TU Delft

Delft University of Technology

Assessing Liquefaction Flow Slides
Beyond Empiricism

de Jager, Richard

DOI
10.4233/uuid:51df13ed-6ba0-49ba-99d7-1c14f8fd022e

Publication date
2018

Citation (APA)
de Jager, R. (2018). *Assessing Liquefaction Flow Slides: Beyond Empiricism*. [Dissertation (TU Delft), Delft University of Technology]. https://doi.org/10.4233/uuid:51df13ed-6ba0-49ba-99d7-1c14f8fd022e

Important note
To cite this publication, please use the final published version (if applicable).
Please check the document version above.

Copyright
Other than for strictly personal use, it is not permitted to download, forward or distribute the text or part of it, without the consent of the author(s) and/or copyright holder(s), unless the work is under an open content license such as Creative Commons.

Takedown policy
Please contact us and provide details if you believe this document breaches copyrights.
We will remove access to the work immediately and investigate your claim.

This work is downloaded from Delft University of Technology.
For technical reasons the number of authors shown on this cover page is limited to a maximum of 10.

Assessing Liquefaction Flow Slides

Beyond Empiricism

Assessing Liquefaction Flow Slides

Beyond Empiricism

Proefschrift

ter verkrijging van de graad van doctor
aan de Technische Universiteit Delft,
op gezag van de Rector Magnificus prof. dr. ir. T. H. J. J. van der Hagen,
voorzitter van het College voor Promoties,
in het openbaar te verdedigen op maandag 18 juni om 12:30 uur

door

Richard Ruben DE JAGER

civiel ingenieur, Technische Universiteit Delft, Nederland
geboren te Sassenheim, Nederland.

Dit proefschrift is goedgekeurd door de promotor:

Prof. dr. M. A. Hicks

Copromotor: Dr. ir. R. B. J. Brinkgreve

Samenstelling promotiecommissie:

Rector Magnificus,	voorzitter
Prof. dr. M. A. Hicks,	Technische Universiteit Delft, promotor
Dr. ir. R. B. J. Brinkgreve,	Technische Universiteit Delft, copromotor

Onafhankelijke leden:

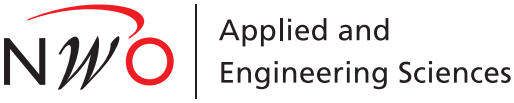
Dr. E.T. Bowman	University of Sheffield
Prof. dr. C. Jommi	Technische Universiteit Delft
Dr. F. Nadim	Norwegian Geotechnical Institute (NGI)
Prof. dr. W. S. J. Uijttewaal	Technische Universiteit Delft

Overig lid:

Prof. dr. ir. F. Molenkamp,	Technische Universiteit Delft

Prof. dr. ir. F. Molenkamp heeft als begeleider in belangrijke mate aan de totstandkoming van het proefschrift bijgedragen.







Keywords: Liquefaction; Flow Slides; Conservation Equations; Finite Element Method; Scale Model Test

Printed by: Ridderprint B.V.

Front & Back: Wendy Ellens (layout), Sam Rentmeester (photograph)

Copyright © 2018 by R. R. de Jager

978-94-6375-013-4

An electronic version of this dissertation is available at
`http://repository.tudelft.nl/`.

I do not wish to convey the impression that I deny the value of experience in foundation engineering in general. But I do wish to differentiate between experience which has proven its merits (...), and such empirical methods which create a conscious or unconscious feeling of uncertainty, perhaps even a suspicion that one's design is, after all, not far from guesswork.

Arthur Casagrande

Conventions

Sign convention

The sign convention from continuum mechanics will be applied with tension and dilation being positive, and compression and contraction being negative. However, for particular cases this convention will be violated. For the sake of visualisation compression is assumed to be positive in plots, illustrating e.g. test results. Furthermore, the sign convention is ignored when defining the principal stresses by numbering the principal stresses based on their absolute magnitude, that is, $|\sigma_1| > |\sigma_2| > |\sigma_3|$.

Notation

This thesis uses both index notation and tensor notation. Index notation is based on the Einstein summation convention, which abbreviates notation by implying summation over indexed terms that appear twice in the same expressions. For instance, matrix multiplication can be expressed by:

$$C_{ij} = A_{ik}B_{kj} = \sum_{k=1}^{N} A_{ik}B_{kj} \tag{1}$$

Index notation is used for the sake of elaboration and implementation. In other cases tensor notation will be used, which suits the frequent use of tensorial quantities in this thesis. Equation 1 reads in tensor notation:

$$\boldsymbol{C} = \boldsymbol{A} \cdot \boldsymbol{B} \tag{2}$$

Frame of reference

This thesis employs a Lagrangian description of physical processes, because it suits the history dependent behaviour of soils. The material time derivative of an arbitrary quantity $\boldsymbol{\psi}$ is expressed by $\dot{\boldsymbol{\psi}}$, which is defined by:

$$\dot{\boldsymbol{\psi}} = \frac{\partial \boldsymbol{\psi}}{\partial t} + \boldsymbol{v}\frac{\partial \boldsymbol{\psi}}{\partial x} \tag{3}$$

Herein, $\boldsymbol{v}$ defines the velocity of the material point.

Subscripts and superscripts

The use of subscripts in variables is reserved for indices, provided that a symbol is only used once. Specifications of variables, such as the concerning constituent or node, are therefore expressed in superscripts. Exceptions are made when symbols are used twice and there can be no unambiguity with the use of indices. For instance, the imposed dilation ratio is expressed by D^i, the relative density based on void ratio by D_e. Furthermore, the use of nodal variable requires the use of both subscripts and superscripts for indices.

Unit tensor

The unit tensor $\boldsymbol{I}$ is a diagonal tensor with value 1 at the diagonal. The unit tensor satisfies the following relationship with, for instance, second-order tensor $\boldsymbol{A}$:

$$\boldsymbol{A} : \boldsymbol{I} = \boldsymbol{I} : \boldsymbol{A} = \boldsymbol{A} \tag{4}$$

Its counterpart in index notation is the Kronecker Delta δ_{ij} or δ^{ij}, which is defined by:

$$\delta_{ij} \text{ or } \delta^{ij} = \begin{matrix} 0 & \text{for } i \neq j \\ 1 & \text{for } i = j \end{matrix} \tag{5}$$

Contents

1 Introduction **1**
- 1.1 Liquefaction flow slides in practice . . . 1
- 1.2 Problem description . . . 3
- 1.3 Research questions . . . 5
- 1.4 Research methodology and contributions . . . 5
- 1.5 Outline . . . 6
- References . . . 7

2 Flow liquefaction and flow slides **11**
- 2.1 A critical review of case histories . . . 11
  - 2.1.1 Pre-failure conditions: geometry . . . 12
  - 2.1.2 Pre-failure conditions: soil properties . . . 13
  - 2.1.3 Triggering of flow liquefaction . . . 14
  - 2.1.4 Development of liquefaction flow slides . . . 15
  - 2.1.5 Post-liquefaction characteristics . . . 15
  - 2.1.6 Flow slides in dense sands and clays . . . 15
  - 2.1.7 Concluding remarks on case histories . . . 18
- 2.2 Scale model testing . . . 19
  - 2.2.1 Model testing in Delft . . . 20
  - 2.2.2 The CANadian Liquefaction EXperiment . . . 25
  - 2.2.3 Concluding remarks on scale model testing . . . 27
- 2.3 Element testing . . . 28
  - 2.3.1 Flow liquefaction and instability . . . 28
  - 2.3.2 Deposition, reconstitution and fabric . . . 33
  - 2.3.3 Stress path, control and drainage . . . 41
  - 2.3.4 Void ratio redistribution . . . 49
  - 2.3.5 Concluding remarks on element testing . . . 53
- 2.4 Assessment of liquefaction flow slides . . . 54
  - 2.4.1 Hypotheses on the initiation of flow slides . . . 54
  - 2.4.2 Methods of assessment . . . 59
- References . . . 62

3 Governing equations of saturated porous media **73**
- 3.1 Starting points and assumptions . . . 73
  - 3.1.1 Introduction . . . 73
  - 3.1.2 Range of applicability . . . 74
  - 3.1.3 Literature review . . . 76

3.2 Governing equations for flow liquefaction . . . 77
3.2.1 Introduction . . . 77
3.2.2 Methodology . . . 77
3.2.3 Stress measures for saturated porous media . . . 80
3.2.4 Interaction . . . 82
3.2.5 Mass equations . . . 89
3.2.6 Momentum equations . . . 90
3.2.7 Alternative derivation of momentum equations . . . 91
3.3 Approximations for liquefaction flow slides . . . 93
3.3.1 Governing set of equations . . . 93
3.3.2 Boundary conditions . . . 94
3.3.3 Hydrostatics . . . 95
3.3.4 Triggering . . . 95
3.3.5 Instability . . . 96
3.3.6 Consolidation . . . 97
3.3.7 Slope failure . . . 98
3.4 Concluding remarks . . . 98
References . . . 99

4 Beyond liquefaction: consistency of framework and limitations 103
4.1 Conservation of energy . . . 103
4.1.1 General . . . 103
4.1.2 Interaction . . . 105
4.1.3 Resulting equations of the conservation of energy . . . 106
4.2 Non-negative entropy production . . . 106
4.2.1 General . . . 106
4.2.2 Interaction . . . 108
4.2.3 Resulting equations . . . 108
4.2.4 Conditions defined by non-negative entropy production . . . 109
4.3 Stress measures for unsaturated soils . . . 115
4.3.1 Introduction . . . 115
4.3.2 Review of stress measures . . . 116
4.3.3 Microstructure, stress and deformation of packing of spheres . . . 118
4.3.4 Suction-induced interparticle forces . . . 123
4.3.5 Capillary-suction-induced intergranular stress . . . 124
4.3.6 Relations between capillary-suction-induced quantities . . . 128
4.3.7 Stress measures for unsaturated granular materials . . . 130
4.3.8 Potential approach for progress toward applications . . . 133
4.3.9 Evaluation of capabilities and limitations of proposed formulation . . . 135
4.4 Stress measures for interparticle sliding and rotation . . . 136
4.4.1 Introduction . . . 136
4.4.2 Momentum equations at the particle scale . . . 137
4.4.3 Definition of the intergranular stress . . . 139
4.4.4 Characteristics of the intergranular stress tensor . . . 140
4.4.5 Example of micro-scale based stresses . . . 141
4.4.6 Conclusions . . . 143

References . . . 144

5 Finite element modelling 149
5.1 Starting points and assumptions . . . 149
5.1.1 Model requirements . . . 149
5.1.2 Literature review . . . 151
5.1.3 General methodology . . . 152
5.2 Composition of stiffness matrix . . . 157
5.2.1 Starting equations . . . 157
5.2.2 Formulation of residuals . . . 158
5.2.3 Newton-Raphson procedure . . . 163
5.2.4 Time discretisation . . . 165
5.2.5 Resulting stiffness matrix . . . 168
5.3 Implementation . . . 169
5.4 Evaluation of model performance . . . 170
5.4.1 General . . . 170
5.4.2 One-dimensional consolidation . . . 170
5.4.3 Conditions for dynamics . . . 187
5.5 Towards modelling of static liquefaction of saturated loose sand . . . 189
5.5.1 Introduction . . . 189
5.5.2 Formulation of model . . . 190
5.5.3 Application of the formulation . . . 193
5.5.4 Demonstration of model capabilities . . . 198
5.6 Closing remarks . . . 200
References . . . 202

6 Development of the liquefaction tank 207
6.1 Objectives and requirements . . . 207
6.2 Design of the liquefaction tank . . . 209
6.2.1 General . . . 209
6.2.2 Structure . . . 212
6.2.3 Fluidisation system . . . 216
6.2.4 Filtering of water . . . 224
6.2.5 Sand . . . 225
6.2.6 Dredging system . . . 226
6.2.7 Triggering systems . . . 229
6.2.8 Instrumentation and data acquisition . . . 231
6.3 Novel sample preparation procedures for triaxial apparatus . . . 238
6.3.1 General . . . 238
6.3.2 Testing procedures . . . 238
6.3.3 Preparation by fluidisation-sedimentation-sand suction . . . 240
6.3.4 Preparation using 1D compression . . . 246
6.3.5 Discussion . . . 248
6.4 Concluding remarks . . . 249
References . . . 250

7 Fluidisation testing **253**
7.1 Response of the sand bed: theory . . . 253
7.1.1 General . . . 253
7.1.2 Theory of fluidisation . . . 254
7.1.3 Aniticipated response sand bed during fluidisation . . . 261
7.2 Preliminary fluidisation tests . . . 268
7.2.1 General . . . 268
7.2.2 Description experiments . . . 269
7.2.3 Results from fluidisation tests in minitank . . . 271
7.2.4 Results from fluidisation tests in permeameter . . . 272
7.3 Measuring the global density of the sand bed . . . 275
7.3.1 General . . . 275
7.3.2 Measurement of soil mass in liquefaction tank . . . 276
7.3.3 Measurement of soil volume in liquefaction . . . 280
7.3.4 Error analysis of global density . . . 280
7.4 Results of fluidisation tests in liquefaction tank . . . 282
7.4.1 General . . . 282
7.4.2 Reference measurements . . . 282
7.4.3 Uniformity of fluidisation pressure . . . 286
7.4.4 Response of sand bed during fluidisation . . . 292
References . . . 298

8 Tilting testing of the liquefaction tank **301**
8.1 Testing programme . . . 301
8.1.1 General . . . 301
8.1.2 Global density . . . 302
8.1.3 Instrumentation and data acquisition . . . 302
8.1.4 Testing procedure . . . 303
8.1.5 Overview of tilting tests . . . 306
8.2 Processing of measurement data . . . 307
8.2.1 General . . . 307
8.2.2 Established density after fluidisation . . . 308
8.2.3 Determination of excess pore water pressures . . . 310
8.2.4 Effect of applied filter . . . 312
8.2.5 Error analysis . . . 313
8.3 Test results . . . 315
8.3.1 General . . . 315
8.3.2 Generic description of response . . . 315
8.3.3 Effect of density . . . 326
8.3.4 Effect of ageing . . . 330
8.3.5 Effect of loading and pre-loading conditions . . . 332
8.3.6 Induced vibrations during tilting . . . 336
8.3.7 Induced water waves during flow slides . . . 337
8.3.8 Concluding remarks for tilting tests . . . 341

8.4 Interpretation and discussion . . . 342
8.4.1 Types of response . . . 342
8.4.2 Triggering of flow liquefaction . . . 345
8.4.3 Factors influencing the response . . . 347
8.4.4 Implications for the assessment of flow liquefaction . . . 348
References . . . 350

9 Conclusions **353**
9.1 Overview of findings . . . 353
9.2 Improving the assessment of liquefaction flow slides . . . 358
9.3 Further implications for engineering practice . . . 359
9.4 Recommendations . . . 361
9.4.1 Research . . . 361
9.4.2 Engineering practice . . . 364

Summary **365**

Samenvatting **371**

Dankwoord **377**

Curriculum Vitæ **379**

List of Publications **381**

List of symbols

Introduction

Density

e,n	void ratio, porosity
D_e,D_n	relative density (void ratio, porosity)
V^p,V^s,V^t	volume pores, particles, bulk
e^{cs},Ψ	void ratio at critical state, state parameter

Testing

D^{50},FC	median grain size, fines content
ϕ	friction angle
x,y,z,t	length, width, height, time
s	sand production rate
N_1	SPT blow count rate

Stresses and strains

$\delta_{ij},\boldsymbol{I}$	kronecker delta, unit tensor
σ'_{ij},τ_{ij}	components effective stress, shear stress
σ'_a,σ'_r	axial, radial effective stress
$\boldsymbol{\sigma}'_1,\boldsymbol{\sigma}'_2,\boldsymbol{\sigma}'_3$	principal effective stresses
p',q	isotropic effective stress, deviatoric stress
K^0,b	neutral earth pressure coefficient, intermediate stress parameter
α,θ	rotation axial stress, imposed stress state
$\epsilon_{ij},\gamma_{ij}$	components strain, shear strain
ϵ_a,ϵ_r	axial, radial strain
$\boldsymbol{\epsilon}_1,\boldsymbol{\epsilon}_2,\boldsymbol{\epsilon}_3$	principal strains
ϵ_p,ϵ_q	isotropic, deviatoric strain
ϵ^{vol},D^i,D^s	volumetric strain; imposed, natural dilation ratio
u	pore pressure

Stability assessment

α,SF	angle infinite slope, safety factor
γ,γ^w	volumetric weight saturated bulk, water
$q_{c1Ncs\text{-}Sr},S_r$	normalised cone resistance, liquefied strength

Theory

Governing equations

M, F	generic expression of mass, linear momentum
m,f	external supply mass, momentum
$\boldsymbol{t}$,$\boldsymbol{b}$	surface traction, body load
$\boldsymbol{X}$,$\boldsymbol{X}^s$,$\boldsymbol{X}^{pf}$	material coordinates bulk, soil skeleton, pore fluid in initial reference state
V,V^s,V^{pf}	volume bulk, soil skeleton, pore fluid in initial reference state
S,S^s,S^{pf}	surface bulk, soil skeleton, pore fluid in initial reference state
$\boldsymbol{x}$,$\boldsymbol{x}^s$,$\boldsymbol{x}^{pf}$	material coordinates bulk, soil skeleton, pore fluid in current state
v,v^s,v^{pf}	volume bulk, soil skeleton, pore fluid in current state
s,s^s,s^{pf}	surface bulk, soil skeleton, pore fluid in current state
t,t^0	time current state, initial reference state
$\boldsymbol{F}$,$\boldsymbol{L}$	deformation gradient, velocity gradient
$\boldsymbol{u}$,$\boldsymbol{u}^s$	displacement general, soil skeleton
$\dot{\boldsymbol{u}}$,$\dot{\boldsymbol{u}}^s$,$\boldsymbol{v}^{pf}$	velocity general, soil skeleton, pore fluid
$\ddot{\boldsymbol{u}}$,$\ddot{\boldsymbol{u}}^s$,$\dot{\boldsymbol{v}}^{pf}$	acceleration general, soil skeleton, pore fluid
$\boldsymbol{v}^{pf\text{-}s}$,$\dot{\boldsymbol{v}}^{pf\text{-}s}$	relative pore fluid velocity, acceleration
e,n	void ratio, porosity
V^p,V^s,V^t	volume pores, particles, bulk
ρ^g,ρ^f	intrinsic volumetric mass soil particles, fluid
ρ,ρ^s,ρ^{pf}	volumetric mass bulk, soil skeleton, pore fluid
$\dot{\rho}^g$,$\dot{\rho}^f$	material time rate of intrinsic volumetric mass soil particles, pore fluid
$\dot{\rho}$,$\dot{\rho}^s$,$\dot{\rho}^{pf}$	material time rate volumetric mass bulk, soil skeleton, pore fluid
ρ^{buoy}	buoyant volumetric mass soil skeleton
ω,ω^{crit}	frequency, critical frequency Poisseulle flow
$\boldsymbol{v}^{pf\text{-}s;crit}$	critical relative pore fluid velocity Poisseulle flow
D^g,r	grain size diameter, pore radius
η,R_e	shear viscosity pore fluid, Reynold's number

Stresses and strains

δ_{ij},$\boldsymbol{I}$	kronecker delta, unit tensor
$\boldsymbol{\sigma}$,$\boldsymbol{p}$	Cauchy stress tensor, pore fluid stress tensor
V^A	total averaging volume
$V^{A;s}$,$V^{A;pf}$	averaging volume soil skeleton, pore fluid
$\boldsymbol{\sigma}^g$,$\boldsymbol{\sigma}^f$	local stress tensor particles, fluid in averaging volume
$\boldsymbol{\sigma}^s$,$\boldsymbol{\sigma}^{pf}$	intrinsic, averaged stress tensor soil skeleton, pore fluid
$\boldsymbol{\sigma}^*$,$\boldsymbol{\sigma}'$,p	intergranular and effective stress tensor, pore fluid stress
$\dot{\boldsymbol{\sigma}}^J$,$\boldsymbol{w}$	Jaumann stress rate tensor, spin tensor
$\dot{\boldsymbol{\sigma}}'$,$\dot{p}$	rate of effective stresses tensor, pore fluid stresses
$\dot{\boldsymbol{\sigma}}^{*J}$,$\dot{\boldsymbol{\sigma}}'^J$	Jaumann intergranular, effective stress rate tensor
$\boldsymbol{\epsilon}^s$,$\boldsymbol{\epsilon}^{pf}$	strains of soil skeleton, pore fluid
$\dot{\boldsymbol{\epsilon}}^s$,$\dot{\boldsymbol{\epsilon}}^{pf}$	rate of strains of soil skeleton, pore fluid
$\dot{\boldsymbol{\epsilon}}^{g;vol}$,$\dot{\boldsymbol{\epsilon}}^{f;vol}$	rate of volumetric strains of soil particles, fluid

$\dot{\boldsymbol{\epsilon}}^{s;vol}$,$\dot{\boldsymbol{\epsilon}}^{pf;vol}$	rate of total volumetric strains of soil skeleton, pore fluid
$\boldsymbol{\epsilon}^{e}$,$\boldsymbol{\epsilon}^{p}$	elastic, plastic part of strain
$\dot{\boldsymbol{\epsilon}}^{e}$,$\dot{\boldsymbol{\epsilon}}^{p}$	material rate of elastic, plastic part of strain
$\boldsymbol{D}$	tangent stiffness tensor
K^{pf},K^{sf}	isotropic stiffness pore fluid, soil skeleton due to channge of pore pressure
C,C^{sf}	generic compressibility, isotropic compressibility soil skeleton
G^{sf}	average shear modulus of particles

Momentum interaction

$\boldsymbol{R}^{pf\text{-}s}$,$\boldsymbol{R}^{pf\text{-}s}$	linear momentum interaction tensor between pore fluid and soil skeleton
$\boldsymbol{R}^{pf\text{-}s;0}$	interaction term for hydrostatics
$\boldsymbol{R}^{pf\text{-}s;\boldsymbol{v}^{pf\text{-}s}}$	interaction term for relative pore fluid flow
$\boldsymbol{R}^{pf\text{-}s;\dot{\boldsymbol{v}}^{pf\text{-}s}}$	interaction term for relative pore fluid acceleration
$S^{A;fs}$,$\mathbf{n}^{fs}$	Boundary between soil skeleton and pore fluid, corresponding normal
$\boldsymbol{g}$	gravitation vector
$\boldsymbol{w}^{pf\text{-}s}$	specific discharge or pore fluid flux
$\boldsymbol{\kappa}$,μ	intrinsic permeability tensor, dynamic viscosity
$\boldsymbol{\sigma}^{f,I}$,$\boldsymbol{\sigma}^{f,D}$	isotropic, deviatoric part of local stress tensor of pore fluid
$K^{pf\text{-}s}$	kinetic energy associated with relative pore fluid velocity
a, K^{tort}	tortuosity factor, kinetic energy transfer due to tortuosity
$\tilde{\boldsymbol{R}}^{pf\text{-}s}$	stress interaction tensor

Approximations for flow slides

$\boldsymbol{Q}$,$\dot{\boldsymbol{Q}}$	rotation matrix, material time rate of rotation matrix
θ	tilting angle with respect to the horizontal
k,ω	permeability soil, frequency loading
K^{s}	volumetric stiffness of soil skeleton as a result of effective stress change
c_x^{und}	wave velocity one-dimensional undrained wave
c_x^{cons}	one-dimensional consolidation coefficient
E^{oed}	oedometric stiffness

Thermodynamics

E,Γ	energy, entropy production rate density
e^{ext}	external energy supply per unit time
$e^{ext;m}$,$e^{ext;q}$	mechanical, thermal contribution external energy supply per unit time
E^{spec},$\dot{E}^{spec}$	specific energy, material rate of specific energy
e,K	specific internal energy, specific kinetic energy
$\dot{e}$,$\dot{K}$	material rate of specific internal energy, specific kinetic energy
e^{str},$\dot{e}^{str}$	internal strain energy, material rate of internal strain energy
e^{pf},e^{s}	specific internal energy pore fluid, soil skeleton
$\dot{e}^{pf}$,$\dot{e}^{s}$	material rate of specific internal energy pore fluid, soil skeleton
c,T	specific heat, temperature
T^{s},T^{pf}	temperature soil skeleton, pore fluid

$\dot{T}, \dot{T}^s, \dot{T}^{pf}$	material rate of temperature general, soil skeleton, pore fluid
$h, \boldsymbol{q}$	specific thermal energy supply by radiation, heat flux
h^{pf}, h^s	specific thermal energy by radiation supplied to pore fluid, soil skeleton
$\boldsymbol{q}^{pf}, \boldsymbol{q}^s$	specific thermal energy by heat flux from pore fluid, soil skeleton
$E^{pf\text{-}s}, E^{s\text{-}pf}$	energy interaction between pore fluid and soil skeleton
$E^{pf\text{-}s;m}$	mechanical part of energy interaction
$E^{pf\text{-}s;q}$	thermal part of energy interaction
η, γ	entropy density, entropy production rate density
γ^{pf}, γ^s	entropy production rate density pore fluid, soil skeleton
$\beta, \boldsymbol{r}$	supply of specific entropy through volume, surface
$\mathscr{D}$	dissipation density
$\mathscr{D}_m, \mathscr{D}_q$	mechanical, thermal dissipation density
$G^{pf\text{-}s}, G^{s\text{-}pf}$	exchange of entropy production between pore fluid and soil skeleton
$\psi, \dot{\psi}$	Helmholtz free energy, material rate of Helmholtz free energy
ψ^{pf}, ψ^s	Helmholtz free energy of soil skeleton, pore fluid
$\dot{\psi}^{pf}, \dot{\psi}^s$	material rate of Helmholtz free energy of soil skeleton, pore fluid
$\hat{\psi}, \hat{\eta}$	constitutive relation of Helmholtz free energy, specific entropy
$\hat{\boldsymbol{\sigma}}, \hat{\boldsymbol{q}}$	constitutive relation of stress, outflow of heat
$\boldsymbol{K}$	thermal conductivity tensor

Unsaturated soil mechanics

P, A	force, average area at intergranular contact
σ'_i, a	normal intergranular stress, contact fraction at intergranular contact
σ'_c	part of normal intergranular stress controlling volume change
p^w, p^g	pore water pressure in the liquid, gas phase
χ	fraction matric suction
$S^w, \dot{S}^w$	degree of saturation of liquid phase, corresponding material rate
S_r^e	degree of saturation of liquid phase in macropores
S_r^m	microstructural threshold of macropore degree of saturation
$R^k, \boldsymbol{f}^k$	radius, force vector at interparticle contact k
$\boldsymbol{n}^k, \boldsymbol{m}^k$	unit normal, tangential vector at interparticle contact k
$\boldsymbol{N}^k, \boldsymbol{T}^k$	normal, tangential component vector at interparticle contact k
$\boldsymbol{A}$	fabric tensor
$\boldsymbol{A}^{iso}, \boldsymbol{A}^{dev}$	isotropic part, deviatoric part of fabric tensor
A_a, A_r	axial, radial component fabric tensor
C, V	number of direct contacts, volume of packing
$\boldsymbol{\sigma}^N, \boldsymbol{\sigma}^T$	intergranular stress tensor due to normal, tangential contact forces
$\boldsymbol{\sigma}^A, \hat{\sigma}$	fabric stress tensor, volume-averaged scalar of normal interparticle force
σ, θ	surface tension, contact angle intersection curve
s, S	surface roughness, dimensionless surface roughness
ψ, ψ^x	general capillary matric suction, specified for unsaturated phase x
$\boldsymbol{F}, \boldsymbol{\Psi}$	dimensionless interparticle force vector, capillary matric suction
p^x, p^b	generalised pore air stress, background pore air stress
$\boldsymbol{\psi}^*$	macroscale, capillary-suction-induced intergranular stress tensor

ψ_p^*, ψ_q^*	isotropic, deviatoric component of $\boldsymbol{\psi}^*$
ψ_a^*, ψ_r^*	axial, radial component of $\boldsymbol{\psi}^*$
$\hat{\chi}$	relative magnitude of deviatoric part of $\boldsymbol{\psi}^*$
$\boldsymbol{X}$	intergranular capillary suction structure tensor
$\hat{\boldsymbol{\sigma}}^*$	intergranular stress tensor due to boundary tractions
$\boldsymbol{n}$	normal outward unit vector of the boundary
$\boldsymbol{\tau}, \boldsymbol{\tau}^*, \tilde{\boldsymbol{p}}$	boundary traction due to total, intergranular, pore fluid stress
$\tilde{\boldsymbol{\psi}}^*$	boundary traction due to capillary-suction-induced intergranular stress
$\boldsymbol{D}^{e;sf}$	tangent, elastic flexibility matrix
$\dot{p}^x, \dot{\boldsymbol{\psi}}^*$	material rate pore air stress, capillary-suction-induced intergranular stress
$\dot{\boldsymbol{p}}^J, \dot{\boldsymbol{\psi}}^{*J}$	Jaumann rate of pore fluid stress
$\dot{\boldsymbol{\psi}}^{*J}$	Jaumann rate of capillary-suction-induced intergranular stress

Interparcle sliding and rotation

P, c	number of particles, contact points per particle
V, S	volume, surface bounding assembly of particles
V^P, S^P	volume, surface of individual particle
f_j^{Pc}, x_i^{Pc}	contact forces, coordinates at contact points particles
F_j^{β}, β	external forces, external contact points
x_i, X_i	coordinates, coordinates of center of mass of particle
r_i, r_i^{Pc}	relative location vector, relative location vector of action points
$w_i^P, \dot{w}_i^P$	axial spin vector of particle, its material rate
$v_i, \dot{v}_i$	velocity, acceleration vector of material point
$v_i^P, \dot{v}_i^P$	velocity, acceleration vector of centre of mass of particle
G_j^P, A_j^P	total body force, acceleration
R_{jk}^P, J_{jk}^P	rotation tensor, moment of inertia tensor
$\bar{\sigma}_{ij}^*, \sigma_{ij}^*$	intergranular stress at macroscale, microscale
t_j^*	microscale intergranular traction
$\boldsymbol{\sigma}^{rf}, \boldsymbol{\sigma}^{rot}$	macroscale stress tensor taking account of interparticle forces, rotation
α, h, d^P	slope angle, thickness layer of granular material, particle diameter
$\boldsymbol{v}, \dot{\gamma}$	surface velocity, average rate of simple shearing
$\zeta^P, \dot{\zeta}^P$	scalar indicating magnitude of spin of particle, its material rate
b	scalar for amount of interparticle rolling and sliding

Finite Element Method

u_i, p	deformation soil skeleton, pore fluid stress
v_i, w_i	relative pore fluid velocity, flux
$\dot{u}_i, \dot{p}$	velocity soil skeleton, material rate pore fluid stress
$\ddot{u}_i, \dot{v}_i, \dot{w}_i$	acceleration soil skeleton, relative acceleration pore fluid, material rate flux
$\boldsymbol{r}, \hat{\boldsymbol{r}}, \boldsymbol{N}$	free variable, nodal free variable, shape function
$t, \Delta t, n$	time, time step, iteration step
$\hat{u}_i^p, \hat{p}^q$	nodal variable of deformation soil skeleton, pore fluid stress
$\hat{v}_i^r, \hat{\dot{v}}_i^r$	nodal variable of relative pore fluid velocity, acceleration

$\dot{\hat{u}}_i^p, \ddot{\hat{u}}_i^p$	nodal variable of velocity, acceleration soil skeleton
$\dot{\hat{p}}^q$	nodal variable of material rate of pore fluid stress
$\boldsymbol{k}, \boldsymbol{p}$	global stiffness matrix, global load vector
$\overline{\boldsymbol{r}}, \overline{\boldsymbol{p}}$	imposed freedom variables, loads
s^f, s^r	part of boundary at which loads, nodal freedom variables are imposed
$\boldsymbol{R}, \boldsymbol{V}, \boldsymbol{U}$	rotation tensor, left, right stretch tensor between initial and new state
$\boldsymbol{R}^0, \boldsymbol{V}^0, \boldsymbol{U}^0$	rotation tensor, left, right stretch tensor between initial and current state
$\hat{\boldsymbol{R}}, \hat{\boldsymbol{V}}, \hat{\boldsymbol{U}}$	rotation tensor, left, right stretch tensor between current and new state
$\boldsymbol{x}, \boldsymbol{x}^0$	material coordinates in new, current state
$\boldsymbol{\sigma}, \boldsymbol{\sigma}^0$	stress in new, current state
$\mathbf{w}_c, \mathbf{w}_b$	Galerkin weighing factors
$\boldsymbol{f}$	residual vector
θ	Crank-Nicholson integration parameter
A, B, C	auxiliary variables for composition global stiffness matrix
$\lvert\hat{\boldsymbol{F}}\rvert, \lvert\hat{\boldsymbol{G}}\rvert$	update of volume, surface from current to new state
$\boldsymbol{N}^p$	shape function for displacements of soil skeleton
$\overline{\boldsymbol{N}}^q, \tilde{\boldsymbol{N}}^r$	shape function for pore fluid stresses, relative pore fluid velocities
$M^t, \overline{M}^s$	shape function applied for boundary conditions
n_u	number of nodes for displacements of soil skeleton
n_p, n_v	number of nodes for pore fluid stresses, relative pore fluid velocities
δ^{ij}	kronecker delta applied for superscripts (nodes)
f^{s_m}	residual vector for conservation of mass
$f_i^{t_lmpf}$	residual vector for linear momentum of pore fluid
$f_i^{u_lmb}$	residual vector for conservation of linear momentum bulk
s^p, s^w	part of boundary at which pore fluid stresses, fluxes are prescribed
s^u	part of boundary at which displacements of soil skeleton are prescribed
B_{ijk}^p	strain-nodal displacement matrix
$\overline{C}_p^{sw}, \tilde{C}_p^{sx}$	coupling matrix
$\overline{K}^{sw}, K_{kp}^{uv}$	stiffness matrix of pore fluid, soil skeleton
$\overline{M}_{ip}^{tv}, \tilde{M}_{ip}^{tx}$	mass matrix of pore fluid
M_{kp}^{uv}	mass matrix of bulk
C_i^{tw}	coupling matrix
N_i^{tw}, Q_{ip}^{tx}	porosity gradient matrix, hydraulic conductivity matrix
$\boldsymbol{L}, \boldsymbol{M}, \boldsymbol{P}$	internal strain, mass, external work matrix
z, c_z	vertical coordinates, consolidation coefficient in vertical direction
h, z^0	sample thickness in 1D-consolidation problem with drainage at one side
q, p^0, σ_z	load, initial excess pore fluid stress, vertical stress
T, T^r	characteristic consolidation time, ramp loading time
u_z, m_z	settlement of top of sample, 1D-compressibility
$\epsilon_z, u_{z;max}$	vertical strain, maximum settlement at the top of sample
w_z	flux through top of sample
Δx	element size
v_z^{tn}, S^{tb}	relative pore fluid velocity, surface at top boundary

r^{er}, r^{cal}, r^{an}	general expression for error, calculated value, analytical value
c^s, G	shear wave velocity, shear modulus soil skeleton
ω	characteristic frequency

Material modelling

e, e^i	void ratio, initial void ratio
e^{cs}, ψ	void ratio at critical state, state parameters
$\boldsymbol{\sigma}^{(k)}$	principal effective stresses
e^p, v^p	plastic deviatoric, isotropic strain
$\dot{e}^p, \dot{v}^p$	plastic deviatoric, isotropic strain rate
S, T	isotropic, deviatoric effective stress vector in the π-plane
$\boldsymbol{\sigma}_a, \boldsymbol{\sigma}_r$	axial, radial effective stress
$\dot{\epsilon}^p_a, \dot{\epsilon}^p_r$	axial, radial plastic strain rate
p^a	mean atmospheric pressure
$T/S\Big\vert^{p}$	deviatoric stress level at the remoulding surface
$T/S\Big\vert^{cs}$	deviatoric stress level at the critical state
$T/S\Big\vert^{\mu}$	deviatoric stress level at the surface of zero-dilatancy
$e^{cs;0}, C^*, C^p$	fit parameters for critical state curve
M^p, β^p	fit parameters for surface of remoulding resistance
C^μ, ζ^μ	fit parameters for surface of surface of zero-dilatancy
E, E^p	fit parameters for initial-plastic hardening phase
$e^{p;vol}, \alpha$	plastic volumetric strain, stress-dilatancy parameter
ϕ_μ	friction angle at zero-dilatancy
N	weighting power for hardening

Experiments

Fluidisation system

$\boldsymbol{k}$, i^{crit}	permeability tensor, critical hydraulic gradient
C	constant related to specific surface of grains
Q^{fl}, A^{tank}	flow into liquefaction tank, surface area of bottom of liquefaction tank
l, N	length, number of fluidisation tubes
p^{int}, p^{ext}	internal, external pressure of tubes in fluidisation system
$p^{int;0}$	pressure at inlet of fluidisation system
D^{tu}, t^{tu}	internal diameter, wall thickness of fluidisation tubes
D^{ho}, l^{ho}	diameter, mutual distance of holes in fluidisation tubes
A^{tu}, v^{tu}	cross-sectional area, velocity of water in tubes
c, A^{ho}	contraction constant, cross-sectional area holes in tubes
s, B, t	characteristic simplified quantities in mass equation of fluidisation
$\bar{p}^{int}, \bar{t}$	imposed quantities at inlet boundary of fluidisation system
$\hat{t}^P, f^P$	nodal value of characteristic quantity, nodal residual
N^P, M^P	shape function for conservation equations, boundary conditions
η	scalar added for consistency units

$\delta f^P, K^{PQ}$	error, stiffness matrix iteration procedure
Δp^{tu}	pressure gradient along tubes

Filtering of water

LT,FT	liquefaction tank, filter tank
BT1,BT2	buffer tanks in filtering system
P01,P02	pumps in filtering system
F01-F03	filters in filtering system
PV	pneumatic valve in filtering system

Sand, dredging and triggering

D^{60}, D^{10}	particle diameter related to cumulative mass percentile
e^{min}, e^{max}	minimum, maximum void ratio according to standard test
FC	fines content
$\theta, \dot{\theta}$	tilting angle, tilting rate of liquefaction tank

Sensors

MT1-MT12	measurement tapes at sides of liquefaction tank
BP1-BP3	fluid pressure sensors in the bottom of liquefaction tank
FP1,FP2	fluid pressure sensors at NW (front) side of liquefaction tank
RP1,RP2	fluid pressure sensors at SE (rear) side of liquefaction tank
FF,FP	flow meter, pressure sensor at inlet of fluidisation system
DFP	differential pressure sensor at end of fluidisation system
TP1,TP2	total load cells at SE (rear) side of liquefaction tank
AF	accelerometer mounted on frame below liquefaction tank
FS	full scale of sensor

Fluidisation procedure triaxial testing

D^{sa}, h^{sa}	diameter, height of sample in mould
h^{ob}, h^{col}	height of overburden, column in tube
K^{ur}	incremental stiffness for unloading and reloading
M, K	deviatoric stress ratio, principal effective stress ratio
M^{com}, M^{ext}	deviatoric stress ratio for triaxial compression, extension
ϕ^{com}, ϕ^{ext}	friction angle for active, passive failure
$\sigma'^{sed;F}_1$	major principal effective stress at transition point F
$\sigma'^{sed;F}_3$	minor principal effective stress at transition point F
$\sigma'^{suc;F}_1$	major principal effective stress at transition point F after sand suction
$\sigma'^{suc;F}_3$	minor principal effective stress at transition point F after sand suction
z^F, K^{ext}	level of transition point F, deviatoric stress ratio at passive failure
p^b, σ^{lc}_v	back pressure, vertical pressure from the top plate

$\sigma'^{C}_{1},\sigma'^{C}_{3}$	principal effective stresses at control point C
$\sigma'^{rmo}_{1},\sigma'^{rmo}_{3}$	principal effective stresses after removal mould
σ'^{mo}_{3}	minor principal effective stress just before removal mould
σ^{mo}_{3}	horizontal stress provided by mould

Fluidisation testing tank

R_e,G_a	Reynold's number, Galileo number
$\dot{u}^{s}_{z},w^{pf\text{-}s}_{z},v^{pf}_{z}$	vertical velocity soil skeleton, flux, velocity pore fluid
σ^{*}_{z}	vertical intergranular stress in soil column
D^{g}	grain size diameter
$w\|^{t>t_0}_{z=0}$	imposed flux at bottom boundary of soil column
V^{s},V^{t}	volume of soil skeleton, bulk
$C,C^{s;mf}$	soil concentration, soil concentration at incipient fluidisation
$w^{pf\text{-}s;mf}_{z}$	flux at incipient fluidisation
$\dot{u}^{g;\infty}_{z},N$	reference settling velocity of single particle, empirical exponent
v^{prop}_{z}	vertical wave propagation velocity
n^{0},n^{1}	initial, steady-state porosity
h^{0},h^{1}	initial, steady-state height of soil column
S	sedimentation flux
C_0,S_0	initial concentration, particle flux
C_D	bed concentration
C_1,C_2,C_3	characteristic concentrations during sedimentation
S_1,S_2,S_3	characteristic sedimentation fluxes during sedimentation
C^{0},S^{0}	concentration, sedimentation flux at fixed bed
C^{1},S^{1}	steady state concentration, sedimentation flux during fluidisation
$\dot{u}^{fl;top},\dot{u}^{fl;bot}$	propagation velocity of fluidisation front at top, bottom of soil
$\dot{u}^{sed;top}$	propagation velocity of sedimentation front at top of soil
$\dot{u}^{sed;bot}$	propagation velocity of sedimentation front at bottom of soil
t^{1}	time required to reach steady state during fluidisation
C^{M},S^{M}	concentration, sedimentation flux at maximum propagation velocity
C_u	uniformity coefficient
γ^{f}	volumetric weight pore fluid
$w^{pf\text{-}s;0.05}_{z}$	discharge through layer submerged under 5 c m water
$\Delta p_z,\Delta p^{0.05}$	pressure drop, imposed pressure for layer submerged under 5 c m water
Δp^{Q}_{z}	flux dependent pressure drop
$\Delta p^{fl;gr;tank}$	pressure drop over fluidised sand in holes of grid in liquefaction tank
$p^{fl;bed}$	stress resulting from fluidised bed
$h^{gr;tank;corr}$	correction in height of grid for calculation stress fluidised bed

Global density tank

$\rho^{s;dry;tank}$	averaged dry density
$M^{s;dry;tank}$	total dry soil mass
$V^{s;tank}$	total volume of soil mass

$M^{s;tot}$	total delivered soil mass
$M^{s;moi}$	mass of moisture in delivered soil
$M^{s;filt}$	mass of sand used in filter tank
$M^{s;fin}$	mass of fines flushed out of sand bed
$h^{s;tank}$	height of the sand bed
M, x_i	general expression mass, variables in error analysis
$\rho^{s;filt}$	volumetric mass of sand in filter tank
$V^{s;filt}$	volume of sand in filter tank
$M^{s;filt;exc}$	mass of excavated dry sand in sand replacement test
$V^{s;filt;exc}$	volume of excavated dry sand in sand replacement test
$V^{s;filt;mesh}$	volume of sand inside mesh of grid in filter tank
$V^{s;filt;up}$	volume of sand above grid in filter tank
$A^{s;filt}$	cross-sectional area of the filter tank
$n^{gr;filt}$	porosity of grid in filter tank
$h^{gr;filt}$	height of grid in filter tank
h^{up}	height of layer on top of grid in filter tank
$V^{s;gr}$	total volume of cells in grid
$V^{s;gr;cell}$	volume of single cell in grid
N	number of samples in error analysis
$h_i^{up;sub}$	height of sand in subdivided parts in filter tank
$V^{s;fin}$	volume of fines in big-bag
$G^{s;fin;sub}$	measured submerged weight of fines in big-bag
$G^{s;fin;sat}$	measured satured weight of fines in big-bag
l^{tank}, w^{tank}	length, width of floor of tank
$n^{gr;tank}$	porosity of grid in liquefaction tank
$h^{gr;tank}$	height of grid in liquefaction tank
$V^{s;mesh;tank}$	volume of soil in mesh of grid in liquefaction tank
$\rho^{s;dry}$	dry volumetric mass of soil

Tilting tests tank

n^{min}, n^{max}	minimum, maximum porosity according to standard test
θ, x	tilting angle, axis along longitudinal direction of liquefaction tank
$p^{hyd}, p^{hyd;0}$	hydrostatic pore fluid pressure for tilted, non-tilted tank
Δp^{hyd}	incremental, hydrostatic pore fluid stress during tilting
θ^{trig}	tilting angle at the start of pore pressure rise
$p^{exc;max}$	peak excess pore pressure
$\delta n, \delta\theta^{trig}$	error in porosity, tilting angle at start pore pressure rise
$\delta p^{exc;max}$	error in peak excess pore pressure
$\delta\theta^{sys}$	error resulting from accuracy imposed tilting angle
$\delta\theta^{init}$	error resulting from accuracy of reading of moment of triggering
δp^{sens}	error resulting from accuracy pore pressure sensors
δp^{meth}	error resulting from method of deducting excess pore water pressure
δp^{filt}	error introduced by low-pass filter

T^{age},$\dot{\theta}$	ageing period, tilting rate
p^{exc}	excess pore fluid stress
n^{av},δn^{av}	average porosity in the liquefaction tank, corresponding error
n^{low},n^{high}	lowest, highest porosity measured in the tank by measurement tapes
ΔP	general total pressure change measured by total load cells
ΔP^{comp}	slow total pressure change as compensated in total load cells
ΔP^{mem}	fast total pressure change as measured by membrane in total load cells
$H^{1/2;trig}$	characteristic height of wave induced by liquefaction failure
$p^{exc;max}$	maximum excess pore fluid stress measured during tilting tests

1

Introduction

1.1. Liquefaction flow slides in practice

A major part of the soil structures worldwide are constructed in or with sandy soils. People value the favourable properties and low cost of sand in man-made structures, such as in flood defences and land reclamations. Sand has a relatively high permeability, stiffness and strength, varying over a narrow range as compared to fine grained soils. It is amply available at many places in the world, can be dredged easily and transported efficiently with ships and pipelines (Figure 1.1).



Figure 1.1: Land reclamation for the extension of the Port of Rotterdam [1]. 240 Mm^3 of sand was used for the construction of "Maasvlakte 2".

Slopes bridge the difference in level between soil structures and their surroundings. In all cases, steeper slopes will provide a more economical use of the space created by the soil structure. With steeper slopes material can be saved during the construction of flood defences, more capacity can be exploited of reclamation areas and more sand can be dredged from sand mining pits. However, slopes also account for the most vulnerable

and heavily loaded part of soil structures. The slope is by definition the part of the soil structure that lacks confinement. It furthermore defines the interface with the environment. The (protected) slopes of land reclamations commonly provide protection against waves and currents. Without proper protection, scour may lead to steeper slopes and, eventually, failure [2]. The consequences of slope failure can be disastrous, with large damage and high numbers of casualties in some cases [3]. During the design of slopes a comparative assessment should be made between economical benefits on the one side and possible damage and safety risks on the other side. This requires knowledge of the possible failure mechanisms.

The liquefaction flow slide is the main geohazard for subaqeous slopes composed of sand. During a liquefaction flow slide the granular soil instantly transforms from a solid-like to a liquid-like behaving material. The underlying mechanism is flow liquefaction, defined as a significant reduction in strength as a result of excess pore water pressures during shear deformation of the soil. There are a number of reasons why liquefaction flow slides are hazardous:

- Liquefaction flow slides occur unexpectedly; a minor trigger may be sufficient to initiate flow liquefaction and flow slides, even for mild slopes.
- Liquefaction flow slides develop rapidly; there is little time to respond.
- Liquefaction flow slides affect large areas; large volumes of soils are displaced over large distances.



Figure 1.2: Damage by flow slide in Leendert Abraham polder (Noord Beveland), the Netherlands in 1966 (Source: https://beeldbank.rws.nl)

It is no surprise that some of the most destructive failures in the history of geomechanics were liquefaction flow slides. They caused considerable financial damage to dams

[4–8], flood defences [2, 9, 10] (Figure 1.2), cuts [11, 12] and berms [13–15]. The financial losses of the Nerlerk Berm failure were over $100 million [16]. Unfortunately, there are also cases where flow slides resulted in casualties, such as the Railway Bridge failure in Weesp [2](41 casualties), the Fort Peck Dam failure [16] (eight casualties) and the failure at Aberfan [4] (144 casualties). Liquefaction flow slides have been an important research topic in geomechanics for decades [1, 17]. Nonetheless, the usual methods for assesments have a fairly poor basis.

1.2. Problem description

The presumed reliability of sand as a construction material seems to contradict the destructive consequences of liquefaction flow slides. Sand has favourable properties, provided that the pore water does not affect its behaviour. If it does, the range of strengths is stretched enormously as a result of changes in pore pressures. Loose sands become unstable at relatively low mobilised strengths and *liquefy*, leaving small residual strengths. This behaviour, frequently observed in the laboratory, can be typified as brittle or sensitive. It corresponds well with the characteristics of liquefaction flow slides, as listed above.

The initiation of flow liquefaction requires the state of the soil to be loose and conditions to be undrained. While undrained conditions can be imposed in the laboratory, the drainage conditions in the field are essentially drained. The undrained condition is merely a convenient approximation in case the time scale of the generation of excess pore pressures is much smaller than the consolidation period of the soil. The assessment of liquefaction flow slides would ideally require a consideration of both time scales. The time scale of the generation of excess pore pressures depends on the rate of loading, but also on the diffusion of the instability through the geometry (see Figure 1.3). It is thereby linked to the other time scale, the rate of consolidation that mainly depends on the permeability of the soil. The likelihood for liquefaction flow slides will increase with decreasing grain size. The permeability of the soil depends quadratically on the grain size [18], whilst loose and unstable structures are more easily created for smaller grain sizes [19, 20].

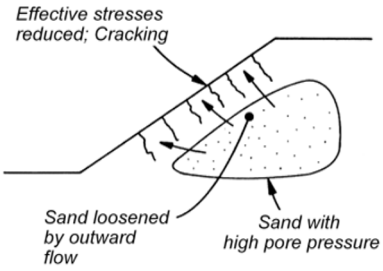


Figure 1.3: Diffusion of instability through geometry after initation [21]

Liquefaction flow slides are in essence fully coupled mechanisms. However, the available methods in engineering practice [11, 22–25] tend to uncouple and simplify the assessment. The lack of advanced models should mainly be attributed to the rather narrow empirical basis. The case histories of liquefaction flow slides provide relatively little information, the reasons being:

- the largest number of liquefaction flow slides happen under water, which complicates observing and monitoring the failure.
- the characteristics of liquefaction flow slides: initated unexpectedly by a minor trigger, followed by a rapidly developing mechanism involving large displacments and volumes.
- ignorance of the soil conditions and properties as a result of:
  - insufficient data from soil investigation.
  - limitations of conventional field methods to measure the in-situ state of the subsoil.
  - disturbance of the soil tested in the laboratory to define its mechanical properties.

Questions have been raised about whether or not liquefaction is the underlying mechanism in particular cases [5, 13]. For a number of flow slides that occurred in the Netherlands in the past, it has been suggested that failure was induced by another mechanism [26]. Unstable breaching seems to leave the same characteristic post-failure geometry, albeit in fine, dense sand [27].

Many of the reported case histories concerned slopes of silty sands, for which recently an alternative view on the initiation of the reported flow liquefaction slides has been suggested [20]. It takes a lot of effort to prepare a sample of clean sand in a liquefiable state in the laboratory, which has raised doubts about the odds of clean sands occurring in this (sensitive) state in nature [20], or about the representativeness of laboratory testing

for field conditions [16]. In one of the few cases in which undisturbed (frozen) samples were tested, only a small proportion of the samples taken from a presumably loose soil mass showed sensitive behaviour during undrained loading [28].

This thesis is an attempt to improve the assessment of liquefaction flow slides in engineering practice. Herein, it will concentrate on the initiation of liquefaction flow slides in a clean, fine sand. The post-failure development of a liquefaction flow slide is beyond the scope of this research. The thesis treats different aspects of liquefaction flow slides, ranging from the fundamentals of saturated porous media to experimental verification by means of scale model testing.

1.3. Research questions

The main research question addressed in this thesis reads:

"How can assessments of liquefaction flow slides be improved?"

The research approach involves answering the key questions:

1. What are the underlying mechanisms of liquefaction flow slides?
2. What are the governing equations for the modelling of liquefaction flow slides?
3. How can the consistency of the framework and its limitations be established?
4. How should the material behaviour and governing equations be implemented in a model?
5. What is required to conduct physical model tests that replicate consistent and reproducible liquefaction flow slides?
6. How does a liquefaction flow slide develop during the physical model tests?
7. What is the role of the trigger during the initiation of liquefaction flow slides?
8. Which aspects govern the triggering of liquefaction flow slides?
9. What are the implications of the physical model tests for the assessment of liquefaction flow slides?

1.4. Research methodology and contributions

The thesis treats a number of separate subjects related to the assessment of liquefaction flow slides. The approach followed is thus not an integral treatment of the subject. An extensive literature review of the observed liquefaction behaviour in the field and the laboratory lays the basis for the subsequent parts. The first subsequent part treats a number of theoretical subjects, while the second part describes the development and results of experiments.

The development of theory aims at answering the first four key questions. A hypothesis is defined with respect to the underlying mechanisms from reported case histories, physical model tests and element tests. Then the underlying mechanisms are formalised by the expression of the governing equations. The gap in the understanding and assessment of liquefaction flow slides is further specified. Furthermore, contributions are made to scientific discussions about the formulation of the governing equations of heterogeneous, saturated, porous media. A recent discussion in literature [29] shows that there are some unresolved issues involving the interaction terms of saturated, porous media. The thesis extends the theory further by considering the consistency of the framework for the conservation of energy and non-negative entropy production. Special attention will be paid to the implication of the formulation of the interaction terms on these fundamental laws. In addition, two novel contributions explore the limits of the stress measures used for porous media and their possible extensions. The Finite Element Method (FEM) [30] is selected for the assessment of liquefaction flow slides. The FEM suits the modelling of boundary value problems with soils; it has a broad basis in soil mechanics with many models being developed and engineers are familiar with the method. However, implementing a fully coupled formulation including statics and dynamics has rarely been done. This thesis will present an initial implementation of the developed framework for saturated porous media. Its performance is evaluated for the simple case of one-dimensional consolidation. Furthermore, a possible extension of the MONOT-model [31] including a critical state formulation is introduced.

The experimental part of the thesis addresses the last five research questions. The experimental verification includes the development of a new, experimental facility: the liquefaction tank. A research facility capable of producing high quality data for the verification of liquefaction flow slides is unique. The thesis addresses the performance of the liquefaction tank in terms of a consistent and reproducible replication of liquefaction flow slides. To this end, in addition to the liquefaction tests, the background, design and preparation of the sand bed are discussed. To the Author's knowledge, this is the first time truly statically triggered liquefaction flow slides have been reproduced at this scale. The results provide a valuable insight into the occurrence and initiation of liquefaction flow slides.

1.5. Outline

The outline of the thesis is presented in Figure 1.4. The thesis starts with the introduction of the research and liquefaction flow slides (Chapters 1 and 2). Chapter 2 also addresses the first research question about the underlying mechanisms of liquefaction flow slides. Chapters 3-5 define the theoretical part of the thesis, involving the formulation of a framework based on the current knowledge of liquefaction flow slides, its consistency and implementation in the finite element method. Research questions 2, 3 and 4 are thus addressed by Chapters 3, 4 and 5 respectively. The experimental part of the research is discussed in Chapters 6-8. As the experimental facility was newly developed during the research, two chapters (5 and 6) are addressed to its design and the preparation of a test (research question 5). Chapter 8 describes the results of the tilting tests, demonstrating the capability of the tank to reproduce liquefaction flow slides. The test series allows the

Author to investigate the triggering of liquefaction flow slides in more detail and thereby answer research questions 6-8. Finally, the thesis concludes with a discussion and conclusions in Chapter 9.

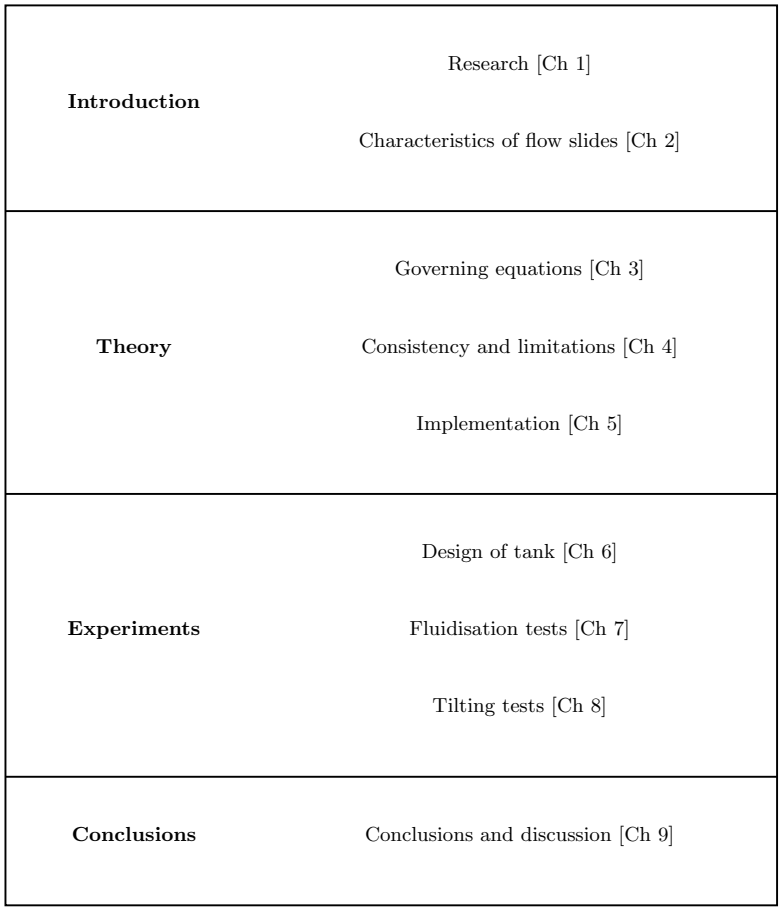


Figure 1.4: Outline of thesis

References

[1] J. van't Hoff and A. Nooy van der Kolff, *Hydraulic Fill Manual: For Dredging and Reclamation Works* (CRC Press, Leiden, the Netherlands, 2012).

[2] A. Koppejan, B. van Wamelen, and L. Weinberg, *Coastal flow slides in the dutch province of zeeland,* in *Proceedings of the 2nd International Conference on Soil Me-*

chanics and Foundation Engineering, Vol. 5 (Rotterdam, the Netherlands, 1948) pp. 89–96.

[3] S. Leroueil, *Natural slopes and cuts: movement and failure mechanisms,* Géotechnique **51**, 197–243 (2001).

[4] A. Bishop, *The stability of tips and spoil heaps,* Quarterly Journal of Engineering Geology and Hydrogeology **6**, 335–376 (1973).

[5] A. Casagrande, *Liquefaction and cyclic deformation of sands, a critical review,* in *5th Pan-American Conference on Soil Mechanics and Foundation Engineering*, Vol. 5 (Buenos Aires, Argentina, 1975) pp. 79–133.

[6] A. Fourie, G. Blight, and G. Papageorgiou, *Static liquefaction as a possible explanation for the merriespruit tailings dam failure,* Canadian Geotechnical Journal **38**, 707–719 (2001).

[7] A. Hazen, *A study of the slip in the calaveras dam,* Engineering News Record **81**, 1158–1164 (1918).

[8] S. Olson, T. Stark, W. Walton, and G. Castro, *1907 static liquefaction flow failure of the north dike of wachusett dam,* Journal of Geotechnical and Geoenvironmental Engineering **126**, 1184–1193 (2000).

[9] A. Andresen and L. Bjerrum, *Slides in subaqueous slopes in loose sand and silt,* Norwegian Geotechnical Institute Publication **081**, 1–9 (1968).

[10] D. Hight, V. Georgiannou, P. Martin, and A. Mundegar, *Flow slides in micaceous sands,* in *Proceedings of the International Symposium on Problematic Soils, IS-TOHOKU* (1999) pp. 945–958.

[11] R. de Jager, F. Mathijssen, F. Molenkamp, and A. Nooy van der Kolff, *Static liquefaction analysis using simplified modified state parameter approach for dredged sludge depot hollandsch diep,* in *Proceedings of the 12th International Conference of the International Association for Computer Methods and Advances in Geomechanics* (2008) pp. 4748–4756.

[12] W. Vlasblom and M. de Groot, *Oeverinstabiliteiten bij Zandwinputten*, Tech. Rep. (CUR commissie C130, 2008).

[13] K. Been, B. Conlin, J. Crooks, S. Fitzpatrick, M. Jefferies, B. Rogers, and S. Shinde, *Back analysis of the nerlerk berm liquefaction slides: Discussion,* Canadian Geotechnical Journal **24**, 170–179 (1987).

[14] M. Hicks and C. Onisiphorou, *Stochastic evaluation of static liquefaction in a predominantly dilative sand fill,* Géotechnique **55**, 123–133 (2005).

[15] J. Sladen, R. D'Hollander, J. Krahn, and D. Mitchell, *Back analysis of the nerlerk berm liquefaction slides,* Canadian Geotechnical Journal **22**, 579–588 (1985).

[16] M. Jefferies and K. Been, *Soil liquefaction: a critical state approach* (Taylor & Francis, 2006).

[17] K. Ishihara, *Liquefaction and flow failure during earthquakes,* Géotechnique **43**, 351–451 (1993).

[18] A. Loudon, *The computation of permeability from simple soil tests,* Géotechnique **3**, 165–183 (1952).

[19] R. Cadle, *Particle size theory and industrial applications, Reinhold Pub* (Reinhold publishing corporation, New York, 1965).

[20] P. Lade and J. Yamamuro, *Evaluation of static liquefaction potential of silty sand slopes,* Canadian Geotechnical Journal **48**, 247–264 (2011).

[21] I. Idriss and R. Boulanger, *Soil liquefaction during earthquakes* (Earthquake engineering research institute, 2008).

[22] J. Chu, S. Leroueil, and W. Leong, *Unstable behaviour of sand and its implication for slope instability,* Canadian Geotechnical Journal **40**, 873–885 (2003).

[23] S. Olson and T. Stark, *Yield strength ratio and liquefaction analysis of slopes and embankments,* Journal of Geotechnical and Geoenvironmental Engineering **129**, 727–737 (2003).

[24] S. J. Poulos, G. Castro, and J. W. France, *Liquefaction evaluation procedure,* Journal of Geotechnical Engineering **111**, 772–792 (1985).

[25] F. Silvis and M. de Groot, *Flow slides in the netherlands: experience and engineering practice,* Canadian Geotechnical Journal **32**, 1086–1092 (1995).

[26] M. de Groot, M. van der Ruyt, D. Mastbergen, and G. van den Ham, *Bresvloeiing in zand,* Geotechniek **Juli**, 34–39 (2009).

[27] J. van Den Berg, A. van Gelder, and D. Mastbergen, *The importance of breaching as a mechanism of subaqueous slope failure in fine sand,* Sedimentology **49**, 81–95 (2002).

[28] P. Robertson, C. Wride, B. List, U. Atukorala, K. Biggar, P. Byrne, R. Campanella, D. Cathro, D. Chan, K. Czajewski, *et al.*, *The canlex project: summary and conclusions,* Canadian geotechnical journal **37**, 563–591 (2000).

[29] M. el Tani, D. Kolymbas, and A. Verruijt, *Hydrostatic paradox of saturated media: Discussion,* Géotechnique **58**, 835–837 (2008).

[30] O. Zienkiewicz, R. Taylor, and J. Zhu, *The Finite Element Method–Its Basis and Fundamentals, volume 1* (Elsevier Butterworth-Heinemann, London, 2005).

[31] F. Molenkamp, *Elasto-plastic double hardening model MONOT*, Tech. Rep. CO-218598 (Delft Geotechnics, Delft, the Netherlands, 1981).

2

Flow liquefaction and flow slides

The assessment of liquefaction flow slides starts with identifying the characteristics and underlying mechanisms. There is a large variation in the soil conditions, triggers of flow liquefaction and subsequent development into a failure mechanism of the reported case histories of liquefaction flow slides. The aim is to explain these variations, while further specifying the gaps in knowledge required to improve the assessment of liquefaction flow slides. This chapter presents the status quo with respect to flow liquefaction and liquefaction flow slides. It provides a basis for the next chapter, in which the underlying physics will be expressed in basic equations.

Liquefaction flow slides and flow liquefaction will be discussed for three, decreasing geometrical scales. First, this chapter considers the initial conditions, triggering and subsequent development of failure in reported case histories. Secondly, the results of scale model tests are discussed. The third geometrical scale concerns the smaller, element tests, which provide the basis for constitutive modelling of soils. Hereafter, the main findings will be related to the assessment of liquefaction flow slides in the last section of this chapter.

2.1. A critical review of case histories

It is not intended to give a complete overview of all case histories of liquefaction flow slides in this section. Literature already provides excellent overviews, for instance [1, 2]. Instead, some case histories are used to expound the main characteristics of liquefaction flow slides. In addition, it is of importance to establish what is actually known about liquefaction flow slides.

This section outlines the characteristics of liquefaction flow slides by clustering information from case histories for the successive phases of the mechanism. The initial con-

ditions and geometry, triggering, development and post-liquefaction characteristics of liquefaction flow slides are consecutively dealt with. The final subsection pays attention to breaching, a mechanism that is believed to be confused with flow liquefaction. The outline is restricted to case histories of subaqeous liquefaction flow slides.

2.1.1. Pre-failure conditions: geometry

Liquefaction flow slides have been initiated at slope angles that would certainly have been stable in conventional (drained) analyses [3]. For instance, both the Fort Peck Dam [1] and Nerlerk berm [4] failed at a slope of 1v:4h, whilst the slopes at the Jamuna Bridge Project ranged between 1v:3.5h and 1v:5h [5]. In contrast to the characteristics of these case histories, the range of pre-failure slope angles can be large for liquefaction flow slides. Wilderom [6] collected data from failures of flood defences in the province of Zeeland in the south western part of the Netherlands. He selected and documented the geometrical features of 145 flow slides, a uniquely vast dataset typifying flow slides in a relatively small region. The characteristic average pre-failure slope angle of the Zeeland flow slides varied between 1v:1.5h and 1v:10h. Wilderom also reported the characteristic steepest slope over a height of 5 m, as being between 1v:1h and 1v:6h. The height of the pre-failure slope also varied significantly with channel depths ranging between 12 m and 52 m below Chart Datum (NAP).

It is generally recognised that an unfavourable slope geometry is one of the prerequisites for the occurrence of a flow slide [7]. However, what can actually be concluded from the pre-failure geometry of case histories? Firstly, it should be concluded that although conventional (drained) slope failures were filtered from the dataset of Wilderom, the case histories in Zeeland were not all initiated by liquefaction. The dataset includes both liquefaction flow slides ("zettingsvloeiingen") as well as superficial mechanisms ("zandregens" or "afkalvingsvloeiing"). These mechanisms, that will be discussed in Subsection 2.1.6, result in the same post-failure geometry but are governed by a completely different (hydraulic) mechanism. It is not known which portion of the documented flow slides in Zeeland were initiated by liquefaction. Secondly, the statistical evidence for the influence of geometrical parameters in Zeeland is poor [8]. Silvis [9] carried out a statistical analysis of the dataset of the flow failures. Wilderom considered the steepest slope over 5 m height as a geometrical parameter, which he based on the characteristic survey lines, i.e. those located at the centre of the flow slide. However, in a number of cases the steepest slopes over 5 m height in adjacent survey lines -yet still inside the area of the flow failure- appeared to be steeper. The relation between the steepest slope angle over 5 m height and the occurrence of the flow slides is therefore questionable. Even more surprising is the comparison between survey lines inside and outside the areas of flow failures. Silvis compared the steepest angles of slopes of more than 5 m height, for slopes that eventually failed and those that did not fail for at least five years after surveying. The slopes that did not fail were even a bit steeper than those that did fail. Apparently, the data of pre-failure slope angles are a general representation of the slope angles occurring in Zeeland, rather than an indication for the initiation of flow liquefaction slides.

2.1.2. Pre-failure conditions: soil properties

Case histories indicate that soils tend to be prone to liquefaction when they are (geologically) young, loosely packed, fine-grained and low-plasticity or non-plastic [10, 11]. Flow slides typically occur in (hydraulic) fills (e.g. Nerlerk Berm, Fort Peck Dam) and dynamic river deltas (Zeeland, Jamuna Bridge). In both cases slopes are raised in a short period, either by (human) disposal methods or (natural) sedimentation, and time effects such as creep and ageing are minimised. In Zeeland the high sedimentation rates of up to 0.5 m to 1.0 m per month have been related to the low density of the soil [9]. The Nerlerk Berm failures illustrate the effect of soil properties and disposal method on the susceptibility to liquefaction of a hydraulic fill [12]. None of the five flow slides penetrated into the core, that was constructed with a slightly coarser sand and using a different placement method than the sand placed over the core. Most of the reported flow slides involve fine-grained sands with D^{50} ranging between 120 µm (Zeeland) and 200 µm (Jamuna, Fort Peck Dam) [10]. However, case histories with median grain size diameters up to 1.50 mm have been reported as well [10]. Lade and Yamamuro [11] recently noted that the vast majority of case histories involve silty sands. They argue that fines promote a loose and unstable structure at low stresses of the soil. Hight et al. [13] also came to the conclusion that the unstable structure of micaeous sands played an important role during the flow slides in Jamuna Bridge.

It is recognised that soil properties complement geometry as a prerequisite for the occurrence of liquefaction flow slides. However, how much is actually known and what can be concluded from case histories? There is a broad consensus that the state (or density) and structure of the soil determine whether or not it is prone to liquefaction. However, it is also known that the direct measurement of both properties is too complex and costly for employment in engineering practice. It would require undisturbed sampling, a delicate operation in cohesionless, loosely packed sands. Instead, engineers tend to rely on index tests, such as the Cone Penetration Test (CPT) and Standard Penetration Test (SPT). Robertson [10] reports 36 case histories, 28 of which include CPT or SPT data. However, the data set is not uniform. The (electrical) CPT is better suited for liquefaction assessments, as it is standardised, reproducible and yields a continuous record with depth [2]. Robertson [10] identified merely six case histories from the data set with detailed electrical CPT records available. From these "Class A" case histories, only four actually contain CPT results that were conducted prior to failure.

Index tests need to be supplemented with laboratory element tests to characterise the site specific material behaviour during liquefaction flow slides. However, this would require undisturbed sampling. None of the documented case histories includes laboratory tests on undisturbed samples. The tests that have been conducted on reconstituted samples do not account for the in-situ structure of the sand and therefore serve as index tests as well, rather than representing in-situ material behaviour. This is further enhanced by the custom in engineering practice to limit laboratory testing to triaxial compression. Both structure and stress path are known to have a great influence on the material behaviour during flow liquefaction [13].

2.1.3. Triggering of flow liquefaction

The trigger is considered to be of minor importance for flow liquefaction slides, hence the synonymous term 'spontaneous liquefaction'. Silvis and de Groot [8] did not consider the trigger condition in their analysis of liquefaction potential, as 'there will always be an initiation mechanism'. Indeed, there are cases in which it is not even clear what the actual trigger was [6]. However, in the vast majority of the documented case histories it was known. Olson [2] documented 33 liquefaction flow slides, 23 of which were caused by earthquakes. Other causes included construction related activities (six cases) and tidal effects (two cases).

The flow slides that occurred in Zeeland are believed to have been caused by a combination of steeper slopes as a result of scour and spring tide [14]. Silvis [9] refuted the effect of scour by comparing the development of cross sections in time prior to failure. The survey data did not show a consistent pattern of steeper slopes in time. In fact, there is a case in which the characteristic steepest slope was considerably steeper three years before failure as compared to the last survey. The effect of tide is apparent; out of 148 cases of flow slides which provide information about water levels, 114 (77 %) coincided with extreme water levels with tidal ranges between 3.3 m and 6.2 m. From a few cases it is known that the flow slide occurred during ebb-tide [14], when the seepage pressures are the highest.

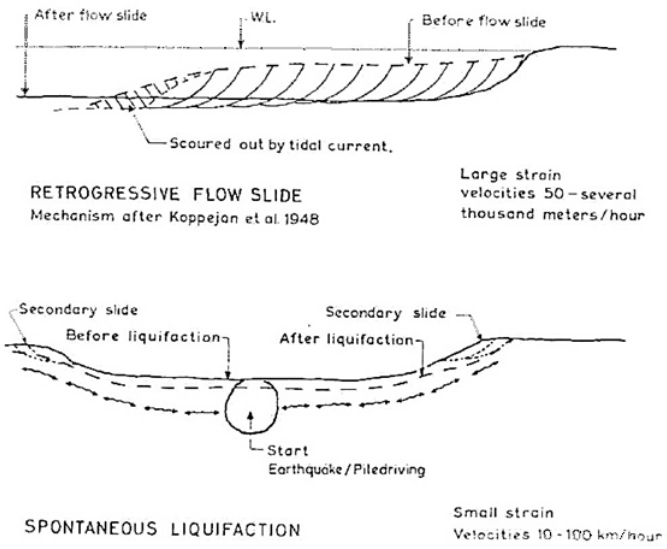


Figure 2.1: Types and rates of liquefaction flow slides [3].

2.1.4. Development of liquefaction flow slides

Liquefaction flow slides propagate at a much faster rate than other failure mechanisms in soils. Using the terminology of Varnes [15], Sladen [16] classified the Nerlerk Berm failures as "very rapid" to "extremely rapid" (from $\mathrm{m\,min^{-1}}$ to $\mathrm{m\,s^{-1}}$). Andresen and Bjerrum [3] distinguished two types of liquefaction flow slides (see Figure 2.1). Retrogressive flow slides consist of a number of shallow failures, moving at a velocity of $50\,\mathrm{m\,h^{-1}}$ to several thousand $\mathrm{m\,h^{-1}}$. The width of the slides often increases as the flow slide retrogresses. Koppejan et al. [14] note that a Zeeland flow slide is a gradual process with soil masses sliding downwards every few minutes.

In general, only when a failure progresses above water can the actual rate be determined. There are only a few cases in which the rate of development of a liquefaction flow slide was recorded under water. These cases [3, 17, 18] are examples of spontaneous liquefaction, moving at velocities of $10\,\mathrm{km\,h^{-1}}$ to $100\,\mathrm{km\,h^{-1}}$ (Figure 2.1). The liquefaction starts at one point and spreads rapidly over vast areas. The breaking of cables and chains on the seabed enabled the rate of a few cases of spontaneous liquefaction to be determined. The liquefaction flow slide in Newfoundland progressed at $20\,\mathrm{km\,h^{-1}}$ to $110\,\mathrm{km\,h^{-1}}$ [18], at Orkdalsfjord at $10\,\mathrm{km\,h^{-1}}$ to $26\,\mathrm{km\,h^{-1}}$, and at Follafjorden at $15\,\mathrm{km\,h^{-1}}$ [17].

2.1.5. Post-liquefaction characteristics

After the liquefaction flow slide has been triggered, the soil mass flows out to form a slope angle as gentle as only a few degrees. Koppejan [14] mentions slope angles of 3° to 4° in the lower part of the post-liquefaction profiles in Zeeland. The upper part consists of much steeper slopes [8], see also Figure 2.1. Wilderom [6] even based his definition of flow slides on the slope of the post-failure profiles. He concluded that profiles with a lower part gentler than 1v:10h had to be flow slides [8], while steeper slopes were classified as conventional slope failures. In the top view in Figure 2.2, liquefaction flow slides typically exhibit a shell shape [3, 19, 20]. Retrogressive flow slides increase in width after being initiated at the toe [3]. Liquefaction flow slides may involve large volumes of displaced soil mass, i.e. in the order of millions of $\mathrm{m^3}$ [3, 14], being displaced over large distances. This observation corresponds with the nature of liquefaction. However, exactly the same characteristics are also observed for a failure mechanism in densely packed sand, as discussed in the next section.

2.1.6. Flow slides in dense sands and clays

The previous sections listed several typical features of liquefaction flow slides extracted from case histories. In a number of these cases [21–23] there have been debates on whether or not liquefaction was the underlying mechanism. It is therefore of interest to establish the distinguishing features of liquefaction flow slides as compared to other, similar failure mechanisms.

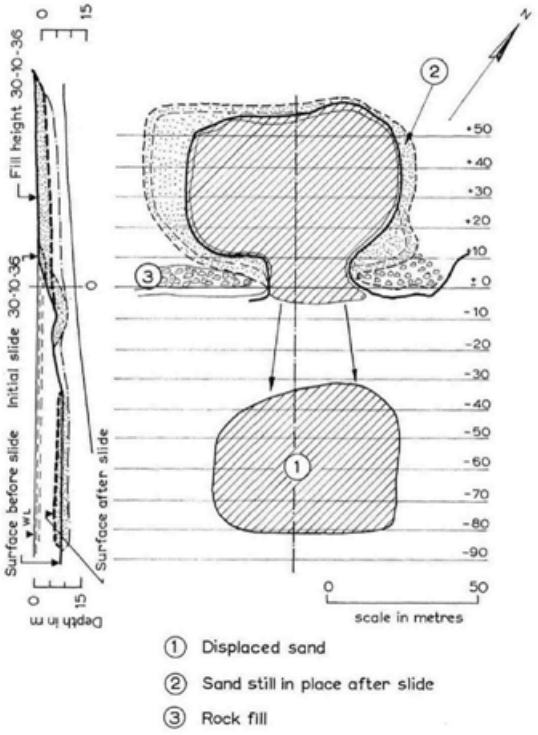


Figure 2.2: Top view of typical shell shape after flow slide in Helsinki Harbor [3].

Breaching is a progressive failure mechanism in densely packed sands (see Figure 2.3). A sufficiently fast, and therefore undrained, development of a locally oversteepened slope or *breach* initiates progressive failure of the sand. Due to suction in the pores of the sand skeleton the slope temporarily remains stable [24]. Consolidation at the surface results in the gradual and retrogressive failure of shallow layers of sand that form a soil-water mixture flowing down the slope. Breaching provides an efficient means of dredging by removing the soil-water mixture after initiation by a moving suction pipe [25]. From a soil mechanics viewpoint, breaching would continue until the angle of repose is restored. However, in dredging practice more gentle slopes have been encountered, which have been attributed to erosion of the slope below the breach [27]. This erosion process may result in an unstable breaching process, provided that the initial breach is sufficiently high and the grain size is sufficiently small. In that particular case, the slope below the breach will become gentler than the existing slope. The consequent increase in height of the breach will enhance erosion and lead to even gentler slopes. The breaching process grows into a large failure mechanism (see Figure 2.3). The post-failure morphology of an unstable breach is typified by a shell shaped failure plane in top view and gentle

slopes in cross section, just like liquefaction flow slides.

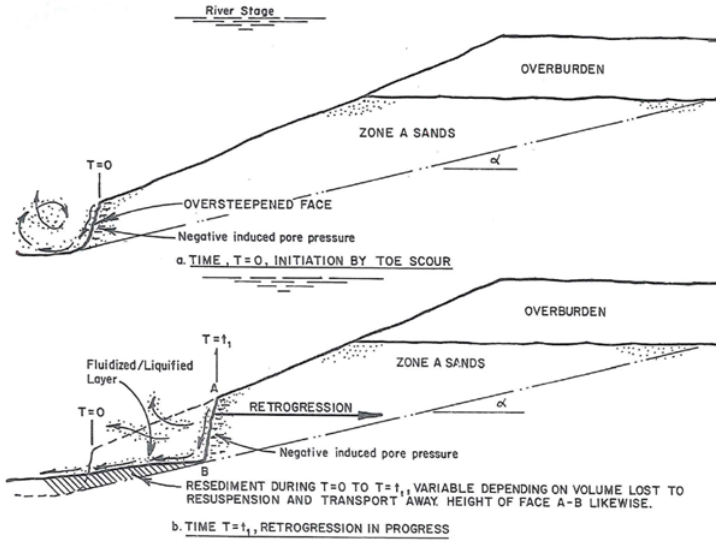


Figure 2.3: Hypothesised failure mechanism in dilative sands of Mississippi River point bars [26].

Recently, the importance of breaching as a failure mechanism in subaqueous slopes has also been raised for natural conditions [28]. Scour or the steep scar left after shear failure or a small liquefaction flow slide may create the conditions necessary for breaching. Breaching is distinguished from liquefaction flow slides by the rate of development, which is governed by the undisturbed permeability k_0 of the sand. For common properties of sand and limited height of the breach the rate of development lies within $20k_0$ to $25k_0$, that is in the order of $\mathrm{mm\,s^{-1}}$ [29]. Unfortunately, it has rarely been possible to determine the rate of development of flow slides. Considering the uncertainties in soil conditions, researchers [27, 28] have argued more and more often that some of the presupposed case histories of liquefaction flow slides may have been cases of breaching. A striking example is the occurrence of flow slides in the Mississippi River point bars [26]. For a long time it had been supposed that liquefaction caused these failures based on the gentle post-failure slopes. However, an extensive field and laboratory testing campaign revealed that it is highly improbable that the subsoil was prone to liquefaction. Furthermore, on a rare occasion the development of a flow slide was observed to last for 12 hours. It was therefore concluded that scour initiated progressive failure in dense sand, which possibly undermined the overlaying cohesive overburden layer (see Figure 2.3). It should be noted that the current state of knowledge does not allow accurate predictions of breaching as a failure mechanism. Physical model tests in the laboratory suffer from limitations in terms of scale [26]. The scarce field evidence does demonstrate a slowly

progressing failure mode in dense sand resulting in a similar post-failure morphology as flow liquefaction slides. Based on the limited information provided by case histories, it is very possible that some were actually cases of breaching. Nowadays, Dutch engineers for instance question the original conclusion that all flow slides in Zeeland were caused by liquefaction.

Flow slides in sensitive clays have not been attributed to flow liquefaction; the geological characteristics are fundamentally different [30, 31]. Nevertheless, the similarities between the mechanisms are striking. Both are initiated by minor disturbances in gentle slopes, develop into an undrained mechanism in a sensitive soil type, either retrogressing or instantly failing at similarly high rates, involving similarly large volumes and sharing the same post-failure morphology [30–32]. Compare for instance the typical post-failure morphology of flow slides in sensitive clays (Figure 2.4) and sands prone to liquefaction (Figures 2.1 and 2.2). Unlike liquefaction flow slides, many flow slides in sensitive clays occur above the water table, while the in-situ soil properties are more easily determined. Consequently, analyses of flow slides in sensitive clays have provided valuable information on the development of retrogressive failures [30–32] and strength redistribution during progressive spreads [33].

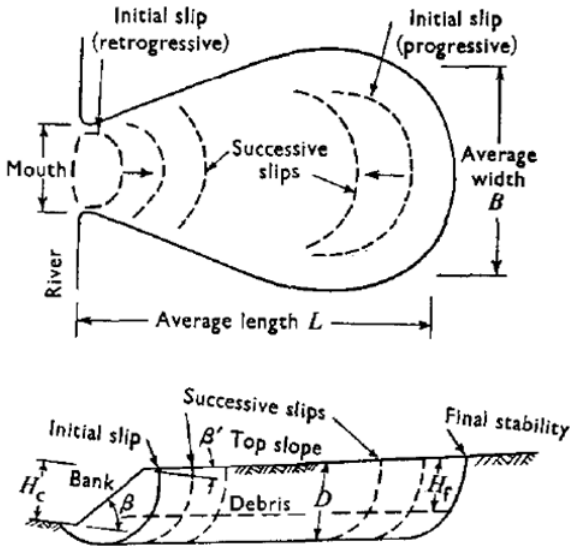


Figure 2.4: Typical retrogressive flow slide in sensitive clay [31].

2.1.7. Concluding remarks on case histories

Liquefaction flow slides are generally recognised as being one of the most hazardous failure mechanisms in soils. The characteristics of liquefaction flow slides complicates

the gathering of information from case histories. From the survey of case histories of flow liquefaction presented above it is concluded that:

- the pre-failure geometry on its own does not define an unambiguous condition for the occurrence of liquefaction flow slides, not even for the same geological conditions;
- a handful of case histories provides information on the susceptibility of the subsoil that is indicative rather than detailed;
- the vast majority of case histories were related to a trigger with a considerable magnitude;
- the post-failure morphology can just as well be related to (unstable) breaching, a failure mechanism occurring in denser sands.

2.2. Scale model testing

The information provided by case histories of liquefaction flow slides is inadequate, particularly as a basis for more advanced assessment methods. Scale model tests conducted under controlled conditions may fill the gaps left by case histories. This section outlines a few, selected scale model tests. As for the previous section, this survey is restricted to tests on subaqueous slopes. Although a few of the major scale model tests on flow liquefaction slides were conducted for rainfall induced slides [34], unfortunately a few fundamental differences with subaqueous flow slides make these tests inappropriate as a reference for this study. For instance, it is believed that liquefaction in these slides is the result of failure (by unsaturated collapse), rather than the cause.

The selected scale tests include tests carried out in Delft and tests carried out as part of the Canadian Liquefaction Experiment (CANLEX). To the Author's knowledge, these have been the most extensive and advanced (scale) testing programs conducted so far. As for the case histories, the quality of the available information is considered with respect to the initial conditions, triggering, development and post-liquefaction characteristics of these laboratory liquefaction flow slides. The scale model tests however allow for studying these properties in more detail. For instance, while case histories provide data from CPTs at best, scale model tests allow for actual measurements of the (relative) density. It should be recognised that the definition of relative density can be based on either the void ratio $e = V^p/V^s$ or porosity $n = V^p/V^t$, with V^p defining the volume of pores, V^s the volume of the particles and $V^t = V^p + V^s$ the volume of the bulk in a unit volume. The relative density based on porosity D_n and void ratio D_e are defined by, respectively:

$$D_n = \frac{n_{max} - n}{n_{max} - n_{min}} \tag{2.1}$$

$$D_e = \frac{e_{max} - e}{e_{max} - e_{min}} \tag{2.2}$$

Note that both may yield a different relative density for equivalent values of n and e. Internationally, it is custom practice to use D_e. Without further notice, the definition of

D_e for the relative density will be adopted and it will be assumed that, in cases where the relative density is not strictly defined in publications, Equation 2.2 applies.

2.2.1. Model testing in Delft

Deltares (more specifically, its predecessors Delft Geotechnics and Delft Hydraulics) carried out three major testing programmes in the 1970's and 1980's. Each yielded liquefaction flow slides in scale models, albeit with different purposes. The three programmes are discussed in chronological order below.

De Groot et al. [35] report the main findings of extensive experimental research in the period 1973-1977. The research was part of the design of the storm surge barrier in the Oosterschelde estuary, where the retrogression length of flow slides occuring in adjacent scour holes played an important role and measures such as compaction were considered. The program comprised 38 tests in a large flume with dimensions (length x width x height) 60 m x 3 m x 3 m and 95 tests in a medium flume with dimensions 30 m x 0.7 m x 1 m. The median grain size D^{50} of the sand bed was either 145 µm, 175 µm or 200 µm. About half of the tests included liquefaction flow slides. De Groot et al. based their paper on reports written in the 1970's, but unfortunately not all details could be retrieved. The paper does provide valuable information, particularly with respect to the development of liquefaction flow slides.

The sand bed was prepared using a fluidisation system in the bottom of the flume to heights varying between 0.63 m (medium flume) to 2.1 m (large flume). The lengths varied between 5 m and 24 m for the medium and large flume respectively, still leaving sufficient length for liquefaction flow slides to run out freely. The slope was fixed at 2v:1h, either by using a steel gate during preparation or dredging while applying suction in the fluidisation system. The established relative densities D_e in the sand bed ranged between −5 % and 25 %, depending on the applied discharge during fluidisation. It should be noted that the uniformity of the sand bed in terms of density was affected by irregularities in the fluidisation system, liquefaction events just after fluidisation, disturbance during the measurement of density by electrical resistivity probes and the possible interaction with boundaries such as the 2v:1h gate. The notion of the disturbing effect of the resistivity probe itself raises questions about the accurary of the density measurements; the calibration of the probes did not account for these local effects.

The envisaged trigger was either the rotation of the gate in the large flume or switching off the suction in the medium flume (see Figure 2.5). Three types of response were observed: liquefaction in the sand and the occurrence of a flow slide, liquefaction but no flow slide, and no liquefaction and no flow slide. It should be noted that 'liquefaction' here means significant excess pore pressures; as there were only pore pressure transducers in the bottom of the flume, it is unknown if the measured excess pore pressures correspond to partial liquefaction over the full height or full liquefaction over a limited height. There appears to be a thin line between the types of response in terms of initial densities; minor differences result in great differences in response. The disturbance of the sand bed seems to affect the response, as some tests that result in liquefaction flow

slides started at higher densities than some tests that did not.

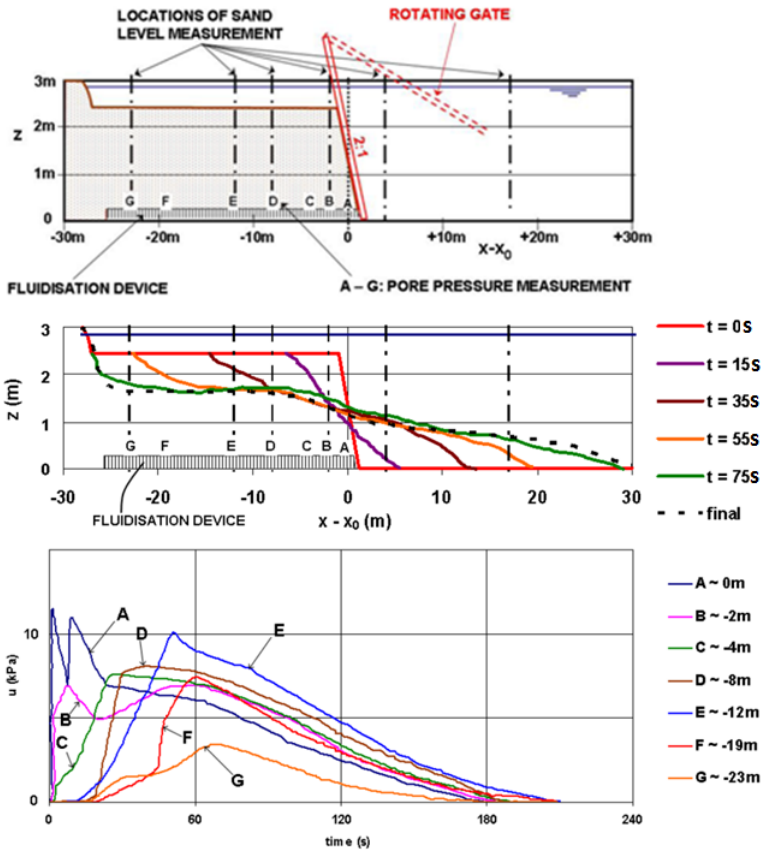


Figure 2.5: Side view of test setup and development of liquefaction flow slide in large flume [35]. The upper subfigure presents the initial configuration of the sand bed, including the rotating gate for the initiation of the flow slide. The middle subfigure displays the development of the sand surface in time during a typical liquefaction flow slide in the flume; the lower subfigure plots the corresponding excess pore water pressure.

The observed development of the liquefaction flow slides subscribes to the field characterisation of case histories. Instantly after triggering, excess pore pressures developed close to the slope (see Figure 2.5). The subsequent development of pore pressures over the length of the flume corresponds with the retrogression of the flow slide at a velocity of approximately 0.40 m/s, that is, in the order of meters per minute ($\mathrm{m\,min^{-1}}$) to meters per second ($\mathrm{m\,s^{-1}}$) (see Subsection 2.1.4). Retrogression continued until either densely packed sand was reached (large flume) or (probably) until the slope became too gentle to continue (medium flume). As for the field cases, the failure included relatively large volumes (up to $21\,\mathrm{m^3\,m^{-1}}$ for the large flume and $1.4\,\mathrm{m^3\,m^{-1}}$ for the medium flume) and gentle post-liquefaction slopes (approximately 1v:20h for the large flume, 1v:10h for

the medium flume). As suggested by these numbers, there was a clear scale effect in the results of the tests. The mechanism in the medium flume tended to be less extensive in size compared to the size of the setup: shallower, smaller in retrogression length, gentler post-liquefaction slopes and (consequently) smaller volumes. In retrospect it is not possible to explain the scale effect unambiguously; it could be the result of physical scale effects, as well as the boundaries or disturbance of the soil during preparations or measurements. The sand profile development in the medium flume suggests that sedimentation of the liquefied sand has an effect; it tends to push the mechanism to the surface (Figure 2.6). Based on hand calculations and the rate of development De Groot et al. [35] postulate that instability of the soil governed the migration of excess pore pressures. Consolidation would govern the subsequent phase of re-sedimentation. During tests that did exhibit excess pore pressures but no resulting liquefaction flow slide, a shallow, liquefied layer was observed at the crest that moved towards the slope before sudden 'freezing'. This observation suggests that consolidation yields an upward moving re-sedimentation front, during which excess pore pressures migrate upwards and liquefy the top layer. Tests that did not result in excess pore pressures nor liquefaction flow slides did show breaching. The rate of development was approximately $0.01\,\mathrm{m\,s^{-1}}$, i.e. one order larger than observed during field cases (Subsection 2.1.6), yet much slower than liquefaction flow slides. Contrary to case histories of unstable breaching, the resulting post-breaching slopes were relatively steep, that is, 1v:3h.

Molenkamp and Van Os [36] conducted a liquefaction test in the Brutus tank at Delft Geotechnics starting in September 1986. The test aimed at verifying the capacity of a finite element model with the constitutive model MONOT [37] for the prediction of the initiation of a liquefaction flow slide and the subsequent initial flow. Molenkamp and van Os report the results of a single test that was eventually carried out after encountering problems during the preparation of the slope. The Brutus tank had an internal size of (length x width x height) 2 m x 1 m x 1 m. The sand bed was prepared to a height of 0.73 m using a fluidisation system, after which a slope of approximately 1v:1.7h and height of 0.44 m was dredged by consecutively removing horizontal layers of sand. The density was measured by using a purpose built set-up, in which a known volume of sand was removed and weighed. This measurement was repeated during several tests to verify the uniformity of the sand bed [38]. Molenkamp and Van Os reported an average porosity equal to $n = 0.453$, implying a loose state for a typical Dutch sand. Irregularities during the dredging of the slope caused liquefaction failure several times before the actual, reported test could be conducted. The measuring system included pore pressure gauges at the bottom as well as in the sand bed and gap sensors to monitor the deformations. It should be noted that the sensors in the sand bed were attached to the tank with wires and were therefore expected to disturb the movement of the slope at larger deformations.

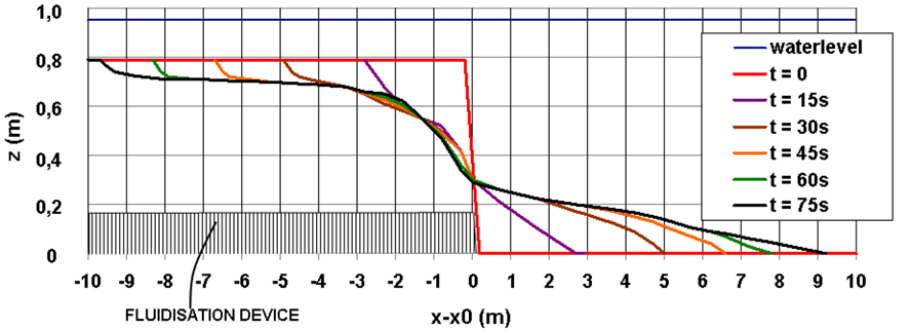


Figure 2.6: Development of surface of sand body along length of medium flume [35]

The liquefaction flow slide was triggered by applying a sudden discharge through the fluidisation system. More specifically, in 2.5 s the discharge was increased to a value equal to approximately 1/6 of the discharge required to fluidise the sand bed. As soon as the flow through the fluidisation system started increasing, the pore pressures in the bottom of the tank and the sand bed increased gradually as well. After 1.35 s the pore pressure gauges in the sand bed started showing deviating values, either a sharp increase or decrease (even down to tension) of the pore pressure. Particularly the decreasing pore pressures underneath the dredged zone next to the toe were conspicuous. After the discharge had reached its final value, all pore pressures increased to values corresponding to full liquefaction. At the same moment the pore pressures started deviating, the deformations measured by the gap sensors sharply increased: the slope failed. After approximately 10 s the sand bed was level again (see Figure 2.7). The sudden discharge through the fluidisation system may have induced a liquefaction flow slide successfully, but it was not a well-defined trigger. The measured excess pore water pressures were the result of both the fluidisation flux and the shear-induced contraction of the bed.

It is hard to determine the rate of development of the flow slide from the measurements of the gap sensors; the rate was simply too high to infer the speed. The data do suggest that the rate was at least in the range of $\mathrm{m\,min^{-1}}$ to $\mathrm{m\,s^{-1}}$ and probably even much higher during the initial stage of development. The porosity of the sand bed after consolidation equalled 0.439, that is slightly denser than before the test.

The third discussed (scale) test series [39, 40] did not primarily aim at testing flow slides. It served the purpose of investigating sedimentation phenomena during the construction of sand fill dams. The observed mild slopes of 1v:10h-1v:30h during the construction of sand fill dams did imply that flow slides affect the fill process. The authors distinguish between the hydraulic and soil mechanics aspect of approximately 10 reported tests, which were conducted at Delft Hydraulics in 1987 and 1988. The experimental setup consisted of a flume with dimensions (length x width x height) 32 m x 0.5 m x 2.5 m. A sand-water mixture was discharged into the flume through a pipe, which was

moved vertically during the experiments. The controlled quantities were therefore the sand concentration, flow rate (or alternatively the result of multiplying these: the sand production rate s) and sand grain size. The pore pressures were measured with six pore pressure gauges mounted at the bottom and seven gauges aligned vertically in the side wall. The porosity was monitored using an electric resistance probe.

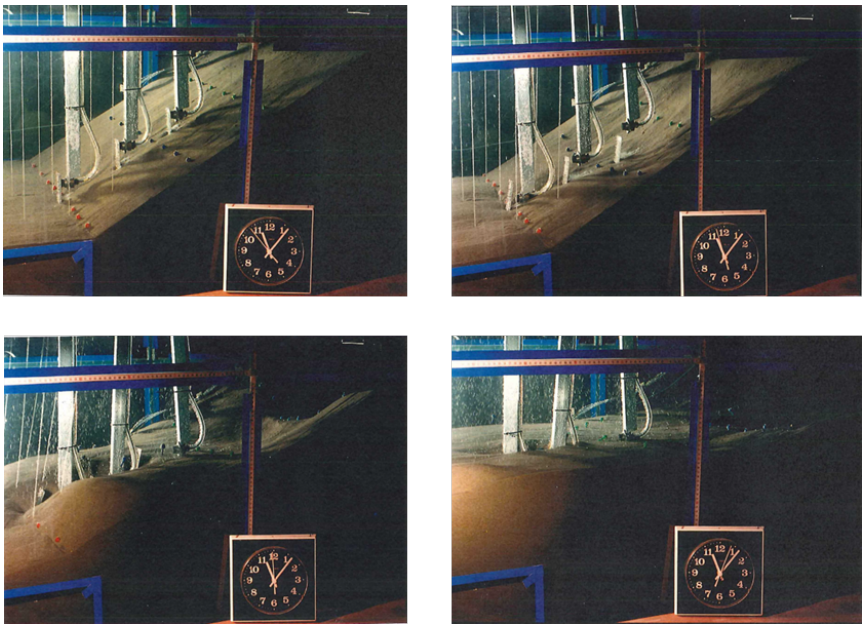


Figure 2.7: Development of liquefaction flow slide in the Brutus tank, starting at time 11:06:53.2 ($t = 0$, top left) and showing subsequently $t = 4$ s (top right), $t = 6.2$ s (bottom left) and $t = 10.5$ s (bottom right) [36].

Irrespective of the selected values of the controlled quantities, the porosity after sedimentation was typified as "very loose" with porosities ranging between 0.435 and 0.49. Mastbergen et al. [39] observe different processes as the under water slope developed. Flow slides governed the development of the slope during the tests with fine sand ($D^{50} = 135\,\mu$m) and low production rates ($s < 10\,\mathrm{kg\,s^{-1}\,m^{-1}}$). From a critical height of 1.5 m, flow slides reduced the slope several times as it reached a critical height (see Figure 2.8). In spite of the low density, flow slides did not occur at all during the tests with coarser sand ($D^{50} = 200\,\mu$m), irrespective of the production rate. The slope developed in a regular way. At high production rates ($s > 25\,\mathrm{kg\,s^{-1}\,m^{-1}}$), the turbulent suspension flow was the dominant transport mechanism and the slope developed in a regular way for all grain sizes.

Bezuijen and Mastbergen [40] elaborate on the liquefaction flow slides that occurred during the tests with fine sand. They state that the main uncertainties of liquefaction flow slides are related to the start (initiation) and end (re-sedimentation). Surprisingly, the pre-failure slope was of minor importance for the initiation of the flow slides. They

occurred at slopes ranging between 1v:2h and 1v:10h. Furthermore, the occurrence of flow slides was not reproducible; the occurrence (and properties) of flow slides differed during two experiments with identical fill conditions. During the liquefaction flow slides excess pore pressures were measured. However, the liquefied area appeared to be much greater than the actual flow slide, which was rather shallow. Note that De Groot et al. [35] report the same observation for the tests described at the beginning of this section. A single recording was available for the determination of the rate of development. Its value (less than $0.05\,\mathrm{m\,s^{-1}}$) is in the aforementioned range of $\mathrm{m\,min^{-1}}$ to $\mathrm{m\,s^{-1}}$. The slight densification of the sand after liquefaction, decreasing by up to 0.03 in terms of porosity, is also in the expected range.

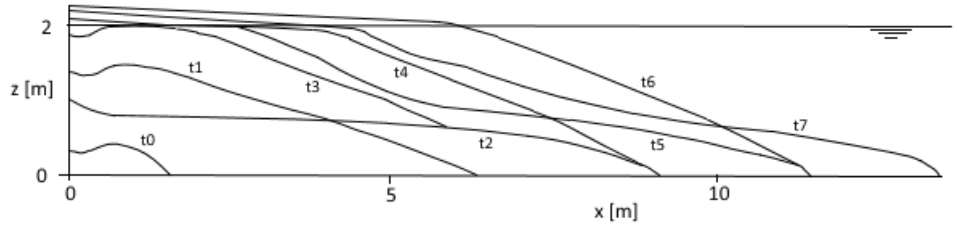


Figure 2.8: Development of slope with time t during discharge of mixture at left top of the flume (redrawn from [39]).

2.2.2. The CANadian Liquefaction EXperiment

The Canadian Liquefaction Experiment (CANLEX) was a collaborative research program between universities, industry and consultants in the period 1993-2000. Its main objective was to study the phenomenon of soil liquefaction [41]. More specifically, three main topics were covered: the characterisation of sand in terms of liquefaction characteristics, the development and calibration of numerical models to predict liquefaction response and a full-scale field test to validate these models [42]. The full-scale event, which is discussed in this section, was preceded by a series of centrifuge model tests.

The purpose of both the full-scale and centrifuge tests was to induce a flow liquefaction failure, while observing the response in terms of pore pressures and displacements [42]. However, both the test set-ups and results differed in many ways. The centrifuge prototype concerned an underwater embankment with slopes 1v:2h founded on a loosely packed layer (see Figure 2.9). At the envisaged acceleration of $50g$ the height of the embankment equalled 5 m, and the thickness of the foundation layer 10 m. Oil was used as a pore fluid to delay the rate of pore pressure dissipation. After spinning up to $50g$ the sand had a relative density of 29 %, a value most probably obtained after averaging the densification of the sand during spinning up over the whole model. Non-uniform densification is a known problem in centrifuge testing, particularly at high stress gradients [43]. Liquefaction was induced by two fast surcharge loads of 60 kPa, the second applied 2.6 s after the first. The surcharge loads instantly led to peaks in the pore pres-

sure responses of the transducer below the crest (Figure 2.9). The response was different below the toe, where the second peak did not occur. The displacement measurements (scaled at 50g) yielded a settlement at the crest (LDT18) of 0.33 m and 0.15 m heave at the toe (LDT19) after applying both surcharge loads. Even though Byrne et al. [42] state the deformation pattern is consistent with a deep seated liquefaction failure, the actual deformations are rather small.

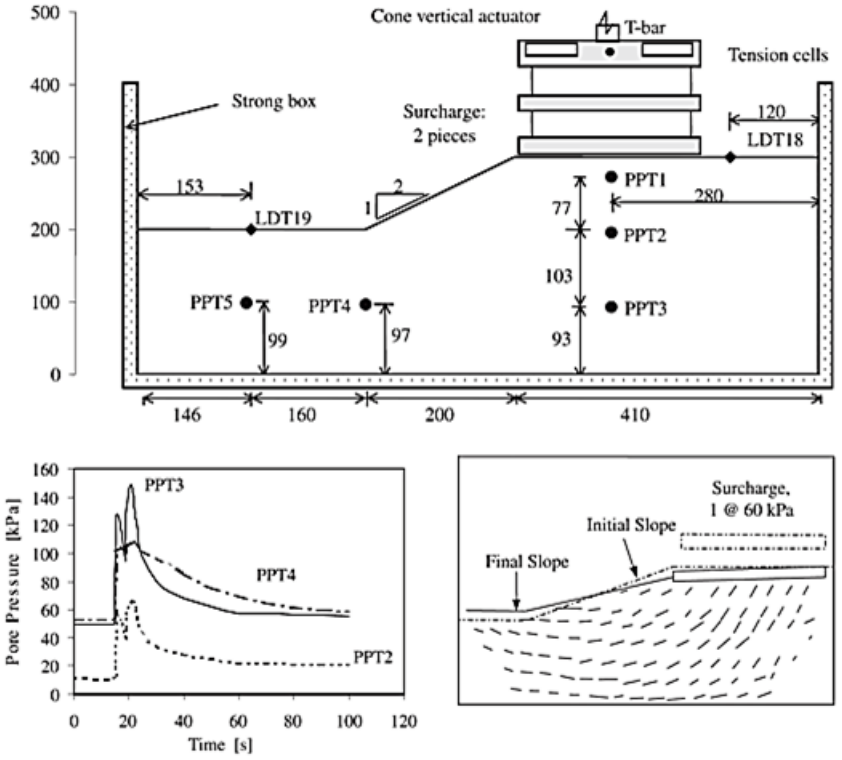


Figure 2.9: Centrifuge modelling CANLEX [42]: geometry and instrumentation (top, dimensions in mm), measured pore pressures (bottom left) and deformation field after first surcharge (bottom right). The technical specifications are provided by Byrne et al. [42] and underlying documents.

The full-scale liquefaction event was constructed by hydraulically placing a loose foundation layer (BBW), covered by a level platform of tailings sands (BAW). An 8 m high clay dyke with slopes of 1v:2.5h was constructed slowly to allow drainage of the underlying layers. To form an enclosure, a containment structure of dense, compacted cell sand was constructed (see Figure 2.10). The intention of the test was to induce liquefaction by pumping tailings behind the clay dyke. The Author believes the created situation resembles the loading of tailings dams, a case notorious for suffering from liquefaction failures. The density of the target sand layer (BBW) was very loose with an average SPT value of $N_1 \approx 3.5$. Nevertheless, liquefaction failure did not occur; the clay dyke experi-

enced a maximum displacement of 5.4 cm. Filling with tailings during 36 hours provided a relatively slow loading rate allowing excess pore pressures in the underlying layers to partially dissipate. Furthermore, the soil response was stronger than anticipated. Byrne et al. [42] hypothesise that this was due to the dominant stress path (compression) during loading. Laboratory testing on undisturbed samples showed a markedly stronger response during triaxial compression as compared to other stress paths. Furthermore, numerical analyses underlined the importance of both incorporating the drainage of the soil and the direction of loading [42].

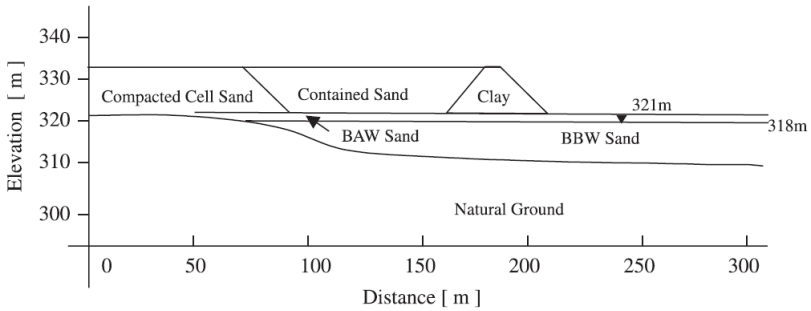


Figure 2.10: Set-up of CANLEX field test [42]

2.2.3. Concluding remarks on scale model testing

Scale model tests confirm the Author's main conceptions about the prerequisites (low density, excess pore pressures) and characteristics (rate of development, gentle post-failure slope) of liquefaction flow slides. Nonetheless, a number of observations stand out:

- It is unduly hard to prepare a sand bed prone to flow liquefaction; the slightest disturbance or densification prevents the occurrence of a liquefaction flow slide;
- The occurrence of laboratory liquefaction flow slides of submerged slopes is unpredictable: questions were raised with respect to the reproducibility of tests conducted under the same conditions, whilst flow slides occurred for a wide range of initial slopes even for similar densities;
- The size and pattern of laboratory flow slides of submerged slopes varied between the instant failure of the entire slope, a shallow failure in a much larger volume of liquefied sand and a deep seated failure resembling conventional shear failures;
- The importance of the trigger: the occurrence of flow slides was governed by the relation between the generation and dissipation of excess pore pressures. However, generation of significant excess pore pressures does not automatically yield a flow slide.
- The (hypothesised) importance of stress paths with varying resistance against liquefaction at different parts of the slope.

2.3. Element testing

Element tests allow flow liquefaction behaviour to be studied in even more detail. It is generally acknowledged that element testing and the measured, corresponding material behaviour provides the key to understanding and assessing liquefaction flow slides. The (presumed) fully controlled conditions during element tests yield liquefaction behaviour in its purest form. But are these results representative for field conditions?

This section addresses element testing with three purposes. Firstly, it defines the key elements of flow liquefaction as an instability mechanism. This consideration is restricted to simple and standard testing methods. Secondly, the variation of these key elements with the fabric of the soil is investigated by considering the effect of the reconstitution method. Thirdly, the scope is further broadened by including the effect of other stress paths imposed by advanced types of element tests, such as the hollow cylinder. Finally, the results from element tests are related to field conditions when addressing *void ratio redistribution*. As for the previous sections, those test results most relevant to the Author's research have been selected from a vast amount of data found in literature. In addition to (relative) density, element testing enables the measurement and/or control of stresses. Two measures that are frequently used in this thesis are the isotropic effective stress p' and the deviatoric stress q, which are defined as functions of the effective stress components σ'_{ij}:

$$p' = \frac{\sigma'_{kk}}{3} \tag{2.3}$$

$$q = \sigma'_{ij} - \frac{\sigma'_{kk}}{3} = \boldsymbol{\sigma}' - p'\boldsymbol{I} \tag{2.4}$$

These expressions simplify to $p' = (\sigma'_1 + \sigma'_2 + \sigma'_3)/3$ and $q = \sigma'_1 - \sigma'_3$ for triaxial test conditions, where the principal stresses σ'_1, σ'_2 and σ'_3 directly follow from the imposed stresses while $\sigma'_2 = \sigma'_3$. Alternatively, one may express both invariants in terms of the axial effective stress $\sigma'_a = \sigma'_1$ and radial effective stress $\sigma'_r = \sigma'_2 = \sigma'_3$, resulting in $p' = (\sigma'_a + 2\sigma'_r)/3$ and $q = \sigma'_a - \sigma'_r$.

2.3.1. Flow liquefaction and instability

Well before flow liquefaction was demonstrated in undrained triaxial tests, Casagrande [44] anticipated its key aspects based on drained test results. He observed the dilation of dense sands and the contraction of loose sands during dry shearing at the same mean effective stress. However, as shearing continued, both sands reached the same constant *critical density*. The same tendency was observed for the shear stresses, with dense sand first exhibiting a peak strength but eventually reaching the same constant *critical state* shear strength as loose sand. Casagrande reasoned that the critical density had to depend on the mean effective stress in a similar way as compression did. Furthermore, he anticipated the same final state would be valid during undrained loading of saturated sand. The corresponding restriction of no volume change yields a reduction of effective stress for sands looser than critical and thereby a reduction in shear strength. Casagrande not only provided a basis for understanding liquefaction, but also a predictive framework (Figure 2.11).

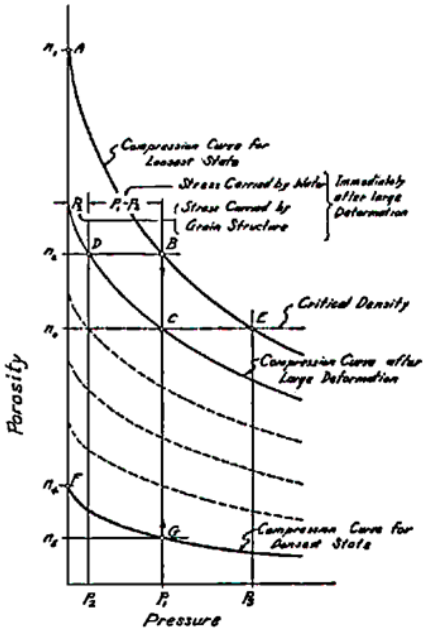


Figure 2.11: Framework of behaviour of cohesionless soils [44], with drained stress paths at constant mean effective stress for dense (G-C) and loose sand (B-C), as well as the anticipated undrained stress path for loose sand (B-D).

Casagrande could not foresee what happened during the generation of excess pore pressure in terms of shear stresses. Figure 2.12 depicts one of the first undrained triaxial tests on loose sands [45]. The test affirms the generation of pore pressures and the related reduction in shear strength. However, more noteworthy is the point of instability. The axial load is gradually increased (stress-controlled) in 14 min, after which the sample collapses and deforms to 20 % axial strain in 0.6 s. The occurrence of instability is the main feature of flow liquefaction behaviour. The Author will consider the point of instability in more detail, starting with its relation to the density of the soil. For now, the density is related to the tendency to dilate (dense) or contract (loose). Later, this will be further formalised. Castro repeated the undrained triaxial tests for varying densities. The results of a series of tests consolidated at the same isotropic stress but different initial densities are shown in Figure 2.13. Castro termed the response for curve *a*, *b* and *c*, 'liquefaction failure', 'limited liquefaction failure' and 'dilative response' respectively. This thesis will use the term 'flow liquefaction' accordingly, that is, whenever a point of instability dictates the effective stress path. Figure 2.13 shows that the point of instability moves to a higher deviatoric stress with increasing density and eventually vanishes. Further along the stress path, suction in the pores increases the resistance for the dilative response significantly. It is clear that the pore water stretches the observed resistance of soils over a wide range under undrained conditions. Furthermore, the resistance depends on the

mobilised strain.

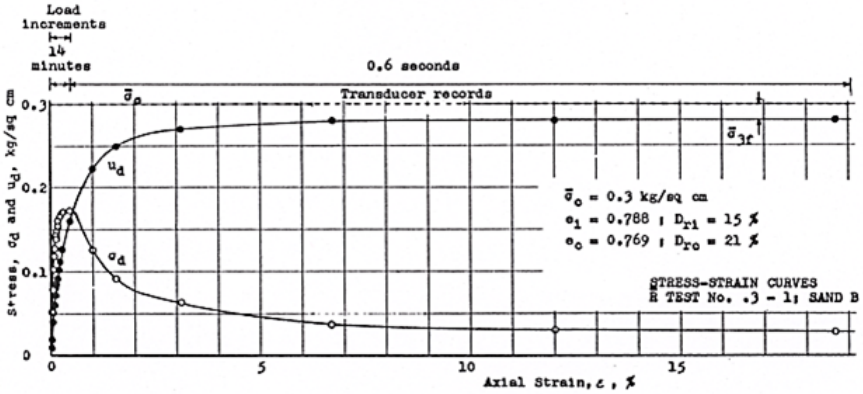


Figure 2.12: Plot of deviatoric stresses $\sigma_d = q$ and pore pressures u_d (vertical axis) versus axial strain ϵ (horizontal axis) during load-controlled, undrained triaxial compression test on isotropically consolidated loose sand [45]. The sample was prepared at an initial void ratio e_i or corresponding relative density D_{ri}. Isotropic consolidation at a radial effective stress $\bar{\sigma}_c$ resulted in a denser packing, as defined by e_c and D_{rc}.

A closer examination of the results of undrained triaxial tests at different densities reveals that the point of instability appears well below the (drained) failure line for loose sand or critical state line, e.g. ϕ=30° in Figure 2.13. This observation has both theoretical and practical relevance. From a theoretical viewpoint, the instability is imposed by drainage constraints rather than being caused by bifurcation. It is typified as *diffusive* instability as opposed to *localised* instability that occurs above the critical state line [46, 47]. The instability during flow liquefaction has been associated with collapse behaviour [48], but this term may be misleading. It suggests the soil skeleton collapses, but in fact the appearance of instability directly follows from known soil behaviour with the restriction of undrained (zero volume change) conditions [1]. The consequent excess pore water pressure generation during undrained deformation reduces the mean effective stress, thus effectively increasing the mobilised deviatoric stress ratio. As a result, the shear hardening becomes progressively smaller. Practically, the notion of instability below the critical state strength is expressed by the instability line [49], a line through the origin in the (q,p')-plane, connecting the points of instability for a particular state of the soil. The instability line may be expressed in terms of (instability) friction angle, which may be as low as 14° for triaxial compression [1]. This low value explains why gentle slopes may suffer from liquefaction flow slides and why only a minor trigger is required. Even shear stresses inferred from stress conditions for level ground (K^0) may exceed this value. The instability line and critical state line create a zone of potential instability in between. In or close to this zone the soil is in unstable equilibrium [44], and any small perturbation leads to instability. At first sight there seems to be a duality in response, since it is known that the soil is perfectly stable under drained conditions below the critical state

line. Subsection 2.3.3 will elaborate further on this peculiarity. The zone of instability is a stress point dependent, rather than a stress path dependent property [51]. No matter how the soil is brought into a (nearly) unstable state, the generation of excess pore pressures will yield liquefaction. This can be explained by the notion that the volumetric tendency, expressed by the stress-dilatancy relation, is stress point dependent as well [51]. Practically, this means that the actual stress path imposed by the trigger is of minor importance for the initiation of flow liquefaction (Figure 2.14).

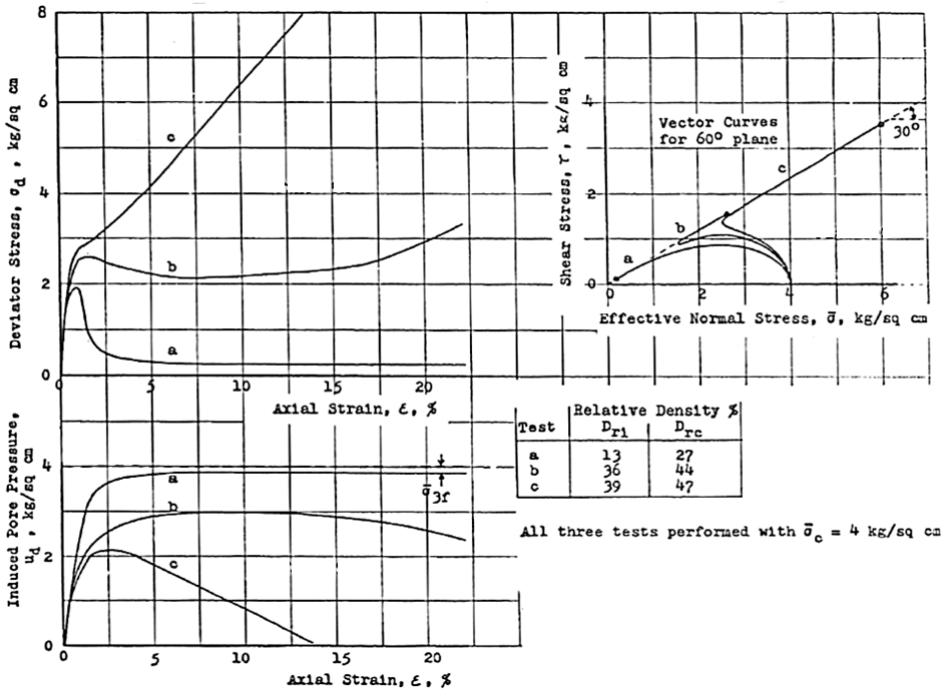


Figure 2.13: Plot of load-controlled undrained triaxial compression tests isotropically consolidated at the same mean effective stress $\bar{\sigma}_c$ but varying densities [45]. The densities are expressed in the initial relative density D_{ri} and relative density after consolidation D_{rc}

Beyond the point of instability the stress path either descends to liquefaction or recovers after descending (limited liquefaction, see Figure 2.13). The difference between both in terms of liquefied strength of the soil is large and has therefore great relevance. The type of response measured during undrained testing is known to depend on a number of (experimental) details. Lindenberg and Koning [52] measured (full) liquefaction during stress-controlled wet critical density tests. However, the calculated response based on displacement-controlled dry density tests at the same initial state resulted in limited liquefaction. They suggest the difference may be attributed to the type of control. Zhang and Garga [53] argue that the recovery during limited liquefaction is the result of

test-induced artefacts, such as end restraints, membrane penetration effects, and compression of the pore fluid. They question if it is real behaviour, all the more since there is no field evidence of a stress recovery after large strains. Others [54] dispute this argumentation. Limited liquefaction can be derived from drained testing and is therefore a feature of real soil behaviour.

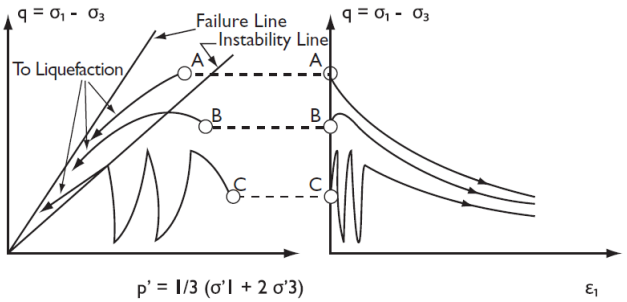


Figure 2.14: Irrelevance of stress path for occurrence of undrained instability of loose sand: (A and B) triggering by monotonic undrained loading; (C) triggering by cyclic undrained loading [50].

The ultimate state of an undrained triaxial test is uniquely defined by the critical state locus, as anticipated by Casagrande [44]. Roscoe et al. [55] defined the critical state as the state at which the soil continues to deform at constant stress and void ratio. It is believed that at the critical state the soil is completely remoulded, resulting in a fabric that allows steady conditions during continuous deformation. The soil has lost its memory of its initial structure. Been et al. [56] showed that the definition of the critical state locus is essentially independent of initial density and fabric, stress path, drainage condition and apparatus control. It is therefore a perfect reference for describing material behaviour. Been and Jefferies [57] defined the state parameter ψ as the difference in void ratio between the current state e and the critical state e^{cs} at the same mean effective stress:

$$\psi = e - e^{cs} \tag{2.5}$$

The state parameter is a predictive parameter for soil behaviour and, hence, for flow liquefaction. The Author considers the state parameter as a step forward compared to (relative) density and, if possible, prefers to use the state parameter from this point on. Unfortunately, this is not always possible as details of critical state lines are sometimes not provided in literature. The higher the value of the state parameter is (in a positive sense), the more excess pore pressures that will be generated before the critical state is reached, and the more likely it is that flow liquefaction will occur. There is one factor the state parameter cannot account for: the effect of the initial fabric on the stress path before the critical state is reached.

The correspondence between the behaviour during undrained triaxial tests on loose sand and liquefaction flow slides is striking. In both cases, flow liquefaction is triggered

at a low mobilised strength, (possibly) by a minor trigger, yielding runaway instability at high rates, and finally resulting in a low liquefied strength and correspondingly gentle slopes. Nonetheless, the representativity of undrained triaxial tests on reconstituted samples for field conditions may be questioned. Drainage conditions and stress path are not strictly imposed in the field. Furthermore, the in-situ fabric is usually unknown as a result of disturbance during sampling. How important are these effects for the prediction of flow liquefaction?

2.3.2. Deposition, reconstitution and fabric

This section elaborates further on the question: what makes soils prone to liquefaction? It is believed that in addition to state, fabric, drainage and stress path should be accounted for. This section addresses the likelihood of a sufficiently loose state and the possible effect of the fabric by considering deposition and reconstitution. The definition of fabric as a description of "particle contacts, their orientations and distribution, and cementation at the contacts" [56] is adopted. Accounting for the effect of cementation on the occurrence of flow liquefaction is outside the scope of this thesis. The fabric tensor expresses the orientation and distribution of particle contacts in one parameter [58]. Although the fabric tensor has proven its value in numerical analyses [59], it has not yet found its way into engineering practice. Actual measurements of the fabric tensor for soils are laborious, whilst the examination of natural soils is hampered by undisturbed sampling. This section therefore treats the subject by comparing observations on the continuum scale without quantifying the underlying fabric.

The previously discussed CANLEX programme also provides an excellent reference when it comes to element testing [41]. The test results allow for studying the effects of the fabric by comparing tests on disturbed and undisturbed samples, as well as by comparing different reconstitution methods from disturbed samples. Undisturbed samples were taken from uniform, loose sand deposits by using the freezing method [60, 61]. The five selected sites have different sedimentary environments, but all contain relatively young, uncemented, normally consolidated sand [41]. The state parameter ranged between (average) values of $\psi = -0.06$ and $\psi = 0$ (D_e from 30 % to 44 %). Out of 51 undrained, displacement-controlled triaxial compression tests conducted on undisturbed samples none showed 'full' liquefaction behaviour, i.e. the behaviour illustrated by curve *a* in Figure 2.13. Four tests showed 'limited' liquefaction behaviour (curve *b*), while the remaining 47 tests were all dilative (curve *c*). It is worth mentioning that the selected test sites were expected to contain loose sand deposits based on past in-situ testing criteria [41]. The apparent lack of susceptibility was attributed to the combined effect of fabric and imposed stress path (see Subsection 2.3.3). This observation raises questions about triaxial compression testing being the most appropriate method and state parameter (or relative density) being the sole governing parameter for the assessment of flow liquefaction. Vaid and co-workers [62–65] report tests that were conducted on samples reconstituted from undisturbed samples. They demonstrate that samples reconstituted by water pluviation yield a response similar to the undisturbed samples and therefore presumably have a similar fabric [65]. Even after pluviation at the loosest possible state undrained triaxial compression tests yield the dilative type of response [63]. This lack of susceptibil-

ity corresponds with the tests conducted on undisturbed samples. The reason there is a vast amount of data from undrained triaxial compression tests in literature that do show liquefaction behaviour relates to the preparation method, and thereby also to the influence of the fabric. It is customary practice to use moist tamping to reconstitute samples. Vaid et al. [64] compared undrained direct simple shear tests conducted at similar states, but prepared by using different reconstitution methods (Figure 2.15). The three methods examined result in different fabrics and therefore different responses. Water pluviation results in the behaviour previously denoted 'dilative response', whereas moist tamping results in 'liquefaction failure' (Figure 2.13).

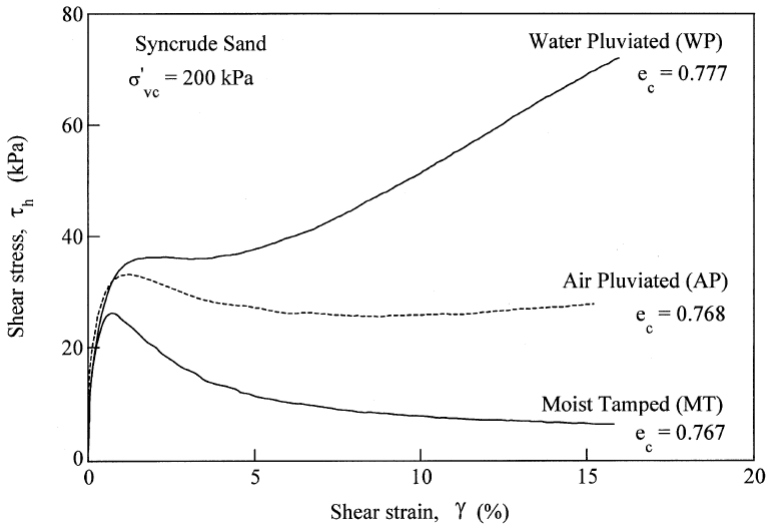


Figure 2.15: Results of undrained direct simple shear tests using different pluviation methods (from [64])

The vast majority of triaxial tests reported in literature were conducted after preparation by moist tamping; see for instance the database provided by Jefferies and Been [1]. Nonetheless, moist tamping has been considered inappropriate for replicating the in-situ soil mass, arguments being:

- Reconstitution using moist tamping introduces strong non-uniformities over the height of the sample [65–68]. The relative density may differ locally by as much as ±10 % from the average. Since the non-uniformities increase with decreasing density, this particularly applies to samples prone to liquefaction.
- Moist tamping introduces a possible error in the calculation of the initial density by not taking account of densification upon saturation [69]. The result is that the actual density is larger than presumed. Sladen and Handford [69] demonstrated that the error, which increases for silty sands and decreasing confining stress, may

be as high as 0.15 in terms of void ratio. Particularly for older studies (before 1987) it is not clear if and how this potential error was taken into account.

- The virgin state of a sample after (moist) tamping may be questioned. Frost and Park [68] demonstrate that tamping introduces peak compression stresses with the same order of magnitude as conventionally applied confining stress, that is up to 150 kPa for a sample with a target relative density of 75 %.
- Moist tamping allows samples to be reconstituted to densities below the minimum density (Figure 2.16). This explains why it is fairly easy to create a sample that is prone to liquefaction using moist tamping, but it is highly unlikely that the in-situ soil mass generally attains a density this low. Often pluvation yields a fabric similar to the in-situ soil mass [65, 70]. Only in particular cases is moist tamping considered representative, e.g. for the construction of fills above water while controlling the moisture content.

Considering the arguments listed above, it is no surprise that literature reports conflicting results from undrained testing using moist tamping. Several researchers [66, 71, 72] publish comparative studies of preparation techniques showing that moist tamping yields a stronger response than dry pluvation under undrained loading. The difference is attributed to the uniformity after preparation [72] or the fabric [66, 73], which are the same arguments as used to explain the contradicting results during CANLEX (Figure 2.15).

The *inherent anisotropy* of soils deposited under the action of gravity is characterised by a strong response in the direction of deposition [74, 75]. Both particle orientation and arrangement have been shown to contribute to the inherent anisotropy. Elongated particles tend to attain a stable configuration by orientation with their long axis in the minor principal stress direction [75, 76]. The contact normals tend to be parallel to the direction of axial compression, the direction in which they are most effective in supporting the load [77]. Mulilis et al. [66] demonstrate that moist tamping introduces a higher degree of contact normals in the direction of the axial load than dry pluvation. However, it is debatable if the anisotropy created is still inherent. Terzaghi [18] postulates that moist tamping creates a 'honeycomb' structure with low possible densities as a result of the adhesion between the particles. The subsequent tamping may affect the fabric by introducing induced anisotropy [78]. Whether the inherent weak fabric or the induced stronger fabric governs the undrained response of sands will depend on amongst other things the target density, soil properties and specifications (layer thickness, moisture content) of moist tamping. Test results obtained from moist tamping illustrate the pronounced effect of fabric on state-dependent (Figure 2.15) and intrinsic (Figure 2.16) susceptibility to flow liquefaction.

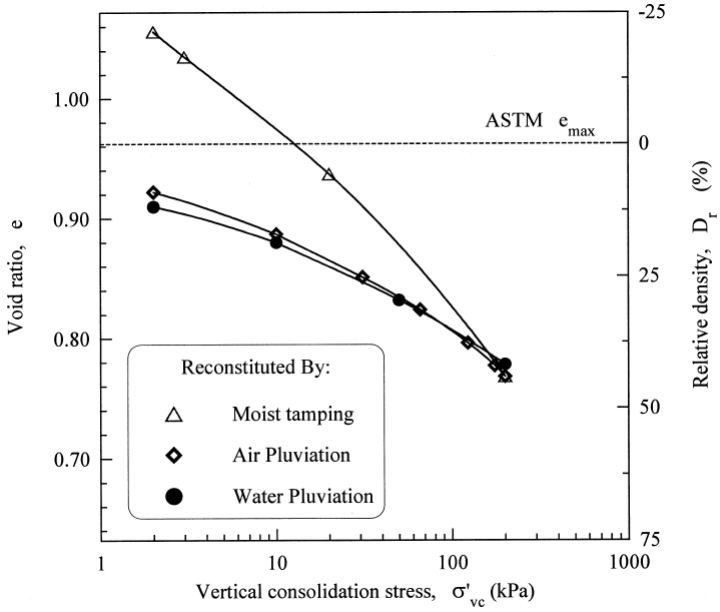


Figure 2.16: Comparison between one dimensional compression from the loosest state for different reconstitution methods [64]

Verdugo and Ishihara [79] define a measure for the intrinsic susceptibility of sands to flow liquefaction by considering the relative position of the critical state line with respect to the isotropic consolidation lines from the loosest and densest states (see Figure 2.17). A sand with a high intrinsic susceptibility will have a critical state line closer to the densest state, thereby having a higher likelihood that a loose state (or high state parameter) is reached. For Toyoura Sand prepared using moist-tamping, Verdugo and Ishihara demonstrate that the intrinsic susceptibility increases with (non-plastic) fines content FC, the percentage by mass of grain sizes equal to or smaller than silt. Without any fines ($FC = 0\,\%$), the critical state line lies relatively close to the minimum density, whereas for a pure silt ($FC = 100\,\%$), the range of loose states is larger than dense states. When comparing a dataset of different sands [1], the same tendency can be observed: the intrinsic susceptibility of clean sands is generally low, but it is higher for sands with a higher fines content. Note that this tendency corresponds with: (1) other investigations showing a transition in (lower) depositional densities for non-plastic soils close to the silt size [11, 18, 80], (2) the test results during CANLEX and (3) the fact that the vast majority of case histories of flow liquefaction include silty sands [11].

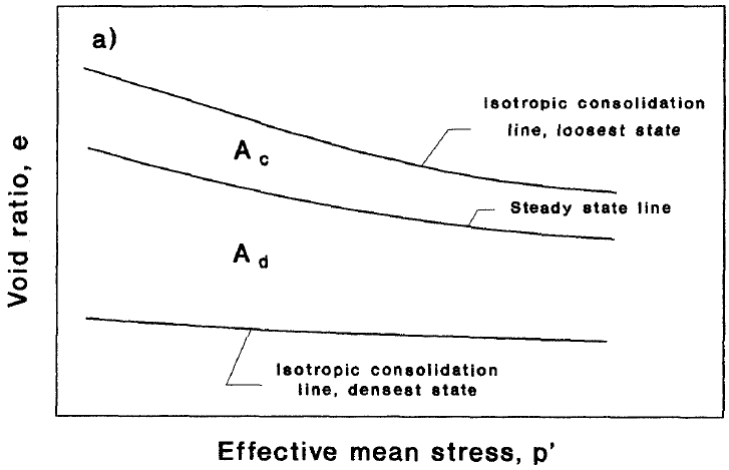


Figure 2.17: Illustration of the intrinsic susceptibility to liquefaction, here defined by the comparison between the contractive domain A_c and dilative domain A_d [79] in the $e-p'$-plane.

The notion that fines increase the susceptibility to liquefaction is controversial; contradicting conclusions are drawn in literature on the influence of non-plastic fines on flow liquefaction resistance [81]. There are various possible explanations for the differences observed. Sadrekarimi [82] elucidates these differences by considering the effect of fines on the critical state line. Fines that have the same properties as the host sand tend to result in a translation of the critical state line in (e,log(p'))-space. Below a threshold value, an increase in fines content results in a translation downwards. However, as the same tendency is expected in the maximum void ratio, the intrinsic susceptibility does not necessarily increase. Sadrekarimi states that natural silts are typically composed of softer minerals and have more angular grain shapes than the host sand. In this case, increasing the fines content below a threshold value will result in a rotation of the critical state line, that is, a steeper critical state line. The actual effect depends on the void ratio and mean effective stress considered, as well as on whether the onset of liquefaction is considered or the final (liquefied) strength. Figure 2.18 illustrates three possible changes in terms of behaviour as the fines content increases, based on a general database of triaxial tests (*a*) and specifically for the case of the Nerlerk berm (*b*). In zone *A* the state parameter decreases for point *A* as a result of the steeper critical state line, whilst the mean effective stress at the critical state increases. Both the resistance against the onset of flow liquefaction and the liquefied strength are therefore increased in zone *A*. In zone *B*, the state parameter does increase for point *B*, but the liquefied strength increases anyway. Finally, for point *C* in zone *C* the state parameter increases and liquefied strength decreases, implying an overall increase in the susceptibility to liquefaction. With respect to the onset of flow liquefaction, Mizanur and Lo [83] publish data showing that with increasing fines content the (equivalent) state parameter indeed increases resulting in a decrease of the slope of the instability line. Sadrekarimi verified the change in liquefied

strengths by considering backcalculated strength values from case histories. The right subfigure (*b*) of Figure 2.18 depicts the effect for the Nerlerk Berm. The rotation of the critical state line from 2% to 12% offers a possible explanation for why a predominantly dilative fill failed; the measured fines content of 12 % alters the state of point *C* from dilative into susceptible to flow liquefaction.

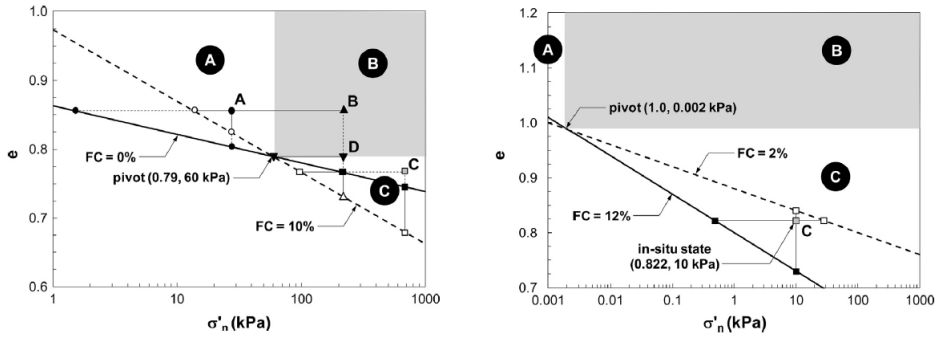


Figure 2.18: Rotation of critical state line around pivot point as a result of increase of fines content: (*a*) general concept based on database, (*b*) case of Nerlerk berm (from [82]).

Another differentiation that can be made concerns the properties of the fines. Yang and Wei [81] demonstrate that the particle shape of both the fines and host sand affects the susceptibility to liquefaction. Round sand grains with round fine particles yield a more unstable response in undrained triaxial testing than angular shapes. Deformation of the soil skeleton requires relative motion of the fines with respect to the sand particles. Yang and Wei hypothesise that the rolling of round fines results in less resistance than for the sliding of angular particles, while less work is required to move along a rounded sand particle than an angular one (Figure 2.19, (*a*)). Hight et al. [13] conducted undrained triaxial tests on sand with plate-shaped fines (mica) to investigate the Jamuna Bridge flow slides. The plate-shaped fines promote an unstable grain structure that is highly anisotropic. The susceptibility to flow liquefaction is particularly high at low effective stresses, as the 'bridging' fines deflect at higher stresses which stabilises the soil skeleton (Figure 2.19, (*b*)). Yamamuro and Lade [84] observe a similar tendency, albeit caused by another mechanism (Figure 2.19, (*c*)). At low effective stresses the fines reside between the contacts of the sand grains, which creates unstable contacts. For increased effective stresses (and densities) the fines reside in the voids between the grains, where they will have a negligible effect on the response of the bulk mass.

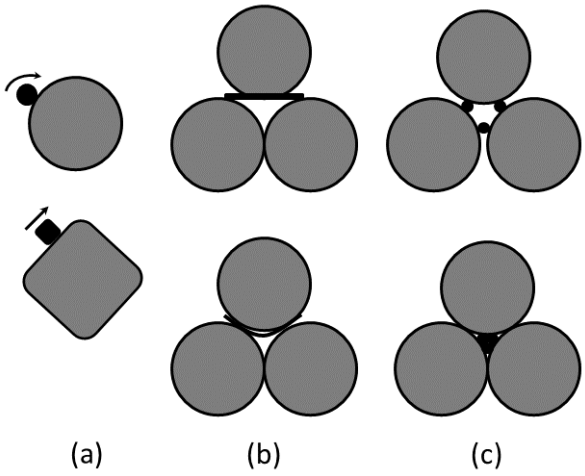


Figure 2.19: Concepts of influence fines on flow liquefaction behaviour: (a) influence of particle shapes (from [81]), (b) mica particles (from [13]) and (c) (un)stable grain contacts (from [84]).

Wood et al. [85] continue the work of Yamamuro and Lade by examining the effect of a number of depositional methods, not including moist tamping, on the undrained response of a silty sand. As for clean sands, differences in response become apparent, particularly at low density, low effective stress and high fines content. Another striking similarity is the response after preparation by water sedimentation, a method similar to water pluviation. None of the samples tested, irrespective of density and fines content, exhibited liquefaction behaviour. It should be noted that Wood et al. encountered segregation of fines during deposition using the conventional methods of water sedimentation and air pluviation. The fines were only evenly distributed after using methods including mixing after deposition. Yamamuro et al. [86] used microscopic analyses to test the hypothesis that the observed response is the result of (un)stable grain contacts. Using a mixture of a host sand with $D^{50} = 140\,\mu$m and non-plastic fines with $D^{50} = 40\,\mu$m, the unstable contacts are defined by the contacts between the larger and smaller grains, whereas contacts between the larger grains provide stable contacts. Indeed, there is a clear relation between the stability of the grain contacts and whether or not flow liquefaction occurs for the tests that Wood et al. conducted. The discussed test results suggest that fines promote an unstable, contractive grain fabric and increase the intrinsic susceptibility to flow liquefaction. However, some remarks need to be made with respect to the representativity of these result for natural soils. Reconstitution by water sedimentation, in many cases considered to be the best representation of in-situ sedimentation conditions, did not yield homogeneous samples nor liquefaction behaviour. Homogeneous samples were only obtained after using methods that replicate high energy and intensity deposition environments in nature, conditions that are also likely to yield higher densities after deposition [87]. It is therefore debatable whether homogeneous, silty samples are representative for in-situ soil conditions susceptible to liquefac-

tion. In the Author's experience in many of the cases of flow liquefaction failure, layered soil strata are encountered. As a consequence it is more likely that the fines content in distinct layers is either very low or very high. Furthermore, the response of the bulk will depend on the scale of layering; the thickness of a silty interlayer will determine whether or not the bulk response is governed by the behaviour of this interlayer. Another remark concerns the custom to use gap graded mixtures to investigate the effect of fines in the laboratory, whereas most natural sands are smoothly graded. The concepts depicted in Figure 2.19 for instance mainly apply to binary mixtures.

Questions raised with respect to representativity can also be raised for numerical analyses using the Discrete Element Method (DEM) [88]. To the Author's knowledge, it has not been possible to capture the generally complex nature of soils and pore fluids using DEM. Instead, simplifications are implemented including the use of spherical or ellipsoidal particles, larger particles to reduce the computational costs, unrealistic values of the initial void ratio and confining stress, and a zero volume change condition instead of undrained conditions including a pore fluid [73]. These simplifications result in deviations in response, as for instance demonstrated by experiments on binary mixtures of round particles [81]. Nevertheless, the DEM has provided valuable insight into concepts such as the critical state and state parameter, the formulation of the yield surface and the (un)importance of interparticle friction and crushing [59, 89, 90]. Its deficiency with regard to a lack of supporting experimental data for validation also, paradoxically, highlights its added value: the DEM complements experiments on particular hard-to-measure properties, such as intergranular stresses. Studies on flow liquefaction using the DEM are rare, presumably because of problems encountered in terms of numerical stability. Yimsiri and Soga [73] examine the effect of fabric on the drained and undrained behaviour of a packing of multi-sized spheres. More specifically, they examine the effect of a certain, imposed fabric (inherent) anisotropy. The imposed distribution of contact normals is varied, while simulating triaxial tests for drained and undrained conditions, under compression and extension, and for 'loose' and 'dense' sand. The results demonstrate that the fabric has a pronounced effect on the response, with the strongest (dilative) response when the major principal stress and concentration of contact normals are aligned and the weakest (contractive) response when they are orthogonal. This observation corresponds with observations during experiments [66, 75, 77]. A feature that is hard to capture during experiments is the evolution of the fabric. Yimsiri and Soga demonstrate that, in both drained and undrained simulations, the transition from a contractive to a dilative volumetric tendency marks a sudden change of the fabric anisotropy, that is, the averaged orientation of the contact normals. Recall that for undrained conditions, this transition is termed the quasi-steady state. Yang and Dai [91] examine the quasi-steady state in more detail by using DEM. Contrary to Yimsiri and Soga, the inherent anisotropy is not pre-defined but created by gravitational deposition. After isotropic compression, the numerical sample is subsequently sheared by constant volume bi-axial loading with the major principal stress in the horizontal direction. The features of flow liquefaction behaviour, including its dependence on void ratio and mean effective stress, are well captured by DEM simulations. Yang and Dai also observe a sudden change in fabric anisotropy, albeit well before the quasi-steady state. At small strains ($< 1\,\%$) the

predominant direction of contact normals suddenly changes from vertical (after deposition) to horizontal (loading direction). Interesting, but impossible to infer from the paper is whether this transition coincides with the moment of instability. Yang and Dai relate the quasi-steady state to a minimum in the average number of contacts per particle, the coordinate number. The generation of excess pore pressures is associated with a decrease of coordinate number, whilst the recovery of strength after the quasi-steady state relates to an increase. In both papers discussed [73, 91], the fabric anisotropy hardly changes after the sudden transition. Yimsiri and Soga state that after the quasi-steady state the remnants of the initial fabric have been destroyed. However, it seems that the occurrence of flow liquefaction is still governed by the initial fabric. More specifically, the initial fabric anisotropy relative to the loading direction governs the occurrence of flow liquefaction.

2.3.3. Stress path, control and drainage

One of the main conclusions of the CANLEX programme concerns the importance of including the direction of loading and drainage in the assessment of flow liquefaction slides [41]. This conclusion corresponds with the findings in the previous section. Reproducing flow liquefaction by undrained triaxial testing may require either artefacts (moist tamping) or silt to create an unstable fabric. However, it is believed that in most cases silt segregates during deposition, which is replicated by (water) pluviation in the lab. The fabric anisotropy created in this way offers the largest resistance in the vertical direction, that is, under triaxial compression. It is therefore of importance to investigate the effect of stress paths on flow liquefaction. The term 'stress path', in the Author's understanding, includes changes in both the magnitude and direction of the principal stresses on a soil element [92]. In the field, the loading conditions are presumably imposed as a combination of stress and strain controlled loads [52]. Therefore, the effect of strain control on flow liquefaction behaviour is also treated. This section considers the effect of the stress path, control and drainage, starting with the simplest case: triaxial loading.

In addition to undrained triaxial compression, undisturbed samples were tested under undrained triaxial extension and simple shear during CANLEX. None of the 106 undisturbed samples tested in total exhibited (full) liquefaction behaviour. However, whilst only a small portion (4/51) of the undrained triaxial compression tests exhibited 'limited' liquefaction, this was considerably larger for the undrained simple shear (7/23) and triaxial extension (13/32) tests. Triaxial extension implies principal stress reversal, with the absolute values of the minor (radial) principal effective stresses σ'_r becoming larger than the major (axial) principal effective stress σ'_a. Generally, both the values of the three principal stresses and their rotations in three directions can be varied. A usual measure to express the relative magnitude of the intermediate principal stress σ'_2 is the parameter b:

$$b = \frac{\sigma'_2 - \sigma'_3}{\sigma'_1 - \sigma'_3} \tag{2.6}$$

Hence, for triaxial extension $b = 1$, while $b = 0$ for triaxial compression. The hollow cylinder apparatus [93] allows for the independent control of the three principal stresses. In

addition to the undrained triaxial compression tests, Vaid and co-workers [62–65] report test results obtained with the hollow cylinder on samples reconstituted from undisturbed samples. Both the value of b and the rotation of the axial stress with the vertical α are varied (see Figure 2.20). The test results show a consistently softer response for increasing values of α and/or b. The extremes are defined by undrained triaxial compression ($\alpha = 0°$, $b = 0$) and extension ($\alpha = 90°$, $b = 1$). Samples that exhibited dilative behaviour under triaxial compression, even for the loosest possible state after water pluviation, exhibit liquefaction behaviour under extension. Both the peak (instability) and minimum strength decrease dramatically as α and/or b are increased.

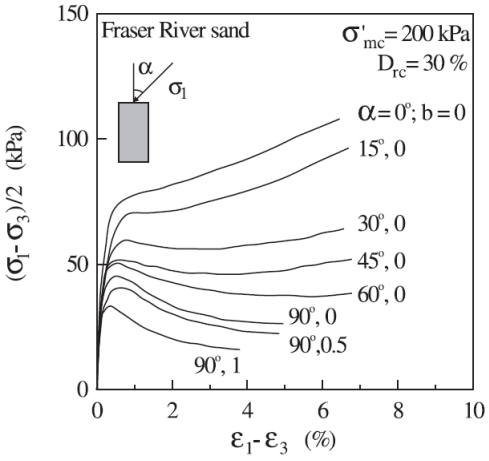


Figure 2.20: Undrained response from hollow cylinder tests for varying rotation α of σ'_1 and σ'_3 and relative value b of σ'_2 [65]. The samples were reconstituted at the loosest state for water pluviation. The tests were conducted using displacment and axial-rotation control.

Similar results were obtained in other studies treating the effect of stress anisotropy on the undrained response of sand [94–97]. In addition to the stress paths depicted in Figure 2.20, literature reports test results aiming at particular aspects of stress path dependence:

- Field loading conditions such as earthquakes amount to simultaneous changes in the direction and magnitudes of the principal effective stresses. During for instance undrained torsional shear [98] and simple shear tests [65], the shear load, the absolute value of the principal effective stresses and their rotation simultaneously vary.

- Yamada and Ishihara [94] varied the magnitudes of the three principal stresses independently, that is, without any rotation. In this case the angle θ in the octohedral or pi-plane expresses the imposed stress state (Figure 2.21). Yamada and Ishihara report tests conducted every $\Delta\theta = 15°$ in the range $\theta = 0° - 180°$. Note that these stress paths define an alternative way of moving from (vertical) triaxial compression to extension as compared to principal stress rotation. Triaxial compression in

the vertical and horizontal directions is defined by $\theta = 0°$ and $\theta = 120°, 240°$ respectively, triaxial extension is correspondingly defined by $\theta = 60°$ and $\theta = 180°, 300°$. By comparing the generated excess pore pressures at different shear stresses τ^{oct} Yamada and Ishihara measured an increasingly weaker response for increasing θ (Figure 2.21), demonstrating anisotropy of the cubical samples.

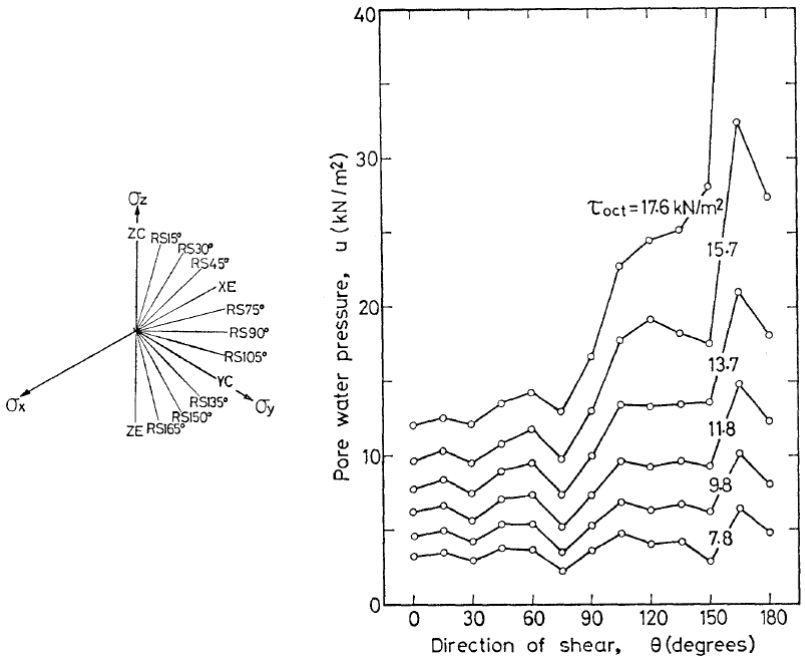


Figure 2.21: Tested effective stress paths in pi-plane (left) with definition of angle θ, and measured relation between generated excess pore pressures at different magnitudes of shear stress τ^{oct} and angle θ (right) [94].

- Uthayakumar and Vaid [96] report results from hollow cylinder tests that isolate the effect of α and b. Figure 2.22 depicts two test series conducted under identical conditions with the exception of α and b, which were either varied or kept constant at an intermediate value. Increasing either of the two variables yields a weaker undrained response. The effect of increasing angle α is greater than increasing b, both in terms of peak and residual strength. The effect of the intermediate stress is most pronounced when b is increased from 0.5 to 1.0. The effect of rotation in principal effective stresses is further isolated by Yang et al. [99], who demonstrate that solely rotating the stresses at a fixed deviatoric stress induces excess pore pressures. Symes et al. [95] demonstrate that the effects of (undrained) rotation and shearing can be superposed. The undrained rotation of the major and minor principal effective stress at a fixed value of the shear stress essentially has the same effect as increasing the shear stress after rotation.

- A case of particular, practical importance concerns plane strain conditions ($\epsilon_2 = 0$). The attained value of b under plane strain conditions is not unique, but depends on the stress path followed. When plane strain conditions are not imposed, they can be retrieved from the stress path that approximates $\epsilon_2 \approx 0$. Yamada and Ishihara [94] relate plane strain conditions to a value of b between 0.5 and 0.732 for a fixed orientation of the principal effective stresses α=0. Uthayakumar and Vaid [96] demonstrate that plane strain conditions are satisfied when $b = 0.4$ for a (fixed) value of $\alpha = 45°$. Yoshimine and co-workers [97, 100] impose plane strain conditions in an automatised hollow cilinder apparatus. Irrespective of the start value of b and the stress path followed (compression, extension, simple shear), at large strains b attains a value of 0.25. Wanatowski and Chu [101] use a purpose-developed plane strain apparatus, which imposes plane strain conditions while measuring the intermediate stress. They conclude that b is not unique under plane strain conditions, but varies between approximately 0.28 and 0.36.

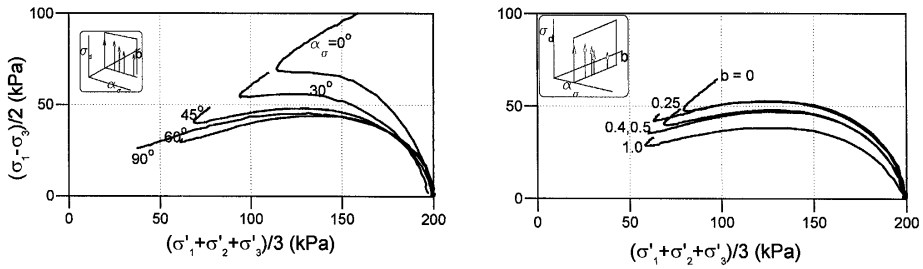


Figure 2.22: Results from undrained hollow cylinder tests conducted on Fraser Sand under identical mean effective stress $p' = 200$ kPa and density $D_e = 30\,\%$, while keeping $b = 0.5$ (for varying α, left figure) and $\alpha = 45°$ (for varying b, right figure) constant, respectively [96].

In general, the results are consistent; the predominant direction of loading relative to the inherent anisotropy of the soil governs its response. Drained true triaxial tests in which the plane of deposition was varied relative to the loading direction confirm this interrelationship [74]. Triaxial compression and extension define the extremes in terms of response for pluviated sands with a horizontal bedding plane. However, these extremes may be stretched further when considering induced anisotropy as well. The influence of induced anisotropy on undrained response has not been examined as extensively as inherent anisotropy. The studies that have been conducted address the effect of drained pre-shearing on the undrained response of loose sand under triaxial compression and extension [102–104]. The behaviour is strongly affected by the magnitude of pre-shearing. Low values of pre-shearing, that is to stress states below the instability line (Figure 2.14), hardly affect the undrained response under triaxial compression or extension. Pre-shearing beyond the instability line, however, has a significant effect even for small changes of density. Drained pre-shearing may either turn an initially contractive response into dilative when pre-sheared in the same direction, or an initially dilative response into contractive when pre-sheared in the opposite direction. Both the

slope of the instability line and the minimum strength decrease significantly when an already contractive specimen is pre-sheared in the direction opposite to the direction of undrained loading.

Provided that no further anisotropy is induced, stress anisotropy during flow liquefaction can be expressed by isolines in three dimensional stress space. Symes et al. [95] define a 'state boundary surface' by connecting the contractant region of the undrained effective stress paths for a constant density in (p',q,α)-space. They demonstrate that an undrained effective stress path remains on the state boundary surface as soon as it hits the surface. The response at the state boundary is not affected by the way it is reached. The behaviour is stress point dependent provided that the soil is loaded and not unloaded. The same stress point dependence (and unimportance of stress path) was noted for the instability line (Figure 2.14), which marks the transition between stable and unstable behaviour on the state boundary surface (Figure 2.23). The post-peak portion of the state boundary surface defines a zone where undrained effective stress paths will exhibit unstable behaviour as soon as the state boundary surface is reached. However, it should be emphasised that the state boundary surface only applies to the contractant region of the effective stress space and does not necessarily exclude limited liquefaction behaviour. The instability line simplifies the onset of instability by a straight line through the origin and a peak of the monotonical undrained effective stress path. This is a safe approximation; stress paths other than the monotonical undrained effective stress path will reach the instability line before reaching the state boundary surface [48].

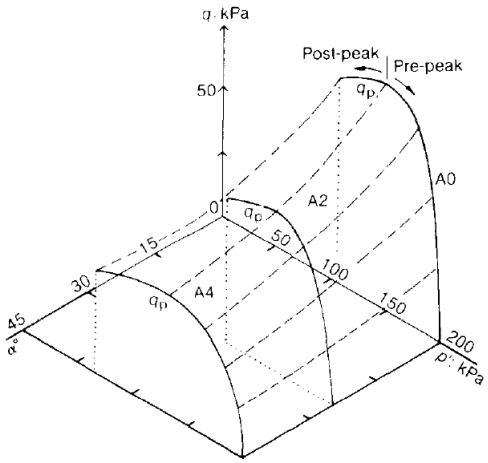


Figure 2.23: Contractant region of state boundary surface as defined by the principal effective stress paths of undrained torsional shear tests A0, A2 and A4 at different, fixed orientations α of the effective stresses [95]. Instability points defining instability lines for constant α are indicated by q_p.

The existence of a state boundary surface defined by monotonical undrained effective stress paths was confirmed by tests conducted under Constant Shear Drained (CSD)

stress paths [48]. The soil is first brought to a particular (anisotropic) stress state by triaxial compression. Then, the deviatoric stress and drainage conditions are maintained whilst the isotropic effective stress is gradually reduced. Using scale model tests, Eckersley [34] demonstrated that flow liquefaction in (unsaturated) slopes may be triggered by raising the water table under essentially drained conditions, i.e. by reducing the mean effective stress. Detailed inspection of the test results reveals that the generation of excess pore pressures is the result rather than cause of instability. Figure 2.24 illustrates a typical result of a CSD test on loose sand [48]. When the stress path reached the state boundary surface the sample rapidly collapsed. Even though the rate of deformation was too high to collect detailed data, it was clear that excess pore pressures were generated and that failure occurred under undrained conditions. Since the test was carried out under drained conditions, instability caused the generation of excess pore pressures and not the other way around. Others [52, 105] report undrained collapse during drained stress paths in which the mean effective stress is held constant while the deviatoric stress is gradually increased. Skopek and co-workers [106] demonstrate that instability during CSD stress paths is essentially a drained phenomenon by conducting CSD tests on dry sand. During instability, strain jumps are observed that would cause the generation of pore pressures in the case when a saturated sand would have been tested. Gajo et al. [105] generalise the observed behaviour by relating the observed collapse to the intersection with the (current) yield locus. The observed relation between the occurrence of flow liquefaction and (the rate of) elastoplastic deformations highlights the importance of advanced constitutive modelling to fully capture liquefaction flow slides. Furthermore, it may be concluded that the generation of excess pore pressure in sand is not necessarily related to the rate of loading of an external agent, but may be the result of slow, drained loading under particular stress paths.

It is of importance to acknowledge that stress control is a prerequisite for the occurrence of undrained collapse during drained loading. Only then can loss of controllability [107] and the generation of excess pore pressures be established. In addition, an inertial loading system is required that is able to keep up with the high rate of deformation during collapse [65, 71, 105]. Lindenberg and Koning [52] report differences in response between wet critical density tests conducted under deformation and stress controlled conditions. Under otherwise identical conditions, a wet critical density test conducted under stress controlled loading results in liquefaction, but shows recovery of the deviatoric stress (limited liquefaction) during strain controlled loading. Casagrande [23] finds different lines at the critical (or steady) state for strain and stress-controlled tests and, as a consequence, a higher critical state strength for strain controlled tests. He attributes the difference to the lack of a consistent flow structure for strain controlled tests. Been et al. [56] refute Casagrande's findings by measurements of the same critical state line for stress and strain-controlled tests. Hanzawa [108] shows that stress control extends the softening part to larger strains during limited liquefaction. Gajo et al. [105] attribute rate effects to the time required for grain contacts to rearrange. Furthermore, the inertia of the loading system during collapse would prevent recovery of the strength. The deceleration of the loading system caused by recovery would yield an additional load on the soil skeleton. CSD tests conducted on dense sand demonstrate that instability occurs

for dense sands as well [105, 109]. As for loose sands, the stress path during undrained, monotonic loading defines a state boundary surface during drained testing. Chu et al. [109] demonstrate that instability occurs as soon as the stress path reaches the state boundary surface. Then, the imposed stress can no longer be sustained and, in spite of the soil dilating, large strains develop. Gajo et al. [105] show that, as for loose sands, the high strain rate during instability may yield undrained behaviour of the dense sand. However, the tendency to dilate results in suction and recovery of the soil skeleton. Chu et al. [109] term the instability of dense sand during CSD loading as 'conditional', since, contrary to loose sands loaded in the instability zone, instability only occurs for particular (decreasing p') stress paths.

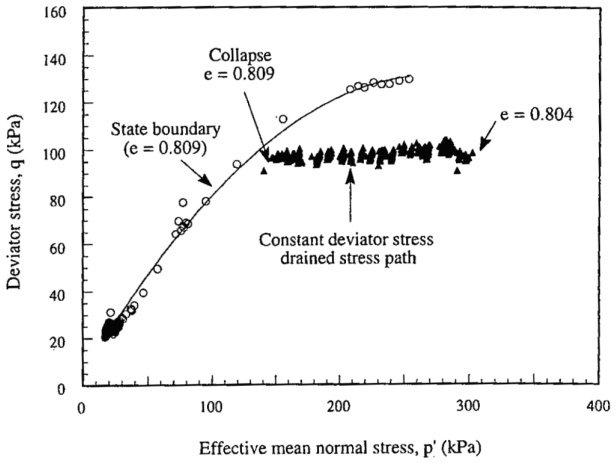


Figure 2.24: Collapse during CSD test conducted on loose sand ($D_e < 10\%$) when stress path reaches state boundary surface [48] defined by effective stress path during undrained test showing liquefaction behaviour.

A third type of control concerns strain path control, that is, an imposed ratio of volumetric strain increment $d\epsilon^{vol}$ over principal strain rate $d\epsilon_1$. Here, D^i is introduced to express the strain increment ratio:

$$D^i = \frac{d\epsilon^{vol}}{d\epsilon_1} \tag{2.7}$$

Note that a ratio of $D^i = 0$ is equal to undrained conditions and a ratio of $D^i = 1$ to oedometric compression. Sasitharan et al. [48] demonstrate that undrained (drainage control) and constant volume (strain path control) triaxial tests conducted under the same conditions yield identical results. In some cases [62, 73], constant volume conditions provide a convenient alternative for complications that may arise during undrained conditions. More generally, strain path control provides a more generic starting point than imposed drainage conditions, which allows the influence of pore water inflow ($D^i < 0$) or outflow ($D^i > 0$) to be treated in the same framework.

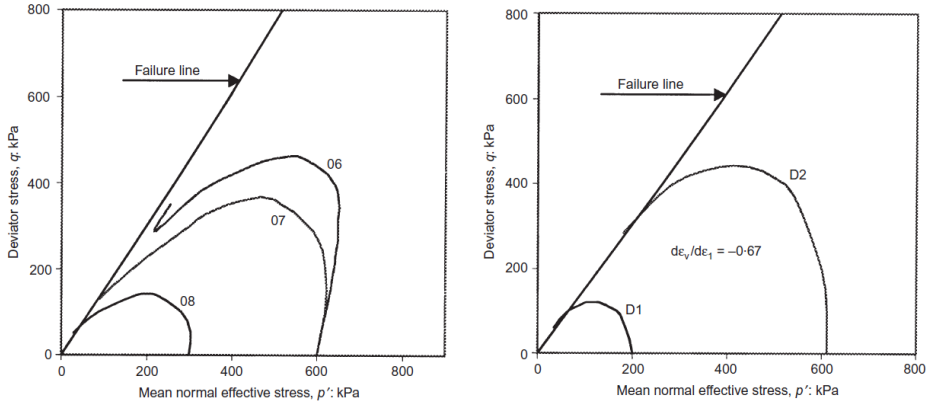


Figure 2.25: Results of undrained triaxial tests on very loose sands (close to minimum density, left) and strain path controlled triaxial tests on very dense sand (close to maximum density, right) [110]

Figure 2.25 depicts both the results of undrained triaxial tests on very loose sand and strain path controlled triaxial tests on very dense sand. The resulting stress paths are similar for both cases, i.e. the tests on very dense sand exhibit (full) liquefaction behaviour under strain path control. The imposed dilation rate of $D^i = -0.67$ is well below the dilation rate that would occur under drained conditions; inflowing pore water enforces additional dilation resulting in instability. However, the loosening of the soil in strain path controlled tests is generally too small to explain the observed instability [65, 111]. Instead, the observed instability should be attributed to soil behaviour under strain path control. A prerequisite for instability of dense sands under strain path control is that the imposed dilation rate D^i is smaller than its 'natural' dilation rate D^s [112]. As D^s depends on the mobilised effective stress ratio σ'_1/σ'_3 and the initial void ratio e [113], the required imposed dilation rate D^i for instability decreases with decreasing shear stress and increasing density [112]. Loose to medium dense sands that exhibit limited liquefaction under undrained conditions are affected by the strain path in a similar way [111]. In case the imposed dilation rate is sufficiently large to suppress the tendency to dilate after the quasi-steady state, limited liquefaction behaviour is turned into full liquefaction behaviour. Conversely, for loose sands a sufficiently high value of D^i, that is extraction of pore water, is required to establish a dilative response [114]. Chu and coworkers [110, 115] demonstrate that, like for loose sands under undrained conditions, runaway instability may occur during strain path controlled loading of dense sands. After bringing a dense sample into a metastable stress state, they maintained the stress state while imposing a sufficiently low value of D^i; a sudden increase was followed by collapse of the sample. It should be stressed that the sample was merely constrained along the certain stress path; injection of water was not actively imposed. The Author concludes that dense sands may exhibit the same (flow liquefaction) behaviour as loose

sands, which requires in both cases strain path control. In the case of dense sands, however, a larger influx of pore water is required, which requires specific boundary conditions.

2.3.4. Void ratio redistribution

The process following the initiation of liquefaction in which water content is redistributed as a result of pore water flow is termed *void ratio redistribution.* Casagrande [23] relates observed differences between strain and stress-controlled undrained triaxial tests to redistribution effects during the 'slow' strain-controlled testing. In addition, he reports isotropically consolidated, cyclic undrained triaxial tests during which water flows from the bottom to the top part of the sample. The bottom part consequently becomes denser and the top part looser. A thin layer of water was observed at moments the effective stresses were zero (liquefaction) and the shear stress reversed in direction. Casagrande attributes void ratio redistribution during element testing to boundary effects, and the stress distribution induced by the triaxial test and the 'pumping action' of the top platen during reversal from compression to extension [23]. Hence, void ratio distribution is considered an artefact.

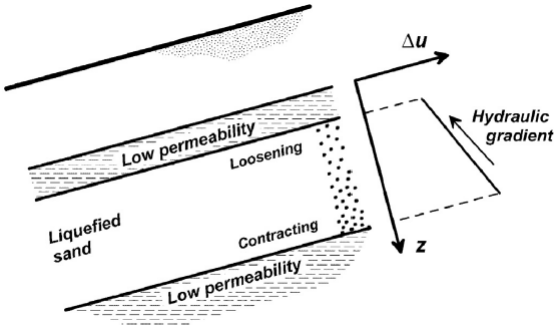


Figure 2.26: Void ratio redistribution in a layer confined by two impermeable layers [116]

Ayoubian and Robertson [117] find the same tendency of void ratio redistribution during monotonical undrained triaxial extension testing. After substantial straining, the upper part of the sample loosened while the lower part densified. The highest void ratio is measured in the zone that fails by necking. Thomson and Wong [72, 118] also attribute undrained failure during triaxial testing to the weakest or loosest zone after void ratio redistribution. However, using X-ray tomography they observe the opposite process of initial non-uniformities being smoothed by void ratio redistribution. This observation throws another light upon the effect of sample preparation techniques on liquefaction behaviour (Figure 2.15). Differences between the undrained response of samples prepared by different sample preparation techniques may be assigned to initial non-uniformities and the effect of void ratio redistribution on the macro response. The *undrained* condition only applies on a global scale, as locally pore water flows from den-

sifying to loosening zones. In this respect, the element test measures the response of a boundary value problem rather than the intrinsic material properties.

Kokusho [119] reports undrained torsional shear tests that aim at replicating the post-liquefaction response of a sand layer sandwiched between two silty seams (Figure 2.26). The vertical movement of the top loading plate is prevented to represent the effect of the overlying silt seam. Undrained, cyclic testing of loose sand yielded liquefaction, followed by re-sedimentation and the formation of a water film layer on top of the sample. As a consequence, shear stresses are no longer transferred through the top plate and the tendency to dilate does not restore the stresses temporarily as it would normally do. The water film acts as a shear stress isolator. The formation of a water film layer below a layer with low permeability was also observed during one-dimensional model tests (Figure 2.27). A cylinder of saturated sand, of height 2 m and diameter 13 cm, liquefied after an impact load by a steel hammer at the base. Figure 2.27 shows the pore pressure development of the soil model with a fine, loose sand and a thin silt interlayer. The silt seam delays pore pressure dissipation in the underlying layer resulting in a large hydraulic gradient over the thin silt layer. The hydraulic gradient pushes the silt seam against the overlying layer of sand, whilst sedimentation takes place in the underlying layer [120]. Consequently, a water film appears immediately after liquefaction and grows in thickness until sedimentation of the underlying layer is completed. The part of the column below the seam that has settled after liquefaction is identified by a constant excess pore pressure. Meanwhile, the water film generates an upward seepage resulting in a gradient in the excess pore pressures with depth in the overlying layer (Figure 2.27). As soon as the sedimentation of the underlying layer has ended the seepage governs the development of the water film that reduces in thickness.

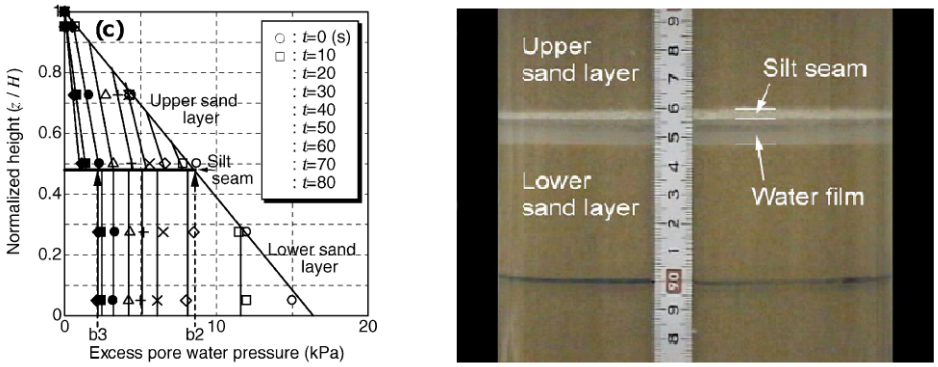


Figure 2.27: Excess pore pressure development after initiation of liquefaction in column of loose sand with silt seam (left [119]); generated water film beneath silt seam (right [121]). Liquefaction induces a gradient in the excess pore water pressure equal to the initial effective stress gradient. At the bottom, the growing settled part is identified by a constant excess pore water pressure. Above the seam, the consolidation of the seam introduces a pore water flow and, as a result, a gradient in the excess pore water pressure.

A second soil model with a layer of fine, loose sand overlying a layer of coarse loose sand did not produce a water film after liquefaction [120]. Instead, turbulence occurred at the boundary between the two layers introducing a thin zone of loosened sand at the bottom of the fine top layer, i.e. as illustrated by Figure 2.26. In both this case and the previous one, liquefaction seems to result in a weakening of the soil conditions. Kokusho [122] demonstrates the effect of void ratio distribution on slope failures using the results from $1g$ shaking table tests. Cases with arc and horizontal silt layers interbedded in a loose packed sandy slope were compared to those without silt layers. In both cases, shaking in the direction perpendicular to the slope yielded the generation of excess pore pressures and deformation of the slope. However, the type, magnitude and duration of movement was strongly affected by the presence of interbedded silt layers. Deformation of the slope without silt layers coincides with the period of shaking and is uniform throughout the geometry. The slopes with interbedded silt layers continue to deform after the shaking has stopped, even though the deformed slopes are gentle. The magnitude of the deformations, that localise around the silt seams, is also larger than for the uniform slope. Kokusho [122] attributes the post-shaking, localised deformation to the observed water film underneath the silt layers which acts as a low-resistance sliding surface. During the test with two horizontal interbedded silt layers the deformation of the slope yielded breakage of silt layers. The consequent upward flow from the water film triggered liquefaction in the upper layer, resulting in further deformation of the slope. Note that the largest deformations are measured during this last phase (Figure 2.28).

Kulasingam et al. [123] elaborated Kokusho's work by conducting centrifuge tests. Properties such as the density, location of silt seams (if any) and intensity and duration of loading were varied during the tests on a slope with (scaled) height of 8 m and slopes of 1v:2h. The deformations of the model slopes without silt seams were limited, even for a relative density of merely 20 %. The response of the slopes with silt seams did develop localised failure just below the silt layer, at least in some cases. As in many of these tests identically high excess pore pressures were generated, the occurrence of failure is attributed to void ratio redistribution. Based on the test results, Kulasingam et al. assign the occurrence of failure to the (inadequate) capacity of the loosening soil underlying the silt layer to dilate and absorb the pore water that is expelled from the densifying layer (Figure 2.26). The strain path imposed by the infiltrating water may yield instability (Figure 2.25) or may increase the susceptibility of the loosening soil. As a consequence, the initial density is not the only factor of importance. Backanalyses of the test results show that the inferred (residual) strength did not correlate solely with the initial density of the sand [123]. The amount of water expelled from the densifying sand also depends on the thickness of the layer, the duration of loading and the sequence of loading, i.e. the susceptibility to liquefaction increases during a loading sequence as the top part of the layer loosens. Furthermore, Kulasingam et al. conclude that the static shear stress is of importance as well. The capacity of the soil to dilate and absorb infiltrating pore water also depends on the thickness of the dilating zone, i.e. the shear band. The notion of localisation during flow liquefaction contradicts the conventional conception of a diffuse mechanism and complicates (numerical) analyses of the development of a failure mechanism [124, 125].

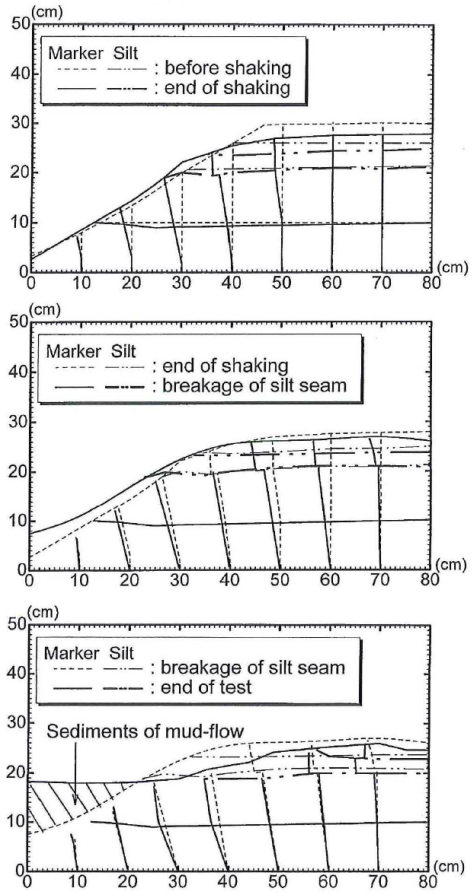


Figure 2.28: Three consecutive phases during 1g shaking table test with two horizontal silt seams: deformations during shaking phase until approximately $t = 1$ s (top), void ratio redistribution from end of shaking until breakage of silt seem at approximately $t = 3$ s (middle) and deformations during final stage of test until $t = 50$ s (bottom) [122].

The occurrence of liquefaction flow failure reflects the response of the entire system, rather than the state of the soil. The limitations of relationships between the (residual) strength and density of case histories of liquefaction flow slides should be acknowledged. During void ratio redistribution the density changes, which means that both the density before and after failure are not necessarily representative measures for the occurrence of a flow slide. Void ratio redistribution provides a plausible explanation for case histories occurring under unusual circumstances. Case histories have been reported with much lower backcalculated strengths than measured during the corresponding laboratory tests [126]. Seid and Byrne [125] note that submarine flow failures occurred in slopes normally less than 5° and sometimes less than 1°. Furthermore, void ratio redistribution explains why liquefaction flow slides have occurred after, rather than during, earthquake shaking [125]. During the well-known case of the Lower San Fernando Dam, flow failure occurred one minute after the strong shaking of the earthquake ceased. Void ratio distribution also addresses the role of fine interlayers. As noted before, many case histories involve sand with fines (see Subsection 2.3.2). The segregation that is likely to occur during deposition in low-energy environments promotes void ratio redistribution. Void ratio distribution is mainly associated with earthquake-induced flow slides. Kokusho [120] demonstrates by one-dimensional column tests that short motions also induce significant void ratio redistribution, provided that the layer thickness is sufficiently large. The test series conducted in Delft [35, 39, 40] stressed the importance of re-sedimentation on the development of liquefaction flow slides (see Subsection 2.2.1). It is likely that void ratio redistribution is not a testing artefact but plays a prominent role in the development from flow liquefaction into a liquefaction flow slide, particularly for layered deposits or slopes that extend above water [119]. However, there is no direct field evidence of void ratio redistribution during flow failures [125]. The effects of void ratio redistribution are not yet fully understood, let alone accounted for in engineering practice [125].

2.3.5. Concluding remarks on element testing

Results from element testing relate flow liquefaction to the occurrence of instability. The peaks of the undrained effective stress paths define a zone of instability in the effective stress space, in which soils susceptible to flow liquefaction collapse under stress-controlled, undrained conditions. However, usually strain-controlled tests are conducted in order to be able to define both the pre- and post-peak portion of the stress path, thereby ignoring possible rate effects. More specifically, it is conventional to conduct isotropically consolidated, undrained triaxial tests on loose sand as prepared by moist tamping to characterise liquefaction behaviour. The Author considers these tests appropriate to reproduce flow liquefaction behaviour, but not necessarily representative for field conditions. Engineering practice usually accounts solely for the effect of density on the susceptibility to liquefaction. This section on element testing has shown that each of the testing specifications affects flow liquefaction behaviour. Density is of importance, but should always be considered in conjunction with the fabric of the soil and the imposed stress path. It is concluded that:

- The fabric of the soil defines another dimension to the susceptibility to flow liquefaction in addition to the density or state parameter. The fabric affects the intrinsic

susceptibility to liquefaction and the possible range of densities. Undrained tests conducted under identical states of the soil may exhibit the full range of possible responses, depending on the initial fabric [64]. Vaid et al. [64] demonstrate that the relative density after using moist tamping can be as low as −20 %.

- The fabric cannot be considered separately from the stress path; the combination of both affects liquefaction behaviour. Hight et al. [13] turned a dilative undrained response under triaxial extension into liquefaction behaviour by adding merely 1 % of mica. Adding the same amount during triaxial compression, however, increased the stability.

- With respect to stress path dependence, triaxial compression defines the upper limit of undrained behaviour, triaxial extension the lower. Sand deposited under water often yields a dilative undrained response during triaxial compression, even for the loosest state [41, 63]. On the other hand, during triaxial extension tests liquefaction behaviour has been noted for relative densities above 60 % [92, 102]. Preshearing may amplify the effect of the stress path. Di Prisco et al. [103] show that sand with a relative density of almost 100 % shows (limited) liquefaction behaviour under extension after substantial preshearing under compression. The undrained shear strength is affected in a similar way; Sadrekarimi [127] reports peak undrained shear strengths under extension a factor of 1.5 to 2 lower than compression, while Byrne et al. [42] report a factor of 5 for the residual undrained shear strengths. Vaid et al. [102] report a test in which the peak undrained shear strength under extension is reduced by a factor of 1.6 as a result of preshearing.

- Flow liquefaction should not strictly be considered an undrained mechanism. It may be the result rather than cause of failure during a (drained) decrease of mean effective stresses [48, 105, 109]. The imposition of undrained conditions merely implies a strain path with a constant volume condition. More severe strain paths, such as imposed dilation, may yield instability of dense sand as well. Chu and Leong [110] report instability of a sample with an initial relative density D_e of nearly 90 %.

- The coupled processes following flow liquefaction may yield further degeneration of the strength of the subsoil due to void ratio redistribution and, eventually, a liquefaction flow slide. Failure may be induced at the top of the liquefied layer, where a dilating strain path is imposed. Void ratio redistribution puts the importance of the initial density of the soil further in perspective; failure reflects the response of the entire system [125].

2.4. Assessment of liquefaction flow slides

2.4.1. Hypotheses on the initiation of flow slides

This chapter is concluded by merging the information gathered in the previous sections into hypotheses of the initiation of liquefaction flow slides. Unlike perhaps suggested by the term initiation, this consideration is not restricted to the triggering of flow slides. The Author believes the initiation to be the response of the entire system, including the

deposition processes of sand and its corresponding layering and properties, the initial geometry, trigger and the possible development into a large failure mechanism. The previous sections have demonstrated the variations both in terms of case histories and underlying processes and mechanisms. It is therefore chosen to treat multiple *hypotheses*, as a single hypothesis would not take account of the complexity of the phenomenon. The analysis is limited to under water slopes, thereby excluding flow slides induced by saturation of the subsoil. Furthermore, it is presumed that the sand is deposited under water in a low-energy environment, which was the case in the vast majority of reported case histories.

Uniform, fresh deposition in the horizontal plane most likely yields:

- Segregation of grain size with depth, with possible silty interlayers due to the variation of the deposition process and, by approximation, clean sand throughout the rest of the profile.
- Mechanical behaviour of the bulk governed by the mechanical properties of the clean sand, thereby implicitly assuming that the amount of fines is relatively small, that is, comprising less than ~ 10 % of the bulk mass [50].
- Loose to medium dense sand with a state parameter just below (dense) of the critical state line ($\psi < 0$) [1].
- Inherent cross-anisotropic soil conditions bounded by the weakest (contractive) response under triaxial extension and the strongest response, presumably even dilative, under triaxial compression for these densities.
- High permeability of the (clean) sand, that is significantly reduced when silty interlayers are present.
- Pre-shearing under compression (K^0 conditions).

The Author concludes that the subsoil is initially stable and that it is unlikely that flow liquefaction is initiated under these conditions. It is worth mentioning that even if the sand would have been deposited in an extremely loose state, an initially metastable state would be unlikely due to the effect of K^0 preshearing [11, 103].

A slope can be created either on (fill) or in (cut) the subsoil. There are fundamental differences between both. The construction of a fill implies another deposition process, albeit at a much faster rate and under a slope angle. The inherent anisotropy of the soil deposited under a slope angle is characterised by a rotation of the preferred directions [128]. Flow liquefaction may be induced if the slope is constructed too fast and too steep, and slope stability can be considered a staged construction problem [108]. Alternatively, flow liquefaction may be induced in the fill sand that experiences a redistribution of pore pressures as a result of sedimentation and (self-weight) consolidation. In addition to the loading rate, expressed by the production rate (Subsection 2.2.1), and slope, the mean grain size plays an important role [39, 40]. Although an unwanted event in some cases, it may be argued that liquefaction flow slides are inevitably part of the development of

slopes during construction of underwater fills, particularly for fine sands. Cut slopes are created by removing part of the subsoil, for instance by erosion or dredging. Unlike fills, the sand in the slope is fully consolidated and characterised by an inherent anisotropy governed by vertical deposition. Furthermore, the cutting of the slope entails an unloading process in terms of mean effective stress. The sand is overconsolidated and instability is presumably triggered at higher mobilised strengths [103].

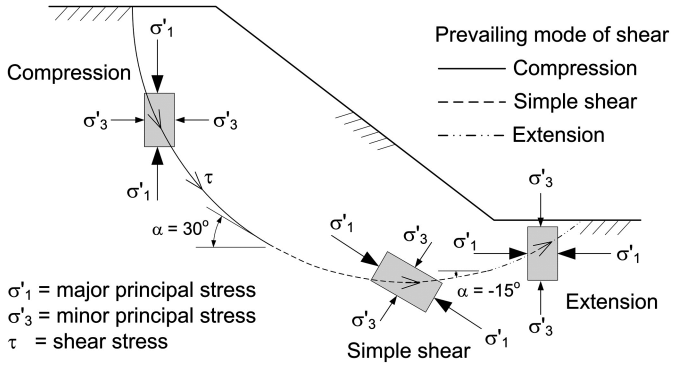


Figure 2.29: Rotation of principal effective stresses along potential slip surface characterised by angle α. The failure mode is subdivided into zones governed by compression ($\alpha > 30°$), simple shear ($30° > \alpha > -15°$) and extension ($\alpha < -15°$) [127].

Irrespective of whether a cut or fill slope is considered, a varying stress anisotropy characterises the stresses in a slope (Figure 2.29). The anticipated undrained response weakens as the element under consideration moves from the crest to the toe of the slope, i.e. as depicted by Figure 2.20. Furthermore, the initial stresses will most likely be restrained by plane strain conditions. An initially stable slope is taken as the starting point, which suggests that the soil is pre-sheared as depicted in Figure 2.29, albeit under drained conditions. Considering that the slope has experienced small perturbations during construction and that drained pre-shearing increases the mobilised strength at instability, it is assumed that the stress states in the slope lie below the zone of instability, i.e. below the instability line or state boundary surface that is depicted by Figure 2.23. Di Prisco et al. [103] demonstrate that spontaneous, undrained collapse of a loose ($D_e = 20\%$) soil element subjected to infinite slope conditions does not occur unless the slope becomes steep (1v:2h).

At this stage matters start becoming complicated. Assuming an undrained response throughout the entire slope, excess pore pressures and a reduction in strength are anticipated in the toe of the slope, whereas a stronger response, perhaps even including suction and strain hardening, are anticipated near the crest. However, the trigger may affect the slope only locally. Hight et al. [13] attribute the flow failures during the construction of Jumuna Bridge to the dredging of the weakest zone of the slope; the toe. The fact that the slope did not fail during the CANLEX field event is partly ascribed to the

high undrained strength of the soil under the dominant loading direction during back filling, i.e. compression [42]. Furthermore, the depth plays an important role during the triggering of liquefaction. The shear stresses are the largest close to the surface, but the susceptibility is likely to increase with increasing depth due to suppressed dilation and decreasing overconsolidation effects.

In addition to construction activities, Subsection 2.1.6 identifies earthquakes and tides as important main trigger mechanisms. Earthquakes contain all ingredients to induce flow failures: sufficiently fast loading to ensure undrained conditions for the entire slope, increased loading of the soil due to inertial effects and cyclic stress rotation during loading. Moreover, earthquakes are global triggers, in that they induce excess pore pressures throughout the entire slope and subsoil which increases the likelihood for secondary effects (void ratio redistribution). The actual effect of tidal variations as a trigger is less obvious. Experience in the Netherlands is that flow slides mainly occur during an extreme, spring ebb tide, i.e. drawdown conditions (see Subsection 2.1.3). The increased water level in the slope induces a pressure gradient and, as a consequence, a pore water flow during the ebb tide (Figure 2.30).

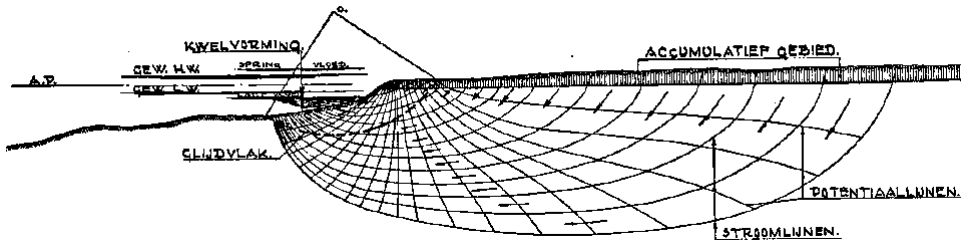


Figure 2.30: Lines of equal flow and potential in a slope during ebb tide [21].

In order to study and quantify the effects of pore water flow on the stability of slopes, the simplified case of a homogeneous, infinite slope is considered. The assessment of the stability of an infinite slope can easily be extended for simple cases of ground water flow [129]. Assuming that the stresses in the slope do not vary in the direction of the slope, the safety factor of an infinite slope with angle α and soil with friction angle ϕ reads for the case without groundwater flow:

$$SF = \frac{\tan\alpha}{\tan\phi} \tag{2.8}$$

Then, the case considered is extended by a uniform, parallel flow directed downslope. When the downstream water level is much lower than the upstream level, $p = 0$ along the surface of the slope and the safety factor is given by:

$$SF = \frac{\gamma - \gamma^w}{\gamma}\frac{\tan\alpha}{\tan\phi} \tag{2.9}$$

Herein, γ and γ^w denote the volumetric weights of the saturated soil and water, respectively. The term $(\gamma - \gamma^w)/\gamma$ equals approximately 0.56 for loose sand, which means that, irrespective of the slope, the stability strongly decreases as a result of groundwater flow. This term is fully attributed to an increase of shear stress as a result of the flow conditions considered. The third case concerns horizontal outflow, while the other conditions are kept the same as in the previous case. Now the safety factor reads:

$$SF = \frac{\gamma - \frac{\gamma^w}{\cos^2 \alpha}}{\gamma} \frac{\tan \alpha}{\tan \phi} \tag{2.10}$$

The term $1/\cos^2 \alpha$ results in a further decrease in the safety factor, which depends on the slope angle or, more specifically, on the angle between the slope and the direction of ground water flow. Hence, the safety factor will decrease when the direction of groundwater flow is rotated further in the clockwise direction. Contrary to the previous case of parallel flow, this decrease is fully attributed to a decrease in normal effective stress.

The Author concludes that groundwater flow during rapid drawdown conditions affects slope stability in two ways: it strongly increases the shear stress exerted on the soil and imposes an excess pore pressure that depends on the direction of flow. Both the implied stress path and magnitudes of these loads suggest that tidal variations may be more than a minor trigger. However, the situation as sketched here also (over)simplifies the conditions during an ebb tide. The tidal range is usually small compared to the height of the slope, whilst the actual gradient depends on the rate of drawdown and permeability of the soil. Assuming normal consolidation the slope stability will be most critical near the surface, where the shear stresses are the largest and the direction of flow lines is approximately perpendicular to the slope (Figure 2.30). As a consequence, ground water flow during an ebb tide may yield wash-out and micro-instability at the surface. The change in geometry may possibly lead to the initiation of a flow slide. In the Netherlands, a common (and successful) mitigating measure against flow slides in tidal waters is the application of scour protection.

The Author postulates that, as for the triggering of liquefaction flow slides, the subsequent development after triggering is governed by redistribution of stresses, anisotropy and consolidation. Loose to medium dense sands are likely to produce localised, retrogressive flow slides (Figure 2.1). The first slide leaves a relatively steep scarp, which may be less stable than the initial slope [32]. The loss of lateral support of the soil in the remaining slope should be compensated by an increase in shear stress. Considering the rapid development of liquefaction flow slides, the first failure is likely to produce (almost) undrained behaviour in the remaining slope. Hence, a first liquefaction flow slide may be the trigger for a subsequent slide where, again, overconsolidation effects at the surface and rotation of the principal effective stresses will be of importance. Excess pore pressures are likely to be generated first within the slope, which may develop into a deep slip plane or may push the mechanism to the surface during consolidation and resedimentation. Eventually, more complex processes will be of importance when considering the further development of liquefaction flow slides, such as three-dimensional effects, erosion and sedimentation (breaching), and possible void ratio redistribution after fail-

ure. These are out of scope when considering the initiation of liquefaction flow slides. Unfortunately, the resulting post-failure cross-sectional profile does play an important role in frequently used assessment methods, as will be explained in the next section.

The assessment of liquefaction flow slides requires accounting for coupling between the effects of state parameter, anistropy, pore pressure generation and redistribution of stresses. The anticipated variation in responses within a slope, even for the same value of the state parameter, complicates assessments. Unlike sometimes suggested, the importance of the trigger is recognised, which specifies the magnitude, direction and rate of loading. The trigger specifies which of the responses governs slope stability.

The hypothetical nature of this subsection is emphasised, which has been based on the current state of knowledge as surveyed in the first part of this chapter. Hence, the hypotheses are based on the most likely field conditions. This does not alter the fact that there are still uncertainties in the understanding and assessment of liquefaction flow slides. Even for homogeneous, controlled conditions laboratory tests yield different, sometimes even opposite results with respect to the effect of the density, fabric, mean effective stress, initial shear stress and stress (and strain) path. Field conditions complicate matters further by introducing heterogeneity, while the actual soil properties and stresses are, at best, uncertain. Consider for instance the different possible hypotheses on the occurrence of liquefaction flow slides of silty slopes. Based on laboratory tests it may be concluded that silty slopes are prone to liquefaction, because of: the (intrinsic) liquefaction potential of silty soils [130], the likelihood for deposition in a loose state [18], the increased susceptibility at high [130] or low mean effective stresses [11] and the increased strength anisotropy at low mean effective stress [13]. Under field conditions the segregation of grain sizes also requires considering the heterogeneity of mechanical properties of the soil [4], reduced permeability [11] and increased likelyhood of void ratio redistribution [119]. Which of these factors -presumably more than one- governs slope stability depends on the case considered, but is generally unknown.

The gap in terms of knowledge between elementary soil behaviour and field response is evident. The results from element tests provide a lot of separate pieces of information that can be put together in different ways. Case histories generally do not provide sufficient information to put the puzzle together.

2.4.2. Methods of assessment

Existing methods for the assessment of liquefaction flow slides commonly address three questions:

1. Susceptibility: Is the subsoil susceptible to flow liquefaction?
2. Triggering: Is flow liquefaction triggered under the conditions considered?
3. Post-triggering: Is the slope stable if flow liquefaction is triggered?

The decoupling of the assessment procedure suits the application of simple methods for slope stability analysis that are commonly employed in engineering practice. The

susceptibility analysis is normally based on SPT and CPT data from case histories, see e.g. [10]. The triggering analysis, if any, assumes undrained conditions a priori. Flow liquefaction is triggered when the instability or peak strength is exceeded locally. The instability strength has also been backcalculated from case histories and can be further supported by laboratory data [131]. The post-triggering analysis implies a slope stability analysis with a representative strength being assigned to the layer that is triggered. Again, strength measures have been derived from both case histories and laboratory tests [116, 132]. Hence, existing assessment methods have a strong empirical basis.

Only few existing methods address each of the three steps listed above [131–133]. Often it is assumed that when the soil is susceptible to liquefaction (Subsection 2.1.2) there will always be an undrained trigger large enough to initiate flow liquefaction [8, 10, 50]. The triggering analysis is ignored. In this case flow liquefaction may be assessed by determining the zone in a slope that is metastable, i.e. in a state of stress above the instability line after stresses are generated under drained conditions [7, 131, 134], but still below the zero-dilatancy line that marks the transition to a dilative response, if any. The question is, what strength value should be assigned to the zone that is presumed to be triggered: the peak (instability) strength or residual (liquefied) strength? Methods that assign the peak strength [49, 109, 135, 136] essentially merge the triggering and post-triggering analysis. These methods were mainly based on the initiation of flow failure, i.e. based on pre-failure geometry and soil properties, during cases induced by a presumably static trigger. Alternatively, a residual strength (ratio) can be assigned. The relation depicted in Figure 2.31 was mainly based on the post-failure cross sections of cases, including those induced by earthquakes. This figure in fact merges all three steps of the assessment in one diagram. It should be noted that Figure 2.31 provides a frequently used tool in engineering practice worldwide [50].

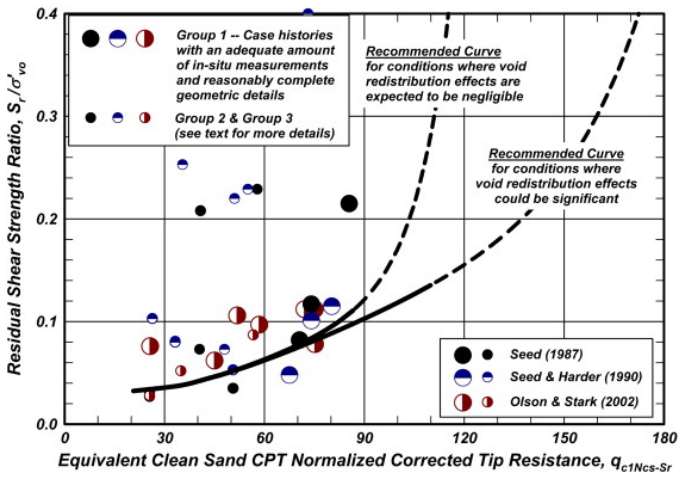


Figure 2.31: Relation between undrained (liquefied) strength ratio and normalised cone resistance [116].

The scatter of data from case histories in Figure 2.31 illustrates the uncertainties of simple assessment methods. As a consequence, the presumed representative relation ('Recommended Curve', Figure 2.31) suggests a brittle relationship between normalised cone resistance $q_{c1Ncs\text{-}Sr}$ and liquefied strength ratio S_r/σ'_{v0}, with extremely low strength values for low resistances. For instance, a value of $S_r/\sigma'_{v0} = 0.10$ corresponds by approximation with a stable, infinite slope of (milder than) 1v:10h (Equation 2.8). The consequent conservative outcome of assessments does not correspond with the notion that many slopes consist of presumably susceptible sands, but have been stable for many years.

The noted conservatism in existing assessment methods is attributed to the shortcuts taken to keep these methods simple. Firstly, the information provided by case histories is poor (see Subsection 2.1.2). For instance, Figure 2.31 only includes four cases where CPT measurements were taken; the other points were derived from correlations with SPT readings. Secondly, the method decouples susceptibility from the triggering of flow liquefaction. The range of presumably susceptible states, as expressed by the cone resistance (CPT) or blow count (SPT), is large as the susceptibility analysis does not discriminate between stress or strain paths, not to mention void ratio redistribution. Thirdly, the method assumes undrained conditions, which is only likely in sands under particular conditions [137]. Fourthly, the Author questions the method used to backcalculate the liquefied strength (ratio) from case histories. Relations such as those depicted in Figure 2.31 are derived from post-failure cross sections [2]. It is thus presumed that the post-liquefaction slope is representative for the liquefied strength of the sand that was originally part of the slope, which may not be the case. During failure the density of the sand can be altered by water entrainment and void ratio redistribution. Besides, the post-failure slope is not only the result of the soil properties but also of the momentum of the slope during failure. The breaching failure mechanism (Subsection 2.1.6) illustrates the unimportance of the initial soil properties for the final slope; breaching occurs in (very) dense sands but yields slopes that can be as gentle as a few degrees. Laboratory testing provides an alternative for the determination of the residual undrained strength for site specific conditions [138]. However, Chu and Wanatowski [137] demonstrate that the residual undrained strength cannot be measured reliably in the laboratory due to severe distortion of the sample at large strains, uncertainties related to stress or strain-controlled response, variations with the type of test conducted and the large variation of strength values with small variations in void ratio.

Ignoring the trigger introduces another source of conservatism to the assessment, which is attributed to the lack of detailed information about triggers from case histories (Subsection 2.1.3). Only in few cases was sufficient information available to analyse the initiation of a liquefaction flow slide from the prefailure geometry. The failure of the San Fernando Dam, initiated after the earthquake shaking ceased, has been backanalysed from both the prefailure and postfailure geometry. The resulting strength values [116, 138] are 36 kPa and 5 kPa respectively, i.e. a difference of more than a factor seven. Using the instability (peak) strength thus provides a much less conservative alternative for the liquefied strength. Whether the peak (instability) strength or residual (liquefied) strength should be used in assessments is a complicated issue, that can only be resolved based

on improved, detailed information from flow slides and advanced models. It is clear that the instability strength should be used with caution, whereas the liquefied strength would result in unduly conservative assessments. That is to say, it would result in conservative assessments provided that void ratio redistribution effects can be neglected. Void ratio redistribution may yield even lower strength values than depicted in Figure 2.31 or a (too) optimistic assessment based on the initial soil condition [137]. Idriss and Boulanger [116] acknowledge that void ratio redistribution is likely to have played a role in the majority of case histories, particularly for loose sands. However, Figure 2.31 suggests an effect at higher densities, while one curve is defined at low densities. The current state of knowledge does not allow to specify the effect of void ratio redistribution in more detail [116].

The above mentioned assessment methods are referred to as screening methods [10]. They suit the assessment of low-risk projects or the first screening of high-risk projects, but what is the alternative if a more advanced approach is required? Advanced stability analyses were applied in the past using the finite element method, see e.g. [42, 139]. However, these analyses also have limitations, e.g. they usually assume undrained behaviour, suffer from numerical instability and demand time and skills to carry out the analysis and interpret the results. The current, mainstream commercial software does not yet provide the means to conduct these analyses, which are commonly thus not applied in engineering practice. An even more fundamental deficiency of advanced methods is the need for extensive input, while its successful application still relies on the same, narrow empirical basis that is used for simple assessment methods. The Author recognises the necessity to apply the finite element method to account for the coupled processes that govern the initiation of liquefaction flow slides. The second prerequisite to improve the assessment of liquefaction flow slides concerns the basis for verification and validation of stability analyses. The existing empirical basis lacks detailed information, particularly with respect to the trigger. Experience has shown that capturing the exact moment of triggering during flow failures is nearly impossible, which leaves the post-failure cross-sectional profile (and soil properties) as the most valuable information. The popularity of assessment methods using the residual undrained strength is hereby explained, but its limitations should be recognised.

References

[1] M. Jefferies and K. Been, *Soil liquefaction: a critical state approach* (Taylor & Francis, 2006).

[2] S. Olson, *Liquefaction analysis of level and sloping ground using field case histories and penetration resistance*, Ph.D. thesis, University of Illinois-Urbana-Champaign (2001).

[3] A. Andresen and L. Bjerrum, *Slides in subaqueous slopes in loose sand and silt,* Norwegian Geotechnical Institute Publication **081**, 1–9 (1968).

[4] M. Hicks and C. Onisiphorou, *Stochastic evaluation of static liquefaction in a predominantly dilative sand fill,* Géotechnique **55**, 123–133 (2005).

[5] P. Robertson, *Submarine slope instability at the west guide bund, Jamuna bridge report*, Tech. Rep. (University of Alberta, 1996).

[6] M. Wilderom, *Resultaten van het vooroeveronderzoek langs de zeeuwse stromen*, Tech. Rep. Nota 75.2 (Rijkswaterstaat, Directie Waterhuishouding en Waterbeweging, District Kust en Zee, Studiedienst Vlissingen, Vlissingen, 1979).

[7] T. Stoutjesdijk, M. de Groot, and J. Lindenberg, *Flow slide prediction method: influence of slope geometry,* Canadian geotechnical journal **35**, 43–54 (1998).

[8] F. Silvis and M. de Groot, *Flow slides in the netherlands: experience and engineering practice,* Canadian Geotechnical Journal **32**, 1086–1092 (1995).

[9] F. Silvis, *Statistische analyse zettingsvloeiingen*, Tech. Rep. CO-416670/12 (Laboratorium voor Grondmechanica, Delft, the Netherlands, 1985).

[10] P. Robertson, *Evaluation of flow liquefaction and liquefied strength using the cone penetration test,* Journal of Geotechnical and Geoenvironmental Engineering **136**, 842–853 (2009).

[11] P. Lade and J. Yamamuro, *Evaluation of static liquefaction potential of silty sand slopes,* Canadian Geotechnical Journal **48**, 247–264 (2011).

[12] J. Sladen, R. D'Hollander, J. Krahn, and D. Mitchell, *Back analysis of the nerlerk berm liquefaction slides,* Canadian Geotechnical Journal **22**, 579–588 (1985).

[13] D. Hight, V. Georgiannou, P. Martin, and A. Mundegar, *Flow slides in micaceous sands,* in *Proceedings of the International Symposium on Problematic Soils, IS-TOHOKU* (1999) pp. 945–958.

[14] A. Koppejan, B. van Wamelen, and L. Weinberg, *Coastal flow slides in the dutch province of zeeland,* in *Proceedings of the 2nd International Conference on Soil Mechanics and Foundation Engineering*, Vol. 5 (Rotterdam, the Netherlands, 1948) pp. 89–96.

[15] D. Varnes, *Slope movement types and processes*, Special report 176 (Transportation Research Board Special Report, Washington, DC, 1978) chapter 2, pp. 12-33.

[16] J. Sladen, R. D'Hollander, J. Krahn, and D. Mitchell, *Back analysis of the nerlerk berm liquefaction slides: Reply,* Canadian Geotechnical Journal **24**, 179–185 (1987).

[17] L. Bjerrum, *Subaqueous slope failures in norwegian fjords,* Norwegian Geotechnical Institute Publ (1971).

[18] K. Terzaghi, *Varieties of submarine slope failures,* in *Proceedings of the 8th Texas Conference on Soil Mechanics and Foundation Engineering* (Austin, USA, 1956) pp. 1–41.

[19] Q. van de Linde, *Oevervallen, zettingsvloeiingen of kwelafschuivingen?, discussie,* Waterbouwkundig Tijdschrift O.T.A.R. **June**, 170–174 (1943).

[20] Q. van de Linde, *Oevervallen, zettingsvloeiingen of kwelafschuivingen (vervolg)?* Waterbouwkundig Tijdschrift O.T.A.R. **July**, 1–6 (1943).

[21] P. Barentsen, *Oevervallen, zettingsvloeiingen of kwelafschuivingen?* Waterbouwkundig Tijdschrift O.T.A.R. **April**, 131–139 (1943).

[22] K. Been, B. Conlin, J. Crooks, S. Fitzpatrick, M. Jefferies, B. Rogers, and S. Shinde, *Back analysis of the nerlerk berm liquefaction slides: Discussion,* Canadian Geotechnical Journal **24**, 170–179 (1987).

[23] A. Casagrande, *Liquefaction and cyclic deformation of sands, a critical review,* in *5th Pan-American Conference on Soil Mechanics and Foundation Engineering,* Vol. 5 (Buenos Aires, Argentina, 1975) pp. 79–133.

[24] K. Meijer and A. van Os, *Pore pressures near moving underwater slope,* Journal of the Geotechnical Engineering Division **102**, 361–372 (1976).

[25] W. van Leussen and J. Nieuwenhuis, *Soil mechanics aspects of dredging,* Géotechnique **34**, 359–381 (1984).

[26] V. Torrey III, J. Dunbar, and R. Peterson, *Retrogressive failures in sand deposits of the Mississippi River. Report 1. Field investigations, laboratory Studies and analysis of the hypothesized failure mechanism*, Tech. Rep. (US Army Engineer Division, 1988).

[27] C. van Rhee and A. Bezuijen, *The breaching of sand investigated in large-scale model tests,* Coastal Engineering Proceedings **1** (1998).

[28] J. van Den Berg, A. van Gelder, and D. Mastbergen, *The importance of breaching as a mechanism of subaqueous slope failure in fine sand,* Sedimentology **49**, 81–95 (2002).

[29] D. Mastbergen and J. van den Berg, *Breaching in fine sands and the generation of sustained turbidity currents in submarine canyons,* Sedimentology **50**, 625–637 (2003).

[30] L. Bjerrum, *Stability of natural slopes in quick clay,* Géotechnique **5**, 101–119 (1955).

[31] G. Meyerhof, *The mechanism of flow slides in cohesive soils,* Géotechnique **7**, 41–49 (1957).

[32] R. Mitchell and A. Markell, *Flowsliding in sensitive soils,* Canadian Geotechnical Journal **11**, 11–31 (1974).

[33] A. Locat, H. Jostad, and S. Leroueil, *Numerical modeling of progressive failure and its implications for spreads in sensitive clays,* Canadian Geotechnical Journal **50**, 961–978 (2013).

[34] D. Eckersley, *Instrumented laboratory flowslides,* Géotechnique **40**, 489–502 (1990).

[35] M. De Groot, J. Lindenberg, D. Mastbergen, and G. Van den Ham, *Large scale sand liquefaction flow slide tests revisited,* in *Eurofuge* (Delft, the Netherlands, 2012) pp. 1–22.

[36] F. Molenkamp and R. van Os, *Liquefaction test in the Brutus Tank*, Tech. Rep. CO-SE-690504/2 (Delft Geotechnics, Delft, the Netherlands, 1987).

[37] F. Molenkamp, *Elasto-plastic double hardening model MONOT*, Tech. Rep. CO-218598 (Delft Geotechnics, Delft, the Netherlands, 1981).

[38] F. Molenkamp, Personal communication (2014).

[39] D. Mastbergen, J. Winterwerp, and A. Bezuijen, *On the construction of sand fill dams—part 1: Hydraulic aspects,* in *International Symposium on Modelling of Soil-Water-Structure Interactions*, edited by P. Kolkman, J. Lindenberg, and K. Pilarczyk (Balkema, Rotterdam, 1988) pp. 353–362.

[40] A. Bezuijen and D. Mastbergen, *On the construction of sand fill dams—part 2: Soil mechanical aspects,* in *International Symposium on Modelling of Soil-Water-Structures Interactions*, edited by P. Kolkman, J. Lindenberg, and K. Pilarczyk (Balkema, Rotterdam, 1988) pp. 363–371.

[41] P. Robertson, C. Wride, B. List, U. Atukorala, K. Biggar, P. Byrne, R. Campanella, D. Cathro, D. Chan, K. Czajewski, *et al.*, *The canlex project: summary and conclusions,* Canadian geotechnical journal **37**, 563–591 (2000).

[42] P. Byrne, H. Puebla, D. Chan, A. Soroush, N. Morgenstern, D. Cathro, W. Gu, R. Phillips, P. Robertson, B. Hofmann, *et al.*, *Canlex full-scale experiment and modelling,* Canadian geotechnical journal **37**, 543–562 (2000).

[43] S.-S. Park and P. Byrne, *Stress densification and its evaluation,* Canadian Geotechnical Journal **41**, 181–186 (2004).

[44] A. Casagrande, *Characteristics of cohesionless soils affecting the stability of slopes and earth fills,* Contributions to Soils Mechanics, 1925-1940 , 257–277 (1940).

[45] G. Castro, *Liquefaction of sands*, Ph.D. thesis, Harvard University, Cambridge, Massachutes (1969).

[46] F. Molenkamp, *Material instability for drained and undrained behaviour, part i: Shear band generation,* International Journal for Numerical and Analytical Methods in Geomechanics **15**, 147–168 (1991).

[47] F. Molenkamp, *Material instability for drained and undrained behaviour, part ii: Combined uniform deformation and shear-band generation,* International Journal for Numerical and Analytical Methods in Geomechanics **15**, 169–180 (1991).

[48] S. Sasitharan, P. Robertson, D. Sego, and N. Morgenstern, *Collapse behavior of sand,* Canadian Geotechnical Journal **30**, 569–577 (1993).

[49] P. Lade, *Static instability and liquefaction of loose fine sandy slopes,* Journal of Geotechnical Engineering **118**, 51–71 (1992).

[50] J. van't Hoff and A. Nooy van der Kolff, *Hydraulic Fill Manual: For Dredging and Reclamation Works* (CRC Press, Leiden, the Netherlands, 2012).

[51] R. de Jager, *The behaviour of soil during static liquefaction*, Master's thesis, Delft University of Technology (2006).

[52] J. Lindenberg and H. Koning, *Critical density of sand,* Géotechnique **31**, 231–245 (1981).

[53] H. Zhang and V. Garga, *Quasi-steady state: a real behaviour?* Canadian Geotechnical Journal **34**, 749–761 (1997).

[54] H. Zhang, V. Garga, Y. Vaid, A. Eliadorani, S. Sivathayalan, M. Uthayakumar, M. Yoshimine, and J. Chu, *Quasi-steady state: a real behaviour?: Discussion,* Canadian Geotechnical Journal **36**, 182–193 (1999).

[55] K. H. Roscoe, A. Schofield, and C. Wroth, *On the yielding of soils,* Géotechnique **8**, 22–53 (1958).

[56] K. Been, M. Jefferies, and J. Hachey, *The critical state of sands,* Géotechnique **41**, 365–381 (1991).

[57] K. Been and M. Jefferies, *A state parameter for sands,* Géotechnique **35**, 99–112 (1985).

[58] M. Satake, *Constitution of mechanics of granular materials through the graph theory,* in *Proceedings of the U.S.–Japan seminar on Continuum Mechanical and Statistical Approaches in the Mechanics of Granular Materials* (Gakujutsu Bunken Fukyu-Kai, Tokyo, Sendai, Japan, 1978) pp. 47–62.

[59] C. Thornton, *Numerical simulations of deviatoric shear deformation of granular media,* Géotechnique **50**, 43–53 (2000).

[60] B. Hofmann, D. Sego, and P. Robertson, *Undisturbed sampling of a deep loose sand deposit using ground freezing,* in *Proceedings of the 47th Canadian Geotechnical Conference, Halifax* (1994) pp. 287–296.

[61] B. Hofmann, D. Sego, and P. Robertson, *In situ ground freezing for undisturbed samples of loose sand–phase ii,* in *Proc. of 48th Canadian Geotechnical Conference, Vancouver, BC* (1995) pp. 192–204.

[62] Y. Vaid, M. Uthayakumar, S. Sivathayalan, P. Robertson, and B. Hofmann, *Laboratory testing of syncrude sand,* in *Proceedings of the 48th Canadian Geotechnical Conference, Vancouver*, Vol. 1 (1995) pp. 223–232.

[63] Y. Vaid, S. Sivathayalan, M. Uthayakumar, and A. Eliadorani, *Liquefaction potential of reconstituted syncrude sand,* in *Proceedings of the 48th Canadian Geotechnical Conference*, Vol. 1 (1995) pp. 319–328.

[64] Y. Vaid, S. Sivathayalan, and D. Stedman, *Influence of specimen-reconstituting method on the undrained response of sand,* ASTM geotechnical testing journal **22**, 187–195 (1999).

[65] Y. Vaid and S. Sivathayalan, *Fundamental factors affecting liquefaction susceptibility of sands,* Canadian Geotechnical Journal **37**, 592–606 (2000).

[66] J. Mulilis, K. Arulanandan, J. Mitchell, C. Chan, and H. Bolton Seed, *Effects of sample preparation on sand liquefaction,* Journal of the Geotechnical Engineering Division **103**, 91–108 (1977).

[67] D.-J. Jang and J. D. Frost, *Sand structure differences resulting from specimen preparation procedures,* in *Geotechnical Earthquake Engineering and Soil Dynamics III* (ASCE, 1998) pp. 234–245.

[68] J. Frost and J.-Y. Park, *A critical assessment of the moist tamping technique,* ASTM geotechnical testing journal **26**, 57–70 (2003).

[69] J. Sladen and G. Handford, *A potential systematic error in laboratory testing of very loose sands,* Canadian Geotechnical Journal **24**, 462–466 (1987).

[70] M. Oda, I. Koishikawa, and T. Higuchi, *Experimental study of anisotropic shear strength of sand by plane strain test,* Soils and Foundations **18**, 25–38 (1978).

[71] V. DeGregorio, *Loading systems, sample preparation, and liquefaction,* Journal of geotechnical engineering **116**, 805–821 (1990).

[72] P. Thomson and R. Wong, *Monitoring void ratio redistribution during continuous undrained triaxial compression by x-ray computed tomography,* Geological Society, London, Special Publications **215**, 191–198 (2003).

[73] S. Yimsiri and K. Soga, *Dem analysis of soil fabric effects on behaviour of sand,* Géotechnique **60**, 483–495 (2010).

[74] J. Arthur and B. Menzies, *Inherent anisotropy in a sand,* Géotechnique **22**, 115–128 (1972).

[75] M. Oda, *Initial fabrics and their relations to mechanical properties of granular material,* Soils and foundations **12**, 17–36 (1972).

[76] A. Mahmood and J. Mitchell, *Fabric-property relationships in fine granular materials,* Clays and Clay minerals **22**, 396–408 (1974).

[77] M. Oda and J. Konishi, *Microscopic deformation mechanism of granular material in simple shear,* Soils and Foundations **14**, 25–38 (1974).

[78] J. Arthur, K. Chua, and T. Dunstan, *Induced anisotropy in a sand,* Géotechnique **27**, 13–30 (1977).

[79] R. Verdugo and K. Ishihara, *The steady state of sandy soils,* Soils and foundations **36**, 81–91 (1996).

[80] R. Cadle, *Particle size theory and industrial applications, Reinhold Pub* (Reinhold publishing corporation, New York, 1965).

[81] J. Yang and L. Wei, *Collapse of loose sand with the addition of fines: the role of particle shape,* Géotechnique **62**, 1111–1125 (2012).

[82] A. Sadrekarimi, *Influence of fines content on liquefied strength of silty sands,* Soil Dynamics and Earthquake Engineering **55**, 108–119 (2013).

[83] R. Mizanur and S. Lo, *Predicting the onset of static liquefaction of loose sand with fines,* Journal of Geotechnical and Geoenvironmental Engineering **138**, 1037–1041 (2011).

[84] J. A. Yamamuro and P. V. Lade, *Static liquefaction of very loose sands,* Canadian Geotechnical Journal **34**, 905–917 (1997).

[85] F. Wood, J. Yamamuro, and P. Lade, *Effect of depositional method on the undrained response of silty sand,* Canadian Geotechnical Journal **45**, 1525–1537 (2008).

[86] J. A. Yamamuro, F. M. Wood, and P. V. Lade, *Effect of depositional method on the microstructure of silty sand,* Canadian Geotechnical Journal **45**, 1538–1555 (2008).

[87] J. Kolbuszewski, *Notes on the deposition of sands,* Research **3**, 478–483 (1950).

[88] P. Cundall and O. Strack, *A discrete numerical model for granular assemblies,* Géotechnique **29**, 47–65 (1979).

[89] M. Bolton, Y. Nakata, and Y. Cheng, *Micro-and macro-mechanical behaviour of dem crushable materials,* Géotechnique **58**, 471–480 (2008).

[90] X. Huang, C. O'Sullivan, K. Hanley, and C. Kwok, *Discrete-element method analysis of the state parameter,* Géotechnique **64**, 954–965 (2014).

[91] J. Yang and B. Dai, *Is the quasi-steady state a real behaviour? a micromechanical perspective,* Géotechnique **61**, 175–183 (2011).

[92] Y. Vaid, E. Chung, and R. Kuerbis, *Stress path and steady state,* Canadian Geotechnical Journal **27**, 1–7 (1990).

[93] D. Hight, A. Gens, and M. Symes, *The development of a new hollow cylinder apparatus for investigating the effects of principal stress rotation in soils,* Géotechnique **33**, 355–383 (1983).

[94] Y. Yamada and K. Ishihara, *Undrained deformation characteristics of loose sand under three-dimensional stress conditions.* Soils and Foundatons **21**, 97–107 (1981).

[95] M. Symes, A. Gens, and D. Hight, *Undrained anisotropy and principal stress rotation in saturated sand,* Géotechnique **34**, 11–27 (1984).

[96] M. Uthayakumar and Y. Vaid, *Static liquefaction of sands under multiaxial loading,* Canadian Geotechnical Journal **35**, 273–283 (1998).

[97] M. Yoshimine, K. Ishihara, and W. Vargas, *Effects of principal stress direction and intermediate principal stress on undrained shear behavior of sand,* Soils and Foundations **38**, 179–188 (1998).

[98] V. Georgiannou, A. Tsomokos, and K. Stavrou, *Monotonic and cyclic behaviour of sand under torsional loading,* Géotechnique **58**, 113–124 (2008).

[99] Z. Yang, X. Li, and J. Yang, *Undrained anisotropy and rotational shear in granular soil,* Géotechnique **57**, 371–384 (2007).

[100] M. Yoshimine, R. Ozay, A. Sezen, and A. Ansal, *Undrained plane strain shear tests on saturated sand using a hollow cylinder torsional shear apparatus.* Soils and Foundations **39**, 131–136 (1999).

[101] D. Wanatowski and J. Chu, *Static liquefaction of sand in plane strain,* Canadian geotechnical journal **44**, 299–313 (2007).

[102] Y. Vaid, E. Chung, and R. Kuerbis, *Preshearing and undrained response of sand.* Soils and Foundations **29**, 49–61 (1989).

[103] C. d. Prisco, R. Matiotti, and R. Nova, *Theoretical investigation of the undrained stability of shallow submerged slopes,* Géotechnique **45**, 479–496 (1995).

[104] S. Sivathayalan and Y. Vaid, *Influence of generalized initial state and principal stress rotation on the undrained response of sands,* Canadian Geotechnical Journal **39**, 63–76 (2002).

[105] A. Gajo, L. Piffer, and F. de Polo, *Analysis of certain factors affecting the unstable behaviour of saturated loose sand,* Mechanics of Cohesive-frictional Materials **5**, 215–237 (2000).

[106] P. Skopek, N. Morgenstern, P. Robertson, and D. Sego, *Collapse of dry sand,* Canadian Geotechnical Journal **31**, 1008–1014 (1994).

[107] R. Nova, *Failure in geomaterials,* European Journal of Environmental and Civil Engineering **13**, 779–802 (2009).

[108] H. Hanzawa, *Undrained strength and stability analysis for a quick sand.* Soils and Foundations **20**, 17–29 (1980).

[109] J. Chu, S. Leroueil, and W. Leong, *Unstable behaviour of sand and its implication for slope instability,* Canadian Geotechnical Journal **40**, 873–885 (2003).

[110] J. Chu and W. Leong, *Pre-failure strain softening and pre-failure instability of sand: a comparative study,* Géotechnique **51**, 311–321 (2001).

[111] Y. Vaid and A. Eliadorani, *Instability and liquefaction of granular soils under undrained and partially drained states,* Canadian Geotechnical Journal **35**, 1053–1062 (1998).

[112] J. Chu, S.-C. Lo, and I. Lee, *Strain-softening behavior of granular soil in strain-path testing,* Journal of Geotechnical Engineering **118**, 191–208 (1992).

[113] P. Rowe, *The stress-dilatancy relation for static equilibrium of an assembly of particles in contact,* Proceedings of the Royal Society of London A: Mathematical, Physical and Engineering Sciences **269**, 500–527 (1962).

[114] P. Guo and X. Su, *Effect of dilatancy on instability, pre-instability strain softening of sand along proportional strain paths,* Soils and foundations **47**, 757–770 (2007).

[115] J. Chu, S.-C. Lo, and I. Lee, *Instability of granular soils under strain path testing,* Journal of Geotechnical Engineering **119**, 874–892 (1993).

[116] I. Idriss and R. Boulanger, *2nd ishihara lecture: Spt- and cpt-based relationships for the residual shear strength of liquefied soils,* Soil dynamics and earthquake engineering **68**, 57–68 (2015).

[117] A. Ayoubian and P. Robertson, *Void ratio redistribution in undrained triaxial extension tests on ottawa sand,* Canadian Geotechnical Journal **35**, 351–359 (1998).

[118] P. Thomson and R. Wong, *Specimen nonuniformities in water-pluviated and moist-tamped sands under undrained triaxial compression and extension,* Canadian Geotechnical Journal **45**, 939–956 (2008).

[119] T. Kokusho, *Current state of research on flow failure considering void redistribution in liquefied deposits,* Soil Dynamics and Earthquake Engineering **23**, 585–603 (2003).

[120] T. Kokusho and T. Kojima, *Mechanism for postliquefaction water film generation in layered sand,* Journal of geotechnical and geoenvironmental engineering **128**, 129–137 (2002).

[121] T. Kokusho, *Water film in liquefied sand and its effect on lateral spread,* Journal of Geotechnical and Geoenvironmental Engineering **125**, 817–826 (1999).

[122] T. Kokusho, *Mechanism for water film generation and lateral flow in liquefied sand layer.* Soils and Foundations **40**, 99–111 (2000).

[123] R. Kulasingam, E. Malvick, R. Boulanger, and B. Kutter, *Strength loss and localization at silt interlayers in slopes of liquefied sand,* Journal of Geotechnical and Geoenvironmental Engineering **130**, 1192–1202 (2004).

[124] R. Boulanger and S. Truman, *Void redistribution in sand under post-earthquake loading,* Canadian geotechnical journal **33**, 829–834 (1996).

[125] M. Seid-Karbasi and P. Byrne, *Seismic liquefaction, lateral spreading, and flow slides: a numerical investigation into void redistribution,* Canadian Geotechnical Journal **44**, 873–890 (2007).

[126] H. B. Seed, *Design problems in soil liquefaction,* Journal of Geotechnical Engineering **113**, 827–845 (1987).

[127] A. Sadrekarimi, *Effect of the mode of shear on static liquefaction analysis,* Journal of Geotechnical and Geoenvironmental Engineering **140**, 420–432 (2014).

[128] D. Lafeber, *Soil structural concepts,* Engineering Geology **1**, 261–290 (1966).

[129] A. Verruijt, *Soil Mechanics* (Screen version, published online at geo.verruijt.net, 2012).

[130] K. Ishihara, *Liquefaction and flow failure during earthquakes,* Géotechnique **43**, 351–451 (1993).

[131] S. Olson and T. Stark, *Yield strength ratio and liquefaction analysis of slopes and embankments,* Journal of Geotechnical and Geoenvironmental Engineering **129**, 727–737 (2003).

[132] S. J. Poulos, G. Castro, and J. W. France, *Liquefaction evaluation procedure,* Journal of Geotechnical Engineering **111**, 772–792 (1985).

[133] T. Youd, I. Idriss, R. Andrus, I. Arango, G. Castro, J. Christian, R. Dobry, W. Finn, L. Harder Jr, M. Hynes, *et al.*, *Liquefaction resistance of soils: summary report from the 1996 nceer and 1998 nceer/nsf workshops on evaluation of liquefaction resistance of soils,* Journal of geotechnical and geoenvironmental engineering **127** (2001).

[134] S. Lignon, F. Laouafa, F. Prunier, H. Khoa, and F. Darve, *Hydro-mechanical modelling of landslides with a material instability criterion,* Géotechnique **59**, 513–524 (2009).

[135] J. Sladen, R. D'hollander, and J. Krahn, *The liquefaction of sands, a collapse surface approach,* Canadian Geotechnical Journal **22**, 564–578 (1985).

[136] R. de Jager, F. Mathijssen, F. Molenkamp, and A. Nooy van der Kolff, *Static liquefaction analysis using simplified modified state parameter approach for dredged sludge depot hollandsch diep,* in *Proceedings of the 12th International Conference of the International Association for Computer Methods and Advances in Geomechanics* (2008) pp. 4748–4756.

[137] J. Chu and D. Wanatowski, *Difficulties in the determination of post-liquefaction strength for sand,* Géotechnique Letters **4**, 57–61 (2014).

[138] S. M. Olson and T. D. Stark, *Liquefied strength ratio from liquefaction flow failure case histories,* Canadian Geotechnical Journal **39**, 629–647 (2002).

[139] M. Hicks and R. Boughrarou, *Finite element analysis of the nerlerk underwater berm failures,* Géotechnique **48**, 169–185 (1998).

3

Governing equations of saturated porous media

Liquefaction flow slides are essentially fully coupled phenomena. Improving the current assessment methods requires taking account of the coupling between the behaviour of the soil and pore water. This chapter presents the formulation of the governing equations for liquefaction flow slides. These form the basis for the finite element model that will be discussed in Chapter 5.

This chapter will start with an overview of the starting points, including the range of applicability, definitions and the results from a literature review. Then, it will deal with the conservation of mass and momentum. The final section of this chapter demonstrates how the resulting equations are related to the different stages of liquefaction flow slides. Chapter 4 will further extend the governing equations by treating the thermodynamic consistency of the formulation.

3.1. Starting points and assumptions

3.1.1. Introduction

A recent discussion in literature [1, 2] inspired the work discussed in this chapter. As a matter of fact, the conservation equations of porous media have been the subject of discussions or even polemics from the moment soil mechanics arose as a separate field in engineering science [3]. The importance of defining the correct conservation equations for saturated, porous media is beyond dispute. Not only in soil mechanics, but in a variety of geosciences such as geomechanics, geophysics and petroleum engineering they form the basis of models. As a consequence, a vast amount of literature is available on the subject. Before providing a concise overview of the relevant literature, first the range of applicability for the topic of flow liquefaction is defined.

The aim is to specify the range of interest without excluding too many aspects a priori.

The previous chapter discussed the sequence of a liquefaction flow slide, which comprises the following stages: initial (hydrostatic) conditions, triggering, (dynamic) development and finally, (hydrostatic) post-failure conditions. Herein the interest is mainly the first part until the slope starts failing. During this stage, the conservation of mass and momentum define the field equations for the initial-boundary value problem considered. However, it is recognised that, in order to verify the consistency of the resulting framework, it is also necessary to take account of the laws of thermodynamics.

The loading history is an elementary part of soil behaviour. The formulation of soil models is therefore based on a Lagrangian (or material) description, while keeping track of the loading history of the soil skeleton. The formulation of the conservation laws are essentially objective, but can be placed in a Lagrangian configuration. This thesis will use a Lagrangian configuration during the derivation of the equations and the selection of (free) variables, thereby anticipating on the description used in the finite element implementation. The displacement of the soil skeleton $\boldsymbol{u}^s$ and *relative* velocity of the pore fluid $\boldsymbol{v}^{pf\text{-}s}$ are selected as free variables. The latter is defined as the difference between the mean velocities of the pore fluid $\boldsymbol{v}^{pf}$ and soil skeleton $\dot{\boldsymbol{u}}^s$ (Figure 3.1):

$$\boldsymbol{v}^{pf\text{-}s} = \boldsymbol{v}^{pf} - \dot{\boldsymbol{u}}^s \tag{3.1}$$

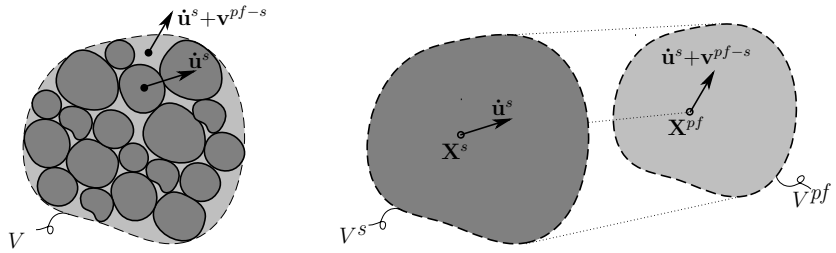


Figure 3.1: Modelling of saturated soil skeleton as superimposed continua

3.1.2. Range of applicability

Consider an assembly of particles, fully saturated by a single pore fluid. The particles are assumed to be impermeable and do not crush nor break at the stress range considered (< 1 MPa). If the volume under consideration is sufficiently large, that is, larger than the Representative Elementary Volume (REV), its properties can be assumed homogeneous and continuous. The saturated soil skeleton, essentially an immiscible mixture, is modelled as superimposed continua; each point in the mixture is simultaneously occupied by a material point of each constituent (Figure 3.1). The contributions of the constituents to the response of the mixture are weighted according to their volume fractions. The general convention in soil mechanics to use the porosity n as a measure of

volume fraction, being defined as the ratio between the volume of pores V^p and the total volume of the assembly V^t, i.e. $n = V^p/V^t$, is followed here. For saturated porous media the volume fraction of the pore fluid is consequently defined by n, and the volume fraction of the soil skeleton by $(1-n)$. For instance, the total volumetric mass of the mixture ρ can be decomposed into contributions from the soil skeleton ρ^s and pore fluid ρ^{pf}. The magnitudes of these depend on the corresponding volume fractions and intrinsic volumetric masses of the soil particles and pore fluid, ρ^g and ρ^f respectively:

$$\rho = \rho^s + \rho^{pf} = (1-n)\rho^g + n\rho^f \tag{3.2}$$

The constitutive equations of the soil skeleton and pore fluid supplement the conservation equations to form a closed set of equations. For now, the constitutive equation of the soil is simply expressed by a generic relation between the rate of effective stresses $\dot{\boldsymbol{\sigma}}'$, tangent stiffness tensor $\boldsymbol{D}$ and rate of strains of the soil skeleton $\dot{\boldsymbol{\epsilon}}^s$ without making any assumptions with respect to these variables:

$$\dot{\boldsymbol{\sigma}}' = \boldsymbol{D} : \dot{\boldsymbol{\epsilon}}^s \tag{3.3}$$

It is noted that in many cases $\boldsymbol{D} = \boldsymbol{D}(\dot{\boldsymbol{\epsilon}}^s)$. The shear stresses of the pore fluid at the continuum scale are neglected. As a consequence, the pore fluid stress p is an isotropic stress measure. A linear constitutive relationship is here assumed between the pore fluid stress increment $\dot{p}$ and the pore fluid strain $\dot{\boldsymbol{\epsilon}}^{pf}$, characterised by stiffness K^{pf}:

$$\dot{p} = K^{pf}\, \dot{\boldsymbol{\epsilon}}^{pf} : \boldsymbol{I} \tag{3.4}$$

Equation 3.4 uses the previously defined unit tensor $\boldsymbol{I}$. Inertial terms are not neglected a priori, but there are limits to the range of application. Firstly, it is assumed that the governing equations are in the low-frequency range. Viscous coupling dominates pore water flow, which is said to be of the Poisseulle type [4, 5]. The upper limit of the Poisseulle flow, the critical frequency ω^{crit} is defined by the viscous skin depth becoming larger than the pore radius r [5]. A first approximation for water ($\rho^f = 1000\,\mathrm{kg\,m^{-3}}$) flowing through a fine sand ($r = 37\,\mu\mathrm{m}$) yields:

$$\omega^{crit} = \frac{2\eta}{\rho^f r^2} \approx 1500\,\mathrm{Hz} \tag{3.5}$$

Herein, $\eta = 0.001\,\mathrm{N\,s\,m^{-2}}$ represents the shear viscosity of the pore fluid. The value of r has been estimated based on the analytical solution for a cubic array of monosized spheres [6] and a grain size diameter of $D^g = 100\,\mu\mathrm{m}$. The implication for $\omega < \omega^{crit}$ is that the terms in the governing equations do not depend on the frequency. Secondly, the pore water flow is assumed to be in the laminar range. To this end, the Reynold's number R_e should be smaller than 1 [7], or the relative pore water velocity $|\mathbf{v}^{pf\text{-}s}|$ smaller than the critical value $\mathbf{v}^{pf\text{-}s;crit}$. A first approximation yields:

$$\mathbf{v}^{pf\text{-}s;crit} = \frac{R_e \eta}{n \rho^f D^g} \approx 0.025\,\mathrm{m\,s^{-1}} \tag{3.6}$$

Herein, the grain size $D^g = 100\,\mu\mathrm{m}$, $n = 0.4$ and $\eta = 0.001\,\mathrm{N\,s\,m^{-2}}$. A flow velocity $|\mathbf{v}^{pf\text{-}s}| < \mathbf{v}^{pf\text{-}s;crit}$ implies that Darcy's Law can be used as a relationship between the pore fluid stress and velocity.

3.1.3. Literature review

Literature provides excellent overviews of the continuity equations and equations of motion of porous media, see e.g. [1, 8, 9]. This section does not intend to give a complete overview. It highlights a few, main contributions, specifies the range of interest for flow liquefaction and indicates the gaps in knowledge that need further attention.

The conservation equations of porous media have been considered from several viewpoints. A first breakdown of methods used to derive the conservation equations is made based on whether seperate entities or a continuum is considered [1]. Discrete [10] and upscaling [8] methods are examples of the first type. These methods attempt to relate (heterogeneous) properties and processes at the smaller scale to the scale of interest. In some cases they are used to justify assumptions made in the second type of methods, i.e. at the continuum scale (e.g. [11]). Within continuum models of saturated, porous media a distinction is made between the phenomenological approach and mixture theory. The phenomenological approach takes the soil skeleton as the starting point and only takes account of the pore fluid as it affects the soil skeleton. The Author considers this approach problem driven, as it fits a particular field of applications. An example is the consolidation of soils after surcharge loading, which yielded a set of equations which essentially define the conservation of mass of saturated soils [12, 13]. Mixture theory is based on general principles of physics of multiphase and multiconstituent media without making any assumptions a priori, see e.g. [14–18].

The phenomenological approach and mixture theory yield the same set of equations for the conservation of mass of saturated porous media, provided that the same assumptions are made [19]. However, a recent discussion in literature [2] shows that the conservation of momentum still leaves points of discussion. The discussion is here narrowed down to three (interrelated) aspects: the hydrostatic paradox, the definition of interaction terms and the stress measures used. It has been noted for a long time that the uplift or buoyancy in a saturated, porous medium with an open, interconnected pore structure and under hydrostatic conditions does not depend on the volume fractions [20, 21]. This notion contradicts the instinctive assumption that stresses should depend on the volumetric masses *and* volumes of the constituents, and is therefore termed the hydrostatic paradox [22]. Practical implications revolve around the question as to what extent uplift should be taken into account during the design of hydraulic structures, which led to polemics and, until recently, erroneous designs [3, 23]. From a more fundamental point of view the hydrostatic paradox seems to conflict with mixture theory, which presupposes that conserved quantities depend on the volume fraction of the constituent under consideration. It should be noted that many significant contributions in literature aim at describing wave propagation and ignore gravitational effects. Among these are Biot [4] and De Josselin de Jong [24], who were -practically simultaneously and independently- the first to derive a (nearly) complete set of equations of motion for saturated soils. However, the hydrostatic paradox is not apparent when gravitational effects are ignored.

The key for refuting the hydrostatic paradox for mixture theory lies in the definition of the interaction terms [2]. It will here be shown that *self-equilibration* cancels out the

term that introduces the paradox to the equations of motion. However, the implications for the laws of thermodynamics are yet unclear [2]. The next chapter will also verify the consistency of the thermodynamic framework that arises from the equations of motion. Furthermore, unification of the phenomenological approach and mixture theory requires the synchronisation of stress measures. Mixture theory starts from phase averaged stresses exerted by the constituents. The phenomenological approach is based on the effective stresses, which by definition describe the deformation of the soil skeleton (Equation 3.3). The pore fluid stresses define the complementary stresses. It will be shown that, by using these stress measures in the phenomenological approach, the hydrostatic paradox is implicitly accounted for. However, how to take account of inertia in the phenomenological approach has not yet been clarified. An alternative derivation of the governing equations from the phenomenological approach will be presented, thereby demonstrating that both approaches yield the same set of equations. Nowadays, the effective stress has also been related to more fundamental approaches [25, 26], while being supported by experimental validation [27]. The next chapter will examine the limits and possible extensions of the effective stress by considering the influence of rotation and (un)saturation.

3.2. Governing equations for flow liquefaction

3.2.1. Introduction

This section addresses the conservation equations of mass and momentum of the pore fluid and soil skeleton of a fully saturated soil. The equations from mixture theory will first be derived. The same methodology will be applied for both equations and both constituents. It is worth noting that the summation of the equations for the constituents should logically end up at the equation for the total mixture, which is a simple, undisputed expression. Hence, the resulting equation for the total mixture can either be used to check the constituent equations, or to derive the complementary equation in case one of the constituent equations is known. In addition to the methodology, the interaction and stress terms are derived and related to the usual measures in mixture theory. The last part of this section will address an alternative derivation of the governing equations, that is, using the phenomenological approach. The reader may for conventions with respect to the signs and notation refer to the preliminary part of this thesis.

3.2.2. Methodology

Consider a deformable body with volume v and surface s at the current spatial state and time t, while the initial reference state at time $t = t^0$ is characterised by volume V and surface S (see Figure 3.2). The adopted description obeys the starting points of Classical Mechanics. A Cartesian triad defines the frame of reference in Euclidean space. For the case of multiple reference frames, these are assumed to differ only by constant velocity or rate of rotation, which confines the consideration to Galilean relativity. If the vector $\boldsymbol{X}$ defines the reference configuration and $\boldsymbol{x}$ the current configuration, the deformation gradient $\boldsymbol{F}$ defines the following relation between both:

$$\boldsymbol{F} = F_{ij} = \frac{\partial x_i}{\partial X_j} = \boldsymbol{x} \otimes \nabla^{\boldsymbol{X}} \tag{3.7}$$

The displacement $\boldsymbol{u}$ from the initial reference state to the current state then reads:

$$\boldsymbol{u} = \boldsymbol{x} - \boldsymbol{X} \tag{3.8}$$

The velocity $\dot{\boldsymbol{u}}$ and acceleration $\ddot{\boldsymbol{u}}$ can be derived from Equation 3.8 by taking the first and second order material time derivatives, respectively. The conservation of mass and linear momentum in volume v are considered, while noting that both quantities also depend on the volume considered. Hence, elaboration of the conservation equations requires taking account of the change of a quantity in volume v, the change of volume v itself and, if necessary, the external supply of mass or linear momentum. The change of volume v will be expressed by referring to the (fixed) initial reference state, that is, by using Equation 3.7. Note that this procedure corresponds with the application of Reynolds' Transport Theorem. The external supply of mass or linear momentum may include terms that act on the entire volume (e.g. gravity), the surface (e.g. imposed boundary loads) and interaction terms for when constituents in a multi-constituent medium are considered.

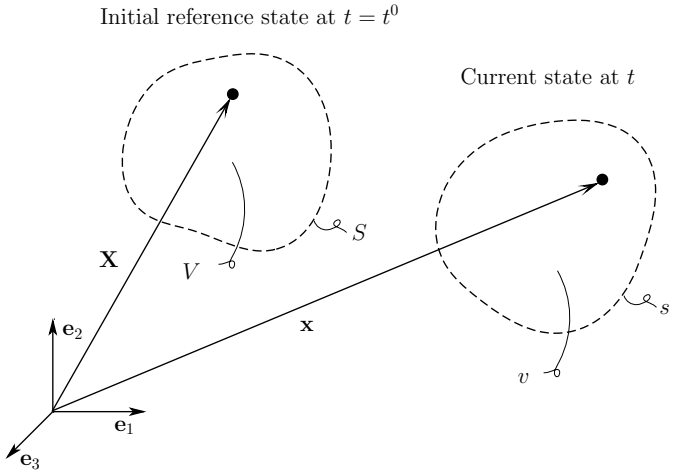


Figure 3.2: Initial reference state and current state of deformable body

The conservation of mass states that the change in mass, expressed by the material time derivative $\mathrm{D}M/\mathrm{D}t$, equals the external supply of mass per unit time m, or:

$$\frac{\mathrm{D}M}{\mathrm{D}t} = \frac{\mathrm{D}}{\mathrm{D}t}\int_v \rho \,\mathrm{d}v = m \tag{3.9}$$

The volume of the current state v is related to volume V in the initial reference state by the determinant of the deformation gradient $\det\boldsymbol{F}$ [28]:

$$v = \det\boldsymbol{F}\, V \tag{3.10}$$

Substitution of Equation 3.10 into Equation 3.9 and subsequent elaboration yields:

$$\begin{aligned}\frac{\mathrm{D}}{\mathrm{D}t}\int_v \rho\,\mathrm{d}v = \frac{\mathrm{D}}{\mathrm{D}t}\int_V \rho\,\det\boldsymbol{F}\,\mathrm{d}V &= \int_v \left(\dot{\rho} + \rho\frac{\dot{\overline{\det\boldsymbol{F}}}}{\det\boldsymbol{F}}\right)\mathrm{d}v \\ &= \int_v \left(\dot{\rho} + \rho\,\nabla\cdot\dot{\boldsymbol{u}}\right)\mathrm{d}v = m\end{aligned} \tag{3.11}$$

The resulting general equation of mass 3.11 is further simplified, by ignoring the supply of mass and interaction between constituents with respect to mass in general, i.e. $m = 0$. Then, the resulting equation is satisfied if the terms under the integral sign equal zero and the equation of mass can be rewritten in its local form:

$$\dot{\rho} + \rho\,\nabla\cdot\dot{\boldsymbol{u}} = 0 \tag{3.12}$$

The equation of linear momentum balance states that the change of linear momentum, expressed by the material time derivative $\mathrm{D}F/\mathrm{D}t$, equals the external supply of momentum per unit time $\boldsymbol{f}$, or:

$$\frac{\mathrm{D}F}{\mathrm{D}t} = \frac{\mathrm{D}}{\mathrm{D}t}\int_v \rho\dot{\boldsymbol{u}}\,\mathrm{d}v = \boldsymbol{f} \tag{3.13}$$

By taking account of the change in volume 3.10 and the conservation of mass 3.12, the left hand side of Equation 3.13 can be further elaborated into:

$$\begin{aligned}\frac{\mathrm{D}}{\mathrm{D}t}\int_v \rho\dot{\boldsymbol{u}}\,\mathrm{d}v = \int_v \left(\frac{\mathrm{D}}{\mathrm{D}t}\left(\rho\dot{\boldsymbol{u}}\right) + \rho\dot{\boldsymbol{u}}\left(\nabla\cdot\dot{\boldsymbol{u}}\right)\right)\mathrm{d}v &= \int_v \left(\rho\ddot{\boldsymbol{u}} + \dot{\boldsymbol{u}}\left(\dot{\rho} + \rho\,\nabla\cdot\dot{\boldsymbol{u}}\right)\right)\mathrm{d}v \\ &= \int_v \rho\ddot{\boldsymbol{u}}\,\mathrm{d}v = \boldsymbol{f}\end{aligned} \tag{3.14}$$

The supply of momentum $\boldsymbol{f}$ in the right hand side of Equation 3.14 is defined by a body and surface load term:

$$\boldsymbol{f} = \int_v \rho\boldsymbol{b}\,\mathrm{d}v + \oint_s \boldsymbol{t}\,\mathrm{d}s \tag{3.15}$$

Herein, $\boldsymbol{b}$ defines the body load and $\boldsymbol{t}$ the surface traction. In order to express Equation 3.14 in its local form, first Cauchy's Theorem is applied and then the Divergence Theorem:

$$\oint_s \boldsymbol{t}\,\mathrm{d}s = \oint_s \boldsymbol{n}\cdot\boldsymbol{\sigma}\,\mathrm{d}s = \int_v \nabla\cdot\boldsymbol{\sigma}\,\mathrm{d}v \tag{3.16}$$

Combining Equations 3.14, 3.15 and 3.16 yields an expression in terms of volume integrals. Omitting the volume integrals leads to the local form of the conservation of linear momentum:

$$\rho\ddot{\boldsymbol{u}} - \nabla\cdot\boldsymbol{\sigma} - \rho\boldsymbol{b} = 0 \tag{3.17}$$

Equations 3.12 and 3.17 are generic formulations of the conservation of mass and linear momentum of geomaterials, respectively. These equations can easily be reformulated for the bulk equations of saturated soils. The constituent equations of the soil skeleton and pore fluid require further consideration. Mixture theory prescribes the application of averaging for the constituents, which results in the introduction of volume fractions,

averaged deformation and corresponding derivatives, and averaged stresses. The term averaging instead of *phase* averaging is here preferred to avoid any premature relation with a particular upscaling method or the interchangeable use of the terms constituents and phases. These averaged quantities will be expressed in more convenient measures, for instance effective stresses in Subsection 3.2.3. Furthermore, interaction terms are introduced to the constituent, which will be specified in Subsection 3.2.4. For all elaborations it is noted that Equations 3.12 and 3.17 are simplified expressions from volume integrands. The specification or introduction of terms should consequently be expressed in terms of volume integrands as well.

3.2.3. Stress measures for saturated porous media

For the expression of stresses the Cauchy or 'true' stress tensor $\boldsymbol{\sigma}$ is used. In the case of large deformations (or rotations) the variance of the Cauchy stress tensor may lead to inconvenience in terms of interpretation or incompatibility with the used strain tensor. The use of the Cauchy stress tensor has therefore been restricted to small strain rates. Note that the Cauchy stress *rate* is used in the generalised constitutive relation 3.3. Unlike the Cauchy stress tensor, its rate is not objective. Alternatively, the objective Zaremba-Jaumann [29, 30] stress rate $\dot{\boldsymbol{\sigma}}^J$ can be used:

$$\dot{\boldsymbol{\sigma}}^J = \dot{\boldsymbol{\sigma}} + \boldsymbol{\sigma} \cdot \boldsymbol{w} - \boldsymbol{w} \cdot \boldsymbol{\sigma} \tag{3.18}$$

Herein, $\boldsymbol{w}$ denotes the rate of rotation as expressed by the spin tensor. Its defintion requires the introduction of the velocity gradient $\boldsymbol{L}$:

$$\boldsymbol{L} = L_{ij} = \frac{\partial v_i}{\partial x_j} = \boldsymbol{v} \otimes \nabla^{\boldsymbol{x}} \tag{3.19}$$

The skew-symmetric part of the velocity gradient $\boldsymbol{L}$ defines the skew tensor $\boldsymbol{w}$:

$$\boldsymbol{w} = \frac{1}{2}\left(\boldsymbol{L} - \boldsymbol{L}^{\mathrm{T}}\right) \tag{3.20}$$

At this stage, it is worth noting that the proposed modelling approach will yield strain and stress increments while keeping track of deformations in a Lagrangian description. This approach enables us to use the Jaumann stress rate to relatively large deformations and rotations, as will be explained in more detail in Chapter 5. For this reason the remaining part of this chapter will use the (Zaremba-Jaumann) stress rate.

This section addresses three types of stress measures for the soil skeleton: the intrinsic, averaged soil stresses $\boldsymbol{\sigma}^s$, intergranular stresses $\boldsymbol{\sigma}^*$ and effective stresses $\boldsymbol{\sigma}'$. The intergranular stresses will be used to derive a relationship between the averaged soil stresses and the effective stresses. The averaged soil stresses and intergranular stresses are defined by the total stresses $\boldsymbol{\sigma}$ and their complementary stress measures, the intrinsic, averaged pore fluid stresses $\boldsymbol{\sigma}^{pf}$ and pore fluid stresses $p\boldsymbol{I}$ respectively, whereas the rate of effective stresses was shown to be related to the deformation of the soil skeleton:

$$(1-n)\boldsymbol{\sigma}^s = \boldsymbol{\sigma} - n\boldsymbol{\sigma}^{pf} \tag{3.21}$$

$$\boldsymbol{\sigma}^* = \boldsymbol{\sigma} - p\boldsymbol{I} \tag{3.22}$$

$$\dot{\boldsymbol{\sigma}}'^J = \boldsymbol{D} : \dot{\boldsymbol{\epsilon}}^s \tag{3.3}$$

Note that, as mixture theory dictates, the intrinsic, averaged stresses are multiplied by the corresponding volume fractions to obtain the stress contributions from the constituents. These volume fractions should consequently also be included when substituting the constituent stress measures in Equation 3.17. The intrinsic, averaged stresses $\boldsymbol{\sigma}^s$ and $\boldsymbol{\sigma}^{pf}$ follow from the averaging of local stress measures $\boldsymbol{\sigma}^g$ and $\boldsymbol{\sigma}^f$ over the constituent, averaging volumes $V^{A;s}$ and $V^{A;pf}$, respectively [31]:

$$\boldsymbol{\sigma}^s = \frac{1}{V^{A;s}} \int_{V^{A;s}} \boldsymbol{\sigma}^g \, \mathrm{d}v \tag{3.23}$$

$$\boldsymbol{\sigma}^{pf} = \frac{1}{V^{A;pf}} \int_{V^{A;pf}} \boldsymbol{\sigma}^f \, \mathrm{d}v \tag{3.24}$$

The averaging volumes $V^{A;s}$ and $V^{A;pf}$ are microscopic properties and should not be confused with the integration volume V used in the previous subsection, which is a macroscopic property. It is assumed that fluid shear stresses are negligible compared to the macroscopic interaction with the soil skeleton. As a consequence, the averaged pore fluid stress tensor $\boldsymbol{\sigma}^{pf}$ is an isotropic stress tensor, as well as being homogeneous over the averaging volume V. In other words, the intrinsic, averaged pore fluid stresses $\boldsymbol{\sigma}^{pf}$ equal the pore fluid stresses $p\boldsymbol{I}$:

$$\boldsymbol{\sigma}^{pf} = p\boldsymbol{I} \tag{3.25}$$

Substitution of Equation 3.25 into Equation 3.21 and subsequently combining Equations 3.21 and 3.22, enables the averaged soil stresses to be expressed in terms of intergranular stresses and pore fluid stresses:

$$(1-n)\boldsymbol{\sigma}^s = \boldsymbol{\sigma}^* + (1-n)p\boldsymbol{I} \tag{3.26}$$

The next step of the elaboration relates the intergranular stresses to effective stresses. Molenkamp et al. [32] present a complete review of stress measures for saturated, porous media, including the effective and intergranular stresses. This thesis confines itself to a concise derivation. Relating the intergranular stress $\boldsymbol{\sigma}^*$ to the effective stress $\boldsymbol{\sigma}'$ requires an understanding of the deformation of the soil skeleton. The strain tensor of the soil skeleton $\boldsymbol{\epsilon}^s$ is defined as a function of the deformations of the soil skeleton $\boldsymbol{u}^s$ [28]:

$$\boldsymbol{\epsilon}^s = \frac{1}{2}\left(\nabla \otimes \boldsymbol{u}^s + \boldsymbol{u}^s \otimes \nabla\right) \tag{3.27}$$

Provided that the particles do not crush, the soil skeleton deforms as a result of either the mutual rearrangement of particles or isotropic deformation of individual particles (see Figure 3.3). The rearrangement of particles is fully attributed to a change in intergranular stress, whilst isotropic deformation of the individual particles may be the result of either a change in pore fluid stresses or (isotropic) intergranular stresses. The stress contributions are separated by considering the deformation of the soil skeleton for cases in which one of the stress increments equals zero:

$$\dot{p}\boldsymbol{I} = 0: \qquad \dot{\boldsymbol{\epsilon}}^s = \boldsymbol{D}^{-1} : \dot{\boldsymbol{\sigma}}'^J = \boldsymbol{D}^{-1} : \dot{\boldsymbol{\sigma}}^{*J} \tag{3.28}$$

$$\dot{\boldsymbol{\sigma}}^{*J} = 0: \qquad \dot{\boldsymbol{\epsilon}}^s = \boldsymbol{D}^{-1} : \dot{\boldsymbol{\sigma}}'^J = \frac{\dot{p}\boldsymbol{I}}{3K^{sf}} \tag{3.29}$$

Herein, the isotropic response of the grains to a pore pressure rate $\dot{p}\boldsymbol{I}$ has been simplified by using a single stiffness term K^{sf}. Superposition of both stress contributions and subsequent elaboration yields a relation between the effective and intergranular stresses:

$$\dot{\boldsymbol{\epsilon}}^{s} = \boldsymbol{D}^{-1} : \dot{\boldsymbol{\sigma}}^{*J} + \frac{\dot{p}\boldsymbol{I}}{3K^{sf}} = \boldsymbol{D}^{-1} : \dot{\boldsymbol{\sigma}}^{\prime J} \tag{3.30}$$

$$\dot{\boldsymbol{\sigma}}^{\prime J} = \dot{\boldsymbol{\sigma}}^{*J} + \frac{\boldsymbol{D} : \boldsymbol{I}}{3K^{sf}}\dot{p} \tag{3.31}$$

The Author concludes that the intergranular stress tensor equals the effective stress tensor when the stiffness K^{sf} is much larger than the components of the tensor $\boldsymbol{D} : \boldsymbol{I}$. For most soils this is indeed the case and it is often assumed that $\dot{\boldsymbol{\sigma}}^{\prime J} = \dot{\boldsymbol{\sigma}}^{*J}$. At this stage, no assumptions will be made regarding the effective stress tensor.

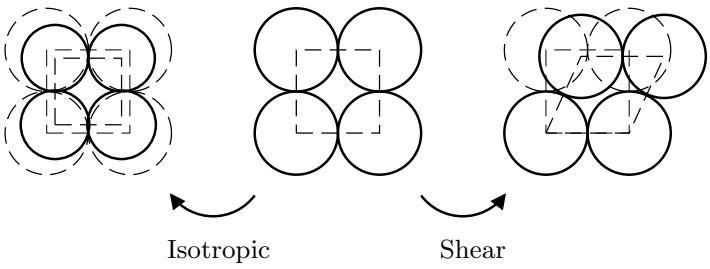


Figure 3.3: Mode of deformation of soil skeleton: isotropic deformation (left) and mutual rearrangement after shear (right) (redrawn from [32])

Terzaghi [12] defines the effective stress according to Equation 3.22, presumably based on observed phenomena in soils. It is worth mentioning that Equation 3.31 also corresponds with other, simplified expressions from literature. Replacing the stiffness tensor $\boldsymbol{D}$ by the inverse of compressibility $1/C$ and stiffness K^{sf} by the inverse of compressibility $1/C^{sf}$ results in:

$$\dot{\boldsymbol{\sigma}}^{\prime J} = \dot{\boldsymbol{\sigma}}^{*J} + \frac{C^{sf}}{C}\dot{p}\boldsymbol{I} \tag{3.32}$$

Molenkamp et al. [32] demonstrate that Equation 3.32 essentially equals expressions found by Biot [13], Skempton [33] and Verruijt [34].

3.2.4. Interaction

In this section the term *interaction* refers to the mutual exchange of linear momentum between the pore fluid and soil skeleton. The Author takes (the change of) the linear momentum of the soil skeleton as the starting point of the derivation of interaction terms that originate from changes in properties of the pore fluid. The linear momentum that is transferred from the pore fluid to the soil skeleton is generally expressed by the tensor $\boldsymbol{R}^{pf\text{-}s}$, and the corresponding reaction force by $\boldsymbol{R}^{s\text{-}pf}$. Newton's second law requires that

$\boldsymbol{R}^{pf\text{-}s} = -\boldsymbol{R}^{s\text{-}pf}$, i.e. the cancellation of interaction terms in the bulk equation. The interaction terms are expressed in terms of force per unit volume to allow substitution in the generic expression 3.17. Specification of the linear momentum equation 3.17 for the soil skeleton and pore fluid, while taking into consideration the phase averaged quantities and interaction $\boldsymbol{R}^{pf\text{-}s}$, yields, respectively:

$$(1-n)\rho^g \ddot{\boldsymbol{u}}^s - \nabla\cdot\left((1-n)\boldsymbol{\sigma}^s\right) - (1-n)\rho^g \boldsymbol{b} - \boldsymbol{R}^{pf\text{-}s} = 0 \tag{3.33}$$

$$n\rho^{pf}\dot{\boldsymbol{v}}^{pf} - \nabla\cdot\left(n\boldsymbol{\sigma}^{pf}\right) - n\rho^{pf}\boldsymbol{b} + \boldsymbol{R}^{pf\text{-}s} = 0 \tag{3.34}$$

The interaction $\boldsymbol{R}^{pf\text{-}s}$ is defined as being the superposed result of three modes, namely hydrostatics $\boldsymbol{R}^{pf\text{-}s;0}$, relative pore fluid flow $\boldsymbol{R}^{pf\text{-}s;\boldsymbol{v}^{pf\text{-}s}}$ and relative pore fluid acceleration $\boldsymbol{R}^{pf\text{-}s;\dot{\boldsymbol{v}}^{pf\text{-}s}}$:

$$\boldsymbol{R}^{pf\text{-}s} = \boldsymbol{R}^{pf\text{-}s;0} + \boldsymbol{R}^{pf\text{-}s;\boldsymbol{v}^{pf\text{-}s}} + \boldsymbol{R}^{pf\text{-}s;\dot{\boldsymbol{v}}^{pf\text{-}s}} \tag{3.35}$$

Upscaling methods provide the means to understand the underlying processes and express interaction in terms of macromechanical properties. Figure 3.4 depicts the simplified case of a single pore fluid channel running through a soil skeleton. This simplified case is used for the sake of illustration and elucidation, but note that implications following from this case also apply to the multiple pore channels that are normally encountered in soils. The field variable under consideration is the local pore fluid stress $\boldsymbol{\sigma}^f$, acting on the soil skeleton at boundary $S^{A;fs}$ with normal $\mathbf{n}^{fs}$. Averaging over the bulk volume V^A requires the volume to be sufficiently large, compared to the grain size, to obtain a smooth function of the field variables. However, it also has to be sufficiently small compared to the wave lengths of typical wave phenomena that need to be captured. Note that these requirements essentially correspond with the aforementioned statements with respect to the range of applicability (see Subsection 3.1.2).

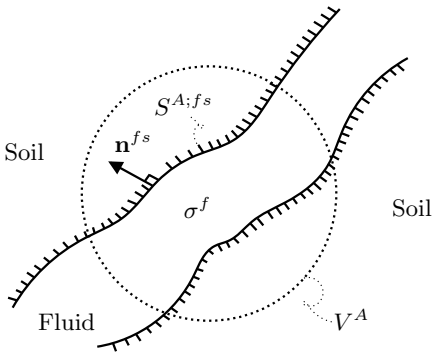


Figure 3.4: Averaging volume V in soil-pore fluid mixture (reworked from [35])

The general relationship expressing the momentum interaction between the pore fluid

and soil skeleton follows from the pore fluid stress acting on the boundary between fluid and soil $S^{A;fs}$. Integration and averaging over volume V^A results in:

$$\boldsymbol{R}^{pf\text{-}s} = -\frac{1}{V^A}\int_{S^{A;fs}} \mathbf{n}^{fs}\cdot\boldsymbol{\sigma}^f \mathrm{d}S \tag{3.36}$$

Note the minus sign that has been added on the right hand side of Equation 3.36 to account for the normal unit vector, that is directed in the opposite direction for the soil phase. Volume averaging enables the elaboration of Equation 3.36. Slattery [36] first derived the theory of volume averaging by considering the gradient of a quantity in the averaging volume, but the elaboration of Equation 3.36 asks for a more generic approach. Gray et al. [37] present a general treatment of the averaging theorem, including an expression for the divergence of a quantity in the averaging volume. The result for the field variable $\boldsymbol{\sigma}^f$ reads (Equation 8.2, [37]):

$$\left(\frac{1}{V^A}\int_{V^A}\boldsymbol{\sigma}^f \mathrm{d}V\right)\cdot\nabla = \frac{1}{V^A}\int_{V^A}\boldsymbol{\sigma}^f\cdot\nabla\,\mathrm{d}V - \frac{1}{V^A}\int_{S^{A;fs}}\mathbf{n}^{fs}\cdot\boldsymbol{\sigma}^f\mathrm{d}S \tag{3.37}$$

Herein, secondary effects at the intersection between the boundary of the averaging volume and the interface between the soil skeleton and pore fluid have been ignored. The second term on the right hand side of Equation 3.37 equals the interaction term $\boldsymbol{R}^{pf\text{-}s}$, as defined in Equation 3.36. Hence, $\boldsymbol{R}^{pf\text{-}s}$ can be expressed in terms of volume averaged quantities:

$$\boldsymbol{R}^{pf\text{-}s} = -\frac{1}{V^A}\int_{V^A}\boldsymbol{\sigma}^f\cdot\nabla\,\mathrm{d}V + \left(\frac{1}{V^A}\int_{V^A}\boldsymbol{\sigma}^f\mathrm{d}V\right)\cdot\nabla \tag{3.38}$$

Now consider each of the interaction terms in Equation 3.35 separately, starting from Equation 3.38. For the first interaction term $\boldsymbol{R}^{pf\text{-}s;0}$ it is assumed that $\boldsymbol{v}^{pf\text{-}s}, \ddot{\boldsymbol{u}}^s, \dot{\boldsymbol{v}}^{pf\text{-}s} = 0$. The pore fluid stress is fully governed by gravity loading. It is inferred from Equation 3.38 that there are two physical contributors to the hydrostatic interaction term, that is, the divergence of both the local pore fluid stress $\boldsymbol{\sigma}^f$ and the volume of pore space $V^{A;pf}$ in the averaging volume. The latter is introduced to the equation by noting that the integration volume V^A can be reduced to the relevant part $V^{A;pf}$, or $V^A = V^{A;pf}$. Both contributors are considered separately by assuming the other to be constant.

First, homogeneity of the pore space is assumed with $\nabla\cdot V^{A;pf} = 0$. The divergence of both the local and averaged pore fluid stress will be the result of gravity loading. The second term on the right hand side of Equation 3.38 reduces to:

$$\left(\frac{1}{V^A}\int_{V^A}\boldsymbol{\sigma}^f\mathrm{d}V\right)\cdot\nabla = \frac{1}{V^A}\int_{V^A}\boldsymbol{\sigma}^f\cdot\nabla\,\mathrm{d}V \tag{3.39}$$

It is concluded that in this case $\boldsymbol{R}^{pf\text{-}s;0} = 0$ and that there is no contribution from the gradient of the local pore fluid stress.

Secondly, heterogeneity of the pore space is assumed, while keeping the gradients of the local and averaged pore fluid stress equal to zero: $\boldsymbol{\sigma}^f\cdot\nabla, \boldsymbol{\sigma}^{pf}\cdot\nabla = 0$. This situation is

for instance valid for horizontal pore channels or presumed constant stresses [38]. The first term on the right hand side of Equation 3.38 equals zero, while the second term can be elaborated further by using Equation 3.24:

$$\begin{aligned}\boldsymbol{R}^{pf\text{-}s;0} &= \left(\frac{1}{V^A}\int_{V^A}\boldsymbol{\sigma}^f \mathrm{d}V\right)\cdot\nabla = \left(n\frac{1}{V^{A;pf}}\int_{V^A}\boldsymbol{\sigma}^f \mathrm{d}V\right)\cdot\nabla = \left(n\boldsymbol{\sigma}^{pf}\right)\cdot\nabla \\ &= \boldsymbol{\sigma}^{pf}\cdot\nabla n = p\boldsymbol{I}\cdot\nabla n \end{aligned} \tag{3.40}$$

Hence, the hydrostatic interaction term $\boldsymbol{R}^{pf\text{-}s;0}$ results from variations in the two complementary volume fractions. To the Author's knowledge, Rakhmatulin [39] was the first to recognise the hydrostatic interaction term. He derived essentially the same term, albeit by using a less rigorous procedure. The resulting Equation 3.40 suggests that heterogeneity of the subsoil introduces interaction between the pore fluid and soil skeleton. As will be shown below, the hydrostatic interaction term refutes the hydrostatic paradox. The linear momentum of the soil skeleton 3.33 and pore fluid 3.34 are elaborated for hydrostatics by neglecting inertial terms and by introducing the pore fluid stress $p\boldsymbol{I}$ and intergranular stress $\boldsymbol{\sigma}^*$ from Equation 3.26:

$$-\nabla\cdot\boldsymbol{\sigma}^* - (1-n)\nabla\cdot\left(p\boldsymbol{I}\right) + p\boldsymbol{I}\cdot\nabla n - (1-n)\rho^g\boldsymbol{b} - \boldsymbol{R}^{pf\text{-}s;0} = 0 \tag{3.41}$$

$$-n\nabla\cdot\left(p\boldsymbol{I}\right) - p\boldsymbol{I}\cdot\nabla n - n\rho^{pf}\boldsymbol{b} + \boldsymbol{R}^{pf\text{-}s;0} = 0 \tag{3.42}$$

At first sight, heterogeneity of the subsoil seems to affect the linear momentum of the pore fluid and soil skeleton through the term $p\boldsymbol{I}\cdot\nabla n$. One knows from actual measurements that the pore fluid stress in the heterogeneous, saturated subsoil solely depends on the depth below the water table and not on the volume fractions. Equations 3.41 and 3.42 make clear that this observation is counter-intuitive, and hence the term hydrostatic paradox. The introduction of the hydrostatic interaction term 3.40 into Equations 3.41 and 3.42 eliminates the term $p\boldsymbol{I}\cdot\nabla n$ from the momentum equations. The introduced linear momentum of heterogeneity of the soil skeleton, if any, is automatically eliminated by an interaction term of the same magnitude but acting in the opposite direction. The term self-equilibration is used for the automatic elimination of the heterogeneous linear momentum term. It is concluded that heterogeneity does not affect the linear momentum equations of saturated, porous media. However, this may not be the case for the conservation of energy and the requirement of non-negative entropy production as a result of the work produced by the interaction term. The next chapter will address this issue in more detail.

For the second viscous interaction term $\boldsymbol{R}^{pf\text{-}s;\boldsymbol{v}^{pf\text{-}s}}$ stationary pore fluid flow is assumed with $\boldsymbol{v}^{pf\text{-}s} \neq 0$, while still $\ddot{\boldsymbol{u}}^s, \dot{\boldsymbol{v}}^{pf\text{-}s} = 0$. Darcy [40] recognised and formalised the effect of relative pore water flow from field experience, resulting in Darcy's Law:

$$\boldsymbol{w}^{pf\text{-}s} = n\boldsymbol{v}^{pf\text{-}s} = \frac{\boldsymbol{\kappa}}{\mu}\left(\nabla\cdot\left(p\boldsymbol{I}\right) + \rho^{pf}\boldsymbol{g}\right) \tag{3.43}$$

where $\boldsymbol{w}^{pf\text{-}s}$ is the specific discharge, $\boldsymbol{\kappa}$ the intrinsic permeability tensor, μ the dynamic viscosity [41] and $\boldsymbol{g}$ the gravity vector that is defined by:

$$\boldsymbol{g} = \begin{bmatrix}0 & 0 & -9.81\end{bmatrix}^T \tag{3.44}$$

Darcy derived an empirical relation between the macroscopic parameters relative pore water flow $\boldsymbol{v}^{pf\text{-}s}$ and pore fluid stress $p\boldsymbol{I}$. In spite of its limited substantiation -one could say using the phenomenological approach- Darcy's Law appears to be widely applicable. Much later, Darcy's Law was also derived from first principles using averaging of the microscopic momentum equation of the pore fluid [41, 42]. These derivations aim at finding the dominant terms in the averaged equations, whilst common assumptions concern the neglect of the internal shear stresses in the pore fluid as compared to the drag at the interface and continuity of velocities at the interface (no slip condition). A detailed treatment of this subject is beyond the scope of this thesis. The findings from Bear and Bachmat [41] are here used to define the second interaction term.

As for the first interaction term, the definition of the viscous interaction force $\boldsymbol{R}^{pf\text{-}s;\boldsymbol{v}^{pf\text{-}s}}$ starts from Equation 3.36. The friction at the soil-fluid interface relates to the deviatoric part of the pore fluid stress. Therefore, the pore fluid stress $\boldsymbol{\sigma}^f$ is decomposed into the isotropic component $\boldsymbol{\sigma}^{f;I}$ and its deviatoric counterpart $\boldsymbol{\sigma}^{f;D}$:

$$-\frac{1}{V^A}\int_{S^{A;fs}}\mathbf{n}^{fs}\cdot\boldsymbol{\sigma}^f\,\mathrm{d}S=-\frac{1}{V^A}\int_{S^{A;fs}}\mathbf{n}^{fs}\cdot\boldsymbol{\sigma}^{f;I}\,\mathrm{d}S-\frac{1}{V^A}\int_{S^{A;fs}}\mathbf{n}^{fs}\cdot\boldsymbol{\sigma}^{f;D}\,\mathrm{d}S \tag{3.45}$$

The viscous interaction term is then defined by:

$$\boldsymbol{R}^{pf\text{-}s;\boldsymbol{v}^{pf\text{-}s}}=-\frac{1}{V^A}\int_{S^{A;fs}}\mathbf{n}^{fs}\cdot\boldsymbol{\sigma}^{f;D}\,\mathrm{d}S \tag{3.46}$$

Bear and Bachman (Equation 2.6.46, [41]) derive an expression for $\boldsymbol{R}^{pf\text{-}s;\boldsymbol{v}^{pf\text{-}s}}$ based on the averaging of a Newtonian pore fluid:

$$\boldsymbol{R}^{pf\text{-}s;\boldsymbol{v}^{pf\text{-}s}}=n^2\mu\boldsymbol{\kappa}^{-1}\cdot\boldsymbol{v}^{pf\text{-}s} \tag{3.47}$$

Substitution of Equations 3.47 and 3.40 into the linear momentum equation of the pore fluid 3.34, while neglecting inertial terms, yields after elaboration:

$$n^2\boldsymbol{v}^{pf\text{-}s}=n\frac{\boldsymbol{\kappa}}{\mu}\left(\nabla\cdot\left(p\boldsymbol{I}\right)+\rho^{pf}\boldsymbol{g}\right) \tag{3.48}$$

A comparison between the resulting Equation 3.48 and Equation 3.43 reveals that including the viscous interaction term $\boldsymbol{R}^{pf\text{-}s;\boldsymbol{v}^{pf\text{-}s}}$ yields Darcy's Law multiplied by the porosity n. The definition of the viscous interaction term 3.47 thus satisfies Darcy's Law, which may replace the linear momentum equation of the pore fluid without loss of validity. Hence, Darcy's Law can be considered an empirical relation, a constitutive relation and a particular case of the linear momentum equation of the pore fluid.

For the last, tortuous interaction term $\boldsymbol{R}^{pf\text{-}s;\dot{\boldsymbol{v}}^{pf\text{-}s}}$ the Author also allows $\ddot{\boldsymbol{u}}^s$, $\dot{\boldsymbol{v}}^{pf\text{-}s}\neq 0$. More specifically, the interaction is considered to be a result of the relative acceleration of the pore fluid $\dot{\boldsymbol{v}}^{pf\text{-}s}$, defined by:

$$\dot{\boldsymbol{v}}^{pf\text{-}s}=\frac{\partial\boldsymbol{v}^{pf\text{-}s}}{\partial t}+\boldsymbol{v}^{pf\text{-}s}\frac{\partial\boldsymbol{v}^{pf\text{-}s}}{\partial\boldsymbol{x}}=\frac{\partial\left(\boldsymbol{v}^{pf}-\dot{\boldsymbol{u}}^s\right)}{\partial t}+\left(\boldsymbol{v}^{pf}-\dot{\boldsymbol{u}}^s\right)\frac{\partial\left(\boldsymbol{v}^{pf}-\dot{\boldsymbol{u}}^s\right)}{\partial\boldsymbol{x}}=\dot{\boldsymbol{v}}^{pf}-\ddot{\boldsymbol{u}}^s \tag{3.49}$$

Interaction between the soil skeleton and pore fluid as a result of a relative acceleration has been related to the *added mass* effect [4]. A solid body mass accelerating through the surrounding fluid requires the fluid to displace around the body. Apart from any frictional interaction at the interface, the solid body experiences an added mass force as a result of the transfer of kinetic energy to the fluid. It can be shown that the interaction adds intertia to the solid body, hence the term added mass [43].

The pore channels of soils are tortuous, diverting the pore fluid flow along particular paths (Figure 3.5). Even though an accelerating pore fluid is considered, the physical implications are similar to those for an accelerating solid body mass. As a result of the tortuosity of the pore channels a part of the kinetic energy of the pore fluid is transferred to the soil skeleton. The tortuous interaction can be derived starting from Equation 3.36, provided that the geometry network is known and can be expressed analytically, see e.g. [35]. As for the added mass effect, the equivalence between the resulting pore fluid pressure and the additional inertia of the soil skeleton can be used to express the interaction term. However, in practice the pore channel network is complex and largely unknown. Therefore, an alternative consideration based on the work of Coussy [18] is presented here.

Referring to Figure 3.5, consider the rate of the relative pore fluid velocity at the microscale $\dot{\boldsymbol{v}}^{f\text{-}s}$ and compare it to the macroscopic equivalent measure $\dot{\boldsymbol{v}}^{pf\text{-}s}$. As a result of the tortuosity of the pore channels, the kinetic energy associated with the averaged microscopic pore fluid acceleration will be larger than the kinetic energy that would be calculated from the macroscopic pore fluid acceleration [18]. If one solely considers the kinetic energy of the relative pore fluid velocity $\boldsymbol{v}^{pf\text{-}s}$, that is, $K^{pf\text{-}s}$, this inequality is mathematically expressed by:

$$K^{pf\text{-}s} = \frac{1}{2}\int_v n\rho^f \boldsymbol{v}^{pf\text{-}s}\cdot\boldsymbol{v}^{pf\text{-}s}\,\mathrm{d}v \leqslant \frac{1}{2}\int_v \left(\int_{V^A}\rho^f \boldsymbol{v}^{f\text{-}s}\cdot\boldsymbol{v}^{f\text{-}s}\,\mathrm{d}V\right)\mathrm{d}v \tag{3.50}$$

The difference between the 'true' and macroscopic kinetic energy is attributed to interaction, which corrects the energy balance. It is worth noting that the relative acceleration will vary along the flow path as a result of variations of the discharge area, which will affect the (rate-dependent) modulus [18]. Hence, the tortuosity also affects the viscous interaction force; both effects are combined in the *dynamic permeability*. However, considering the low-frequency range that is the starting point here, this effect is ignored and the discussion is limited to the *strict tortuosity effect* [18].

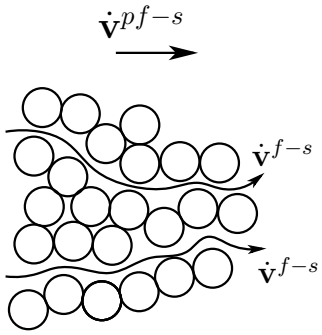


Figure 3.5: Tortuous flow paths through a soil skeleton

The tortuosity effect is expressed by the tortuosity factor a [44]. Coussy [18] demonstrates that a is related to the localised form of Equation 3.50:

$$a = \frac{\int_{V^A} \rho^f \boldsymbol{v}^{f\text{-}s} \cdot \boldsymbol{v}^{f\text{-}s} \mathrm{d}V}{n\rho^f \boldsymbol{v}^{pf\text{-}s} \cdot \boldsymbol{v}^{pf\text{-}s}} \tag{3.51}$$

The kinetic energy K^{tort} may be introduced, which defines the amount of kinetic energy that is transferred from the pore fluid to the soil due to the tortuosity of the pore channels. Based on Equations 3.50 and 3.51, K^{tort} can be defined by:

$$\begin{aligned} K^{tort} &= \frac{1}{2}\int_{V^A} \rho^f \boldsymbol{v}^{f\text{-}s} \cdot \boldsymbol{v}^{f\text{-}s} \mathrm{d}V - \frac{1}{2} n\rho^f \boldsymbol{v}^{pf\text{-}s} \cdot \boldsymbol{v}^{pf\text{-}s} \\ &= \frac{1}{2} an\rho^f \boldsymbol{v}^{pf\text{-}s} \cdot \boldsymbol{v}^{pf\text{-}s} - \frac{1}{2} n\rho^f \boldsymbol{v}^{pf\text{-}s} \cdot \boldsymbol{v}^{pf\text{-}s} \\ &= \frac{1}{2}(a-1) n\rho^f \boldsymbol{v}^{pf\text{-}s} \cdot \boldsymbol{v}^{pf\text{-}s} \end{aligned} \tag{3.52}$$

Then, the corresponding interaction force $\boldsymbol{R}^{pf\text{-}s;\dot{\boldsymbol{v}}^{pf\text{-}s}}$ can be derived from the derivative of K^{tort} with respect to space [4]:

$$\boldsymbol{R}^{pf\text{-}s;\dot{\boldsymbol{v}}^{pf\text{-}s}} = \frac{\partial K^{tort}}{\partial \boldsymbol{x}} = \frac{\partial}{\partial t}\left(\frac{\partial K^{tort}}{\partial \boldsymbol{v}^{pf\text{-}s}}\right) = (a-1) n\rho^f \dot{\boldsymbol{v}}^{pf\text{-}s} \tag{3.53}$$

The tortuosity factor a for strict tortuosity is a function of the geometry of the pore channels. The tortuosity factor a has been derived from the macroscopic response during idealised experiments, where a superfluid was used to isolate viscous and tortuous interaction effects [44]. The results provide an approximate relation between the tortuosity factor a and porosity n, that is, $a = 0.35(1-n)/n + 1$, for a measured range of $0.335 \geq n \geq 0.105$. Detailed experimental data of a for different sands and properties are lacking. Therefore, the simplified relation between a and n is relied on, while noting that its effect is expected to be small for the low frequency range being considered.

By substituting the resulting Equations for the hydrostatic interaction term 3.40, the viscous interaction term 3.47 and tortuous interaction term 3.53 into the definition of the total interaction 3.35, the final result for the interaction between the soil and pore fluid is given as:

$$\begin{aligned}\boldsymbol{R}^{pf\text{-}s} &= \boldsymbol{R}^{pf\text{-}s;0} + \boldsymbol{R}^{pf\text{-}s;\boldsymbol{v}^{pf\text{-}s}} + \boldsymbol{R}^{pf\text{-}s;\dot{\boldsymbol{v}}^{pf\text{-}s}} \\ &= p\boldsymbol{I}\cdot\nabla n + n^2\mu\boldsymbol{\kappa}^{-1}\cdot\boldsymbol{v}^{pf\text{-}s} + (a-1)n\rho^{pf}\dot{\boldsymbol{v}}^{pf\text{-}s}\end{aligned} \tag{3.54}$$

3.2.5. Mass equations

The mass equations follow from elaboration of Equation 3.11 for the soil skeleton and pore fluid. It should be kept in mind that the final result of 3.11 is expressed in terms of material time derivatives. The operator $\frac{\mathrm{D}}{\mathrm{D}t}$ thereby defines the change of a material point co-moving with the constituent under consideration. Material time derivates associated with the other constituent should therefore be corrected, as will be shown below.

Substituting the volume fraction and volumetric mass of the soil skeleton into Equation 3.11 results in:

$$\frac{\mathrm{D}M^s}{\mathrm{D}t} = \int_v \left(\frac{\mathrm{D}}{\mathrm{D}t}\left((1-n)\rho^g\right) + (1-n)\rho^g\nabla\cdot\dot{\boldsymbol{u}}^s \right) \mathrm{d}v = 0 \tag{3.55}$$

The localised form of Equation 3.55 may be elaborated, while noting that all terms can be expressed in terms of material time derivates without any correction:

$$(1-n)\dot{\rho}^g - \dot{n}\rho^g + (1-n)\rho^g\nabla\cdot\dot{\boldsymbol{u}}^s = 0 \tag{3.56}$$

The material time derivative $\dot{\rho}^g$ is related to the volumetric deformation of the grains $\boldsymbol{\epsilon}^{g;vol}$ by:

$$\dot{\rho}^g = -\rho^g\dot{\boldsymbol{\epsilon}}^{g;vol} \tag{3.57}$$

The term $\nabla\dot{\boldsymbol{u}}^s$ is also expressed in terms of strains by using Equation 3.27:

$$\nabla\cdot\dot{\boldsymbol{u}}^s = \frac{\partial\dot{u}_i^s}{\partial x_i} = \dot{\epsilon}_{ii}^s = \dot{\boldsymbol{\epsilon}}^{s;vol} \tag{3.58}$$

Substituting Equations 3.57 and 3.58 into 3.56 yields, after elaboration, the final expression for the conservation of mass of the soil skeleton:

$$\dot{n} - (1-n)\left(\dot{\boldsymbol{\epsilon}}^{s;vol} - \dot{\boldsymbol{\epsilon}}^{g;vol}\right) = 0 \tag{3.59}$$

The mass equation of the pore fluid after substituting the volume fraction and volumetric mass of the pore fluid into Equation 3.11 reads:

$$\frac{\mathrm{D}M^{pf}}{\mathrm{D}t} = \int_v \left(\frac{\mathrm{D}}{\mathrm{D}t}\left(n\rho^f\right) + n\rho^f\nabla\cdot\boldsymbol{v}^{pf} \right) \mathrm{d}v = 0 \tag{3.60}$$

Elaborating Equation 3.60 in terms of material time derivatives requires a correction for the porosity n, which is a property moving with the soil skeleton. The correction term follows from:

$$\frac{D^{pf}}{Dt}n = \frac{\partial n}{\partial t} + \boldsymbol{v}^{pf}\frac{\partial n}{\partial \boldsymbol{x}} = \frac{\partial n}{\partial t} + \left(\dot{\boldsymbol{u}}^s + \boldsymbol{v}^{pf\text{-}s}\right)\frac{\partial n}{\partial \boldsymbol{x}} = \dot{n} + \boldsymbol{v}^{pf\text{-}s}\cdot\nabla n \tag{3.61}$$

Elaboration of Equation 3.60 in its localised form while taking account of Equation 3.61 yields:

$$n\dot{\rho}^f + \dot{n}\rho^f + \rho^f \boldsymbol{v}^{pf\text{-}s} \cdot \nabla n + n\rho^f \nabla \cdot \boldsymbol{v}^{pf} = 0 \tag{3.62}$$

Equation 3.62 is elaborated in a similar way as was done for the soil skeleton. First, it is noted that the material derivative $\dot{\rho}^f$ has to be the result of (volumetric) deformation of the pore fluid. Note also that volumetric deformation is the only possible deformation mode, as expressed by the constitutive relation 3.4. Hence, $\dot{\rho}^f$ is defined as:

$$\dot{\rho}^f = -\rho^f \dot{\boldsymbol{\epsilon}}^{pf;vol} = -\rho^f \frac{\dot{p}\boldsymbol{I}}{K^{pf}} \tag{3.63}$$

The term $\nabla \cdot \boldsymbol{v}^{pf}$ in Equation 3.62 is split into a part related to the soil skeleton and a part related to the pore fluid by using Equation 3.1, that is, $\nabla \cdot \boldsymbol{v}^{pf} = \nabla \cdot \dot{\boldsymbol{u}}^s + \nabla \cdot \boldsymbol{v}^{pf\text{-}s}$. Equation 3.58 relates $\nabla \cdot \dot{\boldsymbol{u}}^s$ to the (rate of) strains of the soil skeleton $\dot{\boldsymbol{\epsilon}}^s$. The complementary term $\nabla \cdot \boldsymbol{v}^{pf\text{-}s}$ may be related to the relative pore water flux $\boldsymbol{w}^{pf\text{-}s}$ that was previously defined in Darcy's Equation 3.43:

$$n\nabla \cdot \boldsymbol{v}^{pf\text{-}s} = \nabla \cdot \boldsymbol{w}^{pf\text{-}s} - \boldsymbol{v}^{pf\text{-}s} \cdot \nabla n \tag{3.64}$$

The expression in terms of flux $\boldsymbol{w}^{pf\text{-}s}$ will simplify the relation with Darcy's equation later on and will eliminate the term $\boldsymbol{v}^{pf\text{-}s} \cdot \nabla n$ from the mass equation. Substituting Equations 3.58, 3.63 and 3.64 into 3.62 and subsequent elaboration yields the final expression of the conservation of mass of the pore fluid:

$$\dot{n} - n\frac{\dot{p}\boldsymbol{I}}{K^{pf}} + n\dot{\boldsymbol{\epsilon}}^{s;vol} + \nabla \cdot \boldsymbol{w}^{pf\text{-}s} = 0 \tag{3.65}$$

It can be seen that the equations of mass of the soil skeleton 3.59 and pore fluid 3.65 can be easily combined through the material derivative of the porosity $\dot{n}$. The result, usually denoted by the *storage equation* [19], reads:

$$n\frac{\dot{p}\boldsymbol{I}}{K^{pf}} - \nabla \cdot \boldsymbol{w}^{pf\text{-}s} + (1-n)\dot{\boldsymbol{\epsilon}}^{g;vol} - \dot{\boldsymbol{\epsilon}}^{s;vol} = 0 \tag{3.66}$$

The storage equation couples the continuity of the pore water and soil skeleton. Both rates of stresses and strains (or fluxes) appear in 3.66. The equation can be further elaborated by introducing a constitutive relation for the soil skeleton and Darcy's equation for the pore fluid. At this stage, the equation may be merely simplified by applying the aforementioned assumption of incompressible particles:

$$n\frac{\dot{p}\boldsymbol{I}}{K^{pf}} - \nabla \cdot \boldsymbol{w}^{pf\text{-}s} - \dot{\boldsymbol{\epsilon}}^{s;vol} = 0 \tag{3.67}$$

3.2.6. Momentum equations

The momentum equations have been specified for the soil skeleton and pore fluid using phase averaged properties in Equations 3.33 and 3.34. The final result of the equations is obtained by substituting the stress measures from Equations 3.25 and 3.26, while the interaction terms are substituted from Equation 3.54. The resulting conservation of linear

momentum of the pore fluid and soil skeleton and the sum of both, the bulk momentum, read respectively:

$$(1-n)\rho^g \ddot{\boldsymbol{u}}^s - \nabla\cdot\boldsymbol{\sigma}^* - (1-n)\nabla\left(p\boldsymbol{I}\right) - (1-n)\rho^g\boldsymbol{b} - n^2\mu\boldsymbol{\kappa}^{-1}\boldsymbol{v}^{pf\text{-}s} - (a-1)n\rho^f\dot{\boldsymbol{v}}^{pf\text{-}s} = 0 \tag{3.68}$$

$$n\rho^f\dot{\boldsymbol{v}}^{pf} - n\nabla\cdot\left(p\boldsymbol{I}\right) - n\rho^f\boldsymbol{b} + n^2\mu\boldsymbol{\kappa}^{-1}\boldsymbol{v}^{pf\text{-}s} + (a-1)n\rho^f\dot{\boldsymbol{v}}^{pf\text{-}s} = 0 \tag{3.69}$$

$$(1-n)\rho^g\ddot{\boldsymbol{u}}^s + n\rho^f\dot{\boldsymbol{v}}^{pf} - \nabla\cdot\boldsymbol{\sigma} - \rho\boldsymbol{b} = 0 \tag{3.70}$$

It is worth noting that the bulk momentum equation reduces to the momentum equation of a single constituent when $\ddot{\boldsymbol{u}}^s = \dot{\boldsymbol{v}}^{pf}$. Next, the Author considers the case of hydrostatics, that is $\boldsymbol{v}^{pf\text{-}s}, \ddot{\boldsymbol{u}}^s, \dot{\boldsymbol{v}}^{pf\text{-}s} = 0$, and defines the intergranular stress $\boldsymbol{\sigma}^*$ and pore fluid stress $p\boldsymbol{I}$ for this particular case. To this end, both inertial and flow terms are neglected in Equations 3.68 and 3.69. In addition, the gravitation vector from Equation 3.44 is substituted, i.e. $\boldsymbol{b} = \boldsymbol{g}$. After isolating the stresses the results read:

$$\nabla\cdot\left(p\boldsymbol{I}\right) = -\rho^f\boldsymbol{g} \tag{3.71}$$

$$\nabla\cdot\boldsymbol{\sigma}^* = -(1-n)\left(\rho^g - \rho^f\right)\boldsymbol{g} \tag{3.72}$$

Hence, for the case of hydrostatics the pore fluid stress $p\boldsymbol{I}$ does not depend on the porosity, whilst the intergranular stress σ^* is defined by the buoyant weight of the soil $\rho^{buoy} = (1-n)\left(\rho^g - \rho^f\right)$. It is common practice in soil mechanics to define the stresses rather than momentum equations, as the intergranular stresses are of importance for the strength and stiffness properties of soils. Equations 3.71 and 3.72 are often starting points for analyses, rather than the momentum equations. The next section will present an alternative derivation of the momentum equation, starting from the effective and pore fluid stresses.

3.2.7. Alternative derivation of momentum equations

Instead of the momentum equation *of* the pore fluid and soil skeleton, this section considers the linear momentum *affecting* the effective stress and pore fluid stress. The starting equations were provided in the previous section by Equations 3.71 and 3.72. Generally, these equations should be defined in terms of the body load $\boldsymbol{b}$ rather than gravitational load $\boldsymbol{g}$:

$$\nabla\cdot\left(p\boldsymbol{I}\right) = -\rho^f\boldsymbol{b} \tag{3.73}$$

$$\nabla\cdot\boldsymbol{\sigma}^* = -(1-n)\left(\rho^g - \rho^f\right)\boldsymbol{b} = -\rho^{buoy}\boldsymbol{b} \tag{3.74}$$

$$\nabla\cdot\boldsymbol{\sigma} = -\rho\boldsymbol{b} \tag{3.75}$$

The key properties of the stresses in a soil skeleton under hydrostatics are the irrelevance of the value of the porosity n for the pore fluid stress $p\boldsymbol{I}$ and the importance of the buoyant volumetric mass ρ^{buoy} for the intergranular stress $\boldsymbol{\sigma}^*$. It will be shown that consistently extending these properties for general conditions will yield essentially the

same equations as derived in the previous section. It is additionally noted that interaction does not appear in Equations 3.73 and 3.74, as the hydrostatic interaction term does not affect the stresses. Interaction is only defined in the case of a relative pore fluid motion. The derivation approaches discussed in the previous and this section converge at the established bulk equation.

First, the hydrostatic case is extended for a uniform acceleration $\ddot{\boldsymbol{u}}^s$ applied on both the soil skeleton and pore fluid. There is no relative motion of the pore fluid and therefore no interaction that affects the effective and pore fluid stresses. Objectivity requires this acceleration to be treated like any other acceleration, including the gravitational acceleration. The term arising from $\ddot{\boldsymbol{u}}^s$ is therefore similarly defined as the body load $\boldsymbol{b}$. The key properties of hydrostatics are thus simply extended for a uniform acceleration:

$$\nabla \cdot \left(p \boldsymbol{I} \right) = -\rho^f \boldsymbol{b} + \rho^f \ddot{\boldsymbol{u}}^s \tag{3.76}$$

$$\nabla \cdot \boldsymbol{\sigma}^* = -\rho^{buoy} \boldsymbol{b} + \rho^{buoy} \ddot{\boldsymbol{u}}^s \tag{3.77}$$

$$\nabla \cdot \boldsymbol{\sigma} = -\rho \boldsymbol{b} + \rho \ddot{\boldsymbol{u}}^s \tag{3.78}$$

Then the pore fluid is allowed to accelerate relative to the soil skeleton, that is, $\dot{\boldsymbol{v}}^{pf\text{-}s} \neq 0$. The relative acceleration introduces the stress interaction term $\tilde{\boldsymbol{R}}^{pf\text{-}s}$, which is related but not equal to the constituent interaction term $\boldsymbol{R}^{pf\text{-}s}$. The acceleration $\dot{\boldsymbol{v}}^{pf\text{-}s}$ simply defines an additional interaction term for the pore fluid, while the bulk equation should be extended by the term $n\rho^f \dot{\boldsymbol{v}}^{pf}$. The additional term arising in the momentum affecting the intergranular stress then follows from the requirement that the sum of the momentum equations affecting the stresses should be equal to the bulk equation. The result reads:

$$\nabla \cdot \left(p \boldsymbol{I} \right) = -\rho^f \boldsymbol{b} + \rho^f \left(\ddot{\boldsymbol{u}}^s + \dot{\boldsymbol{v}}^{pf\text{-}s} \right) + \tilde{\boldsymbol{R}}^{pf\text{-}s} \tag{3.79}$$

$$\nabla \cdot \boldsymbol{\sigma}^* = -\rho^{buoy} \boldsymbol{b} + \rho^{buoy} \ddot{\boldsymbol{u}}^s - (1-n)\rho^f \dot{\boldsymbol{v}}^{pf\text{-}s} - \tilde{\boldsymbol{R}}^{pf\text{-}s} \tag{3.80}$$

$$\nabla \cdot \boldsymbol{\sigma} = -\rho \boldsymbol{b} + \rho \ddot{\boldsymbol{u}}^s + n\rho^f \dot{\boldsymbol{v}}^{pf\text{-}s} \tag{3.81}$$

The term $(1-n)\rho^{pf} \dot{\boldsymbol{v}}^{pf\text{-}s}$ defines the reaction force from the relative pore fluid acceleration reducing $\nabla \cdot \boldsymbol{\sigma}^*$. Its physical meaning can be further elucidated by using the relation $\rho^{buoy} \dot{\boldsymbol{v}}^{pf\text{-}s} = (1-n)\rho^s \dot{\boldsymbol{v}}^{pf\text{-}s} - (1-n)\rho^f \dot{\boldsymbol{v}}^{pf\text{-}s}$. Substitution into Equation 3.80 yields:

$$\nabla \cdot \boldsymbol{\sigma}^* + (1-n)\rho^s \dot{\boldsymbol{v}}^{pf\text{-}s} = -\rho^{buoy} \boldsymbol{b} + \rho^{buoy} \left(\ddot{\boldsymbol{u}}^s + \dot{\boldsymbol{v}}^{pf\text{-}s} \right) - \tilde{\boldsymbol{R}}^{pf\text{-}s} \tag{3.82}$$

The right hand side of Equation 3.82 signifies the effect of a uniform acceleration $\ddot{\boldsymbol{u}}^s + \dot{\boldsymbol{v}}^{pf\text{-}s}$. However, the additional term on the left hand side corrects for the fact that the soil skeleton is not moving, i.e. it holds the soil skeleton in place. An alternative interpretation follows from reconsidering the definition of the frame of reference. So far, the finite element formulation has been anticipated by considering the pore fluid motion relative to the soil skeleton, but this can be turned around. One can even go one step further by tying the reference frame to the uniformly *accelerating* pore fluid. The introduction of this non-inertial reference frame requires the introduction of fictitious or intertia forces in order to account for the objectivity of the conservation of linear momentum. In the

Author's case, this inertia force logically follows from the mass of the soil skeleton accelerated by the relative pore fluid acceleration in the opposite direction, i.e. the term appearing on the left hand-side of Equation 3.82.

The derivation continues by specifying the interaction term $\tilde{\boldsymbol{R}}^{pf\text{-}s}$. It was already noted that the hydrostatic interaction term can be omitted when the momentum affecting the stresses is considered. In addition, the starting point of pore fluid stresses being independent of the volume fraction is recalled. Applying this starting point on the stress interaction term $\tilde{\boldsymbol{R}}^{pf\text{-}s}$ results in:

$$\tilde{\boldsymbol{R}}^{pf\text{-}s} = \frac{\boldsymbol{R}^{pf\text{-}s} - p\boldsymbol{I}\nabla n}{n} \tag{3.83}$$

Substituting $\boldsymbol{R}^{pf\text{-}s}$ from Equation 3.54 into 3.83, and the result into Equations 3.79-3.81 leads after elaboration to the final set of expressions:

$$\nabla\cdot\left(p\boldsymbol{I}\right) = -\rho^f\boldsymbol{b} + \rho^f\dot{\boldsymbol{v}}^{pf} + n\mu\boldsymbol{\kappa}^{-1}\boldsymbol{v}^{pf\text{-}s} + (a-1)\rho^f\dot{\boldsymbol{v}}^{pf\text{-}s} \tag{3.84}$$

$$\nabla\cdot\boldsymbol{\sigma}^* = -\rho^{buoy}\boldsymbol{b} + \rho^{buoy}\ddot{\boldsymbol{u}}^s - n\mu\boldsymbol{\kappa}^{-1}\boldsymbol{v}^{pf\text{-}s} + (n-a)\rho^f\dot{\boldsymbol{v}}^{pf\text{-}s} \tag{3.85}$$

$$\nabla\cdot\boldsymbol{\sigma} = -\rho\boldsymbol{b} + (1-n)\rho^g\ddot{\boldsymbol{u}}^s + n\rho^f\dot{\boldsymbol{v}}^{pf} \tag{3.86}$$

Multiplying the momentum affecting the pore fluid stress 3.84 by the porosity n results in the momentum equation of the pore fluid 3.69. As elimination of n from both sides of the equation will not affect the solution, the equations are thus essentially identical. In other words, provided that all other variables are the same the same pore fluid stress $p\boldsymbol{I}$ will be calculated in both cases. When Equation 3.84 is multiplied by n, the momentum affecting the effective stress 3.85 needs to be reformulated in order to satisfy the (unaltered) bulk equation 3.86. It can be shown that the result equals the momentum equation of the soil skeleton 3.68. Furthermore, the solution of the momentum affecting the effective stress 3.85 must be equal to the momentum of the soil skeleton 3.68, given the identical solutions of the pore fluid (stress) and the (unaltered) bulk equation.

It is concluded that the equations derived using a phenomenological approach, namely starting from and consistently extending the pore fluid and effective stresses for hydrostatics, yield essentially the same equations as derived from first principles in the previous section. The buoyancy effect in porous media is thereby not necessarily restricted to hydrostatics. Nonetheless, it is recognised that the momentum equations 3.68-3.70 provide the necessary sound, theoretical basis, which is generally applicable to multiphase media and allows one to formulate the interaction terms in the same framework. The set of expressions 3.84-3.86 are essentially equal to the momentum equations and can be used interchangeably.

3.3. Approximations for liquefaction flow slides

3.3.1. Governing set of equations

The derived equations provide insight into the physics of liquefaction flow slides. For each stage of a liquefaction flow slide, namely hydrostatics, triggering, redistribution by

consolidation and slope failure, the governing equations can be simplified and elaborated to gain insight into the phenomenon. The governing set of equations is defined by the conservation equations as derived in the previous sections, complemented by the generic constitutive equations of the soil skeleton. Incompressibility of the soil particles furthermore allows the replacement of the intergranular stress $\boldsymbol{\sigma}^*$ by the effective stress $\boldsymbol{\sigma}'$:

$$n\frac{\dot{p}\boldsymbol{I}}{K^f} - \nabla\cdot\boldsymbol{w}^{pf\text{-}s} - \dot{\boldsymbol{\epsilon}}^{s;vol} = 0 \tag{3.67}$$

$$(1-n)\rho^g\ddot{\boldsymbol{u}}^s - \nabla\cdot\boldsymbol{\sigma}' - (1-n)\nabla\left(p\boldsymbol{I}\right) - (1-n)\rho^g\boldsymbol{b} - n^2\mu\boldsymbol{\kappa}^{-1}\boldsymbol{v}^{pf\text{-}s} - (a-1)n\rho^f\dot{\boldsymbol{v}}^{pf\text{-}s} = 0 \tag{3.87}$$

$$n\rho^f\dot{\boldsymbol{v}}^{pf} - n\nabla\cdot\left(p\boldsymbol{I}\right) - n\rho^f\boldsymbol{b} + n^2\mu\boldsymbol{\kappa}^{-1}\boldsymbol{v}^{pf\text{-}s} + (a-1)n\rho^f\dot{\boldsymbol{v}}^{pf\text{-}s} = 0 \tag{3.69}$$

$$\dot{\boldsymbol{\sigma}}'^J = \boldsymbol{D}:\dot{\boldsymbol{\epsilon}}^s \tag{3.3}$$

Incompressibility of the particles is a reasonable approximation for most minerals and will therefore be assumed from now on. Recall that the relative pore fluid flux was defined by $\boldsymbol{w}^{pf\text{-}s} = n\boldsymbol{v}^{pf\text{-}s}$ and the soil skeleton strain by $\boldsymbol{\epsilon}^s = \frac{1}{2}\left(\nabla\otimes\boldsymbol{u}^s + \boldsymbol{u}^s\otimes\nabla\right)$. After discretisation in time and space, the four equations above form a closed set of equations; the amount of free variables, for instance defined by $\boldsymbol{u}^s$, $\boldsymbol{v}^{pf\text{-}s}$, $\boldsymbol{\sigma}'$ and p equals the amount of equations. Depending on the case considered, the bulk equation 3.70 or the momentum equations affecting the stresses, Equations 3.84 and 3.85, may (partly) replace the momentum Equations 3.87 and 3.69.

3.3.2. Boundary conditions

The initial and boundary conditions complement the initial-boundary value problem that is considered, in this case slope stability. Both conditions restrain the set of equations listed above and are thus expressed in terms of the free variables or derived quantities. The initial conditions set a reference for the whole spatial domain. Assuming initially static conditions, the initial conditions are usually defined by calculating $\boldsymbol{\sigma}'$ and p from gravity loading and resetting the deformation variables $\boldsymbol{u}^s$ and $\boldsymbol{v}^{pf\text{-}s}$ to zero. The boundary conditions restrain the spatial domain at its boundaries. Boundary conditions can be both convenient and strictly necessary. They can be expressed in one or more free variables or as a load, provided that these are consistent with the actual problem considered, do not introduce artefacts and provide a well-posed problem. For instance, rigid body motion of the spatial domain would provide non-unique solutions. The boundary conditions will be specified in Chapter 5 (see Table 5.1).

The set of equations will be applied to liquefaction flow slides, which does not imply that its application is restricted to these type of problems. For instance, the equations apply to both diffuse and localised failure, that is, provided that the constitutive equations introduce localised deformation and that evolution of the shear bands is accounted for. Introducing localisation may be established by introducing material rotation, which implies that the stress tensor is no longer symmetrical and the formulation should be

extended with the conservation of angular momentum. An example will be treated in the next chapter, where the post-liquefaction stage of particles rolling over the slope will be considered in more detail.

3.3.3. Hydrostatics

Liquefaction flow slides start from a completely hydrostatic situation. Inertial terms, (relative) flow of the pore fluid and deformations of the pore fluid and soil skeleton are ignored. The set of equations reduces to the aforementioned equations:

$$\nabla \cdot \left(p\boldsymbol{I} \right) = -\rho^{f}\boldsymbol{b} \tag{3.73}$$

$$\nabla \cdot \boldsymbol{\sigma}' = -\rho^{buoy}\boldsymbol{b} \tag{3.74}$$

It is stressed once more that heterogeneity of the subsoil does not affect the hydrostatic situation.

3.3.4. Triggering

The triggering of liquefaction flow slides requires the susceptible soil to be brought into a potentially unstable (metastable) stress state, followed by a perturbation to initiate the event. The phase starts from hydrostatics and ends with instability and the start of a high rate of pore pressure rise and accelerating movement of the soil skeleton. Triggering thus bridges a predominantly static and dynamic phase.

The key equation for describing triggering is given by the constitutive relation of the soil skeleton 3.3, which defines the point of instability. In addition, the undrained response requires the incorporation of the storage equation 3.88. The most simple case of triggering is thus described by the following two equations, while noting that the hydrostatic conditions 3.73 and 3.74 are still valid:

$$n\frac{\dot{p}\boldsymbol{I}}{K^{f}} = \dot{\boldsymbol{\epsilon}}^{s;vol} \tag{3.88}$$

$$\dot{\boldsymbol{\sigma}}'^{J} = \boldsymbol{D} : \dot{\boldsymbol{\epsilon}}^{s} \tag{3.3}$$

Some case histories refer to the gradual steepening of slopes, thereby bringing the soil to an unstable state. The steepening of the slope may be simplified to a uniform rotation of the body mass or, equivalently, to a rotation of the gravity load vector $\boldsymbol{g}$ in the opposite direction in space. If the rotation matrix $\boldsymbol{Q}$ describes the rotation of the gravity load vector $\boldsymbol{g}$, Equation 3.74 should be replaced by:

$$\nabla \cdot \boldsymbol{\sigma}' = -\rho^{buoy}\dot{\boldsymbol{Q}} \cdot \boldsymbol{g} \tag{3.89}$$

$$\boldsymbol{Q} = \begin{bmatrix} \cos\theta & -\sin\theta & 0 \\ \sin\theta & \cos\theta & 0 \\ 0 & 0 & 1 \end{bmatrix} \tag{3.90}$$

Herein, θ defines the tilting angle with respect to the horizontal. The actual triggering could be enclosed in the definition of $\boldsymbol{D}$ in the constitutive relation 3.3, for instance by creep. The loading by gradual steepening provides an unambiguous basis for a triggering

analysis. Alternatively, the soil can be brought into a metastable state by an external load that is either locally applied (a surcharge load) or imposed at the boundary (flux, earthquake). The complexity of the governing equations increases with the complexity of the trigger. A surcharge load adds a term to the momentum equations, the flux requires the extension of both the mass and conservation equations, and earthquakes additionally introduce inertial terms to the governing equations.

3.3.5. Instability

Irrespective of the nature of the trigger, the instability after triggering by itself induces an instant decrease in pore fluid stresses. In the extreme case the soil liquefies completely with a decrease of the pore fluid stresses equal to the effective stress of the soil. As a consequence, the governing equations 3.73 and 3.74 reduce to:

$$\nabla \cdot \left(p\boldsymbol{I} \right) = -\rho^{f}\boldsymbol{g} - \rho^{buoy}\boldsymbol{g} \tag{3.91}$$

$$\nabla \cdot \boldsymbol{\sigma}' = 0 \tag{3.92}$$

Hence, full liquefaction is defined by the transfer of the buoyant, volumetric mass $-\rho^{buoy}$ from the effective stress to the pore fluid stress. The local instability subsequently develops into instability of the entire sand bed. The response of the soil is here considered at two time scales. During and just after instability the response is dynamic with a high rate of change of the pore fluid stress. At a larger time scale, consolidation and pore fluid flow dominate the soil response. Both the dynamics and consolidation can be described analytically based on simplifications of the governing equations.

Essentially, the set of equations listed in 3.3.1 has provided the basis for analyses of (elastic) wave propagation through saturated, porous media from the moment Biot [4] and De Josselin de Jong [24] published their work on the subject. Here, the interest lies in the two compressional waves that characterise the response during periodic loading at the boundary. As a first approximation, one can consider the instant pore pressure rise during instability in a similar way. The soil and pore fluid are locked ('undrained') in the first, fast propagating wave, whereas they move out of phase in the second, slow wave that is damped at a short distance from the boundary [45]. Considering the impact, the first wave is of greater interest here. Verruijt [45] demonstrates the analysis can be further simplified if the permeability k and frequency ω are relatively low. More specifically, if the dimensionless factor $ng/k\omega$ becomes large, the properties of the first, undrained wave can be approximated by an undrained analysis. The anticipated orders of magnitude of the frequency and permeability equal $\omega \sim 1\,\mathrm{Hz}$ and $k \sim 10^{-4}\,\mathrm{m\,s^{-1}}$, respectively. Simplifying the dynamic analysis during and just after instability is thereby justified.

The undrained response of the soil just after triggering assumes no relative displacement between the soil skeleton and pore fluid. The conservation of momentum of the soil skeleton and pore fluid are therefore replaced by the bulk equation, while $\ddot{\boldsymbol{u}}^{s}$ defines the simultaneous acceleration of the pore fluid and the soil skeleton. Assuming that the dynamics of the phenomenon allows for the neglect of the body load term, the resulting

equation results from elaborating Equation 3.86:

$$\nabla \cdot \boldsymbol{\sigma} = -\rho \ddot{\boldsymbol{u}}^s \tag{3.93}$$

Simplifying the constitutive relation for volumetric compression of the soil skeleton to $\dot{\boldsymbol{\sigma}} - \dot{p}\boldsymbol{I} = K^s \dot{\boldsymbol{\epsilon}}^{s;vol}$ and substitution of Equation 3.27 yields:

$$\dot{\boldsymbol{\sigma}} = \left(\frac{K^{pf}}{n} + K^s \right) \nabla \cdot \dot{\boldsymbol{u}}^s \tag{3.94}$$

The obtained set of equations 3.93-3.94 expresses the propagation of an undrained wave through the saturated soil. For one dimension and one point in space, the set of equations reduces to:

$$\frac{\mathrm{d}\sigma}{\mathrm{d}x} = \rho \frac{\mathrm{d}\dot{u}^s}{\mathrm{d}t} \tag{3.95}$$

$$\frac{\mathrm{d}\sigma}{\mathrm{d}t} = \left(\frac{K^{pf}}{n} + K^s \right) \frac{\mathrm{d}\dot{u}^s}{\mathrm{d}x} \tag{3.96}$$

The resulting formulation of the governing set of equations can be solved analytically using the method of characteristics [45], provided that the boundary and initial conditions do not violate the aforementioned assumptions. The key element of the solution is the wave velocity c_x^{und}, which is defined by:

$$c_x^{und} = \sqrt{\frac{\frac{K^f}{n} + K^s}{\rho}} \tag{3.97}$$

Hence, instability yields an undrained wave that travels with velocity c_x^{und}. The propagation of the undrained wave is dominated by the pore fluid as $K^{pf} >> K^s$. For typical values for sands, that is, $n = 0.4$ and $K^{pf} = 2 \times 10^9 \,\mathrm{N\,m^{-2}}$, the wave velocity equals $c_x^{und} \approxeq 2000 \,\mathrm{m\,s^{-1}}$. In the case of a uniform susceptible subsoil, local instability will almost instantly trigger instability throughout the entire geometry and, possibly, global failure. If the subsoil remains stable, (local) instability and the generation of excess pore pressures mark the starting point of consolidation.

3.3.6. Consolidation

The same procedure is applied to derive the governing equations for consolidation, but now a relatively slow process is assumed and the inertial terms are neglected. Furthermore, the focus is on the pore fluid stress $p\boldsymbol{I}$ instead of the total stress $\boldsymbol{\sigma}$. Again, the derivation starts with the mass equation 3.67, albeit without neglecting the flux term $\nabla \cdot \boldsymbol{w}^{pf\text{-}s}$. Again, the constitutive equation of the soil skeleton is simplified to a linear equivalent elastic relationship, which implies that the consideration is restricted to small volumetric deformations. In addition, it is noted that the total stress $\boldsymbol{\sigma}$ does not change during consolidation, which reduces the constitutive relation to $\dot{p}\boldsymbol{I} = -K^s \dot{\boldsymbol{\epsilon}}^{s;vol}$. After substitution the resulting, elaborated mass equation reads:

$$\left(\frac{n}{K^f} + \frac{1}{K^s} \right) \dot{p}\boldsymbol{I} = \nabla \cdot \boldsymbol{w}^{pf\text{-}s} \tag{3.98}$$

The complementary equation follows from the momentum equation affecting the pore fluid stress 3.84, where the inertial terms are neglected:

$$\nabla \cdot \left(p\boldsymbol{I} \right) = -\rho^f \boldsymbol{b} + \mu \boldsymbol{\kappa}^{-1} \boldsymbol{w}^{pf\text{-}s} \tag{3.99}$$

Again, the set of obtained equations are simplified to one dimension and one point in space. Differentiation of Equation 3.99 with respect to space and subsequent substitution into Equation 3.98 results in the *consolidation equation*:

$$\frac{\mathrm{d}p}{\mathrm{d}t} = c_x^{cons} \frac{\mathrm{d}^2 p}{\mathrm{d}x^2} \tag{3.100}$$

Herein, the *consolidation coefficient* is defined by:

$$c_x^{cons} = \frac{1}{\frac{\mu}{\kappa}\left(\frac{n}{K^{pf}} + \frac{1}{K^s} \right)} \tag{3.101}$$

The consolidation coefficient defines the characteristic velocity during the dissipation of excess pore fluid stresses. The notion of $K^{pf} >> K^s$ for sands now leads to the neglect of the stiffness term related to the pore fluid n/K^{pf}. Substitution of usual values for one-dimensional (vertical) consolidation of sands, that is, $\mu \approxeq 10^{-3}\,\mathrm{N\,s\,m^{-2}}$, $\kappa \approxeq 10^{-11}\,\mathrm{m^2}$ and $K^s = E^{oed} = 5 \times 10^4\,\mathrm{N\,m^{-2}}$, results in a consolidation coefficient $c_x^{cons} \approxeq 5 \times 10^{-3}\,\mathrm{m^2\,s^{-1}}$. It is concluded that the characteristic velocity during consolidation is much lower than during undrained loading.

3.3.7. Slope failure

The triggering of flow liquefaction may initiate a liquefaction flow slide. Failure can occur instantly after triggering, that is, by an undrained wave or after consolidation, void ratio redistribution and instability of a loosened layer. In either case instability causes a sudden imbalance between the imposed load, the slope, and the resistance or strength of the soil. Based on the typical rate of deformation as derived from case histories, it is reasonable to assume that undrained conditions will prevail during the actual failure. Hence, the momentum of the slope during failure is approximated by:

$$\nabla \cdot \boldsymbol{\sigma} = -\rho \boldsymbol{g} + \rho \ddot{\boldsymbol{u}}^s \tag{3.102}$$

Equation 3.102 demonstrates that the imbalance driven by the slope causes the saturated subsoil to accelerate. The potential (gravity) energy of the slope is (mainly) converted into kinetic energy [46]. The subsequent stages involve fast and large deformations, followed by re-sedimentation and consolidation until the liquefied sand has settled downstream of the slope.

3.4. Concluding remarks

Chapter 2 described the main characteristics of flow liquefaction and liquefaction flow slides, including the undrained instability after triggering that initiates a transition from a predominant hydrostatic situation into a dynamic failure mechanism. The complete

description of liquefaction flow slides thus requires the coupling between the governing equations of the soil and water phase, while also accounting for the effect of inertia. This chapter has elaborated the governing equations for liquefaction flow slides, namely the conservation of mass and linear momentum equations.

A Lagrangian description has been used to derive the governing equations, which suits the history-dependence of soil and, therefore, the finite element implementation. The conservation of mass equations are combined into a single equation, denoted by the storage equation. The elaboration of the conservation of linear momentum results in separate equations for the soil skeleton and pore fluid or, as an alternative for one of these, the bulk. The heterogeneous interaction term is a conspicuous term in the linear momentum equations that is often overlooked. The effect of heterogeneity is automatically eliminated by this interaction term, which has been described by self-equilibration. However, this is not necessarily the case when considering the thermodynamics. The next chapter will go further into detail on the consistency of the framework.

This chapter also presented an alternative derivation of the momentum equations that highlights the role of buoyancy. The starting point of this derivation is the linear momentum affecting the constituent stresses. The starting point of buoyancy in hydrostatics can be extended to dynamics by requiring the objective treatment of the acceleration terms. Furthermore, the interaction terms should be specified for the effect on the constituent stresses, rather than the linear momentum of the constituents. The resulting set of equations are essentially identical to the set of equations that was derived from first principles. The equations derived from the linear momentum affecting the constituent stresses may provide a convenient alternative in particular cases.

Section 3.3 applied the resulting set of governing equations and the boundary conditions to the different stages of liquefaction flow slides. The initial, hydrostatic situation is described by the momentum equations. The description of triggering requires at least the extension of these equations with the constitutive relation and the storage equation. In general, the required complexity of the governing equations depends on the complexity of the trigger. The consequent undrained instability and generation of excess pore fluid stresses implies a transfer of the buoyant weight of the soil skeleton onto the pore fluid. It should be noted that up to the moment of instability, the momentum equations affecting the constituent stresses provide a convenient set of equations. The migration of pore fluid stresses has been considered at two time scales. Directly after instability, an undrained wave propagates through the soil skeleton at a very high velocity. At a much larger time scale, the consolidation equation describes the dissipation of excess pore fluid stresses. The subsequent stage of failure of the slope is described by the linear momentum of the bulk, while introducing inertial terms to the set of governing equations.

References

[1] M. el Tani, *Hydrostatic paradox of saturated media,* Géotechnique **57**, 773–777 (2007).

[2] M. el Tani, D. Kolymbas, and A. Verruijt, *Hydrostatic paradox of saturated media: Discussion,* Géotechnique **58**, 835–837 (2008).

[3] R. de Boer, R. Schiffman, and R. Gibson, *The origins of the theory of consolidation: the terzaghi& fillunger dispute,* Géotechnique **46**, 175–186 (1996).

[4] M. Biot, *Theory of propagation of elastic waves in a fluid-saturated porous solid. i. low-frequency range,* J. Acoust. Soc. Am **28**, 168–178 (1956).

[5] E. Hughes, T. Leighton, G. Petley, P. R. White, and R. Chivers, *Estimation of critical and viscous frequencies for biot theory in cancellous bone,* Ultrasonics **41**, 365–368 (2003).

[6] S. Gao, J. Meegoda, and L. Hu, *Two methods for pore network of porous media,* International Journal for Numerical and Analytical Methods in Geomechanics **36**, 1954–1970 (2012).

[7] J. Bear and A. Verruijt, *Modeling groundwater flow and pollution* (Springer Science & Business Media, 1987).

[8] J. Berryman, *Comparison of upscaling methods in poroelasticity and its generalizations,* Journal of Engineering Mechanics **131**, 928 (2005).

[9] M. Schanz, *Poroelastodynamics: linear models, analytical solutions, and numerical methods,* Applied Mechanics Reviews **62**, 030803 (2009).

[10] P. Cundall and O. Strack, *A discrete numerical model for granular assemblies,* Géotechnique **29**, 47–65 (1979).

[11] R. Burridge and J. Keller, *Poroelasticity equations derived from microstructure,* The Journal of the Acoustical Society of America **70**, 1140 (1981).

[12] K. Terzaghi, *Erdbaumechanik auf bodenphysikalischer Grundlage* (F. Deuticke, Wien, 1925).

[13] M. Biot, *General theory of three-dimensional consolidation,* Journal of applied physics **12**, 155–164 (1941).

[14] P. Fillunger, *Erdbaumechanik?* (Selbstverlag des Verfassers, Wien, 1936).

[15] C. Truesdell and R. Toupin, *The classical field theories, Encyclopedia of physics vol. III/1, in: Principles of classical mechanics and field theories, ed. S. Flugge* (Springer-Verlag, 1960) pp. 226–790.

[16] R. Bowen, *Theory of mixtures, Continuum Physics Vol. III*, edited by A. Eringen (Academic Press, New York, 1976).

[17] R. de Boer, *Theory of porous media* (Springer, Berlin, 2000).

[18] O. Coussy, *Poromechanics* (John Wiley & Sons, Chichester, 2004).

[19] A. Verruijt, *Theory and problems of poroelasticity* (Screen version, published online at geo.verruijt.net, 2015).

[20] S. Stevin, *Anvang der waterwichtdaet* (Pantijn, Leyden, 1586).

[21] B. Pascal, *Traitez de l'equilibre des liqueurs, et de la pesanteur de la masse de l'air: contenant l'explication des causes de divers effets de la nature qui n'avoient point esté bien connus jusques-icy, & particulierement de ceux que l'on avoit attribuez à l'horreur du Vuide* (Chez Guillaume Desprez, Paris, 1663).

[22] W. Besant, *A treatise on Hydrostatics and Hydrodynamics* (Cambridge University Press, United Kingdom, 1859).

[23] R. de Boer and W. Ehlers, *Uplift, friction and capillarity: three fundamental effects for liquid-saturated porous solids,* International journal of solids and structures **26**, 43–57 (1990).

[24] G. de Josselin de Jong, *Wat gebeurt er in de grond tijdens het heien?* De Ingenieur **68**, B77–B88 (1956).

[25] R. de Boer and W. Ehlers, *The development of the concept of effective stresses,* Acta Mechanica **83**, 77–92 (1990).

[26] R. Borja, *On the mechanical energy and effective stress in saturated and unsaturated porous continua,* International journal of solids and structures **43**, 1764–1786 (2006).

[27] P. Lade and R. De Boer, *The concept of effective stress for soil, concrete and rock,* Géotechnique **47**, 61–78 (1997).

[28] C. Truesdell and W. Noll, *The non-linear field theories of mechanics*, 3rd ed. (Springer, Heidelberg, 2004).

[29] S. Zaremba, *Le principe des mouvement relatifs et les équations de la mécanique physique,* Bull. Int. Acad. Sci. Cracovie **124**, 594–614 (1903).

[30] G. Jaumann, *Elektromagnetische vorgänge in bewegten medien,* Annalen der Physik **324**, 881–917 (1906).

[31] S. Whitaker, *The method of volume averaging* (Kluwer academic publishers, Dordrecht, 1999).

[32] F. Molenkamp, R. de Jager, and F. Mathijssen, *Stress measures affecting deformation of granular materials,* Vadose Zone Journal **13** (2014).

[33] A. Skempton, *Effective stress in soils, concrete and rocks,* in *Pore pressure and suction in soils*, edited by A. e. a. McDonald (Butterworths, London, 1960) pp. 4–16.

[34] A. Verruijt, *Some remarks on the principle of effective stress,* in *IUTAM Conference on Deformation and Failure of Granular Materials, Delft, the Netherlands*, edited by P. Vermeer and H. Luger (A.A. Balkema, Rotterdam, 1982).

[35] S. Pride, A. Gangi, and F. Morgan, *Deriving the equations of motion for porous isotropic media,* The Journal of the Acoustical Society of America **92**, 3278 (1992).

[36] J. Slattery, *Flow of viscoelastic fluids through porous media,* AIChE Journal **13**, 1066–1071 (1967).

[37] W. Gray, A. Leijnse, R. Kolar, and C. Blain, *Mathematical tools for changing spatial scales in the analysis of physical systems* (CRC Press, Florida, 1993).

[38] J. Van der Grinten, *An experimental study of shock-induced wave propagation in dry, water-saturated, and partially saturated porous media*, Ph.D. thesis, Technical University Eindhoven, Eindhoven, the Netherlands (1987).

[39] K. Rakhmatulin, *Fundamentals of gas dynamics of interpenetrating motions of compressible media,* Prikl. Mat. Mekh **20**, 184–195 (1956).

[40] H. Darcy, *Les fontaines publiques de la ville de Dijon* (Victor Dalmont, 1856).

[41] J. Bear and Y. Bachmat, *Introduction to modeling of transport phenomena in porous media* (Springer Science & Business Media, 1990).

[42] S. Whitaker, *Flow in porous media i: A theoretical derivation of darcy's law,* Transport in porous media **1**, 3–25 (1986).

[43] H. Lamb, *Hydrodynamics*, sixth ed. (Dover, New York, 1945).

[44] D. Johnson, T. Plona, C. Scala, F. Pasierb, and H. Kojima, *Tortuosity and acoustic slow waves,* Physical Review Letters **49**, 1840–1844 (1982).

[45] A. Verruijt, *An introduction to soil dynamics* (Springer Science & Business Media, 2010).

[46] F. Molenkamp, *Collapse due to static liquefaction analysed using large deformation elasto-visco-plastic dynamics,* in *Proceedings of the 7th Conference on Numerical Models in Geomechanics* (Balkema, Graz, Austria, 1999) pp. 527–533.

4

Beyond liquefaction: consistency of framework and limitations

The previous chapter considered the framework required to describe and model liquefaction flow slides. This chapter goes one step further by exploring the limits of the framework. There were several reasons to start the research that is described in this chapter. The necessity to demonstrate the consistency of the framework, a discussion in literature and during a conference, and the opportunity to extend the Author's work for a workshop gave rise to investigate these research topics, which were (partly) published in [1–3].

This chapter will start where the previous chapter left off, with the elementary equations of saturated soils. The set of equations are first extended using the first and second law of thermodynamics. The first section treats the conservation of energy, and the second the requirement of non-negative entropy production. These sections aim at investigating the implications of the hydrostatic interaction term $p\boldsymbol{I}\nabla n$ for the laws of thermodynamics. Consistency of the framework also requires the thermodynamical justification of the hydrostatic interaction term. The second part of this chapter will deal with stress measures for porous media. First, the effect of interparticle sliding and particle rolling on the intergranular stress tensor will be examined. Then, the range of applications will be extended to unsaturated conditions. It will be shown that essentially the same stress measures are valid for the full range of degrees of saturation.

4.1. Conservation of energy

4.1.1. General

For the derivation of the conservation of energy of the soil skeleton, pore fluid and bulk soil mass, the same starting points and basic assumptions as used in the previous chap-

ter are used here. The energy equations are therefore derived from mixture theory using the same methodology as discussed in Subsection 3.2.2. In addition, a distinction is made here between mechanical and thermal contributions. Specification and elaboration of all terms would lead to a complete yet unnecessarily laborious treatment of the conservation of energy. This section and the next aim at investigating the implications of the hydrostatic interaction term $p\boldsymbol{I}\nabla n$ for the laws of thermodynamics. Therefore the basis of the thermodynamics of saturated, porous media is presented and terms are only elaborated in more detail if necessary. The resulting energy equations will express the work supplied by $p\boldsymbol{I}\nabla n$, but in order to specify its implications it is also necessary to consider the restriction imposed to the change of energy. Hence, this section will provide a basis for the next section, which will treat the restriction of non-negative entropy production.

The conservation of energy equation generally states that the change of energy, expressed by the material time derivative $\mathrm{D}E/\mathrm{D}t$, equals the external supply per unit of time e^{ext}:

$$\frac{\mathrm{D}E}{\mathrm{D}t} = \frac{\mathrm{D}}{\mathrm{D}t}\int_v \rho E^{spec}\,\mathrm{d}v = e^{ext} \tag{4.1}$$

Before specifying E^{spec} and e^{ext}, it is first noted that the integral term in 4.1 can be simplified using the mass equation. The simplification, which was also used for the conservation of momentum in 3.14, reads:

$$\frac{\mathrm{D}}{\mathrm{D}t}\int_v \rho E^{spec}\,\mathrm{d}v = \int_v \rho \dot{E}^{spec}\,\mathrm{d}v \tag{4.2}$$

The specific energy E^{spec} defines the energy state of the saturated soil skeleton, expressed per unit mass and unit volume. It consists of two parts: the specific internal energy e and specific kinetic energy K:

$$E^{spec} = e + K \tag{4.3}$$

The specific internal energy e specifies the amount of energy stored as a result of thermal and elastic mechanical contributions:

$$\rho e = \rho c T + \frac{1}{2}\boldsymbol{\sigma} : \boldsymbol{\epsilon}^e \tag{4.4}$$

Herein, c defines the specific heat, T the absolute temperature, $\boldsymbol{\sigma}$ the (macro) stress measure and $\boldsymbol{\epsilon}^e$ the elastic strain. The specific kinetic energy K relates to the velocity of a material point $\dot{\boldsymbol{u}}$:

$$K = \frac{1}{2}\dot{\boldsymbol{u}} \cdot \dot{\boldsymbol{u}} \tag{4.5}$$

The material time derivative of the specific energy is required for the energy equation 4.2 and should therefore be applied on both the specific internal energy e and specific kinetic energy K, yielding:

$$\dot{E}^{spec} = \dot{e} + \dot{K} = \dot{c}T + c\dot{T} + \dot{\boldsymbol{\sigma}} : \boldsymbol{\epsilon}^e + \boldsymbol{\sigma} : \dot{\boldsymbol{\epsilon}}^e + \dot{\boldsymbol{u}} \cdot \ddot{\boldsymbol{u}} \tag{4.6}$$

In order to keep the equations concise, the elaborated form of $\dot{e}$ will only be used if necessary. Next the right hand side of Equation 4.1, the external supply of energy e^{ext}, is

considered in more detail. As for the specific energy, the Author distinguishes between mechanical and thermal contributions. The mechanical external energy supply $e^{ext;m}$ is the result of the work done by the body load $\boldsymbol{b}$ and surface traction $\boldsymbol{t}$, variables that also have been included in the momentum equations. Using Cauchy's and the divergence theorems for the traction term, the result reads:

$$e^{ext;m} = \int_v \rho \boldsymbol{b} \cdot \dot{\boldsymbol{u}} \, \mathrm{d}v + \oint_s \boldsymbol{t} \cdot \dot{\boldsymbol{u}} \, \mathrm{d}s = \int_v \rho \boldsymbol{b} \cdot \dot{\boldsymbol{u}} \, \mathrm{d}v + \int_v \nabla \cdot (\dot{\boldsymbol{u}} \cdot \boldsymbol{\sigma}) \, \mathrm{d}v \tag{4.7}$$

The thermal contribution $e^{ext;q}$ also consists of a body and surface supply term, namely the radiation exerted on the volume and outflow of heat through the surface. The rate of thermal energy supply by radiation is defined by ρh and the outflow of heat by $\boldsymbol{q}$. The thermal external energy supply $e^{ext;q}$ is consequently specified by:

$$e^{ext;q} = \int_v \rho h \, \mathrm{d}v - \oint_s \boldsymbol{n} \cdot \boldsymbol{q} \, \mathrm{d}s = \int_v \rho h \, \mathrm{d}v - \int_v \nabla \cdot \boldsymbol{q} \, \mathrm{d}v \tag{4.8}$$

All the components of the energy equation, specified in Equations 4.6, 4.7 and 4.8, are expressed in volume integrals. The energy equation can therefore be written in localised form. Substituting these equations into Equations 4.2 and 4.1 yields the generic energy equation. It can be shown that a part of this equation equals the momentum equation:

$$\begin{aligned} \rho \dot{e} + \rho \dot{\boldsymbol{u}} \cdot \ddot{\boldsymbol{u}} - \rho \boldsymbol{b} \cdot \dot{\boldsymbol{u}} - \nabla \cdot (\dot{\boldsymbol{u}} \cdot \boldsymbol{\sigma}) - \rho h + \nabla \cdot \boldsymbol{q} = \\ \rho \dot{e} - \boldsymbol{\sigma} : (\nabla \otimes \dot{\boldsymbol{u}}) - \rho h + \nabla \cdot \boldsymbol{q} + \left(\rho \ddot{\boldsymbol{u}} - \rho \boldsymbol{b} - \nabla \cdot \boldsymbol{\sigma} \right) \cdot \dot{\boldsymbol{u}} = 0 \end{aligned} \tag{4.9}$$

Substituting the momentum equation into Equation 4.9 yields the final, generic energy equation:

$$\rho \dot{e} - \boldsymbol{\sigma} : (\nabla \otimes \dot{\boldsymbol{u}}) - \rho h + \nabla \cdot \boldsymbol{q} = 0 \tag{4.10}$$

4.1.2. Interaction

Specifying the conservation of energy equation requires amongst other things the introduction of interaction terms. The energy transfer from the pore fluid to the soil skeleton is defined by $E^{pf\text{-}s}$ and its counterpart by $E^{s\text{-}pf}$, while conservation requires that $E^{pf\text{-}s} = -E^{s\text{-}pf}$. In addition, the specification of the energy equation 4.10 for either the soil skeleton or pore fluid will introduce the momentum interaction terms $\boldsymbol{R}^{pf\text{-}s}$ and $\boldsymbol{R}^{s\text{-}pf}$ to the energy equations. Contrary to the generic momentum equation, the constituent momentum equations include an interaction term that needs to be accounted for when substituting the momentum equation into the energy equation. More specifically, the momentum equations can be reformulated by substitution of the momentum interaction tensor $\boldsymbol{R}^{pf\text{-}s}$ from Equation 3.54 into the momentum equations of the soil skeleton and pore fluid, 3.68 and 3.69, respectively:

$$n\rho^f \dot{\boldsymbol{v}}^{pf} - n\nabla \cdot \left(p\boldsymbol{I} \right) - p\boldsymbol{I} \cdot \nabla n - n\rho^f \boldsymbol{b} = -\boldsymbol{R}^{pf\text{-}s} \tag{4.11}$$

$$(1-n)\rho^g \ddot{\boldsymbol{u}}^s - \nabla \cdot \boldsymbol{\sigma}' - (1-n)\nabla \left(p\boldsymbol{I} \right) + p\boldsymbol{I} \cdot \nabla n - (1-n)\rho^g \boldsymbol{b} = \boldsymbol{R}^{pf\text{-}s} \tag{4.12}$$

It is concluded that, when the energy equations are specified for the constituents, the momentum equations introduce the momentum interaction terms to the equations,

rather than being eliminated. The definition of the momentum transfer from the pore fluid to the soil skeleton is recalled from Chapter 3:

$$\boldsymbol{R}^{pf\text{-}s} = p\boldsymbol{I}\cdot\nabla n + n^2\mu\boldsymbol{\kappa}^{-1}\cdot\boldsymbol{v}^{pf\text{-}s} + (a-1)n\rho^f\dot{\boldsymbol{v}}^{pf\text{-}s} \tag{3.54}$$

The tortuous momentum interaction $\boldsymbol{R}^{pf\text{-}s;\dot{\boldsymbol{v}}^{pf\text{-}s}}$ originates from a loss of kinetic energy of the pore fluid, as discussed in Chapter 3. The tortuosity effect therefore defines an energy interaction mechanism by itself, which is however not part of $E^{pf\text{-}s}$. Accounting for the tortuosity effect in the energy equations implies that the kinetic energy of the pore fluid is augmented by $(a-1)n\rho^f\boldsymbol{v}^{pf\text{-}s}\cdot\dot{\boldsymbol{v}}^{pf\text{-}s}$ [4], whilst conservation requires that the tortuosity effect is cancelled out in the conservation of energy of the bulk mass. Combining the additional kinetic energy term with the work supplied by the tortuous momentum interaction demonstrates that this is indeed the case.

4.1.3. Resulting equations of the conservation of energy

The resulting energy conservation equations of the pore fluid, soil skeleton and bulk mass follow from specifying and substituting the variables in Equation 4.10 for the constituents. In addition, the interaction terms should be added to the constituent equations. After elaboration, the resulting equations of the pore fluid, soil skeleton and bulk mass read, respectively:

$$\begin{aligned} n\rho^f\dot{e}^{pf} - np\boldsymbol{I}:\left(\nabla\otimes\boldsymbol{v}^{pf}\right) - n\rho^f h^{pf} + \nabla\cdot\left(n\boldsymbol{q}^{pf}\right) + \\ E^{pf\text{-}s} - p\boldsymbol{I}\nabla n\cdot\boldsymbol{v}^{pf} - n^2\mu\boldsymbol{v}^{pf}\cdot\boldsymbol{\kappa}^{-1}\cdot\boldsymbol{v}^{pf\text{-}s} - (a-1)n\rho^f\dot{\boldsymbol{v}}^{pf\text{-}s}\cdot\dot{\boldsymbol{u}}^s = 0 \end{aligned} \tag{4.13}$$

$$\begin{aligned} (1-n)\rho^g\dot{e}^s - \left(\boldsymbol{\sigma}' + (1-n)p\boldsymbol{I}\right):\left(\nabla\otimes\dot{\boldsymbol{u}}^s\right) - (1-n)\rho^g h^s + \nabla\cdot\left((1-n)\boldsymbol{q}^s\right) - \\ E^{pf\text{-}s} + p\boldsymbol{I}\nabla n\cdot\dot{\boldsymbol{u}}^s + n^2\mu\dot{\boldsymbol{u}}^s\cdot\boldsymbol{\kappa}^{-1}\cdot\boldsymbol{v}^{pf\text{-}s} + (a-1)n\rho^f\dot{\boldsymbol{v}}^{pf\text{-}s}\cdot\dot{\boldsymbol{u}}^s = 0 \end{aligned} \tag{4.14}$$

$$\begin{aligned} n\rho^f\dot{e}^{pf} + (1-n)\rho^g\dot{e}^s - \boldsymbol{\sigma}:\left(\nabla\otimes\dot{\boldsymbol{u}}^s\right) - np\boldsymbol{I}:\left(\nabla\otimes\boldsymbol{v}^{pf\text{-}s}\right) - n\rho^f h^{pf} - (1-n)\rho^g h^s + \\ \nabla\cdot\left(n\boldsymbol{q}^{pf}\right) + \nabla\cdot\left((1-n)\boldsymbol{q}^s\right) - p\boldsymbol{I}\nabla n\cdot\boldsymbol{v}^{pf\text{-}s} - n^2\mu\boldsymbol{v}^{pf\text{-}s}\cdot\boldsymbol{\kappa}^{-1}\cdot\boldsymbol{v}^{pf\text{-}s} = 0 \end{aligned} \tag{4.15}$$

The resulting set of Equations 4.13-4.14 defines a provisional result of the conservation of energy equations. A provisional conclusion is that the tortuosity term indeed drops out of the bulk equation 4.15. The Second Law of Thermodynamics requiring non-negative entropy production will enable further specification of the energy equations.

4.2. Non-negative entropy production

4.2.1. General

This section continues the treatment of the effect of the hydrostatic interaction term $p\boldsymbol{I}\nabla n$ on the thermodynamics of saturated soils. The Second Law of Thermodynamics is considered, stating that the production of entropy must be non-negative. Contrary to the previous conservation laws, the Second Law of Thermodynamics is an inequality related to irreversible processes such as the generation of heat as a result of friction.

In addition to thermal and mechanical processes this section distinguishes between reversible and irreversible processes. Mixture theory is used to define the restriction of non-negative entropy production for the pore fluid, soil skeleton and bulk mass.

The Second Law of Thermodynamics generally states that the entropy production rate Γ in a material volume V must be non-negative, or $\Gamma \geq 0$. The entropy production rate is defined by the change of entropy $\rho\eta$ not related to the supply of entropy through the surface (outflow positive) $\boldsymbol{r} \cdot \boldsymbol{n}$ and volume $\rho\beta$:

$$\Gamma \equiv \frac{\mathrm{D}}{\mathrm{D}t} \int_v \rho\eta \, \mathrm{d}v - \int_v \rho\beta \, \mathrm{d}v + \int_s \boldsymbol{r} \cdot \boldsymbol{n} \, \mathrm{d}s \tag{4.16}$$

In order to rewrite Equation 4.16 in local form, the first term is simplified using the mass equation and the convergence theorem is applied to redefine the third term in a volume integral. Note that both steps have also been applied during the derivation of the conservation of linear momentum and energy equations. Furthermore, the entropy production rate in material volume V is replaced by the entropy production rate density γ to allow a formulation in local form. The resulting inequality reads:

$$\rho\gamma \equiv \rho\dot{\eta} - \rho\beta + \nabla \cdot \boldsymbol{r} \geq 0 \tag{4.17}$$

The entropy supply terms $\rho\beta$ and $\boldsymbol{r}$ are related to the flow of heat $\boldsymbol{q}$ and radiation h according to:

$$\beta = \frac{h}{T} \tag{4.18}$$

$$\boldsymbol{r} = \frac{\boldsymbol{q}}{T} \tag{4.19}$$

Substitution of these definitions 4.18 and 4.19 into the generic expression 4.17 yields the *Clausius-Duhem inequality*:

$$\rho\gamma = \rho\dot{\eta} - \rho\frac{h}{T} + \nabla \cdot \left(\frac{\boldsymbol{q}}{T}\right) \geq 0 \tag{4.20}$$

Elaboration of the divergence term in Equation 4.20, multiplication by the absolute temperature $T > 0$ and subsequent substitution of the generic conservation of energy equation 4.10, involving the replacement of $\nabla \cdot \boldsymbol{q} - \rho h$, yields an expression commonly known as the *dissipation inequality*, introducing the dissipation density $\mathscr{D}$:

$$\mathscr{D} \equiv \rho\gamma T = \rho T\dot{\eta} - \rho\dot{e} + \boldsymbol{\sigma} : (\nabla \otimes \dot{\boldsymbol{u}}) - \frac{\boldsymbol{q}}{T} \cdot \nabla T \geq 0 \tag{4.21}$$

Equation 4.21 defines an alternative general expression of the required non-negative entropy production. However, commonly one distinguishes between the mechanical dissipation density $\mathscr{D}_m$ and thermal dissipation density $\mathscr{D}_q$ with $\mathscr{D} = \mathscr{D}_m + \mathscr{D}_q$. Then, a stronger version of the dissipation inequality requires both the mechanical and thermal parts to satisfy the inequality:

$$\mathscr{D}^m \equiv \rho T\dot{\eta} - \rho\dot{e} + \boldsymbol{\sigma} : (\nabla \otimes \dot{\boldsymbol{u}}) \geq 0 \tag{4.22}$$

$$\mathscr{D}^q \equiv -\frac{\boldsymbol{q}}{T} \cdot \nabla T \geq 0 \tag{4.23}$$

4.2.2. Interaction

The consideration of interaction terms involves the exchanges between the soil and pore water phase per unit of bulk volume of linear momentum $\boldsymbol{R}^{pf\text{-}s}$ (3.54), energy $E^{pf\text{-}s}$, introduced in the energy conservation equations 4.13 and 4.14, and entropy, which will be considered next. The exchange of entropy from the pore fluid to the soil is defined by $G^{pf\text{-}s}$, and its counterpart by $G^{s\text{-}pf}$. The definition of $G^{pf\text{-}s}$ involves the aforementioned exchange of energy $E^{pf\text{-}s}$, which is first decomposed into a mechanical part $E_m^{pf\text{-}s}$ and a thermal part $E_q^{pf\text{-}s}$:

$$E^{pf\text{-}s} = E^{pf\text{-}s;m} + E^{pf\text{-}s;q} \tag{4.24}$$

Conservation also requires the specified terms to satisfy $E^{pf\text{-}s;m} = -E^{pf\text{-}s;m}$ and $E^{pf\text{-}s;q} = -E^{pf\text{-}s;q}$. The definition of $G^{pf\text{-}s}$ involves the exchange of thermal energy $E^{pf\text{-}s;q}$ and the temperature of the (receiving) soil T^s:

$$G^{pf\text{-}s} = \frac{E^{pf\text{-}s;q}}{T^s} \tag{4.25}$$

As the counterpart $G^{s\text{-}pf}$ can be defined in a similar way, it follows that $G^{pf\text{-}s}$ and $G^{s\text{-}pf}$ are related in the following way:

$$G^{pf\text{-}s} = -G^{s\text{-}pf}\frac{T^{pf}}{T^s} \tag{4.26}$$

Hence, for the entropy inequality the exchange of entropy is not necessarily conserved, as expected. Adding both exchange terms yields:

$$G^{pf\text{-}s} + G^{s\text{-}pf} = E^{pf\text{-}s;q}\left(\frac{T^{pf} - T^s}{T^{pf}T^s}\right) \tag{4.27}$$

Assuming that the exchange of energy is driven by a temperature gradient, $E^{pf\text{-}s;q}$ and $T^{pf} - T^s$ will have the same sign, whilst $T^{pf}, T^s > 0$. It is concluded that the sum of exchange terms 4.27 will be non-negative and thereby satisfies the entropy inequality.

The interaction terms related to the exchange of linear momentum and energy are introduced by reformulating and substituting the energy equations 4.13 and 4.14. Reformulation yields:

$$-n\rho^f h^{pf} + \nabla\cdot\left(n\boldsymbol{q}^{pf}\right) = -n\rho^f\dot{e}^{pf} + np\boldsymbol{I}:\left(\nabla\otimes\boldsymbol{v}^{pf}\right) - E^{pf\text{-}s} + R^{pf\text{-}s}\cdot\boldsymbol{v}^{pf} - (a-1)n\rho^f\dot{\boldsymbol{v}}^{pf\text{-}s}\cdot\boldsymbol{v}^{pf\text{-}s} \tag{4.28}$$

$$-(1-n)\rho^g h^s + \nabla\cdot\left((1-n)\boldsymbol{q}^s\right) = -(1-n)\rho^g\dot{e}^s + \left(\boldsymbol{\sigma}' + (1-n)p\boldsymbol{I}\right):\left(\nabla\otimes\dot{\boldsymbol{u}}^s\right) + E^{pf\text{-}s} - R^{pf\text{-}s}\cdot\dot{\boldsymbol{u}}^s \tag{4.29}$$

Note that substitution of the generic energy equation 4.10 into the generic Clausius-Duhem inequality 4.20 previously yielded the dissipation inequality 4.21.

4.2.3. Resulting equations

The resulting equations for non-negative entropy production of the pore fluid and soil skeleton are derived starting from the Clausius-Duhem inequality 4.20. Specifying the

volume fractions and variables and introducing the interaction terms yields for the pore fluid and soil skeleton, respectively:

$$n\rho^f\gamma^{pf} = n\rho^f\dot{\eta}^{pf} - n\rho^f\frac{h^{pf}}{T^{pf}} + \nabla\cdot\left(\frac{n\boldsymbol{q}^{pf}}{T^{pf}}\right) - G^{s\text{-}pf} \geq 0 \tag{4.30}$$

$$(1-n)\rho^g\gamma^s = (1-n)\rho^g\dot{\eta}^s - (1-n)\rho^g\frac{h^s}{T^s} + \nabla\cdot\left(\frac{(1-n)\boldsymbol{q}^s}{T^s}\right) - G^{pf\text{-}s} \geq 0 \tag{4.31}$$

The elaboration of Equations 4.30 and 4.31 requires some intermediate steps. The substitution of the energy equations 4.28 and 4.29 requires the elaboration of the divergence terms, which also involves the temperature in the entropy inequalities 4.30 and 4.31. The resulting equations are multiplied by the appropriate temperatures leading to the dissipation inequalities. Finally, it is noted that combining the entropy and energy interaction terms through Equation 4.25 will eliminate all entropy and interaction terms except for the mechanical energy interaction terms $E^{pf\text{-}s;m}$. The resulting equations for the pore fluid, soil skeleton and bulk mass read, respectively:

$$n\rho^f\gamma^{pf}T^{pf} \equiv \mathscr{D}^{pf} = n\rho^f T^{pf}\dot{\eta}^{pf} - n\rho^f\dot{e}^{pf} + np\boldsymbol{I} : \left(\nabla\otimes\boldsymbol{v}^{pf}\right) - \frac{n\boldsymbol{q}^{pf}}{T^{pf}}\nabla T^{pf} - E^{pf\text{-}s;m} + R^{pf\text{-}s}\cdot\boldsymbol{v}^{pf} - (a-1)n\rho^f\dot{\boldsymbol{v}}^{pf\text{-}s}\cdot\boldsymbol{v}^{pf\text{-}s} \geq 0 \tag{4.32}$$

$$(1-n)\rho^g\gamma^s T^s \equiv \mathscr{D}^s = (1-n)\rho^g T^s\dot{\eta}^s - (1-n)\rho^g\dot{e}^s + \left(\boldsymbol{\sigma}' + (1-n)p\boldsymbol{I}\right) : \left(\nabla\otimes\dot{\boldsymbol{u}}^s\right) - \frac{(1-n)\boldsymbol{q}^s}{T^s}\nabla T^s + E^{pf\text{-}s;m} - R^{pf\text{-}s}\cdot\dot{\boldsymbol{u}}^s \geq 0 \tag{4.33}$$

$$\mathscr{D}^{bulk} = n\rho^f T^{pf}\dot{\eta}^{pf} + (1-n)\rho^g T^s\dot{\eta}^s - n\rho^f\dot{e}^{pf} - (1-n)\rho^g\dot{e}^s + \boldsymbol{\sigma} : \left(\nabla\otimes\dot{\boldsymbol{u}}^s\right) + np\boldsymbol{I} : \left(\nabla\otimes\boldsymbol{v}^{pf\text{-}s}\right) - \frac{n\boldsymbol{q}^{pf}}{T^{pf}}\nabla T^{pf} - \frac{(1-n)\boldsymbol{q}^s}{T^s}\nabla T^s + R^{pf\text{-}s}\cdot\boldsymbol{v}^{pf\text{-}s} - (a-1)n\rho^f\dot{\boldsymbol{v}}^{pf\text{-}s}\cdot\boldsymbol{v}^{pf\text{-}s} \geq 0 \tag{4.34}$$

4.2.4. Conditions defined by non-negative entropy production

The requirement of non-negative entropy production will define conditions on the separate terms occurring in Equations 4.32-4.34. It will be demonstrated that further elaboration will clarify the background and role of the hydrostatic interaction term in the conservation of energy equations. The elaboration comprises a number of generic steps, first elaborated for a single-phase material and later applied on the constituents of the saturated bulk:

1. Distinguishing between the mechanical and thermal parts of the dissipation inequalities 4.22 and 4.23 and applying the strong formulations of the dissipation inequalities.

2. Substitution of the Helmholtz free energy ψ as the thermodynamic potential, generally related to the internal energy e and entropy η by:

$$\psi = e - T\eta \tag{4.35}$$

The Helmholtz free energy measures the useful work available in a thermodynamic system at a constant temperature. It thus allows the conditions for the constitutive relations to be specified. After substitution of the (material derivative of the) Helmholtz free energy, Equation 4.22 can alternatively be written as:

$$\mathscr{D}^m = -\rho\dot{\psi} - \rho\dot{T}\eta + \boldsymbol{\sigma} : (\nabla \otimes \dot{\boldsymbol{u}}) \geq 0 \tag{4.36}$$

3. Introduction of constitutive relations for the primary variables ψ, η, $\boldsymbol{\sigma}$ and $\boldsymbol{q}$. Assuming a deformation-temperature formulation, these variables will be functions of (derivates of) the deformation vector $\boldsymbol{u}$ and temperature T. For illustration purposes, the simple case of a thermoelastic model for a local material will be elaborated. For this case, the values of $\boldsymbol{u}$ and T do not depend on their time history and only to a limited extent (first order) on the values of surrounding points. As material objectivity does not allow constitutive equations to be related to the current position of the material point, the constitutive equations are expressed in terms of deformation gradient or elastic strain $\boldsymbol{\epsilon}^e$, current temperature T and temperature gradient ∇T:

$$\psi = \hat{\psi}(\boldsymbol{\epsilon}^e, T, \nabla T) \tag{4.37}$$

$$\eta = \hat{\eta}(\boldsymbol{\epsilon}^e, T, \nabla T) \tag{4.38}$$

$$\boldsymbol{\sigma} = \hat{\boldsymbol{\sigma}}(\boldsymbol{\epsilon}^e, T, \nabla T) \tag{4.39}$$

$$\boldsymbol{q} = \hat{\boldsymbol{q}}(\boldsymbol{\epsilon}^e, T, \nabla T) \tag{4.40}$$

Then, material derivatives of the primary variables in 4.37-4.40 are obtained by using the partial derivatives with respect to $\boldsymbol{\epsilon}^e$, T and ∇T, for instance:

$$\dot{\psi} = \frac{\partial\hat{\psi}}{\partial\boldsymbol{\epsilon}^e}\dot{\boldsymbol{\epsilon}}^e + \frac{\partial\hat{\psi}}{\partial T}\dot{T} + \frac{\partial\hat{\psi}}{\partial(\nabla T)}\dot{\nabla T} \tag{4.41}$$

4. Definition of conditions for constitutive relations using the Coleman-Noll procedure [5]. First, note that symmetry of the strain tensor $\boldsymbol{\epsilon}$ allows one to apply the definition 3.27 in the last term of Equation 4.36, that is, $\nabla \otimes \dot{\boldsymbol{u}} = \dot{\boldsymbol{\epsilon}}$. Substitution of Equations 4.37-4.40, partial differentiation of material time derivates and rearrangement yields:

$$\mathscr{D}^m = \left(-\rho\frac{\partial\hat{\psi}}{\partial\boldsymbol{\epsilon}^e} + \hat{\boldsymbol{\sigma}}\right) : \dot{\boldsymbol{\epsilon}}^e + \left(-\rho\hat{\eta} - \rho\frac{\partial\hat{\psi}}{\partial T}\right)\dot{T} - \rho\frac{\partial\hat{\psi}}{\partial(\nabla T)}\dot{\nabla T} \geq 0 \tag{4.42}$$

$$\mathscr{D}^q = -\frac{\hat{\boldsymbol{q}}}{T} \cdot \nabla T \geq 0 \tag{4.43}$$

The key observation of the Coleman-Noll procedure implies that $\dot{\boldsymbol{\epsilon}}^e$, $\dot{T}$ and $\dot{\nabla T}$ can be varied independently in thermodynamic processes, while they can attain both

negative and positive values. As the terms multiplying $\dot{\boldsymbol{\epsilon}}$, $\dot{T}$ and $\nabla\dot{T}$ in Equation 4.42 do not depend on these variables, the mechanical part of the dissipation inequality requires that:

$$\boldsymbol{\sigma} = \rho \frac{\partial \psi}{\partial \boldsymbol{\epsilon}^e} \tag{4.44}$$

$$\eta = -\frac{\partial \psi}{\partial T} \tag{4.45}$$

$$\frac{\partial \psi}{\partial (\nabla T)} = 0 \tag{4.46}$$

where for convenience the hats on top of the variables have been omitted. Equations 4.44-4.46 define the relation between the stress $\boldsymbol{\sigma}$ and the Helmholtz free energy ψ, and between the entropy η and Helmholtz free energy ψ, while the Helmholtz free energy ψ cannot depend on the temperature gradient ∇T. The thermal part of the dissipation inequality determines the direction of heat flux depending on the temperature gradient, which is physically consistent. The restriction defined by the thermal part of the dissipation inequality can be further specified by substituting Fourier's model $\boldsymbol{q} = -\boldsymbol{K} \cdot \nabla T$, with $\boldsymbol{K}$ defining the thermal conductivity tensor. The result reads:

$$\frac{(\nabla T) \cdot \boldsymbol{K} \cdot (\nabla T)}{T} \geq 0 \tag{4.47}$$

Since $T > 0$, Equation 4.47 will be satisfied if $\boldsymbol{K}$ is positive semi-definite. Hence, assuming that the constitutive equation of heat $\boldsymbol{q}$ is consistently formulated, only the mechanical part of the dissipation inequality needs further consideration.

5. Distinguishing between reversible and irreversible terms. The possible violation of the entropy inequality during the reversing of processes requires the reversible terms to equal zero. The Helmholtz Free Energy term $\rho\dot{\psi}$, the entropy term $\rho\dot{T}\eta$ and the elastic work term $\boldsymbol{\sigma} : \dot{\boldsymbol{\epsilon}}^e$define the reversible terms. The irreversible terms relate to irreversible or plastic deformations of the soil skeleton and pore fluid. Constitutive equations based on an elastoplastic rather than elastic model are formulated in terms of the total strain tensor, which can be decomposed into an elastic part $\boldsymbol{\epsilon}^e$ and plastic part $\boldsymbol{\epsilon}^p$:

$$\boldsymbol{\epsilon} = \boldsymbol{\epsilon}^e + \boldsymbol{\epsilon}^p \tag{4.48}$$

A conventional approach is to also decompose the other variables in the constitutive equations 4.37-4.40 into conservative and non-conservative parts. The Coleman-Noll procedure will still apply, albeit to the conservative part of the resulting inequality. However, the non-conservative terms cannot be varied independently. Additional relations are needed to specify the non-conservative part, which is required to be non-negative. The formulation of constitutive relations is outside the scope of this part of the thesis. It is therefore assumed that the formulation of elastoplastic constitutive equations is consistent with the dissipation inequality and does not need further consideration.

6. Specification of terms related to the interaction between the pore fluid and soil skeleton. Specification of the dissipation inequality for the constituents introduces interaction terms, which do not appear in the generic formulation of the mechanical part of the dissipation inequality 4.36. Elaboration of the previous steps will only leave the interaction terms for specification, including the hydrostatic interaction term.

Based on these considerations the mechanical part of the dissipation inequality will be elaborated. Reformulating the mechanical part of Equations 4.32 and 4.33 in terms of the Helmholtz free energy ψ and strain tensor $\boldsymbol{\epsilon}$ yields for the pore fluid and soil skeleton, respectively:

$$\mathscr{D}^{m;pf} = -n\rho^f\dot{\psi}^{pf} - n\rho^f\dot{T}^{pf}\eta^{pf} + np\boldsymbol{I} : \dot{\boldsymbol{\epsilon}}^{pf} - (a-1)n\rho^f\dot{\boldsymbol{v}}^{pf\text{-}s}\cdot\boldsymbol{v}^{pf\text{-}s} - E^{pf\text{-}s;m} + R^{pf\text{-}s}\cdot\boldsymbol{v}^{pf} \geq 0 \tag{4.49}$$

$$\mathscr{D}^{s} = -(1-n)\rho^g\dot{\psi}^{s} - (1-n)\rho^g\dot{T}^{s}\eta^{s} + \left(\boldsymbol{\sigma}' + (1-n)p\boldsymbol{I}\right) : \dot{\boldsymbol{\epsilon}}^{s} + E^{pf\text{-}s;m} - R^{pf\text{-}s}\cdot\dot{\boldsymbol{u}}^{s} \geq 0 \tag{4.50}$$

As explained in the aforementioned step-wise elaboration of the dissipation inequality, the reversible terms can be ignored and the (elastoplastic) constitutive equations are presumed to be consistent with the entropy inequality. Omitting these terms reduces the mechanical parts of the dissipation inequality 4.49 and 4.50 to the interaction terms. After elaboration of the momentum interaction term $\boldsymbol{R}^{pf\text{-}s}$, the reduced equations read for the pore fluid and soil skeleton, respectively:

$$-E^{pf\text{-}s;m} + \left(p\boldsymbol{I}\nabla n + n^2\mu\boldsymbol{\kappa}^{-1}\boldsymbol{v}^{pf\text{-}s}\right)\cdot\boldsymbol{v}^{pf} + (a-1)n\rho^f\dot{\boldsymbol{v}}^{pf\text{-}s}\cdot\dot{\boldsymbol{u}}^{s} \geq 0 \tag{4.51}$$

$$E^{pf\text{-}s;m} - \left(p\boldsymbol{I}\nabla n + n^2\mu\boldsymbol{\kappa}^{-1}\boldsymbol{v}^{pf\text{-}s}\right)\cdot\dot{\boldsymbol{u}}^{s} - (a-1)n\rho^f\dot{\boldsymbol{v}}^{pf\text{-}s}\cdot\dot{\boldsymbol{u}}^{s} \geq 0 \tag{4.52}$$

First, the relation $\boldsymbol{v}^{pf} = \boldsymbol{v}^{pf\text{-}s} + \dot{\boldsymbol{u}}^{s}$ is used to elaborate the Darcy term $n^2\mu\boldsymbol{v}^{pf}\cdot\boldsymbol{\kappa}^{-1}\cdot\boldsymbol{v}^{pf\text{-}s}$. One of the two resulting terms $n^2\mu\boldsymbol{v}^{pf\text{-}s}\cdot\boldsymbol{\kappa}^{-1}\cdot\boldsymbol{v}^{pf\text{-}s}$ satisfies the inequality if $\boldsymbol{\kappa}$ is positive definite and can therefore be discarded from Equation 4.51. Elaboration of Equations 4.51 and 4.52 yields:

$$-E^{pf\text{-}s;m} + \boldsymbol{v}^{pf}\cdot p\boldsymbol{I}\cdot\nabla n + n^2\mu\dot{\boldsymbol{u}}^{s}\cdot\boldsymbol{\kappa}^{-1}\cdot\boldsymbol{v}^{pf\text{-}s} + (a-1)n\rho^f\dot{\boldsymbol{v}}^{pf\text{-}s}\cdot\dot{\boldsymbol{u}}^{s} \geq 0 \tag{4.53}$$

$$E^{pf\text{-}s;m} - \dot{\boldsymbol{u}}^{s}\cdot p\boldsymbol{I}\cdot\nabla n - n^2\mu\dot{\boldsymbol{u}}^{s}\cdot\boldsymbol{\kappa}^{-1}\cdot\boldsymbol{v}^{pf\text{-}s} - (a-1)n\rho^f\dot{\boldsymbol{v}}^{pf\text{-}s}\cdot\dot{\boldsymbol{u}}^{s} \geq 0 \tag{4.54}$$

As $\boldsymbol{v}^{pf\text{-}s}$ and $\dot{\boldsymbol{u}}^{s}$ can be varied independently, all terms in equations 4.53 and 4.54 can be either negative or positive. The separate terms do not satisfy the inequality. Therefore, the work done by the momentum interaction terms is related to the mechanical energy interaction $E^{pf\text{-}s;m}$ in order to satisfy the inequality. From Equations 4.53 and 4.54 it follows that the definition of $E^{pf\text{-}s;m}$ will eliminate the Darcy and tortuosity terms, but will always leave a residual term for the work done by hydrostatic interaction. For reasons

clarified later on, the energy interaction term is defined by:

$$E^{pf\text{-}s;m} = \boldsymbol{v}^{pf} \cdot p\boldsymbol{I} \cdot \nabla n + n^2 \mu \dot{\boldsymbol{u}}^s \cdot \boldsymbol{\kappa}^{-1} \cdot \boldsymbol{v}^{pf\text{-}s} + (a-1) n \rho^f \dot{\boldsymbol{v}}^{pf\text{-}s} \cdot \dot{\boldsymbol{u}}^s \tag{4.55}$$

The definition of $E^{pf\text{-}s;m}$ leaves one term in the mechanical part of the dissipation inequality of the soil skeleton to be considered, namely $+\boldsymbol{v}^{pf\text{-}s} \cdot p\boldsymbol{I} \cdot \nabla n$. As the variables in this term can be varied independently, it can be both positive and negative. However, it will be demonstrated that the term as a whole cannot be varied independently from the other terms in the dissipation inequality of the soil skeleton. To this end, recall the equation of mass of the pore fluid 3.62 from Chapter 3:

$$n\dot{\rho}^f + \dot{n}\rho^f + \rho^f \boldsymbol{v}^{pf\text{-}s} \cdot \nabla n + n\rho^f \nabla \cdot \boldsymbol{v}^{pf} = 0 \tag{3.62}$$

The first term in this equation $n\dot{\rho}^f$ was related to the constitutive relation in Equation 3.63. Since $\nabla \cdot \boldsymbol{v}^{pf} = \dot{\boldsymbol{\epsilon}}^{pf;vol}$, the first term is the negative of the last term in Equation 3.62 and both terms are eliminated. The remaining terms are elaborated by eliminating ρ^f, substituting the equation of the conservation of mass of the soil skeleton 3.59 while neglecting the volumetric strain of the grains $\dot{\boldsymbol{\epsilon}}^{g;vol} = 0$ and multiplication by $p\boldsymbol{I}$, yielding:

$$\boldsymbol{v}^{pf\text{-}s} \cdot p\boldsymbol{I} \cdot \nabla n = -(1-n) p\boldsymbol{I} : \dot{\boldsymbol{\epsilon}}^{s;vol} = -(1-n) p\boldsymbol{I} : \dot{\boldsymbol{\epsilon}}^s \tag{4.56}$$

These findings with respect to the entropy inequality and the hydrostatic interaction term lead to the following conclusions. Firstly, it is concluded that Equation 4.56 enables the specification of one term of the mechanical energy interaction $E^{pf\text{-}s;m}$ in Equation 4.55. The mechanical energy interaction ensures that (a part of) the conservative work done by the momentum exchange between the pore fluid and soil skeleton satisfies the entropy inequality. The effects of $\boldsymbol{v}^{pf} \cdot p\boldsymbol{I} \cdot \nabla n$, $n^2 \mu \dot{\boldsymbol{u}}^s \cdot \boldsymbol{\kappa}^{-1} \cdot \boldsymbol{v}^{pf\text{-}s}$ and $(a-1) n \rho^f \dot{\boldsymbol{v}}^{pf\text{-}s} \cdot \dot{\boldsymbol{u}}^s$ on the conservation of energy of the pore fluid and soil skeleton, if any, are exchanged and accounted for, where physically possible, by $E^{pf\text{-}s;m}$. Note that the same was concluded for the term $p\boldsymbol{I} \cdot \nabla n$ in the momentum equations, which was termed *self-equilibration*. The complementary part of the work done by the hydrostatic interaction, $\boldsymbol{v}^{pf\text{-}s} \cdot p\boldsymbol{I} \cdot \nabla n$, is shown to affect the strain energy of the soil skeleton. Secondly, reconsider the energy equations 4.13-4.15 based on the derived definitions 4.55 and 4.56. Substitution and elaboration yields for the pore fluid, soil skeleton and bulk, respectively:

$$n\rho^f \dot{e}^{pf} - np\boldsymbol{I} : \boldsymbol{\epsilon}^{pf} - n\rho^f h^{pf} + \nabla \cdot \left(n\boldsymbol{q}^{pf} \right) - n^2 \mu \boldsymbol{v}^{pf\text{-}s} \cdot \boldsymbol{\kappa}^{-1} \cdot \boldsymbol{v}^{pf\text{-}s} + E^{pf\text{-}s;q} = 0 \tag{4.57}$$

$$(1-n)\rho^g \dot{e}^s - \boldsymbol{\sigma}' : \boldsymbol{\epsilon}^s - (1-n)\rho^g h^s + \nabla \cdot \left((1-n)\boldsymbol{q}^s \right) - E^{pf\text{-}s;q} = 0 \tag{4.58}$$

$$\begin{aligned} n\rho^f \dot{e}^{pf} + (1-n)\rho^g \dot{e}^s - \boldsymbol{\sigma}' : \boldsymbol{\epsilon}^s - np\boldsymbol{I} : \boldsymbol{\epsilon}^{pf} - n\rho^f h^{pf} - (1-n)\rho^g h^s + \\ \nabla \cdot \left(n\boldsymbol{q}^{pf} \right) + \nabla \cdot \left((1-n)\boldsymbol{q}^s \right) - n^2 \mu \boldsymbol{v}^{pf\text{-}s} \cdot \boldsymbol{\kappa}^{-1} \cdot \boldsymbol{v}^{pf\text{-}s} = 0 \end{aligned} \tag{4.59}$$

The obtained set of equations applies for, but is not necessarily restricted to, incompressible soil particles. In the case of compressible particles, the compression of the particles needs to be accounted for in Equation 4.56. In addition, one needs to replace

the effective stress by contributions from the intergranular stress and pore fluid stress according to Equation 3.31. The formulation of a constitutive model would then require the incorporation of different deformation modes of the soil skeleton. Accounting for the compressibility of the particles in Equation 4.56 leads to:

$$\boldsymbol{v}^{pf\text{-}s} \cdot p\boldsymbol{I} \cdot \nabla n = -(1-n)p\boldsymbol{I} : \left(\dot{\boldsymbol{\epsilon}}^{s;vol} - \dot{\boldsymbol{\epsilon}}^{g;vol}\right) \tag{4.60}$$

where $\dot{\boldsymbol{\epsilon}}^{g;vol}$ defines the volumetric compression rate of the particles. Note that the term in between brackets in Equation 4.60 expresses the volumetric strain of the soil skeleton as a result of re-arrangement of the particles. Substitution of this relation into the energy equation of the soil skeleton then yields:

$$(1-n)\rho^g \dot{e}^s - \boldsymbol{\sigma}' : \boldsymbol{\epsilon}^s - (1-n)\rho^g h^s + \nabla \cdot \left((1-n)\boldsymbol{q}^s\right) - E^{pf\text{-}s;q} - (1-n)p\boldsymbol{I} : \dot{\boldsymbol{\epsilon}}^{g;vol} = 0 \tag{4.61}$$

The last term in Equation 4.61 shows that the hydrostatic interaction power term eventually leads to work as a result of the pore fluid stress and compressing particles. It is likely and physically consistent that this work is balanced by the internal energy term of the soil skeleton, $(1-n)\rho^g \dot{e}^s$.

The definitions 4.55 and 4.56 have led to a simplified and concise set of energy equations 4.57-4.59. The bulk equation 4.59 no longer contains contributions from interaction terms. Furthermore, the strain energy terms are strictly separated between the relevant constituent equations. The strain energy term in the energy equation of the pore fluid 4.57 is solely defined by the pore fluid stress and strain, whereas the strain energy term in the energy equation of the soil skeleton 4.58 is solely defined by the effective stress and strain of the soil skeleton. This will have implications for the definition of the constitutive equations, as will be shown below. Thirdly, the mechanical parts of the dissipation inequality of the pore fluid 4.49 and soil skeleton 4.50 are considered. Based on the reformulated energy equations, the mechanical parts of the dissipation inequality of the pore fluid and soil skeleton are formulated by, respectively:

$$\mathscr{D}^{m;pf} = -n\rho^f \dot{\psi}^{pf} - n\rho^f \dot{T}^{pf}\eta^{pf} + np\boldsymbol{I} : \dot{\boldsymbol{\epsilon}}^{pf} + n^2 \mu \boldsymbol{v}^{pf\text{-}s} \cdot \boldsymbol{\kappa}^{-1} \cdot \boldsymbol{v}^{pf\text{-}s} \geq 0 \tag{4.62}$$

$$\mathscr{D}^{m;s} = -(1-n)\rho^g \dot{\psi}^s - (1-n)\rho^g \dot{T}^s \eta^s + \boldsymbol{\sigma}' : \dot{\boldsymbol{\epsilon}}^s \geq 0 \tag{4.63}$$

The conservative part of the constitutive relations can be elaborated using the Coleman-Noll procedure, as explained before. The strict separation of the effective and pore fluid stress for the energy of the soil skeleton and pore fluid, respectively, implies a similar separation when the Coleman-Noll procedure is applied. The pore fluid stress will be strictly related to the Helmholtz free energy of the pore fluid, and the effective stress to the Helmholtz free energy of the soil skeleton:

$$p\boldsymbol{I} = \rho^f \frac{\partial \psi^{pf}}{\partial \boldsymbol{\epsilon}^{pf}} \tag{4.64}$$

$$\boldsymbol{\sigma}' = (1-n)\rho^g \frac{\partial \psi^s}{\partial \boldsymbol{\epsilon}^s} \tag{4.65}$$

It has been demonstrated that the formulation of the hydrostatic interaction term in the momentum equations will have important consequences for the thermodynamic framework. It allows the simplification of the energy equations and, thereby, the derivation of the constitutive equations from thermodynamic restrictions.

4.3. Stress measures for unsaturated soils

4.3.1. Introduction

This section addresses stress measures for granular materials [1], starting from saturated conditions and subsequently extending the concepts to unsaturated conditions. In this thesis, Subsection 3.2.3 treated the stress measures for saturated porous media, which is the primary subject of this thesis. However, flow liquefaction may be initiated by the saturation of unsaturated soils, which is for instance the case during rainfall-induced landslides [6]. This section provides a generic stress framework that applies to both saturated and unsaturated conditions, thus enabling maximum advantage to be taken from the earlier findings on the mechanical characteristics for the saturated case.

The physical relevance of the continuum mechanical measures of stress, deformation, and flow of the pore fluids and stress and deformation of the solid skeleton forms the basis of any constitutive modelling and subsequent application for predictions in geomechanics. For the fluid-saturated case, the calculation of the deformation of the solid skeleton due to a changing pore fluid stress can be achieved by applying the macroscale isotropic pore fluid stress tensor $p\boldsymbol{I}$, at least if the substance composing the particles remains elastic. The intergranular stress tensor $\boldsymbol{\sigma}^*$ and, possibly, a microstructure tensor are derived using micromechanics in combination with volume averaging. The intergranular stress, which accounts for interparticle sliding, is by definition independent of the degree of saturation. The saturated cases, here defined by the fluids air ('dry') and, presumably, water ('wet'), define limit conditions for the unsaturated case. The deformation of the granular skeleton remains identically dependent on the intergranular stress tensor, albeit for a combined measure of both pore fluid stresses. As a consequence, the constitutive relation of a granular skeleton, composed of elastic (or rigid) particles with mainly frictional interaction is considered to remain independent of the degree of saturation.

Furthermore, the measures of stress, deformation, and flow must be consistent with the basic conservation laws of mass, momentum, and energy and the non-negative entropy production law of thermodynamics. The model formulation by Gray and Schrefler [7] satisfies these conditions and implicitly derives the types of required experimental data needed to finally arrive at applications. Another example will be treated in the next section 4.4, where upscaling of conservation laws at the microscale is employed to reconsider the intergranular stress for particle rotation. However, while some experimental capabilities for solid geomaterials do reach the three-dimensional nanometer scale (e.g. [8]), for loose granular materials and multiple pore fluids even the three-dimensional micrometer scale is still rather demanding. Most observations concern macroscale quantities, increasingly supplemented with some microscale data.

This section aims at understanding why and how the saturated stress measures can be extended to keep the unsaturated stress measures physically justified and thereby to keep the amendments to constitutive relations minimal. It will start by reviewing the existing stress measures. Considering the treatment of saturated stress measures in 3.2.3, the review of the stress measures mainly concentrates on unsaturated conditions. The derivation of a generic framework for saturated and unsaturated conditions starts at the description of a pack of spheres at the microscale as applied in the discrete element method. The corresponding macroscale measures such as fabric and intergranular stress will be derived. Then for unsaturated granular materials a microscale description of capillary suction and the consequent interparticle forces is provided, followed by the derivation of the corresponding macroscale intergranular and combined pore fluid stress tensors. Finally, the intended way of application of the derived stress measures will be discussed.

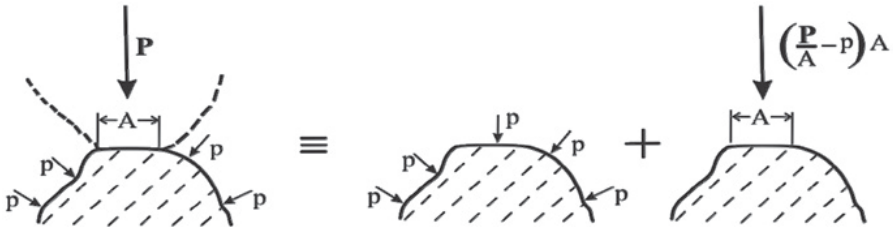


Figure 4.1: Decomposition of forces at an intergranular contact, illustrating average force P and average area A, both per intergranular contact, and pore fluid stress p (after [9], figure 1b).

4.3.2. Review of stress measures

Considering its importance for saturated and unsaturated granular materials, Bishop's treatment of the effective stress [9] provides the starting point for the review. Bishop considered the case of contacts between the particles with non-zero spatial dimensions, illustrated on the left side of Figure 4.1 (after [9], figure 1b), with the average area of the interparticle contacts A, average force per intergranular contact P, and average number of contacts per unit of cross-sectional area N. Bishop indicated the effective contact area of the soil particles per unit cross-sectional area by the contact fraction $a = AN$. Then the resulting average intergranular force per unit of cross-sectional area of the contact plane indicated by normal stress σ'_i is expressed by ([9], equation [4]):

$$\sigma'_i = NP = \sigma - (1-a)p \tag{4.66}$$

Subsequently, Bishop stated: "Now if a soil particle is subjected to a pressure p over the whole of its surface, it undergoes no distortion but a small decrease in volume. Hence it is only that part of the local contact stress ($P/A = \sigma'_i/a$, Author's addition) which is in excess of p that causes deformation of the soil structure." This reasoning is supported by the decomposition of the tractions on a particle, as illustrated on the right side of Figure

4.1. Then continuing: "By summing the corresponding components of the intergranular force per unit of cross-sectional area, [thus $(\sigma'_i/a-p)a$, Author's addition), an expression is obtained for normal stress σ'_c, defined as that part of the normal stress which controls volume change due to the deformation of the soil structure," leading to ([9], equation [6]):

$$\sigma'_c = \sigma'_i - ap \tag{4.67}$$

Next, substituting Equation 4.66 into 4.67 gives, for the normal stress σ'_c, the controlling volume change due to the deformation of the soil structure, in accordance with Bishop ([9], equation [7]):

$$\sigma'_c = \sigma - p \tag{4.68}$$

On this basis, Bishop concluded that "…although the average intergranular force per unit area depends on the magnitude of (contact fraction) a, volume changes due to deformation of the soil structure depend simply on the stress difference $\sigma - p$, whatever the value of a." Consequently, Bishop's theoretical normal stress σ'_c in Equation 4.68 must be the normal component of the intergranular stress tensor because it controls the volume change due to the deformation of the soil structure. The Author concludes that Bishop's theoretical intergranular stress tensor in the soil structure is identical to Terzaghi's proposal of the effective stress tensor $\boldsymbol{\sigma}'$ for incompressible particles.

For unsaturated soils, Bishop [9] recognised that the pore water pressure p^w in the liquid phase, which is lower than that in the gaseous phase p^g, will act only on a reduced area. This notion enabled Bishop to propose the following expression for the normal effective stress:

$$\sigma' = \sigma - p^g - \chi\left(p^w - p^g\right) \tag{4.69}$$

which is the sum of the net stress $\sigma - p^g$ and the product of fraction χ and the matric suction $p^w - p^g$. This fraction χ equals unity for saturated soils and decreases with decreasing degree of saturation S^w to zero. Following this proposal of the normal effective stress, its role in the constitutive modelling of the solid skeleton was disputed while distinguishing the effects of each stress measure occurring in Equation 4.69, net stress and matric suction.

Bishop and Blight [10] demonstrated the determination of the magnitudes of the χ parameter by combining the measured shear strengths of saturated and unsaturated soils in terms of effective stresses. However, a severe shortcoming of the proposed effective stress definition σ' was also recognised [11, 12], namely the impossibility of explaining pore collapse. This is understood to involve the sudden instability phenomenon of volumetric contraction during wetting by reduction in the matric suction.

The simple assumption that fraction χ would be equal to the degree of saturation S^w, i.e. $\chi = S^w$, has been found to be a first rough approximation for sands. To some extent this also applies for silts, but its applicability decreases for clays with increasing plasticity index. The following proposal for fraction χ was investigated [13, 14]:

$$\chi = \left(\frac{p^w - p^g}{\left(p^w - p^g\right)_e}\right)^{-0.55} \tag{4.70}$$

which was applied for matric suctions $p^w - p^g$ larger than the matric suction at air entry $\left(p^w - p^g\right)_e$. Two values were recognised for the matrix suction at air entry, namely one for air entry during drying and the other for air expulsion during wetting. Khalili et al. [15] demonstrated experimentally that with this approximation good predictions of not only the shear strength and volume change of sands and silts are obtained, but also of the critical state line, independent of the degree of saturation. Consequently, these results are in support of Bishop's effective stress proposal 4.69, which significantly simplifies constitutive modelling.

Alonso et al. [16] demonstrated experimentally that, for unsaturated clays, the fraction χ also depends on a measure of the microstructure. The reasoning leading to such a measure involves the notion that during the initial drying of a saturated clay, a bimodal micromechanical deformation mechanism develops spontaneously, as recognised earlier by Jennings and Burland [11]. The initially saturated homogeneous clay structure tends to deform during initial drying into saturated "packets" of clay particles with unsaturated interpacket voids in between. These packets could be seen as deformable particles, while the interpacket capillary interactions determine the induced effective stress. In the terms of Alonso et al. [16], the intra-aggregate micropore spaces contain immobile water, attached to the clay minerals, while the interaggregate macropores contain free water and air. Capillarity, involving the free water, occurs in the macropores. The contribution to the effective stress by capillarity involves the suction of the free water in the macropores. To quantify the degree of saturation S_r^e ([16], equation [12]) of these macropores, the microstructural threshold parameter S_r^m is introduced. This parameter quantifies the lower limit of the degree of saturation $S_r^e = 0$ of the macropores for the case in which the macropores are dry and containing only gas, while the intra-aggregate micropores are still pore water saturated. Following the definition of this degree of saturation S_r^e of the macropores, subsequently fraction χ is assumed equal to the degree of saturation S_r^e of the macropores:

$$\chi = S_r^e \tag{4.71}$$

Experimental evidence, involving the strength and elastic stiffness of the solid skeleton of high-plasticity clays, has also demonstrated the usefulness of the Bishop effective stress 4.69 if the microscale characteristic expressed by the microstructural threshold parameter S_r^m is accounted for.

4.3.3. Microstructure, stress and deformation of packing of spheres

For the development of macroscale stress measures for unsaturated granular materials, first the microscale descriptions of the structures of the solid skeleton and the pores, the interparticle forces, and the capillary microscale stresses in the pore water and pore gas are reviewed. The major part of these descriptions have been developed and applied for the numerical simulation by means of the discrete element method (DEM) [17]. The analytical and numerical investigations have already increased insight into the roles of various microscale characteristics and the corresponding macroscale quantities, such as the evolution of the fabric tensor, intergranular stress, and deformation, see e.g. [18–20].

For the mechanical characteristics of sphere packing with elasto-frictional interaction,

the relative position and the diameters of the spheres in direct contact with each other are of importance, as well as the opposing interparticle forces acting on each of the particles in each interparticle contact. Figure 4.2 illustrates two particles in direct contact, with interparticle contact point r on each side of the interparticle contact point indicated by the sequence number k for $k = (2r-1, 2r)$, respectively. The outward normal unit contact vectors of the material on both sides are indicated by $n(2r-1)$ and $n(2r)$, the corresponding radius vectors by $R(2r-1)$ and $R(2r)$, and the opposing interparticle contact force vectors by $f(2r-1)$ and $f(2r)$, respectively. The microstructure of the packing of spheres can be quantified in terms of the fabric tensor $\boldsymbol{A}$ [21–27]:

$$\boldsymbol{A} = \frac{1}{2C} \sum_{k=1}^{2C} \left(\boldsymbol{n}^k \otimes \boldsymbol{n}^k \right) \tag{4.72}$$

where $C = \max(r)$ represents the number of direct contacts of the packing. Then the corresponding average intergranular stress tensor σ^* is expressed by [18, 28–33]:

$$\boldsymbol{\sigma}^* = \frac{1}{V} \sum_{k=1}^{2C} \left(R^k \boldsymbol{n}^k \otimes \boldsymbol{f}^k \right) \tag{4.73}$$

where V is the sphere packing volume. For the saturated case, the pore space is filled by a pore fluid with isotropic stress tensor $p\boldsymbol{I}$.

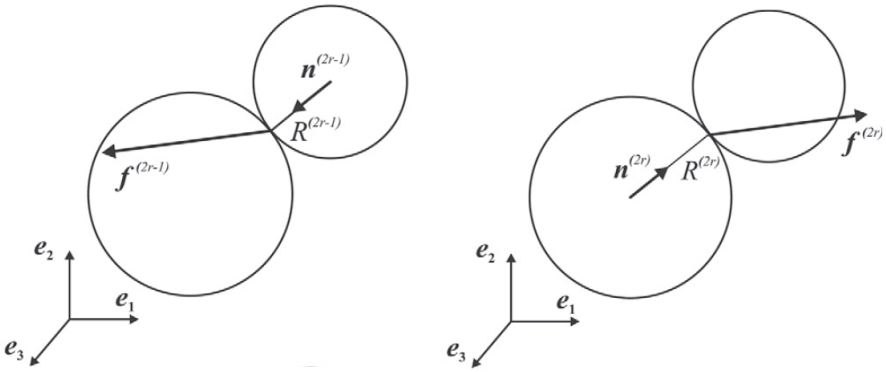


Figure 4.2: Two spheres in contact with opposing interparticle contact force vectors. The upper right particle has radius $R^{(2r-1)}$, and outward normal unit vector $\boldsymbol{n}^{(2r-1)}$ and interparticle force vector $\boldsymbol{f}^{(2r-1)}$ at the contact point, whereas the corresponding quantities of the lower left particle are indicated in the same way using superscript $(2r)$.

Figure 4.3 decomposes the interparticle contact force vector $f^{(2r)}$ into the normal component vector $\boldsymbol{N}^{(2r)} = \boldsymbol{n}^{(2r)} N^{(2r)}$ and tangential component vector $\boldsymbol{T}^{(2r)} = \boldsymbol{m}^{(2r)} T^{(2r)}$ with its unit vector $\boldsymbol{m}^{(2r)}$. Substitution of the normal and tangential component vectors enables the intergranular stress tensor $\boldsymbol{\sigma}^*$ in Equation 4.73 to be decomposed into

the intergranular stress tensors $\boldsymbol{\sigma}^N$ and $\boldsymbol{\sigma}^T$ due to the normal and tangential interparticle contact force vectors, respectively:

$$\boldsymbol{\sigma}^* = \frac{1}{V}\sum_{k=1}^{2C}\left(R^k\boldsymbol{n}^k \otimes N^k\boldsymbol{n}^k + R^k\boldsymbol{n}^k \otimes T^k\boldsymbol{m}^k\right) = \boldsymbol{\sigma}^N + \boldsymbol{\sigma}^T \tag{4.74}$$

In addition to the concept of the intergranular stress tensor $\boldsymbol{\sigma}^N$ due to the normal interparticle contact force vectors $N^{(2r)}$, Thornton [18] introduced the concept of the fabric stress tensor $\boldsymbol{\sigma}^{\mathbf{A}}$. The stresses $\boldsymbol{\sigma}^N$ and $\boldsymbol{\sigma}^{\mathbf{A}}$ are defined by:

$$\boldsymbol{\sigma}^N = \frac{1}{V}\sum_{k=1}^{2C}\left(R^k N^k \boldsymbol{n}^k \otimes \boldsymbol{n}^k\right) \tag{4.75}$$

$$\boldsymbol{\sigma}^{\mathbf{A}} = \frac{1}{V}\sum_{k=1}^{2C}\left(R^k N^k\right)\frac{1}{2C}\sum_{k=1}^{2C}\left(\boldsymbol{n}^k \otimes \boldsymbol{n}^k\right) = \hat{\sigma}\boldsymbol{A} \tag{4.76}$$

where $\hat{\sigma}$ is the volume-averaged scalar measure of the normal interparticle force:

$$\hat{\sigma} = \frac{1}{V}\sum_{k=1}^{2C}\left(R^k N^k\right) \tag{4.77}$$

The fabric tensor $\boldsymbol{A}$ was previously defined in Equation 4.72. Note the similarities between the two stress measures in Equations 4.75 and 4.76. The fabric stress tensor $\boldsymbol{\sigma}^{\mathbf{A}}$ involves the same quantities as used in defining $\boldsymbol{\sigma}^N$, but without the physical correlations embedded in $\boldsymbol{\sigma}^N$.

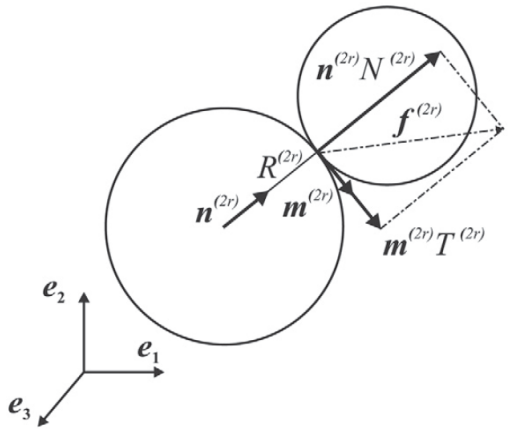


Figure 4.3: Illustration of decomposition of interparticle contact force vector $f^{(2r)}$ into normal component vector $\boldsymbol{N}^{(2r)} = \boldsymbol{n}^{(2r)}N^{(2r)}$ and tangential component vector $\boldsymbol{T}^{(2r)} = \boldsymbol{m}^{(2r)}T(2r)$.

Thornton [18] demonstrated the physical relevance of each quantity by means of Figure

4.4, illustrating various types of deviatoric intergranular stress states in the π plane in principal stress space. The plotted results concern the peak stresses for purely deviatoric loading of an initially dense dry packing of spheres in the numerical simulation of 3D true triaxial tests. The larger locus illustrates the deviatoric peak strength. The locus of the deviatoric part of the intergranular stress tensor $\boldsymbol{\sigma}^N$ is shown to be only marginally smaller than the outer locus. It can be concluded that the contribution by $\boldsymbol{\sigma}^T$ due to the tangential interparticle forces $\boldsymbol{T}$, represented by the difference between the two larger loci, remains relatively small. Furthermore, Figure 4.4 demonstrates the significance of the intergranular fabric in terms of the deviatoric part of the fabric stress tensor $\boldsymbol{\sigma}^{\mathbf{A}}$, represented by the size of the inner locus, which is already about 33% of the outer locus.

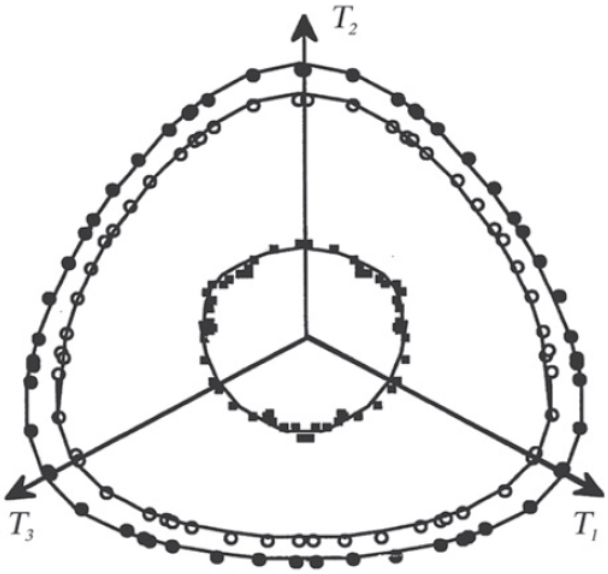


Figure 4.4: Illustration of deviatoric intergranular stress states in the π-plane in principle stress space for peak loading of an initially dense dry granular packing at constant mean intergranular stress. The black dots indicate the total stress tensor $\boldsymbol{\sigma}$, the open dots represent the stress tensor $\boldsymbol{\sigma}^N$ due to the normal contact forces, and the black squares denote the corresponding fabric stress tensor $\boldsymbol{\sigma}^A$ (after Thornton [18]).

Figure 4.5 depicts the corresponding evolution of the deviatoric part of the fabric tensor $\boldsymbol{A}$ as a function of the deviatoric strain measure $\epsilon_a - \epsilon_r$ for the numerical simulation of triaxial compression tests. The deviatoric fabric–strain curve shows a peak of about $A_a - A_r \approx 0.12$ at a strain $\epsilon_a - \epsilon_r \approx 0.07$. At the critical state, the deviatoric fabric value reduces to $A_a - A_r \approx 0.085$. This pattern is similar to the corresponding deviatoric stress–strain behaviour shown in Figure 4.6. The illustrated decomposition of the deviatoric stress into the contributions by the normal and tangential interparticle force components demonstrates the significance of the normal components as depicted in Figure 4.4.

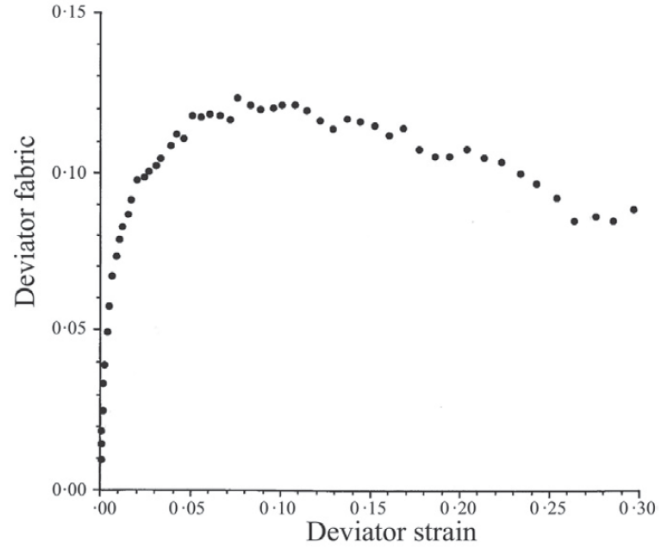


Figure 4.5: Evolution of deviatoric part $A_a - A_r$ of fabric tensor $\boldsymbol{A}$ of an initially dense packing of spheres for purely deviatoric triaxial compression at constant mean stress as a function of deviatoric strain measure $\epsilon_a - \epsilon_r$ (after Thornton [18]).

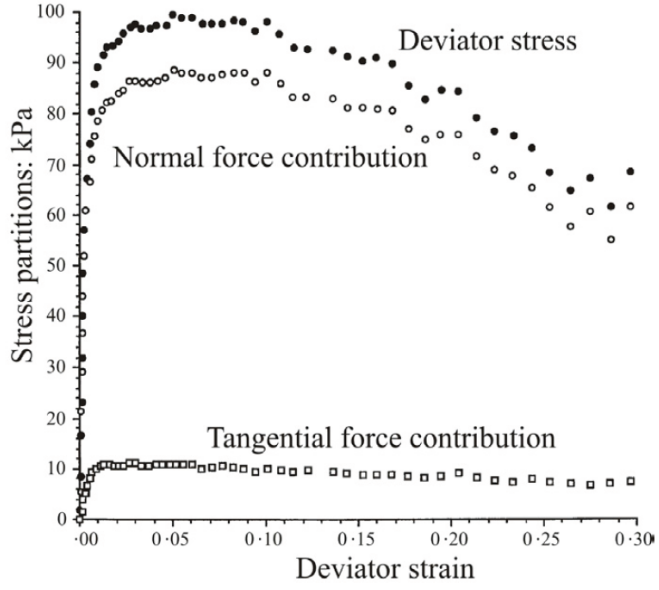


Figure 4.6: Evolution of deviatoric stress $\boldsymbol{\sigma}_a - \boldsymbol{\sigma}_r$ as a function of deviatoric strain measure $\boldsymbol{\epsilon}_a - \boldsymbol{\epsilon}_r$, based on the same discrete element method simulation as used for Figure 4.5, also indicating the decomposition of the deviatoric stress into the contributions by the normal and tangential interparticle forces (after Thornton [18]).

4.3.4. Suction-induced interparticle forces

In unsaturated granular materials for low degrees of saturation, the air phase is continuous while the liquid pore water occurs both as water bridges between neighbouring particles, illustrated in the left part of Figure 4.7, and as isolated pockets of adhesive water at the particle surfaces. This saturation phase is known as the *pendular* phase [34]. The right part of Figure 4.7 illustrates the detailed actions by a water bridge between two rough approximately spherical particles with equal radii R in direct contact. These actions are all induced by the surface tension σ along the interface between the water and air. One major consequence of this surface tension σ is the pore water suction p^w occurring in the pore water composing the water bridge, while in the surrounding air the gas stress p^g occurs. A second consequence of the surface tension σ is the line force acting along the intersection curve of the water surface and the surface of a particle. The orientation of the water surface and the coinciding surface tension σ along the intersection curve, indicated by contact angle θ, depends on the direction of the motion of the intersection curve along the particle surface, due to either wetting or drying. Both the induced pore water suction p^w and surface tension σ acting along the intersection curve pull the particles toward each other and, as a consequence, cause the suction-induced interparticle force vector $\boldsymbol{f}$ as a reaction. Note that, due to the surface roughness s of each particle surface, the representative spheres in contact are kept at a relative distance of $2s$.

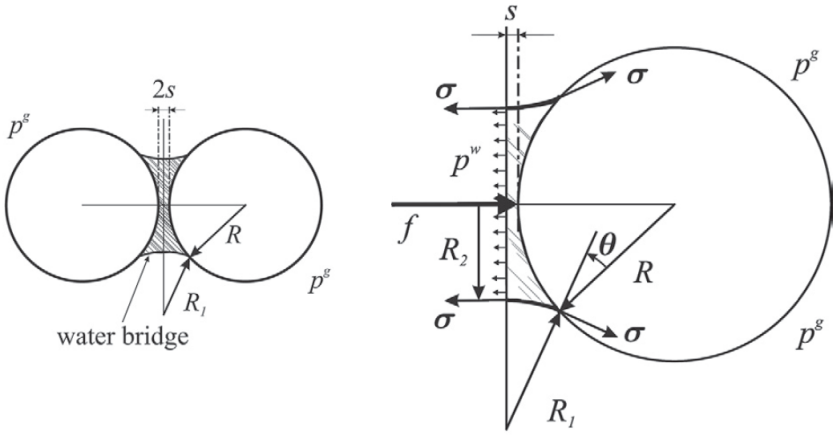


Figure 4.7: Water bridge, with external radius R1 and internal radius R_2, between two neighboring particles with equal radii R at distance $2s$ due to surface roughness, together with the surrounding gas stress p^g. Actions on the right-side particle by the water bridge involve pore water suction p^w, surface tension s directed according to contact angle θ, and suction-induced interparticle contact force vector $\boldsymbol{f}$ (after Molenkamp and Nazemi [35]).

The resulting interparticle force vector $\boldsymbol{f}$ can be expressed in dimensionless form as illustrated in Figure 4.8, namely in terms of $\boldsymbol{F} = \boldsymbol{f}/(\sigma R)$ [35] as a function of dimensionless capillary (matric) suction $\Psi = \psi R/\sigma = \left(p^w - p^g\right) R/\sigma$ and dimensionless surface rough-

ness $S = s/R$, while still depending also on the contact angle θ.

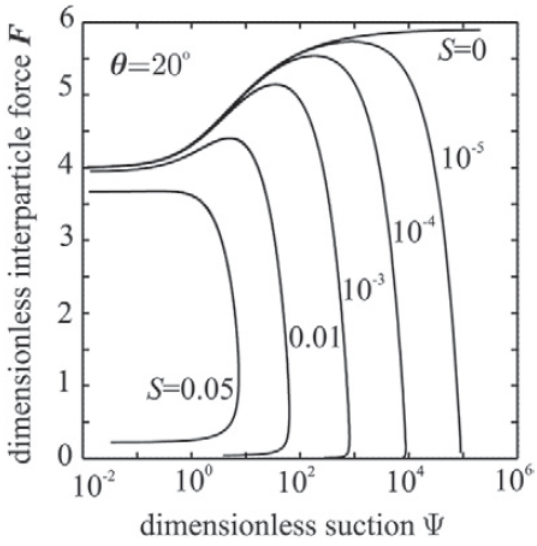


Figure 4.8: Dimensionless suction-induced interparticle force vector $\boldsymbol{F}$ as a function of the dimensionless capillary (matric) suction ψ for a range of the dimensionless particle surface roughness S and also depending on contact angle θ (after Molenkamp and Nazemi [35]).

The curve for smooth particles with zero dimensionless surface roughness, $S = 0$, seems to correspond to the observed behaviour of, e.g., soft clays during severe drought, where during continued drying, solid lumps of clay particles are formed, separated by a developing pattern of cracks due to the shrinking of the lumps. On the other hand, drying of initially saturated sand leads finally to dry sand grains, such as occur higher up sandy beaches, without any suction-induced interparticle forces. Consequently, the curves for the rough particles $S \geq 0.001$ in Figure 4.8 with the dimensionless interparticle force $\boldsymbol{F}$ approaching zero seem to represent the characteristics of sand.

Despite the apparent suitability of the role of surface roughness, the Author believes that the lack of actual physics of surface phenomena at the microscale, occurring at interparticle contacts during drying of sands and clays, warrants further microscale investigation.

4.3.5. Capillary-suction-induced intergranular stress

In unsaturated granular materials, the capillary matric suction needs to be defined for the full range of unsaturation. To this end, the generalised capillary matric suction ψ^x is provisionally defined by:

$$\psi^x = p^w - p^x \tag{4.78}$$

in which the generalised pore air stress p^x is introduced for all phases of unsaturation. Subsequently for the phases of unsaturation, cases a and b are distinguished:

- Case a with a continuous air phase. This range of unsaturated behaviour is subdivided further [34] into the pendular phase, for which the pore water occurs at isolated locations, and the funicular phase, for which the pore water is also continuous. The pore air stress p^g occurs in the continuous air phase throughout the porous network and is usually in open contact with the atmosphere:

$$p^x = p^g \tag{4.79}$$

- Case b with an entrapped air phase in a continuous water phase, known as the insular saturation phase [34]. The pore air stress p^b is the background pore air stress, with a virtual magnitude that would occur if the local pore air would be in open hydrostatic equilibrium with the atmosphere:

$$p^x = p^b \tag{4.80}$$

In unsaturated granular materials, the definition of an unsaturated state involves at least the generalised capillary suction ψ^x (Equation 4.78), the degree of saturation S^w, the contact angle θ, and the magnitudes and spatial distribution of the capillary-suction-induced intergranular force vectors $\boldsymbol{f}^k$, being normal contact forces similar to $\boldsymbol{N}^k$ in Equation 4.74. These force vectors $\boldsymbol{f}^k$ concern a large series of microscale vectors, while all other quantities are scalars defined at the macroscale. The particle surface roughness s is a material parameter.

This subsection aims at replacing the effects of the capillary-suction-induced microscale intergranular force vectors $\boldsymbol{f}^k$ by a representative macroscale capillary-suction-induced intergranular stress tensor $\boldsymbol{\psi}^*$. Such a capillary-suction-induced intergranular stress tensor has already been derived analytically for homogeneous unsaturated pyramidal packing of rough spheres [36] for the pendular saturation phase [34, 37]. These unsaturated state parameters are mutually dependent, so that distinguishing between functionally independent and dependent quantities is merely a matter of convenience. One convenient choice is to consider the contact angle θ depending on both the degree of saturation S^w and its material rate $\dot{S}^w$, enabling us to distinguish between wetting and drying through the latter, that is:

$$\theta = \theta\left(S^w, \dot{S}^w\right) \tag{4.81}$$

Similarly, the functional dependence of the generalised capillary matric suction ψ^x and the macroscale capillary-suction-induced intergranular stress tensor $\boldsymbol{\psi}^*$ can be symbolically expressed by:

$$\psi^x = \psi^x\left(S^w, \dot{S}^w\right) \tag{4.82}$$

$$\boldsymbol{\psi}^* = \boldsymbol{\psi}^*\left(S^w, \dot{S}^w\right) \tag{4.83}$$

Furthermore, it is noted that for unsaturated granular materials composed of spherical particles with the same size at equilibrium in a representative elementary volume,

the pore water suction will be approximately homogeneous. An approximately normal capillary-suction-induced intergranular force vector $\boldsymbol{f}^k$ with approximately equal magnitude at all water bridges between particles in direct contact is thus induced. Here, for the low degrees of the pendular saturation phase, the relative humidity plays an equilibrating role [35]. In such an idealised simple case, the scalar normal magnitudes f^k of the volume-averaged suction-induced interparticle (normal) force vectors $\boldsymbol{f}^k$ can be approximated by the application of the volume-averaged scalar measure $\hat{\sigma}$ of the normal interparticle forces 4.77. Replacing the magnitudes N^k of the normal intergranular forces by the magnitudes f^k of the approximately normal capillary-suction-induced intergranular force vector $\boldsymbol{f}^k$, leads to the following scalar volume-averaged capillary-suction-induced contact force measure:

$$\widehat{\sigma} = \frac{1}{V} \sum_{k=1}^{2C} \left(R^k f^k \right) \tag{4.84}$$

Combining the functional dependence of the capillary-suction-induced intergranular normal force f^k illustrated in Figure 4.8 with the functional form of the contact angle θ according to Equation 4.81 leads to:

$$f^k = f^k(\psi, \theta) = f^k\left(\psi, S^w, \dot{S}^w\right) \tag{4.85}$$

where the effect of the roughness s of the particle surfaces has been assumed to be constant and subsequently for simplicity left out of the following considerations. The corresponding functional form of the volume-averaged suction-induced contact force measure $\widehat{\sigma}$ then becomes:

$$\widehat{\sigma} = \widehat{\sigma}\left(\psi, S^w, \dot{S}^w\right) \tag{4.86}$$

Expanding this idealised simple case even further, the spatial distribution of the water bridges is considered to correspond approximately to the fabric tensor $\boldsymbol{A}$, acting here as an independent state parameter of the granular microstructure. In that particular case, the suction-induced intergranular stress tensor $\boldsymbol{\psi}^*$ will have the same spatial structure as the fabric stress tensor $\boldsymbol{A}$ according to Equation 4.72. Hence, the functional form of $\boldsymbol{\psi}^*$ reads:

$$\boldsymbol{\psi}^* = \widehat{\sigma}\,\boldsymbol{A} = \psi^*\left(\psi, S^w, \dot{S}^w, \boldsymbol{A}\right) \tag{4.87}$$

To arrive at practical relations for the capillary-suction-induced intergranular stress tensor $\boldsymbol{\psi}^*$, recall Bishop's effective stress equation 4.69. Its suction-induced part is considered [9, 10]:

$$\boldsymbol{\psi}^* = -\psi^x \chi\left(S^w, \dot{S}^w\right) \boldsymbol{I} = -\left(p^w - p^x\right) \chi\left(S^w, \dot{S}^w\right) \boldsymbol{I} \tag{4.88}$$

where the generalised capillary suction ψ^x according to Equation 4.82 is combined with Bishop's dimensionless isotropic, intergranular stress function $\chi\left(S^w, \dot{S}^w\right)$. Note that if the generalised capillary suction $\psi = p^w - p^g$ is positive (tension), the corresponding intergranular stress $\boldsymbol{\psi}^*$ is negative (compression), which justifies the minus sign in Equation 4.88.

Next, Equation 4.88 is extended further by also accounting for the deviatoric part $\boldsymbol{A}^{dev}$

of the fabric tensor $\boldsymbol{A}$. To this end the fabric tensor $\boldsymbol{A}$ according to Equation 4.72 is first decomposed into the isotropic part $\boldsymbol{A}^{iso} = A^{iso}\boldsymbol{I}$ and the deviatoric part $\boldsymbol{A}^{dev}$ by:

$$\boldsymbol{A} = \boldsymbol{A}^{iso} + \boldsymbol{A}^{dev} \tag{4.89}$$

$$A^{iso} = \frac{\boldsymbol{A} : \boldsymbol{I}}{3} \tag{4.90}$$

$$\boldsymbol{A}^{dev} = \boldsymbol{A} - A^{iso}\boldsymbol{I} \tag{4.91}$$

Introducing this decomposition in the definition of $\boldsymbol{\psi}^*$ (4.87) yields the following, suggested extension:

$$\boldsymbol{\psi}^* = \widehat{\sigma} A^{iso} \left(\boldsymbol{I} + \hat{\chi}\left(S^w, \dot{S}^w\right) \frac{\boldsymbol{A}^{dev}}{A^{iso}} \right) \tag{4.92}$$

in which the dimensionless scalar function $\hat{\chi}\left(S^w, \dot{S}^w\right)$ has been introduced to account for the relative magnitude of the deviatoric part of the capillary-suction-induced intergranular stress. This scalar function will be defined in more detail below.

Combining Equations 4.92 and 4.88 for the simplified case of $\boldsymbol{A}^{dev} = 0$ leads to:

$$\boldsymbol{\psi}^* \approx \widehat{\sigma} A^{iso} \boldsymbol{I} = -\psi^x \chi\left(S^w, \dot{S}^w\right) \boldsymbol{I} \tag{4.93}$$

The scalar stress measure $\widehat{\sigma}$ can consequently be defined as:

$$\widehat{\sigma} = -\psi^x \frac{\chi\left(S^w, \dot{S}^w\right)}{A^{iso}} \tag{4.94}$$

Backsubstituting Equation 4.94 into Equation 4.92 results in an updated expression for $\boldsymbol{\psi}^*$:

$$\boldsymbol{\psi}^* = -\psi^x \chi\left(S^w, \dot{S}^w\right) \left(\boldsymbol{I} + \hat{\chi}\left(S^w, \dot{S}^w\right) \frac{\boldsymbol{A}^{dev}}{A^{iso}} \right) = -\psi^x \boldsymbol{X} \tag{4.95}$$

In the last term the second-order tensor $\boldsymbol{X}$ has been introduced, which accounts for the intergranular capillary suction structure:

$$\boldsymbol{X} = \chi\left(S^w, \dot{S}^w\right) \left(\boldsymbol{I} + \hat{\chi}\left(S^w, \dot{S}^w\right) \frac{\boldsymbol{A}^{dev}}{A^{iso}} \right) = -\frac{\boldsymbol{\psi}^*}{\psi^x} \tag{4.96}$$

After recognising the physical reality of the existence of a deviatoric part of the capillary-suction-induced intergranular stress tensor $\boldsymbol{\psi}^*$, its practical significance should also be considered, which for unsaturated loose granular materials should at least include its effect on the occurrence of wetting-induced pore collapse. On this topic the Author expects as a provisional speculative guess, before considering wetting, that in general terms the real deviatoric part of the combined intergranular stress tensor may be significantly larger than when completely ignoring the deviatoric part of the capillary-suction-induced intergranular stress tensor $\boldsymbol{\psi}^*$. Then, during subsequent wetting, not only the isotropic part of the combined intergranular stress tensor may decrease but also its deviatoric part, which for loose granular materials will increase the occurrence of volumetric

contraction. This induced-deformation mode, together with the ongoing rate of resaturation, may increase the possibility of the occurrence of a spontaneous instability, as recently investigated by Buscarnera and Nova [6, 38]. This mechanism appears to be somewhat similar to the spontaneous instability leading to flow liquefacton of saturated, loose sand.

4.3.6. Relations between capillary-suction-induced quantities

Some characteristics of unsaturated granular materials are now illustrated for repeated cyclic drying and wetting in triaxial tests. Some synthetic, dimensionless relations are considered for $\chi\left(S^w, \dot{S}^w\right)$, $\hat{\chi}\left(S^w, \dot{S}^w\right)$ and the dimensionless matric suction:

$$\Psi\left(S^w, \dot{S}^w\right) = \frac{\psi D^{50}}{2\sigma} \tag{4.97}$$

where D^{50} defines the median grain diameter.

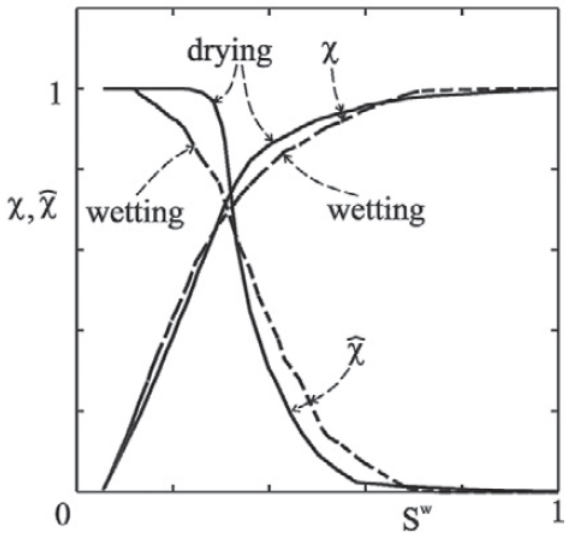


Figure 4.9: Synthetic relations for repeated cycles of drying and wetting in triaxial tests of the dimensionless Bishop's isotropic suction-induced intergranular stress function $\chi\left(S^w, \dot{S}^w\right)$ and the dimensionless fabric related deviatoric suction-induced intergranular stress function $\hat{\chi}\left(S^w, \dot{S}^w\right)$, both as function of the degree of saturation S^w.

The synthetic relations have been composed while taking account of the earlier microscale characteristics according to Figures 3.3, 4.3 and 4.5 together with some experimental data on unsaturated granular materials, particularly concerning the dimensionless relations $\Psi\left(S^w, \dot{S}^w\right)$. In addition, for the corresponding dimensionless capillary-suction-induced intergranular stress tensor $\boldsymbol{\psi}^*$, the following isotropic and deviatoric

components, Ψ_p^* and Ψ_q^* respectively, are distinguished:

$$\Psi_p^* = \frac{\psi_p^* D^{50}}{2\sigma} = \frac{\left(\psi_a^* + 2\psi_r^*\right) D^{50}}{6\sigma} \tag{4.98}$$

$$\Psi_q^* = \frac{\psi_q^* D^{50}}{2\sigma} = \frac{\left(\psi_a^* - \psi_r^*\right) D^{50}}{2\sigma} \tag{4.99}$$

$$\tag{4.100}$$

in which subscripts a and r indicate the axial and radial directions, respectively. Figure 4.9 illustrates the dimensionless isotropic suction-induced intergranular stress function $\chi\left(S^w, \dot{S}^w\right)$ and the corresponding dimensionless fabric-related deviatoric suction-induced function $\hat{\chi}\left(S^w, \dot{S}^w\right)$ for drying and wetting. It is noted that the isotropic Bishop's function χ increases from zero at the dry state with increasing saturation to reach unity at full saturation. The deviatoric fabric function $\hat{\chi}$ on the other hand starts at unity for the dry state and decreases to zero with increasing saturation.

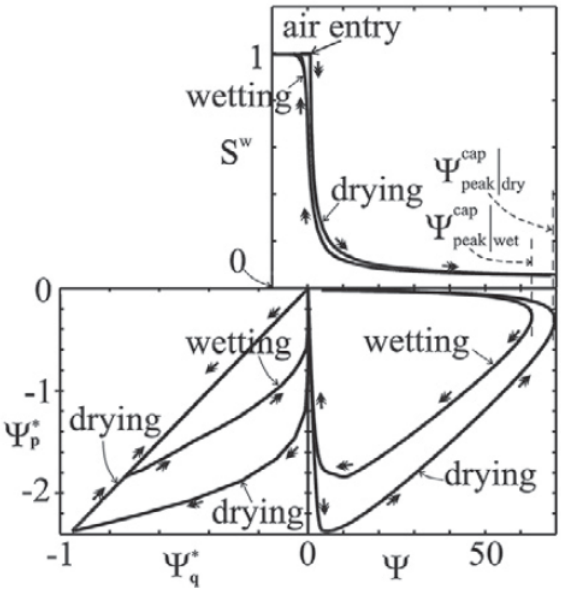


Figure 4.10: Synthetic relations for repeated cycles of drying and wetting in triaxial tests, involving the degree of saturation S^w, the dimensionless capillary pore water suction Ψ (Equation 4.97), and the suction-induced dimensionless isotropic and deviatoric intergranular stress components Ψ_p^* and Ψ_q^* according to equations 4.98 and 4.99.

Figure 4.10 plots the corresponding dimensionless relations of the capillary suction Ψ on the horizontal axis at the right side, the capillary-suction-induced isotropic intergranular stress component Ψ_p^* at the lower vertical axis, and the capillary-suction-induced deviatoric intergranular stress component Ψ_q^* on the horizontal axis at the left side. These

figures are mainly self-explanatory, although the left bottom capillary-suction-induced intergranular stress path is noted to pass through a significant deviatoric stress level during repeated cycles of drying and wetting. From Equation 4.95, the latter is noted to be due to the magnitude of $\left|\boldsymbol{A}^{dev}\right| / A^{iso}$ for which, based on Figure 4.95, $\left|\boldsymbol{A}^{dev}\right| / A^{iso} \approx 0.33$ has been applied.

4.3.7. Stress measures for unsaturated granular materials

From the local equilibrium of unsaturated granular material it follows that the total stress tensor $\boldsymbol{\sigma}$ equals the sum of the combined intergranular stress tensor $\boldsymbol{\sigma}^*$ and the combined pore fluid stress tensor $\boldsymbol{p}$, or:

$$\boldsymbol{\sigma} = \boldsymbol{\sigma}^* + \boldsymbol{p} \tag{4.101}$$

The combined intergranular stress tensor $\boldsymbol{\sigma}^*$ is the sum of the intergranular stress tensor $\hat{\boldsymbol{\sigma}}^*$ due to the boundary tractions and the capillary-suction-induced intergranular stress tensor $\boldsymbol{\psi}^*$:

$$\boldsymbol{\sigma}^* = \hat{\boldsymbol{\sigma}}^* + \boldsymbol{\psi}^* \tag{4.102}$$

Combining Equations 4.101 and 4.102 yields expressions for the total and combined pore fluid stress tensor:

$$\boldsymbol{\sigma} = \boldsymbol{\sigma}^* + \boldsymbol{p} = \hat{\boldsymbol{\sigma}}^* + \boldsymbol{\psi}^* + \boldsymbol{p} \tag{4.103}$$

$$\boldsymbol{p} = \boldsymbol{\sigma} - \boldsymbol{\sigma}^* = \boldsymbol{\sigma} - \hat{\boldsymbol{\sigma}}^* - \boldsymbol{\psi}^* \tag{4.104}$$

The boundary tractions follow from the inner product of the total stress tensor $\boldsymbol{\sigma}$ and the local normal outward unit vector $\boldsymbol{n}$ of the boundary:

$$\boldsymbol{n}\cdot\boldsymbol{\sigma} = \boldsymbol{n}\cdot\boldsymbol{\sigma}^* + \boldsymbol{n}\cdot\boldsymbol{p} = \boldsymbol{n}\cdot\hat{\boldsymbol{\sigma}}^* + \boldsymbol{n}\cdot\boldsymbol{\psi}^* + \boldsymbol{n}\cdot\boldsymbol{p} \tag{4.105}$$

The following boundary traction vectors are inferred from Equation 4.105:

- Due to total stress tensor $\boldsymbol{\sigma}$:

$$\boldsymbol{\tau} = \boldsymbol{n}\cdot\boldsymbol{\sigma} \tag{4.106}$$

- Due to intergranular stress tensor $\boldsymbol{\sigma}^*$:

$$\boldsymbol{\tau}^* = \boldsymbol{n}\cdot\boldsymbol{\sigma}^* \tag{4.107}$$

- Due to the combined pore fluid stress tensor $\boldsymbol{p}$:

$$\tilde{\boldsymbol{p}} = \boldsymbol{n}\cdot\boldsymbol{p} \tag{4.108}$$

- Externally exerted intergranular boundary traction:

$$\hat{\boldsymbol{\tau}}^* = \boldsymbol{n}\cdot\hat{\boldsymbol{\sigma}}^* \tag{4.109}$$

- due to capillary-suction-induced intergranular stress tensor $\boldsymbol{\psi}^*$:

$$\tilde{\boldsymbol{\psi}}^* = \boldsymbol{n}\cdot\boldsymbol{\psi}^* \tag{4.110}$$

Substituting Equations 4.106-4.110 into Equation 4.105 results in a relation between the traction terms:

$$\boldsymbol{\tau} = \hat{\boldsymbol{\tau}}^* + \tilde{\boldsymbol{\psi}}^* + \tilde{\boldsymbol{p}} \tag{4.111}$$

Consider the special case of a pendular boundary condition, expressed in terms of the exerted boundary traction vectors by:

$$\boldsymbol{\tau} = \hat{\boldsymbol{\tau}}^* + p^x \boldsymbol{n} \tag{4.112}$$

where $\hat{\boldsymbol{\tau}}^*$ (Equation 4.109) and p^x (Equation 4.79) are the externally exerted intergranular boundary traction and pore gas stress p^g , respectively. This combined traction corresponds to the total stress tensor $\boldsymbol{\sigma}$, being the sum of the pore gas stress tensor $p^x \boldsymbol{I}$ and the intergranular stress tensor $\hat{\boldsymbol{\sigma}}^*$ due to the boundary tractions:

$$\boldsymbol{\sigma} = \hat{\boldsymbol{\sigma}}^* + p^x \boldsymbol{I} \tag{4.113}$$

Substituting Equation 4.113 into 4.104 leads to:

$$\boldsymbol{p} = \boldsymbol{\sigma} - \hat{\boldsymbol{\sigma}}^* - \boldsymbol{\psi}^* = p^x \boldsymbol{I} - \boldsymbol{\psi}^* \tag{4.114}$$

Next, the expressions for the intergranular stress $\boldsymbol{\sigma}^*$ (Equation 4.102) and the combined pore fluid stress tensor $\boldsymbol{p}$ (Equation 4.114) are elaborated. Substituting the definition of ψ^x (Equation 4.78), the definition of $\boldsymbol{\psi}^*$ (Equation 4.95) and Equation 4.113 into these equations results in:

$$\boldsymbol{\sigma}^* = \hat{\boldsymbol{\sigma}}^* + \boldsymbol{\psi}^* = \boldsymbol{\sigma} - p^x \boldsymbol{I} - \psi^x \boldsymbol{X} = \boldsymbol{\sigma} - p^x \boldsymbol{I} - \left(p^w - p^x\right) \boldsymbol{X} \tag{4.115}$$

$$\boldsymbol{p} = p^x \boldsymbol{I} - \boldsymbol{\psi}^* = p^x \boldsymbol{I} + \psi^x \boldsymbol{X} = p^x \boldsymbol{I} + \left(p^w - p^x\right) \boldsymbol{X} \tag{4.116}$$

Summing both Equations 4.115 and 4.116 yields the total stress tensor $\boldsymbol{\sigma}$. For air-saturated granular materials with $p^x = p^g \cap \boldsymbol{X} = 0$ these equations reduce to:

$$\boldsymbol{\sigma}^* = \boldsymbol{\sigma} - p^g \boldsymbol{I} \tag{4.117}$$

$$\boldsymbol{p} = p^g \boldsymbol{I} \tag{4.118}$$

For water-saturated granular materials with $p^x = p^b \cap \boldsymbol{X} = \boldsymbol{I}$, Equations 4.115 and 4.116 reduce to:

$$\boldsymbol{\sigma}^* = \boldsymbol{\sigma} - p^w \boldsymbol{I} \tag{4.119}$$

$$\boldsymbol{p} = p^w \boldsymbol{I} \tag{4.120}$$

It is concluded that, for both limits of unsaturation, the unsaturated stress measures of the intergranular stress tensor $\boldsymbol{\sigma}^*$ in Equation 4.115 and the combined pore fluid stress tensor $\boldsymbol{p}$ in Equation 4.116 coincide with the respective expressions for saturated geomechanics.

Next the implications of the unsaturated stress measures 4.115 and 4.116 are considered for the constitutive equations. Recall the stress-strain relation 3.31 that was derived in Chapter 3 for saturated conditions. Reformulation and substitution of Equations 4.115

and 4.116 leads to the following expression for the strain rate $\dot{\boldsymbol{\epsilon}}^s$ of the soil skeleton, composed of elastic particles with mainly frictional interaction:

$$\begin{aligned}\dot{\boldsymbol{\epsilon}}^s &= \boldsymbol{D}^{-1} : \dot{\boldsymbol{\sigma}}^{*J} + \left(\boldsymbol{D}^{e;sf}\right)^{-1} : \dot{\boldsymbol{p}}^J \\ &= \boldsymbol{D}^{-1} : \left(\boldsymbol{\sigma}^J - \dot{p}^x \boldsymbol{I} + \dot{\boldsymbol{\psi}}^{*J}\right) + \left(\boldsymbol{D}^{e;sf}\right)^{-1} : \left(\dot{\boldsymbol{p}}^x \boldsymbol{I} - \dot{\boldsymbol{\psi}}^{*J}\right)\end{aligned} \tag{4.121}$$

in which the objective Jaumann stress rates $\dot{\boldsymbol{\sigma}}^{*J}$ and $\dot{\boldsymbol{p}}^J$ have been applied for both the intergranular and combined pore fluid stress tensor, respectively. The corresponding constitutive characteristics are represented by the tangent elasto-visco-plastic flexibility tensor function $\boldsymbol{D}^{-1}$ of the solid skeleton and the tangent elastic flexibility matrix $\boldsymbol{D}^{e;sf}$ of the substance comprising the particles. It is noted that the tangent isotropic linear elastic flexibility matrix $\left(\boldsymbol{D}^{e;sf}\right)^{-1}$ replaces the compressibility $1/K^{sf}$ of the substance comprising the particles, occurring in Equation 3.31. The isotropic pore fluid stress tensor $p\boldsymbol{I}$ is replaced by the combined second-order pore fluid stress tensor $\boldsymbol{p}$. The isotropic linear elastic flexibility matrix of the substance comprising the particles equals, in index format:

$$\left(\boldsymbol{D}^{e;sf}\right)^{-1} = \left(\frac{3\delta_{ik}\delta_{jl} - \delta_{ij}\delta_{kl}}{6G^{sf}} + \frac{\delta_{ij}\delta_{kl}}{9K^{sf}}\right) \boldsymbol{e}_i \otimes \boldsymbol{e}_j \otimes \boldsymbol{e}_k \otimes \boldsymbol{e}_l \tag{4.122}$$

where K^{sf} and G^{sf} are the average bulk and shear modulus of the particles, respectively. Substituting Equation 4.122 into the last term of Equation 4.121 leads to the corresponding part of the strain rate:

$$\left(\boldsymbol{D}^{e;sf}\right)^{-1} : \dot{\boldsymbol{p}}^J = \boldsymbol{I}\left(\frac{\dot{p}^x}{3K^{sf}} - \frac{\boldsymbol{I} : \dot{\boldsymbol{\psi}}^{*J}}{9K^{sf}}\right) - \left(\frac{\dot{\boldsymbol{\psi}}^{*J} - \boldsymbol{I}\left(\boldsymbol{I} : \dot{\boldsymbol{\psi}}^{*J}/3\right)}{2G^{sf}}\right) \tag{4.123}$$

The first term on the right-hand side of Equation 4.123 depends on the bulk stiffness of the particles K^{sf} and is caused by the material rates of both the pore air stress $\dot{p}^x$ and the isotropic part of the capillary-suction-induced intergranular stress $\dot{\boldsymbol{\psi}}^*$. The last term on the right-hand side depends on the shear modulus of the particles G^{sf} and is due to the deviatoric part of $\dot{\boldsymbol{\psi}}^*$. This term is usually assumed to be negligible compared with the deviatoric strain rate resulting from the interparticle deformation mode of the soil skeleton, expressed by the first right-hand term in Equation 4.121.

From Equation 4.121 it is concluded that both developed capillary-based unsaturated stress measures suffice to account for the mechanical effects on the solid skeleton for the full range of unsaturation, including the dry and fully saturated limits. The concept is in general agreement with recently published DEM simulations [39, 40], although the evolution of the spatial distributions of interparticle contact points and water bridges during the loading history may not coincide precisely. For instance, during interparticle slip the local water bridge will at least be distorted due to the dependence of the local contact angle θ on the wetting and drying motions of the capillary interface in contact with the solid surface around the interparticle contact point. This will affect the magnitude and direction of the local capillary-suction-induced interparticle force.

4.3.8. Potential approach for progress toward applications

In principle, the intergranular capillary suction structure tensor function $\boldsymbol{X}$ (Equation 4.96) of the described model framework for unsaturated granular materials could be determined directly on the basis of microscale observations of the evolution of the intergranular structure and the geometries of the interfaces between the pore water, pore air and the particle surfaces. These microscale observations should be sufficient to calculate both the microscale capillary pore fluid stresses and the corresponding suction-induced interparticle forces. Then, subsequent volume averaging of these microscale data should enable the calculation of the macroscale quantities occurring in Equation 4.96. Unfortunately, at present the development of such microscale experimental capabilities seems still far away from geotechnical engineering practice. For instance, Figure 4.11 shows a (state of the art) two-dimensional picture of microsized spheres of about 10 mm diameter with concave and convex water menisci formed simultaneously at contacts for a pore air relative humidity of 88% [41]. Although these type of data are very important to observe essential features of wetting and drying, for the quantification of the complete microstructure three-dimensional geometrical data are needed for both the granular skeleton and the interfaces of water, air, and grains.

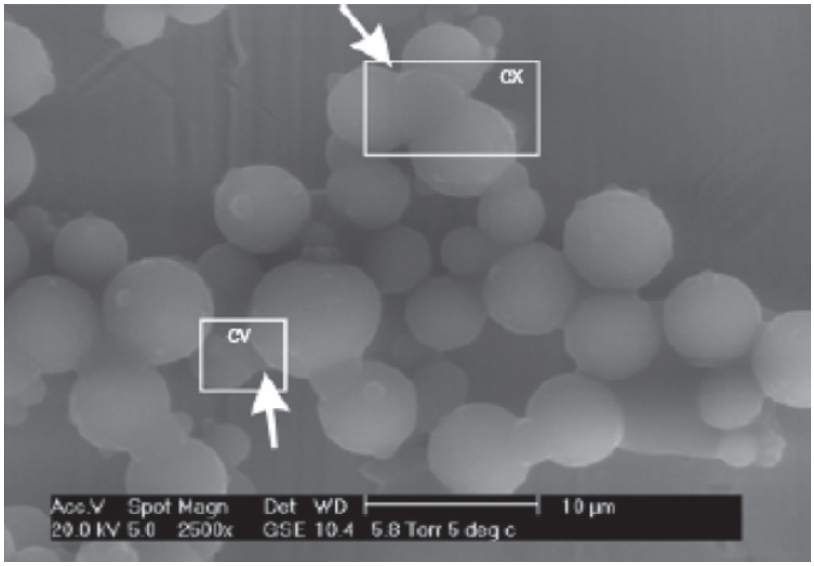


Figure 4.11: Picture of microsized spheres of about 10 mm diameter with concave (cv) and convex (cx) water menisci formed at the contacts for a pore air relative humidity of 88% (after Lourenço et al. [41]).

Therefore another more approximate and less demanding approach for advancing the development of predictive tools for unsaturated sands and silts is considered here. The Author suggests the application of inverse modelling, for which the described model framework for unsaturated granular materials is considered to be potentially useful as a

basis. The method of determination of the χ parameter of Bishop's effective stress (Equation 4.69) can be seen as an early form of such inverse modelling. Bishop and Blight [10] demonstrate that the determination of χ combines measured shear strengths of saturated and unsaturated soils. Inverse modelling by means of the ensemble Kalman filter (e.g. [42, 43]) is expected to allow the simultaneous determination of the macroscale combined capillary characteristics of both pore fluids and the mechanical characteristics of the solid skeleton. This does require the existence of an experimental database containing both saturated and unsaturated data on the mechanical behaviour of the granular skeleton and both pore fluids. In appropriate inverse modelling, all differences between the experimental observations and the model predictions are minimised. For the required modelling predictions occurring in this minimisation process, all stress measures in Equations 4.115 and 4.116 can be used as volume averages. The corresponding deformation modes need to be compatible and thermodynamically justified, minimizing their combined internal energy for equilibrium. Also, the capillary energy stored in the liquid–gas interface must be accounted for at least approximately.

It should be recognised that the major part of this framework for unsaturated conditions concerns the capillary-suction-induced intergranular stress tensor $\boldsymbol{\psi}^*$. Its macroscale quantities are the degree of saturation S^w, the generalised capillary matric suction ψ^x, and the normalised deviatoric fabric tensor $\boldsymbol{A}^{dev}/A^{iso}$ (see Equation 4.96). The corresponding (Bishop) isotropic and deviatoric fitting relations $\chi\left(S^w,\dot{S}^w\right)$ and $\hat{\chi}\left(S^w,\dot{S}^w\right)$ depend also on the wetting and drying modes. However, without microscale three dimensional geometrical data on the microstructure, the fabric tensorial quantity $\boldsymbol{A}^{dev}/A^{iso}$ remains unknown. Nevertheless, application of the proposed model framework in inverse modelling can be expected to enable the approximate determination of $\boldsymbol{A}^{dev}/A^{iso}$ for the following three reasons:

1. The constitutive relations of the solid skeleton of sands and silts are considered to be independent of the degree of saturation. Consequently, the mechanical characteristics of the granular skeleton can be determined by means of inverse modelling based exclusively on the experimental data on saturated behaviour.

2. The anisotropic effect of the microstructure, described by the normalised deviatoric fabric tensor $\boldsymbol{A}^{dev}/A^{iso}$, on the mechanical behaviour of the granular skeleton is maximum for the pendular saturation phase and zero for the insular saturation phase. Consequently, this parameter can be derived by means of inverse modelling from unsaturated experimental data on exclusively the pendular saturation phase, while applying the mechanical characteristics of the granular skeleton according to Point 1.

3. The (Bishop) isotropic and deviatoric fitting curves $\chi\left(S^w,\dot{S}^w\right)$ and $\hat{\chi}\left(S^w,\dot{S}^w\right)$ can be derived by means of inverse modelling using experimental data on the whole range of unsaturation.

Therefore a database of controlled observations is needed for both fully saturated and unsaturated laboratory tests of the same granular materials and for the full range of initial void ratios occurring in engineering practice. In these experiments, the controlled

boundary conditions will concern both pore fluid stresses and total stress, although for the stability of the control [6, 38] other types of control may also be needed to complete the behavioural overview. Having arrived at the best-fitting mechanical characteristics of the solid skeleton and the capillary-suction-induced intergranular stress tensor for unsaturated granular materials, the corresponding intergranular stress tensor $\boldsymbol{\sigma}^*$ and the combined pore fluid stress tensor $\boldsymbol{p}$ can finally be calculated from Equations 4.115 and 4.116.

4.3.9. Evaluation of capabilities and limitations of proposed formulation

This section is concluded by evaluating the capabilities and limitations of the proposed formulation. For the evaluation, first the stress measures for unsaturated granular materials are compared, i.e., Bishop's effective normal stress (Equation 4.69) against the intergranular stress tensor (Equation 4.115). Both are recalled here for convenience:

$$\sigma' = \sigma - p^g - \chi\left(p^w - p^g\right) \tag{4.69}$$

$$\boldsymbol{\sigma}^* = \hat{\boldsymbol{\sigma}}^* + \boldsymbol{\psi}^* = \boldsymbol{\sigma} - p^x \boldsymbol{I} - \psi^x \boldsymbol{X} = \boldsymbol{\sigma} - p^x \boldsymbol{I} - \left(p^w - p^x\right)\boldsymbol{X} \tag{4.115}$$

In both equations, following their last equal signs, the same net stress occurs, namely as the normal stress $\sigma - p^g$ and as the tensor $\boldsymbol{\sigma} - p^x \boldsymbol{I}$. It is noted that $p^x = p^g$ for the pendular and funicular phases and $p^x = p^b$ for the insular phase. The last parts of both Equations 4.69 and 4.115 concern the effects of the matric suction $p^w - p^g$ on the intergranular stress as a normal stress $\chi\left(p^w - p^g\right)$ and as a tensor $\left(p^w - p^g\right)\boldsymbol{X}$. Clearly their main difference concerns the scalar fraction χ and the second-order intergranular capillary suction structure tensor $\boldsymbol{X}$, which equals:

$$\boldsymbol{X} = \chi\left(S^w, \dot{S}^w\right)\left(\boldsymbol{I} + \hat{\chi}\left(S^w, \dot{S}^w\right)\frac{\boldsymbol{A}^{dev}}{A^{iso}}\right) = -\frac{\boldsymbol{\psi}^*}{\psi^x} \tag{4.96}$$

Comparing Equations 4.69 and 4.115, the difference concerns the deviatoric contribution $\chi\left(S^w, \dot{S}^w\right)\hat{\chi}\left(S^w, \dot{S}^w\right)\boldsymbol{A}^{dev}/A^{iso}$, which represents the anisotropic effect of the intergranular fabric on the capillary-suction-induced intergranular stress tensor $\boldsymbol{\psi}^*$. Therefore, it can be concluded that both Equations 4.69 and 4.115 involve the same isotropic capillary-suction-induced intergranular stress, and additionally Equation 4.115 also represents a potential deviatoric contribution.

Thus, for evaluating Equation 4.115 the significance of the deviatoric contribution should be considered. Current experience, involving Bishop's effective stress (Equation 4.69), has shown good predictions of the shear strength, volume change, and critical state lines for sands and silts [15]. At first sight, this would strongly suggest that the significance of the deviatoric part of Equation 4.115 remains relatively small and therefore can be neglected. However, Khalili et al. [15] also expected it to be possible to model pore collapse on wetting by means of a plasticity model by accounting for the hardening effect of matric suction. On this point, the Author would like to remark that the very need for matric suction as a constitutive quantity of the solid skeleton brings Bishop's effective stress

formulation outside the framework considered herein. The Author considers the constitutive models of the granular skeleton to depend exclusively on the state parameters of the solid skeleton, thus being independent of the degree of saturation or the types of pore fluids or the matric suction. It is expected that the additional deviatoric part of Equation 4.115 will enable the modelling of the contraction of the solid skeleton during wetting, because through this deviatoric term wetting will also induce the reversal of deviatoric loading, thereby increasing the tendency of loose sand to contract. Consequently, while recognizing the major modelling capabilities of Bishop's effective stress, it is expected that through its deviatoric part, Equation 4.115 may enable the modelling of some additional physical features, such as pore collapse, without requiring any additional stress measures. In general, for saturated granular materials, the loss of controllability, inducing collapse, occurs for specific combinations of stress and deformation [6, 38]. More complicated granular materials, with the constitutive models of their solid skeletons also depending on the degree of saturation, fall outside the scope of the proposed model framework. Nevertheless, for clays with physical-chemical particle interactions, Bishop's effective stress has been shown to be very useful after accounting for its double-porosity microstructures (e.g. [16, 44]. However, the corresponding microphysics, explaining this microstructure, is still lacking. For peats, composed of organic, partly decomposed, fibrous and bulk substances [45], with potential biochemical actions both within and between the solid components and the pore water and the pore air, the proposed model framework must be considered to be not physically justifiable.

In the longer term, appropriate microscale observations may become possible. Expecting for sands and silts that the capillary phenomenon will remain dominant, detailed microscale observations of the granular fabric, the water–gas interfaces, and their contacts with the particle surfaces may be sufficient for arriving at an effective and physically fully justified model. However, for clays and peats, the required microscale observations and the physical modelling can be expected to involve additional non-capillary physical characteristics.

4.4. Stress measures for interparticle sliding and rotation

4.4.1. Introduction

This section is based on a publication at the conference on Numerical Methods in Geomechanics (NUMGE 2014) [3]. Herein, the limits of the framework that was presented in Chapter 3 are further exploited. The conservation of angular momentum was ignored. The choice for the (symmetric) Cauchy stress ensures the satisfaction of the conservation of angular momentum (Section 2.3.3 in [46]). During the first stage of a liquefaction flow slide, i.e. from hydrostatics to triggering and the initial phase of movement, it is reasonable to assume that interparticle sliding governs the interaction at the particle scale. For this stage the use of the Cauchy stress is justified. However, this may not be the case for the post-liquefaction phase, when the loose, liquefied sand flows down the slope. With decreasing density of granular materials the average number of interparticle contacts per particle decreases [29, 47] and consequently the particle freedoms of rolling

and rotation increase. This section elaborates further on the implications of the complementary deformation mode of interparticle rotation for the stress measure.

Landau and Lifshitz (pages 1-2 in [48]) and Weber [49] defined a global stress measure based on the interparticle force vectors and the location vectors of their points of action. De Saxcé et al. [50] strengthened the derivation of this global stress measure, while also accounting for both gravitational and inertial effects. The microscale approach by Li et al. [27] is extended by applying the conditions of the conservation of linear and angular momentum of all particles. The stress measure for interparticle sliding and particle rotation are derived. The symmetry characteristics of the resulting stress tensor in the continuum will be subsequently considered. Finally, the results are elaborated for the plane case of a simple-shearing flow of a liquefied loose sand layer down a slope.

4.4.2. Momentum equations at the particle scale

Consider an assembly of particles P bounded by a surface S. Its volume V is sufficiently large for the assembly to be assumed a continuum. The particles with surface S^P experience contact forces f_j^{Pc} at their contact points with coordinates x_i^{Pc}. The indices refer to a Cartesian right-handed triad of unit base vector $\boldsymbol{e}_i$ ($i = 1,2,3$). At the boundary, the contact forces should equal the external forces F_j^β that act on the external action points β. Internally, the particles experience opposing action and reaction forces at their contact points, which compensate for one another, resulting in:

$$\frac{1}{V}\sum_{P\in V}\sum_{c\in P} x_i^{Pc} f_j^{Pc} = \frac{1}{V}\sum_{\beta\in S} x_i^\beta F_j^\beta \tag{4.124}$$

Herein, c defines the number of action points per particle, both internally and at the boundary. The center of mass X_i^P of particle P with uniform density ρ is defined by:

$$X_i^P = \frac{1}{V^P}\oint_{V^P} x_i \,\mathrm{d}V^P \tag{4.125}$$

Correspondingly, the relative location vector r_j may be used to define the relative position of material with respect to the centre of mass:

$$x_i = r_i + X_i^P \tag{4.126}$$

For instance, the relative location vector can be used to define the location of the action points x_i^{Pc}:

$$x_i^{Pc} = r_i^{Pc} + X_i^P \tag{4.127}$$

The rotation rate of a rigid particle P is indicated by the axial spin vector w_i^P. The velocity and acceleration vectors of material point (r_i, t) are described by, respectively:

$$v_i(r_i,t) = v_i^P + e_{ijk} w_j^P r_k \tag{4.128}$$

$$\dot{v}_i(r_i,t) = \dot{v}_i^P + e_{ijk}\dot{w}_j^P r_k + w_j^P\left(w_i^P r_j - w_j^P r_i\right) \tag{4.129}$$

in which v_i^P and $\dot{v}_i^P$ define the velocity and acceleration vectors of the centre of mass, respectively.

The conservation of linear momentum of particle P is considered. For the sake of conciseness, the total body force G_j^P and the acceleration force A_j^P are first introduced:

$$G_j^P = \oint_{V^P} \rho b_j \mathrm{d}V^P \tag{4.130}$$

$$A_j^P = \oint_{V^P} \rho \dot{v}_j^P \mathrm{d}V^P \tag{4.131}$$

Note that the latter includes the particle acceleration $\dot{v}_j^P$ rather than the material point $(\boldsymbol{r}, t)$. The complementary parts of Equation 4.129 are equal to zero when considering the linear momentum of the particle:

$$\oint_{V^P} \rho e_{jkl} \dot{w}_k^P r_l \mathrm{d}V^P = 0 \tag{4.132}$$

$$\oint_{V^P} \rho w_k^P \left(w_j^P r_k - w_k^P r_j \right) \mathrm{d}V^P = 0 \tag{4.133}$$

The resulting equation for the conservation of linear momentum of particle P reads:

$$\sum_{c \in P} f_j^{Pc} + G_j^P - A_j^P = 0 \tag{4.134}$$

Equation 4.134 is essentially equal to the general linear momentum equation 3.17 that was derived for a continuum in Chapter 3.

The conservation of angular momentum of particle P simply adds a term to the linear momentum equation, while noting that the spin related terms are not equal to zero for the angular momentum:

$$e_{ijk} \boldsymbol{e}_i \left(\sum_{c \in P} x_j^{Pc} f_k^{Pc} + \oint_{V^P} \rho x_j b_k \mathrm{d}V^P - \oint_{V^P} \rho x_j \dot{v}_k^P \mathrm{d}V^P \right) = \boldsymbol{0} \tag{4.135}$$

Each of the three terms in 4.135 are considered separately. The first summation term is decomposed using the location vector in Equation 4.127:

$$e_{ijk} \boldsymbol{e}_i \sum_{c \in P} x_j^{Pc} f_k^{Pc} = e_{ijk} \boldsymbol{e}_i \sum_{c \in P} r_j^{Pc} f_k^{Pc} + e_{ijk} \boldsymbol{e}_i X_j^P \sum_{c \in P} f_k^{Pc} \tag{4.136}$$

The second volume integral term is reformulated in terms of the total body force G_j^P:

$$e_{ijk} \boldsymbol{e}_i \oint_{V^P} \rho x_j b_k \mathrm{d}V^P = e_{ijk} \boldsymbol{e}_i X_j^P G_k^P \tag{4.137}$$

The third volume integral term requires some further attention. Substituting Equations 4.126 and 4.129 yields an extensive equation that will be abbreviated to:

$$e_{ijk} \boldsymbol{e}_i \oint_{V^P} \rho x_j \dot{v}_k^P \mathrm{d}V^P = e_{ijk} \boldsymbol{e}_i \left(X_j^P A_k^P + R_{jk}^P \right) \tag{4.138}$$

For the sake of conciseness, the non-symmetric tensor R^P_{jk} was introduced, which includes the symmetric momentum of inertia J^P_{jk} in its definition:

$$R^P_{jk} = w^P_m w^P_k J^P_{jm} - w^P_m w^P_m J^P_{jk} + e_{kmn} \dot{w}^P_m J^P_{jn} \tag{4.139}$$

$$J^P_{jk} = \oint_{V^P} \rho r_j r_k \mathrm{d}V^P \tag{4.140}$$

Substituting the three elaborated terms 4.136, 4.137 and 4.138 into the angular momentum expression 4.135 leads to:

$$e_{ijk}\boldsymbol{e}_i \left(\sum_{c\in P} r^{Pc}_j f^{Pc}_k + X^P_j \sum_{c\in P} f^{Pc}_k + X^P_j G^P_k - X^P_j A^P_k - R^P_{jk} \right) = \mathbf{0} \tag{4.141}$$

The second, third and fourth terms in the resulting Equation 4.141 define the linear momentum equation 4.134. The required conservation of linear momentum thus reduces the conservation of angular momentum of a particle to:

$$e_{ijk}\boldsymbol{e}_i \left(\sum_{c\in P} r^{Pc}_j f^{Pc}_k - R^P_{jk} \right) = \mathbf{0} \tag{4.142}$$

4.4.3. Definition of the intergranular stress

In continuum mechanics, the intergranular stress is conventionally defined for a representative elementary volume V with boundary S [50] by volume averaging:

$$\bar{\sigma_{ij}}^* = \frac{1}{V} \oint_V \sigma^*_{kj} x_{i,k} \mathrm{d}V \tag{4.143}$$

Herein, $\bar{\sigma_{ij}}^*$ has been introduced to distinguish the stresses at the macroscale and microscale. Equation 4.143 is further elaborated by subsequently applying partial differentiation, introducing the traction 3.16 and substituting the general momentum equation 3.17. The resulting equation is reformulated in terms of particle summation rather than volume integration:

$$\begin{aligned} \bar{\sigma}^*_{ij} &= \frac{1}{V} \oint_V \sigma^*_{kj} x_{i,k} \mathrm{d}V \\ &= \frac{1}{V} \oint_S x_i t^*_j \, \mathrm{d}S + \frac{1}{V} \oint_V \rho^s x_i \left(b_j - \dot{v}_j \right) dV \\ &= \frac{1}{V} \sum_{\beta\in S} x^\beta_i F^\beta_j + \frac{1}{V} \sum_{P\in V} \oint_{V^P} \rho x_i \left(b_j - \dot{v}_j \right) \mathrm{d}V^P \end{aligned} \tag{4.144}$$

Note that the volume averaged volumetric mass ρ^s has been introduced in the second line to account for the porosity. Furthermore, the traction at the boundary has been discretised by the concentrated forces F^β_j. The right-hand terms in the last line of Equation 4.144 were previously replaced by the body force G^P_j, the acceleration force A^P_j and the tensor R^P_{jk} by Equations 4.130, 4.131 and 4.138. Substitution into Equation 4.144 results in:

$$\bar{\sigma}^*_{ij} = \frac{1}{V} \sum_{\beta\in S} x^\beta_i F^\beta_j + \frac{1}{V} \sum_{P\in V} \left(X^P_i G^P_j - X^P_i A^P_j - R^P_{ij} \right) \tag{4.145}$$

Substitution of the linear momentum equation 4.134 introduces the internal contact forces f_j^{Pc}. In addition, the resulting term is decomposed using the relative location vector at the action points (Equation 4.127):

$$\bar{\sigma}_{ij}^{*} = \frac{1}{V}\sum_{\beta\in S} x_i^{\beta} F_j^{\beta} - \frac{1}{V}\sum_{P\in V}\sum_{c\in P} x_i^{Pc} f_j^{Pc} + \frac{1}{V}\sum_{P\in V}\sum_{c\in P} r_i^{Pc} f_j^{Pc} - \frac{1}{V}\sum_{P\in V} R_{ij}^{P} \tag{4.146}$$

Equation 4.124 cancels out the first two terms on the right-hand side of Equation 4.146, thereby reducing the definition of the intergranular stress to its final formulation:

$$\bar{\sigma}_{ij}^{*} = \frac{1}{V}\sum_{P\in V}\left(\sum_{c\in P} r_i^{Pc} f_j^{Pc} - R_{ij}^{P}\right) \tag{4.147}$$

4.4.4. Characteristics of the intergranular stress tensor

The resulting definition of the intergranular stress 4.147 includes a term related to the interparticle forces and a term related to particle rotation. These will be examined in more detail. But first the stress tensor itself is considered. To this end, notice the similarities between the definition of the intergranular stress tensor 4.147 and the conservation of angular momentum of particle P 4.142. Elaboration of the conservation of angular momentum results in:

$$\begin{aligned}
&\boldsymbol{e}_1\left(\sum_{c\in P} r_2^{Pc} f_3^{Pc} - R_{23}^{P} - \sum_{c\in P} r_3^{Pc} f_2^{Pc} - R_{32}^{P}\right) + \\
&\boldsymbol{e}_2\left(\sum_{c\in P} r_3^{Pc} f_1^{Pc} - R_{31}^{P} - \sum_{c\in P} r_1^{Pc} f_3^{Pc} - R_{13}^{P}\right) + \\
&\boldsymbol{e}_3\left(\sum_{c\in P} r_1^{Pc} f_2^{Pc} - R_{12}^{P} - \sum_{c\in P} r_2^{Pc} f_1^{Pc} - R_{21}^{P}\right) = \boldsymbol{0}
\end{aligned} \tag{4.148}$$

Equation 4.148 is satisfied only if each of the terms in between brackets equals zero. This implies that the off-diagonal terms of the intergranular stress tensor are symmetric, that is for $i \neq j$:

$$\bar{\sigma}_{ij}^{*} = \frac{1}{V}\sum_{P\in V}\left(\sum_{c\in P} r_i^{Pc} f_j^{Pc} - R_{ij}^{P}\right) = \frac{1}{V}\sum_{P\in V}\left(\sum_{c\in P} r_j^{Pc} f_i^{Pc} - R_{ji}^{P}\right) = \bar{\sigma}_{ji}^{*} \tag{4.149}$$

Equation 4.149 shows that the intergranular stress tensor is symmetric, even when accounting for particle rotations.

In order to clarify the role of interparticle sliding and particle rotation, the separate terms in Equation 4.147 are considered in more detail. In addition to the intergranular stress σ_{ij}^{*}, two stress measures are defined. First, consider the stress that follows from the interparticle forces denoted by σ_{ij}^{rf}:

$$\sigma_{ij}^{rf} = \frac{1}{V}\sum_{P\in V}\sum_{c\in P} r_i^{Pc} f_j^{Pc} \tag{4.150}$$

The stress that takes account of the effect of the rotation and inertia of the particles is denoted by σ_{ij}^{rot}:

$$\sigma_{ij}^{rot} = \frac{1}{V} \sum_{P \in V} R_{ij}^{P} \tag{4.151}$$

Based on the definition of the intergranular stress 4.149, the following relation is thus defined between the stresses (in tensor notation):

$$\boldsymbol{\sigma}^{rf} = \bar{\boldsymbol{\sigma}}^{*} + \boldsymbol{\sigma}^{rot} \tag{4.152}$$

Whereas the intergranular stress was shown to be symmetric, the rotation of particles introduces non-symmetry in both other stress measures. As the stress $\boldsymbol{\sigma}^{rf}$ accounts for all interparticle forces, the term *intergranular* stress for $\bar{\boldsymbol{\sigma}}^{*}$ is unsound when both interparticle sliding and particle rotation are of importance. The Author suggests to indicate the stress tensor $\boldsymbol{\sigma}^{rf}$ by the "total non-symmetric intergranular stress". The stress tensor $\boldsymbol{\sigma}^{rot}$ may be referred to as the "non-symmetric rotational part of the total intergranular stress". Finally, it is suggested to denote $\bar{\boldsymbol{\sigma}}^{*}$ by the "symmetric translational part of the total intergranular stress".

The Discrete Element Method (DEM) allows for the quantification of both $\boldsymbol{\sigma}^{rf}$ and $\boldsymbol{\sigma}^{rot}$. Subsequently, the translational part of the intergranular stress $\bar{\boldsymbol{\sigma}}^{*}$ can be calculated using Equation 4.152. The experimental quantification of the stresses is complex. The (divergence of) the translational part of the intergranular stress can be derived based on accurate observation of particle motions at the continuum scale, while the determination of $\boldsymbol{\sigma}^{rot}$ would require the observation of the rotation of all particles. However, for the determination of $\boldsymbol{\sigma}^{rf}$ the interparticle forces would be needed, which may only become possible in the future, for instance using three dimensional photo-elasticity and or inverse modelling at the particle scale.

4.4.5. Example of micro-scale based stresses

The consequences of the derived framework that starts from the conservation of linear and angular momentum and results in the definition of the intergranular stresses will be illustrated by an example. Figure 4.12 depicts a stationary downward flow of a thin layer of granular material with a thickness h and surface velocity $\boldsymbol{v}$ down a slope with angle α. The depicted triad has its unit base vector $\boldsymbol{e}_1$ directed downward along the slope and its unit base vector $\boldsymbol{e}_3$ directed upward normal to the slope surface. The unit base vector $\boldsymbol{e}_2$ is directed horizontally along the slope into the figure. The stress measures during simple shear deformation in plane flow with normal unit base vector $\boldsymbol{e}_2$ will now be considered.

The velocity gradient component L_{13} indicates the average rate of simple-shearing $\dot{\gamma}$ by:

$$L_{13} = \frac{v_1}{h} = \dot{\gamma} \tag{4.153}$$

For the sake of simplicity, the granular material is assumed to be composed of monosized cylindrical particles with diameter d^P and unit length in the direction of the unit

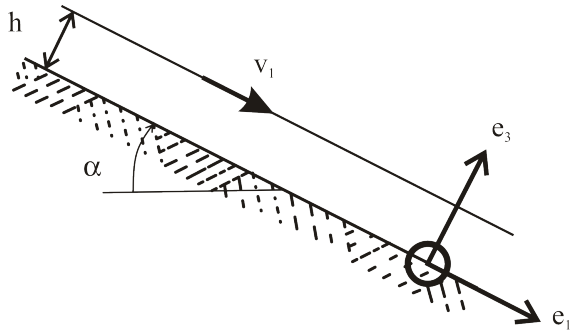


Figure 4.12: Illustration of a slope supporting a stationary downward flow of a thin layer of granular material with a thickness h and surface velocity vector $\boldsymbol{v}$. The Cartesian right-handed reference triad of unit base vectors $\boldsymbol{e}_i$ $(1,2,3)$ is also depicted.

base vector $\boldsymbol{e}_2$. The axial spin vector $\boldsymbol{w}^P$ describes the rotation rate of the particles P along unit base vector $\boldsymbol{e}_2$ by:

$$\boldsymbol{w}^P = \zeta^P \boldsymbol{e}_2 \tag{4.154}$$

where the scalar quantity ζ^P indicates the magnitude of the spin of particle P. If the particles would be rolling on top of each other (no slip) the rotation rate ζ^P would be equal to the rate of simple-shearing, i.e. $\zeta^P = \dot{\gamma}$. This assumption may be realistic for the flow of very loose packings, but for denser packings less rolling and more interparticle sliding is more realistic. To account for this variation, the scalar parameter b is introduced in the following expression:

$$\zeta^P = b\dot{\gamma} \tag{4.155}$$

The range $0 \leq b \geq 1$ is considered to distinguish between loose and dense sand.

The in-plane components $(i, j = 1,3)$ of the stress tensors $\boldsymbol{\sigma}^{rot}$ and $\bar{\boldsymbol{\sigma}}^*$ will now be derived for the simple-shearing flow. The rotational part of the total intergranular stress $\boldsymbol{\sigma}^{rot}$ is derived from Equation 4.151. For a particle P the momentum of inertia J_{ij}^P reads:

$$J_{ij}^P = \oint_{V^P} \rho r_i r_j \mathrm{d}V^P = \rho \int_{\alpha=0}^{\alpha=2\pi} \int_{r=0}^{r=d^P/2} r_i r_j r \,\mathrm{d}\alpha \mathrm{d}r \tag{4.156}$$

Elaboration for $r_1 = r\cos\alpha$ and $r_2 = r\sin\alpha$ gives for $i, j = 1,3$:

$$J_{11}^P = J_{33}^P = \frac{\rho\pi}{64}\left(d^P\right)^4 \tag{4.157}$$

$$J_{13}^P = J_{31}^P = 0 \tag{4.158}$$

Substituting the expressions 4.157 and 4.158 for J_{ij}^P and 4.154 for w_i^P into Equation 4.139 yields for the components of R_{ij}^P:

$$R_{11}^P = -\left(-\zeta^P\right)^2 J_{11}^P + \dot{\zeta}^P J_{13}^P \tag{4.159}$$

$$R_{13}^P = -\left(-\zeta^P\right)^2 J_{13}^P + \dot{\zeta}^P J_{11}^P \tag{4.160}$$

$$R_{31}^P = -\left(-\zeta^P\right)^2 J_{31}^P + \dot{\zeta}^P J_{33}^P \tag{4.161}$$

$$R_{33}^P = -\left(-\zeta^P\right)^2 J_{33}^P + \dot{\zeta}^P J_{31}^P \tag{4.162}$$

The resulting four expressions are substituted into Equation 4.151 to define the stress σ_{ij}^{rot}. Taking into account the definition of the components of inertia in 4.157 and 4.158, the magnitude of the spin by 4.154 and the amount of rolling by 4.155, the result reads:

$$\begin{bmatrix} \sigma_{11}^{rot} & \sigma_{13}^{rot} \\ \sigma_{31}^{rot} & \sigma_{33}^{rot} \end{bmatrix} = \frac{1}{V}\frac{\rho\pi}{64}\sum_{P\in V}\left(d^P\right)^4 \begin{bmatrix} -\left(b\dot{\gamma}\right)^2 & -b\ddot{\gamma} \\ b\ddot{\gamma} & -\left(b\dot{\gamma}\right)^2 \end{bmatrix} \tag{4.163}$$

Herein, it has been assumed that the scalar b is a constant. The in-plane components of σ_{ij}^{rot} depend on the particle diameter to the power 4. Furthermore, the normal stress components depend in a quadratic way on the particle spin ζ, while the shear components depend on the material rate of the spin $\dot{\zeta}$. Equation 4.163 demonstrates that the stress σ_{ij}^{rot} is skew-symmetric.

The derivation of the intergranular stress $\bar{\sigma}_{ij}^*$ for the direction of the unit base vectors $\boldsymbol{e}_1$ and $\boldsymbol{e}_3$ is straightforward. To this end, the field equation of the conservation of linear momentum of classical continuum mechanics, i.e. Equation 3.17, is employed. The body force components depend on the gravitational acceleration g and slope α, giving $b_1 = -g\sin\alpha$ and $b_3 = -g\cos\alpha$. Assuming stationary flow, all time dependent terms and all spatial gradients in the direction of unit base vector $\boldsymbol{e}_1$ are zero. Hence, the field equation of the conservation of linear momentum reduces to a set of one-dimensional field expressions normal to the slope:

$$\frac{\partial\bar{\sigma}_{31}^*}{\partial x_3} - \rho g\sin\alpha = 0 \tag{4.164}$$

$$\frac{\partial\bar{\sigma}_{33}^*}{\partial x_3} - \rho g\cos\alpha = 0 \tag{4.165}$$

4.4.6. Conclusions

It is concluded that the intergranular stress tensor as known in soil mechanics is symmetric, irrespective of whether particle rotations are of importance or not. However, this common, translational, intergranular stress is not sufficient to describe the stresses in an assembly of particles that include both interparticle sliding and particle rotations. In this case the non-symmetric, total intergranular stress tensor, composed of the translational and rotational parts of the intergranular stress, describes the interparticle stresses in the assembly. It is anticipated that the non-symmetric total intergranular stress should be

used for the post-liquefaction phase. The treated example elaborates on the translational and rotational intergranular stress for simple-shear flow. The non-symmetry of the total intergranular stress implies that the conservation of angular momentum should not be ignored as a field equation for mechanisms governed by particle rotations.

References

[1] F. Molenkamp, R. de Jager, and F. Mathijssen, *Stress measures affecting deformation of granular materials,* Vadose Zone Journal **13** (2014).

[2] R. de Jager, F. Mathijssen, and F. Molenkamp, *Hydrostatics and relative motion of pore fluids,* in *Proceedings of the 3rd International Symposium on Computational Geomechanics* (Krakow, Poland, 2013) pp. 359–370.

[3] R. de Jager and F. Molenkamp, *Stress measures for interparticle sliding and particle rolling,* in *Proceedings of the 8th European Conference on Numerical Methods in Geotechnical Engineering*, Vol. I, edited by M. Hicks, R. Brinkgreve, and A. Rohe (CRC Press, Delft, the Netherlands, 2014) pp. 61–66.

[4] O. Coussy, *Poromechanics* (John Wiley & Sons, Chichester, 2004).

[5] B. Coleman and W. Noll, *The thermodynamics of elastic materials with heat conduction and viscosity,* Archive for Rational Mechanics and Analysis **13**, 167 (1963).

[6] G. Buscarnera, *Rainfall induced flow slides: Constitutive modelling, mechanical instability and theoretical interpretation*, Ph.D. thesis, Politecnico di Milano, Milan, Italy (2010).

[7] W. Gray and B. Schrefler, *Analysis of the solid phase stress tensor in multiphase porous media,* International Journal for Numerical and Analytical Methods in Geomechanics **31**, 541 (2007).

[8] G. Desbois, J. Urai, P. Kukla, J. Konstanty, and C. Baerle, *High-resolution 3d fabric and porosity model in a tight gas sandstone reservoir: a new approach to investigate microstructures from mm-to nm-scale combining argon beam cross-sectioning and sem imaging,* Journal of Petroleum Science and Engineering **78**, 243 (2011).

[9] A. Bishop, *The principles of effective stress,* Tek. Ukebl. **106**, 859 (1959).

[10] A. Bishop and G. Blight, *Some aspects of effective stress in saturated and partly saturated soils,* Géotechnique **13**, 177 (1963).

[11] J. Jennings and J. Burland, *Limitations to the use of effective stresses in partly saturated soils,* Géotechnique **12**, 125 (1962).

[12] J. Burland, *Some aspects of the mechanical behaviour of partly saturated soils,* in *Moisture equilibria and moisture changes in soil beneath covered areas*, edited by G. Aitchison (Butterworths, Sydney, 1965) pp. 270–278.

[13] R. Brooks and A. Corey, *Hydraulic properties of porous media and their relation to drainage design,* Trans. ASAE **7**, 26 (1964).

[14] N. Khalili and M. Khabbaz, *A unique relationship of chi for the determination of the shear strength of unsaturated soils,* Géotechnique **48**, 681 (1998).

[15] N. Khalili, F. Geiser, and G. Blight, *Effective stress in unsaturated soils: review with new evidence,* International Journal of Geomechanics **4**, 115 (2004).

[16] E. Alonso, J.-M. Pereira, J. Vaunat, and S. Olivella, *A microstructurally based effective stress for unsaturated soils,* Géotechnique **60**, 913 (2010).

[17] P. Cundall and O. Strack, *A discrete numerical model for granular assemblies,* Géotechnique **29**, 47 (1979).

[18] C. Thornton, *Numerical simulations of deviatoric shear deformation of granular media,* Géotechnique **50**, 43 (2000).

[19] L. Rothenburg and N. Kruyt, *Critical state and evolution of coordination number in simulated granular materials,* International Journal of Solids and Structures **41**, 5763 (2004).

[20] J. Sun, S. Sundaresan, J. Goddard, P. Giovine, and J. Jenkins, *A plasticity model with microstructure evolution for quasi-static granular flows,* in *AIP Conference Proceedings*, Vol. 1227 (AIP, 2010) pp. 280–289.

[21] M. Satake, *Constitution of mechanics of granular materials through the graph theory,* in *Proceedings of the U.S.–Japan seminar on Continuum Mechanical and Statistical Approaches in the Mechanics of Granular Materials* (Gakujutsu Bunken Fukyu-Kai, Tokyo, Sendai, Japan, 1978) pp. 47–62.

[22] M. Satake, *Fabric tensor in granular materials,* in *IUTAM Symposium on Deformation and Failure of Granular materials, Delft, the Netherlands*, edited by P. Vermeer and H. Luger (Balkema, Rotterdam, 1982) pp. 63–68.

[23] M. Satake, *Tensorial form definitions of discrete-mechanical quantities for granular assemblies,* International Journal of Solids and Structures **41**, 5775 (2004).

[24] K. Kanatani, *Distribution of directional data and fabric tensors,* International Journal of Engineering Science **22**, 149 (1984).

[25] M. Oda, S. Nemat-Nasser, and J. Konishi, *Stress-induced anisotropy in granular masses,* Soils and foundations **25**, 85 (1985).

[26] G. Subhash, S. Nemat-Nasser, M. Mehrabadi, and H. Shodj, *Experimental investigation of fabric-stress relations in granular materials,* Mechanics of Materials **11**, 87 (1991).

[27] X. Li, H. Yu, and X. Li, *Macro–micro relations in granular mechanics,* International Journal of Solids and Structures **46**, 4331 (2009).

[28] J. Goddard, *An elastohydrodynamic theory for the rheology of concentrated suspensions of deformable particles,* Journal of Non-Newtonian Fluid Mechanics **2**, 169 (1977).

[29] L. Rothenburg and A. Selvadurai, *A micromechanical definition of the cauchy stress tensor for particulate media,* Mechanics of structured media , 469 (1981).

[30] J. Christoffersen, M. Mehrabadi, and S. Nemat-Nasser, *A micromechanical description of granular material behavior,* Journal of applied mechanics **48**, 339 (1981).

[31] S. Nemat-Nasser, *Fabric and its influence on mechanical behaviour of granular materials,* in *IUTAM Symposium on Deformation and Failure of Granular materials, Delft, the Netherlands*, edited by P. Vermeer and H. Luger (Balkema, Rotterdam, 1982) pp. 37–42.

[32] C. Thornton and D. Barnes, *On the mechanics of granular materials,* in *IUTAM Symposium on Deformation and Failure of Granular materials, Delft, the Netherlands*, edited by P. Vermeer and H. Luger (Balkema, Rotterdam, 1982) pp. 69–77.

[33] N. Kruyt and L. Rothenburg, *Microinechanical definition of the strain tensor for granular materials,* Journal of Applied Mechanics **118**, 706 (1996).

[34] J. Bear, *Dynamics of fluids in porous media* (Elsevier, New York, 1972).

[35] F. Molenkamp and A. Nazemi, *Interactions between two rough spheres, water bridge and water vapour,* Géotechnique **53**, 255 (2003).

[36] F. Molenkamp and A. Nazemi, *Micromechanical considerations of unsaturated pyramidal packing,* Géotechnique **53**, 195 (2003).

[37] J. Nitao and J. Bear, *Potentials and their role in transport in porous media,* Water Resources Research **32**, 225 (1996).

[38] G. Buscarnera and R. Nova, *Modelling instabilities in triaxial testing on unsaturated soil specimens,* International Journal for Numerical and Analytical Methods in Geomechanics **35**, 179 (2011).

[39] B. Chareyre, L. Scholtès, F. Darve, M. Nakagawa, and S. Luding, *Micro-statics and micro-kinematics of capillary phenomena in dense granular materials,* in *AIP Conference Proceedings*, Vol. 1145 (AIP, 2009) pp. 927–930.

[40] B. Kim, S. Park, and S. Kato, *Dem simulation of collapse behaviours of unsaturated granular materials under general stress states,* Computers and Geotechnics **42**, 52 (2012).

[41] S. Lourenço, D. Gallipoli, C. Augarde, D. Toll, P. Fisher, and A. Congreve, *Formation and evolution of water menisci in unsaturated granular media,* Géotechnique **62**, 193 (2012).

[42] G. Evensen, *The ensemble kalman filter: Theoretical formulation and practical implementation,* Ocean dynamics **53**, 343 (2003).

[43] G. Evensen, *Data assimilation: the ensemble Kalman filter* (Springer Science & Business Media, Dordrecht, the Netherlands, 2009).

[44] E. Alonso, N. Pinyol, and A. Gens, *Compacted soil behaviour: initial state, structure and constitutive modelling,* Géotechnique **63**, 463 (2013).

[45] A. Landva and P. Pheeney, *Peat fabric and structure,* Canadian Geotechnical Journal **17**, 416 (1980).

[46] I.-S. Liu, *Continuum mechanics*, 1st ed. (Springer Science & Business Media, 2013).

[47] L. Rothenburg and R. Bathurst, *Analytical study of induced anisotropy in idealized granular materials,* Géotechnique **39**, 601 (1989).

[48] L. Landau and E. Lifshitz, *Statistical Physics: Course of Theoretical Physics 5* (Pergamon Press, Oxford, 1958).

[49] J. Weber, *Recherches concernant les contraintes intergranulaires dans les milieux pulvérulents,* Bulletin de Liaison des Ponts-et-chaussées **20**, 1 (1966).

[50] G. De Saxcé, J. Fortin, and O. Millet, *About the numerical simulation of the dynamics of granular media and the definition of the mean stress tensor,* Mechanics of Materials **36**, 1175 (2004).

5

Finite element modelling

This chapter presents the implementation of the governing equations from Chapter 3 in the finite element model. The Finite Element Method enables the solution of complex boundary value problems by numerical approximations. Selecting appropriate methods of discretisation and implementation yields an error that is acceptable for the considered problem. The error is quantified by verification of known analytical solutions of simple boundary value problems using the model. The resulting finite element model provides a framework in which different constitutive models can be plugged in.

In this chapter, the starting points will first be specified, including the requirements of the model, a literature review and general methodology for composing the model. This methodology will subsequently be applied in order to compose the stiffness matrix. The actual implementation will be discussed in the section thereafter. Then, the performance of the resulting model will be verified. Constitutive modelling will be the subject of the final section of this chapter.

5.1. Starting points and assumptions

5.1.1. Model requirements

The modelling of liquefaction flow slides requires the implementation of the set of governing equations listed at the start of Subsection 3.3.1, which implies that any possible energy related effects are ignored. The initial-boundary value problem of a liquefaction flow slide cannot be solved analytically. The complexity of the geometry and soil behaviour do not allow for this. Instead, approximate methods have to be employed. The finite element Model [1, 2] suits the modelling of history-dependent materials and is therefore most commonly employed in soil mechanics.

The intended model translates a continuous problem into a discrete domain. The conservation of mass and linear momentum of the pore fluid and soil skeleton should be satisfied in the spatial domain. The boundary conditions should be consistent with these

equations and should provide a well-posed problem. Hence, the governing equations, which should be satisfied internally and at the boundaries, form the core of the model. Herein, the constitutive models should be plugged in and may, as a consequence, be considered separately.

Being an approximation, it is essential to know the applicability and accuracy of the numerical model. One conventionally uses analytical solutions of benchmark problems to investigate the convergence towards known solutions. Section 3.3 discussed a few of these cases, being simplifications of the set of governing equations. The consolidation problem (Subsection 3.3.6) will be used to verify the performance of the model in Section 5.4. Furthermore, the numerical stability of the approximation poses restrictions on the step sizes of the discretisation. As for the benchmark problems, the numerical stability applies to simplifications of the full set of equations, e.g. one-dimensional consolidation or wave propagation. Hence, these stability conditions may affect different parts of the (two- or three-dimensional) geometry at different stages of the development of a liquefaction flow slide. It should be noted that wave propagation problems set requirements on the resolution of reproduction of the signal in both time and space, as well as on the possibility of numerical damping. As a consequence of the conservation of energy not being accounted for by the set of governing equations, the discretisation does not necessarily satisfy that fundamental condition.

This chapter discusses the development of a finite element model based on the theoretical framework discussed in Chapters 3 and 4. It was intended to develop a model with a wide range of application. The model should be able to capture the different stages of liquefaction flow slides, namely:

1. Initial quasi-static deformation and consolidation due to changes of boundary conditions up to reaching the sudden occurrence of the approximately undrained instability of flow liquefaction.

2. Sudden, accelerating deformation with approximately undrained pore water pressure generation during a short period of time until reaching the liquefaction flow mode.

3. Relatively fast and large deformation of liquefaction flow with large excess pore water pressure, causing the liquefied sand to almost reach a suspension state.

4. Large, continuous liquefaction flow with consolidation of excess pore water pressure due to re-sedimentation until all liquefied sand has settled downstream of the liquefied slope.

One model that captures all four stages of liquefaction flow slides continuously, while yielding consistent and accurate results seems to be unfeasible at this moment. While providing a generic model, this thesis will concentrate on the above-mentioned first, second and, partly, third stages of liquefaction flow slides. It is anticipated that the tests with the liquefaction tank will provide the data that are required for the evaluation of the model for those stages.

5.1.2. Literature review

This section complements the literature review in Section 3.1.3 on the governing equations. It will consider the discretisation and implementation of the governing equations, the formulation of constitutive models and the application of finite element models on initial-boundary value problems reported in literature. The literature review will concentrate on a number of selected papers in the vast amount of literature on the subject. The main contributions are highlighted, while some of the gaps left by literature are indicated.

In literature, the governing set of equations is usually reduced by introducing assumptions and simplifications. For quasi-static consolidation problems, the omission of inertial terms allows for a direct relation between the pore fluid stress p and relative pore fluid velocity v_i in the conservation of linear momentum of the pore fluid 3.69. Elimination of v_i by substitution into the storage equation 3.67 results in two governing equations, i.e. a so-called $u_i - p$ formulation [3]. This formulation is also applied for low-frequency dynamics problems, such as earthquakes [4]. At the other end of the spectrum, the field of poro-elastodynamics tends to reduce the set of governing equations by assuming simple, elastic constitutive relations [5]. As a consequence, the set of equations may be reduced to a $u_i - p$ or $u_i - v_i$ formulation. The Author's interest lies in capturing the transition from the initial quasi-static phase, towards the relatively fast and large deformation of liquefaction flow (see previous section). Zienkiewicz and coworkers have provided the most important contribution when it comes to modelling the transition from statics to dynamics using the finite element mehthod [4, 6, 7]. Both the governing equations (assuming low frequencies during earthquakes and ignoring the relative pore fluid accelerations), spatial and time discretisation, constitutive modelling and verification of field events and centrifuge tests are treated. However, the collapse of a slope following flow liquefaction was not reported. Other publications that did consider liquefaction flow slides assumed quasi-static conditions (e.g. [8]), undrained conditions (e.g. [9]), or both. More recent efforts concentrate on the formulation of large deformations in the finite element method using, for instance, the material point method (MPM). The results provide useful insights into the development of failure modes [10]. In spite of the promising results so far, MPM analyses using advanced material models for flow liquefaction have not been reported. Furthermore, using formulations for large deformations also requires the incorporation of complex processes, such as for instance the effective stress measure (see Section 4.4), shear banding and the interaction between the soil and water phase.

There are numerous constitutive models that suit the modelling of flow liquefaction, e.g. [11–13], although only the class of elasto-plastic models is discussed here. Provided that the model allows for a non-associated flow rule, flow liquefaction can be modeled by imposing the constraint of a constant volume during shear deformation. Hence, a relatively simple extension of Mohr-Coulomb is sufficient to replicate flow liquefaction (3.4.1, [14]). More advanced models incorporate non-linearity in the formulation of elasticity, the flow rule, plastic potential and (double) hardening rule [12]. The models can furthermore be extended by including for instance the critical state [11], anisotropy and

principal stress rotation [13]. However, with increasing capabilities the complexity of the model and the number of parameters that need to be specified also increases. Olson [15] argues that advanced constitutive models are too complex for common use in engineering practice. Advanced constitutive models are usually exclusively applied by a very limited group of people who know and understand the model. The rise of hypoplastic models, that is, leaving the framework of elasto-plasticity and starting with a general stress-strain (rate) relation, has been attributed to the need for simpler models [16]. On the other hand, advanced features such as stress path-dependence have been shown to be essential for the assessment of liquefaction flow slides (see Subsection 2.2.2). The challenge in material modelling of flow liquefaction thus lies in finding a way to make advanced features accessible to engineering practice.

Material models have proven to be particularly useful for understanding the occurrence of instability during flow liquefaction as a particular, undrained feature of the behaviour of cohesionless, loose soils. Special reference is made to the alternative concept of flow liquefaction as a loss of controllability [17]. The analysis of instability as a loss of controllability allows for an extension of the control that is generally imposed during element tests. This generalisation is useful for the analysis of liquefaction flow slides, where the controlled quantities are not strictly imposed. For instance, Buscarnera and Whittle [18] apply the loss of controllability on the MIT-S1 model to analyze the stability of an infinite slope.

The MONOT model [12] has been the basis of much of the work on liquefaction flow slides carried out in Delft and Manchester [8, 19]. It has a firm theoretical basis with a non-linear elastic component, a yield surface with the form suggested by Lade and Duncan [20], a plastic potential based on Rowe's stress-dilatancy rule [21] and a double hardening rule. The large amount of input parameters can be strongly reduced using the experience gained during calibration. Hicks [22] shows that for practical purposes a maximum of only five parameters is needed, while for the remaining parameters standard default values are suggested. Using the model for an accurate description of the larger deformations following instability would, at least, require the extension with a critical state formulation. The last section of this chapter, 5.5, will propose such a formulation.

5.1.3. General methodology

The Author's model is based on the code *p94_mnr.f95*, that was developed by Molenkamp [23] based on the open source code *p94.f95* provided by Smith and Griffiths [2]. This original code *p94.f95* was written to model a plane strain, coupled consolidation analysis. Molenkamp introduced the Modified Newton-Raphson iteration scheme to the original code to improve its performance for a non-linear response. The Author has extended this model for the set of equations, free variables and boundary conditions corresponding to the governing equations for flow liquefaction, while also introducing an additional type of element.

Preliminaries of finite element method

The finite element method discretises the domain into elements, which are characterised by shape, nodes at the edges and integration points in the interior. The relations between the nodes and integration points are uniquely defined, thus being the key characteristic of the finite element method. The extensive quantities such as the representative stresses in the volume of an element are defined at the integration points, while the displacements are defined at the nodes. The location of the integration points is newly defined based on the displacements of the nodes of the element during each time step. History-dependent materials such as soils require a Lagrangian approach, where the information is stored at points moving with the material that can be traced during deformation of the mesh. Due to geometrical relations between integration points and nodes, both can be handled as points moving with the material. In the finite element method the governing equations are satisfied at the integration points. Shape function $\boldsymbol{N}$ relates the nodal variables $\hat{\boldsymbol{r}}$ to the corresponding quantities $\boldsymbol{r}$ within the element:

$$\boldsymbol{r} = \boldsymbol{N}\hat{\boldsymbol{r}} \tag{5.1}$$

The initial-boundary value problem that is considered entails an incremental change, starting at the current state and changing to a new state, e.g. by a load or changing geometry. Hence, in addition to the current state, a new state will be considered that is solved using two computation loops. Within a time step Δt starting at the current time t, equilibrium is sought at the new state at time $t + \Delta t$ using iterations. The iteration steps are denoted by n. As in Chapter 3, the initial reference state is characterised by a volume V and surface S. The current state is indicated by the initial state with known volume v^0 and surface s^0, and the new state with volume v and surface s (see Figure 5.1).

Formulation of residuals

The development of the model starts from the governing equations that were listed at the start of Section 3.3.1. For the sake of simplicity this set of equations is reformulated, still in terms of general (non-discretised) variables, in matrix format:

$$\boldsymbol{k}\boldsymbol{r} - \boldsymbol{p} = \boldsymbol{0} \tag{5.2}$$

Herein, $\boldsymbol{k}$ denotes the global stiffness matrix, $\boldsymbol{r}$ the freedom variable vector and $\boldsymbol{p}$ the 'load' vector. The elements that are located at the edges of the geometry are affected by the boundary conditions as well, that is, the imposed freedom variables $\overline{\boldsymbol{r}}$ or loads $\overline{\boldsymbol{p}}$. Including Equation 5.2, three equations should thus be satisfied. Equation 5.2 should be satisfied within a particular volume v, while the boundary conditions should be satisfied at the boundary surface s of this volume:

$$g(\boldsymbol{r}, \boldsymbol{p}) = 0 \qquad \text{within domain } v \tag{5.3}$$

$$\boldsymbol{p} - \overline{\boldsymbol{p}} = 0 \qquad \text{at domain } s^f \tag{5.4}$$

$$\boldsymbol{r} - \overline{\boldsymbol{r}} = 0 \qquad \text{at domain } s^r \tag{5.5}$$

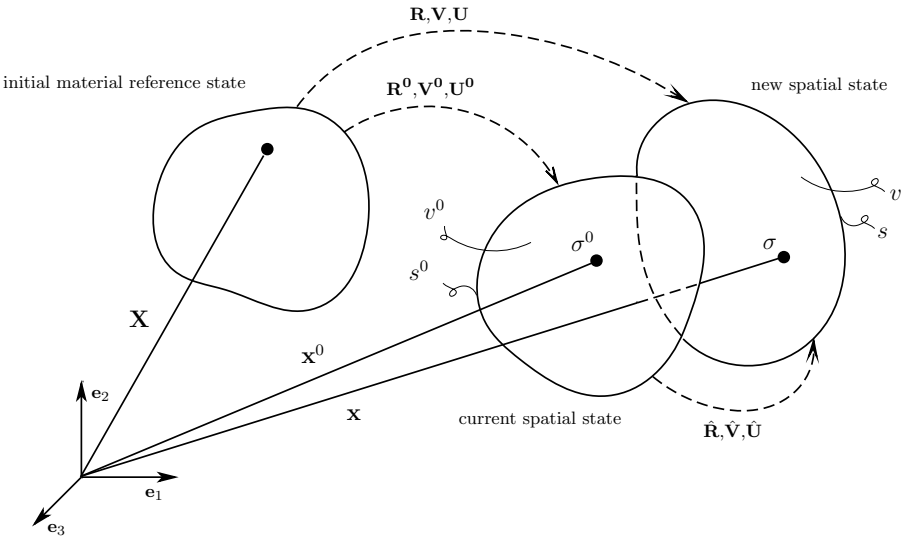


Figure 5.1: Definitions of a body in the initial, current and new spatial state. The deformation of the body is expressed in terms of right and left stretch tensors $\boldsymbol{U}$ and $\boldsymbol{V}$, respectively, material rotation tensor $\boldsymbol{R}$ and the deformation gradient tensor $\boldsymbol{F}$. In addition, the stress at the current state, $\boldsymbol{\sigma}^0$, and new state, $\boldsymbol{\sigma}$ have been displayed.

The domains s^f and s^r, defined for the boundary conditions 5.4 and 5.5, respectively, compose the entire boundary s:

$$s^f + s^r = s \tag{5.6}$$

The method of "Galerkin weighted residuals" is subsequently applied on the set of equations defined by 5.3-5.5 [1]. If each of these is to be satisfied, there must be an arbitrary set of *weighting factors* defined by $\mathbf{w}_c$ and $\mathbf{w}_b$ for the conservation equations and boundary conditions, respectively, for which holds:

$$\int_v \boldsymbol{w}_c^{\mathrm{T}} \boldsymbol{g}(\boldsymbol{r}, \boldsymbol{p})\, \mathrm{d}v = 0 \tag{5.7}$$

$$\int_{s^f} \boldsymbol{w}_{b;f}^{\mathrm{T}} (\boldsymbol{p} - \overline{\boldsymbol{p}})\, \mathrm{d}s = 0 \tag{5.8}$$

$$\int_{s^r} \boldsymbol{w}_{b;r}^{\mathrm{T}} (\boldsymbol{r} - \overline{\boldsymbol{r}})\, \mathrm{d}s = 0 \tag{5.9}$$

An obvious requirement for these factors is that the number of components should equal those of the integral terms or *residuals*. If one of the residuals would be non-zero, there would certainly be a factor which makes one of the terms of 5.7-5.9 non-zero, which proves the validity of Equations 5.7-5.9. This reasoning can be further extended by stating that, if each of the Equations 5.7-5.9 is zero, their sum must be zero as well for an

arbitrary set of weighting factors:

$$\int_v \boldsymbol{w}_c^{\mathrm{T}} \boldsymbol{g}(\boldsymbol{r},\boldsymbol{p})\,\mathrm{d}V + \int_{s^f} \boldsymbol{w}_{b;f}^{\mathrm{T}}(\boldsymbol{p}-\overline{\boldsymbol{p}})\,\mathrm{d}s + \int_{s^r} \boldsymbol{w}_{b;r}^{\mathrm{T}}(\boldsymbol{r}-\overline{\boldsymbol{r}})\,\mathrm{d}s = 0 \tag{5.10}$$

The application of *Galerkin* weighting implies a weakening of Equation 5.10 by replacing the weighting factors by functions of these weighting factors. Furthermore, these functions are specified by the shape functions $\boldsymbol{N}$. The result reads:

$$\int_v \boldsymbol{N}^{\mathrm{T}} \boldsymbol{g}(\boldsymbol{r},\boldsymbol{p})\,\mathrm{d}v + \int_{s^f} \boldsymbol{N}^{\mathrm{T}}(\boldsymbol{p}-\overline{\boldsymbol{p}})\,\mathrm{d}s + \int_{s^r} \boldsymbol{N}^{\mathrm{T}}(\boldsymbol{r}-\overline{\boldsymbol{r}})\,\mathrm{d}s = 0 \tag{5.11}$$

Modified Newton-Raphson procedure

The definition of the residuals in Equation 5.11 defines the starting point for the finite element model. The sum of the residuals should be reduced to zero to satisfy the underlying physics. Solving Equation 5.11 directly is usually not possible as a result of non-linearities caused by non-linear material behaviour (yielding), changing material properties during straining (porosity, permeability), and/or updated volumes and surfaces during straining. In general, a direct solution of Equation 5.11 may only be found for small strain approximations. In other cases an iterative procedure is required for the approximation. To this end, the Modified Newton-Raphson procedure is employed here. If the summed residuals (Equation 5.11) are denoted by the residual vector $\boldsymbol{f}$, the Modified Newton-Raphson procedure implies a minimisation of this term using:

$$\boldsymbol{k}^0\left(\boldsymbol{r}^0-\boldsymbol{r}^1\right) = \left.\frac{\partial \boldsymbol{f}}{\partial \boldsymbol{r}}\right|^0 \left(\boldsymbol{r}^0-\boldsymbol{r}^1\right) = \boldsymbol{f}^0 \tag{5.12}$$

The procedure aims at minimising the residual vector by updating the free variable $\boldsymbol{r}$ after starting from $\boldsymbol{f}^0$ at $\boldsymbol{r}=\boldsymbol{r}^0$. Based on the quantities which were determined during the previous iteration step $\boldsymbol{k}^0$, $\boldsymbol{r}^0$ and $\boldsymbol{f}^0$, a new value $\boldsymbol{r}^1$ is determined. This value is substituted into the expression(s) for the nodal residual vector, leading to a new value $\boldsymbol{f}^1$. Backsubstitution is repeated until the residual vector has reached a sufficiently low value. This procedure is depicted in Figure 5.2. If the stiffness matrix $\boldsymbol{k}^0$ defined by the differential operator is updated for each iteration step, the procedure is formally denoted by Newton-Raphson. As this is however numerically costly, the Modified Newton-Raphson iteration procedure with a constant stiffness term is usually employed.

Time integration

The formulation of the residuals and the stiffness matrix governs the iteration procedure. The Newton-Raphson procedure will be applied on the free variables and their material time derivatives. A time integration scheme is needed to discretise the time dependence. The Crank-Nicholson scheme will be used for this purpose, which implies that an interpolated value $\boldsymbol{r}_\theta\Big|^{n+1}$ at iteration step n is determined by applying weight factors to its value at the start and end of a time step:

$$\boldsymbol{r}\Big|_\theta^{n+1} = \theta \boldsymbol{r}\Big|_1^{n+1} + (1-\theta)\boldsymbol{r}\Big|_0 \tag{5.13}$$

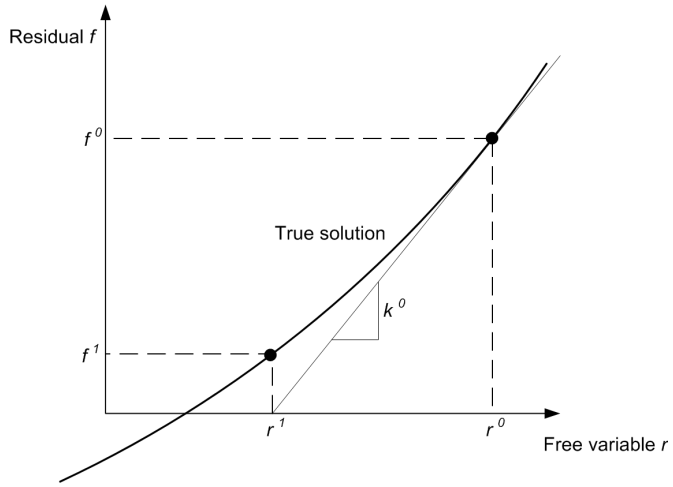


Figure 5.2: Principle of (Modified) Newton-Raphson iteration

This means that all properties are to be considered at time $t_\theta = \theta t_1 + (1-\theta) t_0$, in which θ is the weight factor ($0 < \theta < 1$), time t_0 the time at the beginning and time t_1 the time at the end of time step Δt. The method can also be applied to material time derivatives of $r\big|_\theta^{n+1}$, yielding:

$$\dot{\boldsymbol{r}}\Big|_\theta^{n+1} = \theta \dot{\boldsymbol{r}}\Big|_1^{n+1} + (1-\theta)\dot{\boldsymbol{r}}\Big|_0 = \frac{\boldsymbol{r}\Big|_1^{n+1} - \boldsymbol{r}\Big|_0}{\Delta t} \tag{5.14}$$

$$\ddot{\boldsymbol{r}}\Big|_\theta^{n+1} = \theta \ddot{\boldsymbol{r}}\Big|_1^{n+1} + (1-\theta)\ddot{\boldsymbol{r}}\Big|_0 = \frac{\dot{\boldsymbol{r}}\Big|_1^{n+1} - \dot{\boldsymbol{r}}\Big|_0}{\Delta t} \tag{5.15}$$

The last expression 5.15 requires further attention with respect to the conservation of energy during time integration [24]. The conservation of energy during time integration will be considered after applying time integration on the governing set of equations in 5.2.4. Combining the Modified Newton-Raphson procedure and the Crank-Nicholson time integration scheme implies that the residual should be evaluated at time t_θ:

$$\frac{\partial \boldsymbol{f}}{\partial \boldsymbol{r}}\Big|_0^n \left(\boldsymbol{r}\Big|_\theta^n - \boldsymbol{r}\Big|_\theta^{n+1} \right) = \boldsymbol{f}\Big|_\theta^n \tag{5.16}$$

The left hand-term in Equation 5.16 is reformulated using Equations 5.13-5.15. More specifically, application of the Modified Newton-Raphson procedure will yield terms that depend on $\boldsymbol{r}\Big|_\theta^n - \boldsymbol{r}\Big|_\theta^{n+1}$ and its first and second order material time derivatives. Each of

these is reformulated as follows:

$$\boldsymbol{r}\Big|_{\theta}^{n} - \boldsymbol{r}\Big|_{\theta}^{n+1} = \theta\left(\boldsymbol{r}\Big|_{1}^{n} - \boldsymbol{r}\Big|_{1}^{n+1}\right) \tag{5.17}$$

$$\dot{\boldsymbol{r}}\Big|_{\theta}^{n} - \dot{\boldsymbol{r}}\Big|_{\theta}^{n+1} = \frac{1}{\Delta t}\left(\boldsymbol{r}\Big|_{1}^{n} - \boldsymbol{r}\Big|_{1}^{n+1}\right) \tag{5.18}$$

$$\ddot{\boldsymbol{r}}\Big|_{\theta}^{n} - \ddot{\boldsymbol{r}}\Big|_{\theta}^{n+1} = \frac{1}{\Delta t}\left(\dot{\boldsymbol{r}}\Big|_{1}^{n} - \dot{\boldsymbol{r}}\Big|_{1}^{n+1}\right) = \frac{1}{\theta\Delta t^2}\left(\boldsymbol{r}\Big|_{1}^{n} - \boldsymbol{r}\Big|_{1}^{n+1}\right) \tag{5.19}$$

Anticipating on the composition of the global stiffness matrix, terms related to $\boldsymbol{r}\Big|_{\theta}^{n} - \boldsymbol{r}\Big|_{\theta}^{n+1}$ are represented by A, terms related to $\dot{\boldsymbol{r}}\Big|_{\theta}^{n} - \dot{\boldsymbol{r}}\Big|_{\theta}^{n+1}$ by B and terms related to $\ddot{\boldsymbol{r}}\Big|_{\theta}^{n} - \ddot{\boldsymbol{r}}\Big|_{\theta}^{n+1}$ by C. Then, the time integrated formulation of the Modified Newton-Raphson equation 5.16 reads:

$$\left(\theta A + \frac{1}{\Delta t}B + \frac{1}{\theta}\Delta t^2 C\right)\left(\boldsymbol{r}\Big|_{1}^{n} - \boldsymbol{r}\Big|_{1}^{n+1}\right) = \boldsymbol{f}\Big|_{\theta}^{n} \tag{5.20}$$

5.2. Composition of stiffness matrix

5.2.1. Starting equations

Chapter 3 extensively discussed the governing equations of saturated porous media. If no assumptions are made *a priori* with respect to the inertial terms, three equations solving three free variables provide the physical basis. The obvious choice for the free variables is the pore fluid stress $p\boldsymbol{I}$, the displacements of the soil skeleton $\boldsymbol{u}^s$ and the relative pore fluid velocity $\boldsymbol{v}^{pf\text{-}s}$. The effective stress $\boldsymbol{\sigma}'$ can also be considered a free variable, which is however directly calculated from $\boldsymbol{u}^s$ (or $\boldsymbol{\epsilon}^s$) using a constitutive relation. Chapter 3 demonstrated that there are two equivalent sets of governing equations; the linear momentum of the constituents and the linear momentum affecting the stresses. The linear momentum equations of the bulk and pore fluid are selected here. The linear momentum of the pore fluid will result in a global stiffness matrix that has a higher degree of symmetry than the matrix produced for the linear momentum affecting the pore fluid stress [25].

For the sake of elaboration, the governing equations will be expressed using index notation. Furthermore, the expression of the variables will be simplified. The superscripts referring to the constituents and the unit tensor for the pore fluid stress p will be omitted. Hence, the free variables are expressed by u_i, p and v_i. The starting equations thus read:

$$\frac{n}{K^{pf}}\dot{p} - \dot{u}_{i,i} - w_{i,i} = 0 \tag{3.67}$$

$$np_{,i} + n\rho^f g_i - n^2\mu\kappa_{ij}^{-1}v_j - n\rho^f\ddot{u}_i - an\rho^f\dot{v}_i = 0 \tag{3.69}$$

$$\sigma'_{ji,j} + p_{,i} + \rho g_i - \rho\ddot{u}_i - n\rho^f\dot{v}_i = 0 \tag{3.70}$$

Even though the governing equations have been reformulated, the original labels are used to demonstrate the consistency of the formulation. Note that the linear moment

of the pore fluid 3.69 has been simplified by combining terms that include the relative acceleration of the pore fluid $\dot{v}_i$. To this end, the absolute acceleration of the pore fluid $\dot{\boldsymbol{v}}^{pf}$ is replaced by:

$$\dot{\boldsymbol{v}}^{pf} = \dot{\boldsymbol{v}}^{pf\text{-}s} + \ddot{\boldsymbol{u}}^{s} = \dot{v}_i + \ddot{u}_i \tag{5.21}$$

This elaboration has thus introduced the acceleration of the soil skeleton into the momentum equation of the pore fluid 3.69. Furthermore, the gravitational vector g_i, previously defined in Equation 3.44, is substituted for the body load vector b_i.

The following boundary conditions are relevant for the initial-boundary value problems considered:

- Displacements of the soil skeleton u_i
- Pore fluid stress p
- Flux w
- Total load or traction t

The boundary conditions that are imposed are prescribed values of these variables. Only the displacement of the soil skeleton are used as a constraint, which means that values other than 0 will not be prescribed. The displacement of the soil skeleton and the pore fluid stress are prescribed at nodes, whereas the flux and traction are imposed at the boundary (line) elements for plane problems. Numerical integration is employed to transfer the imposed flux and traction to the nodes. These boundary conditions may affect the governing equations 3.67, 3.69 and 3.70 by imposing a load or prescribing a free variable. The flux w_i implies a load for the mass equation 3.67, while the pore fluid stress p prescribes a free variable. As the displacement of the soil skeleton is only used as a constraint, it will not affect the mass equation. The flux w or the corresponding relative pore fluid velocity v_i implies a prescribed free variable for the linear momentum of the pore fluid 3.69. The load that affects the linear momentum of the pore fluid is the pore fluid stress p or, more specifically, np. The displacement of the soil skeleton u_i and the traction t relate to the linear momentum of the bulk.

Table 5.1: Boundary conditions for governing equations

Residual term	**Imposed nodal freedom**	**Imposed load**
mass pore fluid	pore fluid stress $\overline{p}$	flux $\overline{w}$
linear momentum (LM) bulk	displacement $\overline{u}_i$	traction $\overline{t}_i$
LM of pore fluid	rel. pore fluid velocity $\overline{v}_i$	part. pore fluid stress $n\overline{p}$

5.2.2. Formulation of residuals

General

The residuals are defined by applying the Galerkin weighted residual method 5.11 to the conservation equations 3.67, 3.69 and 3.70 and their corresponding boundary condi-

tions as defined in Table 5.1. The resulting equations are subsequently elaborated in a number of steps, which include:

- Combining of volume and surface integration terms;
- Update of volume and surface at new state;
- Expression of freedom variables in terms of nodal values.

The appearance of divergence terms in the conservation equations 3.67, 3.69 and 3.70 enables the application of Green's theorem and thereby the combination of volume and surface integration terms. Green's theorem is generally expressed by:

$$\int_v \nabla \cdot \boldsymbol{F} \, \mathrm{d}v = \oint_s \boldsymbol{F} \cdot \boldsymbol{n} \, \mathrm{d}s \tag{5.22}$$

For large(r) deformations, the volume v and surface s cannot be considered constants, but need to be updated during the calculations. The current volume v^0 and surface s^0, which are known, are the starting point. The incremental deformation gradient $\hat{\boldsymbol{F}}$ relates the current state $\mathrm{d}\boldsymbol{x}^0$ to the new state $\mathrm{d}\boldsymbol{x}$:

$$\hat{\boldsymbol{F}} = \hat{F}_{ij} = \frac{\partial x_i}{\partial x_j^0} = \boldsymbol{x} \otimes \nabla^{\boldsymbol{x}^0} \tag{5.23}$$

Both the update of volume (from v^0 to v) and surface (from s^0 to s) can be expressed in terms of the incremental deformation gradient $\hat{\boldsymbol{F}}$. These relations read [24]:

$$v = \det\left(\hat{\boldsymbol{F}}\right) v^0 = |\hat{\boldsymbol{F}}| v^0 \tag{5.24}$$

$$s = \frac{\det\left(\hat{\boldsymbol{F}}\right)}{\sqrt{\boldsymbol{n} \cdot \hat{\boldsymbol{F}} \cdot \hat{\boldsymbol{F}}^{\mathrm{T}} \cdot \boldsymbol{n}}} s^0 = |\hat{\boldsymbol{G}}| s^0 \tag{5.25}$$

The integrals may thus be expressed in terms of the volume and surface in the initial reference state, provided that they are multiplied by the correction factors as defined in Equations 5.24 and 5.25, respectively.

The final elaboration concerns the conversion of freedom variables into *nodal* freedom variables. Shape functions usually provide the relation between variables at integration points and the nodes of the element. Since there are three nodal freedom variables, three types of shape function are defined:

$$u_i = \sum_{p=1}^{n_u} N^p \hat{u}_i^p = N^p \hat{u}_i^p \tag{5.26}$$

$$p = \sum_{q=1}^{n_q} \overline{N}^q \hat{p}^q = \overline{N}^q \hat{p}^q \tag{5.27}$$

$$v_i = \sum_{r=1}^{n_v} \widetilde{N}^r \hat{v}_i^r = \widetilde{N}^r \hat{v}_i^r \tag{5.28}$$

The contributions from the element nodes are summed over the number of nodes which are assigned to the nodal freedom variable considered, i.e. n_u, n_p and n_v for the displacements, pore fluid stresses and relative pore fluid velocities respectively. For the sake of clarity the constituent superscripts and summation operators are omitted after the last equal signs. Furthermore, when the Kronecker delta applies to the nodes, superscripts will also be used, i.e. δ^{ij}. This notation will be used hereafter.

Mass equation

Substitution of the conservation of mass of the pore fluid 3.67 and the corresponding boundary conditions from Table 5.1 into the generalised Galerkin's weighted residual equation 5.11 yields:

$$\int_v \overline{N}^s \left(\dot{u}_{i,i} + w_{i,i} - \frac{n}{K^{pf}} \dot{p} \right) \mathrm{d}v + \int_{s^w} \overline{M}^s \left(w_i n_i - \overline{w}^{(n)} \right) \mathrm{d}s + \int_{s^p} \overline{M}^s \left(p - \overline{p} \right) \mathrm{d}s = 0 \tag{5.29}$$

Note that only the flux component normal to the boundary is of importance for the conservation of mass. The flux terms are combined using the aforementioned Green's theorem. To this end, the residual term related to the divergence of flux in the mass equation will be expressed relative to the imposed flux at the boundary. Application of partial differentiation and subsequent application of Green's theorem yields:

$$\begin{aligned} \int_v \overline{N}^s w_{i,i} \mathrm{d}v &= \int_v \left(\overline{N}^s w_i \right)_{,i} \mathrm{d}v - \int_v \overline{N}^s_{,i} w_i \mathrm{d}v \\ &= \oint_s \overline{N}^s w_i n_i \mathrm{d}s - \int_v \overline{N}^s_{,i} w_i \mathrm{d}v \end{aligned} \tag{5.30}$$

Hence, the divergence of the flux is (partly) transferred to the boundary s. Equation 5.29 should be satisfied for any choice of $\overline{M}^s$ and therefore also for $\overline{M}^s = -\overline{N}^s$. This means that the terms including $w_i n_i$ in Equations 5.29 and 5.30 can be combined to:

$$\oint_s \overline{N}^s w_i n_i \mathrm{d}s - \int_{s^w} \overline{N}^s w_i n_i \mathrm{d}s = \int_{s^p} \overline{N}^s w_i n_i \mathrm{d}s \tag{5.31}$$

Equation 5.29 will be automatically satisfied at boundary s^p, where the pore fluid stress p is prescribed. All terms that are valid at boundary s^p can therefore be omitted, which leaves the following equation:

$$\int_v \overline{N}^s \left(\dot{u}_{i,i} - \frac{n}{K^{pf}} \dot{p} \right) \mathrm{d}v - \int_v \overline{N}^s_{,i} w_i \mathrm{d}v + \int_{s^w} \overline{N}^s \overline{w}^{(n)} \mathrm{d}s = 0 \tag{5.32}$$

The final expression of the residual of the mass equation f^{s_m} is obtained by substituting the volume and surface in the reference state through Equations 5.24 and 5.25, and the nodal values through Equations 5.26 and 5.28. Spatial derivatives will only apply on the consequent shape functions, as the spatial derivative of the nodal values equals zero. The result reads:

$$\begin{aligned} f^{s_m} = &\int_{v^0} \overline{N}^s N^p_{,i} \dot{\hat{u}}^p_i |\hat{\boldsymbol{F}}| \mathrm{d}v - \int_{v^0} \overline{N}^s \frac{n}{K^{pf}} \overline{N}^q \dot{\hat{p}}^q |\hat{\boldsymbol{F}}| \mathrm{d}v - \int_{v^0} \overline{N}^s_{,i} \widetilde{N}^r n \hat{v}^r_i |\hat{\boldsymbol{F}}| \mathrm{d}v \\ &+ \int_{s^{w0}} \overline{N}^s \overline{w}^{(n)} |\hat{\boldsymbol{G}}| ds \end{aligned} \tag{5.33}$$

Linear momentum of pore fluid

Substitution of the conservation of the linear momentum of the pore fluid (Equation 3.69) and the corresponding boundary conditions (see Table 5.1) into the generalised Galerkin's weighted residual equation 5.11 yields the residual $f_i^{t_lmpf}$:

$$f_i^{t_lmpf} = \int_v N^t \left(np_{,i} + n\rho^f g_i - n^2 \mu \kappa_{ij}^{-1} v_j - n\rho^f \ddot{u}_i - an\rho^f \dot{v}_i \right) \mathrm{d}v + \int_{s^w} M^t \left(w_i n_i - \overline{w}^{(n)} \right) \mathrm{d}s + \int_{s^p} M^t \left(np - n\overline{p} \right) n_i \mathrm{d}s = 0 \tag{5.34}$$

The same procedure is applied to elaborate the residual of the linear momentum of the pore fluid. Elaboration of the integral term containing $np_{,k}$ by application of partial differentiation and Green's theorem leads to:

$$\int_v N^t np_{,i} \,\mathrm{d}v = \oint_s N^t np\, n_i \mathrm{d}s - \int_v N^t_{,i} np \,\mathrm{d}v - \int_v N^t n_{,i} p \,\mathrm{d}v \tag{5.35}$$

Again, it is assumed that $M^t = -N^t$. Combining the partial pore fluid stress terms in the residual 5.34 that apply on the boundary gives:

$$\oint_s N^t np\, n_i \mathrm{d}s - \int_{s^p} N^t np\, n_i \mathrm{d}s = \int_{s^w} N^t np\, n_i \mathrm{d}s \tag{5.36}$$

The resulting term is automatically satisfied, as the flux is prescribed at boundary s^w. Ignoring all terms related to boundary s^w leaves the following equation:

$$f_i^{t_lmpf} = \int_v N^t \left(n\rho^f g_i - n^2 \mu \kappa_{ij}^{-1} v_j - n\rho^f \ddot{u}_i - an\rho^f \dot{v}_i \right) \mathrm{d}v - \int_V N^t_{,i} np \,\mathrm{d}v - \int_v N^t n_{,i} p \,\mathrm{d}v + \int_{s^p} N^t n\overline{p} n_i \mathrm{d}s \tag{5.37}$$

The final expression is obtained by substituting the volume and surface in the reference state (Equations 5.24 and 5.25) and the nodal values (Equations 5.26 and 5.28). The result reads after multiplication by -1:

$$\begin{aligned} f_i^{t_lmpf} = &- \int_{v^0} N^t n\rho^f g_i |\hat{\boldsymbol{F}}| \mathrm{d}v + \int_{v^0} N^t n^2 \mu \kappa_{ij}^{-1} \widetilde{N}^r \hat{v}_j^r |\hat{\boldsymbol{F}}| \mathrm{d}v + \int_{v^0} N^t n\rho^f N^p \ddot{\hat{u}}_i^p |\hat{\boldsymbol{F}}| \mathrm{d}v \\ &+ \int_{v^0} N^t an\rho^f \widetilde{N}^r \dot{\hat{v}}_i^r |\hat{\boldsymbol{F}}| \mathrm{d}v + \int_{v^0} N^t_{,i} n \overline{N}^q \hat{p}^q |\hat{\boldsymbol{F}}| \mathrm{d}v + \int_{v^0} N^t n_{,i} \overline{N}^q \hat{p}^q |\hat{\boldsymbol{F}}| \mathrm{d}v \\ &- \int_{s^{p0}} N^t n\overline{p} n_i |\hat{\boldsymbol{G}}| \,\mathrm{d}s \end{aligned} \tag{5.38}$$

Note that the formulation of the residual introduces a term that includes the gradient of the porosity, $n_{,i}$. Unlike the hydrostatic interaction term (Subsection 3.2.4), this gradient term arises from the discretisation and will not introduce an *additional* contribution in the case of heterogeneity.

Linear momentum of bulk

The residual of the linear momentum of the bulk $f_i^{u_lmb}$ is defined by substituting the governing equation 3.70 and the corresponding boundary conditions from Table 5.1 into the generalised Galerkin's weighted residual equation 5.11:

$$f_i^{u_lmb} = \int_v N^u \left(\sigma'_{ji,j} + p_{,i} + \rho g_i - \rho \ddot{u}_i - n\rho^f \dot{v}_i \right) \mathrm{d}v + \int_{s^u} M^u \left(u_i - \overline{u}_i \right) \mathrm{d}s + \int_{s^t} M^u \left(t_i - \overline{t}_i \right) \mathrm{d}s = 0 \tag{5.39}$$

The equation will be simplified by combining the stresses in the first integral term of equation 5.39 with the traction at the boundary. To this end, the *total* stress is elaborated:

$$\begin{aligned} \int_v N^u \sigma_{ji,j} \mathrm{d}v &= \oint_s N^u \sigma_{ji} n_j \mathrm{d}s - \int_v N^u_{,j} \sigma_{ji} \mathrm{d}v \\ &= \oint_s N^u t_i \mathrm{d}s - \int_v N^u_{,j} \sigma_{ji} \mathrm{d}v \end{aligned} \tag{5.40}$$

The first integral term in the second line of Equation 5.40 is combined with the traction at the surface. Using the assumption $M^t = -N^t$, the combination of traction terms yields:

$$\oint_s N^u t_i \mathrm{d}s - \int_{s^t} N^u t_i \mathrm{d}s = \int_{s^u} N^u t_i \mathrm{d}s \tag{5.41}$$

As the displacements are prescribed at the part of the boundary s^u, the resulting integral term in Equation 5.41 can be omitted, as well as the prescribed displacements in Equation 5.39 (see Table 5.1). The formulation of the residual 5.39 is updated accordingly:

$$f_i^{u_lmb} = \int_v N^u_{,j} \left(\sigma'_{ji} + p \right) \mathrm{d}v + \int_v N^u \left(\rho g_i - \rho \ddot{u}_i - n\rho^f \dot{v}_i \right) \mathrm{d}v + \int_{s^t} N^u \overline{t}_i \mathrm{d}s \tag{5.42}$$

The expression of the effective stress σ'_{ij} is considered in more detail. The constitutive equation relates effective stress *increments* to strain increments of the soil skeleton by:

$$\dot{\sigma}'_{ij} = D_{ijkl} \dot{\epsilon}_{kl} \tag{5.43}$$

The effective stress in the new state thus results from an effective stress increment with respect to the current state (see Figure 5.1). For small increments in time and strain, the resulting stress can therefore be approximated by:

$$\sigma'_{ij} = \sigma'^0_{ij} + \int_{\Delta t} \dot{\sigma}'_{ij} \mathrm{d}t \approx \sigma'^0_{ij} + D_{ijkl} \Delta\epsilon_{kl} \tag{5.44}$$

The strain increment $\Delta\epsilon_{kl}$ can be related to the nodal displacements of the soil skeleton by using the strain-nodal displacement matrix B^p_{ijk}:

$$\epsilon_{ij} = \frac{1}{2} \left(\frac{\partial u_i}{\partial x_j} + \frac{\partial u_j}{\partial x_i} \right) = \frac{1}{2} (N^p_{,j} \hat{u}^p_i + N^p_{,i} \hat{u}^p_j) = \frac{1}{2} (N^p_{,j} \delta_{ik} + N^p_{,i} \delta_{jk}) \hat{u}^p_k = B^p_{ijk} \hat{u}^p_k \tag{5.45}$$

Using premultiplication by the kronecker delta δ_{ki} and the symmetry of the stress σ_{ij}, the first integral term in Equation 5.42 can be reformulated into:

$$\delta_{ki}\left(N^p_{,j}\sigma_{ij}\right) = \frac{1}{2}\left(\delta_{ki}N^p_{,j}\sigma_{ij} + \delta_{ki}N^p_{,j}\sigma_{ji}\right) = \frac{1}{2}\left(\delta_{kj}N^p_{,i} + \delta_{ki}N^p_{,j}\right)\sigma_{ij} = B^{pT}_{kij}\sigma_{ij} \tag{5.46}$$

Substituting Equations 5.44-5.46 into the residual 5.42 and introducing nodal quantities results in the following updated expression:

$$\begin{aligned} f^{u_lmb}_k = &\int_\nu B^{u\ \mathrm{T}}_{kij}\sigma'^0_{ij}\,\mathrm{d}\nu + \int_\nu B^{u\ \mathrm{T}}_{kij}D_{ijlm}B^p_{lms}\hat{u}^p_s\,\mathrm{d}\nu + \int_\nu N^u_{,k}\overline{N}^q\hat{p}^q\,\mathrm{d}\nu \\ &+ \int_\nu N^u\left(\rho g_i - \rho N^p\ddot{\hat{u}}_i^{\ p} - n\rho^f\tilde{N}^r\dot{\hat{v}}^r_i\right)\mathrm{d}\nu + \int_{s^t} N^u\overline{t}_i\,\mathrm{d}s \end{aligned} \tag{5.47}$$

The last step concerns taking account of the updated volume and surface. However, integrating the residual terms over the initial volume and surface requires that the effect of incremental rotations between the initial and new state are also taken into account. The effective stresses are defined in the local reference frame. Any rotations of the local reference frame with respect to the initial state will affect the expression of the effective stress. To this end, the incremental material rotation $\hat{R}_{ij}$ is introduced:

$$\int_\nu B^{u\ \mathrm{T}}_{kij}\sigma'_{ij}\,\mathrm{d}\nu = \int_{\nu^0} B^{u\ \mathrm{T}}_{kij}\hat{R}_{il}\sigma'_{lm}\hat{R}^{\mathrm{T}}_{mj}|\hat{\boldsymbol{F}}|\mathrm{d}\nu \tag{5.48}$$

Note that this formulation yields an alternative procedure to obtain objectivity of the stress formulation. Molenkamp [26] demonstrates that using the incremental material rotation to update the stress state yields better results than the Zaremba-Jaumann stress rate, which becomes apparent at deviatoric strains above 10%. However, using the material rotation does require a small, local iteration loop to determine the components of $\hat{R}_{ij}$. The final expression of the residual is obtained by updating the surface and volume and including the material rotation in the formulation:

$$\begin{aligned} f^{u_lmb}_k = &\int_{\nu^0} B^{u\ \mathrm{T}}_{kij}\hat{R}_{il}\sigma'^0_{lm}\hat{R}^{\mathrm{T}}_{mj}|\hat{\boldsymbol{F}}|\mathrm{d}\nu + \int_{\nu^0} B^{u\ \mathrm{T}}_{kij}\hat{R}_{il}D_{lmrs}B^p_{rst}\hat{u}^p_t\hat{R}^{\mathrm{T}}_{mj}|\hat{\boldsymbol{F}}|\mathrm{d}\nu + \int_{\nu^0} N^u_{,k}\overline{N}^q\hat{p}^q|\hat{\boldsymbol{F}}|\mathrm{d}\nu \\ &+ \int_{\nu^0} N^u\rho g_k|\hat{\boldsymbol{F}}|\mathrm{d}\nu - \int_{\nu^0} N^u\rho N^p\ddot{\hat{u}}^p_k|\hat{\boldsymbol{F}}|\mathrm{d}\nu - \int_{\nu^0} N^u n\rho^f\tilde{N}^r\dot{\hat{v}}^r_k|\hat{\boldsymbol{F}}|\mathrm{d}\nu + \int_{s^{t0}} N^u\overline{t}_k|\hat{\boldsymbol{G}}|\mathrm{d}s \end{aligned} \tag{5.49}$$

5.2.3. Newton-Raphson procedure

Equations 5.33, 5.38 and 5.49 present the discretised formulations of the governing equations 3.67, 3.69 and 3.70 that need to be satisfied for the considered initial-boundary-value problem. Using the Modified Newton-Raphson procedure, these equations are simplified in order to solve the problem. Consider the subsequent iteration steps n and $n+1$. At the previous iteration step n all quantities are known, including the errors or residuals $\boldsymbol{f}^n$ and the free, nodal variables $\hat{\boldsymbol{r}}^n$. The Modified Newton-Raphson procedure, previously expressed by Equation 5.12, allows for the calculation of the values of the free, nodal variables $\hat{\boldsymbol{r}}^{n+1}$:

$$\left.\frac{\partial \boldsymbol{f}}{\partial \hat{\boldsymbol{r}}}\right|^n \left(\hat{\boldsymbol{r}}^n - \hat{\boldsymbol{r}}^{n+1}\right) = \left.\frac{\partial \boldsymbol{f}}{\partial \hat{\boldsymbol{r}}}\right|^n \mathrm{d}\hat{\boldsymbol{r}} = \boldsymbol{f}^n \tag{5.50}$$

The differential operator $\partial \boldsymbol{f}/\partial \boldsymbol{r}$, from hereon denoted by the stiffness matrix, is thus composed of the derivatives of the residuals with respect to the free variables. Equation 5.50 will be applied to the discretised formulations of the governing equations. At this stage, the material time derivatives of the free variables are not elaborated. These will be considered separately and will be combined in the next section 5.2.4. After calculating the values of $\hat{\boldsymbol{r}}^{n+1}$, backsubstitution into the governing equation will yield the new value of the residuals $\boldsymbol{f}^{n+1}$.

Mass equation

Equation 5.33 defines the residual of the mass equation, f^{s_m}. The Modified Newton-Raphson equation 5.50 is specified as follows for the mass equation:

$$f^{s_m}\Big|^n = \frac{\partial f^{s_m}}{\partial \dot{\hat{u}}_i^p}\Big|^n \mathrm{d}\dot{\hat{u}}_i^p + \frac{\partial f^{s_m}}{\partial \dot{\hat{p}}^q}\Big|^n \mathrm{d}\dot{\hat{p}}^q + \frac{\partial f^{s_m}}{\partial \hat{v}_i^r}\Big|^n \mathrm{d}\hat{v}_i^r \tag{5.51}$$

Elaboration leads to the following expression:

$$\begin{aligned} f^{s_m}\Big|^n = &\left(\int_{v^0} \overline{N}^s N^p_{,i} \delta^{pv} \delta_{ip} |\hat{\boldsymbol{F}}| \mathrm{d}v\right) \mathrm{d}\dot{\hat{u}}_p^v - \left(\int_{v^0} \overline{N}^s \frac{n}{K^{pf}} \overline{N}^q \delta^{qw} |\hat{\boldsymbol{F}}| \mathrm{d}v\right) \mathrm{d}\dot{\hat{p}}^w \\ &- \left(\int_{v^0} \overline{N}^s_{,i} \tilde{N}^r n \delta^{rx} \delta_{ip} |\hat{\boldsymbol{F}}| \mathrm{d}v\right) \mathrm{d}\hat{v}_p^x \end{aligned} \tag{5.52}$$

For the sake of convenience, the integral terms will be expressed in matrix format:

$$f^{s_m}\Big|^n = \overline{C}_p^{sv} \left(\dot{u}_p^v\Big|^n - \dot{u}_p^v\Big|^{n+1}\right) - \frac{n}{K^{pf}} \overline{K}^{sw} \left(\dot{p}^w\Big|^n - \dot{\hat{p}}^w\Big|^{n+1}\right) - n\tilde{C}_p^{sx} \left(\hat{v}_p^x\Big|^n - \hat{v}_p^x\Big|^{n+1}\right) \tag{5.53}$$

Herein, $\overline{C}_p^{sw}$ and $\tilde{C}_p^{sx}$ are coupling matrices, while $\overline{K}^{sw}$ is the stiffness matrix of the pore fluid. Note that the kronecker delta has been added to the integral terms to allow for matrix multiplication.

Linear momentum of pore fluid

Equation 5.38 defines the discretised residual of the linear momentum of the pore fluid, $f_i^{t_lmpf}$. The corresponding Modified Newton-Raphson equation is specified as follows:

$$f_i^{t_lmpf}\Big|^n = \frac{\partial f_i^{t_lmpf}}{\partial \ddot{\hat{u}}_k^p}\Big|^n \mathrm{d}\ddot{\hat{u}}_k^p + \frac{\partial f_i^{t_lmpf}}{\partial \hat{p}^q}\Big|^n \mathrm{d}\hat{p}^q + \frac{\partial f_i^{t_lmpf}}{\partial \hat{v}_k^r}\Big|^n \mathrm{d}\hat{v}_k^r + \frac{\partial f_i^{t_lmpf}}{\partial \dot{\hat{v}}_k^r}\Big|^n \mathrm{d}\dot{\hat{v}}_k^r \tag{5.54}$$

Elaboration yields the following expression:

$$\begin{aligned} f_i^{t_lmpf}\Big|^n = &\left(\int_{v^0} N^t n \rho^f N^p \delta^{pv} \delta_{ip} |\hat{\boldsymbol{F}}| \mathrm{d}v\right) \mathrm{d}\ddot{\hat{u}}_p^v \\ &+ \left(\int_{v^0} N^t_{,i} n \overline{N}^q \delta^{qw} |\hat{\boldsymbol{F}}| \mathrm{d}v + \int_{v^0} N^t n_{,i} \overline{N}^q \delta^{qw} |\hat{\boldsymbol{F}}| \mathrm{d}v\right) \mathrm{d}\hat{p}^w \\ &+ \left(\int_{v^0} N^t n^2 \mu \kappa_{ij}^{-1} \tilde{N}^r \delta^{rx} \delta_{jp} |\hat{\boldsymbol{F}}| \mathrm{d}v\right) \mathrm{d}\hat{v}_p^x + \left(\int_{v^0} N^t a n \rho^f \tilde{N}^r \delta^{rx} \delta_{ip} |\hat{\boldsymbol{F}}| \mathrm{d}v\right) \mathrm{d}\dot{\hat{v}}_p^x \end{aligned} \tag{5.55}$$

The corresponding expression in matrix format reads:

$$f_i^{t_lmpf}\Big|^n = \overline{M}_{ip}^{tv}\left(\ddot{\hat{u}}_p^v\Big|^n - \ddot{\hat{u}}_p^v\Big|^{n+1}\right) + \left(nC_i^{tw} + N_i^{tw}\right)\left(\dot{\hat{p}}^w\Big|^n - \dot{\hat{p}}^w\Big|^{n+1}\right) + Q_{ip}^{tx}\left(\hat{v}_p^x\Big|^n - \hat{v}_p^x\Big|^{n+1}\right) + a\tilde{M}_{ip}^{tx}\left(\dot{\hat{v}}_p^x\Big|^n - \dot{\hat{v}}_p^x\Big|^{n+1}\right) \tag{5.56}$$

Herein, $\overline{M}_{ip}^{tv}$ and $\tilde{M}_{ip}^{tx}$ define mass matrices, C_i^{tw} a coupling matrix, N_i^{tw} the porosity gradient matrix and Q_{ip}^{tx} the hydraulic conductivity matrix. The porosity gradient matrix N_i^{tw} can be further elaborated by treating the porosity as a nodal variable. However, this thesis will only consider simple cases where the current formulation suffices.

Linear momentum of bulk

The discretised residual of the linear momentum of the bulk equation $f_k^{u_lmb}$ was given by equation 5.49. This equation is elaborated using the Modified Newton-Raphson procedure:

$$f_k^{u_lmb}\Big|^n = \frac{\partial f_k^{u_lmb}}{\partial \hat{u}_m^p}\Big|^n \mathrm{d}\hat{u}_m^p + \frac{\partial f_k^{u_lmb}}{\partial \ddot{\hat{u}}_m^p}\Big|^n \mathrm{d}\ddot{\hat{u}}_m^p + \frac{\partial f_k^{u_lmb}}{\partial \dot{\hat{p}}^q}\Big|^n \mathrm{d}\dot{\hat{p}}^q + \frac{\partial f_k^{u_lmb}}{\partial \dot{\hat{v}}_m^r}\Big|^n \mathrm{d}\dot{\hat{v}}_m^r \tag{5.57}$$

The resulting equation reads:

$$f_k^{u_lmb}\Big|^n = \left(\int_{v^0} B_{kij}^{Tu}\hat{R}_{il}D_{lmrs}B_{rst}^p\hat{R}_{mj}^{\mathrm{T}}\delta^{pv}\delta_{tp}|\hat{\boldsymbol{F}}|\mathrm{d}v\right)\mathrm{d}\hat{u}_p^v - \left(\int_{v^0} N^u\rho N^p\delta^{pv}\delta_{kp}|\hat{\boldsymbol{F}}|\mathrm{d}v\right)\mathrm{d}\ddot{\hat{u}}_p^v + \left(\int_{v^0} N_{,k}^u\overline{N}^q\delta^{qw}|\hat{\boldsymbol{F}}|\mathrm{d}v\right)\mathrm{d}\dot{\hat{p}}^w - \left(\int_{v^0} N^u n\rho^f\tilde{N}^r\delta^{rx}\delta_{kp}|\hat{\boldsymbol{F}}|\mathrm{d}v\right)\mathrm{d}\dot{\hat{v}}_p^x \tag{5.58}$$

This equation is reformulated in matrix format:

$$f_k^{u_lmb}\Big|^n = K_{kp}^{uv}\left(\hat{u}_p^v\Big|^n - \hat{u}_p^v\Big|^{n+1}\right) - M_{kp}^{uv}\left(\ddot{\hat{u}}_p^v\Big|^n - \ddot{\hat{u}}_p^v\Big|^{n+1}\right) + C_k^{up}\left(\dot{\hat{p}}^w\Big|^n - \dot{\hat{p}}^w\Big|^{n+1}\right) - \tilde{M}_{kp}^{ux}\left(\dot{\hat{v}}_p^x\Big|^n - \dot{\hat{v}}_p^x\Big|^{n+1}\right) \tag{5.59}$$

5.2.4. Time discretisation

The next step entails the addition of the time dependence using the Crank-Nicolson time stepping scheme. The governing equations will be evaluated at time t_θ, as previously expressed by equation 5.16. The conservation equations of mass (5.53), linear momentum of the pore fluid (5.56) and linear momentum of the bulk (5.59) thus apply to time t_θ. The residuals are calculated using the known values at time t_0 and t_1:

$$\boldsymbol{f}\Big|_\theta^n = \theta\boldsymbol{f}\Big|_1^n + (1-\theta)\boldsymbol{f}\Big|_0 \tag{5.60}$$

The material time derivatives of the free variables are integrated in time, after which the resulting terms are reworked into values at time t_1. Equations 5.17-5.19 expressed these operations, summarised by Equation 5.20.

Mass equation

Applying time integration on the conservation of mass equation 5.53 gives:

$$f^{s_m}\Big|_\theta^n = \frac{1}{\Delta t}\overline{C}_p^{sv}\left(\hat{u}_p^v\Big|_1^n - \hat{u}_p^v\Big|_1^{n+1}\right) - \frac{n}{\Delta t K^{pf}}\overline{K}^{sw}\left(\hat{p}^w\Big|_1^n - \hat{p}^w\Big|_1^{n+1}\right) - n\theta\tilde{C}_p^{sx}\left(\hat{v}_p^x\Big|_1^n - \hat{v}_p^x\Big|_1^{n+1}\right) \tag{5.61}$$

Linear momentum of pore fluid

The conservation of linear momentum of the pore fluid 5.56 reads after time integration:

$$\begin{aligned} f_i^{t_lmpf}\Big|_\theta^n = {} & \frac{1}{\theta\Delta t^2}\overline{M}_{ip}^{tv}\left(\hat{u}_p^v\Big|_1^n - \hat{u}_p^v\Big|_1^{n+1}\right) + \theta\left(nC_i^{tw} + N_i^{tw}\right)\left(\hat{p}^w\Big|_1^n - \hat{p}^w\Big|_1^{n+1}\right) \\ & + \left(\theta Q_{ip}^{tx} + \frac{a}{\Delta t}\tilde{M}_{ip}^{tx}\right)\left(\hat{v}_p^x\Big|_1^n - \hat{v}_p^x\Big|_1^{n+1}\right) \end{aligned} \tag{5.62}$$

Linear momentum of bulk

Time integration yields the following result for the conservation of linear momentum of the bulk 5.59:

$$\begin{aligned} f_k^{u_lmb}\Big|_\theta^n = {} & \left(\theta K_{kp}^{uv} - \frac{1}{\theta\Delta t^2}M_{kp}^{uv}\right)\left(\hat{u}_p^v\Big|_1^n - \hat{u}_p^v\Big|_1^{n+1}\right) + \theta C_k^{uw}\left(\hat{p}^w\Big|_1^n - \hat{p}^w\Big|_1^{n+1}\right) \\ & - \frac{1}{\Delta t}\tilde{M}_{kp}^{ux}\left(\dot{\hat{v}}_p^x\Big|_1^n - \dot{\hat{v}}_p^x\Big|_1^{n+1}\right) \end{aligned} \tag{5.63}$$

Energy consistency of time stepping scheme

The conservation of energy is not explicitly accounted for, but may be violated as a result of time integration. Chapter 4 treated the balance between the internal energy, kinetic energy and external supply of energy. Here, the simplified balance will be related to the time stepping scheme. Ignoring any temperature effects, the conservation of energy reads for a single constituent:

$$\dot{e}^{str} + \dot{K} + e^{ext;m} = 0 \tag{5.64}$$

Herein, e^{str} is the internal strain energy, K the kinetic energy and $e^{ext;m}$ the external supply of energy. The change of energy within a time step may be expressed for each term by:

$$\Delta e^{str} = \frac{1}{2}\left(\boldsymbol{L}_1 + \boldsymbol{L}_0\right)\left(\hat{u}_1 - \hat{u}_0\right) \tag{5.65}$$

$$\Delta K = \frac{1}{2}\left(\dot{\hat{u}}_1^{\mathrm{T}}\boldsymbol{M}\dot{\hat{u}}_1 - \dot{\hat{u}}_0^{\mathrm{T}}\boldsymbol{M}\dot{\hat{u}}_0\right) \tag{5.66}$$

$$e^{ext;m} = \frac{1}{2}\left(\boldsymbol{P}_1 + \boldsymbol{P}_0\right)\left(\hat{u}_1 - \hat{u}_0\right) \tag{5.67}$$

The internal strain matrix $\boldsymbol{L}$ is equivalent to the stiffness matrix $\boldsymbol{K}$ in the bulk equation 5.63. Furhermore, the presumed constant mass matrix $\boldsymbol{M}$ is also a common term in the conservation equations, while the external work matrix $\boldsymbol{P}$ gathers the boundary and

body load terms. The nodal displacement $\hat{u}_1$ is elaborated as follows for a small time step Δt:

$$\ddot{\hat{u}}_1 = \ddot{\hat{u}}_0 + \dddot{\hat{u}}_0 \Delta t \tag{5.68}$$

$$\begin{aligned}\dot{\hat{u}}_1 &= \int \ddot{\hat{u}}_1 \, dt \\ &= \dot{\hat{u}}_0 + \ddot{\hat{u}}_0 \Delta t + \frac{1}{2} \dddot{\hat{u}}_0 \Delta t^2\end{aligned} \tag{5.69}$$

$$\begin{aligned}\hat{u}_1 &= \int \dot{\hat{u}}_1 \, dt \\ &= \hat{u}_0 + \dot{\hat{u}}_0 \Delta t + \frac{1}{2} \ddot{\hat{u}}_0 \Delta t^2 + \frac{1}{6} \dddot{\hat{u}}_0 \Delta t^3\end{aligned} \tag{5.70}$$

Substitution of these equations into the (components) of the conservation of energy equation allows the expression of the equation entirely in terms of the initial nodal incremental displacement $\hat{u}_0$ and its material derivatives. Substitution of Equations 5.68-5.70 into Equations 5.65-5.67 and, subsequently 5.64, and rearrangement leads to:

$$\begin{aligned}&\left\{ \frac{1}{2} \left(\boldsymbol{L}_1 + \boldsymbol{L}_0 - \boldsymbol{P}_1 - \boldsymbol{P}_0 \right) + \ddot{\hat{u}}_0^T \boldsymbol{M} \right\} \dot{\hat{u}}_0 \Delta t + \\ &\left\{ \frac{1}{2} \left(\boldsymbol{L}_1 + \boldsymbol{L}_0 - \boldsymbol{P}_1 - \boldsymbol{P}_0 \right) + \ddot{\hat{u}}_0^T \boldsymbol{M} \right\} \ddot{\hat{u}}_0 \frac{\Delta t^2}{2} + \\ &\left\{ \frac{1}{6} \left(\boldsymbol{L}_1 + \boldsymbol{L}_0 - \boldsymbol{P}_1 - \boldsymbol{P}_0 \right) + \frac{1}{\Delta t} \dot{\hat{u}}_0^T \boldsymbol{M} + \ddot{\hat{u}}_0^T \boldsymbol{M} + \dddot{\hat{u}}_0^T \boldsymbol{M} \frac{\Delta t}{4} \right\} \dddot{\hat{u}}_0 \frac{\Delta t^3}{2} = 0\end{aligned} \tag{5.71}$$

Terms related to the first, second and third material time derivatives of the nodal displacement at the start of the time increment have been assembled. Equation 5.71 will be satisfied unconditionally if each of the these terms equals zero. This is the case if the following equations are satisfied:

$$\frac{1}{2} \left(\boldsymbol{L}_1 + \boldsymbol{L}_0 - \boldsymbol{F}_1 - \boldsymbol{F}_0 \right) + \ddot{\hat{u}}_0^T \boldsymbol{M} = 0 \tag{5.72}$$

$$\frac{1}{6} \left(\boldsymbol{L}_1 + \boldsymbol{L}_0 - \boldsymbol{F}_1 - \boldsymbol{F}_0 \right) + \frac{1}{\Delta t} \dot{\hat{u}}_0^T \boldsymbol{M} + \ddot{\hat{u}}_0^T \boldsymbol{M} + \dddot{\hat{u}}_0^T \boldsymbol{M} \frac{\Delta t}{4} = 0 \tag{5.73}$$

Summing both requirements leads to a relation between the material derivatives of the initial nodal displacements:

$$\dddot{\hat{u}}_0 = -\frac{4 \dot{\hat{u}}_0}{\Delta t^2} - \frac{8 \ddot{\hat{u}}_0}{3 \Delta t} \tag{5.74}$$

Finally, this equation can be substituted into Equation 5.68 to obtain a relation with the nodal acceleration at the end of the time step:

$$\ddot{\hat{u}}_1 = -\frac{4 \dot{\hat{u}}_0}{\Delta t} - \frac{5 \ddot{\hat{u}}_0}{3} \tag{5.75}$$

Considering the sign and magnitude of the right-hand terms, Equation 5.75 predicts oscillations and an ever growing nodal acceleration. This is not consistent with the conservation of energy. In order to exclude unwanted energy effects when using the Crank-Nicolson time stepping scheme, the acceleration terms should not be allowed to vary

during a time step. This means that a single value for the nodal acceleration $\ddot{\hat{u}}\big|_\theta^n$ should be used when calculating $\boldsymbol{f}\big|_\theta^n$, instead of using $\ddot{\hat{u}}\big|_0$ and $\ddot{\hat{u}}\big|_1^n$. The constant acceleration terms during a time step are thus determined by:

$$\ddot{r}\Big|_\theta^{n+1} = \frac{\dot{r}\Big|_1^{n+1} - \dot{r}\Big|_0}{\Delta t} \tag{5.76}$$

In the case of constant acceleration terms during a time step, only Equation 5.72 needs to be satisfied for the conservation of energy. This is the case for $\theta = 0.5$. The left hand terms in Equation 5.72 equal the residual f_θ for $\theta = 0.5$ [24]. Convergence of the residual towards zero thus implies conservation of energy.

5.2.5. Resulting stiffness matrix

Equations 5.61-5.63 formulate the Modified Newton-Raphson equation for the governing set of equations. Combining these three equations, the stiffness matrix relates the residuals to nodal freedom variables. The stiffness matrix thus reads:

$$\begin{bmatrix} \frac{1}{\Delta t}\overline{C}_p^{sv} & \frac{n}{\Delta t K^{pf}}\overline{K}^{sw} & -n\theta\tilde{C}_p^{sx} \\ \frac{1}{\theta\Delta t^2}\overline{M}_{ip}^{tv} & n\theta C_i^{tw} + \theta N_i^{tw} & \theta Q_{ip}^{tx} + \frac{a}{\Delta t}\tilde{M}_{ip}^{tx} \\ \theta K_{kp}^{uv} - \frac{1}{\theta\Delta t^2}M_{kp}^{uv} & \theta C_k^{uw} & -\frac{1}{\Delta t}\tilde{M}_{kp}^{ux} \end{bmatrix} \begin{pmatrix} \hat{u}_p^v\Big|_1^n - \hat{u}_p^v\Big|_1^{n+1} \\ \hat{p}^w\Big|_1^n - \hat{p}^w\Big|_1^{n+1} \\ \hat{v}_p^x\Big|_1^n - \hat{v}_p^x\Big|_1^{n+1} \end{pmatrix}$$

$$= \begin{pmatrix} f^{s_m}\Big|_\theta^n \\ f_i^{t_lmpf}\Big|_\theta^n \\ f_k^{u_lmb}\Big|_\theta^n \end{pmatrix} \tag{5.77}$$

Table 5.2 provides an overview of the components of the stiffness matrix.

Table 5.2: Components of stiffness matrix

$\overline{C}_p^{sv}$	$\int_{v^0} \overline{N}^s N^p_{,i} \delta^{pv} \delta_{ip} \lvert\hat{\boldsymbol{F}}\rvert \mathrm{d}v$	coupling with deform. soil skeleton
$\overline{K}^{sw}$	$\int_{v^0} \overline{N}^s \overline{N}^q \delta^{qw} \lvert\hat{\boldsymbol{F}}\rvert \mathrm{d}v$	stiffness of pore fluid
$\tilde{C}_p^{sx}$	$\int_{v^0} \overline{N}^s_{,i} \tilde{N}^r \delta^{rx} \delta_{ip} \lvert\hat{\boldsymbol{F}}\rvert \mathrm{d}v$	coupling with rel. pore fluid velocity
$\overline{M}_{ip}^{tv}$	$\int_{v^0} N^t n \rho^f N^p \delta^{pv} \delta_{ip} \lvert\hat{\boldsymbol{F}}\rvert \mathrm{d}v$	mass of pore fluid
C_i^{tw}	$\int_{v^0} N^t_{,i} \overline{N}^q \delta^{qw} \lvert\hat{\boldsymbol{F}}\rvert \mathrm{d}v$	coupling with pore fluid stress
N_i^{tw}	$\int_{v^0} N^t n_{,i} \overline{N}^q \delta^{qw} \lvert\hat{\boldsymbol{F}}\rvert \mathrm{d}v$	porosity gradient
Q_{ip}^{tx}	$\int_{v^0} N^t n^2 \mu \kappa^{-1}_{ij} \tilde{N}^r \delta^{rx} \delta_{jp} \lvert\hat{\boldsymbol{F}}\rvert \mathrm{d}v$	hydraulic conductivity
$\tilde{M}_{ip}^{tx}$	$\int_{v^0} N^t n \rho^f \tilde{N}^r \delta^{rx} \delta_{ip} \lvert\hat{\boldsymbol{F}}\rvert \mathrm{d}v$	mass of pore fluid
K_{kp}^{uv}	$\int_{v^0} B^u_{kij} \hat{R}_{il} D_{lmrs} B^p_{rst} \hat{R}^{\mathrm{T}}_{mj} \delta^{pv} \delta_{kp} \lvert\hat{\boldsymbol{F}}\rvert \mathrm{d}v$	stiffness of soil skeleton
M_{kp}^{uv}	$\int_{v^0} N^u \rho N^p \delta^{pv} \delta_{kp} \lvert\hat{\boldsymbol{F}}\rvert \mathrm{d}v$	mass of bulk
C_k^{uw}	$\int_{v^0} N^u_{,k} \overline{N}^q \delta^{qw} \lvert\hat{\boldsymbol{F}}\rvert \mathrm{d}v$	coupling with pore fluid stress
$\tilde{M}_{kp}^{ux}$	$\int_{v^0} N^u n \rho^f \tilde{N}^r \delta^{rx} \delta_{kp} \lvert\hat{\boldsymbol{F}}\rvert \mathrm{d}v$	mass of pore fluid

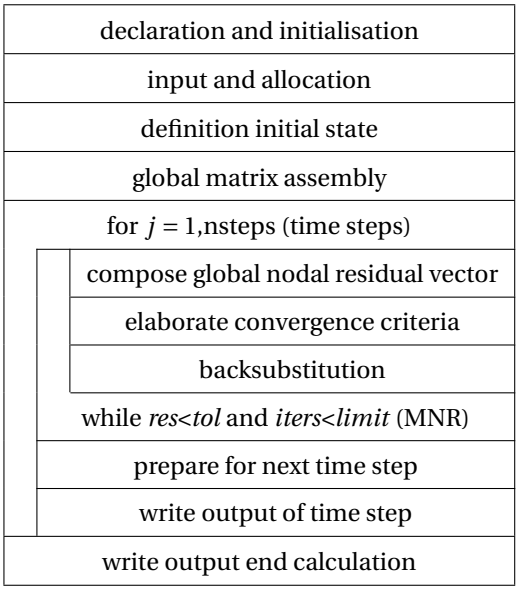
5.3. Implementation

The code *p94_mnr.f95* [23] and the libraries provided by Smith and Griffith [2] form the basis of the implementation of a new code for coupled, two-phase initial-boundary value problems. Molenkamp [23] implemented a Modified Newton-Raphson scheme with a Crank-Nicolson time stepping scheme for statics. The code has here been extended for dynamics and a number of additional options added. This thesis includes a concise description of the implementation. For more details the reader is referred to [25].

Figure 5.3 provides a programming structure diagram PSD of the implementation. The part of the code before the time stepping-loop defines the input for the calculation. After declaration and initialisation, the input allows for further specification of the variables. A separate file defines the input, including the input geometry and mesh, material properties, possible loading functions and boundary conditions. The specification enables the allocation of the allocatable vector and matrix variables. Numerical stability of the selected mesh and time step is verified using the criterion established by Vermeer and Verruijt for consolidation [27]. If necessary, the time step is corrected to ensure numerical stability and accuracy. The subsequent part of the code defines the initial state of the discretised geometry, including the stresses and the components of the global stiffness matrix as provided by Table 5.2. The global matrix assembly combines the contributions of the different components in a single global matrix.

Two loops are used to perform the calculation of the initial-boundary value problem. For each time step, iterations are carried out until the desired convergence has been established. The result is written to the output file for further interpretation using computer graphics.

Figure 5.3: Main structure



5.4. Evaluation of model performance

5.4.1. General

The amendments of the code are evaluated by considering its performance for the well-known initial-boundary value problem of one-dimensional consolidation. The evaluation has been used to test different options of the $u_i - p - v_i$-formulation [25]. This chapter will only describe the results from the formulation described in the previous sections. The evaluation involves the performance of the model with varying number and type of elements for a statics problem. The performance of the model was not evaluated for dynamics. However, the last section will elaborate on the challenges that lie ahead when modelling the dynamic phase of liquefaction flow slides.

5.4.2. One-dimensional consolidation

Analytical solutions

The one-dimensional consolidation problem entails an initial-boundary value problem with a well-known analytical solution that is frequently used to evaluate the performance of numerical models. Subsection 3.3.6 previously considered the derivation of the cor-

responding differential equation from the governing equations of saturated, porous media. The basic assumptions and resulting equations are first recalled:

- The generic set of governing equations is reduced to one dimension.
- The inertial and body load terms are neglected.
- The total stress $\boldsymbol{\sigma}$ remains constant, i.e. $\dot{\boldsymbol{\sigma}} = 0$ and $\dot{\boldsymbol{\sigma}}' = -\dot{p}\boldsymbol{I}$.
- Both the soil particles and pore fluid are assumed to be incompressible.
- The response of the soil skeleton and pore fluid is simplified to linear elasticity.
- The properties of the soil skeleton and pore fluid, expressed by the corresponding compressibilities and hydraulic conductivity, are constant in time and space.

Using the conservation of mass equation 3.67 and the conservation of linear momentum affecting the pore fluid stress 3.84, the consolidation equation is derived:

$$\frac{\mathrm{d}p}{\mathrm{d}t} = c_z \frac{\mathrm{d}^2 p}{\mathrm{d}z^2} \tag{3.100}$$

Herein, the *consolidation coefficient* is defined by:

$$c_z = \frac{1}{\frac{\mu}{\kappa}\left(\frac{n}{K^{pf}} + \frac{1}{K^s}\right)} \tag{3.101}$$

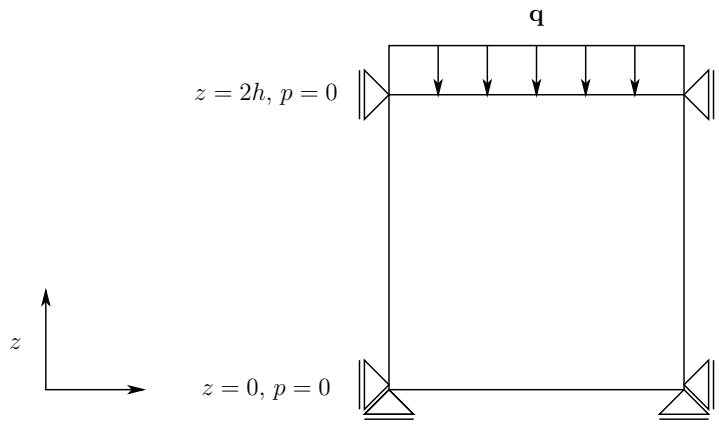


Figure 5.4: Initial-boundary value problem of one-dimensional consolidation.

The initial and boundary conditions complement the initial-boundary value problem (see Figure 5.4). The two boundary conditions concerning the pore fluid stresses read:

$$p = 0 \text{ at } z = 0 \quad ; t \geq 0 \tag{5.78}$$

$$p = 0 \text{ at } z = 2h \; ; t \geq 0 \tag{5.79}$$

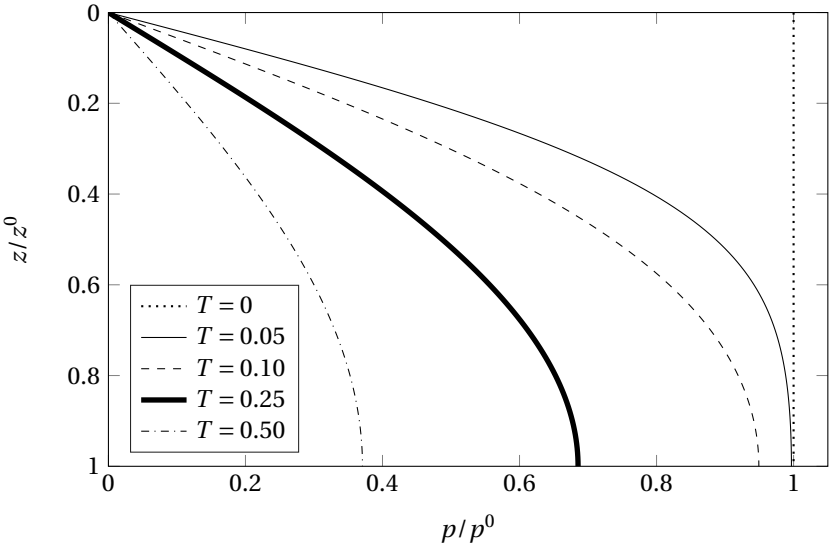


Figure 5.5: Plot of analytical solution of initial-boundary value problem of one-dimensional consolidation for different values of the characteristic time T (see Equation 5.82).

The initial condition is given by the sudden application of load q. As the load is suddenly applied (i.e. during an infinitesimally small time increment dt), initially there can be no flux. The full load is consequently carried by the pore fluid, so that the initial condition is given by:

$$p^0 = q = \sigma_z \text{ at } t = 0 \quad ; 0 < z < 2h \tag{5.80}$$

The problem can be solved by using the Laplace transformation. The solution can be found in many handbooks in soil mechanics [28] and reads:

$$\frac{p}{p^0} = \frac{4}{\pi} \sum_{j=1}^{\infty} \left\{ \frac{(-1)^{j-1}}{2j-1} \cos\left[(2j-1)\frac{\pi}{2}\left(\frac{h-z}{h}\right)\right] \exp\left[-\frac{(2j-1)^2\pi^2}{4}\frac{c_z t}{h^2}\right]\right\} \tag{5.81}$$

Note that, for $z = h$, the excess pore fluid stresses are at their maximum for an arbitrary time t due to the fact that $cos(0) = 1$. The excess pore fluid stress should be zero at $z = 0$ and $z = 2h$, due to the fact that $\cos(\pi/2, 3\pi/2, 5\pi/2 \text{ etc}) = 0$. The pore fluid stress distribution is symmetrical with $z = h$ being the axis of symmetry. One may consequently choose to solve the upper or lower halve of the problem, with a boundary condition at $z^0 = h$ being defined as $p_{,z} = 0$.

Figure 5.5 plots the analytical solution 5.81 of the initial-boundary value problem. The solutions are plotted for five points in time, expressed by the dimensionless characteristic time T:

$$T = \frac{c_z t}{h^2} \tag{5.82}$$

The variables corresponding to the axes have also been normalised to obtain dimensionless quantities. On the vertical axis the pore fluid stresses are normalised by the absolute maximum excess pore fluid stress p^0 that equals the initial surcharge load q, i.e. the same expression used for the solution 5.81. On the horizontal axis the vertical level z has been normalised by $z^0 = h$. In line with common practice, the vertical axis is reversed. Figure 5.5 thus displays the upper half of the boundary value problem in Figure 5.4, while employing the symmetry of the solution. The plot was obtained using the basic file *Terzaghi.f95* [23] that was extended to create the output file.

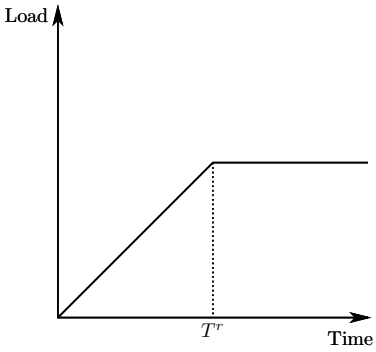


Figure 5.6: Increase of load in time for a ramp load with characteristic time T^r.

A more realistic loading case is provided by a ramp loading scenario. The load is linearly increased from the start ($T = 0$) to the ramp loading time T^r, after which it is held constant (see Figure 5.6). The same solution 5.81 is employed to solve the corresponding development of the pore fluid stresses. To this end, the Author distinguishes between the part where $T \leq T^r$ and $T > T^r$ (see Figure 5.6). For the former part, the cumulative effect of the increasing load is equivalent to the response as a result of the average load:

$$\left.\frac{p}{p^0}\right|_{T \leq T^r} = \frac{\int_0^T \left(p/p^0\right) dT}{T} \tag{5.83}$$

In the case where $T > T^r$, the equivalent average relative pore fluid stress can be calculated by first assuming a ramp load up to T and then subtracting the final part. This will leave the following equation:

$$\left.\frac{p}{p^0}\right|_{T \leq T^r} = \frac{\int_{T-T^r}^T \left(p/p^0\right) dT}{T^r} \tag{5.84}$$

The results of the analytical solution of a ramp load with $T^r = 0.1$ are plotted in Figures 5.7 and 5.9. Figure 5.7 shows the development of the relative pore fluid stress p/p^0 as a function of the characteristic time T for three (relative) levels z/z^0. The reference pore fluid stress p^0 is defined by the final ramp load that is reached at $T^r = 0.1$. Close to the

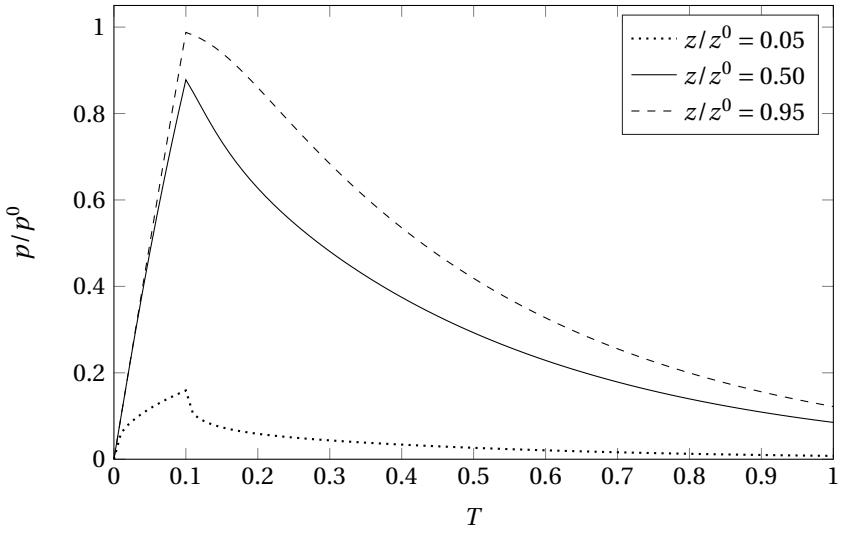


Figure 5.7: Plot of analytical solution of one-dimensional consolidation problem with ramp loading ($T^r = 0.1$) as a function of time T for three levels.

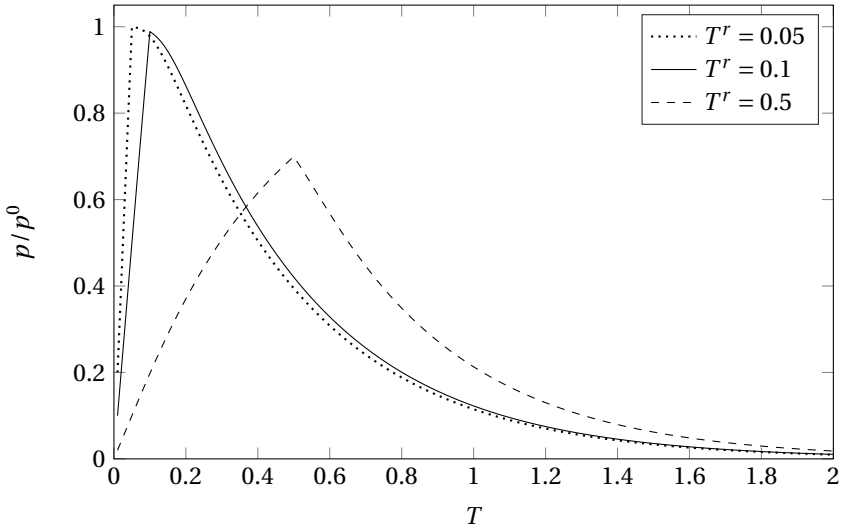


Figure 5.8: Plot of analytical solution of one-dimensional consolidation problem with ramp loading as a function of time T for three characteristic ramp loading times T^r at the lower, impervious boundary ($z/z^0 = 1.00$).

surface ($z/z^0 = 0.05$) consolidation dominates the development of relative fluid stresses that stay well below the maximum value of $p/p^0 = 1$. Close to the centre ($z/z^0 = 0.95$), the loading dominates the development of relative pore fluid stresses up to $T = 0.1$, reaching a value close to $p/p^0 = 1$. Hereafter, consolidation results in decreasing values. Figure 5.8 plots the pore pressure development at $z/z^0 = 1.00$ with time for three characteristic, ramp loading times. As T^r increases, consolidation becomes more pronounced during loading, as manifested by a milder and more non-linear curve during the loading stage.

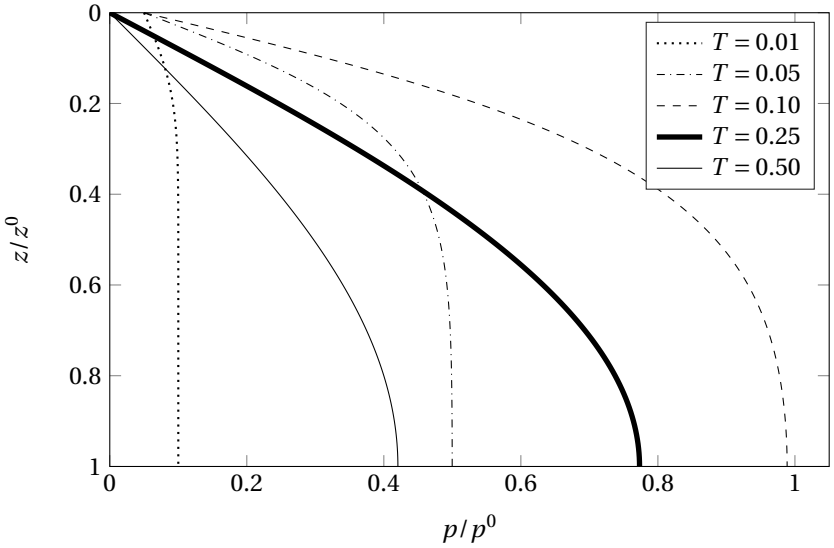


Figure 5.9: Plot of analytical solution of one-dimensional consolidation problem with ramp loading ($T^r = 0.1$) as a function of level z/z^0 for different moments in time T.

Figure 5.9 plots the development of relative pore fluid stresses as a function of the (relative) level for five values of the characteristic time T. The resulting plot is thus comparable to Figure 5.5 for an instantly applied load. The first three curves ($T = 0.01$, $T = 0.05$ and $T = 0.10$) show the increase of relative pore fluid stresses as a result of the ramp load. Then consolidation reduces the pore fluid stresses in the same way as previously depicted by Figure 5.5 ($T = 0.25$ and $T = 0.50$).

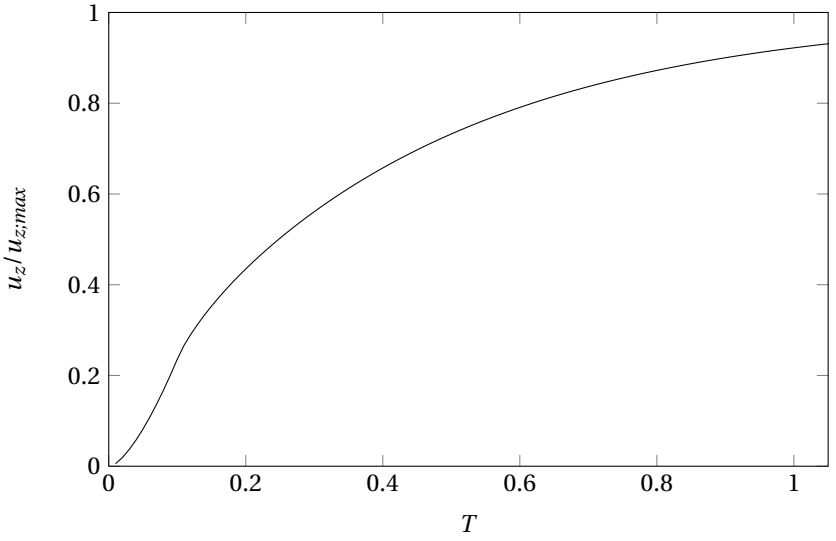


Figure 5.10: Plot of analytical solution of relative settlements $u_z/u_{z;max}$ as a function of time T for ramp load with $t^r = 0.10$ during one-dimensional consolidation.

The analytical solution of the one-dimensional consolidation problem for ramp loading is used as a basis for evaluating the performance of the numerical model. In addition to the development of the relative pore water pressure, the settlement and flux at the top of the sample will be evaluated. The settlement at the top of the sample is the result of the accumulation of strains during consolidation. Using the one-dimensional compressbility $m_z = 1/K^s$, the settlement of the top u_z is elaborated as follows:

$$\begin{aligned} u_z = 2\int_0^h \epsilon_z\, dz &= 2m_z \int_0^h \sigma_z'\, dz \\ &= 2m_z \int_0^h \left(\sigma_z - p\right) dz \\ &= 2m_z q \int_0^h \left(1 - p/p^0\right) dz \end{aligned} \tag{5.85}$$

The last line of Equation 5.85 uses the original starting point that the total stress remains constant and equals both the surcharge load q and reference (maximum) pore fluid stress p^0, i.e. $p^0 = q = \sigma_z$. Substitution of the solution 5.81 into the last line of Equation 5.85 results in an expression for the settlement at the top:

$$\begin{aligned} u_z &= m_z \sigma_z h \left(1 - \left(\frac{8}{\pi^2}\right)\right) \sum_{j=1}^{\infty} \left\{ \frac{1}{(2j-1)^2} \exp\left[-\frac{(2j-1)^2\pi^2}{4} \frac{c_z t}{h^2} \right] \right\} \\ &= u_{z;max} \left(1 - \left(\frac{8}{\pi^2}\right)\right) \sum_{j=1}^{\infty} \left\{ \frac{1}{(2j-1)^2} \exp\left[-\frac{(2j-1)^2\pi^2}{4} \frac{c_z t}{h^2} \right] \right\} \end{aligned} \tag{5.86}$$

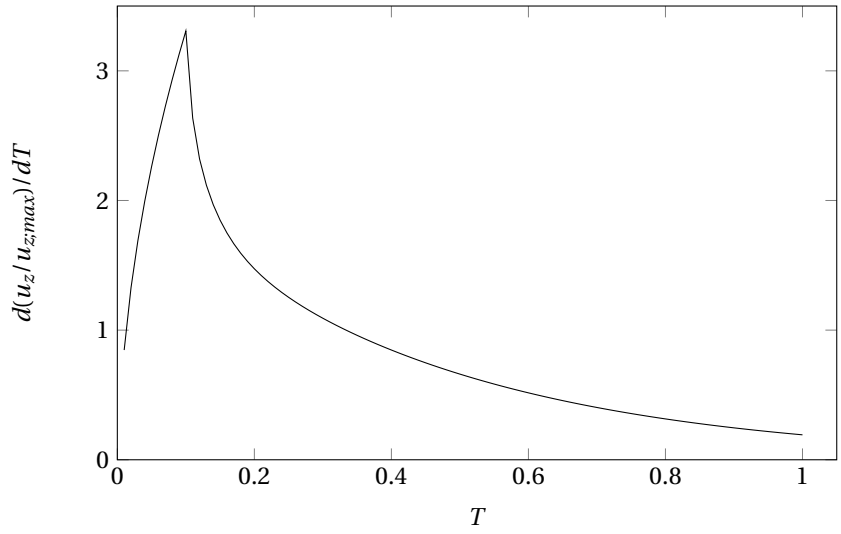


Figure 5.11: Plot of analytical solution of (relative) flux for incompressible pore fluid for ramp load with $T^r = 0.1$ as a function of time T.

The second line of Equation 5.86 introduces the maximum settlement at the top $u_{z;max} = m_z \sigma_z h$, which will be used to normalise the calculated settlements. The resulting plot for a ramp load with t^r is shown in Figure 5.10. Initially, the rate of deformation increases as a result of the ramp load. After $T = 0.1$ the rate of deformation gradually decreases, as would be expected.

The flux through the top of the sample can be calculated if the pore fluid is assumed to be incompressible. In that case continuity requires the flux to be equal to the rate of settlement of the top. The flux w_z thus equals the time derivative of the settlements expressed by Equation 5.86:

$$w_z = \frac{du_z}{dt} = 2u_{z;max} \sum_{j=1}^{\infty} \exp\left[-\frac{(2j-1)^2\pi^2}{4}\frac{c_z t}{h^2}\right] \tag{5.87}$$

Figure 5.11 plots the (relative) fluxes as a function of characteristic time T for a ramp load with T^r. The flux measure at the vertical axis has been calculated from the dimensionless relative settlement and characteristic time T. The results are consistent with Figure 5.10 with a maximum flux at the end of ramp loading $T^r = 0.1$.

Starting points for numerical evaluation

The performance of the code is verified using the aforementioned analytical solutions. The one-dimensional consolidation problem allows verification of the quasi-static part of the implementation. Being based on a simplified set of governing equations, the performance of the code mainly depends on the selected numerical parameters discretising the spatial and time domains.

Table 5.3: Material input parameters

parameter	value	unit
ρ^f	0	$\mathrm{N\,m^{-3}}$
ρ^g	0	$\mathrm{N\,m^{-3}}$
$\kappa\mu^{-1}$	1	$\mathrm{m^4\,N^{-1}\,s^{-1}}$
E	1	$\mathrm{N\,m^{-2}}$
K^{pf}	10^{15}	$\mathrm{N\,m^{-2}}$
c	1000	$\mathrm{N\,m^{-2}}$

The geometry is modelled using a plane strain, two-dimensional geometry of unit dimensions ($1x1$m). The initial boundary conditions are imposed as illustrated in Figure 5.4, albeit for the top half using the symmetry of the problem. The pore fluid stresses are thus zero at the top boundary, but free at the impervious bottom boundary. The displacements are restricted in the horizontal and vertical directions along the bottom boundary and in the horizontal direction along the left and right boundaries. The left and right boundaries are impervious, thereby restraining the fluxes in the horizontal direction. At the top boundary, where there are no restrictions for the flux, a total vertical ramp load q is imposed with $T^r = 0.5$. The actual value of the top load ($1\,\mathrm{N\,m^{-2}}$) is irrelevant, provided that normalised quantities are used to express the development of the consolidation process.

Considering the purpose of the verification, the selection of the soil and pore fluid parameters is based on convenience rather than being a realistic reflection of soil conditions. The default setting of the code is a Mohr-Coulomb material. In order to make sure that the response remains elastic during the analysis a relatively large value of the cohesion as compared to the load is assigned. The Young's Modulus E of the soil is equivalent to the bulk stiffness K^s for oedometric loading. Both the parameters related to the hydraulic conductivity and stiffness of the soil are assigned values equal to one, i.e. $E = 1\,\mathrm{N\,m^{-2}}$ and $\kappa/\mu = 1\,\mathrm{m^4\,N^{-1}\,s^{-1}}$. A very large value is assigned to the stiffness of the pore fluid ($K^{pf} \to \infty$) to ensure that the flux through the boundaries equals the vertical compression of the soil skeleton. Substitution of the parameters into Equation 3.101 yields $c_z = 1\,\mathrm{m^2\,s^{-1}}$ and, as a consequence, $T = t$. In order to eliminate the inertial terms in the implementation, zero values are assigned to the masses of the pore fluid and soil ($\rho^f = 0\,\mathrm{kg\,m^{-3}}$, $\rho^g = 0\,\mathrm{kg\,m^{-3}}$). Table 5.3 provides an overview of the material input parameters.

The numerical parameters that need to be specified concern the element (element size Δx, type of element, number of nodes, number of integration points), time integration (time step Δt, time integration parameter θ, number of time steps) and the required ac-

curacy (convergence tolerances, maximum number of iteration steps). The number of elements are varied between one, two and four. As the problem is one-dimensional, the mesh is only refined in the vertical direction. The selected time step depends on the value of T^r and the numerical stability. The time step should be a fraction of T^r to capture the loading stage accurately. However, numerical accuracy puts a constraint on the choice of the time step Δt. Vermeer and Verruijt [27] derive an accuracy condition for (quasi-static) consolidation:

$$\Delta t \geq \frac{1}{6} \frac{(\Delta x)^2}{\theta c^z} T^r \tag{5.88}$$

The selected values are fractions of $T^r = 0.5$, while still satisfying Equation 5.88 (see Table 5.4). The number of time steps follows from the total, simulated time that equals $T = 3$. The convergence criteria are based on the maximum precision of reals in Fortan 95. When decreasing the time steps the tolerances are relaxed to establish convergence. Table 5.4 provides an overview of the numerical input used in the simulations. Larger numbers of elements were examined, but the results showed only minor differences with the values calculated from four elements.

Table 5.4: Numerical input parameters for varying number of elements (el.)

parameter	**value**			**unit**
	1 el.	2 el.	4 el.	
Δt	0.5	0.125	0.03125	s
number steps	6	24	96	-
T^r	0.5			-
θ	0.5			-
tolerance	10^{-15}	10^{-14}	10^{-12}	-

The calculated relative pore fluid stresses p/p^0, the settlements of the top boundary $u_z/u_{z,max}$ and the normalised fluxes expressed by $d\left(u_z/u_{z,max}\right)/dT$ are compared to the analytical solution. The values of p/p^0 are considered at one of the bottom nodes, i.e. at $z = h$ in Figure 5.4. The output of the fluxes requires further consideration. The selected soil and pore fluid parameters allow a direct comparison between the (dimensionless) normalised fluxes $d\left(u_z/u_{z,max}\right)/dT$ and the calculated fluxes expressed in $\mathrm{m\,s^{-1}}$. There are two ways to calculate the fluxes through the top boundary using the finite element model. The calculated nodal mass residual f^{s_m} at the top boundary is the result of a flux. The sum of the two residuals thus yields the total flux through the top boundary. It should be noted that the residuals are calculated at the interpolated time $t_\theta = \theta t_1 + (1-\theta) t_0$:

$$w_z\Big|_\theta = -\sum_{s=1}^{2} f^{s_m} \tag{5.89}$$

The minus sign accounts for the notion that an upward flux corresponds with a negative value of the residuals, but a positive value of the flux. Alternatively, the fluxes are calculated using the relative pore fluid velocity at one of the top nodes. In this case, the relative pore fluid velocity in the vertical direction v_z^{tn} should be multiplied by the (presumed constant) porosity and integrated along the top boundary S^{tb}:

$$w_z\Big|_t = \int_{S^{tb}} n v_z^{tn} dS \tag{5.90}$$

The absolute values of p/p^0, $u_z/u_{z,max}$ and $w_z\Big|_t$ will be compared to the analytical solutions. A more detailed view on the results is provided by using the error of the variable under consideration. The error r^{er} is defined using the normalised, absolute value of the difference between the calculated value r^{cal} and analytical value r^{an}, expressed as a percentage:

$$r^{er} = \frac{\left| r^{cal} - r^{an} \right|}{r^{peak}} * 100\% \tag{5.91}$$

The next section will examine the performance of the code by verifying the output for different levels of refinement of the mesh. The type of element that will be used is the quadrilateral element [1]. The displacements are calculated at eight nodes, while the pore fluid stresses and relative pore fluid velocities are calculated at the four corner nodes. In the subsequent section, other types of elements that may be useful when moving on to dynamics are considered.

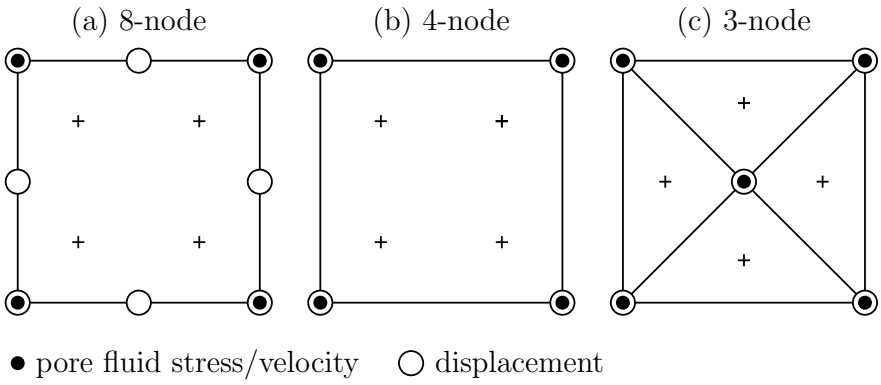


Figure 5.12: Types of elements varied: (left) conventional, quadrilateral element ('8 node'), (center) four-node quadrilateral element ('4 node'), (right) four-node quadrilateral element subdivided into four triangular elements ('3 node').

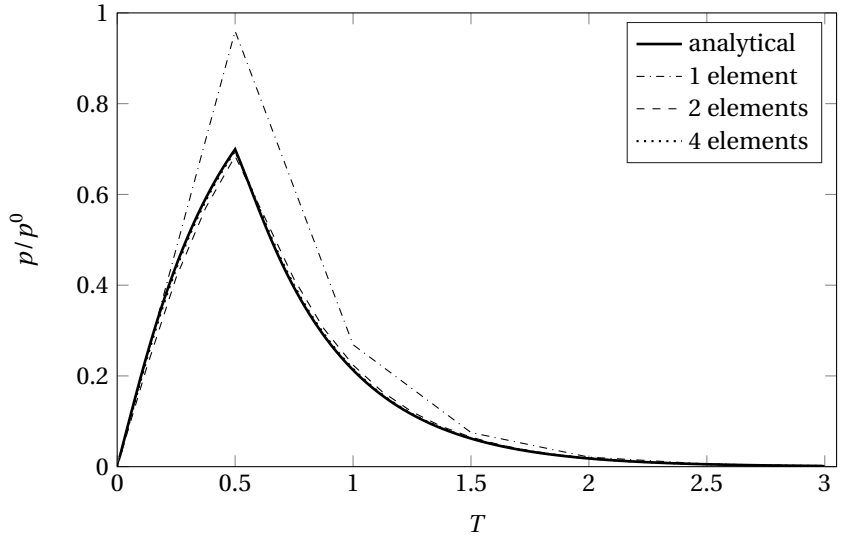


Figure 5.13: Results of normalised pore fluid stresses p/p^0 at level $z/z^0 = 1$ as a function of the characteristic time T for a ramp loading time $T^r = 0.5$ and different levels of refinement.

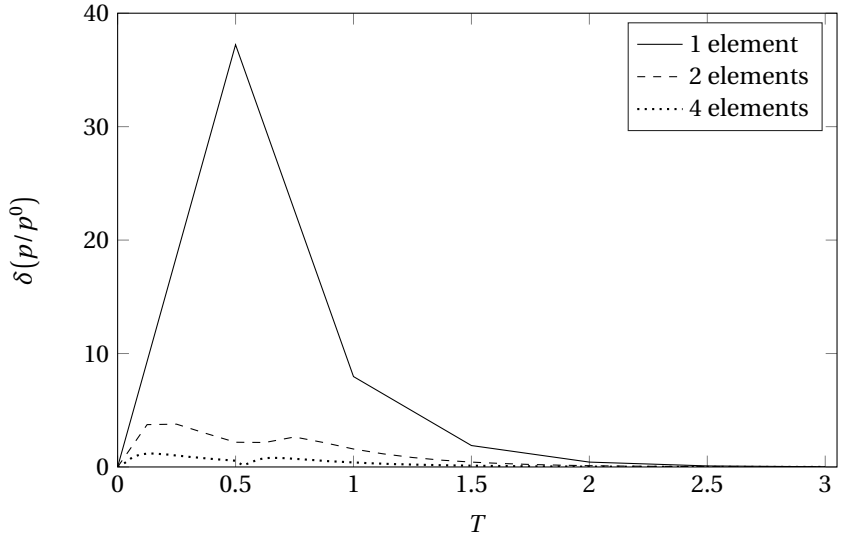


Figure 5.14: Error of p/p^0 at level $z/z^0 = 1$ for a ramp loading time $T^r = 0.5$ and for three levels of refinement.

Number of elements

In quasi-static consolidation problems one conventionally uses quadrilateral elements, where displacements are assigned to eight nodes and pore fluid stresses to four nodes [2] (see Figure 5.12 (a)). Four integration points are assigned to both, which means that the pore fluid stresses are fully integrated, while the displacements are under-integrated. Considering the close relation to the pore fluid stresses, the pore fluid velocities are also assigned to the four corner nodes with full integration. Using these conventional elements, the performance of the model for one, two and four elements was considered.

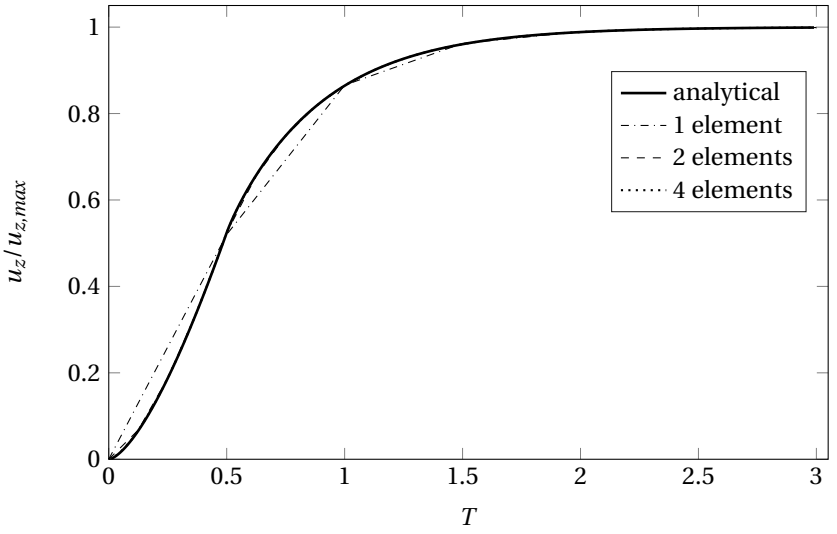


Figure 5.15: Normalised settlements $u_z/u_{z,max}$ during ramp loading with $T^r = 0.5$ for one, two and four elements.

Figure 5.13 plots the development of the relative pore fluid stress p/p^0 at level $z/z^0 = 1$ for different numbers of elements and for the analytical solution. The model with a single element strongly overestimates p/p^0 at $T^r = 0.5$. The overestimate gradually decreases for larger values of T. The deviation is attributed to the relatively large time step that equals the characteristic ramp loading time, that is $\Delta t = T^r$. The model is not able to correct the calculated values within the ramp loading time. Furthermore, the mesh is relatively coarse with pore fluid stresses only being calculated (or imposed) at the top and bottom boundary. The results with two and four elements seem to fit the analytical solution well. Figure 5.14 shows the corresponding errors and thereby allows for a more detailed consideration of these results. The error indeed decreases with an increasing number of elements, leaving an error of 1% or lower for four elements. In all three cases considered, the largest error is produced during the first time step. Then, the error rapidly decreases. The model with two and four elements shows a subsequent increase just after $T^r = 0.5$. Apparently, the error is sensitive to abrupt changes in the loading conditions. The last part of the time series shows a gradual decrease of the error towards zero.

The corresponding normalised settlements $u_z/u_{z,max}$ are shown in Figure 5.15. Similar conclusions can be drawn with respect to the settlements. There is a clear deviation for the model with one element, which seems to be caused by the coarse discretisation. The errors are relatively small compared to the pore fluid stresses, which is related to the more gradual development of the settlements that accumulate in time. The results for two and four elements are the same, as the curves practically coincide.

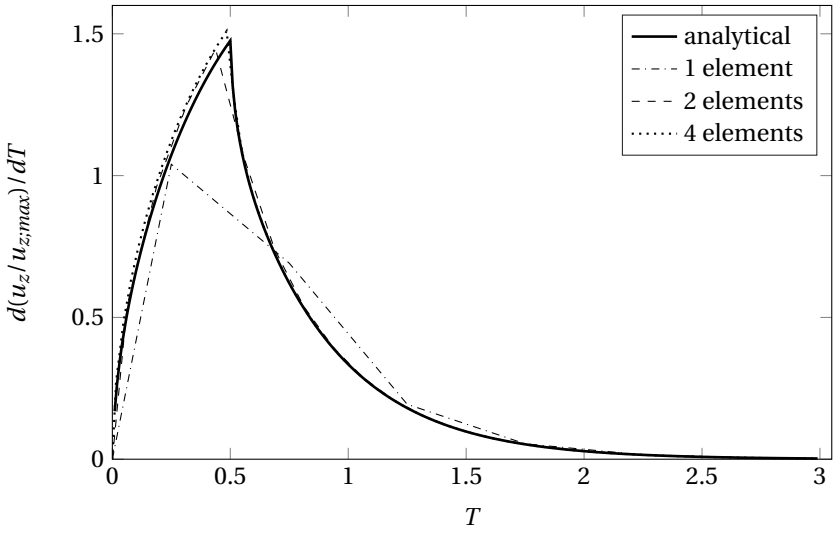


Figure 5.16: Normalised fluxes derived from residuals at interpolation points t_θ for ramp loading with $T^r = 0.5$ and different levels of refinement.

The fluxes are depicted for the values derived from the residuals (Equation 5.89, Figure 5.16) and the relative pore fluid velocities (Equation 5.90, Figure 5.17). The residuals are defined at the interpolation time $t = \theta t_1 + (1-\theta) t_0$, which clearly affects Figure 5.16. The simulation with one element does not reproduce the peak at $T^r = 0.5$, but well reproduce the points before ($T^r = 0.25$) and after the peak ($T^r = 0.75$). Only the values at the interpolation points are plotted, which is where the model aims to obtain accurate results. The values at the time steps, which are not plotted, oscillate around the values at the integration points depicted in Figure 5.16. Refinement of the mesh into two or four elements leads to a good fit with the analytical solution. Calculating the fluxes from the relative pore fluid velocity (Figure 5.17) also leads to an accurate fit. The model with a single element suffers from the coarse discretisation, but nonetheless follows the trend from the analytical solution. Mesh refinement leads to relatively accurate results. Hence, both options to calculate the flux from the finite element model produce good fits with the analytical solution.

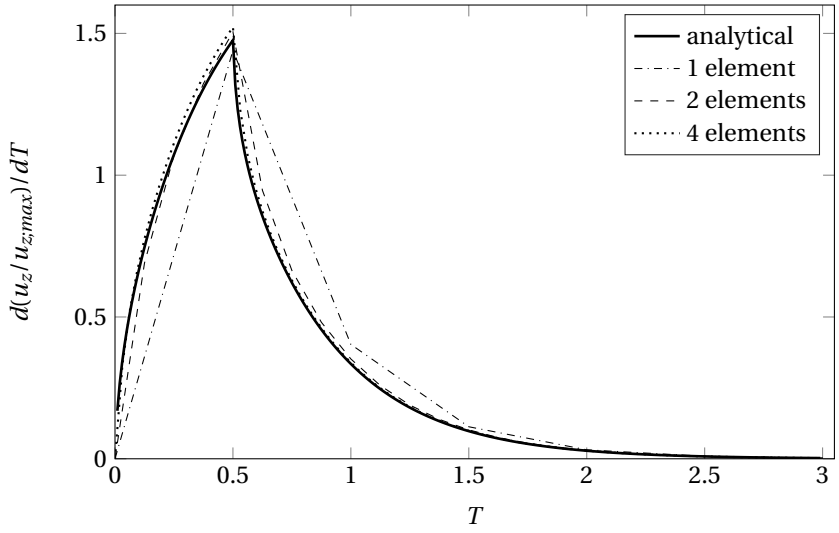


Figure 5.17: Normalised fluxes derived from nodal relative pore fluid velocities for ramp loading with $T^r = 0.5$ and different levels of refinement.

Type of elements

The second variation that will be considered concerns the type of elements. The element will be modified step-wise. First, the four nodes will be assigned to the displacements, thereby creating a uniform element where all nodal free variables are fully integrated ('4 node', Figure 5.12, (b)). Then, the resulting element is subdivided by including a cross and a node in the center ('3 node'). As a consequence, four triangular elements are created with three nodes applied to each of the nodal freedom variables (Figure 5.12 (c)). Each of the triangular elements is assigned one integration point, which implies that each of the nodal freedom variables is fully integrated. The Author believes that the resulting elements suit dynamic analyses. However, their performance for quasi-static consolidation analyses is to be investigated.

Even though it is common to assign eight nodes to displacements and four to pore fluid stresses, it is unclear what the actual effects are of assigning four nodes to all nodal freedoms. Potts and Zdravkovic [29] state there is no theoretical basis to assume that the performance will be much poorer when four nodes are assigned to displacements. Zienkiewicz et al. [1] on the other hand expect inaccuracies (oscillations) for pore fluid stresses when these elements are used. The performance of the four-node and subdivided elements will be compared with the conventional quadrilateral, eight-node element for the aforementioned case of one-dimensional consolidation during ramp loading with $T^r = 0.5$. An objective comparison requires a similar amount of freedom variables for the types of elements. Referring to the nodal displacements, the performance of two quadrilateral elements (Figure 5.12, (a)) will be compared to four elements of the other types (Figure 5.12, (b) and (c)) in the vertical z-direction. For a detailed comparison, the results will mostly be compared in terms of the error (Equation 5.91).

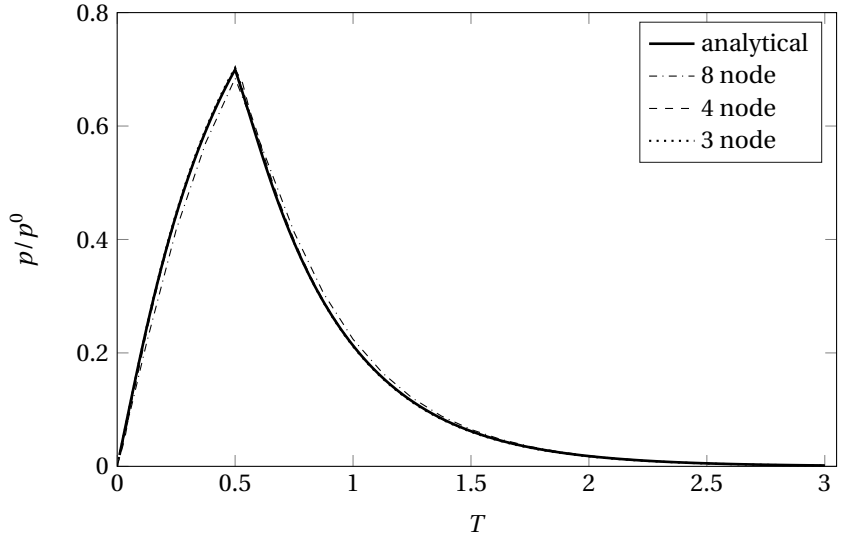


Figure 5.18: Relative pore fluid stresses during ramp loading with T^r for analytical solution and three types of element.

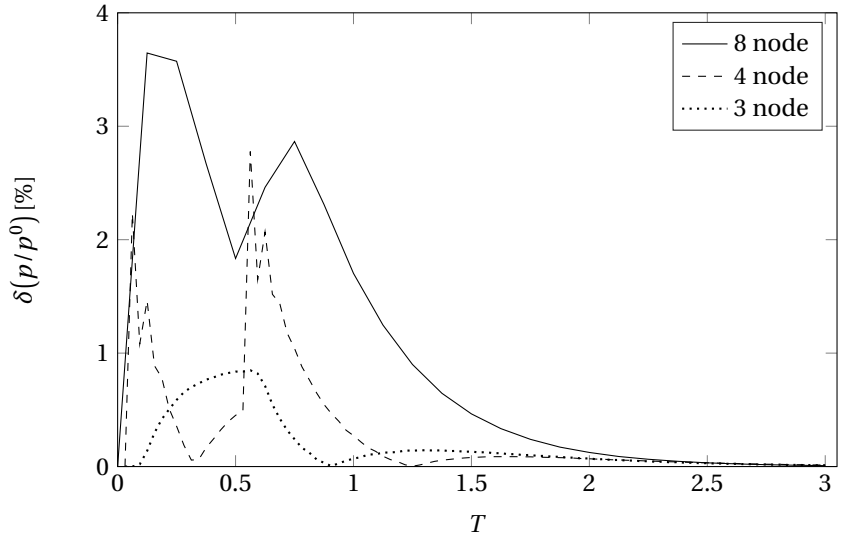


Figure 5.19: Error of relative pore fluid stresses during ramp loading with T^r for three types of element.

For the sake of completeness, Figure 5.18 plots the development of the relative pore fluid stresses p/p^0 for the analytical solution and the three types of element. Even though there are small deviations from the analytical solution, the performance in all three cases seems to be rather good. Figure 5.19 allows for a more detailed consideration of the results by comparing the corresponding errors. Recall the performance of the conventional, '8-node' element from Figure 5.14. The error shows a peak after the first time step, decreases rapidly to a minimum at $T^r = 0.5$ and subsequently increases once more, suggesting a reduced performance after abrupt changes in the loading conditions. Figure 5.19 once more shows the error in the relative pore fluid stresses for the two '8-node' elements. The '4-node' elements show a similar tendency, albeit with an oscillation around the peaks. As for the '8-node' elements, the solution converges rather rapidly after the ramp loading time T^r. The response for the subdivided three-node ('3-node') elements differs from the others. The error after the first time step is very small. The maximum error is reached at the ramp loading time T^r, rather than just after. It seems that this type of element can cope well with abrupt changes in the loading conditions. Overall, the performance of each of the three types of elements in terms of the error $\delta(p/p^0)$ seems satisfactory, but the '3-node' elements are the most accurate. It should be noted that the model with the '3-node' elements also has the highest number of freedom variables for the pore pressures.

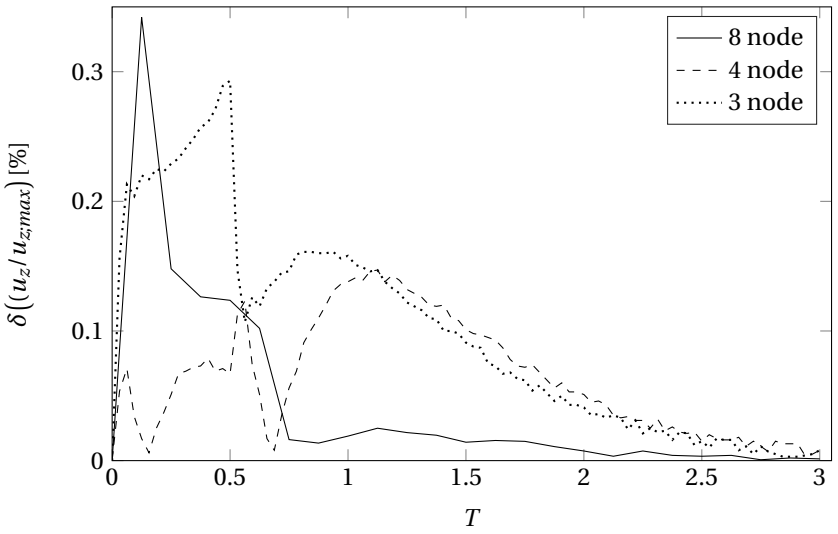


Figure 5.20: Error in settlements during ramp loading with $T^r = 0.5$ for three types of element.

Figure 5.20 plots the corresponding error in terms of normalised settlements $u_z/u_{z;max}$ for the three types of elements. The errors in terms of relative settlements are generally very small. The peak error after the first time step is the largest for the '8-node' elements, which has the best performance during the last part of the plot ($T \geq 0.7$). The error with

the '4-node' elements fluctuates before gradually decreasing after $T \geq 1$. The '3-node' elements show a peak in the error of normalised settlements at the ramp loading time $T^r = 0.5$ and a gradual decrease from $T \approxeq 0.9$.

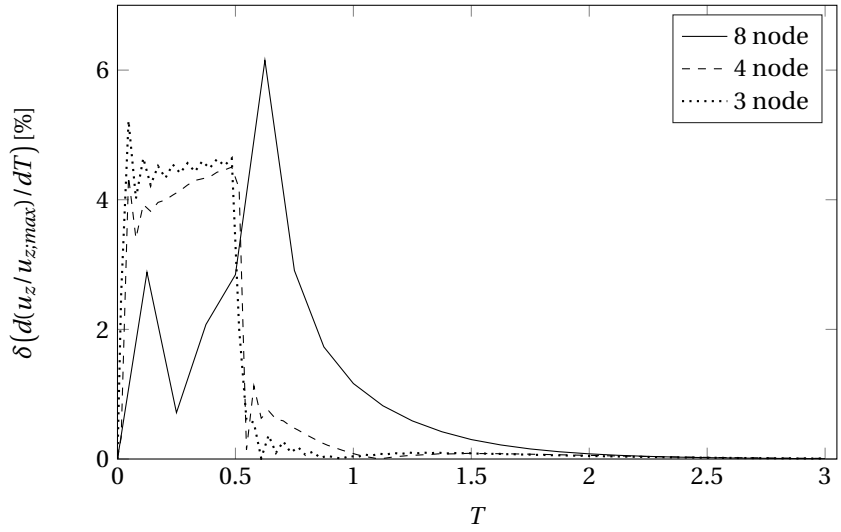


Figure 5.21: Error of normalised fluxes as derived from nodal relative pore fluid velocities for ramp loading with $T^r = 0.5$.

Finally, the error of the normalised fluxes are plotted in Figure 5.21 for the three types of element. The values of the normalised fluxes were derived from the nodal, relative pore fluid velocities as previously done in Figure 5.17. The response of the '3-node' and '4-node' elements is very similar. During the first part ($T \leq 0.5$), the error is more or less constant around 4%, after which it rapidly decreases to values close to zero. The '8-node' elements on the other hand show peaks after the first time step and the time step after the ramp loading time. It is concluded that discretisation using quadrilateral elements with four nodes does not have a significant effect on the performance of the model. When it comes to abrupt changes in the loading conditions, the subdivided, triangular elements have the best performance in terms of pore fluid stresses. This characteristic thus suggests the good performance of these elements for dynamic (undrained) analyses.

5.4.3. Conditions for dynamics

Verification of the code for dynamics is beyond the scope of this thesis. The accuracy and numerical stability will be treated, albeit concisely. This subsection aims at defining the conditions that are set by the accuracy and numerical stability when combining both the quasi-static and subsequent dynamics stage during the start of movement of the bed.

First, some starting points are recalled. For the sake of (numerical) energy consistency

an interpolation parameter has been selected equal to $\theta = 0.5$, while the parameter range $0.5 \leq \theta \leq 1$ is unconditionally stable [30]. As a consequence, the following accuracy condition applies for quasi-static consolidation [27]:

$$\Delta t \geq \frac{1}{6} \frac{(\Delta x)^2}{\theta c^z} \tag{5.88}$$

In addition, the following Courant-condition applies for the numerical simulation of dynamic wave propagation:

$$\Delta t \geq \frac{2\Delta x}{\pi c_s} \tag{5.92}$$

Herein, c^s defines the shear wave velocity which, for elasticity, depends on the shear modulus of the soil skeleton G and the bulk volumetric mass ρ:

$$c^s = \sqrt{\frac{G}{\rho}} \tag{5.93}$$

On the other hand, the time step should be sufficiently small to capture the dynamic phenomenon with a sufficiently high resolution. If ω denotes the characteristic frequency of the signal considered, the Nyquist-frequency defines the upper bound of the time step:

$$\Delta t \leq \frac{2}{\omega} \tag{5.94}$$

It is concluded from Equations 5.92 and 5.94 that the conditions for accuracy and stability during dynamics are satisfied if the selected element size Δx is sufficiently small:

$$\Delta x \leq \frac{\pi c^s}{\omega} \tag{5.95}$$

Considering the instant of transition from statics to dynamics, both Equations 5.88 and 5.92 should be satisfied simultaneously, which gives:

$$\Delta x = \frac{12\theta}{\pi} \frac{c_z}{c^s} \tag{5.96}$$

Typical, approximate values for a loose sand are $c_z = 10^{-4}\mathrm{m}^2\,\mathrm{s}^{-1}$ and $c^s = 10^2\mathrm{m}\,\mathrm{s}^{-1}$, which leads to an optimum element size of the order of $\Delta x = 10^{-6}\mathrm{m}$. The corresponding time step will be of the order of $\Delta t = 10^{-8}\mathrm{s}$. Both values are very small, which would make the simulation numerically costly. Furthermore, the requirement of modeling both the static consolidation and dynamic wave propagation phase simultaneously may imply conflicting requirements with respect to the refinement of the mesh size. For the accurate modelling of consolidation phenomena, the element size Δx should be a minimum where the gradients of the pore fluid stress and deviatoric strain are a maximum. The dynamic phenomena with propagating compressional and shear waves reach all elements in the mesh, thereby requiring the element mesh size Δx to be distributed uniformly. Molenkamp [9] suggests an alternative approach by limiting the maximum deviatoric strain increment at all integration points, thereby imposing a restraint on the

maximum time step Δt. The corresponding maximum element size Δx follows from the Nyquist-frequency (Equation 5.94) and the Courant stability condition for wave propagation (Equation 5.92):

$$\Delta x \leq \frac{\Delta t \pi c^s}{2} \tag{5.97}$$

The calculation should be terminated as soon as the element size Δx becomes too large during subsequent reductions of time step Δt towards instability. The only way to continue the calculation is by constructing a finer mesh.

5.5. Towards modelling of static liquefaction of saturated loose sand

5.5.1. Introduction

This section is based on a paper published at the conference COMGEO in 2011 [31]. The paper addresses a formulation that can be used to model the evolution of the void ratio towards the critical state for monotonical, deviatoric loading. Such a formulation is required when describing the stage following the occurrence of (undrained) instability, i.e. the post-stability flow during liquefaction flow slides. The formulation is developed to extend the existing MONOT-model [12] with a critical state formulation. Some of the parameters presented in this section are compliant with the MONOT-model.

In engineering practice the concept of "State Parameter" [32, 33] has been shown to be versatile for quantifying the possible occurrence of undrained instability of static liquefaction of saturated sands, not least due to the apparent correlation with the in-situ density as estimated based on measured cone penetration resistance. This "State Parameter" is expressed by the scalar variable quantifying the difference between the current void ratio e and the critical void ratio at the current mean effective stress e^{cs}, namely

$$\psi = e - e^{cs} \tag{2.5}$$

This section describes the modelling of the change of void ratio of sands during monotonically increasing deviatoric deformation towards the critical state in a way compatible with this "State Parameter" concept. In this study a frictional elasto-plastic model is developed with two state parameters, namely the void ratio and the mean effective stress. One classical main characteristic of this constitutive model concerns a relation between the rates of volume change and deviatoric deformation according to the stress-dilatancy theory [21, 34, 35]. The second more novel characteristic concerns a description of the remoulding resistance towards the critical state, involving a relation between the mean effective stress, the deviatoric stress and the void ratio. In particular, the latter has been missing in similar aimed developments in the literature [36–39].

For monotonically increasing deviatoric deformation of initially loose sands the combined formulation results in hardening due to contractant remoulding towards the critical state. Furthermore, for initially dense sands the post-peak softening towards the critical state is considered to occur due to dilatant remoulding. However, for dilatant mate-

rial states localisation of deformation usually occurs as shear bands tend to develop and subsequent plastic deformation remains mainly limited to the shear bands [40]. In such cases the globally observed post-peak softening of the whole specimen seems more brittle than of the actual uniformly deforming material in the shear bands [41], depending on, for example, the ratio of applied specimen size to mean grain size. Unfortunately, this phenomenon of shear band formation in dense sands also implies that, for proper experimental validation of the softening aspect of the constitutive model, micro-mechanical testing and observations may be indispensable. Nevertheless, combining the concepts of stress-dilatancy and remoulding resistance in the frictional elasto-plastic model guarantees that, for any monotonically increasing type of uniform deviatoric deformation, a critical state is always reached. This formulation is expected not only to enable the appropriate simulation of static liquefaction, but also the subsequent post-stability liquefied flow.

5.5.2. Formulation of model

Surface of remoulding resistance

For the considered constitutive model, first the existence of a surface of remoulding resistance is postulated. This surface of remoulding resistance is considered to be approached gradually for any drained proportional deviatoric deformation with fixed principal strain directions and at any constant mean effective stress, producing correspondingly fixed principal directions of effective stress. However, for simultaneously rotating principal strain directions different surfaces of remoulding resistance may be expected [42]. For fixed principal strain directions the surface of remoulding resistance is a function of the principal effective stresses $\boldsymbol{\sigma}^{(k)}$, the void ratio e and the plastic deviatoric strain e^p for a sufficiently large magnitude, e.g. $e^p >> 1$. Consequently this surface is formally described by a function of the following form:

$$f\left(\boldsymbol{\sigma}^{(k)}, e\right) = 0 \tag{5.98}$$

Such a surface of remoulding resistance is illustrated in Figure 5.22 for drained purely deviatoric triaxial compression at constant mean effective stress. For this frictional material model the maximum remoulding resistance is expressed in terms of the deviatoric stress level $T/S\Big|^p$, involving both the principal deviatoric stress vector in principal stress space, directed in the π-plane with scalar magnitude T, and the principal isotropic effective stress vector along the space diagonal in principal stress space with scalar magnitude S. These magnitudes are expressed in terms of the axial and radial effective stresses $\boldsymbol{\sigma}_a$ and $\boldsymbol{\sigma}_r$, respectively, by:

$$T = \sqrt{\frac{2}{3}}\,(\boldsymbol{\sigma}_a - \boldsymbol{\sigma}_r) \tag{5.99}$$

$$S = \sqrt{\frac{1}{3}}\,(\boldsymbol{\sigma}_a + 2\boldsymbol{\sigma}_r) \tag{5.100}$$

Similar types of deviatoric and isotropic quantities in principal strain space can be expressed for triaxial strain rates based on the axial and radial plastic strain rates $\dot{\epsilon}_a^p$ and $\dot{\epsilon}_r^p$,

respectively. Then the magnitudes of the deviatoric and isotropic strain rates are respectively:

$$\dot{e}^p = \sqrt{\frac{2}{3}}\left(\dot{\epsilon}_a^p - \dot{\epsilon}_r^p\right) \tag{5.101}$$

$$\dot{v}^p = \sqrt{\frac{1}{3}}\left(\dot{\epsilon}_a^p + 2\dot{\epsilon}_r^p\right) \tag{5.102}$$

Then the scalar plastic deviatoric strain e^p is obtained by integration in time, namely:

$$e^p = \int_0^t \dot{e}^p \, dt \tag{5.103}$$

Figure 5.22 illustrates a decreasing remoulding resistance with increasing void ratio e.

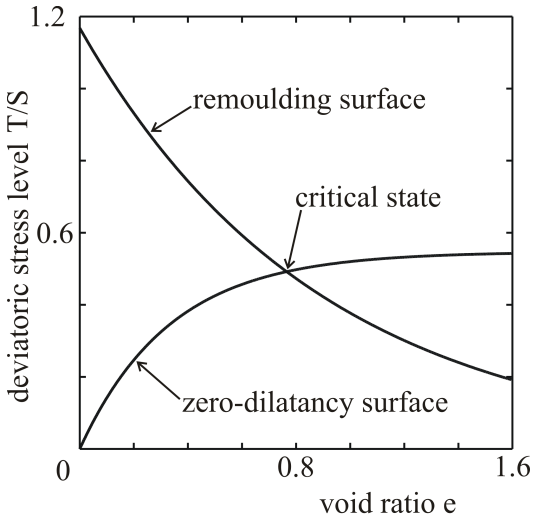


Figure 5.22: Illustration of remoulding and zero-dilatancy surfaces with their "critical state" intersection point. Illustration refers to a isotropic stress level of $S/p^a = \sqrt{3}$ with the mean atmospheric pressure equal to $p^a = 100\,\text{kPa}$.

Surface of zero-dilatancy

In Figure 5.22 a zero-dilatancy surface [21, 34] for triaxial compression is also illustrated, considering the mobilised friction level at zero-dilatancy to increase from zero at zero void ratio e to reach its maximum value at a void ratio around $e = 1$. It may be noted that, for the experimental determination of the zero-dilatancy surface, standard macroscopic laboratory tests on sand specimens may suffice because shear band generation will usually occur at effective stress states above this surface. However, for the determination of the surface of remoulding resistance, due to the occurrence of shear bands microscopic specimens and measurement methods [41] may be necessary.

The intersection point of the surfaces of remoulding resistance and zero-dilatancy concerns the critical state. This is understood by considering that on the left side of this intersection point the remoulding resistance occurs above the zero-dilatancy surface; thus it involves dilation during continuing distortion, inducing loosening due to dilation and thus an increasing void ratio. On the other hand, on the right hand side of the intersection point the surface of remoulding resistance occurs below the zero-dilatancy surface, thus inducing contraction during continuing distortion until a state of constant volume is reached at the intersection point, which is completely consistent with the definition of the critical state.

Critical state curve

The critical state curve shows the dependence of the critical void ratio e^{cs} on the isotropic stress level S/p^a as illustrated in Figure 5.23. This relation is approximated by the following expression, namely:

$$e^{cs} = f\left(\frac{S}{p^a}\right) = \left(1 + e^{cs;0}\right) \exp\left(-C^* \left(\frac{S}{p^a}\right)^{C^p}\right) - 1 \tag{5.104}$$

For the illustration in Figure 5.23 the following parameter values have been applied, namely $e^{cs;0} \approx 0.82$, $C^* = 0.026$ and $C^p \approx 0.3$. All soil parameters are collected in Table 5.5.

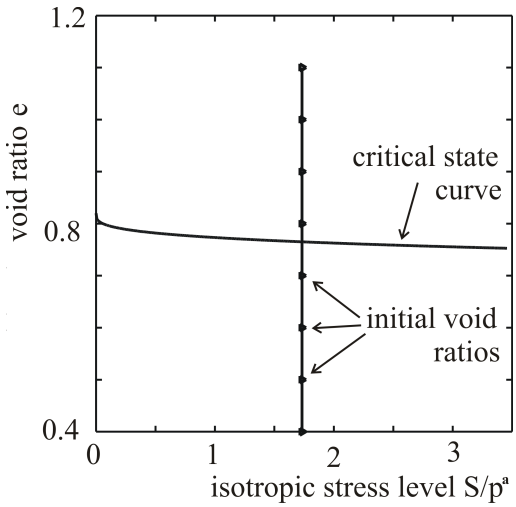


Figure 5.23: Illustration of critical state curve and the considered range of initial void ratios e^i at isotropic stress level $S/p^a = \sqrt{3}$.

To demonstrate the effects of the combined concepts of stress-dilatancy and remoulding resistance, a series of numerical simulations of drained purely deviatoric triaxial compression with monotonically increasing deviatoric plastic strain will be considered later

in this section. These simulations will be done for a range of initial void ratios, namely $0.4 \leq e^i \leq 1.1$, and a constant isotropic effective stress level $\frac{S}{p^a} = \sqrt{3}$, where p^a is the mean atmospheric pressure and $p^a \approx 100\,\text{kPa}$. These initial states are also indicated in Figure 5.23.

It is noted that, for the above-mentioned parameter values and the isotropic effective stress level $\frac{S}{p^a} = \sqrt{3}$, the corresponding critical void ratio e^{cs} according to Equation 5.104 reads $e^{cs} \approx 0.765$, which is represented by the intersection point of both curves in Figure 5.23.

Formulation of surfaces

For the considered cases of triaxial compression in Figure 5.22, the deviatoric stress level $T/S\Big|^p$ of the surface of remoulding resistance at $S/p^a = \sqrt{3}$ is related to the void ratio e by:

$$\frac{T}{S}\Big|^p = M^p \exp\left(-\beta^p e\right) \tag{5.105}$$

with model parameters M^p and β^p. Then, for the slope of the remoulding surface in the direction of void ratio it follows that:

$$\frac{\mathrm{d}\left(T/S\Big|^p\right)}{\mathrm{d}e} = -\beta^p M^p \exp\left(-\beta^p e\right) = -\beta^p \left(T/S\Big|^p\right) \tag{5.106}$$

The corresponding relation between the deviatoric stress level $T/S\Big|^\mu$ for zero-dilatancy and the void ratio e, illustrated in Figure 5.22, reads:

$$\frac{T}{S}\Big|^\mu = C^\mu \left(1 - \exp\left(-\zeta^\mu e\right)\right) \tag{5.107}$$

with model parameters C^μ and ζ^μ. Then for the slope of the zero-dilatancy surface in the direction of void ratio it follows that:

$$\frac{\mathrm{d}\left(T/S\Big|^\mu\right)}{\mathrm{d}e} = \zeta^\mu C^\mu \exp\left(-\zeta^\mu e\right) \tag{5.108}$$

5.5.3. Application of the formulation

Parameter determination based on critical state

The critical state is reached at the intersection of the surfaces of remoulding resistance and zero-dilatancy, at the critical state void ratio $e = e^{cs}$ and deviatoric stress level:

$$\frac{T}{S}\Big|^{cs} = \frac{T}{S}\Big|^p = \frac{T}{S}\Big|^\mu \tag{5.109}$$

Then, at the intersection point, from 5.105 and 5.107 the following relation is obtained:

$$\frac{T}{S}\Big|^{cs} = M^p \exp\left(-\beta^p e\right) = C^\mu \left(1 - \exp\left(-\zeta^\mu e\right)\right) \tag{5.110}$$

Table 5.5: Mathematical and physical (dimensionless) material parameters

parameter	value	equation	description
critical state curve			
e^{cs}	0.765[(a)]	5.104	critical state void ratio
C^*	0.026	5.104	fitting parameter
C^p	0.3	5.104	fitting parameter
$e^{cs;0}$	0.82	5.104	cs void ratio at $S/p^a = 0$
$(T/S)\Big\vert^{cs}$	0.492[(a)]	5.110	cs deviatoric stress level
initial plastic hardening phase			
E	0.0025	5.122	fitting parameter
E^p	4.2	5.122	fitting parameter
deviatoric stress-plastic strain			
N	3.0	5.126	weighting power
remoulding resistance			
M^p	1.168	5.105,5.111	fitting parameter
β^p	1.13	5.105,5.113	fitting parameter
$\left(\mathrm{d}(T/S)\Big\vert^{p}/\mathrm{d}e\right)\Big\vert^{cs}/(T/S)\Big\vert^{cs}$	-1.13[(a)]	5.113	ratio defining β^p
zero-dilatancy			
C^μ	0.547	5.107,5.111	fitting parameter
ζ^μ	3.00	5.107	fitting parameter
$\left(\mathrm{d}(T/S)\Big\vert^{\mu}/\mathrm{d}e\right)\Big\vert^{cs}/(T/S)\Big\vert^{cs}$	0.336[(a)]	5.114	ratio defining ζ^μ

[(a)] For stress level $\frac{S}{p^a} = \sqrt{3}$

from which it follows for the parameters M^p and C^μ that:

$$M^p = \frac{T/S\Big|^{cs}}{\exp\left(-\beta^p e\right)} \tag{5.111}$$

$$C^\mu = \frac{T/S\Big|^{cs}}{1-\exp\left(-\zeta^\mu e\right)} \tag{5.112}$$

The expressions 5.111 and 5.112 show that parameters M^p and C^μ can be derived based on the observed deviatoric stress level of the critical state $T/S\Big|^{cs}$ if the parameters β^p and ζ^μ are known. Furthermore, from Equation 5.106 the parameter β^p can be expressed in terms of the ratio of the slope $\left(\mathrm{d}(T/S)\Big|^p/\mathrm{d}e\right)\Big|^{cs}$ of the remoulding surface at the critical state and the deviatoric stress level $(T/S)\Big|^{cs}$ at the critical state, namely:

$$\left(\frac{\mathrm{d}(T/S)\Big|^p}{\mathrm{d}e}\right)\Big|^{cs} = -\beta^p \frac{T}{S}\Big|^{cs} \rightarrow \beta^p = \frac{\left(\frac{\mathrm{d}(T/S)\Big|^p}{\mathrm{d}e}\right)\Big|^{cs}}{T/S\Big|^{cs}} \tag{5.113}$$

Similarly, based on Equations 5.108, 5.111 and 5.112 for the ratio of the slope of the zero-dilatancy surface at the critical state $\left(\mathrm{d}\left(T/S\Big|^\mu\right)/\mathrm{d}e\right)\Big|^{cs}$ and the deviatoric stress level $(T/S)\Big|^{cs}$ at the critical state, it follows that:

$$\frac{\left(\mathrm{d}\left(T/S\Big|^\mu\right)/\mathrm{d}e\right)\Big|^{cs}}{(T/S)\Big|^{cs}} = \frac{\zeta^\mu \exp\left(-\zeta^\mu e^{cs}\right)}{1-\exp\left(-\zeta^\mu e^{cs}\right)} \tag{5.114}$$

In principle, from 5.113 and 5.114 parameters β^p and ζ^μ can also be derived if the left slope terms are known, based on experimental data. When applying Equation 5.107 and the last expression of Equation 5.110 the deviatoric stress level at zero-dilatancy $(T/S)\Big|^\mu$ can also be expressed with respect to the critical state resistance $(T/S)\Big|^{cs}$ and critical void ratio e^{cs} at the same isotropic stress level S/p^a by:

$$\frac{T}{S}\Big|^\mu = \frac{T}{S}\Big|^{cs} - C^\mu\left(\exp\left(-\zeta^\mu e\right) - \exp\left(-\zeta^\mu e^{cs}\right)\right) \tag{5.115}$$

This relative form has similarities to the formulation using the State Parameter Ψ (Equation 2.5, [32, 33]). Applying this relative form also for the remoulding resistance $(T/S)\Big|^p$ gives:

$$\frac{T}{S}\Big|^p = \frac{T}{S}\Big|^{cs} + M^p\left(\exp\left(-\zeta^\mu e\right) - \exp\left(-\zeta^\mu e^{cs}\right)\right) \tag{5.116}$$

Stress-dilatancy for triaxial compression

The relation between the increments of the void ratio de and the plastic volumetric strain d$e^{p;vol}$ reads, when applying the sign conventions of continuum mechanics with stretching, tension and thus dilation positive:

$$\mathrm{d}e = (1+e)\mathrm{d}e^{p;vol} \tag{5.117}$$

The increment of the plastic volumetric strain d$e^{p;vol}$ is related to the scalar norm de^p of the incremental plastic deviatoric strain by:

$$\mathrm{d}e^{p;vol} = \sqrt{3}\mathrm{d}v^p = 3\alpha\mathrm{d}e^p \rightarrow \alpha = \frac{1}{\sqrt{3}}\frac{\mathrm{d}v^p}{\mathrm{d}e^p} \tag{5.118}$$

in which the principal incremental isotropic plastic strain vector along the space diagonal in principal strain space has scalar magnitude dv^p and the scalar α is quantified by the application of the stress-dilatancy theory [21, 34], which expresses the dilatancy ratio dv^p/de^p. When applying the sign-convention of continuum mechanics the dilatancy ratio dv^p/de^p for triaxial compression is expressed by [12]:

$$\frac{\mathrm{d}v^p}{\mathrm{d}e^p} = -\frac{2\sqrt{2}\sin\phi_\mu - (3-\sin\phi_\mu)T/S}{(3+\sin\phi_\mu) - 2\sqrt{2}\sin\phi_\mu T/S} \tag{5.119}$$

In the concept of the zero-dilatancy surface the friction angle ϕ_μ at zero-dilatancy is considered to be a function of both the void ratio e and the isotropic stress level S/p^a. This friction angle ϕ_μ is related to the deviatoric stress level $T/S\big|^\mu$ at zero-dilatancy by:

$$\frac{T}{S}\bigg|^\mu = \frac{2\sqrt{2}\sin\phi_\mu}{3-\sin\phi_\mu} \leftrightarrow \sin\phi_\mu = \frac{3T/S\big|^\mu}{2\sqrt{2}+T/S\big|^\mu} \tag{5.120}$$

Then substitution of Equation 5.118 into Equation 5.117 leads to the relation between the incremental plastic deviatoric strain de^p and the increment of the void ratio de as expressed by:

$$\mathrm{d}e = (1+e)\mathrm{d}e^{p;vol} = (1+e)\sqrt{3}\mathrm{d}v^p = (1+e)3\alpha\mathrm{d}e^p \tag{5.121}$$

Deviatoric stress-plastic strain relation

For the initial plastic hardening phase of triaxial compression the following deviatoric stress-deviatoric plastic strain relation is applied [12], namely:

$$e^p = E\left(\frac{T}{S}\bigg|^0\right)^{E^p} \leftrightarrow \frac{T}{S}\bigg|^0 = \left(\frac{e^p}{E}\right)^{\frac{1}{E^p}} \tag{5.122}$$

for which the applied values of parameters E^e and E^p are indicated in Table 5.5. From Equation 5.118 follows the incremental relation between the deviatoric stress level of the initial hardening phase $(T/S)\big|^0$ and the plastic deviatoric strain e^p:

$$\frac{\mathrm{d}\left(T/S\big|^0\right)}{\mathrm{d}e} = \frac{T}{S}\bigg|^0 \frac{1}{E^p e^p} = \frac{1}{EE^p}\left(\frac{T}{S}\bigg|^0\right)^{1-E^p} \tag{5.123}$$

After large deviatoric distortion in triaxial compression the remoulding resistance $T/S\Big|^{p}$ (Equation 5.116) is approached. Differentiation of Equation 5.116 with respect to the void ratio e for a constant isotropic stress level S/p^a gives:

$$\frac{\mathrm{d}\left(T/S\Big|^{p}\right)}{\mathrm{d}e} = -\beta^p M^p \exp\left(-\beta^p e\right) \tag{5.124}$$

Combining Equations 5.121 and 5.124 gives an incremental relation between the deviatoric stress level $(T/S)\Big|^{p}$ and the plastic deviatoric strain e^p, namely:

$$\frac{\mathrm{d}\left(T/S\Big|^{p}\right)}{\mathrm{d}e^p} = \frac{\mathrm{d}\left(T/S\Big|^{p}\right)}{\mathrm{d}e}\frac{\mathrm{d}e}{\mathrm{d}e^p} = 3(1+e)\alpha\beta^p M^p \exp\left(-\beta^p e\right) \tag{5.125}$$

At this stage the incremental relations between, on the one hand the deviatoric stress levels for both the initial plastic hardening phase $(T/S)\Big|^{0}$ (Equation 5.123) and the remoulding resistance after large deviatoric deformation $(T/S)\Big|^{p}$ (Equation 5.124) and, on the other, the plastic deviatoric strain e for purely deviatoric loading in triaxial compression at constant isotropic stress level S/p^a, have been formulated. Next the combined incremental plastic deviatoric stress-strain relation is derived. To this end, first for any deviatoric plastic strain e^p the combined deviatoric stress level T/S can be expressed by:

$$\frac{T}{S} = \frac{(T/S)\Big|^{0}(T/S)\Big|^{p}}{\left(\left((T/S)\Big|^{0}\right)^{N} + \left((T/S)\Big|^{p}\right)^{N}\right)^{1/N}} \tag{5.126}$$

in which the weighting power N is larger than unity. Here, this weighting power N is roughly estimated as $N \approx 3$. Furthermore, it may be noted that in Equation 5.126 T/S describes the yield surface as a function of the stresses for purely deviatoric loading in triaxial compression, while its right-hand side quantities concern functions of the corresponding plastic deviatoric deformation.

Based on 5.126 the following relation between the increments of the deviatoric stress level $\mathrm{d}(T/S)$ and the plastic deviatoric strain $\mathrm{d}e^p$ for purely deviatoric loading in triaxial compression at constant isotropic stress level S/p^a is derived, namely:

$$\frac{\mathrm{d}(T/S)}{\mathrm{d}e^p} = \frac{\mathrm{d}\left(\dfrac{(T/S)\Big|^{0}(T/S)\Big|^{p}}{\left(\left((T/S)\Big|^{0}\right)^{N} + \left((T/S)\Big|^{p}\right)^{N}\right)^{1/N}}\right)}{\mathrm{d}(T/S)\Big|^{0}}\frac{\mathrm{d}(T/S)\Big|^{0}}{\mathrm{d}e^p} + \frac{\mathrm{d}\left(\dfrac{(T/S)\Big|^{0}(T/S)\Big|^{p}}{\left(\left((T/S)\Big|^{0}\right)^{N} + \left((T/S)\Big|^{p}\right)^{N}\right)^{1/N}}\right)}{\mathrm{d}(T/S)\Big|^{p}}\frac{\mathrm{d}(T/S)\Big|^{p}}{\mathrm{d}e^p} \tag{5.127}$$

in which:

$$\frac{\mathrm{d}\left(\dfrac{(T/S)\Big|^0\,(T/S)\Big|^p}{\left(\left((T/S)\Big|^0\right)^N+\left((T/S)\Big|^p\right)^N\right)^{1/N}}\right)}{\mathrm{d}(T/S)\Big|^0}=\frac{\left(T/S\Big|^p\Big|\right)^{N+1}}{\left(\left((T/S)\Big|^0\right)^N+\left((T/S)\Big|^p\right)^N\right)^{(1/N)+1}} \tag{5.128}$$

and:

$$\frac{\mathrm{d}\left(\dfrac{(T/S)\Big|^0\,(T/S)\Big|^p}{\left(\left((T/S)\Big|^0\right)^N+\left((T/S)\Big|^p\right)^N\right)^{1/N}}\right)}{\mathrm{d}(T/S)\Big|^p}=\frac{\left(T/S\Big|^0\Big|\right)^{N+1}}{\left(\left((T/S)\Big|^0\right)^N+\left((T/S)\Big|^p\right)^N\right)^{(1/N)+1}} \tag{5.129}$$

while $\mathrm{d}(T/S)\Big|^0/\mathrm{d}e^p$ and $\mathrm{d}(T/S)\Big|^p/\mathrm{d}e^p$ are described by Equations 5.123 and 5.125, respectively. Finally substituting equations 5.116, 5.125, 5.128 and 5.129 in 5.127 gives the required expression relating the increment of the deviatoric stress level $\mathrm{d}(T/S)$ to the increment of the plastic deviatoric strain $\mathrm{d}e^p$, namely:

$$\begin{aligned}\frac{\mathrm{d}(T/S)}{\mathrm{d}e^p}=&\frac{\left(T/S\Big|^p\Big|\right)^{N+1}}{\left(\left((T/S)\Big|^0\right)^N+\left((T/S)\Big|^p\right)^N\right)^{(1/N)+1}}\frac{1}{EE^p}\left(\frac{T}{S}\Big|^0\right)^{1-E^p}+\\&\frac{\left(T/S\Big|^0\Big|\right)^{N+1}}{\left(\left((T/S)\Big|^0\right)^N+\left((T/S)\Big|^p\right)^N\right)^{(1/N)+1}}3(1+e)\alpha\beta^pM^p\exp\left(-\beta^pe\right)\end{aligned} \tag{5.130}$$

5.5.4. Demonstration of model capabilities

The frictional elasto-plastic material model (Equation 5.130), combining the concepts of remoulding resistance 5.116 and zero-dilatancy 5.119, has been elaborated for purely deviatoric triaxial compression at constant isotropic stress level S/p^a. For any initial void ratio e^i and any isotropic stress level S/p^a this model describes an increment of the deviatoric stress level $\mathrm{d}(T/S)$ as a function of an increment of plastic deviatoric strain $\mathrm{d}e^p$. In this subsection the capabilities of this constitutive model are demonstrated by means of various calculated results for drained purely deviatoric triaxial compression, to reach the critical state for monotonically increasing purely deviatoric large plastic deformation at the ultimate state of monotonic deviatoric plastic flow.

Figure 5.24 illustrates the paths of deviatoric stress level T/S versus void ratio e, starting from the same isotropic effective stress state with $S/p^a=\sqrt{3}$ and for a range of initial

void ratios e^i, namely $0.4 \leq e^i \leq 1.1$. In the initial phase of deviatoric deformation the plastic deviatoric strain e^p is expressed by Equation 5.122. The corresponding change in the void ratio e is calculated using the stress-dilatancy theory as expressed by Equations 5.118, 5.119 and 5.121. Figure 5.24 illustrates that, for the applied scale of the void ratio, the change of void ratio is hardly observable as the paths are practically vertical. When the paths approach the surface of remoulding resistance, rather than intersecting this surface the paths start to bend gradually towards this surface. This characteristic of gradual approach is achieved by the application of Equation 5.126 in combination with Equation 5.130, but becomes less gradual with increasing weighting parameter $m >> 1$. For Figure 5.24 $N = 3$ has been used.

When approaching the surface of remoulding resistance even further, the increasing plastic deviatoric deformation causes decreasing changes of the deviatoric stress level T/S as governed by the local slope of the surface. However, the effect of the corresponding change of the void ratio as expressed by the dilatancy theory 5.119 remains active, causing the paths to proceed towards the critical state, where the plastic dilation rate becomes zero, while the monotonically increasing purely plastic deviatoric deformation can continue.

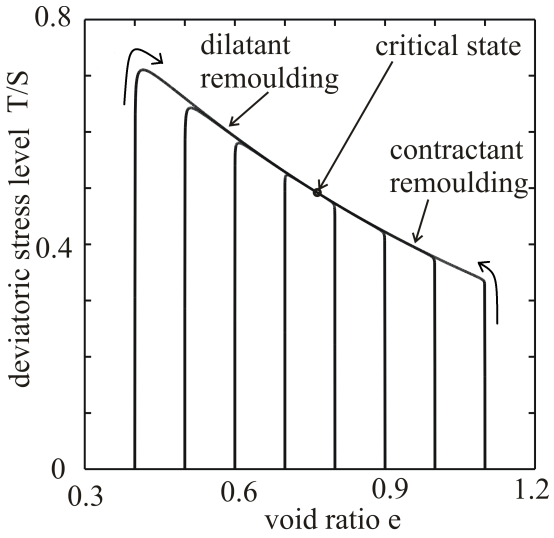


Figure 5.24: Calculated paths of deviatoric stress level T/S and void ratio e towards the critical state for drained purely deviatoric triaxial compression with monotonically increasing deviatoric deformation at constant isotropic stress level $S/p^a = \sqrt{3}$ for a series of initial void ratios $0.4 \leq e^i \leq 1.1$.

The corresponding relation between the deviatoric stress level T/S and the plastic deviatoric strain e^p is shown in Figure 5.25. All stress-strain paths are shown to approach the same critical state, reaching it at very large plastic flow. For the considered initial states looser than critical, the critical state is approached by plastic contraction along

the contractant part of the surface of remoulding resistance. This plastic contraction induces the monotonic plastic hardening illustrated in Figure 5.25 for the considered large initial void ratios: $e^i \geq 0.8$. On the other hand, for the initial small void ratios $e^i \leq 0.8$ peaks are shown to occur in the deviatoric stress-plastic strain paths, as also observed experimentally. Subsequently gradual softening is simulated, which may be much more elongated than observed experimentally when considering element testing. This difference has been explained before to be due to the occurrence of shear band generation, in which the plastic deformation becomes concentrated within the shear bands [41].

Figure 5.26 depicts the calculated paths of the plastic dilatancy ratio $\mathrm{d}v^p/\mathrm{d}e^p$ and the deviatoric stress level T/S. It is noted that the left part concerns contraction and the right dilation. The inclined lines from contraction towards dilation are based on the stress-dilatancy relation 5.119. These inclined stress-dilatancy lines reach their upper limits on a curve fully related to the surface of remoulding resistance. For the initially dense void ratios $e \leq 0.7$ this upper limit concerns softening by dilatant remoulding, while for the initially loose void ratios $e \geq 0.8$ along the upper limit hardening by contractant remoulding occurs. Both parts of the upper limit curve carry the paths to the critical state. All material parameters have been collected in Table 5.5. Apart from the respective equation numbers for their definition, two types of material parameters are indicated; namely, the parameters occurring in the mathematical expressions of the model and the more physical parameters, which in the background are affecting the magnitudes of most other mathematical parameters. The determination of the links between both types of parameters and the physical parameters for observed undrained behaviour is the subject of future research.

5.6. Closing remarks

This chapter was aimed at the development of a finite element model that should be able to capture the initiation of liquefaction flow slides and the first phase of movement of the slope. The corresponding requirements are the coupling of mass and linear momentum, and the incorporation of both statics and dynamics. The modelling of liquefaction using the Finite Element Method involves a number of aspects. This chapter has treated the implementation of the governing equations in a model, its performance for statics, the accuracy conditions for statics and dynamics, and a formulation to extend the material model MONOT. For the sake of overview, the main findings are summarised below. Furthermore, this final section will give an outlook on the work that still needs to be done before the model for the assessment of liquefaction flow slides can be applied.

The framework of governing equations from Chapter 3 was the starting point for the development of the finite element model. The residiuals were derived from the governing equations and the boundary conditions using the method of "Galerkin weighted residuals". Subsequently, the stiffness matrix was composed to approximate the residuals using an iteration procedure. Two loops were identified for the selected iteration procedure. Within a time step, the Modified Newton-Raphson method was employed to account for non-linearities. Time integration was established using the Crank-Nicholson scheme. Provided that the acceleration terms do not vary during a time step, the Crank-

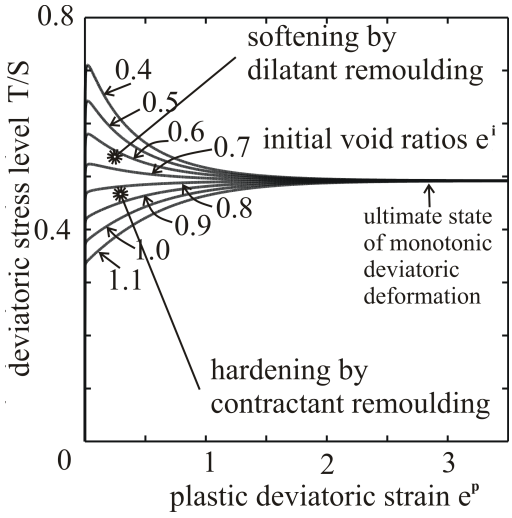


Figure 5.25: Calculated paths of deviatoric stress level T/S and plastic deviatoric strains e^p towards the critical state for drained purely deviatoric triaxial compression with monotonically increasing deviatoric deformation at constant isotropic stress level $S/p^a = \sqrt{3}$ for a series of initial void ratios $0.4 \leq e^i \leq 1.1$.

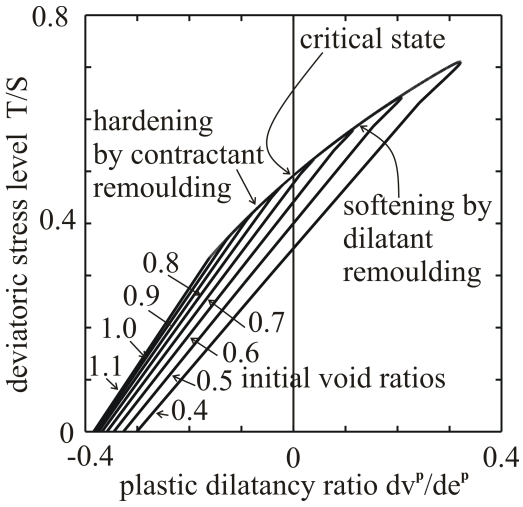


Figure 5.26: Calculated paths of deviatoric stress level T/S and plastic dilatancy ratio $\mathrm{d}v^p/\mathrm{d}e^p$ towards the critical state for drained purely deviatoric triaxial compression with monotonically increasing deviatoric deformation at constant isotropic stress level $S/p^a = \sqrt{3}$ for a series of initial void ratios $0.4 \leq e^i \leq 1.1$.

Nicholson scheme does not introduce any unwanted energy inconsistencies. The residuals and the stiffness matrix form the basis of the implementation in the finite element code. The result is a basic model, which accounts for the coupled response and the transition from statics to dynamics during liquefaction flow slides.

It would be fairly easy to extend the presented implementation. For instance, by updating the surfaces and volumes of the elements ('Updated-Lagrange') and by correcting for material rotations for the effective stress, the model can also handle larger deformations. Plugging in different material models enables various aspects of material behaviour to be accounted for. However, before these extensions are considered, the performance of the basic formulation itself should be verified, that is, for a simple problem involving small deformations and a simple (elastic) material response. To this end, the basic model has been benchmarked against the one-dimensional consolidation problem. It has been concluded that the model performed well. The results provide insight into the expected errors and the effect of the number and types of elements. In order to use the model for the assessment of liquefaction flow slides, it is recommended to perform additional benchmarks including dynamics.

The incorporation of both statics (consolidation) and dynamics (wave propagation) in the model introduces strict requirements with respect to the numerical accuracy and stability. It has been demonstrated that the resulting optimum element size and time step are extremely small and, thereby, numerically costly. Furthermore, conflicting requirements with respect to the refinement of the mesh may be imposed. Therefore, it is recommended to apply an adaptive strategy for both the mesh size and time step as the dynamic stage of a liquefaction flow slide is approached.

The modelling of large deformations in the dynamic phase of liquefaction flow slides requires a material model with a critical state formulation. Section 5.5 presented the extension of the existing MONOT-model with a critical state surface. The resulting formulation is compatible with the concept of the state parameter. The resulting material model may thus benefit from both the firm, theoretical basis of the MONOT-model, and the practical implications of the state parameter concept.

Hence, this chapter has presented a basic finite element implementation, and has indicated which steps still need to be taken towards dynamics and large(r) flow deformations. However, the Author acknowledges that, even after these extensions, the performance of the model depends entirely on the input parameters. The material model should be calibrated using the results of element tests. The outcome for a particular initial-boundary value problem should subsequently be evaluated using scale model tests and case histories. Without the experimental basis, the model has great potential, but little practical significance.

References

[1] O. Zienkiewicz, R. Taylor, and J. Zhu, *The Finite Element Method–Its Basis and Fundamentals, volume 1* (Elsevier Butterworth-Heinemann, London, 2005).

[2] I. Smith and D. Griffiths, *Programming the finite element method*, 4th ed. (John Wiley & Sons Ltd., Chicester, 2004).

[3] I. Smith and R. Hobbs, *Biot analysis of consoidation beneath embankments,* Géotechnique **26**, 149–171 (1976).

[4] O. Zienkiewicz, A. Chan, M. Pastor, D. Paul, and T. Shiomi, *Static and dynamic behaviour of soils: a rational approach to quantitative solutions. i. fully saturated problems,* Proceedings of the Royal Society of London A: Mathematical, Physical and Engineering Sciences **429**, 285–309 (1990).

[5] M. Schanz, *Poroelastodynamics: linear models, analytical solutions, and numerical methods,* Applied Mechanics Reviews **62**, 030803 (2009).

[6] O. Zienkiewicz, C. Chang, and P. Bettess, *Drained, undrained, consolidating and dynamic behaviour assumptions in soils,* Géotechnique **30**, 385–395 (1980).

[7] O. Zienkiewicz and T. Shiomi, *Dynamic behaviour of saturated porous media; the generalized biot formulation and its numerical solution,* International Journal for Numerical and Analytical Methods in Geomechanics **8**, 71–96 (1984).

[8] M. Hicks and C. Onisiphorou, *Stochastic evaluation of static liquefaction in a predominantly dilative sand fill,* Géotechnique **55**, 123–133 (2005).

[9] F. Molenkamp, *Collapse due to static liquefaction analysed using large deformation elasto-visco-plastic dynamics,* in *Proceedings of the 7th Conference on Numerical Models in Geomechanics* (Balkema, Graz, Austria, 1999) pp. 527–533.

[10] B. Wang, P. Vardon, and M. Hicks, *Investigation of retrogressive and progressive slope failure mechanisms using the material point method,* Computers and Geotechnics **78**, 88–98 (2016).

[11] M. Jefferies, *Nor-sand: a simple critical state model for sand,* Géotechnique **43**, 91–103 (1993).

[12] F. Molenkamp, *Elasto-plastic double hardening model Monot*, Tech. Rep. CO-218598 (Delft Geotechnics, Delft, the Netherlands, 1981).

[13] J. Pestana and A. Whittle, *Formulation of a unified constitutive model for clays and sands,* International Journal for Numerical and Analytical Methods in Geomechanics **23**, 1215–1243 (1999).

[14] D. M. Wood, *Geotechnical modelling*, 1st ed. (CRC Press, London, 2003).

[15] S. Olson, *Liquefaction analysis of level and sloping ground using field case histories and penetration resistance*, Ph.D. thesis, University of Illinois-Urbana-Champaign (2001).

[16] D. Kolymbas (ed.), *Constitutive modelling of granular materials*, 1st ed. (Springer-Verlag, Germany, 2000).

[17] R. Nova, *Failure in geomaterials,* European Journal of Environmental and Civil Engineering **13**, 779–802 (2009).

[18] G. Buscarnera and A. Whittle, *Constitutive modelling approach for evaluating the triggering of flow slides,* Canadian Geotechnical Journal **49**, 499–511 (2012).

[19] M. Hicks and R. Boughrarou, *Finite element analysis of the Nerlerk underwater berm failures,* Géotechnique **48**, 169–185 (1998).

[20] P. Lade and J. Duncan, *Elastoplastic stress-strain theory for cohesionless soil,* Journal of the Geotechnical Engineering Division **101**, 1037–1053 (1975).

[21] P. Rowe, *The stress-dilatancy relation for static equilibrium of an assembly of particles in contact,* Proceedings of the Royal Society of London A: Mathematical, Physical and Engineering Sciences **269**, 500–527 (1962).

[22] M. Hicks, *Experience in calibrating the double-hardening constitutive model Monot,* International journal for numerical and analytical methods in geomechanics **27**, 1123–1151 (2003).

[23] F. Molenkamp, *Implementation for consolidation of Modified-Newton-Raphson scheme,* Tech. Rep. (Delft University of Technology, Delft, the Netherlands, 2006).

[24] F. Molenkamp, *Continuum mechanics* (Lecture notes, Delft, the Netherlands, 2010).

[25] R. de Jager, *Flow slides of submerged slopes composed of loose sands: intermediate report,* Tech. Rep. (Delft University of Technology, the Netherlands, 2012).

[26] F. Molenkamp, *Limits to the jaumann stress rate,* International journal for numerical and analytical methods in geomechanics **10**, 151–176 (1986).

[27] P. Vermeer and A. Verruijt, *An accuracy condition for consolidation by finite elements,* International Journal for numerical and analytical methods in geomechanics **5**, 1–14 (1981).

[28] A. Verruijt, *Soil Mechanics* (Screen version, published online at geo.verruijt.net, 2012).

[29] D. Potts and L. Zdravković, *Finite element analysis in geotechnical engineering: Theory* (Thomas Telford Ltd., London, 1999).

[30] J. R. Booker and J. Small, *An investigation of the stability of numerical solutions of biot's equations of consolidation,* International Journal of Solids and Structures **11**, 907–917 (1975).

[31] R. de Jager, L. Braakenburg, M. Hicks, and F. Molenkamp, *Towards modelling of static liquefaction of saturated loose sand,* in *Proceedings of the 2nd International Symposium on Computational Geomechanics* (Dubrovnik, Croatia, 2011) pp. 1–13.

[32] K. Been and M. Jefferies, *A state parameter for sands,* Géotechnique **35**, 99–112 (1985).

[33] M. Jefferies and K. Been, *Soil liquefaction: a critical state approach* (Taylor & Francis, 2006).

[34] P. Rowe, *Theoretical meaning and observed values of deformation parameters for soil,* Proceedings of the Roscoe Memorial Symposium , 143–194 (1971).

[35] G. De Josselin de Jong, *Rowe's stress—dilatancy relation based on friction,* Géotechnique **26**, 527–534 (1976).

[36] D. Muir Wood, K. Belkheir, and D. Liu, *Strain softening and state parameter for sand modelling,* Géotechnique **44**, 335–339 (1994).

[37] R. Wan and P. Guo, *A simple constitutive model for granular soils: modified stress-dilatancy approach,* Computers and Geotechnics **22**, 109–133 (1998).

[38] X. Li, *A sand model with state-dependent dilatancy,* Géotechnique **52**, 173–186 (2002).

[39] Y. Yao, D. Sun, and T. Luo, *A critical state model for sands dependent on stress and density,* International Journal for Numerical and Analytical Methods in Geomechanics **28**, 323–337 (2004).

[40] J. Desrues, R. Chambon, M. Mokni, and F. Mazerolle, *Void ratio evolution inside shear bands in triaxial sand specimens studied by computed tomography,* Géotechnique **46**, 529–546 (1996).

[41] S. Hall, M. Bornert, J. Desrues, Y. Pannier, N. Lenoir, G. Viggiani, and P. Bésuelle, *Discrete and continuum analysis of localised deformation in sand using x-ray μct and volumetric digital image correlation,* Géotechnique **60**, 315–322 (2010).

[42] P. V. Lade, J. Nam, and W. P. Hong, *Shear banding and cross-anisotropic behavior observed in laboratory sand tests with stress rotation,* Canadian Geotechnical Journal **45**, 74–84 (2008).

6

Development of the liquefaction tank

This chapter introduces the liquefaction tank to the thesis. The liquefaction tank is an experimental facility developed to conduct physical scale model tests of liquefaction flow slides. The liquefaction tank was developed, designed, built and tested during the PhD-research. The liquefaction tank is a unique facility of its kind, bridging the gap between the detailed but specific soil response from element testing and the relevant but largely unknown soil response during field events.

The background of the liquefaction tank will be elaborated in the first section, by discussing the objectives and requirements. The subsequent section addresses the design of separate parts of the tank and the sand used during testing. Finally, this chapter will conclude with the design of the triaxial cell that was developed to conduct triaxial tests on sand with the same soil structure and at the same stress level as the liquefaction tank.

6.1. Objectives and requirements

Chapter 2 reviewed the case histories of liquefaction flow slides, demonstrating its importance in engineering practice. Nonetheless, the case histories lack the detailed information required to verify and validate advanced models. The soil conditions are usually unknown or uncertain, whilst the importance of the trigger is evident but can hardly be quantified due to a lack of detailed information. Improving the assessment of liquefaction flow slides demands a shift away from empiricism and a taking account of aspects such as the direction of loading and consolidation effects.

Element tests do provide detailed information on the soil response during flow liquefaction. It is beyond doubt that element tests provide valuable information, demonstrating the importance of soil structure, and imposed stress and/or strain paths. The focus on specific stress and/or strain paths of element tests also raises questions about their rele-

vance for the boundary value problem of slope stability. The roles of the effective stress and strain paths depend on a number of complex phenomena, including the coupling of the hydro-mechanical behaviour in the slope, the nature of the trigger, and the redistribution of excess pore pressures and density during and after consolidation of the soil. In spite of some noteworthy efforts, element tests can only account for these aspects to a very limited extent.

Physical scale model testing may bridge the gap between element testing and the real boundary value problem encountered. The laboratory conditions allow control over the boundary and loading conditions, as well as the preparation of the sand bed. There are only a few reported cases of physical scale model tests of liquefaction flow slides. In Chapter 2 the shortcomings of these tests were listed, including the lack of documentation, insufficient control over the preparation of the sand bed and lack of knowledge of the trigger. It is noted that, in addition, the lack of a vast amount of experimental results is by itself a major shortcoming. The physical scale model tests that have been conducted so far were all part of testing programmes. The scale model tests were no longer used after the cessation of these programs. The Author notes that a certain, critical mass of experimental data is required in order to verify the reproducibility and consistency of test results and to vary the experimental input variables.

The development of the liquefaction tank aims at the verification of advanced, numerical models, and has been developed for the long term. A large, open-source database of high-quality experimental data should allow researchers worldwide to test the performance of numerical models. The liquefaction tank is not intended to be a replication of field conditions. The experimental set-up will be scaled in terms of geometry, whilst the uniform and controlled laboratory conditions that are necessary to obtain reproducible results will not be encountered in the field. Instead, the liquefaction tank should provide a stepping stone from element testing to the boundary value problem of slope stability. Its primary objective is to reproduce the phenomenon of liquefaction flow slides and its susceptibilities, and to be able to relate these to the results of element tests. Extrapolation to larger scales should be accounted for by conducting element tests at field stresses and densities, used as input for advanced, numerical analyses for the boundary value problems encountered in the field.

The objectives of the liquefaction tank lead to a number of basic requirements, which serve as the basis for the design:

- Reproducing liquefaction flow slides requires:
  - the soil to be susceptible to flow liquefaction;
  - sufficiently large triggers;
  - the types of boundary conditions similar to those occurring in both nature and engineering practice.
- Reproducibility of experiments requires:
  - uniform and known soil conditions;

  - the trigger to be well-defined at each stage of failure.

- Evaluation of numerical models requires:
  - known initial conditions;
  - the trigger to be reproducible in the model;
  - monitoring of the free variables.

- Compatibility with element tests requires:
  - a similar density, soil structure and effective stress history after preparation in both cases;
  - an equal initial stress level.

- The practicality of the set-up requires:
  - the size of the tank and the volume of the sand to be manageable;
  - a limited time frame for conducting a test.

The possibility is left open to extend the research with the liquefaction tank beyond this PhD. For instance, the dimensioning of the tank takes account of the post-triggering phase, during which the liquefied sand-water mixture is allowed to run out freely. Furthermore, the need to investigate flow liquefaction slides in unsaturated slopes, triggered by saturation, is anticipated.

The design of the liquefaction tank based on these requirements is considered in the next section. However, a preliminary choice that has to be made first concerns the type of test; that is, a $1g$-test or centrifuge test. The advantages of a centrifuge test set-up are the ability to vary the dimensions by scaling and the manageable size of the model. Nonetheless, it was decided to develop a $1g$-test facility. The preparation of a very loosely packed, uniform sand bed in the centrifuge test is complicated by the limited options for preparation techniques, vibrations during spinning up and non-uniformities at higher g-levels (see Subsection 2.2.2). The required scaling of the hydraulic conductivity of the saturated soil using a pore fluid with an increased viscosity also affects the free water next to the slope. As a consequence, the artificially induced support by the free water will affect the response, particularly at larger deformations. If flow liquefaction is triggered by creep, as observed in element tests, the yet unresolved scaling of creep time complicates flow liquefaction slides in the centrifuge [1]. The same accounts for erosion and sedimentation during the post-liquefaction phase, which lacks experimental validation. Hence, a $1g$-test facility has been developed, while relying on the experiences gained during previous research projects in Delft.

6.2. Design of the liquefaction tank

6.2.1. General

The design of the liquefaction tank is elaborated further herein. In this first subsection, the contours of the liquefaction tank are drawn. The separate components are further

detailed in the following subsections.

The sand bed is prepared using a fluidisation system (Figure 6.1). Past experience with the Brutus tank has shown that fluidisation can yield extremely loose packings and a uniform distribution, provided that the system is properly designed. In addition, fluidisation can be employed to flush out the fines of the soil. An overflow to keep the water level in the tank constant and to transport the fines out of the tank was envisaged. The removal of the fines limits the segregation of grain sizes after sedimentation and reduces the turbidity of the free water in the liquefaction tank. The expansion of the sand bed during fluidisation sets requirements on the dimensions of the tank. The dimensions of the tank were selected based on a minimum effective stress level that can be reached in an element test, that is, 5 to 10 kPa. Section 6.3 will provide the background to these values, while elaborating on the accuracy of undrained triaxial tests at low effective stresses. Selecting larger dimensions would affect the manageability of the set-up. A representative stress range of 5 to 10 kPa is reached for a slope with a (crest) height of 1.5 m. Based on the anticipated expansion of the sand bed, the selected height of the set-up equals 2 m. The inevitable boundary effects from the sides of the tank are minimised in two ways. First, the selected width of 2 m is sufficiently large to reduce arching to a minimum in the middle of the tank. Secondly, the friction along the (transparent) sides is kept to a minimum by using hardened glass and a single sheet per side to avoid joints. The length of the tank should be considerably larger than its width and height to allow free movement of the slope without end effects. A slope with a height of 1.5 m and a slope of $1v:2h$ will have a length of approximately 3 m. If 1 m for the crest and the toe is accounted for, the selected length of the tank equals 5 m. In short, the selected dimensions of the liquefaction tank read 5 m, 2 m and 2 m for length, width and height, respectively.

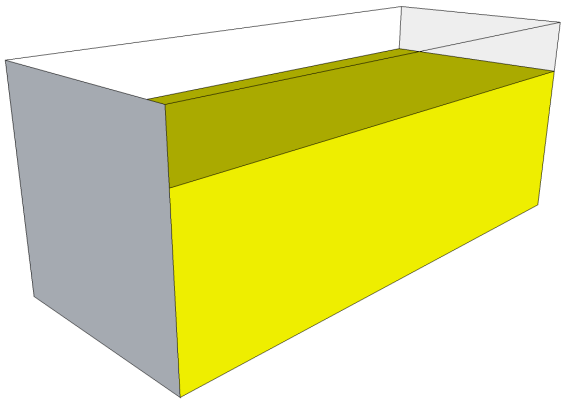


Figure 6.1: Sketch of liquefaction tank after fluidisation

The envisaged method to create a slope is by dredging, which is the same method used previously in the Brutus tank. For the subsequent triggering of the slope, two options were originally considered. The first is by tilting the tank. The rotation of the entire slope geometry during tilting yields a uniform, well-defined trigger. Furthermore, the finite element method can reproduce tilting easily by rotating the gravity vector in the reverse direction. The second option for triggering flow liquefaction is a shock load at the crest. Defining this trigger requires more effort. The slope will deform during loading which will affect the magnitude and direction of the trigger. Hence, in order to define the trigger and to model it, its properties need to be monitored in detail. Note that, contrary to tilting, the trigger is applied locally. Figure 6.2 depicts a sketch of the tank in the tilted position. The tank is placed on a frame to allow its rotation by two jack-up screws.

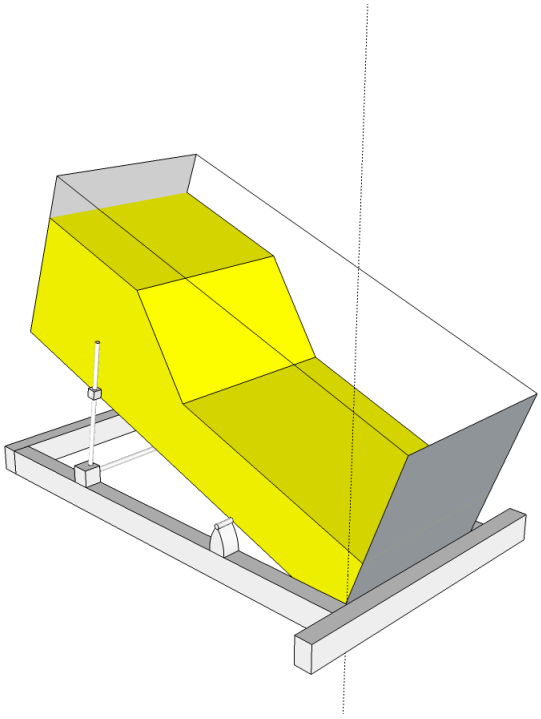


Figure 6.2: Sketch of liquefaction tank after tilting

The development of the liquefaction tank started with a basic design that was modified several times as a result of new insights. For instance, during its development a $1:10$ scale model, referred to as the *minitank*, was used to test the flushing of the sand, fluidisation, dredging and triggering. Preliminary results obtained with the minitank will be elaborated in Subsection 6.2.6 to substantiate the design. Generally, this thesis concentrates on the final design of the liquefaction tank, while only mentioning the process if strictly necessary.

6.2.2. Structure

The structure facilitates the sand bed, as well as the other components of the liquefaction tank, such as the fluidisation system, the trigger, the dredging system and instrumentation. The previous subsection drew the outline of the tank, including its dimensions and the triggers, based on the requirements discussed in Section 6.1. In addition, minimising the effects of the boundary conditions requires the tank to be stiff, both during loading by the triggers and during changing stresses in the sand bed, for instance during liquefaction.

The structure comprises the base frame, tank frame, glass sheets and components connecting these. It was recognised that the liquefaction tank is part of a working environment, i.e. the laboratory, but also provides a working environment itself. The development of the liquefaction tank required considering the interaction with other setups, and minimising possible interference. A low wall was constructed around the liquefaction tank to retain possibly leaked water, as well as a curtain to control possible splashing. Safety considerations required, amongst other things, the construction of a purpose-designed staircase and a working platform on top of the tank. For the sake of overview, Figure 6.3 shows the side view of the tank.

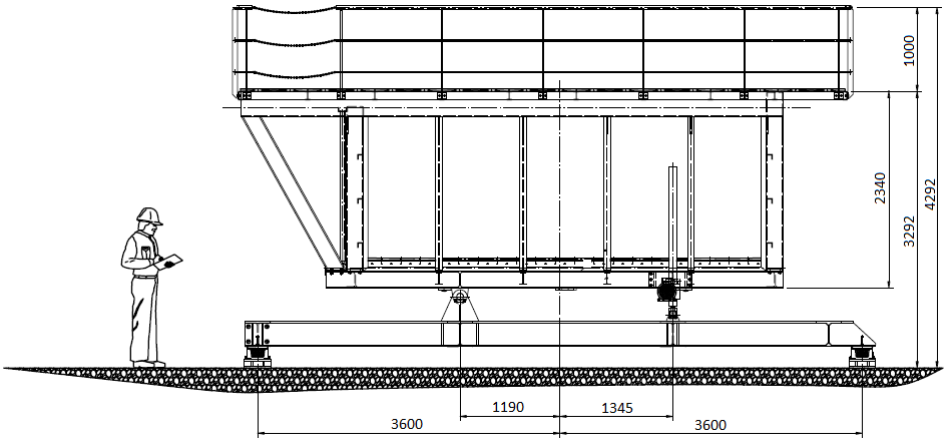


Figure 6.3: Building plan in side view of the liquefaction tank with measures in mm

When completely filled with sand and water the liquefaction tank has a total weight of approximately 50 ton, meaning that the bearing capacity of the floor in the laboratory will be exceeded. Additional steel columns were designed and installed in the basement of the laboratory to transfer the loads to the foundation. The grid of foundation piles centred at $7.2x3.6$ m defined the minimum dimensions of the lower steel frame. The deformations of the newly installed steel columns were monitored during the filling of the tank with water, in order to evaluate the design. An additional function of the steel base frame is the elevation of the liquefaction tank to allow for rotation. The base frame was

eventually constructed from six HE300B steel beams, two in the longitudinal and four in the width-wise direction of the tank. The frame is wider at the front side of the tank (the left side in Figure 6.3) to reach the aforementioned 3.6 m. The width of the rest of the frame is defined by the total width of the tank it supports and measures 2.77 m. The width does not increase at the rear of the tank, as a (stiff) bearing wall transfers the loads to the foundation.

The required low density of the sand bed requires that the liquefaction tank is isolated from vibrations that are externally induced. Hence, the base frame is supported by (sets of) isolator springs. The criterion for the selection of these isolator springs is the passing of vibrations with frequencies much lower than the eigenfrequency of the slope. The calculated, required stiffness of approximately $14\,\mathrm{MN\,m^{-1}}$ is provided by sets of four isolator springs under each of the four corners of the frame. Later, the performance of these isolators could be verified when accelerometers were installed onto the frame.

The lower frame connects to the liquefaction tank by two hinges at the front and by two jack-up screws at the rear. The jack-up screws of type TP-8010 (Unimec) have an outer diameter of 98 mm and a stroke of 1200 mm. The lower hinges of the steel screws are sunken in the lower base frame, which has been reinforced at these positions. A box beam was welded at both sides of the tank and connected to the bevel houses of the jack-up screws by hinges. During tilting the bevel houses move upwards along the screws, thereby rotating the tank. A cylindrical cross bar driven by an electric motor connects the two screws, which therefore move at the same pace. Further details of the tilting system will be given in Subsection 6.2.7 on the triggering mechanisms.

The bottom of the liquefaction tank consists of four HE-200B steel beams welded in a rectangular frame, reinforced by four IPE-160 beams in the width-wise direction and strips in the longitudinal direction. A plate was welded at the top and bottom side of the frame, thereby creating a box structure. The bottom is bolted to four, vertical HE-200B beams at the corners of the tank. In the longitudinal direction these beams are overlain by two box beams of $500x300$ mm (Figure 6.4). Four vertical IPE-160 profiles were placed between the bottom and the horizontal box beams at each (longitudinal) side of the tank to provide support for the glass sheets. At the front side of the tank the box beams have been extended and an additional, diagonal beam connects the box beams to the bottom. This extension provides both stiffness to the tank and a place for the dredging machine to be stationed. The front and rear side of the tank are closed by plates that are bolted to the vertical beams in the corners and the bottom of the tank. It was decided to bolt the plates instead of welding, to allow dismantling of the tank if necessary, and to allow the glass sheets to be lifted into the frame from the front. A walking grid with railing on top of the tank provides a safe access and working platform for the tank.

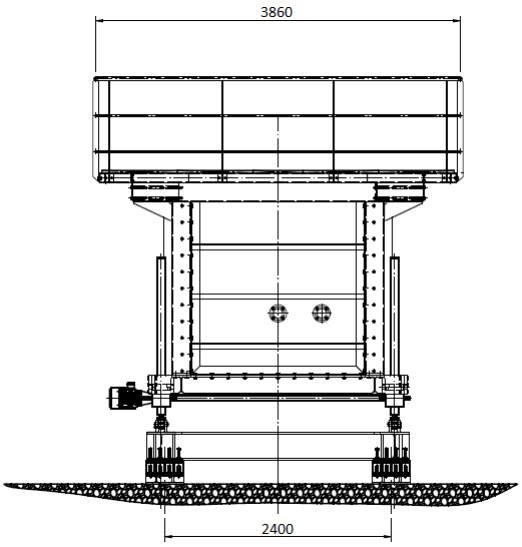


Figure 6.4: Rear view of the liquefaction tank with measures in mm. The motor was later moved to the other side of the tank and two sensors were added to the rear end plate.

The design of the glass sheets asks for further consideration. It is common practice for glass sheets of a certain thickness to be composed of thinner layers of glass with intermediate layers of foil. Finite element calculations showed that glass sheets of 30 mm thickness will withstand the load exerted by a fully liquefied sand bed. A thickness of 40 mm was selected to include a safety margin. However, hardened glass is highly susceptible to breakage by point loads at the edges. These may result from irregularities in the rebates or a bump during the transport or lifting of the sheets. Hence, a rubber profile was placed around the edges of the glass sheets before lifting them into the structure. The actual operation of placing the glass sheets into the structure was considered a risk due to the lack of space and the necessity to rotate the sheets twice. The sheets were delivered standing in a vertical position on a frame; they had to be lain horizontally on a frame to glue the rubber profiles and were then rotated back vertically to be moved into their final position in the tank (Figure 6.5).



Figure 6.5: Lifting glass sheets from frame after glueing rubber profiles (left), glass sheets after placement in structure (right)

The U-profiles are made of stiff, ethylene propylene rubber (EPDM80) with a thickness of 10 mm. The rubber profile was sawn to fit the corners of the sheets and glued afterwards. The strength of the established, glued connections at the corners was tested in a tension test. The strength was governed by the rubber and therefore does not create a weak link. The creep behaviour of the rubber was also tested, which may induce stresses in the glass sheets in the long term. The effect of creep was found to be negligible. The strength of the glass sheets was evaluated by conducting loading tests on glass sheets of hardened glass (see Figure 6.6). In order to mimic the situation in the liquefaction tank, the loading force was spread by a plate and the glass sheet supported by EPDM80 rubber. The test was repeated with a nut shoved between the rubber and the glass sheet at the bearing to investigate the effect of an irregularity at the edge of the sheet. Both the outcome of the basic test and the test with the nut were satisfactory; in both cases the plate could be loaded far beyond the expected load in the liquefaction tank.

However, the protection of the glass sheets by rubber introduced a problem of unforeseen proportions. Sealant does not stick to EPDM80 rubber, which reduced the possibilities for sealing the liquefaction tank for water tightness. This was (by far) the biggest issue during the development of the liquefaction tank, causing a delay of approximately two years. Several measures were taken in an attempt to solve this problem. Auxiliary steel strips were placed to increase the area for the sealant and the movement of the glass sheets was restrained by applying special, stiff sealant at the outside of the sheets. There were several attempts of sealing the tank using different types of sealant and contractors. The sealing of the end plates also appeared to be an issue, presumably caused by the grease used to squeeze the plates into position. This issue was (partly) resolved by welding the end plate at the rear end to the bottom of the tank. Finally, the leakage of the tank was step-by-step reduced until it reached acceptable proportions. Figure 6.7 depicts the liquefaction tank after assembly.

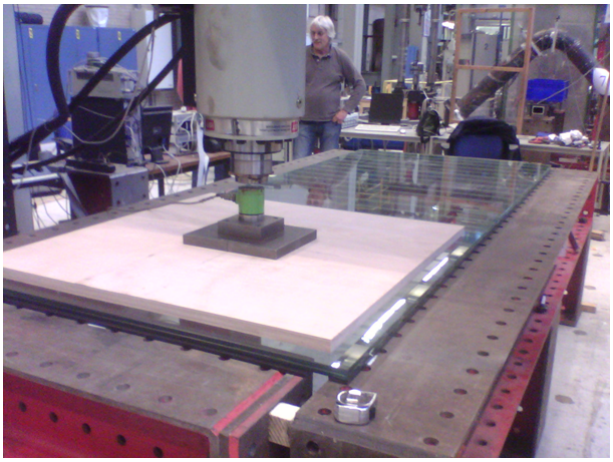


Figure 6.6: Load test on glass sheet to evaluate strength

6.2.3. Fluidisation system

The fluidisation system aims at creating a sand bed that is sufficiently loose to induce flow liquefaction, and sufficiently uniform to obtain reproducible results. Even though the liquefaction tank may appear impressive in terms of its size, it is still substantially smaller than most field situations. Chapter 2 treated the effect of the isotropic effective stress on the susceptibility to flow liquefaction, elaborating on the traditional view based on Critical State Soil Mechanics and the conflicting recent view based on silty sands. Since the current research will be dealing with clean sands, the traditional view based on Critical State Soil Mechanics will be adopted. Considering the relatively low stresses in the liquefaction tank, the packing needs to be extremely loose to induce flow liquefaction. It is expected that these densities cannot be obtained using traditional (pluviation) methods; hence the choice for fluidisation which is expected to yield looser packings. This subsection treats the design of the fluidisation system. The next chapter will go further into detail on the mechanism of fluidisation and the performance of the system. This subsection anticipates the response of the system, whereas the next chapter will concentrate on the response of the sand. The contents of this subsection were published in [2].

Based on experiences in the past with the Brutus tank [3], a fluidisation system consisting of several perforated tubes, embedded in one or more filter layers, was envisaged. In addition to the basic requirements, the robustness of the tubes and the filter layer(s) determine the requirements of the system. However, the main concern of the design is the relative size of the perforation holes in the tubes. These holes should allow for an outflow that is sufficiently large to induce fluidisation. However, the outflow of water will create a pressure gradient along the tubes, that should remain relatively small to ensure uniform fluidisation of the sand bed. It is assumed here that a uniform pressure in the fluidisation system yields a uniform packing in the sand bed.

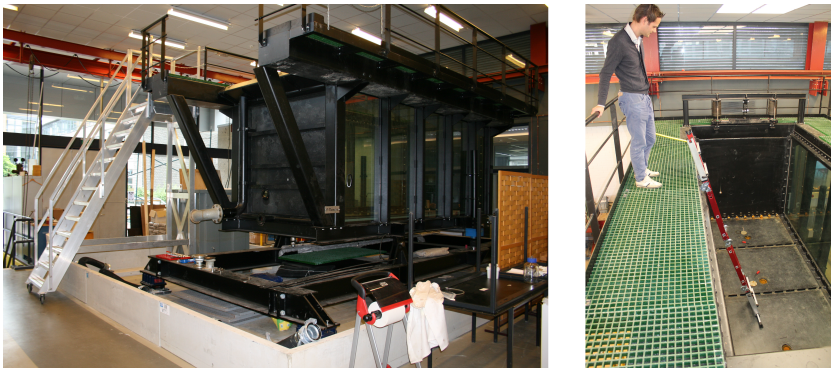


Figure 6.7: The liquefaction tank after assembly: outside (left) and inside (right)

The total loss of vertical effective stress, that is, $\sigma'_{zz} = 0$, marks the initiation of fluidisation. The flow is assumed to be stationary and uniform, which implies that the absolute and relative pore fluid acceleration equals zero: $\dot{\boldsymbol{v}}^{pf}, \dot{\boldsymbol{v}}^{pf\text{-}s} = 0$. Considering the interest in fluidisation and the presumed uniformity of flow, the situation is further simplified to a one-dimensional analysis in the vertical (z) direction. Elaboration of the momentum equation of the pore fluid 3.69, while fluidisation requires $p_{,z} = \sigma_{zz,z} = \rho^g$, yields:

$$w_z^{pf\text{-}s} = -k_{zz}\left(\frac{\rho - \rho^f}{\rho^f}\right) \tag{6.1}$$

Equation 6.1 defines the momentum equation of the pore fluid for fluidisation, expressed in terms of flux $\boldsymbol{w}^{pf\text{-}s} = n\boldsymbol{v}^{pf\text{-}s}$ and permeability $\boldsymbol{k}/\gamma^f = \boldsymbol{\kappa}/\mu$ with $\gamma^f = \rho^f \boldsymbol{g}$. The term between the brackets is usually denoted by the *hydraulic gradient* i^{crit}. The value of i^{crit} depends on ρ and, thereby, increases with decreasing porosity n. The opposite is true for k_{zz}, which increases with increasing porosity. The effect of the latter is greater, which means that the design situation is given by the maximum, anticipated porosity n. Assuming an initial porosity of $n = 0.4$ and a bed expansion from 1.5 m to 2.0 m, the design porosity equals $n = 0.55$. The Kozeny-Carman equation [4] is employed to estimate the permeability k_{zz}:

$$k_{zz} = \frac{Cn^3\left(D^g\right)^2}{(1-n)^2}\frac{\gamma^f}{\mu} \tag{6.2}$$

Herein, $C \approx 0.0072$ relates to the specific surface of the grains, $D^g \approx 100\,\mu\text{m}$ specifies the representative grain diameter and $\mu \approx 0.001\,\text{N}\,\text{s}\,\text{m}^{-2}$ the dynamic viscosity of the pore fluid. Substitution of $n = 0.55$ yields a permeability of $k_{zz} = 5.8 \times 10^{-4}\,\text{m}\,\text{s}^{-1}$, a critical hydraulic gradient of $i^{crit} = 1.74$ and a required flux of $w_z^{pf\text{-}s} = 1 \times 10^{-3}\,\text{m}\,\text{s}^{-1}$. The required flow into the tank Q^{fl}, expressed in litres per second where $1\,\text{s}^{-1} = 10^{-3}\,\text{m}^3\,\text{s}^{-1}$, equals:

$$Q^{fl} = w_z^{pf\text{-}s} A^{tank} \approx 10\ \text{l}\,\text{s}^{-1} \tag{6.3}$$

It was provisionally chosen to compose the fluidisation system of ten horizontal PVC tubes at the bottom of the liquefaction tank, aligned in the longitudinal direction of the tank. The water is pumped to an inlet at the front side of the tank, where it is divided into the 10 tubes. At the rear end of the tank, the tubes are closed by plug screws that allow flushing. The pressure gradient will be much greater in the longitudinal direction than in the perpendicular, horizontal direction at the inlet. Therefore, it is assumed that the pressure at the inlet $p^{int;0}$ is evenly distributed over the tubes. The difference between the internal pressure p^{int} in the tubes and the pressure in the tank at the same level p^{ext} determines the outflow of water.

The design of the fluidisation system is first directed at the uniformity of p^{int} along the tubes. The PVC tubes are characterised by an internal diameter D^{tu} and wall thickness t^{tu}. Pairs of holes are drilled in both sides of the tubes with a diameter D^{ho} and a mutual distance l^{ho}. In the case that the total outflow area defined by both D^{ho} and l^{ho} is relatively small compared to the flow area of the tube defined by D^{tu}, the pressure gradient will be relatively small. This criterion will be elaborated in more detail, while taking account of the required inlet pressure $p^{int;0}$ and realisability of the design.

The equation describing the variation of pressure along the tubes follows from the conservation of mass. An infinitesimally small stretch dx of one of the tubes is considered with constant cross-sectional area A^{tu}, which is fully saturated by an incompressible fluid. The positive direction of the x-axis is defined by the direction of flow in the tube v^{tu}. The change of the mass related to the flow equals $dv^{tu}\,A^{tu}$. The mass per unit length flowing out of the (pairs of) drilled holes equals $2Q^{ho}/l^{ho}$, with the total mass being $2\left(Q^{ho}/l^{ho}\right)dx$. The governing equation reads:

$$\frac{dv^{tu}}{dx}A^{tu} + 2\frac{Q^{ho}}{l^{ho}} = 0 \tag{6.4}$$

Both contributions can be expressed in terms of pressure p^{int} by using the conservation of energy. First, the exact solution of the Navier-Stokes equation provided by Hagen-Poisseulle flow defines a relation between v^{tu} and p^{int} for laminar flow conditions:

$$v^{tu} = -\frac{\left(D^{tu}\right)^2}{32\mu}\frac{dp^{int}}{dx} \tag{6.5}$$

Second, the energy balance for a hole allows Q^{ho} to be expressed in terms of the pressure difference:

$$Q^{ho} = cA^{ho}\sqrt{\frac{2\left(p^{int} - p^{ext}\right)}{\rho^f}} \tag{6.6}$$

The constant $c \approx 0.62$ accounts for the contraction of the flow. Substitution of Equations 6.5 and 6.6 into the mass equation 6.4, and subsequent elaboration, yields:

$$\frac{d^2p^{int}}{dx^2} - \frac{64\mu\left(D^{ho}\right)^2 c}{\left(D^{tu}\right)^4 l^{ho}}\sqrt{\frac{2\left(p^{int} - p^{ext}\right)}{\rho^f}} = 0 \tag{6.7}$$

Unfortunately, there are no simple analytical solutions to solve Equation 6.7. In order to solve the equation numerically, it is transformed in two steps. First, the equation is simplified to:

$$\frac{d^2 s}{dx^2} - B\sqrt{s} = 0 \tag{6.8}$$

Herein, s and B are defined by, respectively:

$$s = \frac{\left(p^{int} - p^{ext}\right)}{p^{ext}} \tag{6.9}$$

$$B = \frac{64\mu\left(D^{ho}\right)^2 c}{\left(D^{tu}\right)^4 l^{ho}} \sqrt{\frac{2}{\rho^f p^{ext}}} \tag{6.10}$$

Second, the dimensionless quantity $t = \sqrt{s}$ is introduced. Substitution into the first term of Equation 6.8 and elaboration leads to:

$$\frac{d^2 s}{dx^2} = \frac{d^2 t^2}{dx^2} = 2\left(\left(\frac{dt}{dx}\right)^2 + t\frac{d^2 t}{dx^2}\right) \tag{6.11}$$

Hence, Equation 6.8 can be simplified to:

$$\frac{d^2 t}{dx^2} + \frac{1}{t}\left(\frac{dt}{dx}\right)^2 - \frac{B}{2} = 0 \tag{6.12}$$

The non-linear differential equation 6.12 can be solved numerically. Before considering the discretisation of the equation, the boundary conditions are first addressed. These are first expressed in terms of the field variable p^{int} and then in terms of the auxiliary variable t. The stress p^{int} is imposed at the start boundary $x = 0$, i.e. $p^{int} = \bar{p}^{int}$. The restrained velocity $v^{tu} = 0$ at the end boundary $x = 5$ requires $dp^{int}/dx = 0$ according to Equation 6.5. Using the definition of t, the boundary conditions are defined by:

$$\text{At } x = 0: \quad t = \bar{t}\Big|_0 = \sqrt{\frac{\bar{p}^{int}}{p^{ext}} - 1} \tag{6.13}$$

$$\text{At } x = 5: \quad \frac{dt}{dx} = \overline{\frac{dt}{dx}}\Big|_5 = 0 \tag{6.14}$$

Garlerkin's approach is employed to discretise the set of equations given by 6.12, 6.13 and 6.14 to suit implementation in a finite element code. The conservation equation 6.12 applies to the domain and should be integrated over the length of the tube l. The boundary conditions 6.13 and 6.14 are point values. The governing equations can be multiplied by any arbitrary weighting function without loss of validity. The shape function N^P is selected for the conservation equation and M^P for the boundary conditions. The weak formulation of the set of equations is obtained by requiring the sum to be equal to zero:

$$\int_l N^P\left(\frac{d^2 t}{dx^2} + \frac{1}{t}\left(\frac{dt}{dx}\right)^2 - \frac{B}{2}\right)dx - M^P\eta\left(t - \bar{t}\Big|_0\right)\Big|_0 + M^P\left(\frac{dt}{dx} - \overline{\frac{dt}{dx}}\Big|_5\right)\Big|_5 = 0 \tag{6.15}$$

Note that a scalar η with dimension $[1/m]$ has been added to ensure consistency in terms of units. Furthermore, the boundary terms have opposite signs due to the directions of the normal vectors. The divergence theorem allows the double integral term in 6.15 to be simplified. The term is first reformulated using partial differentiation, after which the divergence theorem can be applied on part of the resulting expression:

$$\int_l N^P \frac{d^2 t}{dx^2} dx = \int_l \frac{d}{dx}\left(N^P \frac{dt}{dx}\right) dx - \int_l \frac{dN^P}{dx}\frac{dt}{dx} dx \tag{6.16}$$

$$\int_l \frac{d}{dx}\left(N^P \frac{dt}{dx}\right) dx = \left(N^P \frac{dt}{dx}\right)\Big|_5 - \left(N^P \frac{dt}{dx}\right)\Big|_0 \tag{6.17}$$

By defining $M^P = -N^P$, substituting Equations 6.16 and 6.17 into 6.15 and simplifying, the resulting equation is:

$$\int_l \left(-\frac{dN^P}{dx}\frac{dt}{dx} + N^P\left(\frac{1}{t}\left(\frac{dt}{dx}\right)^2 - \frac{B}{2}\right)\right) dx + N^P \overline{\frac{dt}{dx}}\Big|_5 - \left(N^P \frac{dt}{dx}\right)\Big|_0 + N^P \eta\left(t - \bar{t}\Big|_0\right) = 0 \tag{6.18}$$

The equation is further simplified by considering the boundary conditions. At $x = 0$, the free variable t is prescribed which means that all terms applying to $x = 0$ are obsolete. Equation 6.14 prescribes the gradient $\overline{dt/dx} = 0$ at $x = 5$, which also can be discarded. After multiplication by -1, the resulting equation reads:

$$\int_l \frac{dN^P}{dx}\frac{dt}{dx} dx - \int_l N^P\left(\frac{1}{t}\left(\frac{dt}{dx}\right)^2 - \frac{B}{2}\right) dx = 0 \tag{6.19}$$

The free variable t is discretised by assuming a relation with the nodal values $\hat{t}$ through N^P:

$$t = N^P \hat{t}^P \tag{6.20}$$

Substitution into Equation 6.19, applying partial differentiation and elaboration yields in index notation:

$$f^P = \int_l N^P_{,i} N^Q_{,i} dx\, \hat{t}^Q - \int_l N^P \left(\frac{N^Q_{,i}\hat{t}^Q N^R_{,i}\hat{t}^R}{N^S \hat{t}^S} - \frac{B}{2}\right) dx = 0 \tag{6.21}$$

The term f^P is the *residual*, which the finite element code aims to minimise. To this end, the error δf^P is expressed in terms of the error of the free variable $\delta\hat{t}^P$ by partial differentiation:

$$\delta f^P = \frac{\partial f^P}{\partial \hat{t}^U}\delta\hat{t}^U = \int_l \left(N^P_{,i} N^Q_{,i} - 2N^P \frac{N^R_{,i}\hat{t}^R}{N^S\hat{t}^S} N^Q_{,i} + N^P \frac{N^U_{,i}\hat{t}^U N^R_{,i}\hat{t}^R}{\left(N^S\hat{t}^S\right)^2} N^Q\right) dx\, \delta\hat{t}^Q = K^{PQ}\delta\hat{t}^Q \tag{6.22}$$

The Newton-Raphson procedure is employed to reduce δf^P to a value close enough to zero. For iteration step $n+1$, the value of $\hat{t}^Q$ can be estimated using the following relationship:

$$K^{PQ}\left(\hat{t}^Q\Big|^n - \hat{t}^Q\Big|^{n+1}\right) = f^P\Big|^n \tag{6.23}$$

A uniform, initial pressure at the first iteration step $n = 0$ results in the singularity of K^{PQ}. The initial pressure distribution was assumed to decrease linearly from the boundary condition at $x = 0$ to a value approximately 10% lower at the boundary at $x = 5$. Based on the aforementioned discretisation of the governing equations, a finite element code named *p91_tube1.f95* was developed, using parts of the code and libraries provided by Smith and Griffith [5]. The code varies the values of $\bar{p}^{int}$ at $x = 0$ and the internal diameter of the tubes D^{tu}. The design external pressure p^{ext} is defined by a fully fluidised bed of 2 m thickness and equals 35 kPa. Given the number of tubes $N = 10$, the design flux $Q^{fl} = 10$ ls^{-1} specifies the ratio $(D^{ho})^2/l^{ho}$ by Equation 6.6.

Figure 6.8: Structure of code *p91_tube1.f95*

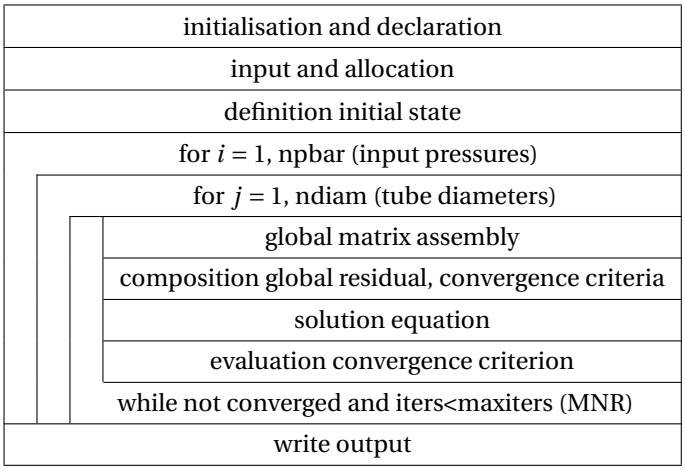


Figure 6.8 depicts the structure of *p91_tube1.f95*. The input pressure $\bar{p}^{int}$ is varied between 50 and 100 kPa, and the inner tube diameter D^{tu} between 25 mm and 50 mm. The results of the finite element calculations demonstrate that the pressure gradient along the tube Δp^{tu} is small, even for $D^{tu} = 25$ mm. For the considered input pressures, the resulting relative pressure drop $\Delta p^{tu}/p^{tu}$ ranges between 0.3% and 0.5%. Nonetheless, a tube diameter of $D^{tu} = 40$ mm was selected. The calculated pore fluid velocities v^{tu} at $x = 0$ decrease from 2.1 m s^{-1} to 0.2 m s^{-1} when D^{tu} is increased from 25 mm to 50 mm. The corresponding Reynold's number R_e decreases from approximately 5.2×10^4 to 1.7×10^4, which is still well above the threshold value for turbulent flow. To limit the energy losses as a result of turbulence, a larger value of D^{tu} is preferred. A value of $D^{tu} = 40$ mm was selected to still fit the tubes in the envisaged 50 mm thick filter layer. The actual energy losses due to turbulence will be governed by the Reynold's number R_e and the tube roughness. The drilled holes will affect the roughness of the smooth PVC tubes. Hence, the amount of holes should be minimised or the distance l^{ho} maximised to minimise turbulence. However, larger values of l^{ho} will have a negative impact on the uniformity of the distribution of water. A value of $l^{ho} = 5$ cm was still considered acceptable. This value is of the same order as the thickness of the overlying filter layers.

Furthermore, the upward decreasing permeability of the filter layers towards the overlying sand bed will result in uniformisation of the pressure. The corresponding value of $D^{ho} = 1.4\,\text{mm}$ is based on the minimum considered pressure of $\bar{p}^{int} = 50\,\text{kPa}$. In this way the load on the filter bed is limited, which depends on the pressure gradient by Equation 6.6.

The resulting design measures of the tubes are summarised in Table 6.1. It is concluded that the pressure distribution in the fluidisation system is expected to be uniform for these values. A shortcoming of our analysis is the energy loss as a result of turbulence, which has not been accounted for. The pressures in the fluidisation system have been monitored to verify its performance and the effect of turbulence (see Subsection 6.2.8 and Chapter 7).

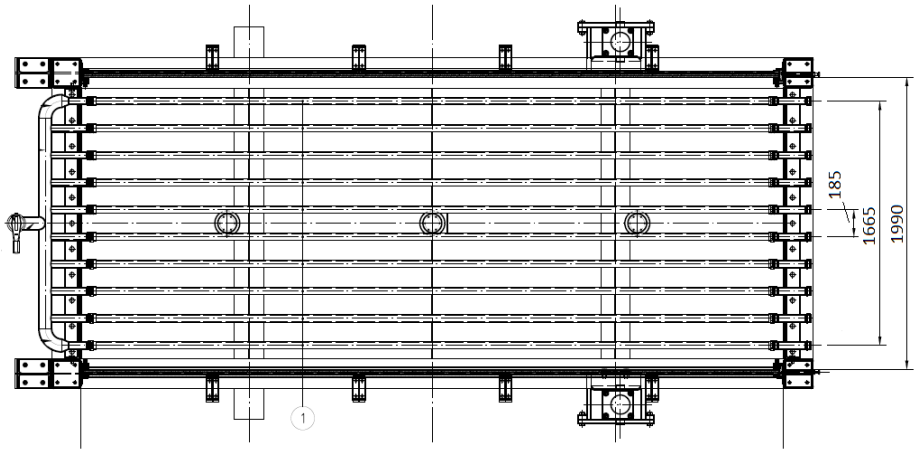


Figure 6.9: Building plan of fluidisation system in top view with measures in mm. The water inlet is depicted on the left.

Figure 6.9 shows the top view of the fluidisation system. The pump transports the water to the front end of the tank, where a welded pipe distributes the water over the tubes. Steel pipes running through the front end plate connect the distribution pipe to the PVC tubes inside the tank. The steel pipes running through the rear end plate and connected to the PVC tubes allow flushing of the fluidisation system. Note that holes were also drilled in the steel parts protruding into the tank. However, for practical reasons the holes are larger, directed diagonally upward and drilled at a larger mutual distance. The PVC tubes are embedded in two layers of granular filter material. The simple rule for a geometrically closed filter consisting of monosized filter layers has been applied, which states that the ratio of representative particle diameters should not be larger than 5. Assuming a minimum, median grain size of $D^{50} = 100\,\mu\text{m}$, industrial filter sand with ranges of 1.7 mm-2.5 mm and 0.2 mm-0.63 mm are applied from the bottom to the top, respectively. The different layers of granular material are separated by geosynthetic filter

layers. On top of the upper granular filter layer with diameter range 0.2 mm-0.63 mm a non-woven Ten Cate TS80 filter was placed, and in between the granular filter layers a woven Ten Cate PE 525. As the non-woven TS 80 filter lacks strength, an additional PE 525 was placed on top of this layer. In order to make sure that finer particles do not affect the fluidisation system, a TS 80 filter was also wrapped around the PVC tubes. On top of the granular and geosynthetic filter layers, a walking grid enables access to the (empty) tank without damaging the filter layers. The walking grid also provides sufficient resistance against flotation of the TS 80 layer, which has a low permeability. Finally, Table 6.1 provides an overview of the specifications of the fluidisation system.



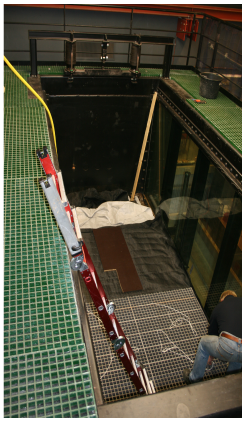


Figure 6.10: Construction of the first (lowest) granular filter layer. The fluidisation tubes are wrapped in a (white) geotextile, while a black geosynthetic layer separates the first and second granular filter layer.

Table 6.1: Composition of fluidisation system from top to bottom

component	**specification**
walking grid	synthetic, height: 37 mm, grid: 34 mm, wall: 8 mm
geosynthetic filter layer	PE525 Ten Cate, pore size: 0.35 mm
geosynthetic filter layer	TS80 Ten Cate, pore size: 0.09 mm
granular filter layer	Sand, thickness: 5 cm, grain diameter: 0.2 mm-0.63 mm
geosynthetic filter layer	PE525 Ten Cate, pore size: 0.35 mm
granular filter layer	Sand, thickness: 5 cm, grain diameter: 1.7 mm-2.5 mm
geosynthetic filter layer	around tubes, TS80 Ten Cate, pore size: 0.09 mm
fluidisation tubes	PVC, amount: 10, pressure class: 16 bar, internal diameter: 40 mm, length: 5 m, flow: 10 ls^{-1}, $D^{ho} = 1.6$ mm, $l^{ho} = 5$ cm

6.2.4. Filtering of water

During fluidisation, an overflow mounted on top of the end platen at the lower end of the tank discharges the presumably turbid water. The design of the liquefaction tank provides a filtering system in which the turbid water is filtered and the resulting clean water recirculated into the system. The dredging system also employs the filtering system to recirculate the water.

Figure 6.11 provides a schematic overview of the flow through the filtering system during fluidisation. The mixture overflowing from the liquefaction tank (LT) is directed to the filter tank (FT) in the basement, a cylindrical tank with an effective height of 2.30 m and a diameter of 1.90 m. The filter tank has a coarse filter layer at the bottom, overlain by a thin layer of the same sand that is used in the liquefaction tank. These granular layers form the first filter layer in the system. The hydraulic head in the filter tank promotes the water flow through these layers. The square tank BT1 with a volume of approximately 1.5 m^3 buffers the water from the filter tank and provides a reservoir for the first pump P01. This centrifugal pump with a flow capacity of 40 $m^3 h^{-1}$ at a pressure of 2.5 bar pumps the water through three levels of filters. The first, F01, consists of a small tank with filter bags aiming at filtering particles larger than 50 µm. The flow is subsequently directed through two candle filters, F02 and F03, filtering particles larger than 10 µm and 1 µm respectively. The second buffer tank BT2 with a volume of approximately 7 m^3 stores the clear water. Finally, for continued fluidisation the second pump P02, which is identical to P01, pumps the water from the basement to the liquefaction tank.

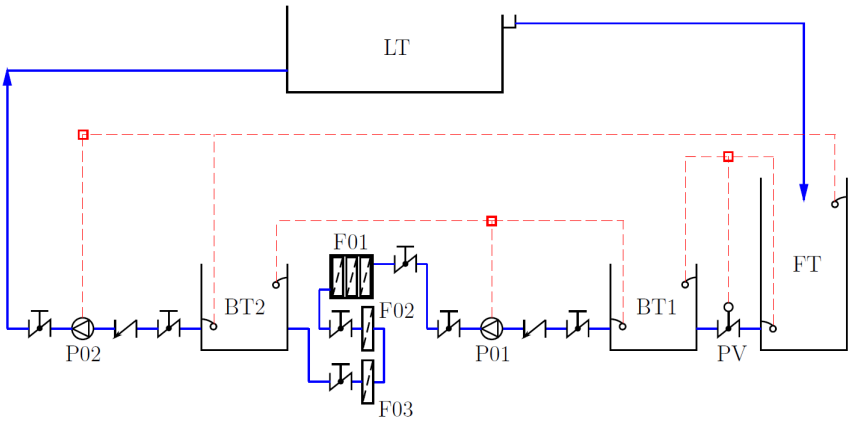


Figure 6.11: Schematic overview of filtering system with water flow depicted with the blue line and interrelations by the red dashed lines

Figure 6.11 also depicts a number of valves and switches that are used to control the filtering system. In between the filter tank (FT) and first buffer tank (BT1) a pneumatic valve (PV) has been installed. This valve controls the lower level switch in the filter tank

and the upper level switch in the buffer tank. The valve is automatically closed as soon as the water level in the filter tank becomes too low or the level in the buffer tank too high. It thus prevents the filter tank running dry and the overflowing of buffer tank BT1. In a similar way, the connection of pump P01 to level switches prevents the running dry of buffer tank BT1 and the overflowing of BT2. A butterfly valve controls the flow (and pressure) that is supplied by pump P01. The second pump P02, which is also controlled by a butterfly valve, is automatically switched off as the water level in the filter tank FT becomes too high or the water level in the buffer tank BT2 too low. Hence, the filtering system can run autonomously and safely, as level switches prevent the tanks in the system from running dry or overflowing. The system contains a number of additional valves which can be used to close of particular parts from the system, for instance during maintenance of the filters.

6.2.5. Sand

The test series addressed in this thesis were conducted on one type of sand. The performance in terms of (re)reproducibility of liquefaction flow slides in the tank governed the selection of the sand. Based on the experiences gained in engineering practice (Chapter 2), it was decided to opt for a fine, poorly graded sand with (sub)rounded grains. Considering the required availability of the sand, now and in the future, an industrially available sand was preferred over the excavation of a 'new' resource. *Geba Sand* was selected from several options. The company Eurogrit (www.eurogrit.com) supplies the sand, that is mined in a quarry in the south of Germany. The product sheet describes Geba Sand as a fine crystal, quartz sand with a SiO_2 content of 99%. The sand is washed and sieved after being mined. The product sheet refers to Geba Sand as a round shaped sand with a particle unit weight of $2650\,\mathrm{kg\,s^{-1}}$ and a median grain size diameter of $D^{50} = 103\,\mu$m. These properties of Geba Sand have been verified during this and related research projects [6–8]. Furthermore, Deltares has used the same type of sand for other scale model tests, for which the properties were also verified. The measurement error, applied methodology and soil variability, as well as the possible removal of fine particles by flushing, yield a variation in results. Table 6.2 provides an indicative overview of the main measured soil properties and their variations. The characterisation of the particle shape refers to Powers' method [9]. The determination of the minimum and maximum dry density have been carried out using the methods conventionally used at the labs of Delft University based on the Japanese method (JGS), and Deltares. A thorough description of both methods can be found in [10], p.119.

Table 6.2: Main properties of sand

D^{50}	D^{60}/D^{10}	e^{max}	e^{min}	FC	particle shape
µm	-	-	-	%	-
120 ± 18	1.45 ± 0.12	1.01 ± 0.06	0.64 ± 0.03	2 ± 1	subangular-subrounded

6.2.6. Dredging system

The envisaged next step during the preparation of the sand bed concerns the creation of a slope geometry by dredging. Originally, it was thought that tilting a level sand bed to 10° would not be sufficient to trigger a liquefaction flow slide in the tank. The dredging system thus aims at creating a slope by dredging, while the disturbance of the sand bed should be kept to a minimum. The experience previously gained during the experiments in the Brutus tank (see Subsection 2.2.1) was used to develop the dredging system. Three main components constitute the dredging system: the suction heads, pumps and supporting structure.

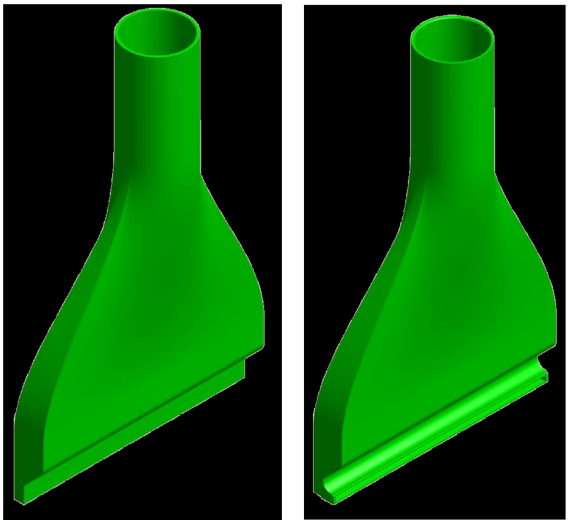


Figure 6.12: Three dimensional illustration of suction heads for vertical (left) and horizontal dredging (right).

The Brutus tank employed a single suction head to dredge a slope [3]. For the sake of uniformity, a system with multiple suction heads covering the full width of the liquefaction tank was preferred. The design first concentrated on the performance of a single suction head, that was tested in the minitank. It was decided to dredge the slope in two steps, which required the development of two types of suction heads. First, a suction head is moved vertically downwards to the planned level of the toe, thereby creating a natural slope in the sand bed. The suction head used for this first step requires an opening directed downwards. Then, the system is moved horizontally to create additional space in front of the slope. The second type of suction head thus requires an opening directed horizontally. Figure 6.12 depicts both types of suction head. The reason for using two steps in the dredging is the instrumentation that is installed in the sand bed. The sensors should be installed during fluidisation, which means that the dredging should take account of the wires that stick out of the sand bed. By dredging a natural slope the need for accessing the entire geometry with the suction heads has been resolved. The system does require the interchange of suction heads when the required depth has been

reached. Furthermore, the method of dredging by creating a small breach and letting the sand flow towards the suction head poses a risk of disturbance of the sand bed and failure of the slope during dredging. The risk depends on the rate of progress of the advancing suction heads.

The design of the suction heads requires the flow within the heads to be uniform. Except for the opening, the flow area of the suction head should be uniform over its height and equal to or larger than the area of the pipe connecting the head to the rest of the system. Furthermore, the geometry of the suction head should be smooth and continuous to minimise energy loss. These requirements lead to a complex geometry of the suction head. Fortunately, 3D-printing provides the possibility to reproduce complex geometries accurately. The suction heads were printed using stereo lithography of a transparent polymer in two parts, which were glued together. The height of the sand suction opening was selected at 3.5 mm, which is sufficiently large to prevent the jamming of particles during dredging. It is on the other hand sufficiently small to make sure that the area of the opening is much smaller than the area of the rest of the suction head. As a consequence, the pressure drop over the opening will be much larger than in the rest of the suction head, leading to a well-distributed flow over the width of the head.

The required flow velocity for the erosion of particles was estimated from Shield's diagram [11]. Assuming uniform flow conditions and a horizontal bed, a critical flow velocity of approximately $1\,\mathrm{cm\,s^{-1}}$ is obtained iteratively for a grain size diameter of $D^g = 120\,\mu\mathrm{m}$. A minimum value of $10\,\mathrm{cm\,s^{-1}}$ was selected to take account of the uncertainties. The required corresponding flow rate in the minitank equals $0.1\ \mathrm{l\,s^{-1}}$, whereas in the liquefaction tank it would be $1\ \mathrm{l\,s^{-1}}$. These are unusually low values for pumps that transport mixtures of sand. For the minitank, a self-priming centrifugal pump was selected with a flow capacity of $0.2\ \mathrm{l\,s^{-1}}$ at a feed pressure equal to 95 kPa for water. Considering the much lower feed pressures required for the minitank, a needle valve reduced the feed pressure while keeping the flow rate within the intended range. The actual flow rate was measured using a simple float, flow meter.

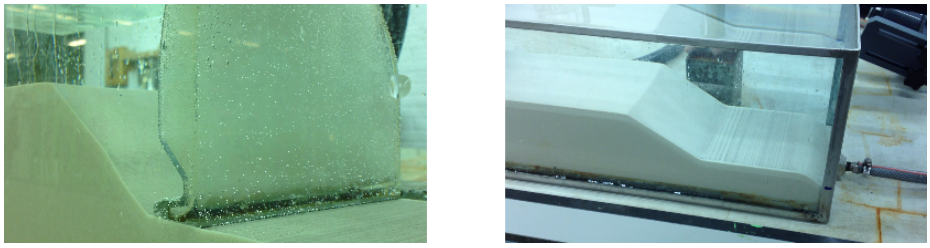


Figure 6.13: Sand suction in the minitank: sand suction in action (left) and resulting slope (right). The upstanding 1 kg steel block behind the minitank (visible behind the slope) in the right subfigure is pushed over to induce flow liquefaction.

Figure 6.13 demonstrates the performance of the dredging system in the minitank. The

actual flow rate that was applied equalled 750 ls^{-1}, or a flow velocity of 20 $cm\,s^{-1}$, which is well above the critical velocity. The pump could not provide lower values without starting to shake. Additional tests that were performed at lower flow rates did show that a flow rate of 0.1 ls^{-1} amply suffices to erode the sand bed. The left hand side of Figure 6.13 shows the horizontal suction head in action. The suction head initiated a small breach that feeds the head while progressing upwards. The suction was very well distributed over the width of the head. The right hand side of Figure 6.13 shows the dredged profile, which confirms the good performance of the suction heads. It should be noted that dredging did yield some disturbance of the sand bed; the surface of the approximately 10 cm high sand bed settled 4 mm. Nevertheless, the sand bed appeared to be highly susceptible to flow liquefaction. During a few tests the slope failed as a result of irregularities caused by dredging. The slope depicted on the right-hand side of Figure 6.13 failed after pushing over the 1 kg block that is shown behind the minitank. The falling block did not affect the minitank directly, but produced vibrations that triggered failure of the slope.



Figure 6.14: The dredging system for sand suction in the liquefaction tank

For the liquefaction tank, the suction heads were somewhat scaled up to fit the full width with eight suction heads (see Figure 6.14). In order to impose a relatively low and stable suction pressure (and flow rate), each of the eight suction heads is equipped with a venturi system. Water is pumped into a central pipe that distributes the water over eight hoses that are looped to the central outflow pipe. The venturis provide a narrowing part in the hoses where the flow accelerates and, as a consequence, the pressure decreases. A cross pipe connects the narrowing part with each suction head. The applied suction can be controlled by adjusting the flow rate that is pumped through the central system. A total suction flow rate of 1 ls^{-1} provided by the eight suction heads requires a flow rate of approximately 10 ls^{-1} to be supplied by the pump. The flow rate is similar to the flow rate required for fluidisation, which means that the same pump can be used. The out-

let of the dredging system is connected to the filter tank. Both the hoses connecting the inlet and outlet of the dredging system are hung freely on a rail connected to the ceiling of the laboratory, which prevents any vibrations being introduced into the liquefaction tank through these hoses.

A four-wheeled frame supports the dredging system and allows it to be moved in the lateral direction along the tank. During the changing of suction heads or after the dredging has ended, the dredging system should be lifted out of the water and rotated horizontally. Initially, a manual system with a chain and tensioner was used to rotate the system. Furthermore, the chain was used to keep the dredging system stable during dredging, as it had the tendency to tilt over. However, the system also appeared unstable in its rotated configuration, when it had the tendency to tilt back. Some adjustments have been suggested, including an extension of the supporting frame and the replacement of the chain by a control mechanism involving an electric, linear actuator (see Figure 6.15). However, as the dredging machine was never actually used during this research project, the further development was left to the subsequent research project.

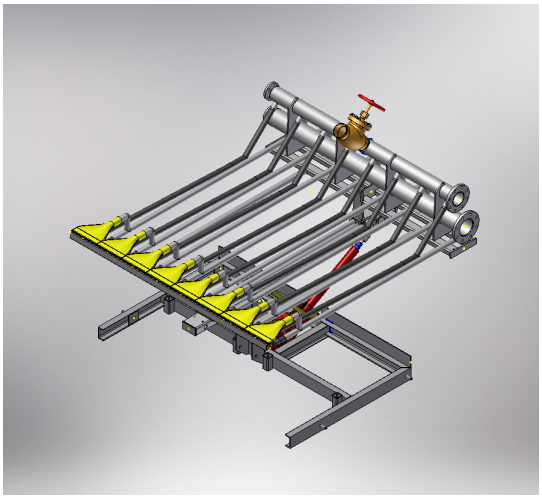


Figure 6.15: Design of tilting mechanism for dredging machine with control mechanism in red

6.2.7. Triggering systems

The liquefaction tank has been developed to test several types of triggers, e.g. drawdown of the water table, horizontal seepage flow through the slope, etc. During this research project the focus was on the development of two types of triggers: tilting of the tank and a strip load on the crest. This subsection will describe both, even though only the former was actually applied during this research (see Chapter 8).

A pure, static trigger implies that the load is applied at a slow rate and without any form of disturbance. The loading brings a part of the slope to a metastable stress state, af-

ter which any perturbation yields instability, inducing fast motion of the unstable bulk soil mechanism with an almost undrained response of the soil. Therefore, the design of the tilting system was principally aimed at a vibration-free, slow and uniform tilting system. A system consisting of two screw jacks that are interconnected by a cross beam to ensure a synchronous motion was selected. Electrically driven screw jacks tend to induce less vibrations than hydraulic systems. Contrary to hydraulic systems, they are also self-locking in the case of a power breakdown. However, although a uniform tilting rate may be appealing from a theoretical viewpoint, it is no guarantee that flow liquefaction is initiated. The system was additionally designed for alternative tilting rates, that is, a quadratic and cubic dependence of the tilting angle θ in time. The option of a sudden halt of the tank during rotation was also included, which will introduce additional momentum of the slope. It was decided to base the required power on a maximum tilting rate of $\dot{\theta} = 0.115\,^{\circ}\mathrm{s}^{-1}$ for uniform, quadratic and cubic tilting profiles. Based on the anticipated loads, two trapezoidal Unimec TP8010 screwjacks were selected with a diameter of 98 mm, a stroke of 1200 mm and a total transmission of 0.33 mm rotation^{-1}. The required power is governed by the tilting profile, mass of the tank filled with water and sand, and the efficiency of the components in the system. A Kollmorgen AKM 83T servomotor with a maximum couple of 70 N m and a maximum power of 16.1 kW was selected. The tilting system was elaborately and successfully tested before conducting the tilting tests. However, the design conditions, that is, cubic tilting of the completely filled tank had not been tested yet.

The second triggering system that was developed is the fast loading of a strip footing along the crest of the slope. There are two essential differences compared to the discussed tilting of the tank. The loading of a strip footing is a trigger that is applied locally and at a high rate. During the initial stage of load buildup it is likely that undrained conditions will prevail. However, in time the slope will start to deform which will affect the magnitude and direction of loading. It is therefore important to monitor the properties of the trigger during its application.

The crest load system hangs on a frame that is mounted on the steel box beams on top of the liquefaction tank (see Figure 6.16). Several holes drilled in the box beams enable the positioning of the crest load system along the liquefaction tank. The center part of the crest load system consists of two bellows, a cross beam and the system that allows the release of the trigger. The two Firestone 1T15M-9 bellows supply the loads during triggering. The pressure that is applied in the bellows defines the load that will be exerted upon release. Depending on the initial height of the bellows, the load can be maintained over a substantial period of time after release. The two bellows are connected by a cross beam, that is connected vertically to the system that allows the release of the trigger. This system contains a shackle, which is held in position by a pin. When the pin is removed, the shackle will be disconnected and the bellows will release their force on the crest.

The lower part of the crest load system contains the instrumentation, two rods and the plate that lies on the crest. Two trapezium rods connect the plate on the crest to the center part of the crest load system. The length of the rods can be adjusted using a tight-

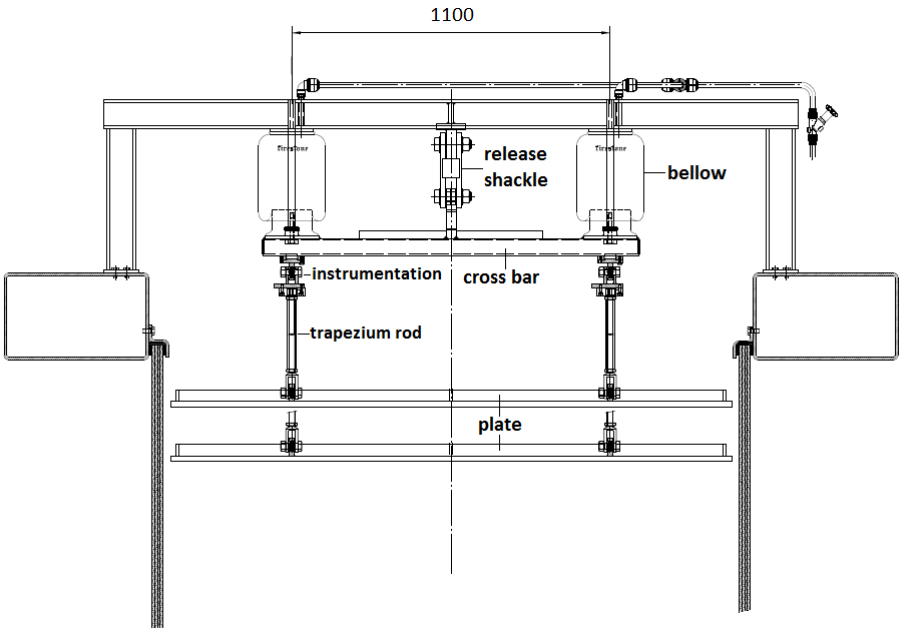


Figure 6.16: Building elevation of crest loading system in front view with measures in mm

ening screw to make sure that the lower plate rests on the crest. The instrumentation is mounted between the rods and the cross bar. A load cell measures the load that is transferred from the bellows to the crest. A spherical hinge on top of the load cell excludes the possibility that a moment is exerted on the load cell. A displacement and inclinometer measure the vertical displacement and rotation of the load cell, respectively. The plate on the crest, with a width of 14 cm and thickness of 15 mm, is connected to the rods, but can rotate freely in the direction of the slope. The rotation, which allows the plate to keep its orientation parallel to the crest surface during deformation of the slope, is measured by another inclinometer. The loading of a strip footing has been developed, but not tested nor used during this research project.

6.2.8. Instrumentation and data acquisition

The instrumentation provides the information required for the simulation by means of finite element models. The selection of the sensors therefore aims at measuring displacements and stresses. These are to be measured at both (a) fixed positions at the contact surface between the slope area and the tank, and (b) within the sand bed. This research has mainly concentrated on the fixed sensors measuring stresses, which will be considered in more detail. In addition, the data acquisition system that has been developed will be elaborated. Only a part of the sensors and data acquisition has actually been used during the fluidisation and tilting tests.

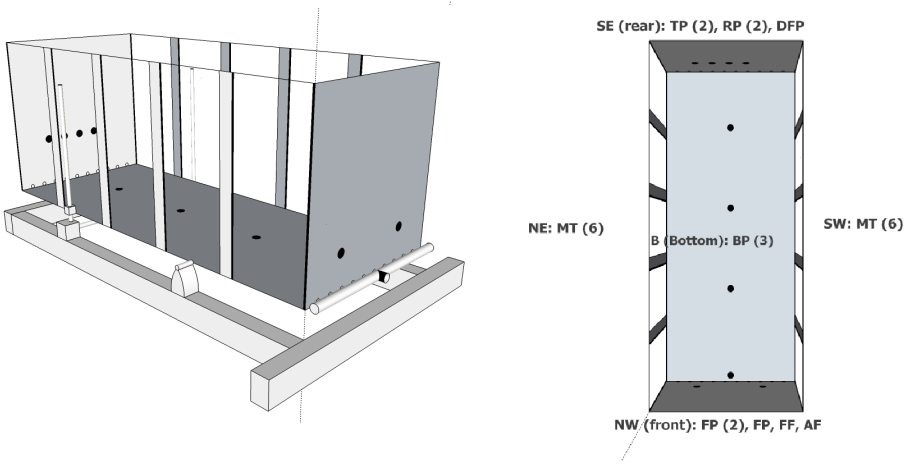


Figure 6.17: Sketches of the liquefaction tank with instrumentation. The three dimensional sketch on the left provides a general overview of the locations of the instrumentation, while the top view (right) specifies the orientation of the sides of the tank and the sensors. The pressure sensors are indicated by the circular filter plates. Note that one of the filter plates at the bottom is used for the drain, rather than a sensor.

Figure 6.17 gives an overview of the fixed sensors in the liquefaction tank. For the sake of clarity, each of the four sides of the liquefaction tank (in top view) is indicated by its orientation. The front is directed to the northwest (NW), and the rear to the southeast (SE). The sides are directed to the northeast (NE) and southwest (SW). From here on, each of the sides will be referred to by its orientation.

The liquefaction tank allows for measurements in the fluidisation system, at the bottom and end platens, and at the transparent sides. The sensors in the fluidisation system measure the fluidisation flow rate (FF) and pressure (FP) in the inlet pipe at the front, and the differential pressure between the fluidisation tube and the tank at the rear (DFP). Fluid pressures are measured at two positions at the front (FP), three positions at the bottom (BP) and two locations at the rear (RP). The total stress is also be measured at two locations at the rear (TP). Six vertical measurement tapes (MT) have been glued on each of the transparent sides of the tank to monitor the vertical displacements of the sand bed.

Figure 6.18 specifies the locations of the sensors in more detail. The measurement tapes MT1-MT12 have been glued at the front sides of the vertical beams and are therefore evenly distributed along the tank. The resolution of the tapes is 1 mm, while the accuracy of reading depends on the variability of the level of the sand bed (in time and space) and the skill of the reader. In order to minimise the reading error, the level of the bed is monitored at eye level.

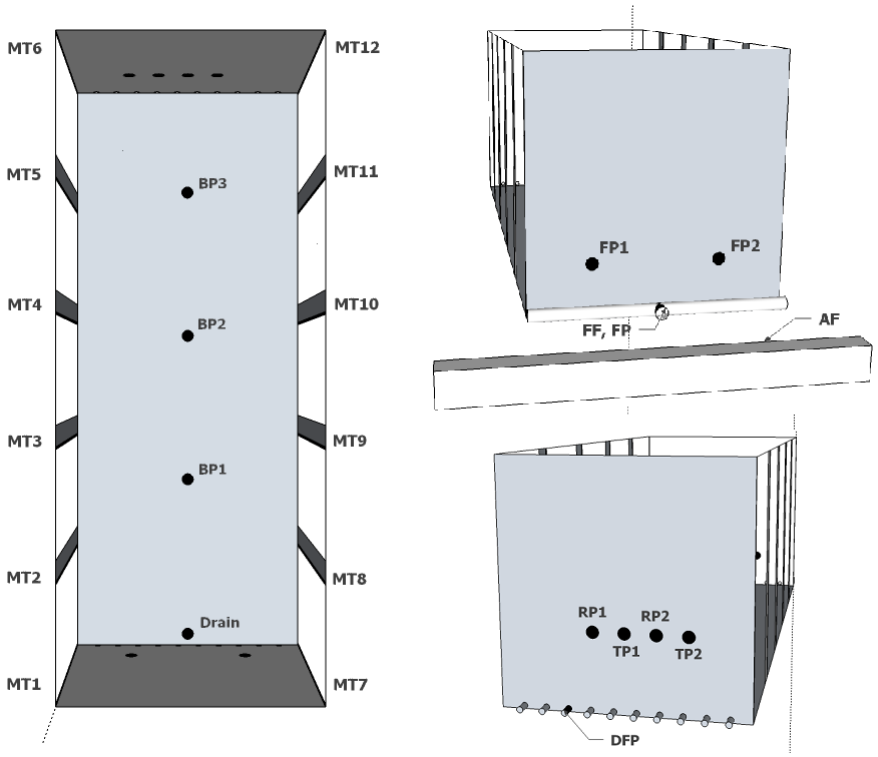


Figure 6.18: Designation of sensors in top view (left), front view (right, top) and rear view (right, bottom). The acceleration sensor AF is mounted on the frame below the tank.

The bottom of the tank contains a drain and the fluid pressure sensors BP1-BP3. The drain is positioned close to the platen at the NW-side, the sensor BP1 at 1 m from this platen. The mutual distance between the BP sensors is 1.3 m. The interface between the sensor and the tank was designed to allow for the removal of the sensor from outside the tank. Flanges mounted at the bottom of the tank allow the sensors to be screwed into a fitting, overlain by a filter plate to protect the sensors from the sand in the tank. The chambers in between the sensor and the filter plate can be saturated from the outside using a tube and de-aired water. The anticipated pressure resulting from 2 m of liquefied sand governs the pressure range of 0-50 kPa of the selected PR-25Y Keller sensors. The corresponding accuracy equals 0.5% of the full scale, i.e. 0.25 kPa. Four additional fluid pressure sensors are located at the end platens. Sensors FP1 and FP2 are located at the NW-side, symmetrically at 0.5 m from the sides and 0.4 m from the bottom. Sensors RP1 and RP2 are symetrically positioned at the SE-side at 0.75 m from the sides and at a level of 0.65 m from the bottom. The design of the interface with the tank and the selected types of sensors (PR-25Y Keller) are identical to the sensors at the bottom of the tank.

The sensors in the fluidisation system primarily aim at verifying and controlling the fluidisation process. The verification of the design of the fluidisation system (Subsection 6.2.3) requires the measurement of the fluidisation flow rate and the internal and external pressure in the fluidisation system at both the front and rear end of the tank. The flow meter FF is placed in the hose connecting the pump P02 with the entrance pipe at the NW-side of the tank. The selected Krohne Optiflex 2100C sensor has a range of 0-20 $\mathrm{l\,s^{-1}}$ and an accuracy of 0.5% of the full range, i.e. 0.1 $\mathrm{l\,s^{-1}}$. During the tilting tests, the fluidisation flow rate will be used to control the initial density of the sand bed. The pressure sensor FP measures the fluid pressure in the entrance pipe at the NW side of the tank. The selected Keller PR-33X sensor has a pressure range of 0-100 kPa, corresponding to the anticipated pressure range during fluidisation (see Subsection 6.2.3), and an accuracy of 0.1% of the full range or 0.1 kPa. The differential pressure sensor DFP accounts for both the internal and external pressure at the rear end by measuring the difference. The GDS Instruments Kit wet-wet pressure transducer has a range of 0-69 kPa and an accuracy of 0.25% of the full range or 0.17 kPa. It should be noted that both pressure sensors in the fluidisation system also appeared to be useful during tilting (see Subsection 6.2.3).

Unlike the sensors specified above, the total load cells TP1 and TP2 were developed in-house. The total pressures measured by these sensors are combined with the adjacent fluid pressure sensors RP1 and RP2 to determine the horizontal, intergranular stress. The two key requirements of the total load cell are the minimisation of the disturbance of the sand bed during measurement and the possibility to capture both gradual and fast changes of the total horizontal stresses. The undisturbed measurement of the total horizontal stress requires the load cells to remain essentially undeformed, as the smallest deformations will affect the stress development in the bed. Hence, the deformations of the sensor required to measure the stresses need to be compensated. The horizontal stress is likely to change gradually during the fluidisation phase. During and after triggering it may change both gradually, for instance during reconsolidation, and fast as (undrained) waves propagate through the sand bed. Both stages need to be captured by the load cells.

The design of the total compensated load cells is based on the measurement of horizontal stresses in the lateral stress oedometer [12]. In the referenced research, three diaphragms fitted with strain gauges on the inside were machined on an oedometer ring. Behind the diaphragms oil filled reservoirs were connected to three independent pressure control pumps. These kept the diaphragms in line with the boundary by controlling the oil pressure, which should equal the lateral stress exerted on the ring. The same concept was applied herein, albeit with some modifications. The two load cells have been scaled up to the same size in terms of contact area with the sand bed as the adjacent water pressure sensors. The response of the diaphragm has been used to capture fast phenomena. Initially, a steel diaphragm was also applied and the strain gauges used to measure instant changes in the horizontal, total stress. An air instead of oil filled reservoir allowed the instant deformation of the diaphragm. A peristaltic pump controls the air pressure that is used to bring the diaphragm back to its original state. The steel diaphragms were manufactured as thin as practically possible using turning, that is, a 0.15 mm thickness. Assuming the diaphragm to deform like a clamped plate, the

response of the strain gauges can be calculated in terms of stresses. Note that both pressure and tension can be monitored in this way. Unfortunately, the response of the diaphragms appeared to be unstable during the testing of the total load cells. The manufacturing of the diaphragms presumably yielded residual stresses, which caused the buckling of the diaphragms.

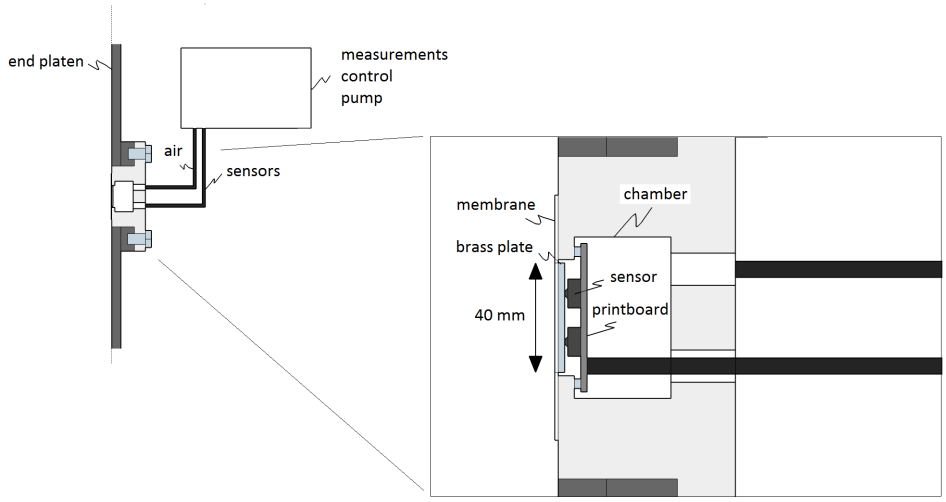


Figure 6.19: Layout of load cell with overview (left) and components specified (right)

The steel diaphragms and strain gauges were replaced by a load-controlled system. The circular gap that was left by the diaphragm was closed using a thin, latex membrane that has been glued at the outside of the load cell. The latex membrane provides a simple alternative to seal the sensor from the water in the tank, but also has different properties than the end plate itself. Penetration of the grains affects the development of stresses in the sand bed. It is assumed that this effect is relatively small. At the inside of this membrane a 2 mm thick, circular brass plate has been glued that is just (1 mm in radius) smaller than the original, steel membrane. The brass plate thus almost covers the gap left by the diaphragm, but is still able to deform freely in the direction of the horizontal stress (see Figure 6.19). Three Honeywell FSS1500NSB force sensors support the brass plate inside the chamber. Any change in horizontal pressure exerted on the brass plate is thus instantly recorded by these sensors. Using these sensors instead of strain gauges yields a much stiffer, instant response and therefore less disturbance of the sand bed during measurement. The three sensors have been soldered to a printboard, which has been stiffly screwed to the wall of the chamber using brass collars. The permeable print board does not impede the influx and outflux of air. The print board produces the average output of the three sensors. Any possible disparity between the sensors is thus accounted for.

A separate unit processes the measured force (or stress) and controls the influx and outflux of air. The signal from the sensors is processed along two paths. After being amplified, the signal is sent both to the data acquisition system, which processes the 'fast' measurement, and to the micro controller. The latter has a set point for the signal, which corresponds to the initial, undeformed configuration of the brass plate. A deviation from the set point, i.e. a change in the measured total horizontal stress, triggers the peristaltic pump that will control the pressure in the chamber until the set point has been reached once again. The pressure in the chamber provides the 'slow' measurement.

It should be noted that the sensors have been modified during the test series. During the tilting tests, only one of the two total load sensors (TP1) was modified, whereas the other (TP2) was still operating with a steel membrane and strain gauges. The latter yielded an unstable response and could not be used. The total load cells were calibrated using a PVC tube filled with water. Even though both the 'fast' and 'slow' measurements have been calibrated, the interest in this thesis lies mainly in the latter. Determining the accuracy of this 'slow' measurement is not straightforward, as it concerns a controlled quantity that depends on various factors. The accuracy is here defined for a stationary situation. In the case when the stress changes over time, there will be a phase lag between the 'slow' and 'fast' measurements. The consequent 'error' in the slow measurement depends on the rate of change of the horizontal stress and needs to be determined for the specific situation. The stationary accuracy is estimated by considering the measurements conducted during the tilting tests (Chapter 8). During the initial stage, i.e. before fluidisation, the water level is constant and any fluctuations in the measurements are believed to be the result of the (in)accuracy of the load cell. The corresponding error is the summed result of contributions from the load sensors, pump, etc. After considering several test results, the estimate of the maximum deviation from the true vale is 0.1 kPa. Assuming a full scale of 50 kPa, the accuracy is 0.2%FS.

The accelerometer (AF), depicted in Figure 6.18, has been attached to the frame at the NW-side of the tank. Its purpose is to verify whether any vibrations are induced from inside or outside the tank that may disturb the sand bed. The stiff tank structure and frame make the actual location of the sensor irrelevant. The accelerometer consists of two sensors, which allow the measurement in three directions. The axes of the sensors are aligned in the logitudinal (SE-NW), transverse (NE-SW) and vertical directions. The possible measurement range is 0.5g in all directions, while the accuracy equals 1 mg. Table 6.3 specifies the range and accuracy of the sensors.

Table 6.3: Specification of sensors

sensor	**label**	**type**	**range**	**accuracy**
pore water pressure	BP, FP, RP	Keller PR-25Y	0-50 kPa	0.5% FS
measurement tape	MT	NA	0-200 cm	0.05% FS
pore water pressure	FP	Keller PR-33X	0-100 kPa	0.1% FS
total pressure cell	TP	in-house	0-50 kPa	0.2% FS
diff. water pressure	DFP	GDS wet-wet kit	0-69 kPa	0.25% FS
flow meter	FF	Krohne optiflex 2100C	0-20 ls^{-1}	0.5% FS
accelerometer frame	AF	Sherborne A710,A720	$\pm 0.5g$	0.2% FS

A data acquisition system was developed based on the future functional requirements of the instrumentation in the liquefaction tank. These functional requirements mainly concern the number of sensors, the sampling frequency and the triggering of the acquisition system during a flow slide. In addition to the sensors depicted in Figure 6.17, the data acquisition system should allow the processing of the output from sensors in the sand bed, the crest loading system and a camera system. The sampling frequency should be as large as 1 kHz to capture the propagation of fast phenomena (the undrained wave) during the triggering of flow liquefaction. However, sampling at a high frequency results in a great amount of data, a part of which will be abundant. Therefore, the system should trigger the high frequency sampling at the moment the flow liquefaction is triggered, i.e. as the excess pore water pressures and/or accelerations in the sand bed instantly increase. During the fluidisation and tilting tests another, provisional data acquisition system was used. The use of this system allowed the fluidisation and tilting tests to be conducted while the intended system was still under development. Even though the provisional system did not provide the convenience of the intended system, its performance was not inferior to it for the tests that were performed. Both in terms of (connection) capacity and sampling frequency, the provisional system met the requirements, although it was necessary to use separate systems for data acquisition and control of the tilting mechanism. As a consequence, the tilting mechanism and measurements had to be synchronised during the post-processing (see Subsection 8.2.3). Furthermore, the high sampling frequencies could not be triggered during testing, which occasionally led to large amounts of stored data.

The data acquisition system used during the fluidisation and tilting tests consists of two NI USB 6211 data acquisition modules connected to a desktop computer. An in-house software package ("MP3") was used to process the data acquired by the acquisition modules. The sampling rate of the modules was set at 2 kHz in order to capture the noise generated by the system voltage of approximately 50 Hz. From a specified cut-off value, the higher frequencies are filtered out using a first-order low pass filter. By using the double entry input of the acquisition modules the system neutralised the disturbance caused by the tilting motor. The tilting rate of the motor was controlled using Labview software

installed on a separate laptop. The software allowed for tilting at a rate of $0.11\,\mathrm{deg\,s^{-1}}$ and $0.011\,\mathrm{deg\,s^{-1}}$.

6.3. Novel sample preparation procedures for triaxial apparatus

6.3.1. General

One of the key requirements of the liquefaction tank is its compatibility with element testing in terms of density, soil micro-structure (fabric) and effective stress (history) of the sand bed. The compatibility between both promotes the understanding of the outcome of the liquefaction tank tests and allows for its extension to field conditions by means of computational models. This section will treat the development of novel sample preparation procedures that are compatible with the preparation procedure of the model slope in the liquefaction tank. A suitable preparation procedure requires the following quantities to be reproduced sufficiently well:

- The low density involves the way the grains are deposited during sample preparation. Various methods exist for achieving very low densities. In particular, very loose states can be created by means of moist tamping.
- The soil micro-structure (fabric) of the sand is rather more problematic, because the fabric of natural (sub-angular) sand cannot be quantified mathematically and measured objectively as yet. Nevertheless, it is anticipated that for uniform sand, fluidisation and sedimentation provide a reasonably reproducible preparation procedure. It seems reasonable to expect that the corresponding micro-structure of the sand is reproducible as well, although this assumption cannot be proven as yet.
- The mean effective stress involves the ratio of the geometrical scales of the slope in the liquefaction tank and the representative soil element for element testing, assuming that the accuracy of the sensors can be selected as sufficient.

The choice for the *triaxial* test as an element test is motivated by the frequent use of the test in engineering practice and the relative simplicity of its interpretation. The experience that will be gained with the development of the triaxial apparatus may be employed for the development of novel versions of more advanced element tests in the future. Only the main principles behind the development of the novel triaxial sample preparation procedures are discussed here. The elaboration of the design, production and assembly of the new components is beyond the scope of this thesis. An internal report provides details on the design [13], while the production and assembly is left for a future research project. This section aims at answering the questions on how compatibility can be established and to what extent and accuracy.

6.3.2. Testing procedures

The preparation of the sample, the application of the effective stresses during consolidation and the undrained loading of the sample should mimic the situation as close as

possible for a representative sample in the liquefaction tank. Being a reference for the material response, the soil properties and imposed stresses should be well-defined and uniformly distributed over the sample. The key challenge of developing this novel triaxial apparatus lies in the extremely low stresses and densities that are anticipated in the liquefaction tank while satisfying these requirements.

The structure and density in the liquefaction tank can be approximated in the triaxial tests by also using fluidisation to prepare the sample. To the Author's knowledge, this preparation method has not been applied before in the triaxial test. Applying fluidisation requires a number of amendments to the pedestal [13], which will not be discussed in more detail. Furthermore, the expanding sand column requires an expansion of or attachment to the preparation mould. Two preparation procedures will be investigated.

The first procedure corresponds closely with the fluidisation-sedimentation-sand suction process that is employed in the liquefaction tank. The design of the liquefaction tank assumes an expansion of the sand bed to 2.0 m during fluidisation, followed by sedimentation resulting in a thickness of 1.5 m. A representative soil sample at center-height corresponds with an expanded column of 1.0 m and a sedimented column of 0.75 m height. Practically, this will be established by mounting a transparent fluidisation tube on top of the mould. The tube with a height of 0.8 m has an overflow to enable a continuous fluidisation process and to flush out the fines. A siphon tool is used for the layer-by-layer sand suction [13]. Note that the same tool was actually used to determine the density established in the permeameter tests that were conducted to investigate the fluidisation process (see Subsection 7.2.2, Figure 7.11).

The second procedure does employ fluidisation, but does not employ sand suction to prepare the sample. This procedure is more similar to conventional preparation techniques than the first. The sample with an initial height of 20 cm is fluidised inside the mould, after which one-dimensional compression is used to consolidate the sample to the desired stress level. A short, transparent fluidisation tube with an overflow is mounted on top of the mould to facilitate the fluidisation process. Both procedures will be considered in the subsequent sections to investigate the anticipated performance in terms of stress paths, disturbance and uniformity of stresses and density.

Irrespective of the procedure, the preparation will result in an extremely loose and sensitive sand sample. In conventional triaxial testing, the back pressure is applied to keep the sample stable when the split mould is removed. However, it is expected that this procedure would disturb the highly sensitive soil sample; hence, the back pressure will be kept to a relatively low value to minimise disturbance. The cell will be split into a lower and upper half. The lower part of the cell will be put in position and filled with water to support the sample before removing the mould. The mould should be removed slowly and carefully to allow the cell water to enter the space between the mould and the sample. To this end, a special mould has been designed that can be opened by rotating a bolt connected to a system of cog-wheels. Considering the limited amount of space between this mould and the cell wall, its removal will be a delicate task [13].

The final stage of testing is a conventional triaxial test. After closing the cell by connecting the upper part to the lower part, the sample will be saturated using an increased back pressure while keeping the intergranular stress constant. Next, the sample can be consolidated to arrive at any desired effective stress state. However, the possible disturbance of the sample should be accounted for when selecting the initial, effective stress state. If this stress state differs substantially from the stress states reached during the previous stages, the sample will most likely be disturbed. The subsequent sections will elaborate the effective stress paths that are imposed during the stages of fluidisation, sedimentation, removal of the mould and triaxial testing.

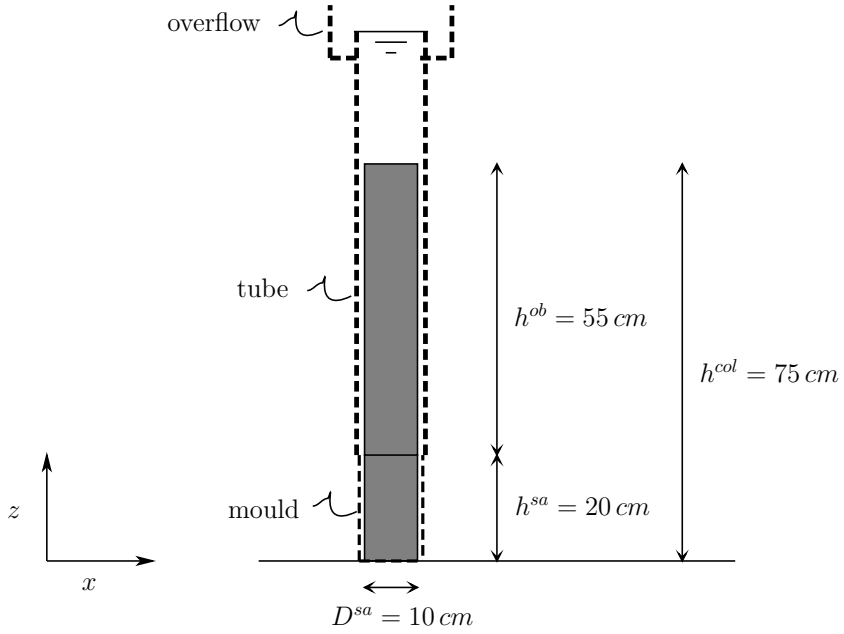


Figure 6.20: Measures of soil column after fluidisation in novel triaxial cell.

6.3.3. Preparation by fluidisation-sedimentation-sand suction

General

The effective stress paths during fluidisation, sedimentation and sand suction will be considered. The effective stress paths are expressed in terms of the isotropic, effective stress p' and deviatoric stress q. These invariants, previously defined by Equations 2.3 and 2.4, reduce for principal directions and triaxial conditions to:

$$p' = \frac{\sigma'_1 + 2\sigma'_3}{3} \tag{6.24}$$

$$q = \sigma'_1 - \sigma'_3 \tag{6.25}$$

where the principal effective stress σ'_1 is defined by the axial, effective stress and $\sigma'_3 = \sigma'_2$ by the radial, effective stress. Figure 6.20 provides an overview of the main measures of the soil column after sedimentation and defines the reference triad. During and after fluidisation the soil column is fully submerged. The buoyant weight of the soil determines the value of the major principal effective stress σ'_1 at a level z in a column of soil with height h^{col}:

$$\sigma'_1 = \rho^{buoy} g(h^{col} - z) = (1-n)\left(\rho^g - \rho^f\right) g(h^{col} - z) \tag{6.26}$$

It is assumed that the minor principal stress σ'_3 after sedimentation is defined by K^0-conditions, leading to:

$$\sigma'^{sed}_3 = K^0 \sigma'_1 \tag{6.27}$$

During the removal of the sand column in the tube by sand suction, the soil column below will be unloaded with a presumably stiffer rebound of the soil. The incremental stiffness measure K^{ur} for unloading-reloading defines the stress path during unloading:

$$K^{ur} = \frac{\Delta\sigma'_1}{\Delta\sigma'_3} \tag{6.28}$$

These stress ratios may also be expressed in terms of the deviatoric stress q and isotropic effective stress p'. To this end, the deviatoric stress ratio M is introduced:

$$M = \frac{q}{p'} = \frac{3(\sigma'_1 - \sigma'_3)}{\sigma'_1 + 2\sigma'_3} \tag{6.29}$$

By dividing both the numerator and denominator by σ'_1 a relation is derived between M and the (generic) principal effective stress ratio $K = \sigma'_3/\sigma'_1$:

$$M = \frac{3-3K}{1+2K} \leftrightarrow K = \frac{3-M}{2M+3} \tag{6.30}$$

The failure locus, specified by the friction angle ϕ, bounds the stress space. The friction angle can also be expressed in terms of the deviatoric stress ratio M, yielding a value for failure under triaxial compression M^{com} and extension M^{ext}:

$$M^{com} = \frac{6\sin\phi}{3-\sin\phi} \tag{6.31}$$

$$M^{ext} = -\frac{6\sin\phi}{3+\sin\phi} \tag{6.32}$$

Combining Equations 6.31 and 6.32 with Equation 6.30 allows failure to be expressed in terms of the stress ratio K. For instance, substituting a friction angle $\phi = 30°$ corresponds with $K = 1/3$ for compression and $K = 3$ for extension. One usually refers to active and passive failure when using these stress ratios.

Fluidisation and sedimentation

A porosity of $n = 0.5$ has been assumed after the column sedimented to a height of $h^{col} = 0.75\,\text{m}$ (see Figure 6.20). Substituting these values into Equation 6.26 results in:

$$\sigma'_1 = 8093(0.75 - z) \tag{6.33}$$

where the resulting stress is expressed in terms of Pa and level z should be expressed in m. Assuming a value of $K^0 = 0.5$, the corresponding minor principal stress after sedimentation reads:

$$\sigma'_3 = 4046(0.75 - z) \tag{6.34}$$

For the top ($z = 0.2\,\text{m}$) and bottom ($z = 0\,\text{m}$) of the sample in the mould, the pricipal stresses are calculated and expressed in terms of isotropic effective stress p' and deviatoric stress q using Equations 6.24 and 6.25. Figure 6.21 plots the resulting stress path for the top (T) and bottom (B) of the sample. The boundaries for active (ϕ^{com}) and passive (ϕ^{ext}) failure are drawn for a friction angle of $\phi = 30°$, while using Equations 6.31 and 6.32.

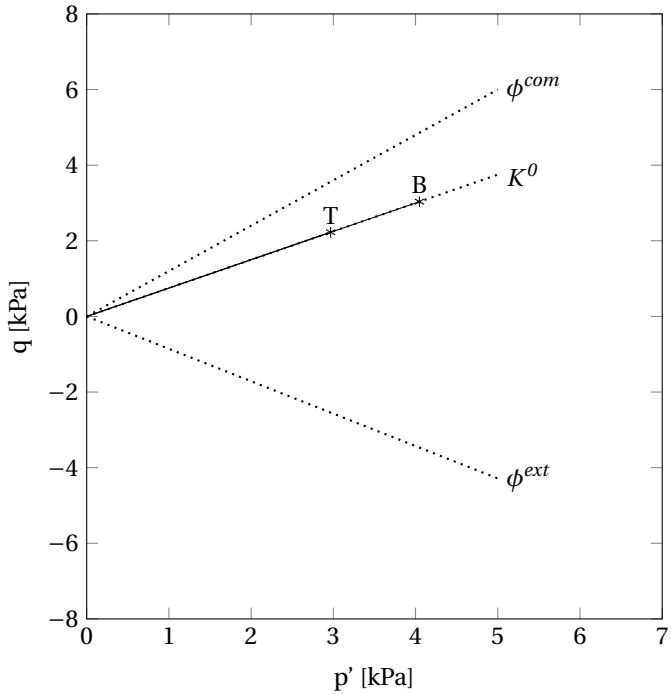


Figure 6.21: Stress path during sedimentation at top (T) and bottom (B) of sample in the mould

Sand suction

The stresses at the top and bottom of the sample in the mould will be lowered during sand suction. The decrease of the major principal effective stress σ'_1 will be de-

termined by the decrease of the buoyant weight on top of the sample, while the decrease of the minor principal effective stress σ'_3 is defined by Equation 6.28. A value of $K^{ur} = 0.2$ is assumed during unloading, which lies in the approximate order of magnitude $0.3 \geq K^{ur} \geq 0.1$. As a consequence, the stress path during unloading will be steeper than during K^0-loading (sedimentation) in the (p', q)-plane. At the top of the sample, the final stress point will lie at the origin after the removal of the entire overburden. It is inferred that the stress path of the top of the sample in the mould during unloading will hit the (passive) failure locus, which will be followed until the origin is reached (see Figure 6.22). The bottom of the sample will remain within the presumed elastic domain. Somewhere between the bottom and top of the sample in the mould, there will be a transition level at which the sample just reaches passive failure illustrated by point F in Figure 6.22. Above this level the sample fails passively, whereas below, it will be elastically unloaded. After sedimentation the principal effective stresses at this transition level (F) equal:

$$\sigma'^{sed;F}_1 = (1-n)\rho^{buoy} g (h^{col} - z^F) \tag{6.35}$$

$$\sigma'^{sed;F}_3 = K^0 \sigma'^{sed;F}_1 \tag{6.36}$$

Due to removal of the sand column in the tube by means of sand suction these effective stresses will decrease as follows:

$$\sigma'^{suc;F}_1 = \rho^{buoy} g \left(h^{sa} - z^F\right) \tag{6.37}$$

$$\sigma'^{suc;F}_3 = \sigma'^{sed;F}_3 - K^{ur} \Delta\sigma'^{suc;F}_1 = K^0 \rho^{buoy} g \left(h^{sa} - z^F\right) + \left(K^0 - K^{ur}\right) \rho^{buoy} g h^{ob} \tag{6.38}$$

in which h^{ob} is the height of the sand column after sedimentation in the tube, as indicated in Figure 6.20. Passive failure is reached when the stress ratio equals K^{ext}:

$$K^{ext} = \frac{\sigma'^{suc;F}_3}{\sigma'^{suc;F}_1} = \frac{K^0 \left(h^{sa} - z^F\right) + \left(K^0 - K^{ur}\right) h^{ob}}{\left(h^{sa} - z^F\right)} \tag{6.39}$$

Elaborating Equation 6.39 and substituting $K^0 = 0.5$, $h^{sa} = 0.2\,\text{m}$, $K^{ur} = 0.2$ and $h^{ob} = 0.55\,\text{m}$, results in:

$$z^F = h^{sa} - \frac{K^0 - K^{ur}}{K^{ext} - K^0} h^{ob} = 0.134\,\text{m} \tag{6.40}$$

It is thus concluded that approximately the top third of the sample will deform passively during the removal by suction of the overburden sand column. Figure 6.22 depicts the corresponding stress paths.

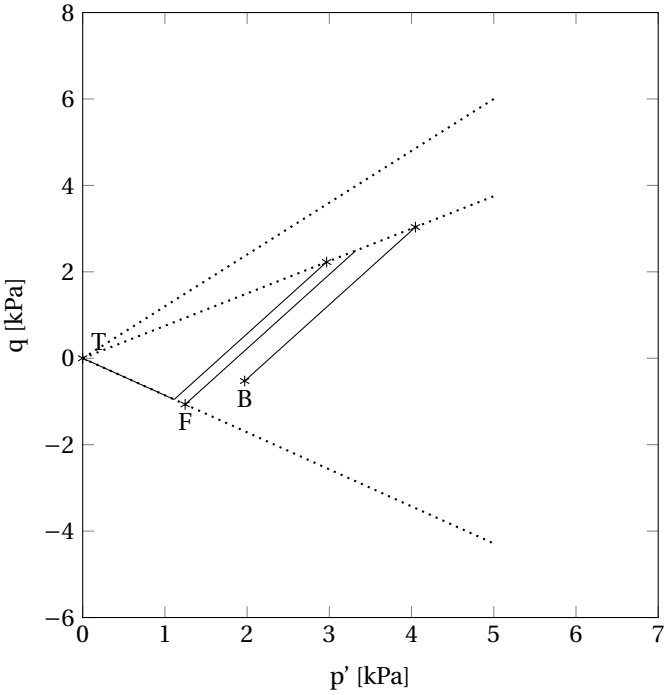


Figure 6.22: Stress path during sand suction at top (T), bottom (B) and transition level (F) of sample in the mould

Removal of mould

The fluidisation, sedimentation and sand suction in the triaxial cell mimic the situation in the tank. The next steps, the removal of the mould, and the saturation and consolidation of the sample, are steps strictly related to the triaxial test. Particularly the removal of the mould from the loose and sensitive sample requires further consideration. The previous stages leave a sample that is still supported by the submerged mould in the water-filled lower half of the cell. The removal of the mould will allow the cell water to infiltrate in between the mould and the sample, thereby equalising the pore pressures inside and outside the sample. This should be established gradually to avoid disturbance. Furthermore, additional support should replace the mould before removal. To this end, the back pressure p^b and the vertical pressure from the top plate that is measured by the load cell, σ_v^{lc} will be applied. The disturbance of the sample also plays an important role for the selection of the values that will be applied.

The stress point according to Equations 6.33 and 6.34 at the bottom of the sample ($z = 0\,\text{m}$) after K^0-consolidation is defined as the 'control point' (C). Directing the effective stress path towards this point will minimise the disturbance at the bottom of the sample. The resulting effective stress paths at the top and transition point need to be determined. The control point lies at $\sigma'^C_1 = 6070\,\text{Pa}$ and $\sigma'^C_3 = 3035\,\text{Pa}$, with the corresponding

triaxial invariants being $p' = 4047\,\text{kPa}$ and $q = 3035\,\text{kPa}$. After removing the mould, the minor principal effective stress σ'^{rmo}_3 is completely defined by the back pressure, while the major principal effective stress σ'^{rmo}_1 is affected by both the back pressure and the vertical stress from the top plate:

$$\sigma'^{rmo}_1 = \sigma^{lc}_v + \rho^{buoy} g \left(h^{sa} - z\right) - p^b \tag{6.41}$$

$$\sigma'^{rmo}_3 = -p^b \tag{6.42}$$

The values of the back pressure p^b and vertical stress σ^{lc}_v for the control point can be calculated using the aforementioned values of $\sigma'^{C}_1 = 6070\,\text{Pa}$ and $\sigma'^{C}_3 = 3035\,\text{Pa}$. The result reads:

$$p^b = -3035\,\text{Pa} \tag{6.43}$$

$$\sigma^{lc}_v = 1416\,\text{Pa} \tag{6.44}$$

Just before removing the mould, when the back pressure and vertical stress have just been applied, the mould still supports the sample. Horizontal equilibrium requires the following expression between the effective stress σ'^{mo}_3, the back pressure p^b, the hydrostatic pressure in the mould $\rho^f g \left(h^{sa} - z\right)$ and the support provided by the mould σ^{mo}_3:

$$\sigma'^{mo}_3 = -p^b - \rho^f g \left(h^{sa} - z\right) + \sigma^{mo}_3 \tag{6.45}$$

Comparing Equations 6.42 and 6.45 leads to the conclusion that the stress provided by the mould compensates the hydrostatic pore fluid stress in the sample. This support should be replaced by the water in the cell, which leaves the effective stress in the sample unaffected. Figure 6.23 shows the resulting effective stress paths for the top (T), transition level (F) and bottom (B) of the sample. As expected, the effective stress path at the bottom follows the unloading-reloading curve back to the control point. For the sake of simplicity, it is assumed that there is no hysteresis during unloading and reloading. The effective stress path at the transition level slightly deviates from the unloading path. However, at the top of the sample, the increase in isotropic effective stress is significant.

The conventional way of preparing a sample without any cell water would have led to even more disturbance. For this case, Equation 6.42 should be modified into:

$$\sigma'^{rmo}_3 = -p^b - \rho^f g \left(h^{sa} - z\right) \tag{6.46}$$

As a consequence, the required suction provided by the back pressure increases, while the vertical stress on the top plate decreases. The result reads for the control point:

$$p^b = -4997\,\text{Pa} \tag{6.47}$$

$$\sigma^{lc}_v = -546\,\text{Pa} \tag{6.48}$$

The isotropic effective stress will be increased much further as compared to the situation with water in the cell. Furthermore, tension needs to be applied by the top platen. For the case without cell water, the final stress point for the top of the sample T would lie

lower and further to the right as compared to the situation drawn up in Figure 6.23. The variation of stress state over the sample would be considerably larger than with the water in the cell during preparation. The effective stress state in the sample as depicted in Figure 6.23 would form the starting state for the subsequent standard undrained triaxial test with constant cell pressure and vertical displacement control.

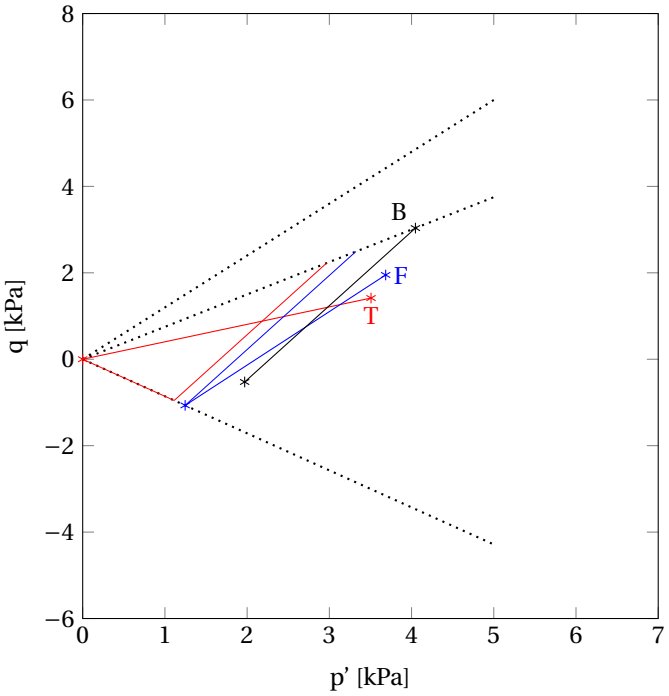


Figure 6.23: Stress path during removal of the mould at top (T), bottom (B) and transition level (F) of sample in the mould. The stress paths during sand suction (see Figure 6.22) are indicated by the faint lines.

6.3.4. Preparation using 1D compression

An alternative preparation procedure using 1D compression is considered in the same way. Contrary to the previous procedure, preparation using 1D compression does not mimic the sand suction in the liquefaction tank. The sample is fluidised in an extended mould of 30 cm. Sedimentation of the sample to a height of 20 cm yields a K^0 stress state, previously expressed by Equations 6.26 and 6.27. The effective stresses at the top of the sample after sedimentation equal zero, while the stresses at the bottom can be calculated from Equations 6.26 and 6.27 with $z = 0$ and $h = h^{sa}$.

Next, the sample is loaded by the top plate to the desired stress level. At this stage the sample is still in the mould, which implies a 1D compression situation. The pore pressure at the top platen, controlled by the back pressure, is kept at atmospheric pressure to allow free drainage. The same control point defined by $\sigma'^{C}_{1} = 6070\,\text{Pa}$ and $\sigma'^{C}_{3} = 3035\,\text{Pa}$

is used, which represents a K^0 stress situation at the bottom of the sample. At the top of the sample, the K^0 loading path is also followed as a result of the lateral constraint by the mould. As the mould is about to be removed, the controlled back pressure and vertical load are set to the values previously expressed by Equations 6.43 and 6.44. Hence, the stress points just before and after removal of the mould coincide with those previously plotted in Figure 6.23. At the bottom of the sample, the stress point does not move when the controlled quantities are adjusted for the removal of the mould. For both situations, the stress point lies at the K^0-line. However, the stress point at the top of the sample does move, as the minor effective stress σ'_3 changes from a K^0 stress state into a state fully governed by the backpressure p^b.

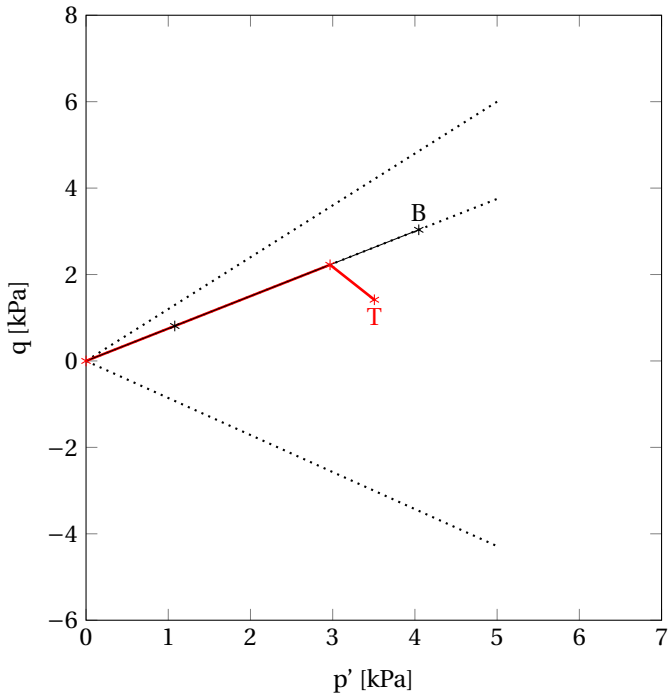


Figure 6.24: Stress path for procedure using 1D-compression at top (T) and bottom (B) of sample in the mould

Figure 6.24 plots the effective stress paths for the top and bottom of the sample. The bottom remains essentially undisturbed, as the stress point remains at its initial position after 1D-compression. The top shows an increase in mean effective stress and a decrease in the deviatoric stress, which is likely to cause some contraction of the loose sample. The change in stress state is caused by an increase in minor effective stress $\Delta\sigma'_3$ from 1D compression σ'^{1D}_3 to the controlled value before removal σ'^{rmo}_3:

$$\Delta\sigma'_3 = \sigma'^{rmo}_3 - \sigma'^{1D}_3 = K^0\left(\sigma'^{C}_1 - \rho^{buoy} g h^{sa}\right) + p^b \tag{6.49}$$

Hence, the stress difference varies linearly from the bottom to the top of the sample for this second sample preparation procedure. It is concluded that the disturbing effect varies gradually over the sample and is less severe at the top than for the first sample preparation procedure as illustrated by Figure 6.23.

6.3.5. Discussion

The principles of two alternative sample preparation procedures for the representative triaxial test for the sand in the liquefaction tank have been discussed. Application of the same fluidisation and sedimentation processes for the preparation of the sand of the slope in the liquefaction tank, as well as for the triaxial sample, seems to control not only the reproducibility of the sand density, but probably also the sand's micro-structure. Both procedures can be considered representative for a part of the slope in the liquefaction tank in terms of achieved mean effective stress state. The first procedure, including sand suction, represents the lower part and toe of the slope. The second procedure includes 1-D compression and represents the upper part and crest of the slope. It is concluded from Figures 6.23 and 6.24 that the first procedure is the more complex of the two by far in terms of induced stress paths and, as a consequence, disturbance. Therefore, the Author will concentrate on the performance of the second procedure. At this stage, the consideration is concentrated on the stress paths, and other factors, such as the accuracy of the sensors and control, will be ignored.

The response of the representative sand sample will be measured in the triaxial apparatus as an averaged response over the sample. It should be stressed that this is not a specific feature of the triaxial cell, but a generic feature for element testing. Sample preparation will always introduce non-uniformities to some extent. Subsection 2.3.2 discussed the moist-tamping technique, which may result in fluctuations of the relative density of $\pm 10\,\%$ around the mean value. The local response differs from the global response in the case of non-uniformities of the soil sample. For instance, the globally imposed undrained condition does not exclude the possibility of an internal flux from looser to denser parts. The question is to what extent non-uniformities affect the global response.

The preparation method by 1D-compression will also introduce both non-uniformities in terms of effective stresses and density. These are related, as a highly non-uniform stress state over the sample is likely to introduce similar variations in terms of density. The transition from 1D-compression to the controlled state before the removal of the mould introduces some densification towards the top. However, a small effect is expected. The deviation of the stress path does not come close to failure, nor does it reach the passive extension zone of the effective stress space. The effect would be more pronounced in the case that the variation of density would lead to different undrained responses over the sample, e.g. dilation at the top and liquefaction behaviour at the bottom. Considering the very loose initial density after fluidisation and sedimentation, and the relatively small densification during the subsequent step, the type of response is expected to be still rather uniform.

The effective stresses at the start of undrained triaxial testing will also be relatively uniformly distributed over the sample. The variation of the isotropic, effective stress at the top (T) and bottom (B) is well below the 10 % around the mean value in the sample. This suggests that for the selected geometric scale of the liquefaction tank reasonably accurate liquefaction-related mechanical characteristics of the loose sand composing the slope may be measured by means of triaxial tests. The corresponding variation in deviatoric stress is considerably larger, around 35 %. Nonetheless, both stress points lie in the same zone between the isotropic axis and the instability line for compression. The effective stress paths during undrained triaxial compression starting from these stress points are thus expected to be similar. During undrained triaxial extension, the initial similarities will be even greater. The anticipated stress path in Figure 6.24 starting from point B will run approximately through point T.

The preliminary conclusion is that similar effective stress paths are anticipated at the top and bottom of the sample during undrained triaxial testing after sample preparation by 1D compression. This conclusion would justify the averaging of the soil response. Nevertheless, it is recommended to consider both the effective stress paths at the top and bottom of the sample, which define the upper and lower boundaries of the average response.

The preliminary conclusion is based on expectations derived from the generic conception of soil behaviour in the triaxial cell. It seems that the tests that will be conducted in the triaxial cell will be the first ones using fluidisation and sedimentation as a sample preparation method and are also unique in terms of the (low) stress level. Gaining experience with the triaxial apparatus is essential for its development. It is recommended to first compose a database using fluidisation and 1D compression at moderate stress levels ($p' = 10 - 50$ kPa), drained and undrained conditions, and under compression and extension. Furthermore, it is recommended to interpret the results using finite element analyses, which allows the effects of non-uniformities to be studied in more detail. These results may also allow comparisons to be made with data from other triaxial tests on samples prepared by different sample preparation methods, initial effective stress states and initial densities. Using these results, insight will be gained into the performance of the novel triaxial apparatus, which can be employed when tests will be carried out at extremely low stress levels.

6.4. Concluding remarks

The final part of the thesis addresses the experimental facility denoted by the liquefaction tank (see Figure 1.4). It is recognised that there is a large gap between the fundamental knowledge obtained from element tests and the empirical basis that is provided by case histories. The improvement of liquefaction flow slides requires this gap to be closed. To this end, the liquefaction tank was developed.

This chapter defined the five key requirements of the experimental setup, which served as the basis for the design of the liquefaction tank. The first obvious requirement is that the experimental set-up should reproduce liquefaction flow slides. Therefore, the soil

should be susceptible to flow liquefaction and the flow slide should be triggered. In addition, the second requirement states that the liquefaction tank should yield reproducible results. As a consequence, the soil conditions and the trigger should be well-controlled and well-defined. Thirdly, the set-up should be manageable in terms of size and the time required to conduct a test. This third requirement complicates the reproduction of liquefaction flow slides, as the susceptibility to liquefaction flow slides is known to increase with the mean effective stress, and therefore, with the height of slopes. Hence, the preparation of the sand bed in a sufficiently loose state is of utmost importance.

The filtering and fluidisation system were designed to control the preparation of the sand bed. The filtering system enables the recirculation of clean water. Furthermore, the fines can be flushed out to create a uniform grading. The fluidisation system is aimed at the preparation of a sufficiently loose and uniform sand bed. It is assumed that a uniform pressure along the fluidisation system will also provide a uniform sand bed. The design thus attempted to keep the inevitable pressure drop acceptably small. Section 6.2.3 presented a finite element analysis that was carried out to quantify the pressure drop.

The fourth requirement states that the experiments should allow for the evaluation of numerical models. As a consequence, special attention has been paid to the triggering mechanisms (6.2.7) and the monitoring system (6.2.8). The most simple and unambiguous trigger concerns the uniform rotation of the liquefaction tank. In addition, a fast load applied on a strip was discussed. The interaction between the strip and the underlying soil body requires this trigger to be monitored during loading. The instrumentation in the liquefaction tank should provide the information about the output variables in the finite element analysis, i.e. stresses and displacements. A total compensated load cell was developed to measure the development of the stresses in the soil.

Finally, the fifth requirements is that the experiments in the liquefaction tank should be compatible with element tests. It is recognised that the liquefaction tank is significantly smaller than the slopes encountered in engineering practice. In order to extrapolate the results obtained with the liquefaction tank, element tests are indispensable. However, the extremely low stresses and the preparation by fluidisation pose challenges in element testing. Section 6.3 treated novel sample preparation procedures for the triaxial apparatus. The disturbance of the sample was judged by analysing the stress paths that are anticipated during the preparation of the sample.

References

[1] J. Garnier, G. Gaudini, S. Springman, P. Culligan, D. Goodings, D. Konig, B. Kutter, R. Phillips, M. Randolph, and L. Thoreli, *Catalogue of scaling laws and similitude questions in geotechnical centrifuge modelling,* International Journal of Physical Modelling in Geotechnics **3**, 1 (2007).

[2] R. De Jager and F. Molenkamp, *Fluidization system for liquefaction tank,* in *Eurofuge 2012, Delft, The Netherlands, April 23-24, 2012* (Delft University of Technology and Deltares, 2012).

[3] F. Molenkamp and R. van Os, *Liquefaction test in the Brutus Tank*, Tech. Rep. COSE-690504/2 (Delft Geotechnics, Delft, the Netherlands, 1987).

[4] P. Carman, *Permeability of saturated sands, soils and clays,* The Journal of Agricultural Science **29**, 262 (1939).

[5] I. Smith and D. Griffiths, *Programming the finite element method*, 4th ed. (John Wiley & Sons Ltd., Chicester, 2004).

[6] P. Lamens, *Fluidization before liquefaction: a study of sand bed uniformity*, Bsc. thesis, Delft University of Technology (2015).

[7] S. Noriega, *Characterisation of saturated loose sand samples prepared by fluidization*, Master's thesis, Delft University of Technology (2015).

[8] C. Krapfenbauer, *Experimental investigation of static liquefaction in submarine slopes*, Master's thesis, ETH Zurich (2016).

[9] M. Powers, *A new roundness scale for sedimentary particles,* Journal of Sedimentary Research **23** (1953).

[10] K. Petropoulos, *Earthquake induced liquefaction susceptibility of carbonate sands, experimental study: cyclic behaviour of carbonate materials used as hydraulic fills*, Master's thesis, Delft University of Technology (2013).

[11] G. Schiereck, *Introduction to bed, bank and shore protection*, 1st ed. (Spon Press, New York, 2003).

[12] A. Rohe, L. Gareau, and F. Molenkamp, *Lateral oedometer testing of anisotropic clay as affected by surface roughness,* Géotechnique **59**, 703 (2009).

[13] R. de Jager and F. Molenkamp, *Prepatory study of protocol and equipment for undrained triaxial testing of saturated sand samples prepared by fluidization*, Tech. Rep. (Delft University of Technology, the Netherlands, 2015).

7

Fluidisation testing

The performance of the fluidisation system is essential for obtaining reproducible, experimental liquefaction flow slides in the liquefaction tank. Therefore, the fluidisation system was elaborately designed and tested before conducting the tilting tests. The previous chapter discussed the design of the fluidisation system in Subsection 6.2.3. This chapter will elaborate on the experimental verification of the system performance.

In the first section the theory behind the mechanism of fluidisation will be described by considering both the available literature and governing equations based on the theoretical framework in Chapter 3. The elaboration of the test results in the subsequent sections consists of three parts: the preliminary, small-scale experiments, the measurement of the global density in the liquefaction tank and the actual fluidisation tests in the liquefaction tank.

7.1. Response of the sand bed: theory

7.1.1. General

In sedimentology one uses the term *liquidisation* for the mechanisms liquefaction and fluidisation [1], i.e. effecting the change from a solid-like to liquid-like state of soils. The difference between both is the opposite role of the pore fluid and soil skeleton. Whereas liquefaction is actively induced by the soil skeleton, fluidisation is the result of an externally enforced pore fluid flow. Contrary to liquefaction, fluidisation can be induced in any type and state of cohesionless soil, provided that the hydraulic gradient is sufficiently large.

This section continues where the design of the fluidisation system (6.2.3) left off. It will concentrate on the response of the sand bed. Sedimentological or chemical rather than geotechnical approaches usually address the phases following incipient fluidisation, including bed expansion and resedimentation. Nonetheless, the basic physics are the same. The process of fluidisation will be discussed from both viewpoints, thereby

benefiting from the experiences in both fields. The treatment of fluidisation will be subdivided into a part on the theoretical background and a part concerning its application for this research, to hypothesise the anticipated response of the sand bed in the tank.

7.1.2. Theory of fluidisation

The fluidisation of a water-saturated sand bed by water is considered, thereby ignoring the gas phase and the influence of bubbles. Furthermore, the fluidisation process is assumed to be stationary and isothermal. The definition of stationary fluidisation adopted here is that the centre of gravity of the sand does not move vertically, nor horizontally [1]. Internal motions are however not precluded. For the sake of simplicity the sand bed is first assumed to be characterised by a single particle diameter (monodisperse response), while noting that the same principles also apply on polydisperse systems.

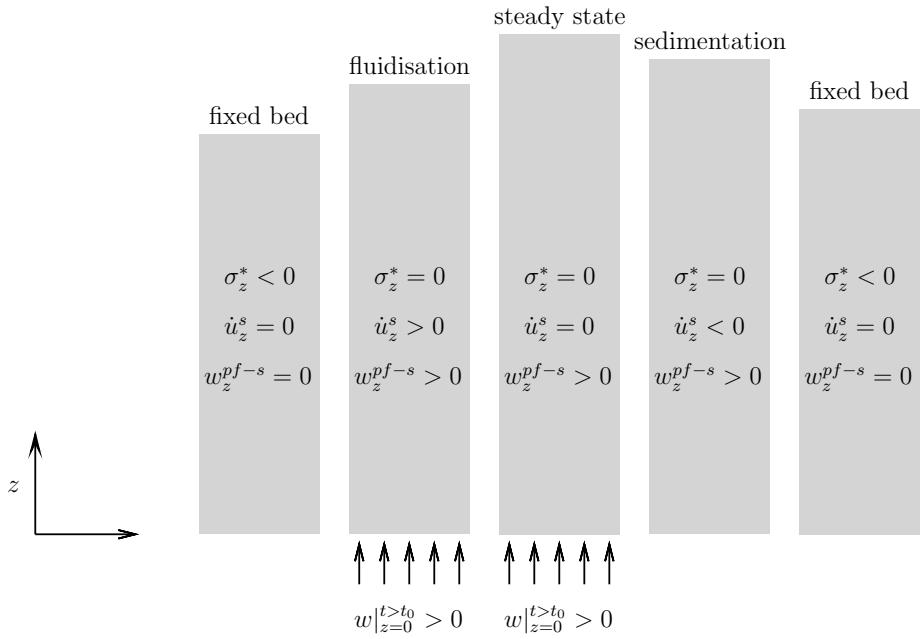


Figure 7.1: Consecutive stages of fluidisation of a column of soil.

Figure 7.1 defines the initial-boundary-value problem that will be considered. The sand bed is simplified as a one dimensional soil column. The vertical z-axis of the reference triad is directed upwards with $z = 0$ at the bottom of the soil column. This subsection discusses the theory of fluidisation by addressing the subsequent phases of (incipient) fluidisation, steady state expansion and sedimentation. The main variables of the soil bed are the vertical intergranular stress σ_z^*, the velocity of the soil skeleton $\dot{u}_z^s$ and the flux $w_z^{pf\text{-}s}$. The imposed fluidisation flux $w|_{z=0}^{t>t_0}$ defines the boundary condition at the

bottom of the column. It is assumed that both the soil particles and pore fluid are incompressible.

Incipient fluidisation

The field of soil mechanics conventionally describes the very first and last part of the cycle depicted in Figure 7.1. Switching on the fluidisation flux effects an increase of the vertical intergranular stress towards zero, while the opposite process governs the sedimentation and self-weight consolidation of the soil bed after switching off the fluidisation flux. Recall the analysis of incipient fluidisation from Subsection 6.2.3. The required flux $w_z^{pf\text{-}s}$ for incipient fluidisation was derived using the linear momentum of the pore fluid and the criterion $\sigma_z^* = 0$:

$$w_z^{pf\text{-}s} = -k_{zz}\left(\frac{\rho - \rho^{pf}}{\rho^{pf}}\right) \tag{6.1}$$

Equation 6.1 is based on the assumption of a laminar flow regime. Inertial effects at higher values of the Reynold's number introduce the trend of decreasing values of k_{zz} with increasing values of $w_z^{pf\text{-}s}$. Vardoulakis [2] measured a sudden increase of the permeability as the flux was increased towards incipient fluidisation. However, the permeability k_{zz} decreased (or resistivity increased) as the flux was further increased as a result of inertial effects.

Sedimentology conventionally addresses sedimentation from the steady state condition of a mixture, as depicted by the third ('steady state') and fourth ('sedimentation') column in Figure 7.1. Objectivity of the description allows a similar consideration of the fluidisation process. Sedimentation thus describes the three intermediate stages in Figure 7.1. The governing equations follow from the conservation of mass of the soil phase, as will be shown in more detail in the next subsection. The concentration C is a conventional measure in sedimentology. Being defined by the ratio between the volume of the particles V^s and total grain assembly V^t, the concentration C relates to the porosity n and void ratio e:

$$C = \frac{V^s}{V^t} = 1 - n = \frac{1}{1+e} \tag{7.1}$$

Note that the definition of incipient fluidisation according to Equation 6.1 is not strictly unambiguous. There is a stage in between the incipient fluidisation of the fixed bed and the gradual expansion during continued fluidisation. Depending on the initial density or concentration, the sand bed may first expand upon incipient fluidisation, resulting in an increased permeability k_{zz} and requiring a larger value of the flux $w_z^{pf\text{-}s}$ for fluidisation. To allow for an unambiguous definition of incipient fluidisation, the volumetric grain concentration measure $C^{s;mf}$ is introduced, that marks both the initiation of fluidisation ($\sigma_z^* = 0$) and the gradual expansion of the bed ('minimum fluidisation'). The value of $C^{s;mf}$ is typically around the loosest random packing [1]. Here, following Allen [1], $C^{s;mf} = 0.55$ is assumed. The introduction of $C^{s;mf}$ enables one to define $w_z^{pf\text{-}s} = w_z^{pf\text{-}s;mf}$ unambiguously. As the bed does not expand at $C^s = C^{s;mf}$ and for $w_z^{pf\text{-}s} = w_z^{pf\text{-}s;mf}$, the

permeability k_{zz} and bulk volumetric mass ρ are constants. Allen [1] refers to the following simplified expression for uniform spheres and velocities in the laminar range:

$$w_z^{pf\text{-}s;mf} = -0.00114 \frac{\left(\rho^g - \rho^f\right) g \left(D^g\right)^2}{\mu} \tag{7.2}$$

Equation 7.2 is practically identical to 6.1 for $C^{s;mf} = 0.55$ and the values for the Cozeny-Karman equation as assumed in 6.2.3.

Governing equations of fluidisation and sedimentation

During the fluidisation tests generally $w|_{z=0}^{t>t_0} > w_z^{pf\text{-}s;mf}$ and the sand bed will expand. Equation 6.1 still applies, albeit for increasing values of k_{zz} and reducing values of the bulk volumetric mass ρ as the sand bed expands while the assumption of a laminar flow regime is still satisfied. The development of the expansion comes down to an exchange of volume fraction between the soil skeleton and pore fluid, described by the continuity equations. The continuity equations are considered in the vertical (z) direction and the pore fluid and soil particles are assumed to be incompressible. Recall the conservation of mass equation of the soil skeleton 3.59, which reduces for incompressibility of the grains into:

$$\dot{n} - (1-n)\dot{\boldsymbol{\epsilon}}^{s;vol} = 0 \tag{7.3}$$

Note that the term $\dot{n}$ originates from calculating the material time derivative of the volume fraction of the soil skeleton, $1-n$. Furthermore, following soil mechanics' conventions the mass conservation of the soil skeleton is expressed in material form. Reformulating Equation 7.3 in terms of $1-n$, in spatial form and in the vertical direction yields:

$$\begin{aligned} -\frac{\partial(1-n)}{\partial t} - \dot{u}_z^s \frac{\partial(1-n)}{\partial z} - (1-n)\frac{\partial \dot{u}_z^s}{\partial z} = \\ -\frac{\partial(1-n)}{\partial t} - \frac{\partial(1-n)\dot{u}_z^s}{\partial z} = 0 \end{aligned} \tag{7.4}$$

This formulation of the conservation of mass of the soil skeleton is conventionally applied in sedimentology. It should be stressed that Equations 7.3 and 7.4 are essentially identical. The sudden application of a fluidisation flux $w|_{z=0}^{t>t_0} > 0$ creates an unsteady situation. The sand will not fluidise over the entire height at once, but the start of fluidisation at the bottom defines a disturbance that travels upwards. Slis et al. [3] consider the propagation velocity based on Equation 7.4. Objectivity requires fluidisation to be identical to settling, as in both cases the fluid moves upward with respect to the particles. The empirical Richardson-Zaki equation [4] defines a relationship between the settling velocity of a particle in a dispersion, conventionally expressed in terms of flux $w_z^{pf\text{-}s}$, and concentration C:

$$w_z^{pf\text{-}s} = |\dot{u}_z^{g;\infty}| (1-C)^N \tag{7.5}$$

Herein, $\dot{u}_z^{g;\infty}$ defines the reference settling velocity of a single particle under the effect of gravity, and N is an empirical exponent depending on the Reynold's number R_e [5]. The absolute sign neutralises the minus sign of $\dot{u}_z^{g;\infty}$. The Reynold's number is expressed by:

$$R_e = \frac{|\dot{u}_z^{g;\infty}| D^g \rho^f}{\mu} \tag{7.6}$$

It is assumed that the well-known Stokes' equation [6], valid for $R_e < 1$ and spherical particles, gives a good approximation of $|\dot{u}_z^{g;\infty}|$:

$$|\dot{u}_z^{g;\infty}| = \frac{\left(D^g\right)^2 \left(\rho^g - \rho^f\right) g}{18\mu} \tag{7.7}$$

The value of the empirical exponent N ranges between 2.4 for high values of R_e and 4.65 for low values. More specifically, N and R_e are related as follows [1]:

$$R_e < 0.2: \quad N = 4.65 \tag{7.8}$$

$$0.2 < R_e \leq 1: \quad N = 4.4 R_e^{-0.03} \tag{7.9}$$

$$1 < R_e \leq 500: \quad N = 4.4 R_e^{-0.1} \tag{7.10}$$

$$R_e > 500: \quad N = 2.4 \tag{7.11}$$

Herein, any wall effects are neglected as the dimensions of the set-ups will be much larger than the nominal grain size. The flux (or settling velocity) $w_z^{pf\text{-}s}$ is positive for an upward relative pore fluid motion. The Richardson-Zaki equation predicts an initial increase of $w_z^{pf\text{-}s}$ with increasing concentration C, which turns into a reversed trend at a particular value of the concentration as a result of hindered settling [5]. In terms of porosity n, the Richardson-Zaki equation reads:

$$w_z^{pf\text{-}s} = n\left(v_z^{pf} - \dot{u}_z^s\right) = |\dot{u}_z^{g;\infty}| n^N \tag{7.12}$$

Continuity requires the imposed fluidisation $w|_{z=0}^{t>t_0}$ to be equal to:

$$w|_{z=0}^{t>t_0} = n v_z^{pf} + (1-n)\dot{u}_z^s \tag{7.13}$$

At this stage, the essential assumption is made that the Richardson-Zaki equation 7.12 also applies for the unsteady situation just after a sudden change of the fluidisation flux. Then, combining Equations 7.12 and 7.13 yields a revised formulation that applies at any stage during fluidisation:

$$w|_{z=0}^{t>t_0} - \dot{u}_z^s = |\dot{u}_z^{g;\infty}| n^N \tag{7.14}$$

Equation 7.14 enable the mass equation 7.4 to be expressed in terms of the known properties $w|_{z=0}^{t>t_0}$, $\dot{u}_z^{g;\infty}$ and n:

$$\left(\left(N n^{N-1} - (N+1) n^N\right) |\dot{u}_z^{g;\infty}| + w|_{z=0}^{t>t_0}\right) \frac{\partial n}{\partial z} + \frac{\partial n}{\partial t} = 0 \tag{7.15}$$

Equation 7.15 describes a wave propagating with velocity v_z^{prop}, which equals:

$$v_z^{prop} = \left(N n^{N-1} - (N+1) n^N\right) |\dot{u}_z^{g;\infty}| + w|_{z=0}^{t>t_0} \tag{7.16}$$

Note that Equations 7.14-7.16 apply for any change in fluidisation flux, including a decrease or stepwise change. As the imposed flux $w|_{z=0}^{t>t_0}$ is changed, Slis et al. [3] assume an instant and uniform change of porosity from the initial value n^0 to the steady state

value n^1 at the bottom. The assumption of an instant change is mathematically convenient, but in reality the initial loosening will require some time. The second assumption concerning a uniform response is valid for fluidisation in the *particulate* regime [1]. The *Galileo* number G_a defines the type of regime:

$$G_a = \frac{\rho^f \left(\rho^g - \rho^f\right) g \left(D^g\right)^3}{\mu^2} \tag{7.17}$$

Allen [1] specifies the transition from the particulate to the non-uniform, *aggregative* regime at $G_a > 180$, which is well above the anticipated values for the experiments in this research. Hence, the assumed, uniform response is justified.

The discontinuity described by Equation 7.16 may propagate upwards as a sharp or broadening front, depending on the initial conditions and how $w|_{z=0}^{t>t_0}$ is varied. Consider a front where the propagation velocity v_z^{prop} is governed by steady state fluidisation conditions at the bottom, while the porosity decreases towards the top still characterised by the original porosity. If the propagation velocity v_z^{prop} is larger for the steady state conditions induced by fluidisation as compared to the overlying part, the propagation velocity at the lower part will tend to overtake the front at the higher part resulting in a sharp front. Vice-versa, the front will broaden as it moves upward. Note that the propagation velocity v_z^{prop} reaches its maximum value for $n = (N+1)/(N-1)$. Eventually, the steady state is reached, that is, if $w|_{z=0}^{t>t_0} < |\dot{u}_z^{g;\infty}|$. The steady state implies $\dot{u}_z^s = 0$, while the steady state-porosity n^1 can be deduced from Equation 7.14. Furthermore, the conservation of soil mass requires the following equation between the initial porosity n^0 and thickness of the sand bed h^0, and the steady state values n^1 and h^1, respectively:

$$\left(1 - n^0\right) h^0 = \left(1 - n^1\right) h^1 \tag{7.18}$$

Combining Equations 7.18 and 7.14 with $\dot{u}_z^s = 0$ for the steady state allows the definition of the relative bed expansion h^1/h^0:

$$\frac{h^1}{h^0} = \frac{1 - n^0}{1 - \left(w|_{z=0}^{t>t_0} / |\dot{u}_z^{g;\infty}|\right)^{1/N}} \tag{7.19}$$

The expansion of the sand increases drastically as the fluidisation flux $w|_{z=0}^{t>t_0}$ approximates the settling velocity of a single particle $|\dot{u}_z^{g;\infty}|$, as expected. As soon as $w|_{z=0}^{t>t_0} \geq |\dot{u}_z^{g;\infty}|$, the particles are flushed away by the fluid, which is denoted by *elutriation*. For these or larger values the steady state will not be reached and the sand bed continues expanding indefinitely. Elutriation is used to clean the sand from fines, which have a smaller settling velocity than the median sized particles. Note that Equation 7.19 provides an alternative to the soil mechanical approach used in Subsection 6.2.3, where the expansion was related to the permeability and bulk volumetric mass of the soil. The soil mechanical approach is here preferred during the phase of incipient fluidisation, where the response is governed by the soil skeleton. As the sand bed expands, the sand bed is considered a mixture, which is preferably described by Equation 7.19.

The final stage concerns the sedimentation after ceasing the fluidisation. The sedimentation can be considered in the same way and using the same equations as fluidisation. Indeed, reducing the fluidisation flux to $w|_{z=0}^{t>t_0} = 0$ merely defines a particular application of Equation 7.15.

Graphical method Kynch

The formulation of Equation 7.15 is consistent with the well-known Kynch's theory of sedimentation [7]. Kynch provides a graphical alternative for the mathematical approach presented above. Kynch's graphical method will be used to gain insight into the propagation of the fluidisation and sedimentation front and to provide an overview of the development of the concentration (or porosity) of the sand bed during the cycle depicted by Figure 7.1. Without specifying the propagation velocity v_z^{prop}, Kynch derives the following generic equation for sedimentation:

$$v_z^{prop}\frac{\partial C}{\partial z} + \frac{\partial C}{\partial t} = 0 \tag{7.20}$$

Kynch introduces the particle flux S, defined by the concentration and particle velocity $\dot{u}_z^s$ that is assumed to be a function of the (local) concentration:

$$S = C\,\dot{u}_z^s(C) \tag{7.21}$$

Furthermore, Kynch states v_z^{prop} to be related to S and C by:

$$v_z^{prop} = \frac{dS}{dC} \tag{7.22}$$

Equations 7.20-7.22 define a framework that is consistent with the previously derived, characteristic equation 7.15. Substituting Equation 7.21 into Equation 7.22, while specifying $\dot{u}_z^s$ by the Richardson-Zaki equation through 7.14 yields the derived definition of v_z^{prop} in Equation 7.16. The set of Kynch's equations 7.20-7.22 is thus consistent with the analysis by Slis et al. as expressed by Equations 7.14-7.16.

Kynch's graphical method employs Equation 7.21, i.e. it plots the particle flux S against the concentration C. Figure 7.2 illustrates the method [1]. The initial conditions of the sand bed are characterised by a uniform concentration C_0 and corresponding sedimentation flux S_0. It is obvious that above the dispersion $C = S = 0$, i.e. the origin of the plot $(0,0)$. At the bottom a sand bed is assumed to be formed with a constant concentration C_D. The curve has thus been cut off at $C = C_D$ where the sedimentation flux should be zero, $S = 0$. The sedimented sand bed is thus characterised by $(0, C_D)$.

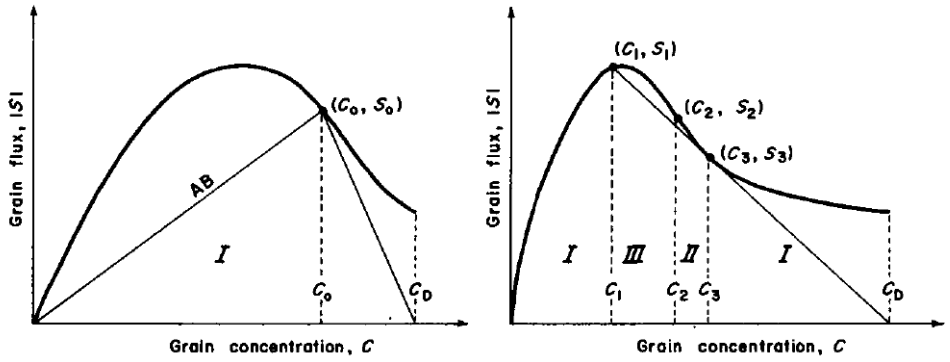


Figure 7.2: Two types of discontinuities during sedimentation of a mixture [1]: a sharp front (left) and wide front (right)

When the point (C_0, S_0) connects to the origin $(0,0)$ and $(0, C_D)$ directly without intersecting the curve, a sharp front characterises the settling of the top of the dispersion and the upward propagation of the formed sand bed. The propagation velocities v_z^{prop} are then defined by the linear curves between the points, as illustrated on the left hand side of Figure 7.2. The line connecting the origin and (C_0, S_0) (AB) represents the settling of the top, while the line connecting (C_0, S_0) and $(C_D, 0)$ represents the formation of the bed. However, the curve may contain a 'sheltered' part as illustrated on the right hand side of Figure 7.2. When (C_0, S_0) lies in the region between (C_1, S_1) and (C_3, S_3), an additional interlayer is formed between the sand bed at the bottom and the dispersion. Now, the formation of the sand bed propagates with a velocity defined by (C_3, S_3), whereas the top of the dispersion still settles with a velocity defined by (C_0, S_0). When (C_0, S_0) lies in region II, the tangent of the curve which defines the propagation velocity gradually increases from (C_3, S_3) to (C_0, S_0). The front thus broadens during sedimentation and the interlayer grows at the expense of the dispersion with constant concentration C_0. The situation becomes more complex in the convex part of the sheltered region III. Here, the velocity at (C_0, S_0) tends to be lower than the adjacent part at higher concentrations, which means that a sharp front is likely to be formed between the interlayer and the dispersion. Whether a sharp boundary is formed between the interlayer and the sand bed at the bottom depends on whether the local propagation velocity at (C_0, S_0) is higher or lower than the propagation velocity of the sand bed.

During the formation of the sand bed it will be slightly compressed by self-weight consolidation, followed by creep. Both mechanisms will be ignored, as the effect is expected to be small in sands, at least in terms of settlement. The theory does not provide any guidance on how to quantify the established, final density. Kynch's theory requires the bed density to be defined as an input rather than an output parameter. It is likely that the final density will increase with increasing bed expansion, provided that the flux precludes elutriation. The whole sand bed is lifted during elutriation, thereby increasing the

drop height during subsequent sedimentation and the anticipated density.

7.1.3. Aniticipated response sand bed during fluidisation

This subsection applies the theory on the fluidisation of the sand bed in the liquefaction tank. The response of a monodisperse system will be treated first, which is a reasonable assumption considering the low, anticipated coefficient of uniformity of the sand and removal of the fines by flushing. Later, the effect of varying grain sizes, i.e. a polydisperse response, will also be considered.

Table 7.1: Values of variables used as input for fluidisation analysis

description	**variable**	**value**	**unit**	**Equation**
particle diameter	D^g	120	µm	input
dynamic viscosity water	μ	1	$\mathrm{mN\,s\,m^{-2}}$	input
(single) particle settling velocity	$\lvert\dot{u}_z^{g;\infty}\rvert$	13	$\mathrm{mm\,s^{-1}}$	7.7
Reynold's number	R_e	1.6	-	7.6
Concentration exponent	N	4.2	-	7.10
Flux incipient fluidisation	$w_z^{pf\text{-}s;mf}$	0.27	$\mathrm{mm\,s^{-1}}$	7.2

Table 7.1 gives an overview of the variables that are used for the fluidisation analysis. The particle diameter and fluid dynamic viscosity are input variables, whereas the other variables are calculated from equations discussed in the previous subsection. Note that the Reynold's number (just) exceeds the requirement of $R_e < 1$ that applies for Stokes' equation 7.7. Nonetheless, Stokes' equation is applied as the deviation is expected to be small. Furthermore, it is worth noting that elutriation is highly unlikely for these variables, as this would require a fluidisation flow rate of 122 $\mathrm{l\,s^{-1}}$ which is considered unrealistic.

Expansion of sand bed

The steady state-porosity during fluidisation n^1 is calculated from Equation 7.14 for $\dot{u}_z^s = 0$, and the steady state-bed expansion h^1/h^0 subsequently from Equation 7.19. The initial porosity is assumed to be $n^0 = 0.45$, which is the value that corresponds with the presumed reference value $C^{s;mf}$. This value is both convenient due to the unambiguous definition of $w_z^{pf\text{-}s;mf}$ and applicable to the test series with common values around $n^0 = 0.45$. The value of $C^{s;mf}$ can be considered to mark the transition from a predominantly solid to a predominantly liquid response. However, this does not mean that the sand bed starts expanding at $w|_{z=0}^{t>t_0} = w_z^{pf\text{-}s;mf}$ and $n^0 = 1 - C^{mf}$, that is, if the theory is applied using the input variables given in Table 7.1. Figure 7.3 depicts the response in terms of steady state-porosity n^1 and bed expansion h^1/h^0 as a function of the flow rate $Q^{fl} = w|_{z=0}^{t>t_0} * A^{tank}$. The anticipated required flow rate for an incipient bed expansion of 4.2 $\mathrm{l\,s^{-1}}$ ($h^1/h^0 = 1$) is well above the predicted value of 2.5 $\mathrm{l\,s^{-1}}$ (see Table 7.1). Hence, the theory predicts an intermediate range of flow rates between incipient fluidisation

and incipient bed expansion. This apparent flaw in the theory is attributed to the uncertainties that arise in this intermediate region for pure soil and fluid mechanical theories. Furthermore, it is acknowledged that an important parameter, the structure, is missing in both the Kozeny-Carman and Richardson-Zaki equations. The intermediate flow range may be related to the change or loss of structure that is required for the expansion of the sand bed.

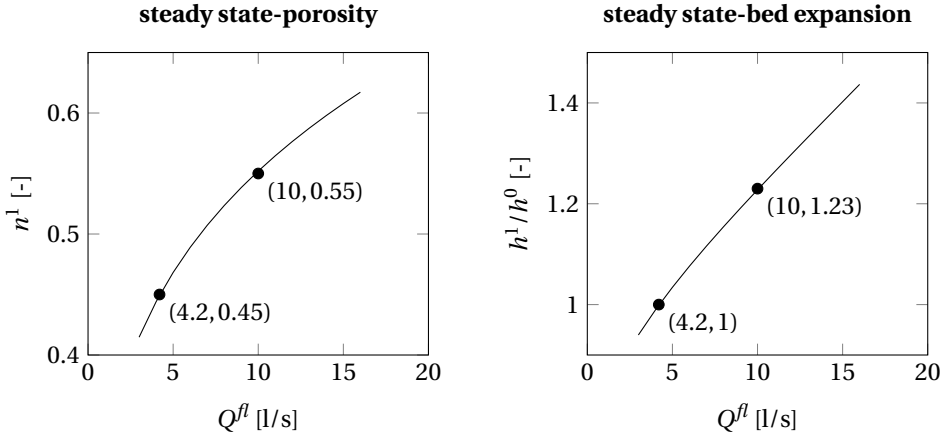


Figure 7.3: The steady state-porosity n^1 and relative bed expansion h^1/h^0 as a function of the fluidisation flow rate Q^{fl} for input parameters provided by Table 7.1 and calculated using equations 7.14 and 7.19. The points for incipient fluidisation and steady-state fluidisation have been marked in the plots.

The fluidisation and sedimentation process are considered in more detail for the design flow rate, namely $Q^{fl} = 10$ ls^{-1}. The resulting steady state-properties read $n^1 = 0.55$ and $h^1/h^0 = 1.23$. It is worth noting that $h^1/h^0 = 1.34$ for $Q^{fl} = 10$ ls^{-1} and $n^0 = 0.40$, i.e. the design values from Chapter 6. These values correspond with the presumed expansion of the sand bed from 1.5 m to 2.0 m, even though for the design a purely soil mechanical approach was used.

Application of graphical method of Kynch

Kynch's graphical method is used to illustrate the fluidisation and sedimentation process. Two curves are constructed from Equations 7.21 and 7.14. The curve for sedimentation ($w|_{z=0}^{t>t_0} = 0$) resembles the theoretical curve in Figure 7.2, whereas fluidisation ($w|_{z=0}^{t>t_0} = Q^{fl}/A^{tank}$) defines the second curve. Figure 7.4 shows the resulting plot. The vertical axis has negative values of the sedimentation flux S in an upward direction due to the applied sign convention. The sedimentation curve has $S = 0$ at $C = 0$, as expected. Furthermore, the formation of the sand bed cuts the curve short at $C^0 = 0.55$, with a sudden jump to $S = 0$. The introduction of a fluidisation flux moves the curve downwards with $S > 0$, that is, an expanding sand bed for higher values of C. The steady state during fluidisation implies $S = 0$, meaning that the steady state-point (C^1, S^1) lies on the line $S = 0$.

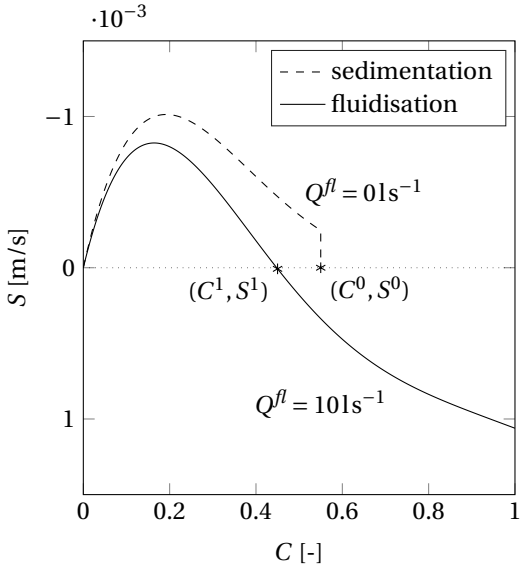


Figure 7.4: Sedimentation flux S as a function of concentration C for sedimentation and fluidisation for input defined in Table 7.1

The path that is followed during the process of fluidisation and resedimentation is considered. The established porosity after fluidisation and re-sedimentation is assumed to be $n_D = 1 - C_D = 0.50$. Referring to Figure 7.5, point A defines the initial state of the sand bed. As soon as the fluidisation system is turned on, the fluidisation rather than sedimentation curve applies to the response of the sand bed (point B). The vertical line between points A and B suggests this transition to be instant. Subsequently, the concentration at the bottom of the sand bed reduces to its steady state-value indicated by point C. As the upward propagation velocity v_z^{prop} increases from B to C, a sharp front is predicted with $C = C^0$ above and $C = C^1$ below the front. Assuming fluidisation is continued until the whole sand bed reaches the steady state, the fluidisation is turned off and the response of the sand bed instantly moves to point D. Following Kynch's sedimentation theory (Figure 7.2, left part), sedimentation is anticipated to be governed by a sharp front defined by point E propagating upwards.

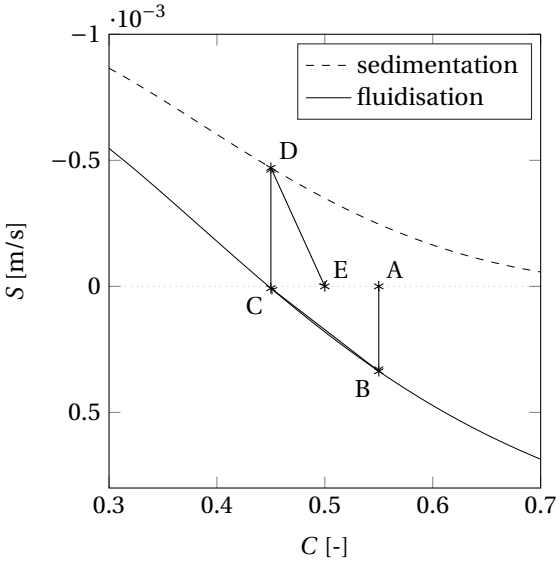


Figure 7.5: Path followed during fluidisation and re-sedimentation with: the initial state (A), original concentration during fluidisation (B), steady state during fluidisation (C), fluidised state during sedimentation (D) and fixed bed after sedimentation (E).

Figure 7.5 provides insight into the different stages before, during and after fluidisation. In addition, the propagation velocities can be retrieved from these curves. Figure 7.6 elaborates further on the propagation velocities. The aforementioned upward propagation velocities during fluidisation and sedimentation are indicated by $\dot{u}^{fl;bot}$ and $\dot{u}^{sed;bot}$ respectively. The propagation velocities of the top of the sand bed have also been included. During fluidisation the top of the sand bed propagates upwards with a constant velocity $\dot{u}^{fl;top}$, whereas during sedimentation it settles with a velocity $\dot{u}^{sed;top}$. These velocities are particularly useful, as the top of the sand bed can be monitored easily. The time required to reach the steady state t^1 can be calculated by using either $\dot{u}^{fl;bot}$ or $\dot{u}^{fl;top}$. The steady state height of the sand bed h^1 should be passed by the fluidisation front propagating upwards with velocity $\dot{u}^{fl;bot}$. Alternatively, the steady has been reached once the top of the sand bed has been expanded from h^0 to h^1 with velocity $\dot{u}^{fl;top}$:

$$t^1 = \frac{h^1}{\dot{u}^{fl;bot}} = \frac{h^1 - h^0}{\dot{u}^{fl;top}} \tag{7.23}$$

For instance, for $h^0 = 50\,\text{cm}$, $h^1 = 61.3\,\text{cm}$ is calculated from Equation 7.19, and $\dot{u}^{fl;bot} = 3.3\,\text{mm}\,\text{s}^{-1}$ and $\dot{u}^{fl;top} = 0.6\,\text{mm}\,\text{s}^{-1}$ using Equations 7.14, 7.22 and 7.21. Substitution into Equation 7.23 gives $t^1 = 186\,\text{s}$. The variation of t^1 with the fluidisation flow Q^{fl} is relatively small. For a considered range of $Q^{fl} = 5 - 15\ 1\text{s}^{-1}$, the period t^1 varies between $176 - 210\,\text{s}$.

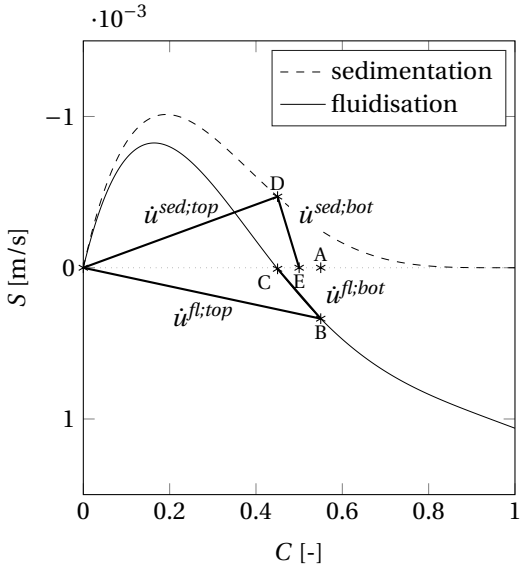


Figure 7.6: Velocities at bottom and top of sand bed during fluidisation and re-sedimentation: Upward propagation velocity of fluidisation front $\dot{u}^{fl;bot}$, upward velocity of top sand bed during fluidisation $\dot{u}^{fl;top}$, upward velocity of sedimentation front $\dot{u}^{sed;bot}$ and downward velocity of top sand bed during sedimentation $\dot{u}^{sed;top}$.

Polydisperse system: influence of grain size

Next, the response of a polydisperse system with a median particle diameter of $D^g = 0.12\,\text{mm}$ is considered. In spite of the uniformity of the sand used for testing, the grain size does vary, albeit over a limited range. For instance, less than 60% by mass of the sand lies between $0.106 - 0.150\,\text{mm}$, suggesting a relatively large contribution of other grain sizes. The actual contribution by volume is unknown, which limits this analysis to a qualitative assessment. The basis starting points, i.e. the steps taken, equations used and assumed bed porosities n^0 and n_D, are the same for the monodisperse and polydisperse responses. Figure 7.7 plots the expansion of the sand bed at the steady state for different grain sizes. Note that (the right part of) Figure 7.3 previously depicted the plot for a monodisperse system with $D^g = 0.12\,\text{mm}$. A decrease of the grain size has an increasing effect on the magnitude of the bed expansion. This effect becomes stronger for an increasing fluidisation flow rate Q^{fl}. For higher values of Q^{fl} and/or decreasing particle diameter, the limit of an infinitely expanding sand bed or *elutriation* will be approached.

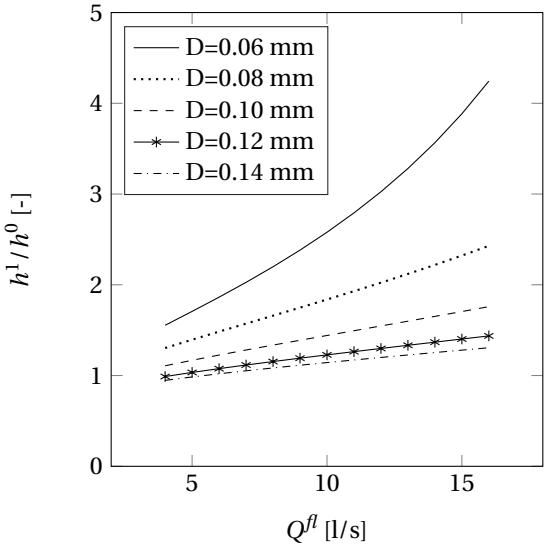


Figure 7.7: Relative bed expansion h^1/h^0 as a function of fluidisation flow rate Q^{fl} for different grain sizes

It is likely that the starting situation for the fluidisation testing is a segregated sand bed in terms of particle size. The smaller particles tend to be pushed further up during fluidisation than the larger ones, while the settling velocity is smaller. Hence, the extensive flushing before fluidisation is likely to yield a gradient in particle sizes. Referring to Figure 7.7, the relative expansion of the bed increases towards the top of the sand bed. Ideally, one can select the fluidisation flow rate and initial bed height in such a way that all particles below a particular, selected size are flushed from the sand bed.

Using Kynch's graphical method, the sedimentation curve will be compressed vertically for smaller grain sizes. As a consequence, the curve for fluidisation will also plot below the reference curve depicted in Figure 7.4. The rate of expansion, expressed by the velocity of the top of the sand bed $\dot{u}^{fl;top}$, will thus increase with decreasing grain size. Nonetheless, the time required to reach the steady state t^1 will increase as a result of the large increase in expansion of the sand bed. The actual response becomes complicated for smaller grain sizes.

Consider the particle flux S during fluidisation for a particle diameter $D^g = 60\,\mu$m in Figure 7.8. Unlike the curve considered for $D^g = 120\,\mu$m the theory does not predict a sharp fluidisation front. In between the initial state B(C^0, S^0) and the steady state C(C^1, S^1) the propagation velocity v_z^{prop}, defined by the derivative, reaches its maximum at (C^M, S^M). The derivative of the propagation velocity v_z^{prop} defines the value of C^M:

$$\frac{dv_z^{prop}}{dC} = 0 \rightarrow C^M = 1 - \frac{N-1}{N+1} = 0.385 \tag{7.24}$$

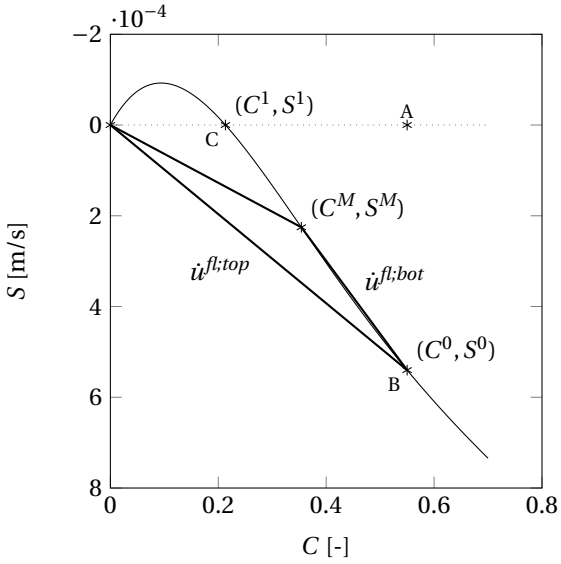


Figure 7.8: Graphical illustration of response during fluidisation of soil with small grain size diameter $D^g = 60\,\mu$m

As the sand bed expands from C^0 to C^M, the propagation velocity increases and a sharp front is formed propagating upwards with $\dot{u}^{fl;bot}$. However, as the sand bed expands further to C^1, the propagation velocity reduces to the local value at (C^1, S^1) and the front broadens. Initially, the top of the sand bed moves upwards with a constant velocity $\dot{u}^{fl;top}$ defined by the initial state (C^0, S^0). As soon as the top end of the front reaches the top of the sand bed, its concentration drops to C^M and so does $\dot{u}^{fl;top}$. The top of the sand bed absorbs the front, while gradually reducing its concentation to C^1 and its velocity to $\dot{u}^{fl;top} = 0$. Hence, the top of the sand bed is first predicted to move upwards at a constant velocity, and then suddenly to reduce its velocity, which is thereafter gradually decreasing to zero.

The type of response illustrated in Figure 7.8 applies whenever $C^M > C^1$. In the case considered here, the transition grain size diameter approximately equals $D^g = 100\,\mu$m. As this value lies close to the median grain size $D^g = 120\,\mu$m, the smaller grain sizes are expected to have a distinct effect on the global response.

Based on the elaboration of theory in this subsection, the following is concluded with respect to the anticipated response of the sand bed during the fluidisation experiments. Generally, with increasing fluidisation flow Q^{fl}, the rate of expansion, defined by the response of the top of the sand bed, tends to increase as well as the total expansion and the time required to reach the steady state. It has been assumed that the initial sand bed will be segregated in terms of grain sizes, with the larger grain sizes at the bottom. As a consequence, the rate of expansion tends to increase in time. As a uniform sand is being used for the tests herein, the rate of expansion is expected to be fairly constant during

a large part of the test. As the fluidisation front reaches the smaller grains in the upper part of the sand bed, the rate of expansion first increases. Then, as the front reaches the top, the rate of expansion will gradually decrease to zero. The time required to reach the steady state t^1 strongly depends on the (volume) fraction of smaller grain sizes. A uniform sand bed with $D^g = 120\,\mu$m reaches the steady state for $Q^{fl} = 10$ ls^{-1} in $t^1 = 186$ s, whereas for a grain size of $D^g = 60\,\mu$m this value increases to $t^1 = 804$ s.

7.2. Preliminary fluidisation tests

7.2.1. General

A preliminary stage of testing in small scale set-ups preceded the fluidisation tests in the liquefaction tank. There are several motives for including a preliminary stage. It was felt that there was a need to evaluate the method and its presumed performance, for instance with respect to the flushing of the sand bed and the established, uniform density. In addition, the assumed input parameters in the theory and design of the fluidisation system need to be verified. Smaller and simplified set-ups suit these purposes better than the laborious and complex tests in the liquefaction tank. An intermediate stage also allows for possible corrections that need to be made in the tank. Small scale experiments may simplify fluidisation to a one-dimensional process, while enabling local measurements to be taken.

This section addresses two experimental set-ups: a scale experiment of the liquefaction tank referred to as the minitank and a modified permeameter. These set-ups will first be concisely described. The results from both set-ups are then discussed. Finally, some conclusions are drawn from the preliminary tests.

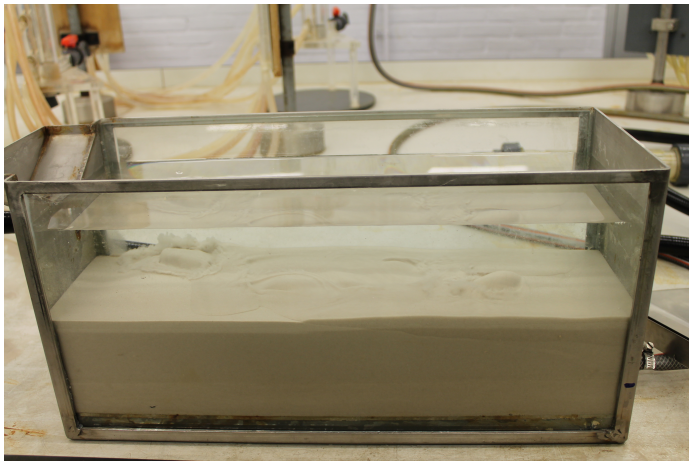


Figure 7.9: Initial stage of fluidisation in minitank

7.2.2. Description experiments

The minitank is a 1 : 10-scale model of the liquefaction tank. Its dimensions thus measure $20x20x50$ cm. It was developed to test several components, but here only the part related to the fluidisation system is discussed.

The minitank (Figure 7.9) consists of a metal frame, which has been closed by metal plates at the ends and the bottom. Along the long sides glass sheets have been glued to enable the observation of the sand bed from the sides. The fluidisation system consists of a thick PVC plate mounted on the bottom plate and overlain by a stainless steel, sintered plate. In between the PVC and steel plates a cavity was created by grinding a part of the top of the PVC plate. This cavity connects to a pipe at the outside of the minitank, which can be connected to the de-aired water supply through a hose. The fluidisation flow rate can be controlled by a valve, albeit to a limited extent. The minitank has an overflow by which the fluidisation flow rate can be monitored.

The principle objective of the fluidisation tests conducted in the minitank was to gain insight into the fluidisation process for a similar, scaled geometry as used in the liquefaction tank. The boundary effects are expected to be negligible, as the ratio between particle size and representative length measure of the boundaries, e.g. the width of 20 cm, is still very small. More specifically, the fluidisation tests in the minitank aimed at the performance of the fluidisation system, the flushing of the sand bed and the expansion of the sand bed.

The tests conducted with the modified permeameter were part of a BSc.-thesis research project [8]. The used set-up (Figure 7.10) is a standard permeameter with a height of 50 cm and a diameter of 6 cm that was modified to allow for the testing of fine sands. A first test showed that the original, coarse filters had to be replaced by finer filters for the fine sand used for testing. One commonly applies the permeameter for the measurement of the permeability of the soil. To this end, the hydraulic head above the sand column is held constant by an inflow of de-aired water through tap 1A and an overflow that connects to the outlet. By opening tap 2 a downward flow through the sand column is created, which is monitored by recording the piezometric levels at different positions. Alternatively, the inflow of water can be directed to the bottom of the sand column by using tap 1B and closing tap 2. The upward flow may induce fluidisation of the sand column.

The experiments were aimed at the established properties of the sand bed before and after fluidisation, rather than a detailed investigation of the fluidisation process itself. In addition to the piezometric levels, the density and grain size distribution were measured using a siphon tool (Figure 7.11). A small tube was used to gently remove a certain volume of sand layer-by-layer, while controlling the suction pressure by the level of the storage container. The mass and volume of the removed sand define its density. The batches of sand were sieved to obtain a profile of the grain size distribution over the height of the sand column.

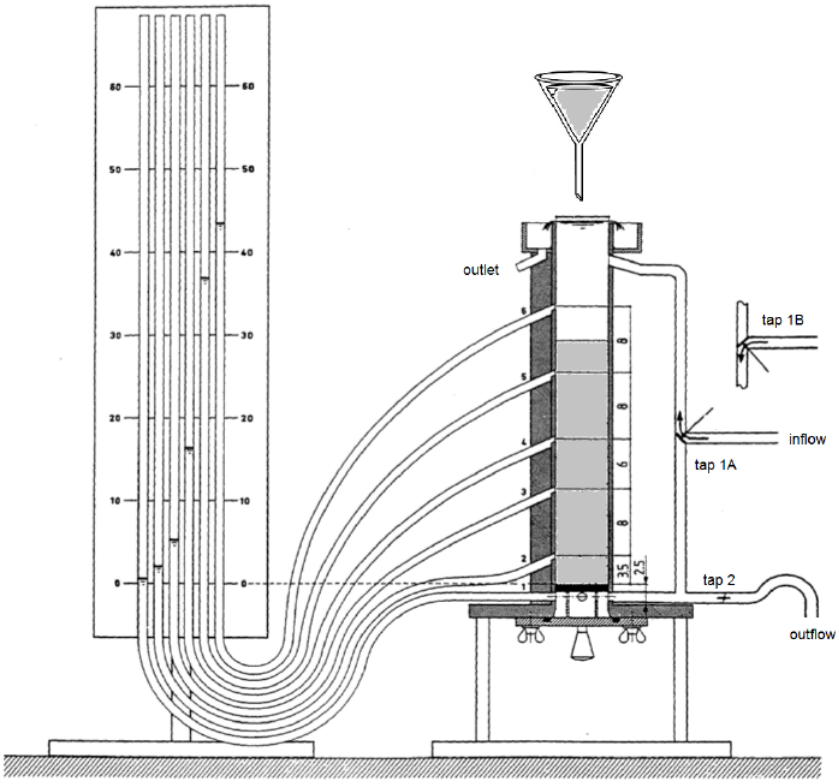


Figure 7.10: Permeameter set-up used for fluidisation testing [8]

Before preparing the sand column, the sand was sieved and any silt particles $D^g < 63\,\mu$m were removed. The sand column was prepared using a water-pluviation technique with a funnel and a constant drop height of 50 cm. Section 2.3.2 previously discussed the preparation methods, including water pluviation. The initial permeability, density and grain size distribution were measured using the aforementioned procedures. A large upward flow rate was subsequently applied to ensure that the sand bed fluidized. The turbidity of the water was reduced by flushing out the fines that were left or newly generated in the sand bed. However, the large flow rate also led to a large expansion of the bed, and the flow had to be muted now and then to prevent overflow of the sand column. The fluidisation of the sand was maintained for ten minutes and then it was allowed to settle for another 10 minutes. The measurement of the permeability, density and grain size distribution was repeated for the fluidised sand bed.

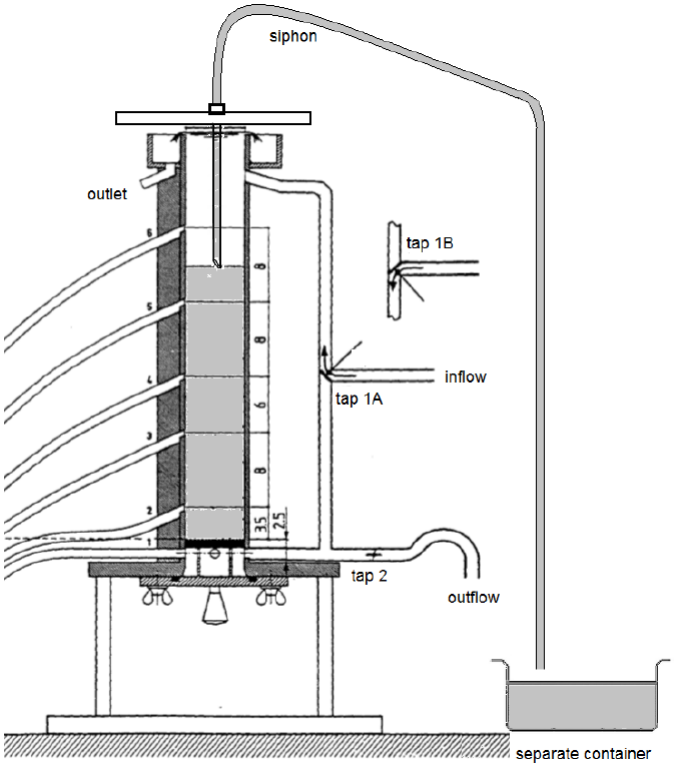


Figure 7.11: Siphon tool used for determining density over height [8]

The principle objective of the fluidisation tests in the modified permeameter is to provide insight into the uniformity of the sand bed after fluidisation. The term uniformity refers to one, namely the vertical, dimension. It is believed that a uniformly applied fluidisation system in the liquefaction tank will yield similar conditions. More specifically, the tests in the modified permeameter aim at the development of the permeability, density and grain size distribution as a result of fluidisation.

7.2.3. Results from fluidisation tests in minitank

The minitank was filled approximately halfway with sand. During the first stage of flushing the valve was fully opened to maximise the fluidisation flow rate. The system performed well. The sand bed expanded uniformly until the steady state was reached. After maintaining the steady, fluidised state for a while the initially turbid water gradually cleared. It was observed that the sand bed was fully fluidised, with the exception of dead zones at the edges where the porous plate is supported. Closing the valve produced a sand bed approximately 10% looser than the original state and a uniform, level surface. It also became clear that the sand segregated in terms of grain size, as could be seen by the distinct colour of the top layer (see Figure 7.9).

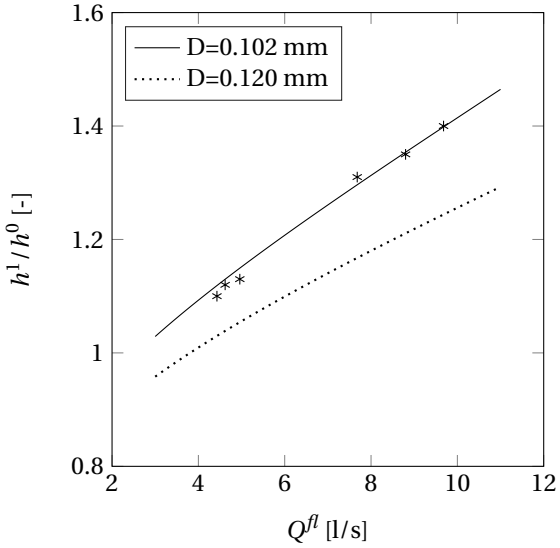


Figure 7.12: Relative bed expansion in minitank as a function of flow rate scaled to dimensions of liquefaction tank. The measurements are marked by asterisks, the curves depict theoretical relations.

Subsequent experiments were conducted where the valve was partly closed. It was observed that the rear part of the sand did not fluidise uniformly as the fluidisation flow rate was further reduced, while the front part did. Apparently, the pressure drop along the fluidisation system caused a non-uniform fluidisation response. The relative, steady state-expansion of the sand bed was measured for different flow rates. Figure 7.12 depicts the results for a scaled flow rate Q^{fl}. Two theoretical curves are drawn based on Equation 7.19.

The anticipated curve for $D^g = 120\,\mu$m lies well below the data points, which fit to the curve for $D^g = 102\,\mu$m. This observation is related to the observed segregation of particle sizes and the notion that the bed expands increasingly for decreasing particle size (see Figure 7.7). Apparently, the net effect of segregation results in an expansion of the bed governed by the smaller particles. The segregation of particle sizes over the height of the bed was confirmed by sieving tests for samples taken from different levels after fluidisation. Segregation will be considered in more detail for the permeameter tests in the next subsection.

7.2.4. Results from fluidisation tests in permeameter

The main objective of the study conducted with the modified permeameter is the determination of the uniformity of the sand bed after fluidisation. The initial sand bed prepared by water pluviation is used as a reference for the state of the sand bed after fluidisation. The density and segregation of particle sizes are compared for the fluidised and water pluviated ('non-fluidised') sand column. Before discussing the uniformity of

the sand bed, the global response of a permeameter test is considered.

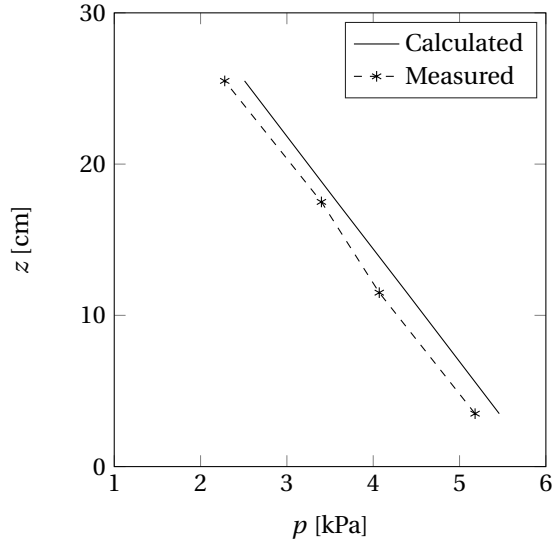


Figure 7.13: Measured pressure in permeameter and calculated pressure for complete fluidisation

A sample with a height of approximately 15 cm and an initial porosity of 0.51 was prepared in the permeameter using water pluviation. First, a conventional permeameter test was conducted resulting in a permeability of $k_{zz} = 3.1 \times 10^{-4}\,\mathrm{m\,s^{-1}}$, which is below the theoretical permeability $k_{zz} = 5.5 \times 10^{-4}\,\mathrm{m\,s^{-1}}$ based on Kozeny-Carman. During the test the sample slightly densified yielding an initial porosity of $n^0 = 0.50$ for the subsequent fluidisation test. The flow was reversed and the sample fluidised for 10 minutes to ensure it reached the steady state. The scaled fluidised flow rate equaled 27.5 $\mathrm{l\,s^{-1}}$, which is well above the range considered before. However, the corresponding flux of $w_z^{pf\text{-}s} = 2.9\,\mathrm{mm\,s^{-1}}$ is still well below the threshold value for elutriation. Moreover, the contribution of the velocity head can be neglected. At the steady state the sand bed had expanded to 32.5 cm, which corresponds to a porosity of $n^1 = 0.78$. As for the minitank experiments, the relative bed expansion of $h^1/h^0 = 2.24$ is well above the value that would be expected based on theory and $D^g = 120\,\mu$m. The relative bed expansion does correspond to a value of 100 μm, which is close to the value that was used to fit the results from the minitank fluidisation tests. It is concluded that the response during fluidisation corresponds well with the minitank tests, in spite of the significant differences in terms of geometry and applied flow rates.

Figure 7.13 depicts the measured and calculated pressures p as a function of the level z during steady state-fluidisation. The measured pressures are calculated from the measured head h and the level z, while the calculated pressures are determined based on the presumption of a fluid response of the completely fluidised soil column. Based on the small difference between both curves, the soil column was almost completely flu-

idised. The corresponding permeability during fluidisation equals $k_{zz} = 8.4 \times 10^{-3}\,\mathrm{m\,s^{-1}}$. Note that this value is significantly higher than the calculated value in Subsection 6.2.3 of $5.8 \times 10^{-4}\,\mathrm{m\,s^{-1}}$, which is explained by the significantly higher flow rate applied during the tests in the permeameter resulting in a larger porosity during fluidisation.

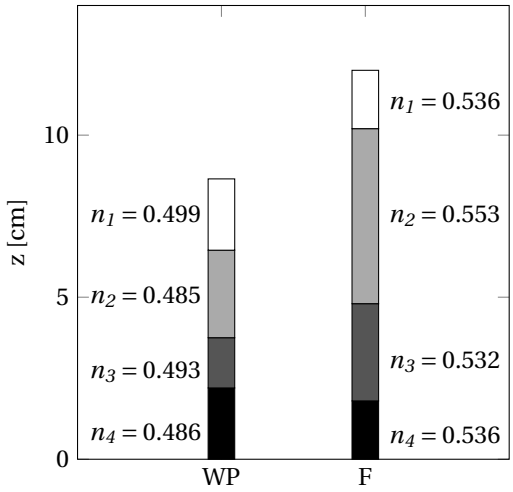


Figure 7.14: Measured porosity over height after water pluviation (WP, left) and fluidisation (F, right)

The uniformity of the sand bed before and after fluidisation was examined by decomposing the sand bed layer-by-layer using the siphon tool. Figure 7.14 shows the four layers of the water pluviated sand column ('WP'), and the column after fluidisation and resedimentation ('F'). It should be noted that the two columns were obtained during separate tests. The difference in height between the two columns should not be attributed to the density of the sand alone, as the total mass of sand used for the right column was slightly larger. Nonetheless, the porosity after fluidisation ('F') is significantly larger as compared to water pluviation ('WP'), which confirms the anticipated effect of fluidisation. In both cases the density is distributed uniformly along the column. There is no increase of density with depth. The water pluviated column is slightly more uniform, which agrees with observations in literature of a decreasing uniformity with increasing porosity.

The same layers of sand were sieved to determine the variation of the grain size distribution over the height. Figure 7.15 shows the results in terms of retained, cumulative mass. Layer 1 refers to the top layers in Figure 7.14, layer 4 to the bottom layers. The grain size distribution is rather uniform for the water pluviated sand column. However, there is a clear segregation of particle sizes after fluidisation. In terms of the median grain size D^{50}, the value for layers 1-4 read, respectively, 88 μm, 119 μm, 141 μm and 157 μm. The distinct segregation is striking, considering the relatively uniform sand that is used during testing. The coefficient of uniformity of $C_u = D^{60}/D^{10}$ of a representative sample of the original sand equals approximately 1.35, which is extremely low. The observed segregation does support the measured response during the minitank and permeameter

tests, where the measured bed expansion was much larger than anticipated based on the representative particle size.

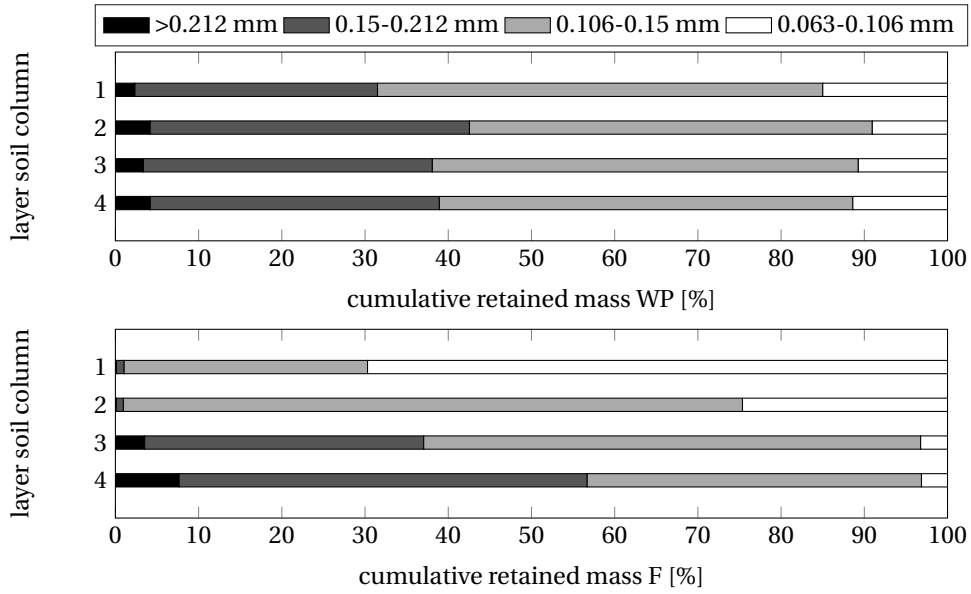


Figure 7.15: Distribution of grain sizes over height after water pluviation (WP, upper) and fluidisation (F, lower)

Comparing Figures 7.14 and 7.15 demonstrates that there is no relation between the established density and particle segregation. Based on literature, one might expect lower densities for smaller particles (see Chapter 2). The particle segregation does relate with the permeability. Additional tests were conducted where the permeability profile was determined over the height of the sample. Fluidisation yields a reduction of permeability of approximately 20% at the top and a similar increase at the bottom, while the density was more or less constant over the height. The gradient in permeability is attributed to the segregation of particle sizes.

7.3. Measuring the global density of the sand bed

7.3.1. General

It is known from engineering practice that the in-situ measurement of the density of cohesionless soils is hampered by sample disturbance. One usually relies on correlations, for instance based on the cone resistance, to determine the in-situ density. Assuming that fluidisation will provide a uniform packing of the sand bed, the state of the sand is characterised by its global density. The definition of the global density refers to the averaged dry volumetric mass $\rho^{s;dry;tank}$, being equal to the fraction of dry soil mass in the

liquefaction tank $M^{s;dry;tank}$ and the volume it takes in the liquefaction tank $V^{s;tank}$:

$$\rho^{s;dry;tank} = \frac{M^{s;dry;tank}}{V^{s;tank}} \tag{7.25}$$

The actual mass $M^{s;dry;tank}$ will decrease as fines are filtered out of the sand bed. For practical reasons, measurements of the amount of fines were taken after extensive flushing events, while assuming that in between the mass of the sand in the liquefaction tank was constant. During experiments, the determination of the dry volumetric mass $\rho^{s;dry;tank}$ thus reduced to the measurement of the volume $V^{s;tank}$, or, for a constant area, the height of the sand bed $h^{s;tank}$. Both the starting points and the procedures to measure $M^{s;dry;tank}$ and $V^{s;tank}$ will be discussed in more detail in the next subsections. Both the results and an error analysis will be presented as an indication of the accuracy of the measured global dry volumetric mass $\rho^{s;dry;tank}$. The spatial variation of the density of the sand in the tank is generally not known; the variation of $h^{s;tank}$ in the tank will provide a rough indication, at best. The development of a method to take undisturbed measurements of the density of the sand is beyond the scope of this research. It is noted that the global density appeared to be an appropriate and representative measure for the susceptibility to flow liquefaction, as will be demonstrated in the next chapter.

7.3.2. Measurement of soil mass in liquefaction tank

The sand was delivered in a batch of five big-bags with a total mass of $M^{s;tot}$. In between the delivered mass $M^{s;tot}$ and the dry mass in the liquefaction tank $M^{s;dry;tank}$, the mass decreases for a number of reasons. Firstly, the delivered sand is not completely dry, but contains a certain mass of moisture $M^{s;moi}$. Secondly, a part of the sand with a mass $M^{s;filt}$ has been used as a filter material in the filter tank FT (see Figure 6.11). Thirdly, fines are washed out during the flushing of the sand bed with a mass $M^{s;fin}$. The dry mass of sand in the liquefaction tank $M^{s;dry;tank}$ equals:

$$M^{s;dry;tank} = M^{s;tot} - M^{s;moi} - M^{s;filt} - M^{s;fin} \tag{7.26}$$

In Equation 7.26 a few other possible contributions were ignored, such as the sand that was lost during the transport of the sand to the liquefaction tank, the fine material that dissolved in the water and stuck to the walls of the liquefaction tank, and the fine material that was filtered by the finer filters of 50µm, 10µm and 1µm by the filter system in the basement. These contributions are believed to be small, but nonetheless note that the value obtained by 7.26 provides an upper bound.

The procedures to determine each of the masses at the right hand side of Equation 7.26 will be discussed. The masses M are indicated with an estimated error δM to facilitate the global error analysis later on. If possible, the error δM is estimated directly from mass measurements. In the case that the determination of the mass is related to other variables, that is, $M = M(x_i)$, the propagation of errors δx_i defines the magnitude of δM. The resulting error will always be smaller than [9]:

$$\delta M \leqslant \left| \frac{\partial M}{\partial x_i} \delta x_i \right| \tag{7.27}$$

In the case that the error contributions prove to be independent and random, the error reduces to:

$$\delta M = \sqrt{\left(\frac{\partial M}{\partial x_i}\delta x_i\right)^2} \tag{7.28}$$

The sand was delivered in big bags of 1500 kg each. The mass was verified using a load cell, resulting in an estimated deviation of ±3 kg. The mass $M^{s;tot}$ therefore equals:

$$M^{s;tot} = 7500\,\text{kg} \pm \sqrt{5 * (3\text{kg})^2} = 7500 \pm 7\text{kg} \tag{7.29}$$

For the second mass component, $M^{s;moi}$ samples were taken from the big-bags and dried to determine the moisture content. The measured average moisture content was 7.5×10^{-4}, while a possible deviation of 30% was assumed. The mass $M^{s;moi}$ therefore equals:

$$M^{s;moi} = 7500\,\text{kg} * \frac{7.5e-4}{1+7.5e-4} \pm \left(0.3 * 7500\,\text{kg} * \frac{7.5e-4}{1+7.5e-4}\right) = 6 \pm 2\text{kg} \tag{7.30}$$

The mass of sand used as the top filter layer in the filter tank, $M^{s;filt}$, was determined by measuring the volumetric mass $\rho^{s;filt}$ and the corresponding volume $V^{s;filt}$:

$$M^{s;filt} = \rho^{s;filt} V^{s;filt} \tag{7.31}$$

The volumetric mass $\rho^{s;filt}$ was very high and uniform as a result of the numerous flushing events, where water seeped continuously through the filter tank. Therefore, one measurement of $\rho^{s;filt}$ was taken, which was assumed to be representative for the whole filter layer. The volumetric mass was measured during a sand replacement test involving the mass of excavated, dry sand $M^{s;filt;exc}$ and its corresponding volume $V^{s;filt;exc}$:

$$\rho^{s;filt} = \frac{M^{s;filt;exc}}{V^{s;filt;exc}} = \frac{2.972\,\text{kg}}{1.716 \times 10^{-3}\,\text{m}^3} = 1732\,\text{kg}\,\text{m}^{-3} \tag{7.32}$$

For the corresponding error analysis, the error of the measured dry mass was estimated to be $\delta M^{s;filt;exc} = 0.005\,\text{kg}$. The *relative* error of the volume of the excavated sand was assumed to be $\delta V^{s;filt;exc}/V^{s;filt;exc} = 0.05$. These measurements cannot be considered independent and therefore the upper limit 7.27 is used to estimate the propagated error:

$$\begin{aligned}\delta\rho^{s;filt} &= \frac{\delta M^{s;filt;exc}}{V^{s;filt;exc}} + \frac{M^{s;filt;exc}}{(V^{s;filt;exc})^2}\delta V^{s;filt;exc} = \frac{\delta M^{s;filt;exc}}{V^{s;filt;exc}} + \frac{\delta V^{s;filt;exc}}{V^{s;filt;exc}}\rho^{s;filt} = \\ &= \frac{0.005\,\text{kg}}{1.716 \times 10^{-3}\,\text{m}^3} + 0.05 * 1732\text{kg}\,\text{m}^{-3} = 89\,\text{kg}\,\text{m}^{-3}\end{aligned} \tag{7.33}$$

The volume of the sand in the filter tank $V^{s;filt}$ consists of contributions from the volume inside the mesh of the grid $V^{s;filt;mesh}$ and the upper volume above the grid $V^{s;filt;up}$. Both quantities depend on the cross-sectional area of the filter tank $A^{s;filt}$:

$$V^{s;filt} = V^{s;filt;mesh} + V^{s;filt;up} = \left(n^{gr;filt} h^{gr;filt} + h^{up}\right) A^{s;filt} \tag{7.34}$$

Herein, $n^{gr;filt}$ defines the porosity of the grid. The radius of the filter tank equals 0.94 m, with an error of ±1 mm based on a conventional measurement tape. The resulting error in terms of cross-sectional area will be very small. The resulting area $A^{s;filt} = 2.776\,\mathrm{m}^2$ is therefore considered accurate. The complementary measures of the grid, $n^{gr;filt} = 0.878$ and $h^{gr;filt} = 30\,\mathrm{mm}$, are also considered accurate. The error of the dimensions of a single cell of the prefabricated grid is likely to be random and small, whilst the combined error averages out when considering a large number of cells, i.e. the grid. If the error of a single reading, for instance $\delta V^{s;gr;cell}$, is random and small, the combined error $\delta V^{s;gr}$ decreases with increasing number of samples N:

$$\delta V^{s;gr} = \frac{\delta V^{s;gr;cell}}{\sqrt{N}} \tag{7.35}$$

The error analysis of the height of the sand bed above the grid, h^{up}, does require further consideration. The surface of the sand bed is seen to fluctuate in height. In order to increase the accuracy of the measurement of h^{up}, the area $A^{s;filt}$ was subdivided into 13 equal parts, while measuring h^{up} at the center of gravity of each part. The measurement error during each reading was assumed to be relatively high, $\delta h^{up;sub} = 5\,\mathrm{mm}$, because of the difficult conditions during reading. The reading conducted before fluidisation testing yielded the following result:

$$h^{up} \pm \delta h^{up} = \frac{\sum_i^{13} h_i^{up;sub}}{N} \pm \frac{\sum_i^{13} \delta h_i^{up;sub}}{\sqrt{N}} = 6.7 \pm 0.1\,\mathrm{cm} \tag{7.36}$$

Substituting the average values into Equation 7.31 yields an average value of $M^{s;filt} = 449\,\mathrm{kg}$. The upper limit of the error $\delta M^{s;filt}$ follows from the application of Equation 7.27 and substituting the error contributions:

$$\begin{aligned}
\delta M^{s;filt} &= V^{s;filt}\delta\rho^{s;filt} + \rho^{s;filt}A^{s;filt}\delta h^{up} \\
&= \left((0.878 * 0.03\,\mathrm{m} + 0.067\,\mathrm{m}) * 2.776\,\mathrm{m}^2\right) * 89\,\mathrm{kg\,m^{-3}} + \\
&\quad 1732\,\mathrm{kg\,m^{-3}} * 2.776\,\mathrm{m}^2 * 0.0014\,\mathrm{m} \\
&= 30\,\mathrm{kg}
\end{aligned} \tag{7.37}$$

Hence, the mass contribution of the sand in the filter tank reads:

$$M^{s;filt} = 449 \pm 30\,\mathrm{kg} \tag{7.38}$$

The final mass contribution concerns the mass of the fines that are removed after flushing of the sand bed, $M^{s;fin}$. The fines have an effect on the performance of the filtering process, as a result of the clogging of the filter sand in the filter tank. Therefore, the top layer in the filter tank was scraped off several times until the sand was considered sufficiently clean. It should be noted that fluidisation by itself is expected to generate fines due to wear of the particles. As for the measurement of the mass of the filter sand, the monitoring of the mass of the fines should be continued during the use of the liquefaction tank. Here, the measurements that were conducted before the fluidisation tests are discussed.

The removed fines are stored in a submerged big-bag in a separate tank. The measurement of $M^{s;fin}$ by oven-drying the sand would be (too) laborious, considering its large volume. An alternative procedure is therefore suggested. The dry mass of removed fines $M^{s;fin}$ as stored in a submerged big-bag is defined by:

$$M^{s;fin} = (1-n)\rho^g V^{s;fin} \tag{7.39}$$

Herein, $V^{s;fin}$ defines the volume of the fines in the big-bag. It can be shown that $M^{s;fin}$ can be determined by simply measuring the submerged weight of the fines in the big-bag. To this end, consider two measurement situations. During the first, the submerged big-bag is lifted with a crane until it is no longer supported by the floor of the tank. It is ensured that the fines are still fully submerged. The submerged weight of the big-bag is ignored and the submerged weight of the fines $G^{s;fin;sub}$ is measured using a load cell. The measured weight is related to the soil properties by:

$$G^{s;fin;sub} = (1-n)\left(\rho^g - \rho^f\right) g V^{s;fin} = M^{s;fin} g - (1-n)\rho^f g V^{s;fin} \tag{7.40}$$

Next, the big-bag is lifted out of the water and the permeable big-bag is left for a while until all the water adhering to the big-bag has been drained off. At this stage, it is likely that the fines are still fully saturated due to the high expected capillary forces. Again, the weight of the fines $G^{s;fin;sat}$ is measured, which is related to the soil properties by:

$$G^{s;fin;sat} = \left(n\rho^f + (1-n)\rho^g\right) g V^{s;fin} = M^{s;fin} g + n\rho^f g V^{s;fin} \tag{7.41}$$

The set of equations defined by 7.40 and 7.41 leaves two unknowns, the porosity n and volume $V^{s;fin}$. However, elaboration of the equations and substitution into 7.39 reveals that $M^{s;fin}$ only depends on the submerged weight $G^{s;fin;sub}$ by:

$$M^{s;fin} = \frac{\rho^g}{\rho^g - \rho^f} \frac{G^{s;fin;sub}}{g} \tag{7.42}$$

It is assumed that the presumed values of the volumetric masses ρ^g and ρ^f are accurate. The error in $M^{s;fin}$ is therefore solely related to the error in $G^{s;fin;sub}$, which is easy to measure. By repeating the measurement and, in order to check the consistency of the assumptions and measurement, by measuring both $G^{s;fin;sub}$ and $G^{s;fin;sat}$, the magnitude of $M^{s;fin}$ is established as:

$$M^{s;fin} = 325 \pm 3\,\text{kg} \tag{7.43}$$

As all the mass contributions in Equation 7.26 are known with their respective error estimates, the mass of dry sand in the liquefaction tank $M^{s;dry;tank}$ can be determined. All the contributions were measured independently, which allows the determination of the propagated error using Equation 7.28. Substitution of Equations 7.29, 7.30, 7.38, 7.43 into Equations 7.26 (average values) and 7.28 (errors) yields:

$$\begin{aligned} M^{s;dry;tank} &= (7500 - (6 + 449 + 325)) \pm \sqrt{7^2 + 2^2 + 30^2 + 3^2}\,\text{kg} \\ &= 6720 \pm 31\,\text{kg} \end{aligned} \tag{7.44}$$

7.3.3. Measurement of soil volume in liquefaction

The soil volume $V^{s;tank}$ is closely related to the dimensions of the liquefaction tank. The floor area of the tank A^{tank} defines the base of the sand bed. The complementary dimension of the sand bed, the height $h^{s;tank}$, varies with the mass and state of the sand. Six measurement tapes were attached at each of the glass sides of the tank to monitor the height $h^{s;tank}$. These measurement tapes were positioned above the walking grid on the bottom of the tank, the open volume of which should also be taken into account when determining the volume of the sand bed.

The floor area of the liquefaction tank A^{tank} was determined by taking measurements of the length and width of the tank, l^{tank} and w^{tank}, respectively, at different positions. The assumed error for each of the width measurements was ± 1 mm, and for each of the length measurements it was ± 2 mm. The errors of the average measures of the width and length are equal to or less than these magnitudes according to Equation 7.27. The resulting dimensions are $l^{tank} = 4781 \pm 2$ mm and $w^{tank} = 1971 \pm 1$ mm, yielding an estimated floor area of:

$$A^{tank} = 9.424 \pm 0.009\,\mathrm{m}^2 \tag{7.45}$$

As for the grid in the filter tank, the error of the grid porosity is expected to be negligibly small. Based on accurate values of $n^{gr;tank} = 0.65$ and $h^{gr;tank} = 36.7$ mm, the volume of the mesh $V^{s;mesh;tank}$ equals:

$$V^{s;mesh;tank} = n^{gr;tank} h^{gr;tank} A^{tank} = 0.65 * 0.0367\,\mathrm{m} * 9.424\,\mathrm{m}^2 = 0.225\,\mathrm{m}^3 \tag{7.46}$$

The error in $V^{s;mesh;tank}$ is extremely small and will therefore be ignored.

The positions of the zero readings of the measurement tapes with respect to the top of the grid have been measured. Hence, the measurement of $h^{s;tank}$ has two sources of error: the positions of the measurement tapes and the actual reading. It is assumed that both have an error equal to ± 1 mm resulting in a total error of maximally ± 2 mm. It is concluded that the volume of sand in the tank equals:

$$V^{s;tank} = 0.225\,\mathrm{m}^3 + \left(9.424 \pm 0.009\,\mathrm{m}^2\right)\left(h^{s;tank} \pm 0.002\,\mathrm{m}\right) \tag{7.47}$$

7.3.4. Error analysis of global density

The average global volumetric mass in the liquefaction tank $\rho^{s;dry;tank}$ and the corresponding error $\delta\rho^{s;dry;tank}$ follow from the corresponding values of the mass 7.44 and volume 7.47. Both quantities were measured independently, which justifies the use of Equation 7.28 to determine the propagated error:

$$\delta\rho^{s;dry;tank} = \sqrt{\left(\frac{\delta M^{s;dry;tank}}{V^{s;tank}}\right)^2 + \left(\frac{M^{s;dry;tank}}{\left(V^{s;tank}\right)^2}\delta V^{s;tank}\right)^2} \tag{7.48}$$

The actual magnitude of $\delta\rho^{s;dry;tank}$ depends on the value of $h^{s;tank}$, which will be varied during the experiments. At this stage, the error is related to the range of values of $h^{s;tank}$

after sedimentation as observed during experiments, that is, $44\,\text{cm} \leqslant h^{s;tank} \leqslant 52\,\text{cm}$. Assuming that the area of the tank A^{tank} and the height of the sand bed $h^{s;tank}$ are independent measures with random errors, the resulting volume $V^{s;tank}$ equals:

$$4.372 \pm 0.023\,\text{m}^3 \leqslant V^{s;tank} \leqslant 5.125 \pm 0.023\,\text{m}^3 \tag{7.49}$$

Then, the resulting density and its error can be calculated by substituting the mass and volume into Equations 7.25 and 7.49 to end up with:

$$1311 \pm 9\,\text{kg}\,\text{m}^{-3} \leqslant \rho^{s;dry;tank} \leqslant 1537 \pm 11\,\text{kg}\,\text{m}^{-3} \tag{7.50}$$

It is concluded that the relative error in terms of dry, volumetric mass is relatively small, i.e. $< 1\%$. The mass and volume contribute approximately equally to the total error. Consider for instance the error of $9\,\text{kg}\,\text{m}^{-3}$ at the lower end of Equation 7.50. The related first square root term on the right-hand side of Equation 7.48 equals 37, while the second square root term equals 36. The error in the volume $\delta V^{s;tank}$ is governed by the measurement of the sand bed, depending both on the error in the measurement itself and the position of the measurement tape. The error in the mass $\delta M^{s;dry;tank}$ is mainly governed by the error in the mass of the sand in the filter.

The meaning of the result 7.48 is further elucidated when expressing these numbers in terms of porosity n or void ratio e. The calculation of the porosity is rather straightforward:

$$n = 1 - \frac{\rho^{s;dry}}{\rho^{g}} \tag{7.51}$$

As ρ^{g} is assumed to be accurate, the error δn can be calculated from $\delta\rho^{s;dry}$. The void ratio e and its corresponding error can then be calculated using the following relation with porosity n:

$$e = \frac{n}{1-n} \tag{7.52}$$

The following ranges are derived with respect to porosity and void ratio, respectively:

$$0.420 \pm 0.004 \leqslant n \leqslant 0.505 \pm 0.003 \tag{7.53}$$

$$0.724 \pm 0.012 \leqslant e \leqslant 1.021 \pm 0.013 \tag{7.54}$$

The error in terms of porosity n or void ratio e is relatively small. Using the global, average density moreover provides a stable measure to characterise the state of the sand bed. If the error is doubled in terms of measured mass and volume, the error in terms of either $\delta\rho^{s;dry}$, δn or δe will approximately double as well. Even then, the magnitudes would be acceptable. The large mass and volume reduce the errors in the global, average density (and related quantities), which will be even more the case when the liquefaction tank is filled with larger amounts of sand in the future. However, whether the global, average density provides sufficient level of detail to describe the response of the sand bed is questionable. In the next chapter, it will be shown that the global, average density relates well with the observed and measured responses during tilting tests.

7.4. Results of fluidisation tests in liquefaction tank

7.4.1. General

A series of fluidisation experiments was conducted on the sand bed with a dry mass of $M^{s;dry;tank}$. The main objective of the experiments was the verification of the performance of the fluidisation system. Practical issues that asked for verification were the removal of the fines by flushing of the sand bed and the effect of the filter bed.

The flushing was discussed in the previous section. It is worth noting that the flushing reduced the turbidity of the water significantly, but did not yield a fully transparent view. This may be attributed to the combination of the limited duration of continuous fluidisation and the relatively small height of the sand bed. The discharge capacity of the first filter layer in the large storage tank appeared insufficient during larger fluidisation flow rates. The relatively small bed height on the other hand requires a long period of continuous flushing to cover the distance of 1.5 m to the overflow. It is anticipated that this issue will be resolved when the thickness of the sand bed will be increased.

The filter layers provide a stable basis for the fluidisation process, but also introduce additional resistance in the system. In order to interpret the fluidisation experiments correctly, it is first necessary to establish the pressure loss in the filter layers. Subsection 7.4.2 will address the results of reference measurements to determine the resistance of the filter layers in more detail.

Secondly, the performance of the fluidisation system will be considered in terms of the uniformity of the fluidisation pressure in the system. The design of the system (Subsection 6.2.3) accounts for the pressure gradient in the fluidisation system as a result of the flux imposed on the sand bed. It is argued that a uniform pressure in the fluidisation system will lead to a uniform density in the sand bed. During the fluidisation tests the fluidisation pressure at the front and rear end of the tank was measured to verify its uniformity. Finally, the response of the sand bed during and just after sedimentation is considered in the final Subsection 7.4.4. The response of the sand will be compared with the theory from Section 7.1 and the results from the preliminary tests as discussed in Section 7.2. The information concerning the soil mass and volume from Section 7.3 enables a measured height of the sand bed to be expressed in terms of porosity n, including its estimated error. During the liquefaction testing, the initial porosity of the sand bed will be controlled by varying the fluidisation process.

7.4.2. Reference measurements

The filter consists of two granular layers, with geosynthetic filter layers in between and above the granular layers (see Table 6.1). Tests were conducted with only the filter installed to verify its resistance. Before discussing the results, the anticipated resistance in the filter will be addressed. Assuming stationary conditions, the pore fluid stress difference Δp_z over each of the components of the filter can be deduced from the momentum

affecting the pore fluid stress 3.84:

$$\Delta p_z = \left(1 + \frac{w_z^{pf\text{-}s}}{k_{zz}}\right)\gamma^f \Delta z \tag{7.55}$$

Equation 7.55 expresses the pore water stress difference in terms of vertical (tensor) components.The resistance of each of the components is calculated for $Q^{fl} = 10\ \mathrm{l\,s^{-1}}$. The permeability of the granular layers is estimated using the Kozeny-Carman equation 6.2 and $n = 0.4$. The permeability of the geosynthetic layers is specified by a standardised test described in [10]. The geosynthetic layer is submerged under 5 cm water ($\Delta p^{0.05}$), while measuring the discharge through the layer $w_z^{pf\text{-}s;0.05}$. Assuming that the resulting permeability also applies for much larger fluxes, the pressure drop Δp_z can be directly calculated from these measures:

$$\Delta p_z = \frac{w_z^{pf\text{-}s}}{w_z^{pf\text{-}s;0.05}} \Delta p^{0.05} \tag{7.56}$$

Table 7.2 quantifies the pressure drop for each of the components of the filter for $Q^{fl} = 10\ \mathrm{l\,s^{-1}}$. It should be noted that the walking grid at the bottom of the liquefaction tank increases the pressure drop in the combined, geosynthetic top layer. The grid directs the flow through the holes, thereby increasing the flux and the pressure drop. The total, anticipated pressure drop over the filter layer equals approximately 1 kPa. It is concluded from Table 7.2 that the upper granular filter layer governs the anticipated pressure drop in the filter layer. The contributions of the geosynthetic layers is relatively small. The fixed component of the pressure drop, i.e. the component defined by the hydrostatic pressure $\gamma^f \Delta z$, accounts for approximately 3/4 of the total pressure drop, with the variable, flux dependent component accounting for the complementary 1/4.

Table 7.2: Pressure drop over filter layers above fluidisation system due to flow

component	k_{zz} [mm s^{-1}]	$w_z^{pf\text{-}s;0.05}$ [mm s^{-1}]	Δp_z [Pa]
geosynthetic layer PE525+TS80	NA	300+55	17
granular filter layer $D^{50} = 0.39$ mm	2	NA	763
geosynthetic layer PE525	NA	300	2
granular filter layer $D^{50} = 2.15$ mm	58	NA	250

During the tests the fluidisation flow rate, the water pressures at the bottom, the total water pressure and differential water pressure in the fluidisation system, and the total pressures at the rear end plate of the tank were measured, and the rise of the phreatic level using the measurements tapes at the sides of the tank was monitored. The resistance of the filter is verified by considering the increment in measured water pressures after turning on the fluidisation system. In this way, the influence of the level of the

sensors can be ignored. Thus the variable part of the anticipated pressure drop is verified as presented in Table 7.2. Isolating the variable parts of the pressure drop of each component in Table 7.2, i.e. the flux dependent part in Equation 7.55, and subsequent summation yields:

$$\Delta p_z^Q = 30\, Q^{fl} \tag{7.57}$$

Herein, Δp_z^Q is expressed in Pa, and Q^{fl} in $\mathrm{l\,s^{-1}}$. Two test series were conducted to verify the reproducibility of the results. Here, the result of the second series is discussed.

During the test, the fluidisation flow rate Q^{fl} was stepwise increased from 7.6 $\mathrm{l\,s^{-1}}$ to 15.0 $\mathrm{l\,s^{-1}}$. In between the four steps, the fluidisation flow rate was held constant for at least 60 s. The readings were sampled with an interval of 1 s. Two sensors showed a deviant response. The filter plate on top of one of the sensors in the bottom of the tank appeared to be clogged, resulting in a slow response of this sensor. One of the total load sensors at the rear end of the tank yielded an unstable response, even though the average response was well captured. Apart from these sensors, the response of the sensors was consistent. The performance of the sensors was verified by considering the gradual increase of the pressure during the periods in which the fluidisation flow rate was held constant.

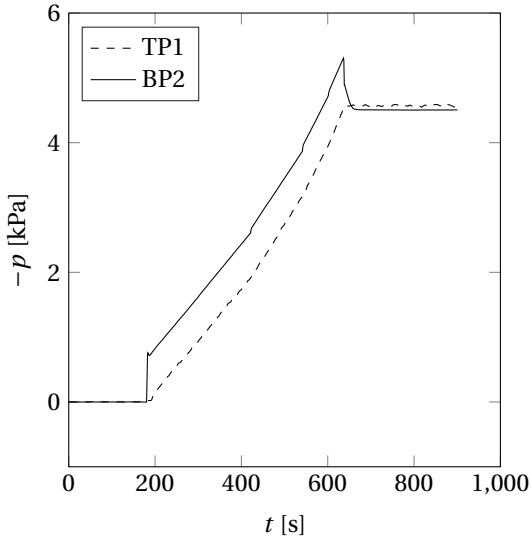


Figure 7.16: Response from pressure sensors in terms of pressure increment during reference tests with only filter installed.

The response of the middle sensor at the bottom of the tank (BP2) and the total pressure sensor TP1 are now considered. Figure 7.16 shows the response of both sensors in time. After approximately 180 s the fluidisation system is turned on, as can be seen by the sudden pressure increase of BP2. The pressure increase is much larger than anticipated based on Equation 7.57. The first series of tests, starting at a fluidisation flow rate

of only $Q^{fl} = 2.5$ ls^{-1}, showed a similar increase. The relatively large pressure increase is attributed to a small amount of sand that was left in the holes of the synthetic grid. These tests were carried out after removing the sand bed, but a small amount of sand was left in the holes of the synthetic grid. To eliminate the effect of fluidised sand in the holes of the synthetic grid, only the subsequent flow (and pressure) increments are considered. Starting from a fluidisation flow rate of $Q^{fl} = 7.7$ ls^{-1} at time=200 s, the fluidisation flow rate was stepwise increased to 9.7 ls^{-1}, 12.7 ls^{-1} and 15 ls^{-1} at time=420 s, 540 s and 600 s, respectively. The instant increase in measured pressure by BP2 is compared to the anticipated value based on Equation 7.57. Table 7.3 gives an overview of the results. Considering the uncertainties of the soil properties and measurement accuracy of the sensors, the result correspond well, particularly at low flow rates.

Table 7.3: Measured and calculated pressure drop over filter layers above fluidisation system

Time [s]	ΔQ^{fl} [ls^{-1}]	Δp_z^{meas} [Pa]	Δp_z^{calc} [Pa]
420	2	58	59
540	3	71	89
600	2.3	44	68

During fluidisation of the sand bed, the interpretation of the *absolute* pressure readings at the bottom of the tank requires that account is taken of two additional contributions. Firstly, the hydrostatic part in between the fluidisation holes in the tubes and the pore pressure sensors equals 441 Pa for an approximate distance of 4.5 cm between the holes and the sensor. Note that this contribution can be ignored if the incremental pressure at the moment the fluidisation system is turned on is considered. Secondly, the pressure drop over the holes in the walking grid at the bottom of the tank should be accounted for. The hydrostatic pressure drop over the cells with a height of $h^{gr;tank} = 3.67$ cm equals 360 Pa. Again, this component can be ignored if the incremental pressure is considered. Furthermore, the sand in the holes of the synthetic grid fluidises, thereby creating an additional pressure drop in between the pressure sensors and the fluidising bed. Fluidisation (or liquefaction) of the sand implies the transfer of the buoyant weight from the intergranular stress to the pore fluid stress (Equation 3.91). Hence, the incremental pressure $\Delta p^{fl;gr;tank}$ during fluidisation of the sand depends on the porosity n and height of the grid $h^{gr;tank}$:

$$\Delta p^{fl;gr;tank} = \rho^{buoy} g h^{gr;tank} = (1-n)\left(\rho^{g} - \rho^{f}\right) g h^{gr;tank} \tag{7.58}$$

After substituting a porosity of $n = 0.55$ during fluidisation and a thickness of $h^{gr;tank} =$ 36.7 mm, the pressure drop over the fluidised sand in the holes of the synthetic grid equals 267 Pa. Alternatively, consider the fluidisation of the entire sand bed including the sand in the holes. Provisionally ignoring the grid, the incremental pressure of a uni-

form sand bed with height $h^{s;tank}$ during fluidisation equals:

$$p^{fl;bed} = -(1-n)\left(\rho^g - \rho^f\right) g h^{s;tank} = -\frac{\rho^{s;dry}}{\rho^g}\left(\rho^g - \rho^f\right) g \frac{V^{s;tank}}{A^{tank}}$$
$$= -\frac{M^{s;dry;tank}}{V^{s;tank}\rho^g}\left(\rho^g - \rho^f\right) g \frac{V^{s;tank}}{A^{tank}} = -\left(\frac{\rho^g - \rho^f}{\rho^g}\right)\frac{M^{s;dry;tank}}{A^{tank}} g \tag{7.59}$$

The last expression of Equation 7.59 allows one to calculate the incremental pressure during fluidisation (or liquefaction) from the dry sand mass $M^{s;dry;tank}$. However, the contribution of the sand in the holes is erroneously taken into account. Equation 7.59 presumes that the contribution of the sand in the holes is smeared out over the total area of the tank, thereby underestimating the height of the cells and the pressure drop. The correction that needs to be applied in terms of height equals:

$$h^{gr;tank;corr} = h^{gr;tank} - \frac{V^{s;mesh;tank}}{A^{tank}} = 0.0367 - \frac{0.225}{9.424}\text{m} = 1.3\,\text{cm} \tag{7.60}$$

Substituting this correction into Equation 7.58 yields the additional pressure drop that needs to be added when using Equation 7.59 to calculate the anticipated pressure increment during full fluidisation or liquefaction of the sand bed, p^{fl}. The result reads:

$$p^{fl} = -\left(\frac{\rho^g - \rho^f}{\rho^g}\right)\frac{M^{s;dry;tank}}{A^{tank}} g - (1-n)\left(\rho^g - \rho^f\right) g h^{gr;tank;corr}$$
$$= -\left(\frac{2650\text{kg m}^{-3} - 1000\text{kg m}^{-3}}{2650\text{kg m}^{-3}}\right) * \frac{6720\text{kg}}{9.424\text{m}^2} * 9.81\text{m s}^{-2} -$$
$$(1-0.55) * \left(2650\text{kg m}^{-3} - 1000\text{kg m}^{-3}\right) * 9.81\text{m s}^{-2} * 0.013\text{m}$$
$$= -4.36 - 0.09\text{kPa} = -4.45\,\text{kPa} \tag{7.61}$$

Note that the correction term in Equation 7.61 depends on the porosity n. The value of n can be calculated using the theoretical steady-state value from Equation 7.14 with $\dot{u}_z^s = 0$. The substituted value $n = 0.55$ corresponds to a steady-state value for $D^g = 120\,\mu$m and $w|_{z=0}^{t>t_0} * A^{tank} = 10\ \text{l s}^{-1}$. Considering the effect of segregation and the varied fluidisation flow rate, the correction term is uncertain and variable. However, the sensitivity with grain size and fluidisation flow rate is relatively small. For instance, a coarser grain size of $D^g = 140\,\mu$m yields a value of -0.10 kPa, and an increased flux of $w|_{z=0}^{t>t_0} * A^{tank} = 15\ \text{l s}^{-1}$ a value of -0.08 kPa. Hence, the value calculated in Equation 7.61 will be retained.

7.4.3. Uniformity of fluidisation pressure

The uniformity of the pressure in the fluidisation system is a prerequisite for a uniform density of the sand bed. The main conclusions from the design of the fluidisation tank in 6.2.3 are recalled. Based on design calculations a relative pressure difference $\Delta p/p$ along the fluidisation tubes of well below 1% is expected, or an absolute pressure difference in the order $\Delta p \sim 0.1$ kPa. For the considered range of input pressures of 50 kPa to 100 kPa the absolute pressure is more or less constant, while the relative measure decreases with increasing input pressure. The main uncertainty in the calculations is the

presumed laminar flow. The calculated Reynold's number (order 10^4) is well above the threshold value for turbulent flow.

This section verifies the uniformity of the fluidisation pressure during fluidisation experiments. Experiments conducted with and without the sand bed installed will be considered. During the experiments the entry pressure in the fluidisation system was measured by pore pressure transducer FP, while the differential pressure at the rear of the system was measured by the differential pressure transducer DFP (see Figure 6.18). Ideally, the difference between the entry pressure and differential pressure should equal the pressure in the tank at the level of the fluidisation tubes. Hence, the difference between the actual measured pressure in the bottom and the pressure deducted from the sensors to assess the pressure gradient are compared. The middle pore pressure sensor in the bottom, BP2, is used for the consideration. The sensor closest to the rear end, BP3, showed a delayed response due to the clogging of the overlying filter plate. Again, the *incremental* pressure is considered to eliminate the influence of the levels of the sensors.

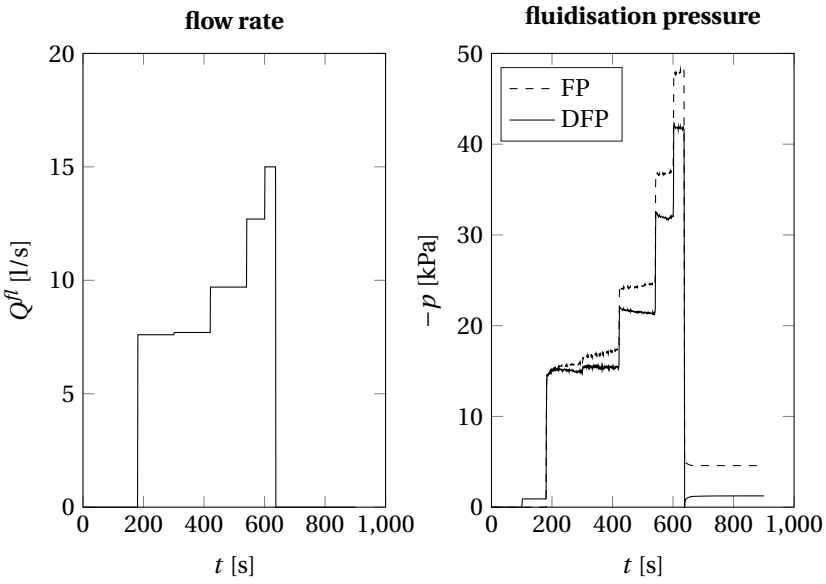


Figure 7.17: Fluidisation flow rate Q^{fl} (left) and incremental pore fluid stress $-p$ (right), as measured by sensors FP and DFP during test FT2. The fluidisation flow rate has consecutively been raised at $t = 120$ s ($Q^{fl} = 7.5$ l s^{-1}), $t = 240$ s ($Q^{fl} = 7.7$ l s^{-1}), $t = 360$ s ($Q^{fl} = 9.4$ l s^{-1}), $t = 480$ s ($Q^{fl} = 12.3$ l s^{-1}) and $t = 600$ s ($Q^{fl} = 14.4$ l s^{-1}). At time $t = 620$ s the fluidisation flow has been switched off.

Uniformity of pressure without sand bed

Figure 7.17 shows a typical response in terms of fluidisation flow rate and fluidisation pressures. Test FT2 was conducted to measure the resistance of the filter layer only, i.e. without a sand bed, during a stepwise increase of the fluidisation flow rate. The plots of the fluidisation pressures are based on raw, yet filtered, data. The differential pressure

shows an anomaly (increase) around $t = 120\,\mathrm{s}$, presumably due to an external cause. Nonetheless, the observed tendency meets the expectations. Both the entry pressure (FP) and differential pressure (DFP) instantly respond to changes in the fluidisation flow rate. The difference between the two increases as a result of the rising water level (the tank was not completely filled beforehand) and the pressure difference that appears as a result of the decreasing pressure along the fluidisation tubes. The rising water table has no effect on the differential fluid pressure, but it does affect the fluid pressure measured by FP.

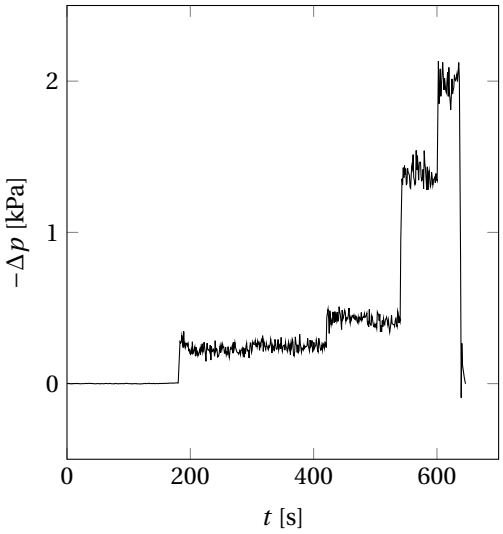


Figure 7.18: Difference between differential pressure (DFP) at the rear of the tank and pressure (FP) at the front for test FT2. The fluidisation flow rate has consecutively been raised at $t = 120\,\mathrm{s}$ ($Q^{fl} = 7.5\ \mathrm{l\,s^{-1}}$), $t = 240\,\mathrm{s}$ ($Q^{fl} = 7.7\ \mathrm{l\,s^{-1}}$), $t = 360\,\mathrm{s}$ ($Q^{fl} = 9.4\ \mathrm{l\,s^{-1}}$), $t = 480\,\mathrm{s}$ ($Q^{fl} = 12.3\ \mathrm{l\,s^{-1}}$) and $t = 600\,\mathrm{s}$ ($Q^{fl} = 14.4\ \mathrm{l\,s^{-1}}$). At time $t = 620\,\mathrm{s}$ the fluidisation flow has been switched off.

Figure 7.18 plots the difference in pressure between the front and rear ends of the fluidisation system. The figure has been reworked to have a clear picture of Δp over the length of the fluidisation tubes. Anomalies in the differential pressure sensor before starting and after ending fluidisation have been removed. The same applies for the large peaks measured by BP2 just after changing the fluidisation flow rate. Furthermore, Figure 7.18 compensates for the increasing water table. The measured response is consistent. The pressure difference Δp is negative (decrease pressure) and fairly constant during periods in which the fluidisation flow rate is constant. For the two initial fluidisation flow rates ($Q^{fl} = 7.6\ \mathrm{l\,s^{-1}}$, $Q^{fl} = 7.7\ \mathrm{l\,s^{-1}}$) the pressure difference fluctuates around the relatively low value of $-\Delta p = 0.2\,\mathrm{kPa}$. However, as the fluidisation flow rate is stepwise increased to $Q^{fl} = 9.7\ \mathrm{l\,s^{-1}}$, $Q^{fl} = 12.7\ \mathrm{l\,s^{-1}}$ and $Q^{fl} = 15\ \mathrm{l\,s^{-1}}$, the pressure difference increases significantly. The increase to $Q^{fl} = 9.7\ \mathrm{l\,s^{-1}}$ still yields a relatively small pressure difference of $-\Delta p = 0.5\,\mathrm{kPa}$. However, the two subsequent steps yield values of $-\Delta p = 1.4\,\mathrm{kPa}$ and $-\Delta p = 2.0\,\mathrm{kPa}$, respectively. The relative pore pressure difference $\Delta p/p$ increases from

approximately 1.5% for $Q^{fl} = 7.6$ ls^{-1} to over 4% for $Q^{fl} = 15$ ls^{-1}. These differences were not expected based on the design calculations. It is concluded that turbulence indeed affects the pressure gradient over the fluidisation tubes significantly. It seems that turbulence becomes increasingly important for flow rates higher than $Q^{fl} = 10$ ls^{-1}.

Uniformity of pressure with sand bed

Next, the measured fluidisation pressures during test FT3 that was conducted with the first batch of sand installed is considered. Figure 7.19 depicts the fluidisation flow rate and fluidisation pressures. The fluidisation flow rate was again stepwise increased, this time starting at the relatively low value of $Q^{fl} = 2.7$ ls^{-1}. It is noted that the final fluidisation flow rate could only be retained for a short period; its value of $Q^{fl} = 12.6$ ls^{-1} is therefore uncertain. The measurements are consistent with those conducted without the sand bed installed (Figure 7.17). During the fifth step the fluidisation flow rate was increased to $Q^{fl} = 9.4$ ls^{-1}, which is close to the value imposed at the third step in Figure 7.17 where $Q^{fl} = 9.7$ ls^{-1}. The measured fluidisation pressures are similar. However, the water level was rising during test FT2, while it was constant during test FT3. In addition, the fluidisation flow rate was higher during test FT2, which will also have an effect on the fluidisation pressures. Hence, the fluidisation pressures are higher for the test with the sand bed installed, as expected.

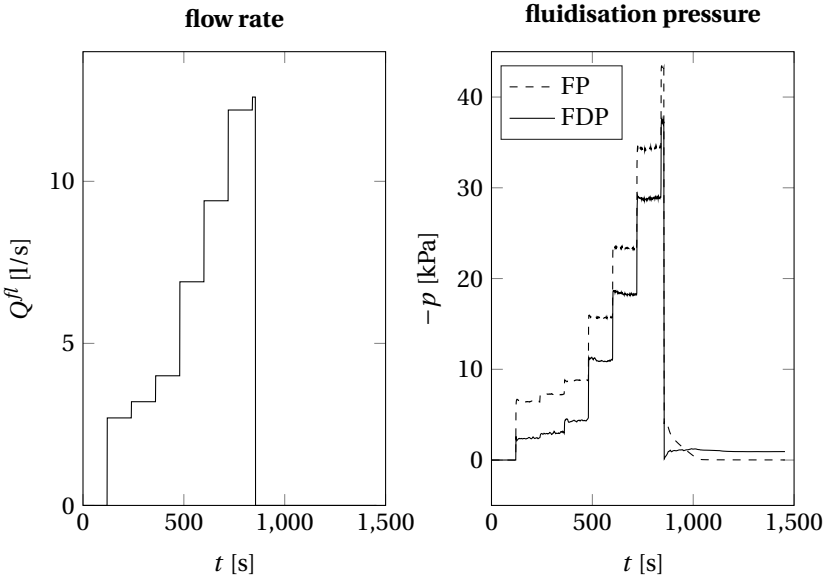


Figure 7.19: Fluidisation flow rate Q^{fl} (left) and incremental pore fluid stress $-p$ (right), as measured by sensors FP and DFP during test FT3. The fluidisation flow rate has consecutively been raised at $t = 120$ s ($Q^{fl} = 2.7$ ls^{-1}), $t = 240$ s ($Q^{fl} = 3.2$ ls^{-1}), $t = 360$ s ($Q^{fl} = 4.0$ ls^{-1}), $t = 480$ s ($Q^{fl} = 6.9$ ls^{-1}), $t = 600$ s ($Q^{fl} = 9.4$ ls^{-1}), $t = 720$ s ($Q^{fl} = 12.2$ ls^{-1}) and $t = 840$ s ($Q^{fl} = 12.6$ ls^{-1}). At time $t = 855$ s the fluidisation flow has been switched off.

Figure 7.20 plots the pressure difference Δp over the fluidisation tubes. The data were

reworked by removing the peaks between the transitions between fluidisation flow rates. The response is highly irregular, particularly at lower fluidisation flow rates. It is hard to distinguish the transitions between flow rates. The first step $Q^{fl} = 2.7$ ls^{-1} after turning on the fluidisation system even yields a small, negative pressure difference. During subsequent steps, the difference first increases after changing the flow rate but then tends to decrease in time as the flow rate is maintained. The difference does seem to stabilise more and more as the flow rate is increased. Its response is stable during the last step but one when $Q^{fl} = 12.2$ ls^{-1}.

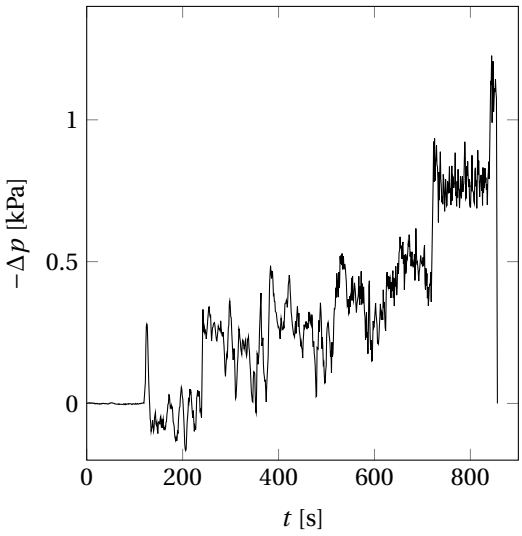


Figure 7.20: Difference between differential pressure (DFP) at the rear of the tank and pressure (FP) at the front for test FT3. The fluidisation flow rate has consecutively been raised at $t = 120$ s ($Q^{fl} = 2.7$ ls^{-1}), $t = 240$ s ($Q^{fl} = 3.2$ ls^{-1}), $t = 360$ s ($Q^{fl} = 4.0$ ls^{-1}), $t = 480$ s ($Q^{fl} = 6.9$ ls^{-1}), $t = 600$ s ($Q^{fl} = 9.4$ ls^{-1}), $t = 720$ s ($Q^{fl} = 12.2$ ls^{-1}) and $t = 840$ s ($Q^{fl} = 12.6$ ls^{-1}). At time $t = 855$ s the fluidisation flow has been switched off.

The irregular pressure difference is attributed to the response of the sand bed. The response of the fluidisation pressures (Figure 7.19) is stable, whilst the pressure measured at the bottom (BP2) is highly irregular. The first three steps are below the anticipated fluidisation threshold value of $Q^{fl} = 4.2$ ls^{-1} (see Figure 7.3). The response stabilises as the fluidisation flow rate passes the threshold value. The actual measured pressure difference equals approximately $\Delta p = 0.8$ kPa for $Q^{fl} = 12.2$ ls^{-1}. Recall that a value of $\Delta p = 1.4$ kPa was established for the test without the sand bed installed, albeit for a slightly higher flow rate of $Q^{fl} = 12.7$ ls^{-1}. Before drawing any premature conclusions, another series of tests is first considered.

Uniformity of pressure for different, constant flow rates

The fluidisation flow rate was held constant during the last series of tests considered, FT5. During three tests (FT5a, FT5b and FT5c), the sand bed was fluidised using initial fluidisation flow rates of $Q^{fl} = 6.2\ \mathrm{l s^{-1}}$, $Q^{fl} = 9.4\ \mathrm{l s^{-1}}$ and $Q^{fl} = 12.7\ \mathrm{l s^{-1}}$, respectively. The fluidisation system was turned on for as long as the storage capacity of filtered water allowed. Figure 7.21 shows the pressure difference over the tubes Δp for the three tests. All three tests show a more or less stable value of Δp. Surprisingly, there is hardly any difference between the tests conducted at $Q^{fl} = 6.2\ \mathrm{l s^{-1}}$ and $Q^{fl} = 9.4\ \mathrm{l s^{-1}}$, with an approximate value of $\Delta p = 0.7\,\mathrm{kPa}$. There is a clear difference with the test which was conducted at $Q^{fl} = 12.7\ \mathrm{l s^{-1}}$, which yields an approximate value of $\Delta p = 1.3\,\mathrm{kPa}$. This value corresponds well with the value found for the same flow rate but without the sand bed installed (FT2, Figure 7.18). The value found for $Q^{fl} = 9.4\ \mathrm{l s^{-1}}$ ($\Delta p = 0.7\,\mathrm{kPa}$) is slightly higher for both the value found during test FT2 ($Q^{fl} = 9.7\ \mathrm{l s^{-1}}$,$\Delta p = 0.5\,\mathrm{kPa}$) and test FT3 ($Q^{fl} = 9.4\ \mathrm{l s^{-1}}$, $\Delta p = 0.5\,\mathrm{kPa}$), but the difference is acceptable.

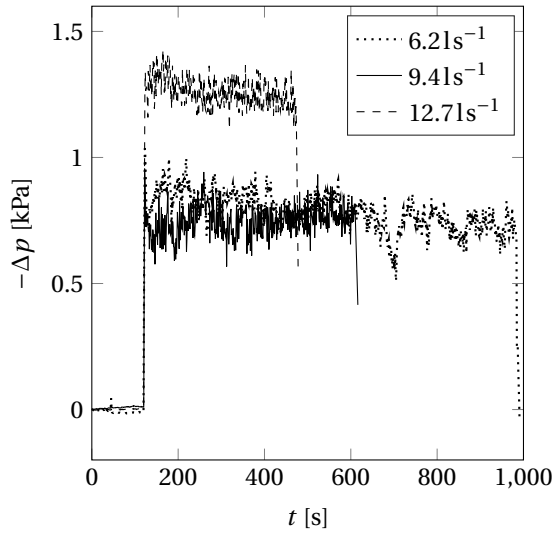


Figure 7.21: Difference between differential pressure (DFP) at the rear of the tank and pressure at the front (FP) for tests FT5a, FT5b and FT5c.

The following conclusions are drawn with respect to the fluidisation tests. Turbulence governs the magnitude of the pressure gradient along the fluidisation tubes. The pressure loss between the front and rear end of the fluidisation is relatively small for fluidisation flow rates below 9 $\mathrm{l s^{-1}}$. Relatively speaking, the pressure loss increases rapidly as the flow rate is increased beyond this value. Hence, from the viewpoint of pressure uniformity the magnitude of the fluidisation flow rate should be kept as low as reasonably possible.

No significant differences in terms of pressure loss were observed between the tests con-

ducted with and without the sand bed installed. The strongly irregular measurement results at low fluidisation flow rates reflects the non-uniform fluidisation response of the sand bed. The test results indicate that the fluidisation flow rate should be larger than 6 $\mathrm{l s^{-1}}$ to yield a uniform response. Particularly at low fluidisation flow rates the initial state of the sand bed is of importance, with a more regular and predictable response for a looser and more uniform initial state. Hence, from the viewpoint of the fluidisation response of the sand bed, the magnitude of the flow rate should be as large as reasonably possible.

It is concluded that the optimum fluidisation flow rate lies somewhere in the range between 6 $\mathrm{l s^{-1}}$ to 12 $\mathrm{l s^{-1}}$. The question is how relevant is the anticipated pressure loss for the uniformity of the sand bed. This issue is addressed by considering the consequent gradient in fluidisation flow rate for the design value of 10 $\mathrm{l s^{-1}}$. The (square root of the) differential pressure between inside and outside the tubes determines the magnitude of the actual fluidisation flow rate (Equation 6.6). For $Q^{fl} = 10$ $\mathrm{l s^{-1}}$, the differential pressure equals approximately 20 kPa and the pressure loss is 1 kPa, as can be seen from the measurement results in Figures 7.18 and 7.20. The differential pressure is thus reduced from 20 kPa to 19 kPa at the end of the tube; a reduction of 5%. Considering the flow rate relates to the square root of the differential pressure (through Equation 6.6), the anticipated difference in terms of flow rate equals 2.5%. Imposing a fluidisation flow rate of 10 $\mathrm{l s^{-1}}$ at the front of the fluidisation system will effect a flow rate of 9.75 $\mathrm{l s^{-1}}$. It is highly unlikely that this difference will result in great non-uniformities.

7.4.4. Response of sand bed during fluidisation

While the previous subsection concentrated on the measured pressures in the fluidisation system, this section deals with the actual response of the sand bed. The incipient fluidisation flow rate, bed expansion, sedimentation and established density for different fluidisation flow rates will be considered. The mass and volume measurements from 7.3.2 are used to express the bed height in terms of density and porosity. Again, the incremental measurements after starting fluidisation will be plotted, unless otherwise noted.

The total, dry mass of the sand bed equals $M^{s;dry;tank} = 6720$ kg (Equation 7.44). Fluidisation of the entire sand bed implies that the buoyant weight of the soil skeleton is transferred from the effective stress to the pore fluid stress (see Equation 3.91). Also taking into account the resistance of the filter bed leads to the following anticipated pressure increase:

$$-\Delta p^{Q} = 4.45 + 0.03\, Q^{fl} \tag{7.62}$$

The pressure increase Δp^{Q} is expressed in terms of kPa, and the fluidisation flow rate in $\mathrm{l s^{-1}}$. The linear coefficient equal to 0.03 thus has dimensions $\mathrm{kPa\,l s^{-1}}$. Note that Equation 7.62 combines the results of Equations 7.57 and 7.61.

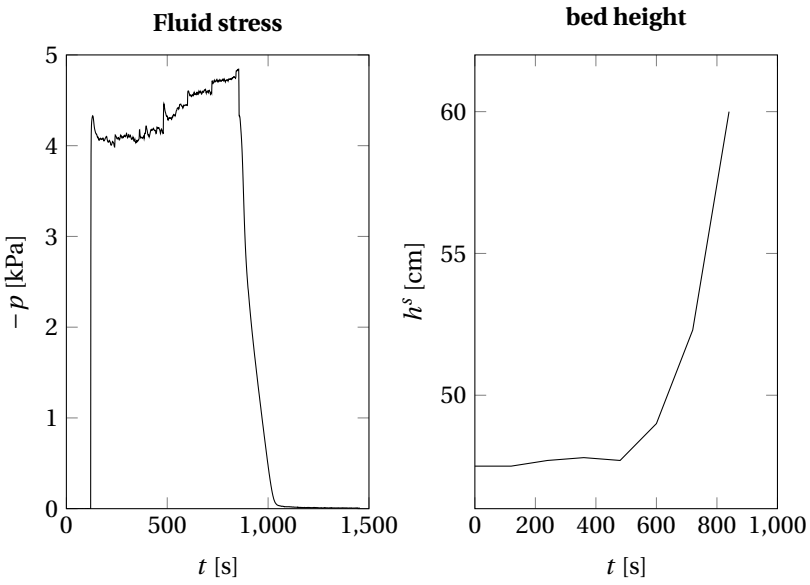


Figure 7.22: The incremental fluid stress measured by BP2 (left) and development of bed height during test FT3 (right).

Threshold expansion of sand bed

The test results from test FT3 are used to consider the initial response of the sand bed during fluidisation. Figure 7.19 previously depicted the fluidisation scheme for this test, characterised by a stepwise increase of the flow rate. Figure 7.22 shows the incremental fluid pressure at the bottom as measured by sensor BP2 and the development of the bed height. The bed height was recorded at each moment the fluidisation flow rate was adjusted. The initial bed height of 47.5 cm implies an average porosity of $n = 0.461$. Instantly after starting fluidisation ($Q^{fl} = 2.7$ ls^{-1}) the fluid pressure increases by just over 4 kPa. However, it is unlikely that the sand bed was fluidised at this stage, as the sand bed does not expand. The pressure rise is the result of the encountered resistance of the sand bed during upward flow. The fluctuations are presumably caused by the fluidisation of the sand within the holes of the synthetic grid, where the flow contracts.

The measurements show little change for the subsequent steps up to and including $Q^{fl} = 4.0$ ls^{-1}. This observation corresponds to the threshold value for incipient fluidisation of $Q^{fl} = 4.2$ ls^{-1} (see Figure 7.3). The increase to $Q^{fl} = 6.9$ ls^{-1} yields both an additional increase in fluid stress and bed expansion. The gradual increase in fluid stress following the increase of flow rate supports the notion of the onset of fluidisation of the sand bed. Every additional increase hereafter results in an instant increase of the fluid stress and an increase in the rate of bed expansion. Finally, at the final step (assumed $Q^{fl} = 12.6$ ls^{-1}) the bed has expanded to 60 cm ($n = 0.569$). The total increase in fluid stress of 4.84 kPa is close to the value that would be expected for full fluidisation of the sand bed (4.83 kPa).

Unlike predicted by theory, the initial stage of fluidisation in the tank was not a gradual process. Presumably as a result of initial non-uniformities in the sand bed, incipient fluidisation involved the appearance of sand boils at the surface. Initially only a few were noted, after which the process homogenised and (smaller) boils were observed all over the surface. Note that boils were observed in the minitank as well (Figure 7.9). It is assumed that the initial non-uniform response is part of a fluidisation process in a 3D setup. It is likely to yield some degree of non-uniformity of the final state of the sand bed, as will be discussed later on.

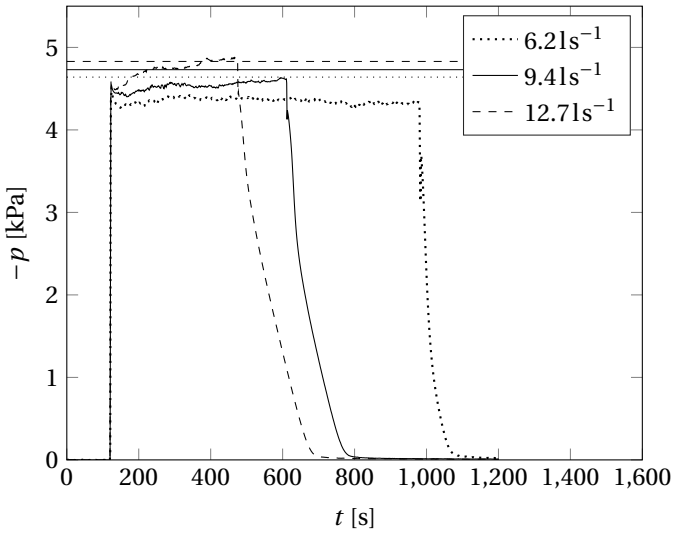


Figure 7.23: Measured incremental pressure during fluidisation tests with constant flow rates. The horizontal lines correspond to the anticipated pressure increment during full fluidisation.

Extent of fluidisation

The response of the sand bed during fluidisation is considered in more detail using the measurements of the test series FT5. The response of the sand bed was monitored during three tests conducted under different but constant fluidisation flow rates (see Figure 7.21). Figure 7.23 shows the fluid stress at the bottom (BP2) for the three tests carried out. In addition, the boundary fluid pressures for fluidisation of the entire bed are plotted, based on Equation 7.62. The flow rate-dependent resistance of the filter bed leads to small differences between these boundary values for the three tests. The observed tendency is consistent. The test conducted at $Q^{fl} = 6.2$ ls^{-1} stays ~ 0.3 kPa below the boundary line, indicating a (small) part of the bed had not been completely fluidised. The test conducted at $Q^{fl} = 9.4$ ls^{-1} reaches a value ~ 0.1 kPa below the boundary line, while the test conducted at $Q^{fl} = 12.7$ ls^{-1} does reach full fluidisation. Note that the entire sand bed may be in a fluidised state, while not having expanded completely yet (see 7.1.3).

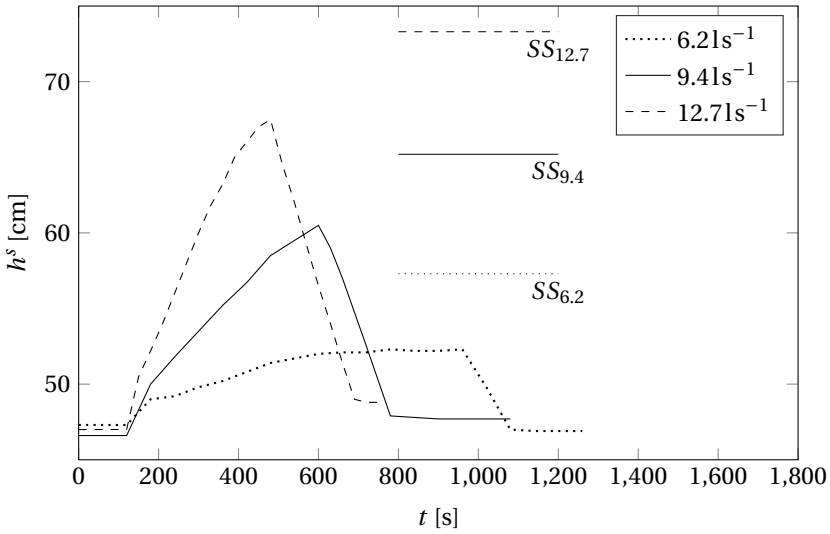


Figure 7.24: Development of top sand bed h^s during three tests with different, constant fluidisation rates. The respective steady-state heights of the sand bed are indicated by $SS_{Q^{fl}}$.

Bed expansion

The results of the bed expansion will be compared with the theory that was elaborated in Section 7.1. The development of the top of the sand bed was monitored during the fluidisation tests. Recall the theoretical elaborations of the top of the sand bed from Section 7.1. The value of the steady-state height was predicted using Equation 7.19. Furthermore, the rate of development of the top of the sand bed was expressed by $\dot{u}^{sed;top}$ for sedimentation and $\dot{u}^{fl;top}$ for fluidisation. The values are calculated using the particle flux S and concentration C at the corresponding curves (see Equation 7.22 and Figure 7.6). Conclusions with respect to the anticipated response were drawn at the final part of Subsection 7.1.3.

The actual, measured bed expansion is plotted in Figure 7.24. At first sight, the resulting plots seem to contradict with those in Figure 7.23. The test conducted at $Q^{fl} = 6.2$ ls^{-1} does reach a constant value of expansion, whereas the other two tests do not. However, this is not the bed expansion that was anticipated. The anticipated, steady state-bed heights are also plotted, based on Equation 7.19 and the experience gained during the preliminary testing (Section 7.2). The values are thus based on a representative grain size of $D^g = 100\,\mu$m. The test conducted at $Q^{fl} = 6.2$ ls^{-1} stays well below the anticipated value. The reason is most likely that not the entire bed fluidised at this flow rate. Recall Figure 7.23 showing that the measured pressure stayed well below the value that is expected for complete fluidisation of the bed.

The two tests conducted at higher fluidisation flow rates are characterised by roughly three stages. During the first stage of a few tens of seconds, the rate of expansion is the

highest. It was observed that during this stage the sand bed is lifted as a rigid body by the upward flux. The second stage of a few hundreds of seconds is characterised by a constant rate of expansion. Fitting the measured rate of expansion to a representative grain size using theory ($\dot{u}^{fl;top}$, Figure 7.6) gives exactly the same results for both tests, namely $D^g = 140\,\mu$m. During the third stage the expansion rate is governed by a smaller grain size. First, the expansion rate seems to increase, but the measurements are not detailed enough to draw conclusions. Note that this increase was predicted for a polydisperse system and the notion that the expansion rate increases with decreasing grain size (see Subsection 7.1.3). Then the expansion rate gradually decreases, which is attributed to the (widened) front reaching the top of the sand bed.

The fluidisation tests were terminated before reaching steady state-conditions, as the filtered water supply ran short. The measured bed expansion suggests the major part of the bed did expand fully, while a top layer was still expanding. It is probable that a relatively thin layer was responsible for the remaining, anticipated expansion in Figure 7.24, considering segregation and a large effect of the grain size (Figure 7.7).

The termination of fluidisation is followed by a phase of sedimentation. The rate of sedimentation is approximately constant. The largest rate of sedimentation is measured for the test conducted at $Q^{fl} = 12.7\ \mathrm{l\,s^{-1}}$, which is consistent with the conclusions drawn in Section 7.1. The theory predicts for this range of porosities a larger rate of sedimentation for a larger porosity that follows from a larger flow rate (see Figure 7.6). During fluidisation it was concluded that the steady state-bed expansion fits a representative grain size of $D^g = 100\,\mu$m (Section 7.2), while above it was concluded that the rate of expansion is governed by a larger grain size of $D^g = 140\,\mu$m. The rate of sedimentation will be governed by a smaller grain size fraction. The level of the top of the sand bed was measured. Unlike fluidisation, the underlying layers hardly affect the response of the finer top layer during sedimentation. Hence, the rate of sedimentation of the top of the sand bed is governed by the finer top layer. A measured sedimentation rate of $0.70\,\mathrm{mm\,s^{-1}}$ and $0.88\,\mathrm{mm\,s^{-1}}$ for $Q^{fl} = 9.4\ \mathrm{l\,s^{-1}}$ and $Q^{fl} = 12.7\ \mathrm{l\,s^{-1}}$, respectively, is derived. Based on theory ($\dot{u}^{sed;top}$, Figure 7.6) and $D^g = 100\,\mu$m the calculated rates of sedimentation equal $1.00\,\mathrm{mm\,s^{-1}}$ and $1.35\,\mathrm{mm\,s^{-1}}$, respectively. The finer top layer thus indeed governs the rate of sedimentation.

Density after sedimentation

Figure 7.24 suggests there is a relation between the bed expansion (or flow rate) and the density after sedimentation. The bed heights at the stage before fluidisation, maximum bed expansion and after sedimentation have been determined and reworked in terms of porosity. Figure 7.25 shows the result. It should be noted that the readings of the bed height before and during fluidisation were taken at the same measurement tape, that appeared to be representative for the sand bed. However, the top level of the sand bed tended to fluctuate after sedimentation. Therefore, readings from all measurement tapes were taken and the average calculated.

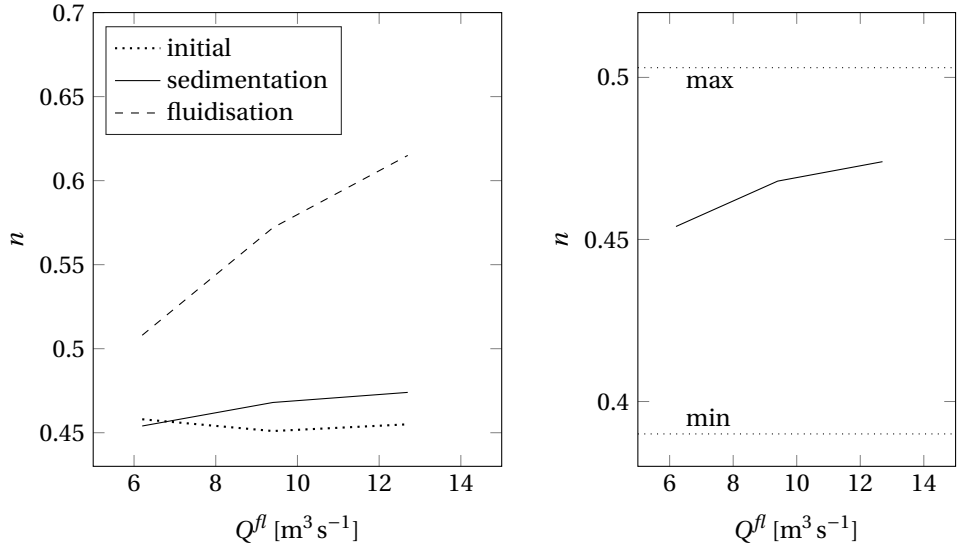


Figure 7.25: Measured porosities n as a function of flow rate Q^{fl}: overview of different stages (left) and after sedimentation (right)

The left-hand subfigure of 7.25 plots the relation between the porosity and flow rate for the three stages. The right hand subfigure zooms in on the porosity after sedimentation. For the sake of reference, the minimum and maximum porosity (corresponding to the minimum and maximum void ratio in Table 6.2) have been drawn in.

The initial porosity of the three tests was similar, namely just above $n = 0.45$ or a relative density of $D_e = 48\%$ (Equation 2.2). It should be stressed that the relative density is based on the void ratio e, rather than porosity n. Figure 7.25 shows that fluidisation only effects loosening of the sand after sedimentation at flow rates higher than 7 ls^{-1}. The porosity after sedimentation follows the same tendency as the bed expansion during fluidisation and increases for higher flow rates. The test conducted at $Q^{fl} = 12.7$ ls^{-1} results in a relative density of $D_e = 29\%$ after sedimentation. Even higher values of porosity n can be reached if the bed is allowed to expand further, either by increasing the flow rate or the duration of fluidisation (see next chapter).

The established densities in the liquefaction tank are higher than those measured in the permeameter (see Figure 7.14). In terms of relative density those tests established densities below $D_e = -60\%$. This gap is attributed to the difference in flow rate and layer thickness, i.e. self-weight compression. The scaled flow rate applied in the permeameter equalled 27.5 ls^{-1}. The height of the sand in the liquefaction tank is approximately five times higher than the sand column tested in the permeameter, which results in a larger densification during (self-weight) consolidation. Note that the tests conducted to determine the minimum and maximum porosity have approximately the same scale as the permeameter test.

Figure 7.25 also puts the pressure loss considered in the previous subsection in perspective. Recall that the measured pressure gradient effecting a decrease of 0.25 $\mathrm{l s^{-1}}$ is expected for a fluidisation flow rate of $Q^{fl} = 10$ $\mathrm{l s^{-1}}$ (see conclusions Subsection 7.4.3). Figure 7.25 indicates that, as a consequence, the established porosity would be approximately 0.0006 lower at the rear end of the tank as compared to the front. This corresponds to a decrease in relative density of approximately 0.8%. It is concluded that the pressure loss in the fluidisation system does not produce non-uniformities in the sand bed. Nonetheless, significant variations in terms of height were seen across the sand bed. For instance, the average porosity measured after sedimentation at $Q^{fl} = 12.7$ $\mathrm{l s^{-1}}$ was 0.474, but it varied between 0.458 and 0.503. These porosities were derived from the values of the bed height at the measurement tapes, and thus indicate fluctuations at the surface of the bed. Different wave phenomena at the surface were observed during fluidisation and sedimentation. Interference of surface waves may have caused fluctuations in bed height. The observed random distribution of the fluctuations across the largest part of the tank during the tests supports this supposition. There is one exception. All tests show an elevation just behind the front end of the tank. The larger, diagonally upward directed holes that were drilled in the steel pipes protruding into the tank (see 6.2.3) presumably caused the elevation, which marked the highest point of the bed. Nevertheless, the average density (or porosity) is used as the measure to characterise the sand bed during the tilting tests. Whether the variations in bed level have implications for the measured response should become apparent during the tilting tests.

References

[1] J. Allen, *Sedimentary structures, their character and physical basis*, Vol. 2 (Elsevier, 1982).

[2] I. Vardoulakis, *Fluidisation in artesian flow conditions: Hydromechanically stable granular media,* Géotechnique **54**, 117–130 (2004).

[3] P. Slis, T. W. Willemse, and H. Kramers, *The response of the level of a liquid fluidized bed to a sudden change in the fluidizing velocity,* Applied Scientific Research, Section A **8**, 209–218 (1959).

[4] J. Richardson and W. Zaki, *The sedimentation of a suspension of uniform spheres under conditions of viscous flow,* Chemical Engineering Science **3**, 65–73 (1954).

[5] J. Allen, *Sedimentary structures, their character and physical basis*, Vol. 1 (Elsevier, 1982).

[6] G. Batchelor, *An introduction to fluid dynamics*, first cambridge mathematical library edition ed. (Cambridge university press, Cambridge, United Kingdom, 2000).

[7] G. Kynch, *A theory of sedimentation,* Transactions of the Faraday society **48**, 166–176 (1952).

[8] P. Lamens, *Fluidization before liquefaction: a study of sand bed uniformity*, Bsc. thesis, Delft University of Technology (2015).

[9] J. Taylor, *An introduction to error analysis: the study of uncertainties in physical measurements*, 2nd ed. (University Science Books, Sausalito, CA, USA, 1997).

[10] *NEN-EN-ISO 11058: Geotextiles and geotextile-related products - Determination of water permeability characteristics normal to the plane, without load*, 2nd ed. (2010).

8

Tilting testing of the liquefaction tank

The final, paramount verification of the performance of the liquefaction tank was established by a series of tilting tests. These were conducted on the level sand bed created by fluidisation. The tests were initially intended as an intermediate step before conducting tests in which a slope is dredged. However, somehow unexpectedly the tilting tests on a level sand bed yielded liquefaction flow slides at very gentle slopes. The Author believes the results of these tests provide valuable insight into the occurrence and initiation of liquefaction flow slides and allow conclusions on the reproducibility of testing in this facility.

The next section will start off by discussing the testing programme, including an update on the sand mass in the liquefaction tank, the sensors employed during the programme and an overview of the tests. The subsequent section will address the procedure applied during the elaboration of the measurements. The test results will be discussed subsequently. First the general response of the sand bed is considered, followed by subsections considering specific properties, such as density, ageing and tilting rate. The chapter concludes with the interpretation of the test results and a discussion on their implications.

8.1. Testing programme

8.1.1. General

The testing programme was not strictly defined from the start, but gradually evolved on the basis of the results that were obtained. As the tests were limited to a maximum tilting angle of 10°, the first question addressed was if a liquefaction flow slide could be triggered under these conditions. This appeared to be the case at, somewhat unexpectedly, tilting angles well below the value of 10°, which was the general ultimate tilting angle. The testing programme was subsequently extended by considering the reproducibility

of the results and the effect of density. The weekends and holidays were used to consider the effect of time in between preparation and testing ('ageing'). The final stage of the testing programme included tests that were conducted to interpret and understand the outcome of the testing series hitherto. By the end, the testing programme comprised 32 tests.

8.1.2. Global density

The tilting tests were carried out a few months after the fluidisation series. Before starting the tests, the sand bed was flushed extensively. Considering the period in between and the notion that fluidisation itself is expected to generate fines by the wearing of the particles, the tilting series was started by determining the reference soil mass in the liquefaction tank. The global density at the start of the tests was thus known.

The elaboration of global density before fluidisation testing (Section 7.3) is recalled. The dry mass in the liquefaction tank $M^{s;dry;tank}$ is calculated by subtracting the mass of moisture in the sand $M^{s;moi}$, the dry mass of sand used in the filter $M^{s;filt}$ and the dry mass of fines flushed out of the bed $M^{s;fin}$ from the total sand mass that was delivered $M^{s;tot}$ (Equation 7.26). The total mass and mass of moisture remain unaltered and need no renewed consideration. The dry masses of the filter sand and fines were remeasured.

The dry mass of sand in the filter tank $M^{s;filt}$ was previously defined by the volumetric mass of the dry sand $\rho^{s;filt}$ and its volume $V^{s;filt}$ (Equation 7.31). The volumetric mass was assumed to be the same as measured before the fluidisation tests, as the continuous, downward flow through the filter layer will yield a steady state in which the sand reaches a constant, high density. The volume of the filter layer was remeasured using the same procedure as discussed in Subsection 7.3.2. The resulting dry mass in the filter layer and its corresponding error read:

$$M^{s;filt} = 492 \pm 32\text{kg} \tag{8.1}$$

The dry mass of the fines was determined from measuring the submerged weight of the fines in the big-bag, the same procedure as explained in Subsection 7.3.2. Two subsequent measurements yielded exactly the same results, meaning that the anticipated error is small. The resulting dry mass and its error read:

$$M^{s;fin} = 413 \pm 1\text{kg} \tag{8.2}$$

The renewed determinations of $M^{s;filt}$ and $M^{s;fin}$ allows the redefinition of the total, dry sand mass in the liquefaction tank $M^{s;dry;tank}$ and its error:

$$M^{s;dry;tank} = 6589 \pm 33\text{kg} \tag{8.3}$$

The determination of the volume of sand in the liquefaction tank $V^{s;tank}$ according to Equation 7.47 remains unaltered. The resulting porosity n of the sand bed and its error will depend on the height of the sand bed $h^{s;tank}$.

8.1.3. Instrumentation and data acquisition

Subsection 6.2.8 discussed the instrumentation and data acquisition system of the liquefaction tank. A part of the installed sensors and a provisional data acquisition system

were used during the tilting tests. Referring to Figure 6.18, the following sensors were used:

- Fluid pressure fluidisation system: FP, DFP;
- Fluid pressure bottom: BP1, BP2, BP3;
- Measurement tapes MT1-MT12;
- Total, compensated pressure sensor TP1;
- Accelerometer frame AF (only for two final tests).

The measurement tapes were used to measure the susceptibility to flow liquefaction of the sand bed by its global average density. The response of the sand bed during tilting was measured using the sensors BP1-BP3. In addition to monitoring the fluidisation process, the sensors in the fluidisation system FP and DFP appeared to be useful for the identification of the exact moment of the start and end of tilting. The sensor FP showed an instant peak in the response at these moments, presumably caused by (electrical) interference with the motor. The total, compensated pressure sensor TP1 was also used to monitor the tilting stage. The accelerometer in the frame AF was installed at the end of the test series, when questions were raised about possible vibrations induced during the tilting of the tank. During the first of two tests conducted with the sensor AF installed, the signal was disturbed by the motor. A filter enabled the undisturbed measurement of accelerations during the second test.

The deformation of the sand bed was not monitored in detail. A conventional video camera directed at one of the transparent sides of the tank recorded the type of failure. The quality of the measurement was however insufficient to consider the deformation of the slope quantitatively.

The data acquisition system allowed the specification of the sampling rate and the cut-off frequency of the low-pass filter. The sampling rate of fluid pressures during the major part of the testing series equaled 1 Hz during fluidisation and 10 Hz during tilting. The cut-off frequency was either 1 Hz or 20 Hz.

8.1.4. Testing procedure

The tilting tests comprise three phases: fluidisation, resting and tilting. Figure 8.1 depicts these phases. The tests start from an uneven and unprepared sand bed. The water table is well below the overflow, because the capacity of the overflow cannot cope with the discharge at the high tilting rate applied during most tests. Turning on the fluidisation system yields uniformisation and expansion of the sand, and a gradual rise in the water table. Turning off the fluidisation system initiates the phase of resedimentation, which ends when all excess pore water pressures have been dissipated. Resedimentation typically lasts for approximately 250 s.

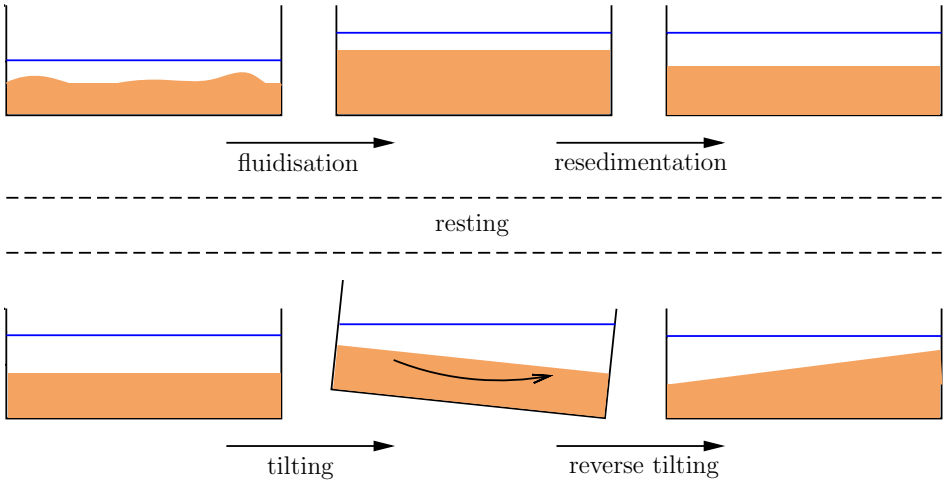


Figure 8.1: Subsequent stages during a tilting test: fluidisation, resedimentation, tilting and reverse tilting.

As soon as the excess pore water pressures have dissipated the sand bed would be ready for tilting. However, a 'resting' phase of at least 14 min was always included to eliminate possible time effects just after resedimentation. The end of the resting phase marks the start of the third phase of tilting. The density is recorded by taking measurements of the height of the sand bed using the measurement tapes. Then, the tank is tilted at a constant rate to a maximum tilting angle of 10° with the horizontal. After a short period of resting, the tank is tilted reversely to its original, horizontal position. Liquefaction of the sand bed during tilting levels the bed and, as a consequence, leaves a slope after reversed tilting. It should be noted that during some tests the slope also (partially) failed during reverse tilting.

Figure 8.1 illustrates the standard procedure that was followed during the tilting tests. The procedure was varied to examine amongst other things the effect of ageing and the density of the sand bed. By simply extending the resting period ageing was examined, while adjusting the fluidisation procedure enabled different densities to be established. In the loose regime, the density of the sand bed was varied by varying the flow rate and duration of fluidisation. The expansion of the sand was used to assess the anticipated density, while keeping the fluidisation flow rate in the range of $7.4 - 10.6$ ls^{-1}. A slightly higher density was established by the stepwise lowering of the fluidisation flow rate. One or more short stages of approximately 5 s of fluidisation yielded even higher densities. The density increased with the number of pulses of fluidisation. However, after more than three pulses the surface of the sand bed became irregular indicating non-uniformities of the density.

Table 8.1: Overview of tilting tests

test	fluidisation	resting	average porosity	tilting rate
TT01	uniform	17 min	0.469	$0.115\,°s^{-1}$ [a]
TT02	1 pulse	15 min	0.455	$0.115\,°s^{-1}$
TT03	1 pulse	14 min	0.460	$0.115\,°s^{-1}$
TT04	uniform	21 min	0.479	$0.115\,°s^{-1}$
TT05	1 pulse	19 min	0.462	$0.115\,°s^{-1}$
TT06	stepwise lowered	25 min	0.472	$0.115\,°s^{-1}$ [b]
TT07	stepwise lowered	24 min	0.468	$0.115\,°s^{-1}$
TT08	uniform	22 min	0.482	$0.115\,°s^{-1}$
TT09	uniform	43 h	0.479	$0.115\,°s^{-1}$
TT10	1 pulse	43 min	0.458	$0.115\,°s^{-1}$ [c]
TT11	3 pulses	19 min	0.449	$0.115\,°s^{-1}$
TT12	uniform	23 min	0.469	$0.115\,°s^{-1}$
TT13	uniform	68 h	0.479	$0.115\,°s^{-1}$
TT14	uniform	21 min	0.474	$0.115\,°s^{-1}$
TT15	uniform	16 min	0.474	$0.115\,°s^{-1}$
TT16	uniform	22 min	0.479	$0.115\,°s^{-1}$
TT17	uniform	26 min	0.481	$0.115\,°s^{-1}$
TT18	uniform	41 h	0.475	$0.115\,°s^{-1}$
TT19	1 pulse	66 h	0.460	$0.115\,°s^{-1}$
TT20	stepwise lowering	20 min	0.465	$0.115\,°s^{-1}$
TT21	3 pulses	40 h	0.449	$0.115\,°s^{-1}$
TT22	6 pulses	26 min	0.443	$0.115\,°s^{-1}$ [d]
TT23	uniform	23 min	0.478	$0.115\,°s^{-1}$
TT24	1 pulse	19 min	0.459	$0.115\,°s^{-1}$ [e]
TT25	uniform	65 h	0.471	$0.115\,°s^{-1}$
TT26	uniform	33 min	0.478	$0.0115\,°s^{-1}$ [f]
TT27	3 pulses	42 h	0.449	$0.115\,°s^{-1}$ [g]
TT28	uniform	22 min	0.481	$0.0115\,°s^{-1}$
TT29	uniform	12 days	0.475	$0.115\,°s^{-1}$
TT30	3 pulses	40 h	0.449	$0.115\,°s^{-1}$
TT31	uniform	35 min	not recorded	$0.115\,°s^{-1}$ [h]
TT32	uniform	20 min	0.479	$0.115\,°s^{-1}$

[a] Tilting temporarily halted at 5° and then continued to 10°
[b] Sampling rate of data acquisition system erroneously set on 0.033 Hz
[c] Discharge opened after fluidisation to densify the sand bed
[d] From test TT22 the cut-off frequency of the filter set at 20 Hz
[e] Tank tilted twice
[f] Tank tilted twice, the second time at a rate of $0.115\,°s^{-1}$ until 11°
[g] Sand bed disturbed by falling hose during tilting
[h] Vibrations measured during tests TT31 and TT32

8.1.5. Overview of tilting tests

Table 8.1 provides an overview of the fluidisation, resting and tilting characteristics of the 32 tests that were conducted. Fluidisation controls the initial density before starting the actual tilting. Table 8.1 provides an overview of the average porosity of the sand bed. The details (variations) of the established density will be further elaborated in Subsection 8.2.2.

As mentioned, the procedure distinguishes between uniform fluidisation, the number of fluidisation pulses and stepwise lowering. It is noted that during test TT10 another procedure for densification was tested. The discharge of the liquefaction tank was temporarily opened to compact the sand bed by the induced, downward flow. However, the established compaction was very small and therefore this procedure was not further employed.

The resting period between the end of resedimentation and the start of tilting varies between 14 min and 12 days. The tests are categorised based on the order of the resting period. The majority of tests were conducted after a resting period of well within an hour. These reference tests are assumed to provide similar starting conditions with respect to the ageing of the sand bed. The second, 'aged' category of tests incorporates a resting period varying between 40 and 68 h, that is, in the order of a few days. Test TT29 was left to rest over the Christmas Holidays, resulting in a resting period of approximately 12 days. Hence, test TT29 provides the ultimate case of ageing within the current testing programme.

A uniform tilting rate of $0.115\,^{\circ}\,s^{-1}$ defines the reference condition with respect to tilting. The first test TT01, during which the procedures were still under development, included a stepwise tilting profile. The tank was first tilted to 5° where it was left for a few minutes. Then the tank was tilted further to 10°. Test TT24 examined the effect of multiple cycles by tilting the tank twice. The tilting rate was reduced by a factor of 10 during tests TT26 and TT28. Test TT26 also incorporated a second tilting cycle, albeit by a rate of $0.115\,^{\circ}\,s^{-1}$. During this second cycle, an additional step to 11° was carried out.

Table 8.1 contains a number of footnotes. Tests TT06 and TT27 will be discarded, as the results are affected by an erroneous setting of the sampling rate and disturbance of the sand bed by a falling hose, respectively. The frequency of the low pass filter used for the raw measurements was increased from 1 Hz to 20 Hz during test TT22. From that moment, all tests were conducted using a cut-off frequency of 20 Hz. Subsection 8.2.4 will elaborate further on the influence of the filter. The two last tests TT31 and TT32 were conducted to measure the possible vibrations in the frame during tilting. The former, TT31, aimed at testing the installed sensors and data acquisition system. This test will be discarded when elaborating the test results. The latter did provide useful information on the vibrations induced during tilting.

8.2. Processing of measurement data

8.2.1. General

The 32 tilting tests have been elaborated and documented systematically. The height of the sand bed has been recorded using the measurement tapes after the fluidisation and resting phase. In some cases additional measurements have been taken, for instance after densification by pulses or after tilting of the tank. Even though the variability of the height of the sand bed was considered, it was assumed that the average of the 12 measurements defines the characteristic density of the sand bed. The essential, underlying assumption is that the liquefaction flow slide may be considered a stability problem where the scale of the mechanism is much larger than the scale of fluctuation. As a consequence, spatial variations of soil properties are averaged out when considering the stability. This is an assumption that requires experimental verification, which will be delivered in the next section 8.3. Section 8.2.2 will provide an overview of the porosities before entering the tilting phase.

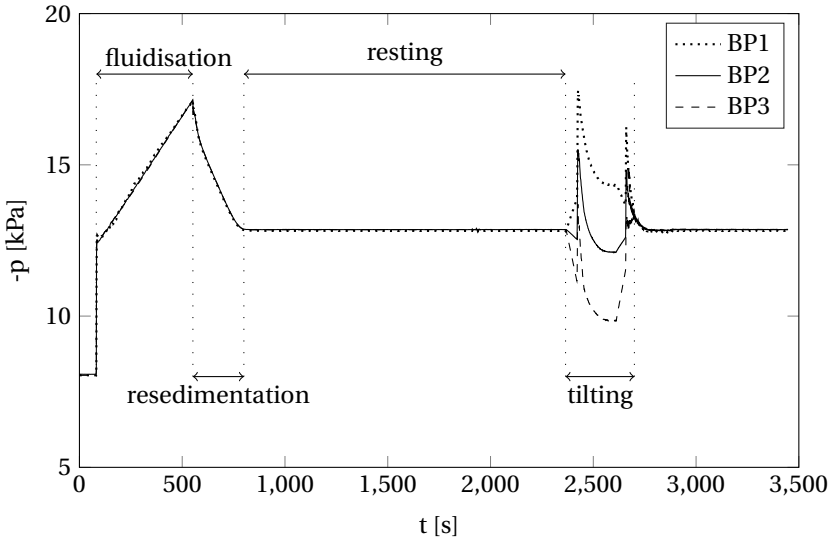


Figure 8.2: Measured pore pressures $-p$ as a function of time for different stages of tilting test TT17.

The measured fluid pressures have been elaborated for each phase of the tilting tests. Both the absolute fluid pressure and the incremental value as compared to the initial pressure were considered. Figure 8.2 depicts the absolute fluid pressure measured by the sensors in the bottom of the tank as a function of time for test TT17. The figure shows the typical response of a very loose sand bed during fluidisation, resedimentation, resting and tilting (see also Figure 8.1). The initial water level equals around an 80 cm water column above the sensors. Turning on the fluidisation system instantly yields an increase in the fluid pressure. The subsequent, gradual increase is attributed to the rising water table during fluidisation. Turning off the fluidisation system initiates the phase of

resedimentation. The pressure after resedimentation corresponds with the new water level in the liquefaction tank, which is maintained during the phase of resting. The subsequent tilting alters the fluid pressures measured by the three sensors that rotate with respect to the horizontal water table. At a particular stage, the pore pressures of all three sensors instantly and simultaneously increase, indicating the triggering of a liquefaction flow slide. The excess pore water pressures dissipate as the tank is rotated further to its maximum inclination. After a short period of resting, the tank is tilted back into its original position with the same rate of rotation. Note that during reverse tilting the three sensors also measure an instant, peak excess pore water pressure. The next section will consider the tilting phase in more detail. The final water pressure corresponds to the hydrostatic situation that was measured during the resting phase, thereby implying that all excess pore water pressures have dissipated.

The main interest lies in the excess pore water pressure rather than the absolute pressure. In order to eliminate any variations related to the level of the sensors or an offset in the calibration, the fluid pressure change after starting the test was considered, i.e. the incremental fluid pressure. The determination of the excess pore pressure should in addition account for the rotation of the tank (see Subsection 8.2.3). The level of the sensors with respect to the water table changes as a result of the rotation of the tank.

The third parameter that will be used to describe the response of the sand bed during tilting is the angle of rotation with the horizontal. While the porosity of the sand bed is a measure of its density, the excess pore water pressure a measure of the (change in) isotropic effective stress, and the rotation angle is a measure of the shear stress exerted on the sand bed. As mentioned, the response of the pressure sensor FP was used to mark the start and end of tilting. The interference with the motor causes a peak in the pressure measured by FP (see Figure 6.18) at the moment it is turned on or off, thereby indicating the start and end of tilting.

8.2.2. Established density after fluidisation

Table 8.1 provided an overview of the main characteristics of the tilting test, including the fluidisation phase. It distinguishes between uniform fluidisation, a stepwise lowering of the fluidisation flow rate and pulses to densify the sand bed. Figure 8.3 shows the consequent porosities just before starting the tilting test including their variations. It is noted that the resting time hardly affected the porosity of the sand bed. The maximum, measured mean porosity decrease after resting (creep) is approximately $\Delta n = 0.002$.

Measurements were taken at the 12 measurement tapes around the tank (see Figure 6.18). Figure 8.3 depicts the average porosity and the range of porosities that is derived from the separate measurements. The local height of the sand bed is thus assumed to correspond to a local value of the porosity, that is, the average porosity in the column of soil around the measurement tape. As expected, the average porosity is the highest for the tests with uniform fluidisation, the lowest for the tests where the bed was densified by pulses and intermediate values are obtained using stepwise lowering of the fluidisation flow rate. The average porosity ranges between $n = 0.443$ and $n = 0.482$. Based on the

minimum and maximum porosity, $n^{min} = 0.39$ and $n^{max} = 0.502$ respectively, the corresponding range in relative densities (based on void ratio e) equals $D_e = 22\% - 58\%$. The highest porosities were obtained after allowing the largest expansion of the sand bed, while the lowest porosities were obtained by increasing the amount of pulses. In both cases, the effect diminishes with increasing efforts. Hence, using these testing procedures, the range of porosities can hardly be stretched any further. The range of porosities is somewhat larger than the range that was obtained during the fluidisation tests (Figure 7.24), but the maximum porosity is well below the value obtained by the permeameter tests (Figure 7.14). This is mainly attributed to the significantly larger mean effective stresses in the liquefaction tank.

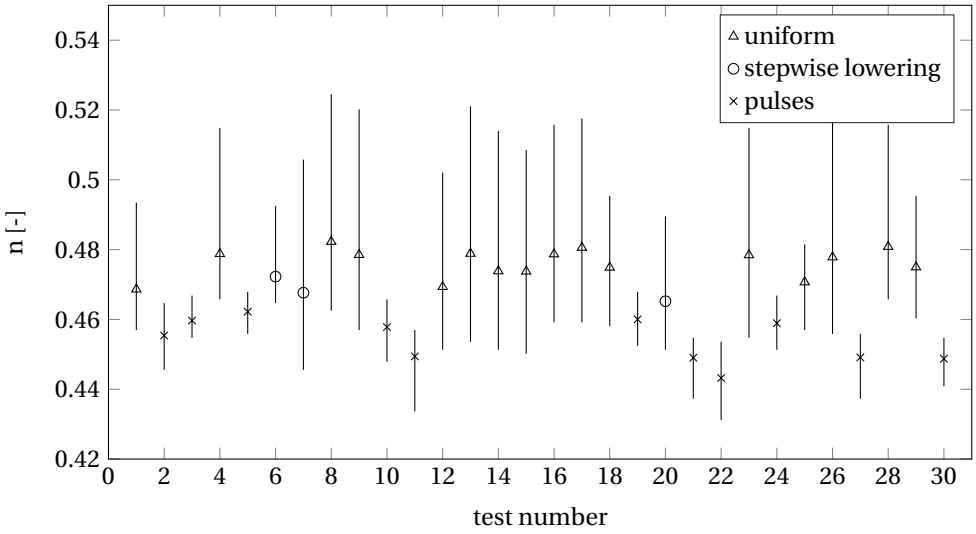


Figure 8.3: Porosity range with average value indicated for test series

There is a large difference between the range of porosities after uniform fluidisation and after applying pulses. The porosity ranges up to $\Delta n = 0.067$ for the former and up to $\Delta n = 0.023$ for the latter. There seems to be a correlation between the average porosity and the range found. Note that literature has reported a similar tendency for element tests (see Subsection 2.3.2). The range of porosities in individual tests is even larger than the range of average porosities in the test series. The variability of the porosity is partly systematic; in every case of uniform fluidisation the sand bed had a bump around the line defined by measurement tapes MT2 and MT8 (see Figure 6.18). In general, the effect extended to the entire NW-part of the tank, where the porosity was higher than in the SE-part of the tank. This flaw is attributed to the larger holes that had to be drilled in the connection pipes between the end platen and the fluidisation system. One can see the effect of the bump in the average porosities, which typically lie in the lower part of the porosity ranges in Figure 8.3. To what extent the variability of the sand bed affects the response during tilting is left for Section 8.3.

8.2.3. Determination of excess pore water pressures

The excess pore water pressure is defined as the difference between the measured fluid pressure and the anticipated, hydrostatic fluid pressure. The latter should also account for the changing hydrostatic water pressure during the tilting of the tank. The hydrostatic pressure at sensor BP3 will decrease with increasing tilting angle θ, whereas the pressure at BP1 will increase (Figure 8.4).

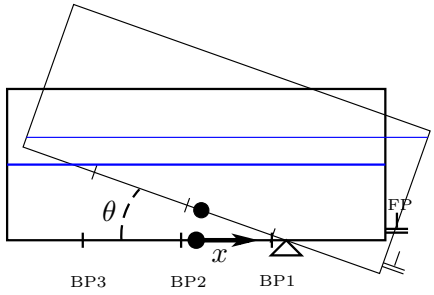


Figure 8.4: Water table for tank in horizontal and tilted positions for pore pressure transducers at bottom of tank

The relation between the hydrostatic fluid pressure p^{hyd} and the tilting angle θ is a function of the position of the sensors. Considering the tank in its horizontal (non-tilted) position, the Author concentrates on the longitudinal direction and ignores any possible variations in the vertical direction. An axis x is defined along the longitudinal direction of the tank, with the origin midway along the bottom of the tank (see Figure 8.4). Using a simple mass balance, one can demonstrate that the distance between the origin of the axis and the water table perpendicular to the axis is constant. The relation between hydrostatic fluid pressure p^{hyd}, tilting angle θ and coordinate x reads:

$$p^{hyd} = p^{hyd;0}\cos\theta - x\gamma^{f}\sin\theta \tag{8.4}$$

Herein, $p^{hyd;0}$ defines the uniform, hydrostatic pressure at the bottom of the tank in its (non-tilted) horizontal position. Note that the sign convention of pressure being negative has been applied. The coordinates of the sensors (and the exact position of the origin of the axis) are only known by approximation. In order to reduce the error induced by the uncertainty in the position of the sensors, Equation 8.4 was calibrated using the measured response of the sensors. Test TT26 was conducted at a reduced tilting rate of $0.011\,^{\circ}\mathrm{s}^{-1}$, which prevented the generation of excess pore pressures (see Subsection 8.3.5). As the measurements are expressed in terms of incremental fluid pressure, the calibration was based on a derived formulation of Equation 8.4:

$$\Delta p^{hyd} = p^{hyd} - p^{hyd;0} = p^{hyd;0}(\cos\theta - 1) - x\gamma^{f}\sin\theta \tag{8.5}$$

The incremental, hydrostatic pore fluid stress is expressed by Δp^{hyd}, which is positive for a decrease in pressure. Figure 8.5 depicts the calibration that was carried out for sensor

BP3. Note that $-\Delta p^{hydr}$ is plotted on the vertical axis, which corresponds with the (incremental) pressure. The measurements correspond very well with the calibration curve for $x = -1.6\,\text{m}$. The calibration curves for sensors BP1 ($x = 1.02\,\text{m}$), BP2 ($x = -0.29\,\text{m}$) and PF ($x = 2.72\,\text{m}$) have a similar quality. The calibrated values of x correspond quite well with the anticipated values, with deviations of less than or equal to 0.02 m (see Subsection 6.2.8).

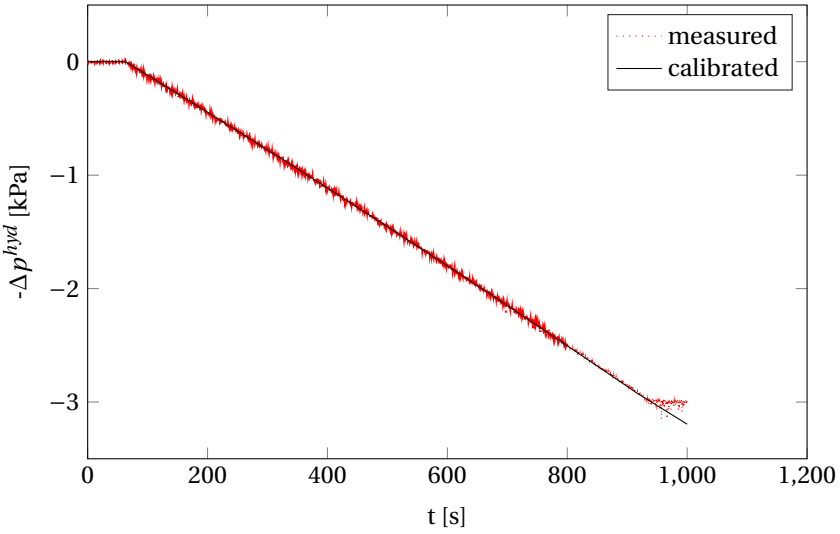


Figure 8.5: Calibration of distance of pore pressure sensor BP3 based on development of hydrostatic pore pressure during tilting

Figure 8.6 shows the comparison between measured (incremental) pressures and derived excess pore pressures. The figure depicts the result of test TT17 for the 'tilting' part in Figure 8.2. The left subfigure plots the incremental pressure. Initially, tilting only yields a hydrostatic change of the incremental pressure, which depends on the position of the sensors. The incremental pressures instantly rise at approximately $t = 2420\,\text{s}$ as a result of flow liquefaction. After reaching the peak, the incremental pressures gradually dissipate. At approximately $t = 2450\,\text{s}$, a subtle kink in the curves marks the end of tilting at $\theta = 10°$.

The right subfigure plots the corresponding excess pressures using Equation 8.5 and the calibration. Up to and just after the moment of instability the response of the three sensors coincide. The peak excess pore pressure hereafter is affected by the failure of the sand bed and the corresponding redistribution of (liquefied) soil. As a result, the three curves no longer coincide during dissipation, even though there is a similar tendency in excess pore pressure decay. The response in terms of excess pore pressures is characterised by two points: the triggering of flow liquefaction at the initiation of excess pore pressure rise ('trigger') and the peak excess pore pressure ('peak'). In the next Section 8.3

these points will be used to characterise the response during the tilting tests. Note that using the term 'instability' is avoided, although it is often used to describe the response in element tests. Instability refers to collapse of the sand bed. As the deformations are not measured in detail in this testing programme, the term 'trigger' is preferred to designate the instant rise in excess pore water pressure.

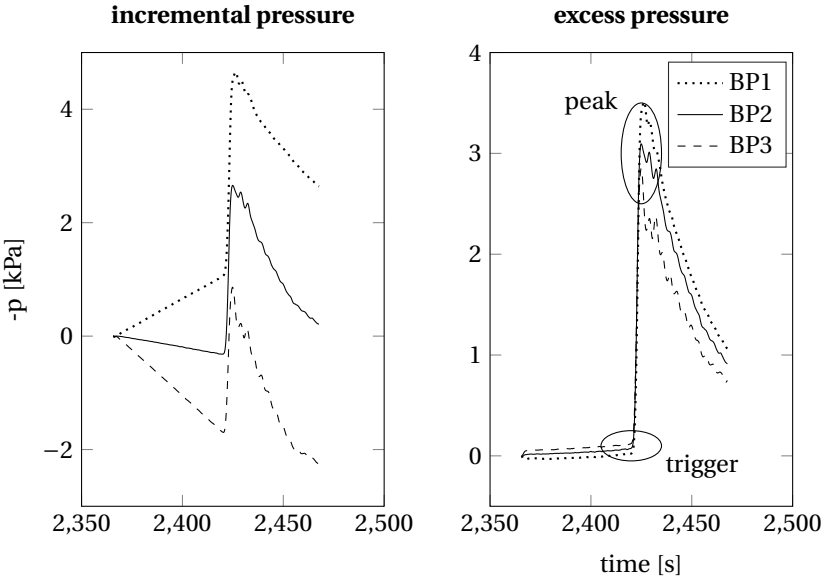


Figure 8.6: Elaboration of measured pore pressures (left) into excess pore pressures (right) for test TT17.

8.2.4. Effect of applied filter

The data acquisition system contains a first order low-pass filter to smooth the measurement results. Unlike a perfect low-pass filter, the first-order low pass filter contains a transition region between the passed and filtered signals. By definition, the cut-off frequency of a first order low-pass filter is defined at −3 dB or an attenuation of approximately 70% of the input signal. It should be noted that the filter primarily applies to the input and output voltages, i.e. an electronic filter. As a result of the presumed linear relation between output voltage and measured quantity, the filter can be applied in the same way on the derived pressure.

A cut-off frequency of 1 Hz was used for tests TT1-TT21, which was increased to 20 Hz for tests TT22-TT32. The results suggest that the rise in excess pore pressure during the triggering of flow liquefaction occurs in a few seconds. The main phenomenon is thus captured for both applied cut-off frequencies. However, filtering will introduce an error during signal processing. The error will most likely be manifested in a delay and smoothening of the signal. It is assumed that the error introduced for a cut-off frequency of 20 Hz is negligible. Whether this is also the case for a cut-off frequency of 1 Hz needs

to be investigated. To this end, the measurement results of test TT23 that were obtained applying a cut-off frequency 20 Hz were considered. The results were filtered for a cut-off frequency of 1 Hz applying a first-order, low pass filter created in the software package MATLAB. The error in terms of the delay of the signal is investigated by considering the initiation of flow liquefaction, while the peak pore fluid pressure is considered to investigate the effect of smoothening.

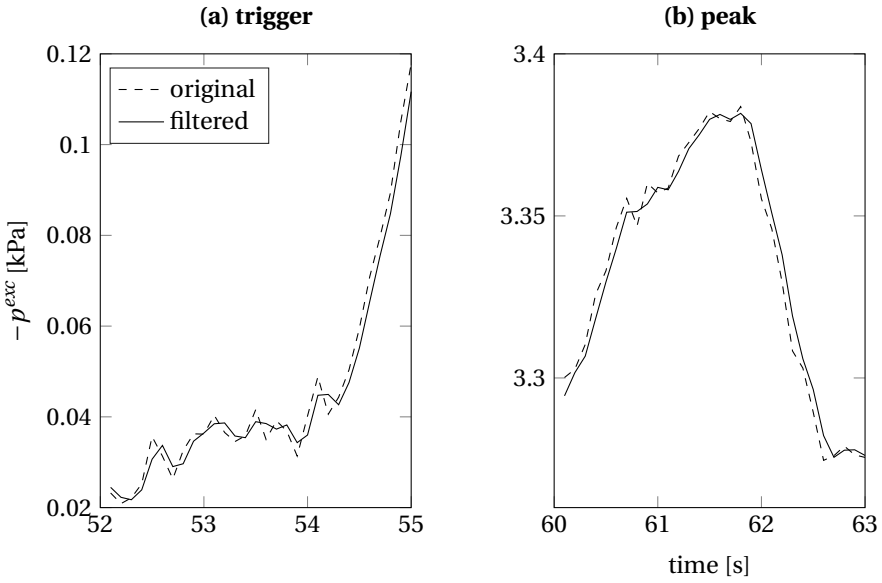


Figure 8.7: Plot of excess pore pressures of original results of test TT23 using a lowpass filter with cut-off frequency of 20 Hz and filtered results for a cut-off frequency of 1 Hz. The left subfigure (a) plots the triggering of excess pore water pressure around time=54.2 s, while the right subfigure (b) shows the peak around time=61.5 s, see also Figure 8.6.

Figure 8.7 plots the excess pore fluid stresses measured by sensor BP1 at the instant increase of excess pore pressures and at the peak. Both the original results for a cut-off frequency of 20 Hz and the filtered results (1 Hz) are depicted. Filtering clearly yields a delay and smoothening of the original signal. The introduced error is however small. The delay at the initiation of flow liquefaction equals 0.2 s, which implies that the error in terms of tilting angle equals $0.02 \pm 0.01°$. The error in amplitude at the peak is small, as the excess pore pressure develops gradually. The actual peak as a result of flow liquefaction is reached at 60.9 s, after which the excess pore pressure increases further as a result of the movement of liquefied sand to the lower end of the tank. The error is largest at this preliminary peak and equals 0.006 ± 0.002 kPa.

8.2.5. Error analysis

The main interest lies in the moment of initiation, expressed by the titling angle at the start of the pore pressure rise θ^{trig}, and the peak excess pore pressure $p^{exc;max}$ (see Figure

8.6). These will be expressed as a function of the porosity in the next Section 8.3. In addition to the previously considered error of the porosity δn, this subsection considers the error in terms of the trigger tilting angle $\delta\theta^{trig}$ and peak excess pore pressure $\delta p^{exc;max}$. The error is determined for a representative test, that is, using a sampling rate of 10 Hz and a filter with a cut-off frequency of 1 Hz.

The error $\delta\theta^{trig}$ depends on the accuracy of the imposed tilting angle and on the accuracy of reading the actual moment of triggering. The corresponding errors are defined by $\delta\theta^{sys}$ and $\delta\theta^{init}$, respectively. Only the random parts of these errors are considered, while accounting for the systematic part (by filtering) directly in the test results. Hence, the summed error $\delta\theta^{trig}$ is determined by:

$$\delta\theta^{trig} = \sqrt{(\delta\theta^{sys})^2 + \left(\delta\theta^{init}\right)^2} \tag{8.6}$$

Both contributions are further elaborated. The error $\delta\theta^{sys}$ depends on the accuracy of imposing an angle by the control system and on the estimate of the start of tilting. For smaller tilting angles < 10° the former is negligible. The start of tilting is estimated using the response of sensor FP, which shows a sudden, artificial peak caused by electrical interference as the tilting takes off. After studying the response of the different sensors, this method seems rather accurate. A related error smaller than 0.02° is estimated, i.e. $\delta\theta^{sys} = 0.02°$.

The error $\delta\theta^{init}$ consists of the uncertainty in the filtering error (0.01°) and a contribution related to the determination of the actual moment of initiation, which is estimated at 0.02°. The summed error and thereby the total error $\delta\theta^{trig}$ equals:

$$\delta\theta^{trig} = 0.03° \tag{8.7}$$

The error $\delta p^{exc;max}$ has three possible sources of error: the accuracy of the pore pressure sensors BP1-BP3, the accuracy of the methodology of deducting an excess pore water pressure (Subsection 8.2.3) and the error introduced by the filter (Subsection 8.2.4). The corresponding errors are denoted by δp^{sens}, δp^{meth} and δp^{filt}, respectively. Again, only the random parts of these errors will be considered, while accounting for the systematic parts directly in the test results. Hence, the error $\delta p^{exc;max}$ is calculated using:

$$\delta p^{exc;max} = \sqrt{\left(\delta p^{sens}\right)^2 + \left(\delta p^{meth}\right)^2 + \left(\delta p^{filt}\right)^2} \tag{8.8}$$

Table 6.3 specifies the accuracy of the sensors, which equals 0.5% FS or $\delta p^{sens} = 0.25$ kPa for the BP sensors. The excess pore water pressure is determined using the calibration illustrated by Figure 8.5. Considering the close fit of the calibration curve, a relatively small error of $\delta p^{meth} = 0.02$ kPa is anticipated. Finally, the filter introduces a random error of $\delta p^{filt} = 0.002$ kPa, as discussed in Subsection 8.2.4. Hence, the accuracy of the sensor governs the summed error $\delta p^{exc;max} = 0.25$ kPa. Compared to the accuracy of the sensors, the errors introduced by the filter and derivation of excess pore pressure are negligible.

Table 8.2 provides an overview of the errors of the main quantities used during the interpretation of the tilting tests. Note that the error of the porosity n, which was previously expressed by Equation 7.53, depends on the actual value of the initial porosity.

Table 8.2: Error of main quantities used during interpretation of tilting tests

description	**parameter**	**error**
initial porosity	δn	0.003-0.004
tilting angle at triggering	$\delta\theta^{trig}$	0.03°
maximum excess pore pressure during tilting	$\delta p^{exc;max}$	0.25 kPa

8.3. Test results

8.3.1. General

After drawing up the framework for the processing of measurement data, the actual measured and observed response of the tilting tests will be elaborated. This section aims at providing a thorough description of the results, verifying their consistency and identifying possible tendencies. The interpretation of the results will be put in a broad perspective in the next Section 8.4.

During the test series different types of response have been identified. These will be related to the variables that were imposed. During the tilting test the (average) density of the sand bed, the duration of the 'resting' period and the loading characteristics were varied. The corresponding input variables are thus the porosity n just before tilting, the ageing period T^{age} and the tilting rate $\dot{\theta}$. Table 8.1 summarised the characteristics of the tilting tests for each phase, while Figure 8.3 specified the input porosities n. The two final tests in the test series included measurements of the induced vibrations during tilting. These will be examined to exclude the possibility of externally induced excess pore water pressures, for instance due to vibrations of the foundation or irregularities in the tilting system. The final subsection addresses the effect of failure on the free water surface. The occurrence of a wave just after liquefaction failure was observed and measured. This wave provides indirect information on the failure mechanism, while the wave may provide a hazard itself in practice when a tsunami is initiated.

8.3.2. Generic description of response

The response of the sand bed is typified by its observed (and taped) deformations and the measured excess pore water pressures. The Author distinguishes between 'liquefaction', 'partial liquefaction' and 'dilation' in terms of responses. Figure 8.8 illustrates the corresponding responses of the sand bed. The instant liquefaction and levelling of the sand bed during tilting defines the 'liquefaction' response. The 'dilation' response does not involve failure of the sand bed. An instant change during tilting turning the surface of the sand bed from flat into irregular was observed. This change suggests the instant generation of excess pore water pressures. 'Partial liquefaction' describes the intermediate response; the left part of the sand bed in Figure 8.8 exhibits a 'dilation' response,

whereas the right part liquefies. The three types of response will be considered in more detail.

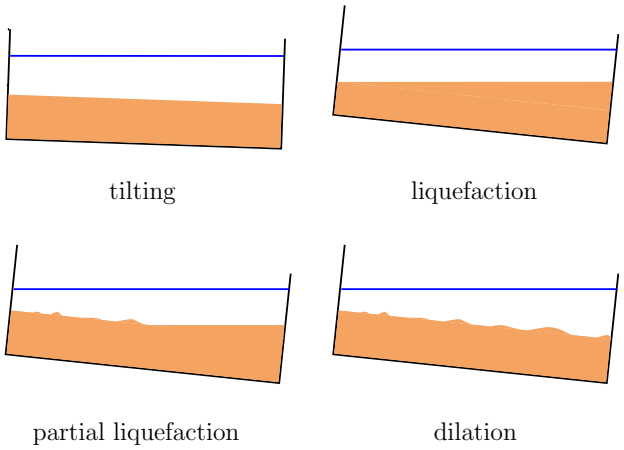
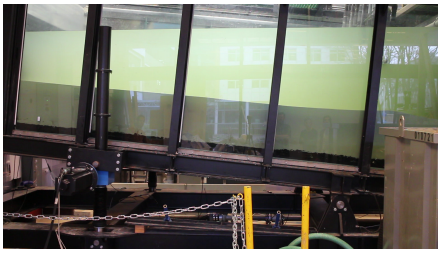


Figure 8.8: Three different types of responses observed during the tilting of the sand bed: liquefaction, partial liquefaction, dilation.

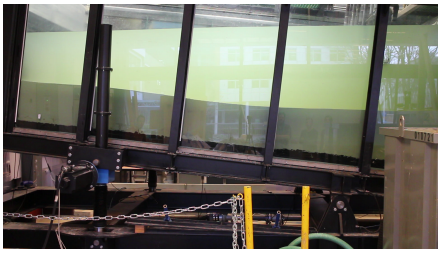
Liquefaction

The results of test TT08 are used to illustrate the properties of the 'liquefaction' response. The NE-side of the tank was filmed during tilting. With respect to the designation of the sides of the tank, refer to Figure 6.17. The resulting frames provide a good indication of the movement of the sand bed. The mechanism seemed to be plane strain, but detailed measurements of the displacements along the width of the sand bed should be conducted to confirm this presumption.

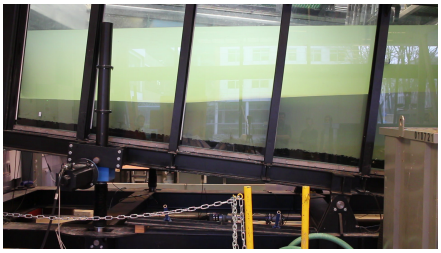
Figures 8.9a-8.9d present four subsequent time frames with a time interval of 4 s. The first frame ($t_1 = 0$ s, by definition) shows the sand bed just before it started moving. The first sign of failure of the sand bed is observed at the lower, NW-side of the tank. A local failure produces a disturbance that travels both in the upper, SE-direction (the trough in the sand bed) and in the lower, NW-direction (the peak of sedimented material). The frame at $t_2 = 4$ s displays the wave in the surface of the sand bed. The rate of regression is estimated at approximately 1 m s^{-1}, which is in agreement with the experience gained from case histories and scale model tests (see Chapter 2). The development of the mechanism is clearly affected by the boundaries at the lower and upper ends, where the waves are reflected ($t_3 = 8$ s). Eventually, a stationary situation is almost reached when the surface of the sand bed is completely horizontal ($t_4 = 12$ s). At this stage, a surficial wave can be observed that moves in the direction of the lower end of the tank. The tank is further tilted to its final position, while the surface remains horizontal. Note that maintaining a horizonal sand bed during tilting requires a constant flux of liquefied sand from the upper to the lower half of the tank.



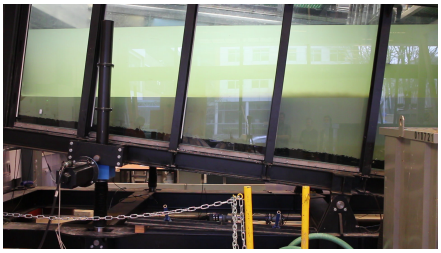
(a) $t_1 = 0\,\mathrm{s}$



(b) $t_2 = 4\,\mathrm{s}$



(c) $t_3 = 8\,\mathrm{s}$



(d) $t_4 = 12\,\mathrm{s}$

Figure 8.9: Liquefaction failure of sand bed during test TT08 at four subsequent time frames, starting just before failure is initiated.

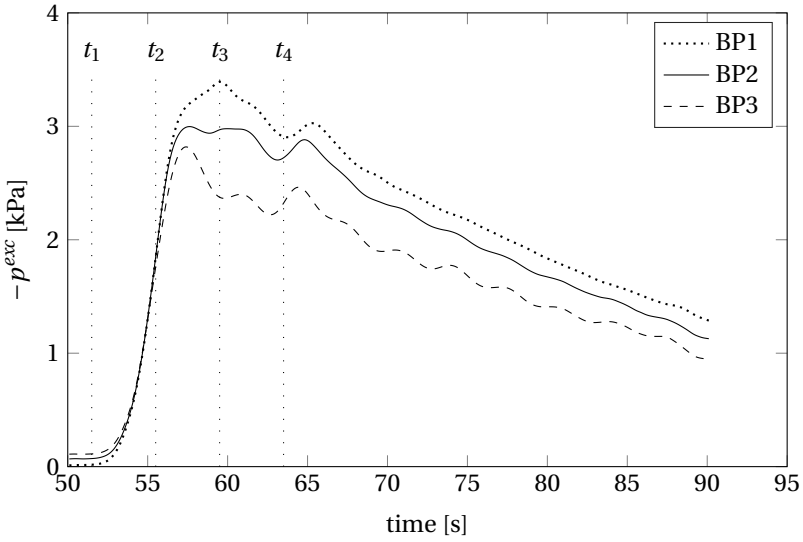
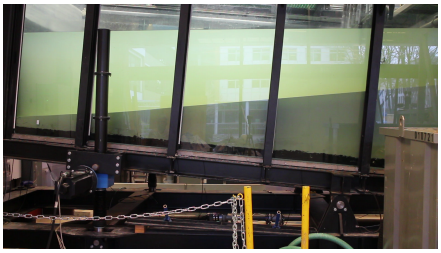


Figure 8.10: Excess pore pressures measured by pore pressure transducers at bottom during test TT08.

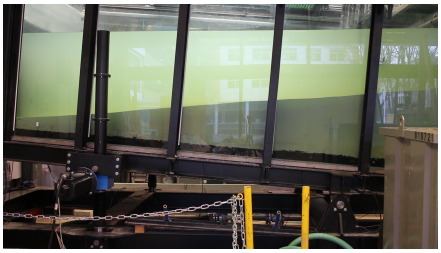
Figure 8.10 plots the corresponding excess pore water stresses. The time on the x-axis was started 0.5 s before tilting started. The moment of initiation of the liquefaction flow failure, as derived from the time frames in Figure 8.9a, practically coincides with the rise of excess pore water pressures in Figure 8.10. Thus the time frames t_1-t_4 are plotted in Figure 8.10. In between t_1 and t_2 the measured response is identical for the three sensors, even though the frame at t_2 suggests a different response along the sand bed. These differences do become apparent in between t_2 and t_3, when the movement of the sand bed governs the pore pressure response. All three sensors reach an initial peak at time≈57 s, which is slightly higher for sensor BP1 and slightly lower for sensor BP3. The average excess pore water pressure of approximately 3 kPa is well below the maximum possible value of 4.45 kPa for full liquefaction (see Equation 7.61). Then the excess pore pressure increases further for sensor BP1 as a result of the increasing thickness of the (liquefied) sand bed at that location. The opposite trend can be seen for BP3, while the response of BP2 lies in between the others. At time t_3 the effect of the movement of the sand bed is at its maximum, as is the excess pore water pressure for BP1. The response in between t_3 and t_4 is affected by different mechanisms. The measured decrease in excess pore pressures implies the increasing effect of consolidation, but the values still fluctuate. Just after time t_4, when the sand bed is horizontal, the excess pore pressures show a distinct peak that is attributed to the water wave generated by the liquefaction flow slide. The wave, which was clearly noticed during testing, marks the end of the bed movement at t_4. It moves from BP3 to BP1 with a velocity of approximately 2.5 m s^{-1} and an amplitude of approximately 20 c m. Consolidation governs the subsequent final part of tilting, during which the water wave attenuates.

After reaching the final tilting position, the sand bed was left to consolidate for another 237 s. By then, the excess pore pressures have been dissipated. The (average) porosity of the reconsolidated bed was not measured. Other tests that did include the recording of the sand bed after failure suggest a small decrease in porosity after tilting. For instance, test TT13 showed a densification from $n = 0.479$ to $n = 0.464$. The liquefied, horizontal sand bed creates a perfect slope when the tank is tilted back. Figures 8.11a-8.11d show the response during reverse tilting. The first Subfigure 8.11a shows the tank just before the sand bed showed signs of movement. Surprisingly, the first movement was noticed at the toe of the slope. Even though the sand started boiling and air bubbles were released during tilting, the toe of the slope remained practically stable. The crest did liquefy, as shown by the gradual leveling during reverse tilting ($t_1 - t_4$). The surface of the crest waved after liquefaction, which was presumably induced by the water wave generated by the (partial) liquefaction flow slide.

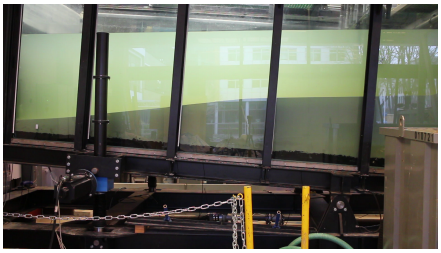
Figure 8.12 plots the corresponding excess pore pressures. Again, the first sign of movement coincides with the increase of excess pore pressures. The magnitude of the peak excess pore pressures are significantly lower as compared to tilting. The gradient in initial bed thickness results in slight differences during the generation of excess pore water pressures and significant differences at the peaks. The bed movement seems to have little effect on the measured pore pressures, even though the noticeable, induced water wave does suggest some movement of the sand bed.



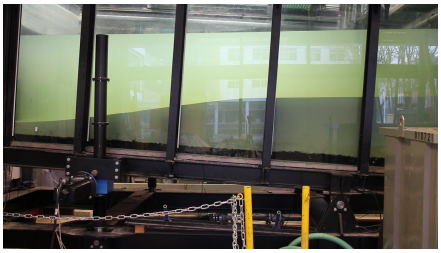
(a) $t_1 = 0\,\mathrm{s}$



(b) $t_2 = 4\,\mathrm{s}$



(c) $t_3 = 8\,\mathrm{s}$



(d) $t_4 = 12\,\mathrm{s}$

Figure 8.11: Partial failure depicted by four time frames during reverse tilting of test TT08

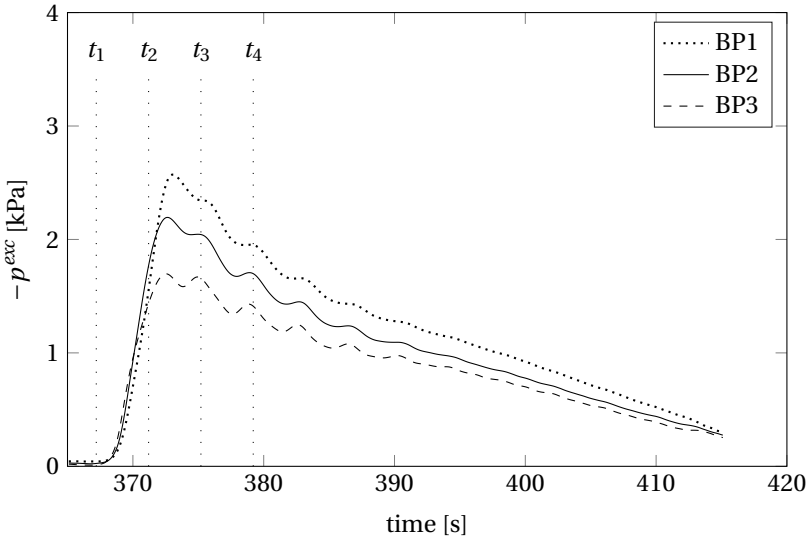


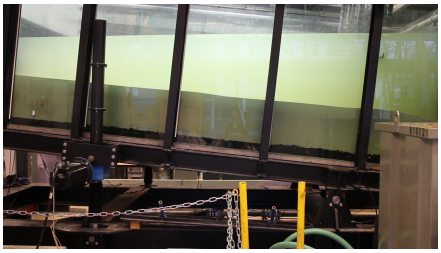
Figure 8.12: Excess pore pressures measured during reverse tilting of test TT08.

Partial liquefaction

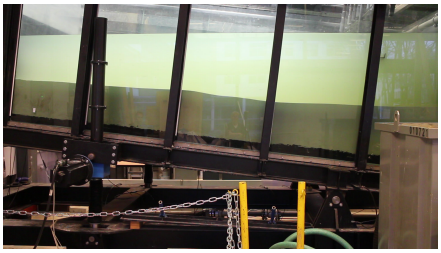
Test TT07 is used to illustrate the typical response during partial liquefaction. For the sake of comparison, both the frames (Figures 8.13a-8.13d) and excess pore water pressures (figure 8.14) are depicted in the same way as the previously discussed test TT08. Figures 8.13a-8.13d present four frames starting just before the bed shows signs of movement. The axes of Figure 8.14 have the same ranges as Figure 8.10.

The frame at t_4 is identical to the corresponding frame 8.9b during test TT08. Liquefaction flow failure is initiated at the lower, NW-side of the tank, resulting in a disturbance moving both in the NW (lower) and SE (upper) directions. The subsequent frames however differ. The liquefaction response, characterised by the level bed, remains limited to the lower, NW-side of the tank. The upper, SE-half of the bed indeed subsides, but does not level afterwards. The slope that is left suggests a residual strength that is larger than in the liquefied part of the sand bed.

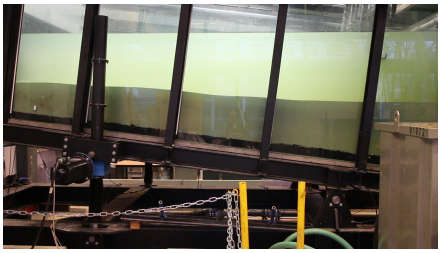
The first part of the plot 8.14 is also practically identical to test TT08, even though the pore pressure increase starts approximately 3 s later. The peak excess pore pressures are slightly lower and remarkably uniform. The response of sensors BP2 and BP3 is identical at the peak, while BP1 only shows a minor difference. Based on the clear differences depicted by the frames in Figures 8.13a-8.13d, a larger difference between the measured excess pore pressures was anticipated. Between t_2 and t_3, the difference in bed movement does yield differences in the excess pore pressures. The bed movement has ended by t_3, as indicated by the water wave that appears between t_3 and t_4. The amplitude of the wave is smaller compared to test TT08, and there is a clear difference between the sensors that corresponds with the bed response. The water wave first passes sensor BP1, where it is considerably larger than at sensors BP2 and BP3. Consolidation governs the final part of the plot with excess pore pressures depending on the thickness of the bed.



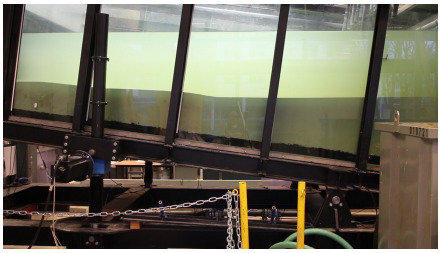
(a) $t_1 = 0\,\mathrm{s}$



(b) $t_2 = 4\,\mathrm{s}$



(c) $t_3 = 8\,\mathrm{s}$



(d) $t_4 = 12\,\mathrm{s}$

Figure 8.13: Partial liquefaction of the sand bed illustrated in four, subsequent time frames of test TT07. The first frame is taken just before failure is induced.

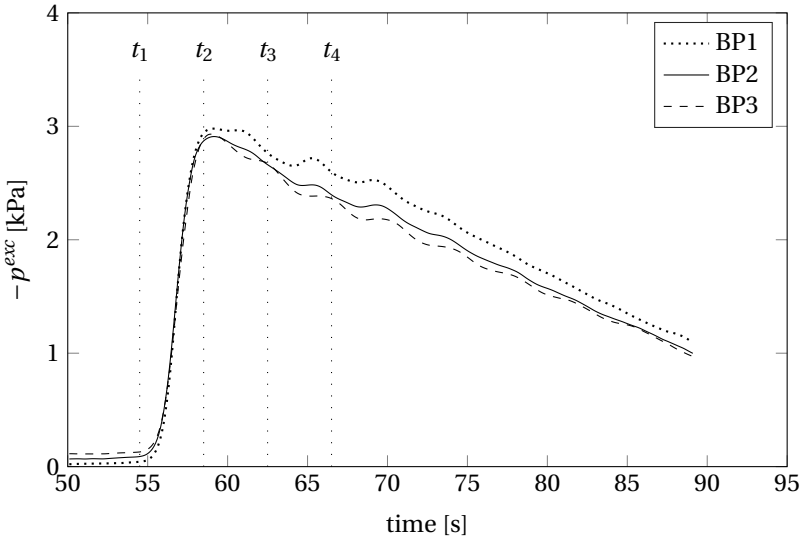
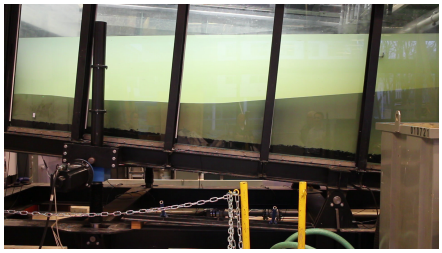
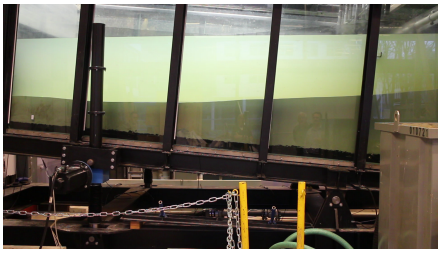


Figure 8.14: Corresponding excess pore pressures and time frames during partial liquefaction of test TT07.

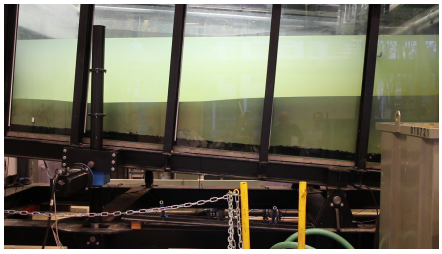
The sand bed was left to consolidate for another 146 s. Reverse tilting created a slope at the NW-side of the tank. Figures 8.15a-8.15d display the frames during reverse tilting. A modest failure is induced in the middle of the tank at time t_2, followed by a smooth, diffusive mechanism. Eventually, liquefaction leads to a gentle slope, but does not completely level the slope. Figure 8.16 plots the corresponding excess pore fluid stresses. Unlike the previous plots, Figure 8.16 also includes the period before t_1. While the excess pore pressures were constant before t_1 in the previous plots, they gradually and uniformly increase in Figure 8.16. The part of the plot starting from t_1 is similar to the previous plots. The differences in bed thickness on top of the sensors leads to a difference in (peak) excess pore pressures. The magnitude of the peaks, on average approximately 2.5 kPa, is higher than the values measured during reverse tilting of test TT08 (Figure 8.12). This is a remarkable conclusion, as the initial density was higher for test TT07. Furthermore, the excess pore pressures increase approximately 4 s earlier than during test TT08. Another difference between both tests is the relative small influence of the water wave for the measured excess pore pressures during test TT07. This notion confirms the occurrence of a relatively smooth and modest failure. Finally, the excess pore pressures have almost dissipated at the end of the plot, i.e. during the final stage of reverse tilting. The previously discussed plots all showed higher values of excess pore pressures near the end of tilting.



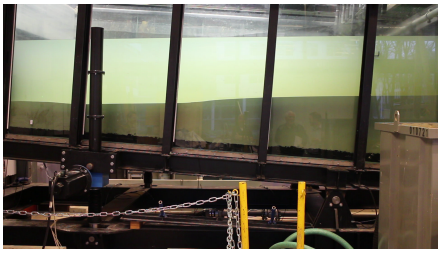
(a) $t_1 = 0$ s



(b) $t_2 = 4$ s



(c) $t_3 = 8$ s



(d) $t_4 = 12$ s

Figure 8.15: Partial liquefaction during reverse tilting of the tank for test TT07, illustrated by four subsequent time frames.

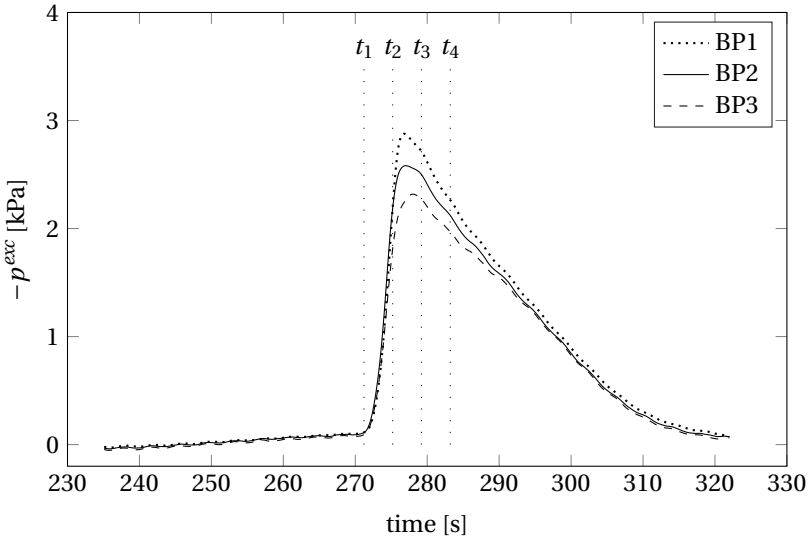


Figure 8.16: Excess pore pressures during reverse tilting of the tank of test TT07, corresponding to Figures 8.15a-8.15d.

Dilation

The results from test TT11 are used to illustrate a typical dilation response. The sand bed was densified by three 'pulses' of fluidisation, leading to a denser and apparently more uniform sand bed. As the dilation response does not include failure of the sand bed, two instead of four frames are used to describe the reponse in Figures 8.17a and 8.17b. The excess pore water pressures have been plotted on the same scales in Figure 8.18 as previously used for tests TT07 and TT08.



(a) $t_1 = 0\,\text{s}$



(b) $t_2 = 4\,\text{s}$

Figure 8.17: Dilation response of the sand bed during test TT11 before (a) and after (b) the rise of excess pore pressures.

Figures 8.17a and 8.17b display the sand bed just before and after the generation of excess pore water pressures. Even though the sand bed does not fail as a whole, the excess pore water pressures do affect the sand bed. Several local failures create a pattern of sub-

sidences alternated with elevations. Unlike the liquefaction response, these local failures do not yield failure of the entire sand bed. The result is a highly irregular surface of the sand bed at t_2, which does not change any further thereafter. The local failures caused a small but clearly visible water wave.

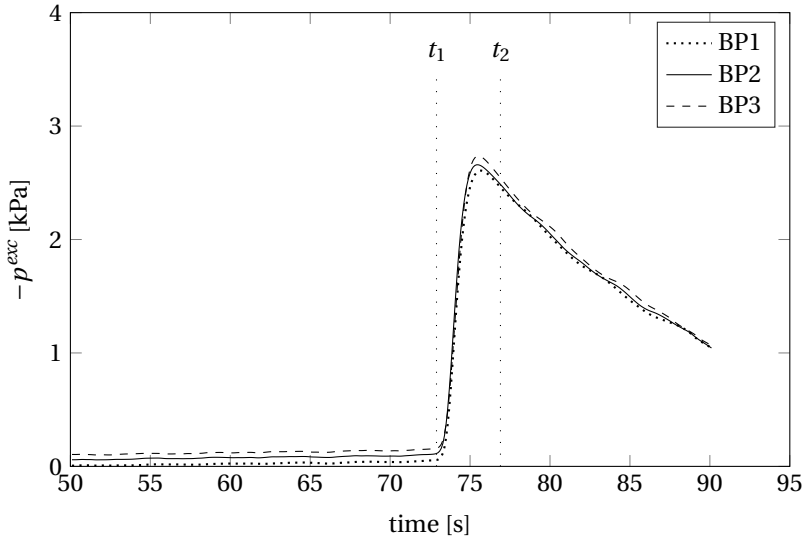


Figure 8.18: Corresponding excess pore water pressures during test TT11.

Figure 8.18 shows that the pore pressures rise at a much later stage than previously observed during test TT08 (see Figure 8.10) and TT07 (see Figure 8.14). Another, subtle difference is the build up to pore pressure rise. The excess pore pressures show a slight and gradual increase, which becomes stronger towards t_1. This increase is much stronger as compared to the looser tests, where the increase can hardly be identified. Considering the difference in density, this conclusion is remarkable. After triggering at t_1, the excess pore pressures develop uniformly over the sand bed, with negligible differences between the sensors. The magnitude of the peak excess pore pressure is slightly smaller as compared to test TT07, which confirms the tendency of decreasing peak values for increasing densities. However, in spite of the much larger density there is still an excess pore pressure that is significant, that is, more than 60% of the maximum excess pore pressure that corresponds to full liquefaction or zero effective stress. Recall from Equation 7.61 that full liquefaction involves a pressure increase of $p^{fl} = -4.45\,\text{kPa}$. The observed water wave can hardly be idenitified in the excess pore pressures that develop gradually and uniformly towards the end of tilting.

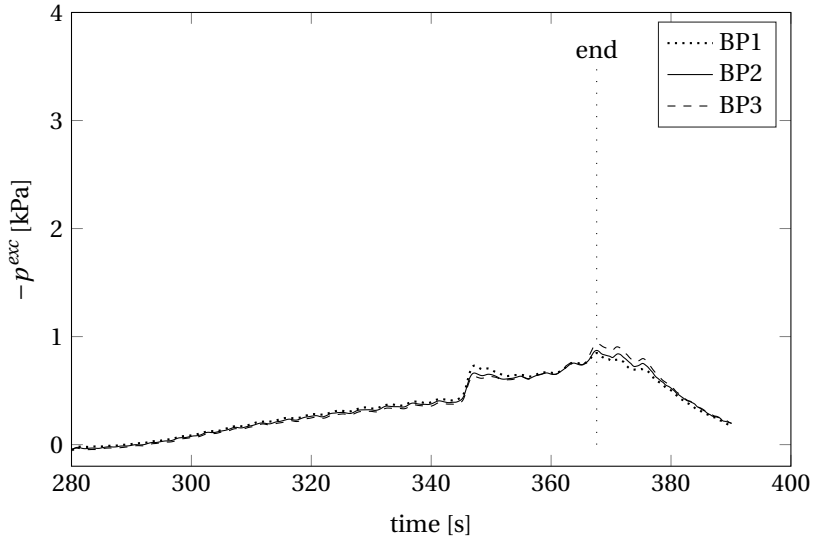


Figure 8.19: Excess pore pressures during reverse tilting after dilation response of test TT11.

The sand bed was allowed to consolidate for another 192 s, before reverse tilting was started. Contrary to the previously discussed tests, reverse tilting does not create a slope but diminishes the slope angle and thereby yields unloading of the sand bed. No movements of the sand bed were observed during reverse tilting. Excess pore pressures were induced, as plotted in Figure 8.19. The end of reverse tilting is indicated in the figure by 'end'. As soon as the reverse tilting is started, the excess pore pressures gradually increase. The same tendency was observed during tests TT07, albeit to a lesser extent. Around time = 345 s, the excess pore pressures show an instant, small increase. After a slight decrease as a result of consolidation, the excess pore pressures rise again. This peak is well below the magnitudes seen in the previous plots. The moment of the peak is remarkable; the peak coincides with the end of reverse tilting, which suggests that the peak is induced by the inertial effect towards the end of reverse tilting. However, other dilation tests show a peak well after the end of reverse tilting, which suggests that the peak is induced by void ratio redistribution. After the peak at the end of reverse tilting, the excess pore pressures first fluctuate as a result of the induced water wave, followed by a period governed by consolidation.

Figure 8.19 represents the typical, dilation response during reverse tilting. A gradual increase of excess pore pressures is alternated with instant rises. However, the actual development of the excess pore pressure does vary with the loading history. Subsection 8.3.5 will treat the effect of loading history in more detail.

8.3.3. Effect of density

The tendencies in the observed response that were suggested in the previous section are now elaborated. This section considers the effect of density, and will concentrate on the type of response (liquefaction, partial liquefaction and dilation), the moment of pore pressure increase and the average, maximum pore pressure during the tilting of the tank. In addition, the consistency and reproducibility of the tests are verified. This section only considers the tests that were conducted after a standard waiting time (order of minutes) and a uniform tilting rate ($0.115\,^{\circ}\mathrm{s}^{-1}$).

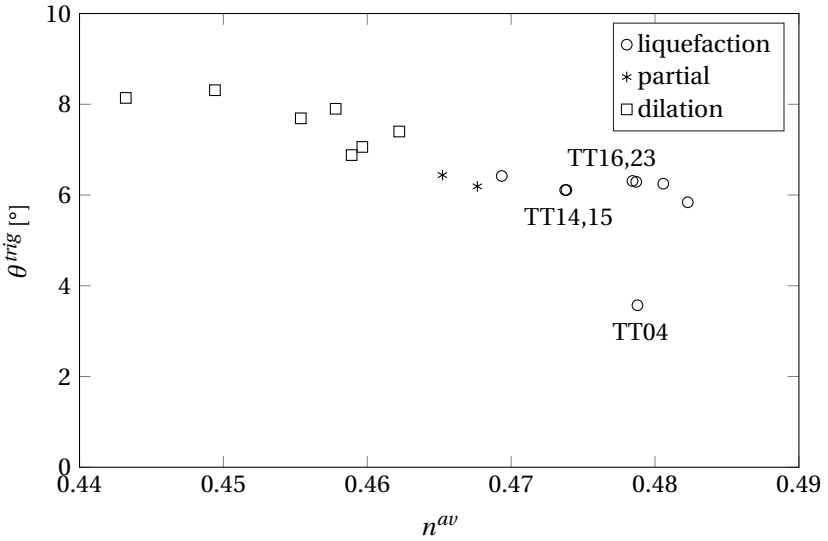


Figure 8.20: Angle θ^{trig} at which instant rise of excess pore pressure is triggered plotted as a function of the average porosity n^{av}. The results of tests TT01-TT05, TT07-TT08, TT10-TT12, TT14-TT17, TT20 and TT22-TT24 have been plotted.

Figure 8.20 plots the tilting angle at the triggering of excess pore water pressures θ^{trig} as a function of the average porosity n^{av}. If necessary, θ^{trig} was corrected for the filter settings (see 8.2.4). A number of conclusions can be drawn from Figure 8.20. The types of response can be distinguished based on the values of n^{av}. The range $n^{av} < 0.463$ is governed by the dilation response, and the range $n^{av} > 0.468$ by liquefaction. In between, partial liquefaction has been observed. In spite of the different ranges and responses, θ^{trig} relates continuously to n^{av} with relatively small differences between the liquefaction and dilation response. Generally, θ^{trig} and n^{av} thus correlate very well, with one exception. Test TT04 plots well below the rest of the tests with $\theta^{trig} = 3.59°$. Nonetheless, nothing unusual could be found in the preparations or measurements of the test that could explain this deviation. Two additional tests (TT16 and TT23) were conducted at the same initial porosity n^{av}. These tests did plot at the anticipated value θ^{trig}, that is, they plotted within $\Delta\theta^{trig} = 0.02°$. The excellent reproducibility of the tests is confirmed by another set of tests, TT14 and TT15. These yielded exactly the same value of

$\theta^{trig} = 6.11$ at $n^{av} = 0.475$. Thus test TT04 is considered to be an outlier that does not affect the consistency of the observed tendency.

Even though there is a clear trend, a trend line was not plotted to avoid any preliminary conclusions with respect to the raw results. A trend line does provide insight into the consistency of the trend. The statistics of the results based on a linear 'best fit' trend line of the results in Figure 8.20 have been considered, while excluding test TT04. Note that the choice for a linear correlation is rather arbitrary, because there is no physical basis to assume a particular type of correlation. The coefficient of determination of the test data with respect to this line is $R^2 = 0.82$, which means that the linear 'best fit' trend line replicates the test results quite well. The trend line also allows for a definition of the error ranges. The standard deviation is used as a measure of the error. The standard deviation of the triggering angle with respect to the trend line is $\delta\theta^{trig} = 0.34°$. Alternatively, the error is expressed in terms of the standard deviation of the average porosity: $\delta n^{av} = 0.005$. This value is somewhat larger than the error of $\delta n^{av} = 0.003-0.004$ that was derived before (see Table 8.2). Considering the different mechanisms that are captured and the arbitrariness of a linear correlation, the error range is satisfactory.

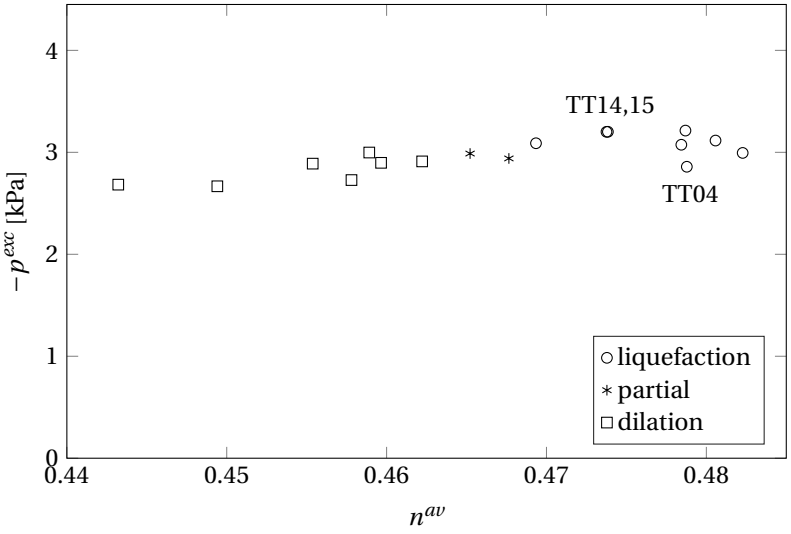


Figure 8.21: Average peak excess pore pressure as a function of average porosity. The results of tests TT01-TT05, TT07-TT08, TT10-TT12, TT14-TT17, TT20 and TT22-TT24 have been plotted.

Figure 8.21 plots the corresponding, characteristic excess pore fluid stresses p^{exc} as a function of the average porosity n^{av}. The plotted excess pore fluid stresses are the averaged values of the three sensors just before the movement of the sand bed. This point is assumed to coincide with the peak value of sensor BP2. For instance, the average value at time = 57 s was taken for test TT08 (Figure 8.10). The vertical scale in Figure 8.21 corresponds with the range of possible values of excess pore pressures. Hence, the largest value on the vertical axis indicates full liquefaction at $p^{fl} = -4.45$ kPa. The conclusions

drawn from Figure 8.20 also apply to Figure 8.21. There is a consistent correlation between the characteristic excess pore water pressure $-p^{exc}$ and the average porosity n^{av}. Test TT04 plots below the trend, albeit with a relatively small difference. The tests that were conducted at approximately the same porosity, TT16 and TT23, plot close to one another and somewhat above TT04. The set of tests that yielded almost perfect reproducibility in Figure 8.20, tests TT14 and TT15, also produce the same value of p^{exc} in Figure 8.21. Hence, it is concluded that the measured excess pore fluid stresses are consistent and reproducible. Note that all values correspond with a relative, excess pore fluid pressure larger than 60% of the maximum value of $p^{fl} = -4.45\,\text{kPa}$.

Again, the statistics of the results based on a linear 'best fit' trend line are considered, while excluding test TT04. The coefficient of determination of the test results with respect to the trend line is $R^2 = 0.71$, which is below the value previously found for the triggering angle θ^{trig}. The standard deviation of the characteristic excess pore water pressure with respect to the trend line is $\delta p^{exc} = 0.09\,\text{kPa}$. Alternatively, the error range is expressed in terms of the standard deviation of the average porosity, resulting in $\delta n^{av} = 0.007$. This value is larger than the value previously found based the correlation with the triggering angle θ^{trig}. Hence, the error range is somewhat larger than found for the triggering angle. However, the uncertainty in the determination of the excess pore water pressure is also larger than the triggering angle (see Table 8.2).

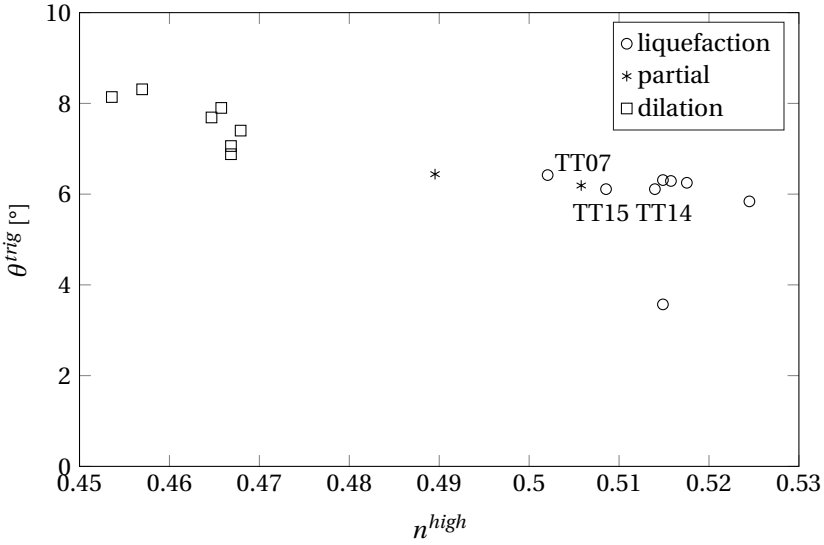


Figure 8.22: Angle at triggering of excess pore pressure rise as function of highest porosities in the liquefaction tank

Considering the suggested variability of the initial porosity in Figure 8.3, the uniformity of the plotted results is remarkable. It is thus suggested that the average porosity is a proper measure for the bed response. This presupposition is further investigated by con-

sidering the response as a function of the lowest and highest density as measured in the tank by the measurement tapes. The highest porosity as measured by the tapes will be indicated as n^{high}, whereas the lowest will be indicated by n^{low}. Special attention will be given to the tests that exhibited the 'partial liquefaction' response, i.e. where the bed failed at the part with the highest porosity but remained stable at the part with the lowest porosity.

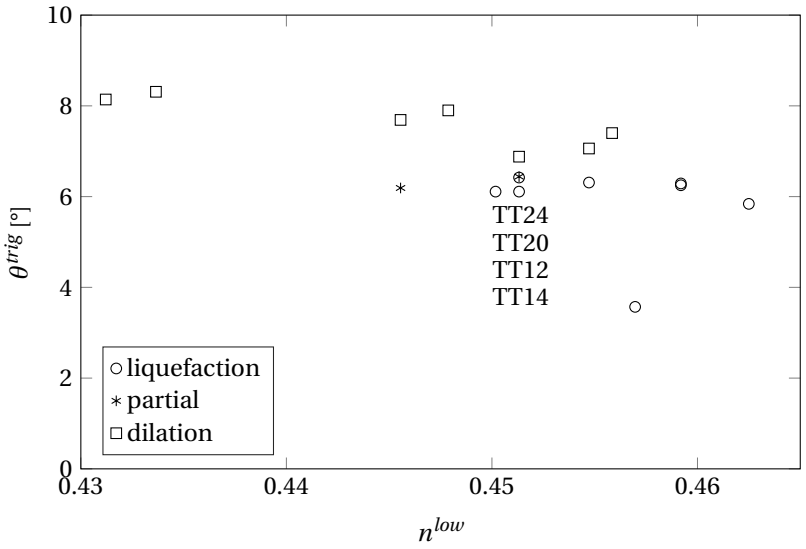


Figure 8.23: Angle at triggering of excess pore pressure rise as function of lowest porosities in the liquefaction tank

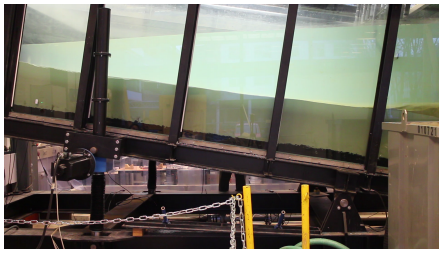
Figures 8.22 and 8.23 depict the triggering angle θ^{trig} as a function of the highest and lowest porosity, respectively. Plotting the results as a function of n^{high} extends the porosity range at the higher end and confines the porosity range at the lower end. The gap between the looser and denser tests increases significantly. This representation of the results yields the same tendency and consistency as observed in Figure 8.20. Test TT07, which yielded the 'partial liquefaction' response, now plots between two 'liquefaction' tests. Tests TT14 and TT15 no longer plot at the same point, as n^{high} differs by approximately 0.006. Plotting the results as a function of n^{low} significantly increases the scatter of the test results (Figure 8.23). The different responses can no longer be distinguished. Tests TT12, TT14, TT20 and TT24 start at the same value of $n^{low} = 0.451$, but yield different types of response. The porosity range of the 'dilation' tests is significantly increased, and the range of 'liquefaction' tests reduced.

Based on the comparison between Figures 8.22 and 8.23, and the observed responses, it is concluded that the response is governed by the looser part of the bed. This was also suggested by the frames, which showed that failure is triggered in the looser NW-side of the tank. However, for the entire bed response the average porosity n^{av} is the pre-

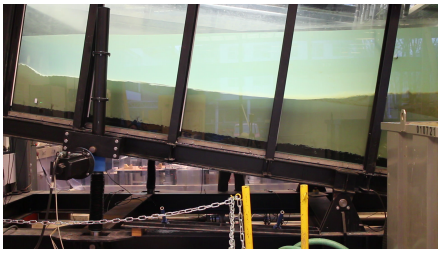
ferred measure. It enables one to distinguish between the types of response that were observed, while both θ^{trig} and p^{exc} are best reproduced in terms of n^{av}. The perception of one, averaged response is supported by the relatively small differences in excess pore pressures as measured along the bed. It is suspected that variations in the height of the sand bed are caused by surficial waves that propagate at the surface during fluidisation. Final conclusions on the influence of spatial variability of the soil conditions can only be drawn after measuring the actual, local density in detail.

8.3.4. Effect of ageing

A total of nine tests were conducted after a considerably longer waiting time. In eight cases, the waiting time was in the order of a few days, and in one case it was 12 days (see Table 8.1). One test (TT27) was disturbed by a falling hose, which instantly led to the generation of excess pore pressure. This subsection considers the remaining eight tests. The tests are treated in the same framework as the 'standard' tests, that is, by considering the types of response, the triggering angle θ^{trig} and characteristic excess pore fluid stress p^{exc}.



(a) $t_1 = 2\,\mathrm{s}$



(b) $t_2 = 4\,\mathrm{s}$

Figure 8.24: Two frames taken just after liquefaction failure of test TT29.

Even though the response of the aged tests can be considered in the same framework as the standard tests, liquefaction was usually triggered at a higher tilting angle θ^{trig}. Furthermore, the response was more brittle. The cases in which the bed failed appeared more spectacular and energetic. An example (test TT29) is shown by the frames taken approximately 2 s and 4 s after failure. Figure 8.24a displays the former. It can be seen that, even though the surface levels first at the lower, NW-side of the bed, the entire sand bed becomes unstable at the same instant. As the color of the top surface of the sand bed has changed in time, presumably due to some biological activity, the movement of the sand bed can be traced during the first stage of failure (Figure 8.24b).

The resulting triggering angle θ^{trig} is plotted as a function of the average porosity n^{av} in Figure 8.25. For the sake of comparison, the results of the previously discussed tests are plotted in the background. The bold symbols represent the tests with a longer resting time, the thick 'o' the test with a waiting time of 12 days. The plotted values of n^{av} were measured just before tilting, i.e. after resting. The densification as a result of creep ranged between $\Delta n^{av} \approx -0.001$ and $\Delta n^{av} \approx -0.002$ for the tests conducted after a resting

time of a few days. The distinction between bed responses also holds for the aged sand bed, with the transition between the responses at approximately the same porosity. Tests in the 'partial liquefaction' range were not conducted.

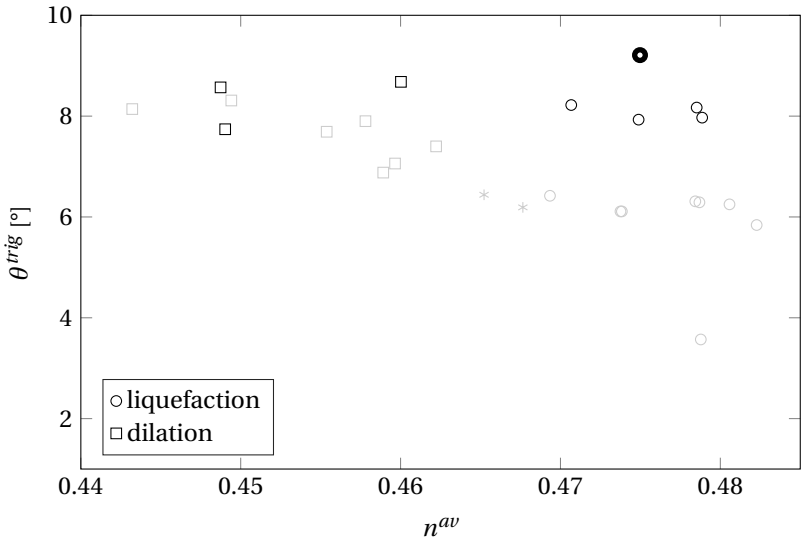


Figure 8.25: Triggering angle for 'aged' tests. The 'aged' tests are plotted by bold markers, the previous set is plotted in the background. The following tests have been added in this plot: TT09, TT13, TT18-TT19, TT21, TT25, TT29, TT30. An extra thick marker is used for the test conducted after an extremely long waiting time of 12 days.

Figure 8.25 suggests that ageing increases the resistance against triggering and diminishes the variations with porosity. For instance, at the higher end of n^{av} the triggering angle θ^{trig} equals approximately 6° for a resting time of tens of minutes, increases to 8° for a resting time of tens of hours and increases further to over 9° for a waiting time of 12 days. However, at the lower end of porosities θ^{trig} hardly increases with waiting time. Hence, the effect of the density on the triggering angle θ^{trig} diminishes with increased ageing of the bed.

The characteristic, excess pore fluid stress is hardly affected by the increased waiting time (Figure 8.25). All tests fit the previously observed tendency well. Furthermore, the measured values reproduce quite well for similar values of the average porosity. It is thus concluded that ageing may postpone the triggering of liquefaction, but will eventually yield the same excess pore fluid stress as would be expected for freshly deposited sand.

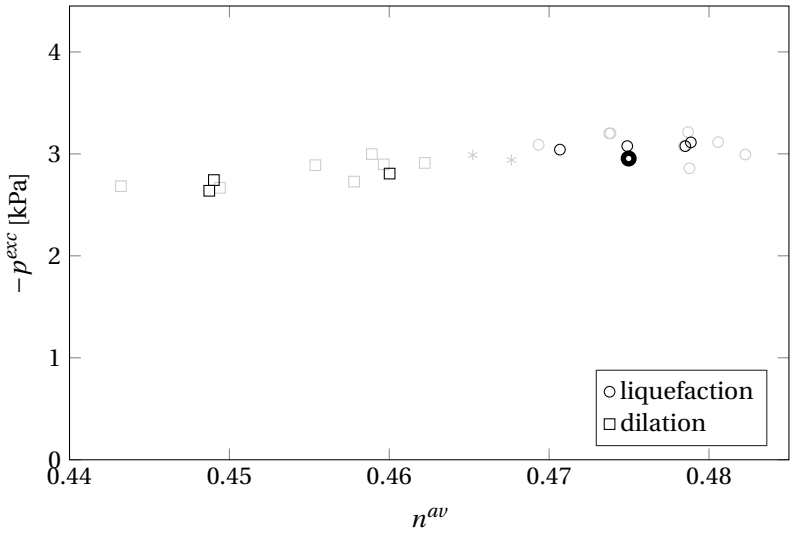


Figure 8.26: Peak excess pore pressures for 'aged' tests, with conventional set plotted at the background. The following tests have been added in this plot: TT09, TT13, TT18-TT19, TT21, TT25, TT29, TT30.

8.3.5. Effect of loading and pre-loading conditions

The Author will now go further into the details of the test results by considering the influence of the loading and pre-loading conditions. These include the loading history during tilting, the tilting rate and the response during reverse tilting. This subsection aims at improving understanding of the triggering of excess pore water pressures and failure. It furthermore introduces the structure of the soil skeleton as a factor of influence in addition to the (global) density.

Tests TT26 and TT28 were conducted at a reduced tilting rate of $0.0115°s^{-1}$, i.e. at a rate 10 times slower than the other tests. As the previous tests showed very little excess pore pressure build-up before triggering an instant rise, it was suspected that there were no rate effects. Test TT26 was carried out to test this presupposition.Test TT28 was conducted later to verify the reproducibility of test TT26. Both test TT26 and TT28 were conducted at porosities well within the 'liquefaction' range (see Figure 8.3).

Figure 8.27 plots the excess pore fluid stresses in time during tilting of the tank. No excess pore pressures were measured whatsoever. This finding was later verified and confirmed by the results of test TT28. Hence, there is a determining rate effect in the triggering of an instant rise in excess pore pressures. Note that the tilting rate hardly affects the initial pore pressure build-up before triggering, which is very small.

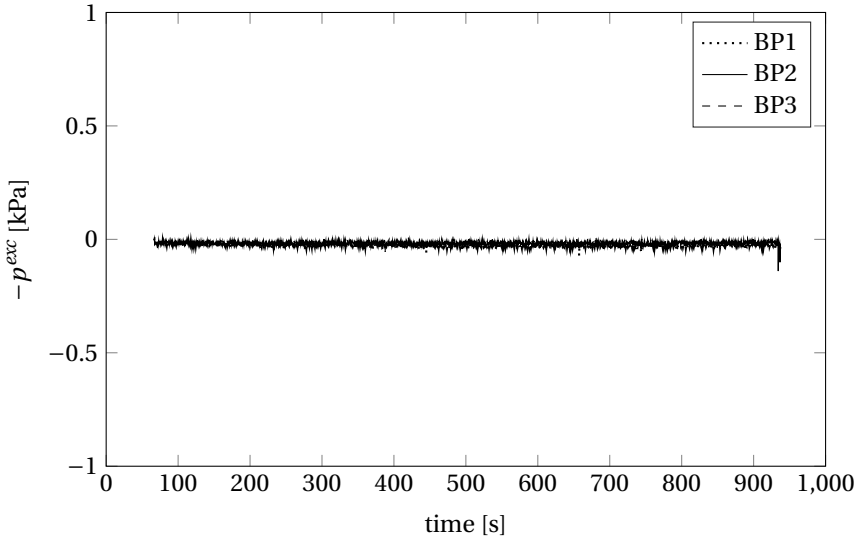


Figure 8.27: Excess pore water pressures during test TT26 at a tilting rate 10 times lower than applied during the other tests. The excess pore pressures are plotted for a time range starting just before the tilting was started and ending just after the tank reached an inclination of 10°.

Reverse tilting did not lead to any excess pore pressures during both tests. The levels of the bed height were recorded when the tank was back in its horizontal position. For both test TT26 and TT28, the densification was very small ($\Delta n^{av} = -0.002$). Test TT26 included an additional tilting cyclus to investigate the pre-loading effect. The tank was tilted to 10° at the usual (high) rate of $0.115\,°\,s^{-1}$. After neither movement nor excess pore pressures were observed, the tank was tilted further to 11° at the same rate. Again, there was no notable response by the sand bed. During reverse tilting some excess pore pressure build-up was observed, albeit small. The recordings of the bed levels after the tank reached its initial position demonstrated that there was no additional densification after the second cycle of tilting. Considering the negligible amount of densification between the first and second cycle of tilting, there must be another explanation for the lack of response. For the first stage of tilting to 10° during the second cycle of tilting, an elastic response upon reloading may offer an explanation. For the subsequent tilting to 11° it does not. Apparently, the changed structure of the soil skeleton yields a stronger response, in a similar way as observed during the 'aged' tests. While the 'aged' tests eventually liquefied, these tests did not show any sign of failure.

The effect of the loading history depends on the direction of pre-shearing. The tilting of the tank during test TT01 was interrupted at 5° and restarted after 20 s. The triggering of excess pore water pressures occurred relatively late, i.e. $\theta^{trig} = 7.07°$ for $n^{av} = 0.469$, presumably as a result of hardening by pre-shearing. On the other hand, reversing the direction of tilting seems to result in an enhanced buildup of excess pore pressures, as discussed in Subsection 8.3.2.

Test TT24 was carried out to study the effect of pre-shearing in more detail. The sand bed was prepared using a single pulse of fluidisation resulting in a (medium) dense sand bed. The tilting phase included two cycles, that is, the tank was tilted and reverse tilted twice at the usual (high) rate of $0.115\,^{\circ}\,s^{-1}$. Figure 8.28 plots the excess pore water pressures as measured by sensor BP2. The results of sensors BP1 and BP3 coincided with the curve in Figure 8.28, which is common for the 'dilative' tests. The first cycle of tilting and reverse tilting shows the weakening of the sand bed as the shearing direction is reversed. At the instant that reverse tilting commences, the excess pore water pressures gradually rise, followed by peaks at $\theta^{trig} = 5.77^{\circ}$ (time 275 s) and $\theta^{trig} = 1.58^{\circ}$ (time 320 s) (see Figure 8.28). Furthermore, the excess pore water pressures at the latter peak during reverse tilting are slightly larger than the peak excess pore pressure during tilting. Subsequently, the tank is tilted and reverse tilted once more. The second stage of tilting yields a lower value of the peak excess pore water pressure. However, contrary to the first stage of tilting, the excess pore water pressures rise from the start and the peak occurs much earlier at $\theta^{trig} = 3.09^{\circ}$ (time 469 s). Finally, the second stage of reversed tilting yields a minor response in terms of excess pore water pressure. This is presumably caused by densification of the bed, as the excess pore pressure response resembles the response of other tests at lower porosities (see e.g. Figure 8.19).

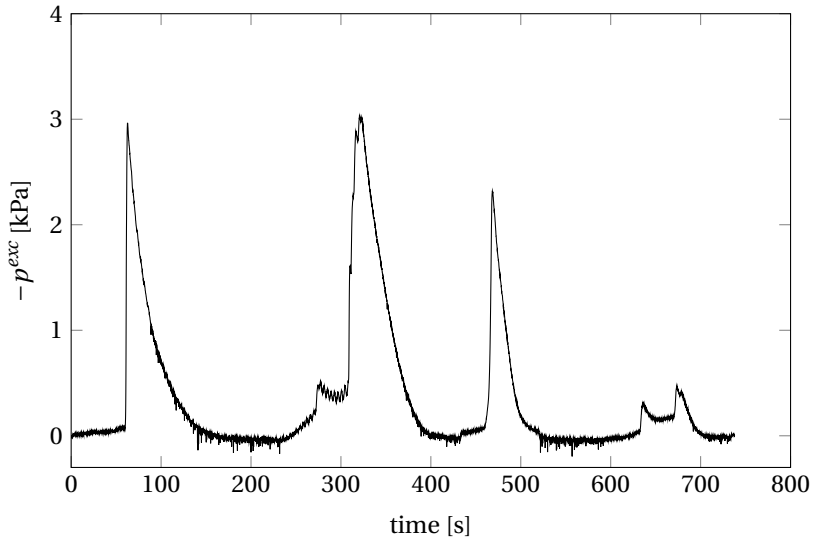


Figure 8.28: Excess pore water pressure during two subsequent cycles of tilting and reverse tilting. The following stages are identified: (1) tilting: time=0 – 88 s, (2) resting 88 – 236 s, (3) reverse tilting: 236 – 322 s, (4) resting: 322 – 433 s, (5) tilting: 433 – 520 s, (6) resting: 520 – 593 s, (7) reverse tilting: 593 – 680 s.

It is concluded that the loading direction with respect to the loading history has an important effect on the development of the excess pore water pressure, that is, its initial buildup, the moment of triggering and the value of the peak. However, the response

during reverse tilting is not as consistent as the response during tilting. For instance, the triggering angle θ^{trig} of the peaks varies significantly during reverse tilting. The lack of consistency is attributed to the disturbance of the bed during the foregoing phase of tilting. It is therefore not opportune to draw firm conclusions about the effect of loading and pre-loading conditions, other than observing trends. Furthermore, it is noted that the effect depends on the initial porosity of the bed. Liquefaction remoulds the sand bed during tests at higher porosities, thereby introducing uncertainties with respect to the soil conditions at the start of reverse tilting. At the lower porosities, the excess pore water pressure response is governed by the density rather than the loading direction, as illustrated by Figures 8.18 and 8.19.

The importance of the loading direction is further illustrated by the results of test TT02, displayed by Figure 8.29. Only the excess pore pressures of sensor BP2 are plotted, as the response of the three sensors practically coincided. The sand bed was prepared using a single pulse to level and densify the bed, yielding a 'dilation' response. Reverse tilting was initiated relatively soon after tilting. Even though the excess pore pressures had not been fully dissipated yet, reverse tilting induced a gradual rise in pore pressures. These excess pore pressures increase stepwise to a peak value that is considerably larger than the first peak and appears well after the end of reverse tilting. Figure 8.29 thus suggests that the loading and preloading conditions also have an effect on the redistribution of excess pore water pressures.

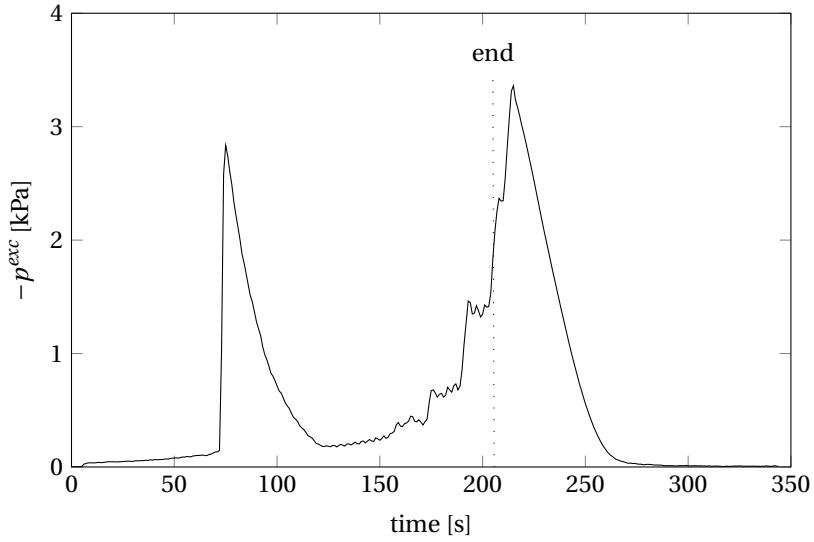


Figure 8.29: Excess pore pressure during tilting and reverse tilting of the dilation test TT02. The peak excess pore pressure during reverse tilting appears well after the tank has reached its original, horizontal position ('end').

8.3.6. Induced vibrations during tilting

The final tests of the series, TT31 and TT32, were conducted with the accelerometer AF installed on the frame (see Figure 6.18). These tests were aimed at verifying the possibility of vibrations induced during tilting that may affect the response of the sand bed. Test TT31 was used to fine-tune the settings of the sensors, leading to optimal settings for test TT32. The latter will be studied in more detail.

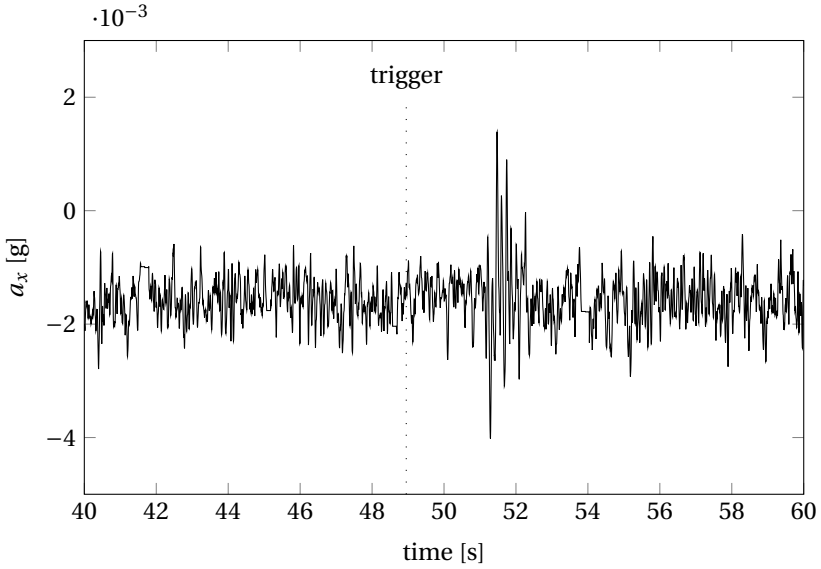


Figure 8.30: Accelerations in longitudinal direction of tank during reverse tilting of test TT32, measured on the frame. The moment of triggering of partial liquefaction failure is indicated.

The sand bed before tilting was relatively loose with $n^{av} = 0.479$. The response during tilting was as anticipated; the bed liquefied at an angle of $\theta^{trig} = 6.56°$ and liquefied partially during reverse tilting. During the entire tilting cycle were measured, amongst other things, the accelerations in three directions at a sampling frequency of 200 Hz. As both the sensors and screw jacks are attached to the supporting frame, any possible vibrations should be instantly measured by the sensors. By simply tapping on the frame, the sensitivity of the sensors could easily be tested, which appeared to be excellent.

During the tilting of the tank no significant accelerations were measured. Each of the sensors showed a regular noise with a maximum amplitude of $0.001g$. It should be noted that due to unknown reasons, the data acquisition system did not sample for a duration of approximately 0.2 s just after the triggering of excess pore pressures. However, it is expected that vibrations induced by failure of the bed should have been measured a few seconds later. This is also illustrated by the response during reverse tilting. Figure 8.30 plots the accelerations in the longitudinal direction, expressed as a fraction of the gravitational acceleration g. A few seconds after triggering the plot shows an excitation,

presumably caused by movements in the sand bed and in the water. This excitation was only measured in the longitudinal direction. Surprisingly, no such response was measured during tilting of the tank, when the whole sand bed failed. Apparently, there is a dependence on the direction of movement.

The measurements show that no vibrations are induced during tilting of the tank. The measured accelerations, if any, are in the same order of magnitude as the accuracy of the sensor (see Table 8.2). This is an order of magnitude lower than the range that is considered of interest for cyclic loading of soils. The measured excitations in Figure 8.30 show the excellent performance of the sensors.

8.3.7. Induced water waves during flow slides

The observed water waves are analyzed using the measurements of the total load sensor TP1 (see Figure 6.18). These include both the compensated ('slow') total pressure and the average pressure measured behind the membrane ('fast'). The performance of both measurements is illustrated by Figures 8.31 and 8.32, respectively. These depict the measurements during the tilting cycle of test TT17. The pressure change $-\Delta P$ is on the vertical axis, it being negative for a decrease in total pressure.

Figure 8.31 clearly shows the tilting profile, first resulting in a decrease of total pressure and then, after a period of rest, an increase to its initial value. A closer look at the plot shows a ripple in the plot around time = 125 s and a few smaller ripples from approximately time = 360 s. The ripples, which appear just after triggering, represent the water waves induced by bed movement. The compensated pressures in Figure 8.31 display an indirect measure of the wave. The pressures behind the membrane provide a direct measure (Figure 8.32). Before tilting the pressures behind the membrane remain constant. The peak in $-\Delta P^{mem}$ marks the start of tilting around time= 70 s. Even though $-\Delta P^{mem}$ develops more irregularly during tilting, the compensating pressures result in relatively small deviations from zero. The induced water wave marks a large peak around time = 125 s, which attenuates afterwards. Around time = 360 s another peak arises, representing the water wave induced by bed movement during reverse tilting. These do not attenuate like the first wave, presumably as a result of subsequent waves induced by subsequent bed movements. It is concluded that Figures 8.31 and 8.32 are consistent, each clearly showing the induced water waves.

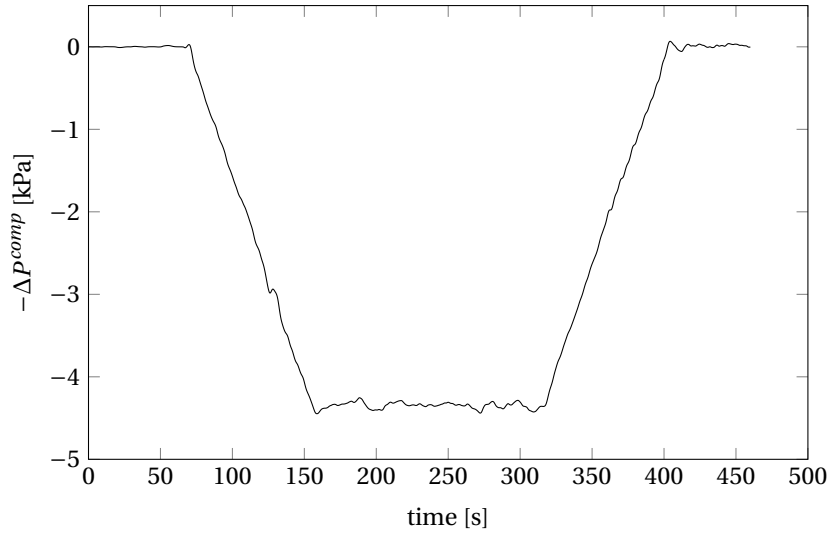


Figure 8.31: Slow measurement of total, compensated pressure by TP1 during test TT17

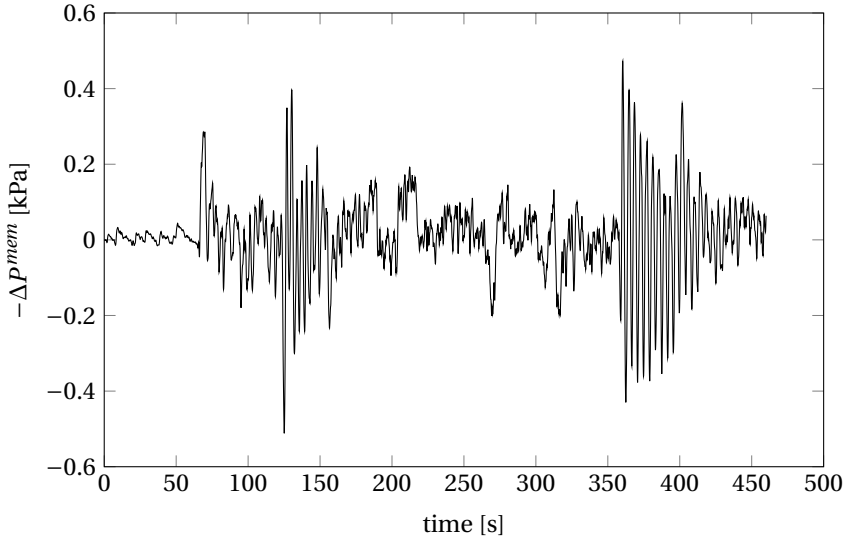


Figure 8.32: Fast measurement of total pressure by TP1 during test TT17.

Figure 8.33 zooms in on the ranges of interest from Figure 8.32. The water wave during tilting is characterised by a decrease (trough) in pressure, whereas the wave during reverse tilting is characterised by an increase (peak). These extremes, i.e. half of the wave height, are used to quantify the wave induced by the bed movement. A full cycle or full wave height would introduce the possible disturbance by the compensating pressure; hence the choice of using the extreme value. The characteristic wave heights for test TT17 thus measure 5.2 cm and 4.8 cm during tilting and reverse tilting, respectively.

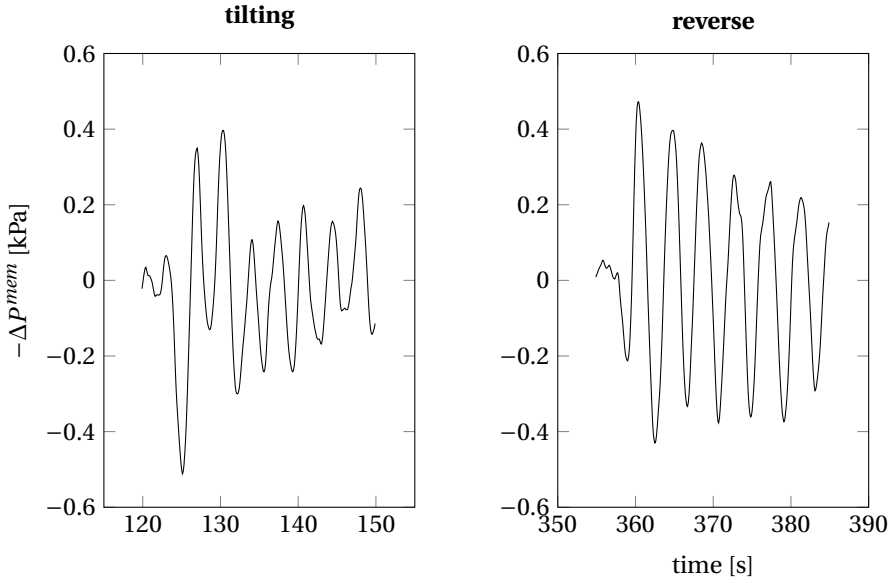


Figure 8.33: Zoomed plots of pressure difference in Figure 8.32 during tilting (left) and reverse tilting (right).

The characteristic wave height, from hereon expressed by the absolute variable $H^{1/2;trig}$, depends on the density, triggering angle and, possibly, the water depth. The effect of the density, which determines the type of response, is obvious. The triggering angle determines the amount of potential energy that is transferred into kinetic energy. For instance, the aged tests that yielded liquefaction induce larger waves than the standard tests. The outlying test TT04, which failed at an extremely low angle θ^{trig}, resulted in a wave of merely $H^{1/2;trig} = 2.3$ cm. The water depth may affect the propagation of the wave. However, this requires knowledge of the complex interaction with the (liquefying) sand bed. Furthermore, the choice of the characteristic wave height just after triggering minimises the effect of wave propagation. Test TT10 was affected by the water depth, which was low after using the discharge to densify the sand bed. The water wave resulted in partial submergence of the sensor and, as a result, in an extreme decrease of the measured pressure. Both tests TT04 and TT10 will thus be left out of the consideration.

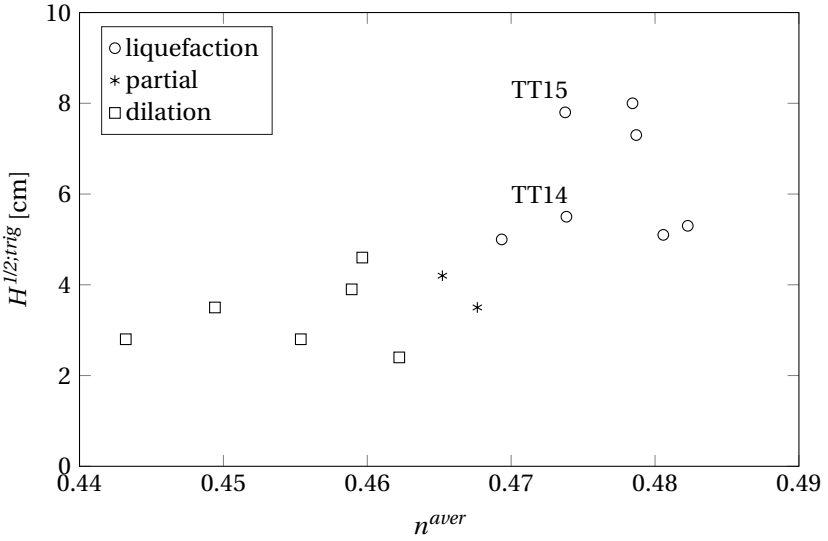


Figure 8.34: Half amplitude of wave induced by bed movements as a function of the average porosity. The results of the following tests have been plotted: TT02, TT03, TT05, TT07, TT08, TT11, TT12, TT14-TT17, TT20, TT22-TT24.

The wave heights $H^{1/2;trig}$ during the tests conducted after a standard waiting time and a uniform tilting rate, i.e. the tests discussed in Subsection 8.3.3, are plotted in terms of porosity n^{aver} in Figure 8.34. There is an upward trend with increasing porosity. Each of the tests showed a clear deflection in the pressure measurements at or just after triggering, even for a dilation response. The transition between dilation and liquefaction responses is smooth, with an approximate value of $H^{1/2;trig} = 5\,\mathrm{cm}$ that marks the transition. The smooth transition suggests that the value of $H^{1/2;trig}$ is not just governed by the amount of displaced sand, which is much larger for the liquefaction response. It underlines the Author's observation that there is some initial movement during the dilation response, even though it does not develop into a flow slide.

The scatter in Figure 8.34 reflects the indirect relation between both variables. For instance, tests TT14 and TT15 yielded identical values of porosity n^{aver}, angle θ^{trig} and peak excess pore fluid stress $-p^{exc}$, but resulted in $H^{1/2;trig} = 5.5\,\mathrm{cm}$ and $H^{1/2;trig} = 7.8\,\mathrm{cm}$ respectively. In spite of the clear trend, the quality of reproducibility of the results is less for $H^{1/2;trig}$ as compared to the directly related variables θ^{trig} and $-p^{exc}$.

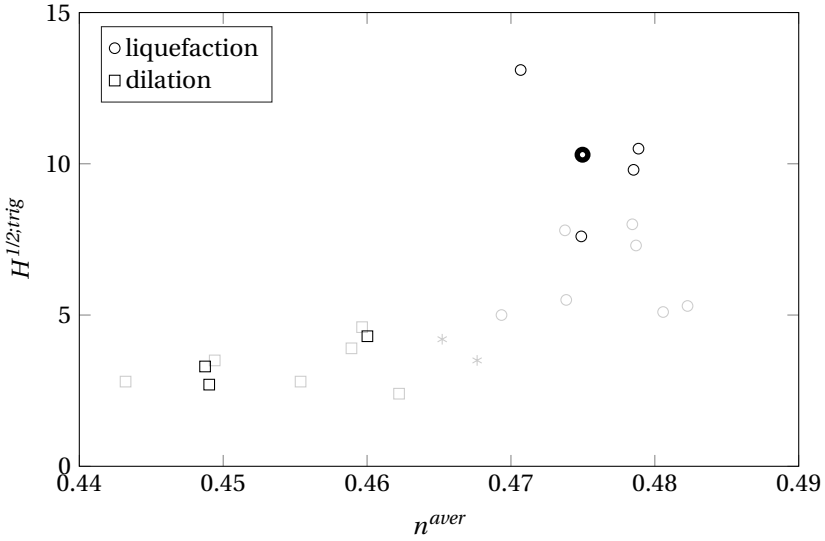


Figure 8.35: Half amplitude of wave induced by bed movements as a function of the average porosity for aged tests.

The effect of angle θ^{trig} on the wave height $H^{1/2;trig}$ is considered by including the tests that were conducted after a longer resting time. These tests yielded a more or less constant value of θ^{trig} (see Figure 8.25). Figure 8.35 plots the results of the aged tests as bold symbols, using an even bolder symbol for the test that was conducted after a waiting time of 12 days. The results demonstrate very little effect for a dilation response, but a clear effect when the bed liquefied. The maximum value reads $H^{1/2;trig} = 13.1\,\mathrm{cm}$ for the aged tests and $H^{1/2;trig} = 8\,\mathrm{cm}$ for the standard set. Hence, provided that the sand bed liquefies, θ^{trig} has a strong effect on $H^{1/2;trig}$.

8.3.8. Concluding remarks for tilting tests

A total of 32 tilting tests were conducted, covering a range of relative densities of $D_e = 22 - 58\%$, resting times between 14 min and 12 days, and tilting rates of $0.115^\circ\mathrm{s}^{-1}$ and $0.0115^\circ\mathrm{s}^{-1}$. The tests have resulted in a wealth of information on the triggering of liquefaction flow slides. The results are summarised using the following concluding remarks:

- The liquefaction tank is capable of replicating liquefaction flow slides by the slow and uniform tilting of a loosely packed, level sand bed. The observed liquefaction flow slides are accompanied by an instant rise of the excess pore water pressure.

- The observed response depends on the initial, average porosity of the sand bed. Decreasing the porosity from the looser states first yields a limited liquefaction response, followed by a stable bed response (dilation) for the lower, average porosities.

- Irrespective of the initial, average porosity of the sand bed, all tests exhibited an

instant rise in excess pore water pressure. However, the angle at which the instant rise is triggered, θ^{trig}, as well as the peak excess pore water pressure $-p^{exc}$, vary with the porosity. Unlike suggested by the different types of bed responses, these measures vary continuously with the initial, average porosity and the range of variation is relatively small.

- The variation of the type of bed response, triggering angle θ^{trig} and peak excess pore water pressure $-p^{exc}$ with the initial, average porosity of the sand bed is consistent and reproducible. That is, two tests conducted at the same density and conditions will yield practically the same type of bed response and values of θ^{trig} and $-p^{exc}$.

- Increasing the resting time has a pronounced effect on the triggering angle θ^{trig}, even for the relatively small 'ageing' periods of a few days that have been considered. Ageing increases the triggering angle θ^{trig} uniformly for different initial, average porosities, thereby overruling the variation of θ^{trig} with density. Nonetheless, the relation between the initial, average porosity and type of response is consistent with the tests conducted at the standard, short waiting periods.

- The triggering of liquefaction flow slides in the liquefaction tank is rate dependent. Tests conducted at a tilting rate that is 10 times lower do not exhibit any sign of excess pore pressure increase or bed movement.

- The loading direction with respect to the loading history of the sand bed has an effect on the development of excess pore pressures, that is: its initial rise (if any), the triggering angle θ^{trig} and the peak excess pore water pressure $-p^{exc}$. Furthermore, a pore pressure rise is observed during reverse tilting well after the tank reached its final, horizontal position.

- The possibility of (external) vibrations affecting the excess pore water pressure development has been ruled out by the measurements with the accelerometers.

- A water wave is observed and measured after the triggering of excess pore water pressures for all tests that were conducted. The wave height depends on the type of bed response and value of the triggering angle, i.e. on the initial, average porosity and resting time.

8.4. Interpretation and discussion

The previous sections demonstrated the consistency and reproducibility of the results. This section puts the results in the broader perspective of element tests, physical model tests and case histories (see Chapter 2).

8.4.1. Types of response

The Author distinghuishes between the 'liquefaction', 'partial liquefaction' and 'dilation' responses (see Figure 8.8). In all three cases the excess pore water pressure developed similarly; an initial stage of zero excess pore water pressures is followed by an instant rise and a stage governed by consolidation. Even though the peak excess pore pressure

increases with increasing porosity (Figure 8.21), the differences seem to be too small to explain the pronounced difference in type of response. How then can the difference in type of response be explained?

The development of excess pore water pressures resembles the response during element tests as discussed in Subsection 2.3.3. Recall the response under a Constant Shear Drained (CSD) stress path, as displayed in Figure 2.24. The soil is brought into an unstable state by drained loading at a constant deviatoric stress, after which the rate of collapse of the sample induces excess pore water pressures and liquefaction. Detailed measurements of the deformations of the sand bed during the liquefaction flow slides are not available, which are required to draw firm conclusions on the instability behaviour of the sand bed. Nonetheless, the similarities between the excess pore water response in the liquefaction tank and during these element tests suggest a similar instability mechanism.

Both in element testing and in the liquefaction tank the occurrence of failure will depend on the strength that can be mobilised after the triggering of the excess pore water pressure. The residual or liquefied strength has been used in engineering practice to assess the stability of slopes (see Figure 2.26). In element testing, the liquefied strength is determined by the friction angle at failure and the normal effective stress or, indirectly, by the excess pore water pressure. Recall the different types of responses for undrained triaxial tests as defined by Castro [1] in Figure 2.13. During 'liquefaction' behaviour at a loose packing the sample collapses after instability, as the liquefied strength is lower than the load imposed at the moment of instability. However, during the 'limited liquefaction' behaviour of a medium dense sample there is an instability response without failure. The residual strength is higher and the sample can be loaded further without failing. The higher density of the sample results in a tendency to dilate and, as a consequence, a decrease of the excess pore water pressure. During the 'dilation' tilting tests an instant excess pore pressure rise without failure of the bed was also observed. Therefore, it is hypothesised that these tests were governed by 'limited liquefaction' behaviour of the sand.

It should be noted that the authenticity of the medium dense, 'limited liquefaction' response has been disputed in literature [2, 3]. The existence of the 'quasi-steady state' has been attributed to experimental artifacts, while it has been stated that field evidence is lacking. The results of the tilting tests may provide this evidence, which would also elucidate the differences in the observed response.

In order to test the hypothesis, it is necessary to study the pore pressure development during the tilting tests in more detail. More specifically, it is necessary to find out whether the post-peak decrease of excess pore pressure during the 'dilation' tilting tests is the result of consolidation, or could also be caused by the tendency to dilate. To this end, the consolidation responses of tests TT24 and TT11 are compared (Figure 8.36). Two 'dilation' tests were selected, as the measured pore pressure response is not disturbed by the failure of the bed. For the sake of comparison, the plots are synchronised at the start of

instability (time = 10 s). Furthermore, the excess pore pressures are normalised by plotting $p^{exc}/p^{exc;max}$ on the vertical axis. This normalisation enables a comparison between the tests, but is also a convenient measure when studying the consolidation response that is conventionally expressed in terms of the degree of consolidation $p^{exc}/p^{exc;max}$. Test TT11 was conducted at an initial porosity of $n^{av} = 0.449$, while test TT24 was substantially looser with $n^{av} = 0.459$.

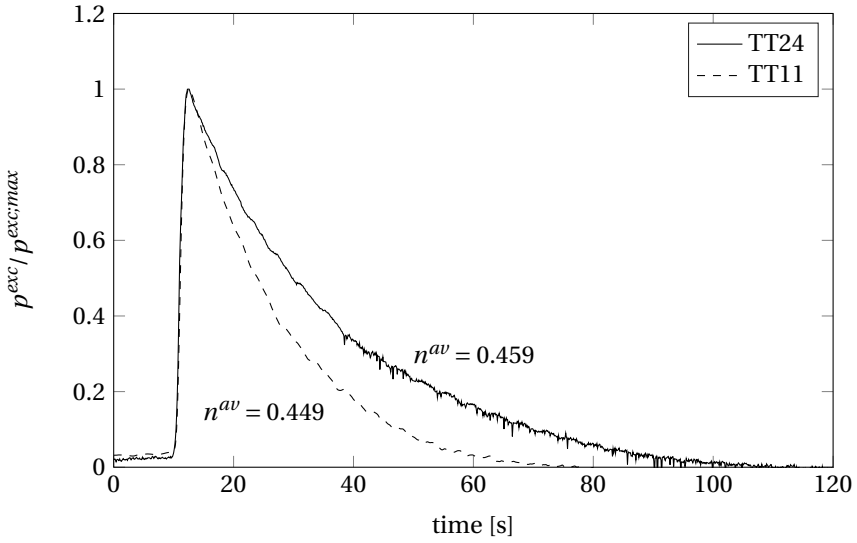


Figure 8.36: Consolidation of excess pore pressures for tests TT24 and TT11 with decreasing porosity.

The responses of tests TT24 and TT11 coincide during the initial stage of instability. However, the decrease of excess pore pressure is significantly higher for the denser of the two tests, TT11. Hence, Figure 8.36 endorses the hypothesis that the tendency to dilate may also affect the post-peak decrease of excess pore water pressure, in addition to consolidation. Figure 8.36 provides a sign of limited liquefaction behaviour, which may be held accountable for the stable bed response during the 'dilation' tests. However, there are some uncertainties. It is not clear whether the extent of the tendency to dilate is indeed sufficient to keep the sand bed stable. Furthermore, the difference in initial, average porosity may also affect the consolidation process itself. Assuming that the consolidation coefficient is an appropriate measure for the description of the consolidation process, the rate of consolidation is affected by the permeability of the soil and its compressibility (see Equation 3.101). The net effect of the density on the consolidation coefficient is not easy to assess, because the density has a reversed effect on the consolidation coefficient through these quantities.

It is recommended to conduct additional tests in the future, preferably enhanced by numerical simulations, to further test the hypothesis. The measurements should include accelerometers in the sand bed indicating the start of instability and pore pressure trans-

ducers in the sand to follow the consolidation process. It is anticipated that limited liquefaction behaviour will be more easily distinguished when the thickness of the sand bed is increased. The consolidation time depends quadratically on the thickness of the bed and will thus increase significantly.

8.4.2. Triggering of flow liquefaction

The instant increase of excess pore pressures during the tilting tests appeared seemingly spontaneous. This corresponds with both field observations and the results of element tests. Literature has reported cases where flow liquefaction occurred without a clear trigger; hence the term 'spontaneous liquefaction' [4]. During element tests this behaviour has been mimicked by pre-shearing the loose sample before closing the drainage valves. The subsequent, sudden liquefaction collapse has been attributed to creep of the sample [5]. The question is, what exactly triggered liquefaction during the tilting tests?

The following, possible triggering mechanisms are considered:

- an external trigger;
- undrained loading;
- groundwater flow;
- rate dependent plasticity in the low shear stress regime;

Possible external triggers include externally induced vibrations and boundary effects. The possibility of externally induced vibration can be excluded based on the measured accelerations (see Subsection 8.3.6). In addition, it is unlikely that the bottom of the tank would allow movements of the sand bed. The fixed walking grid protrudes into the bed, thereby creating a rough bottom boundary.

A second possible explanation is the generation of excess pore water pressures during tilting before instability. There is a clear rate effect, as the reduced tilting rate did not yield any excess pore pressures. Furthermore, a slight increase in excess pore pressures is observed before instability is triggered. Figure 8.37 provides a closer look at the pre-triggering phase for test TT23. It should be noted that, while the measurements of BP2 are depicted, all three fixed sensors at the bottom showed the same, consistent tendency. In general, the measurements of BP1 lie slightly below those of BP2, while the measurements of BP3 lie slightly above those of BP2. The difference is constant and relatively small, and approximately 0.02 kPa.

Before instability, the excess pore water pressures show a relatively fast increase at the start, a more gradual increase in the middle part and an increasing rate towards the triggering of liquefaction failure. Considering the ongoing consolidation, the excess pore pressure response suggests the occurrence of an increasing rate of contraction as a result of tilting. The rate of contraction depends on the characteristics of the soil skeleton reacting to the increase of shear stresses and rotation of the principal effective stresses. The compressibility of the pore water may also play a role, as the level of saturation may

be limited. However, in that case one would expect a different response for the three water pressure sensors in the bottom of the tank as a result of the varying hydrostatic pressure along the tank. Note that towards the moment of triggering there are signs of an increasingly unstable response, as the curve becomes more and more irregular. Nonetheless, the excess pore pressures before triggering are still very small, i.e. 0.07 kPa or 1.7% of the maximum excess pore pressure at complete liquefaction. It is concluded that the pre-triggering increase in excess pore pressure is the result of a more unstable structure in the sand bed, but cannot be held accountable for the subsequent, instant instability.

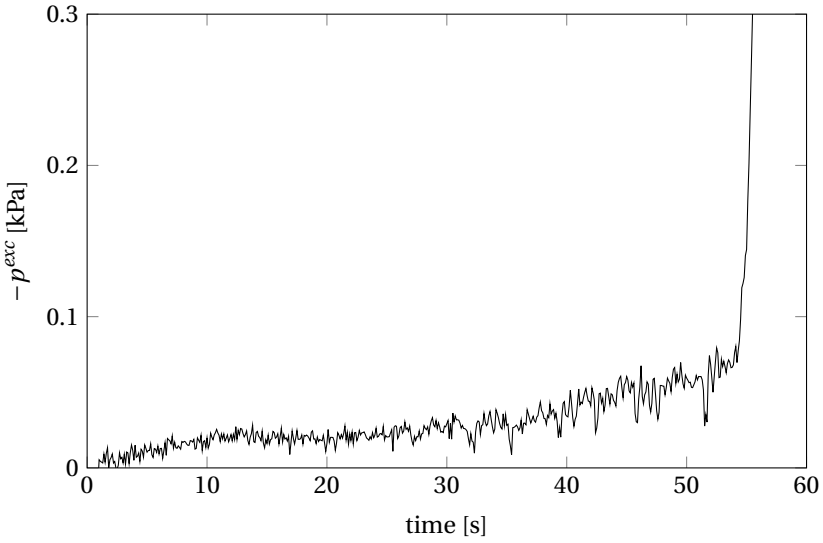


Figure 8.37: Slight increase in excess pore pressure before failure for test TT23.

The third option that is considered is the possible flow of water through the bed. The tilting of the tank reduces the water level at the upper end and increases it at the lower end. The required flow is likely to occur above the sand bed where the resistance is the lowest. Any flux inside the sand bed should be associated with a pressure gradient, which is not apparent from the pore pressure measurements. In addition, tilting yields a decrease in the total isotropic stress at the upper end and an increase at the lower end. The effect on the soil behaviour depends on the compressibility of the grains (see Equation 3.31), which is likely to be low. Hence, the possibility of groundwater flow as the triggering agent can be ruled out.

The last option, alternatively denoted by creep, asks for a further specification. Tilting entails a continuous increase of the shear load, which complicates the distinction of creep. However, the shear load stays well below the natural slope of approximately 32° that was observed during the tests in the minitank. Hence, the term *creep* is here defined as the re-arrangement of particles and contacts in this low-shear region. Whether this

is truely creep is a semantic discussion, which is not of importance at this stage. Lade and Liu [6] stress the common features of creep and plastic behaviour and demonstrate that both can be described in a hardening plasticity framework. The separation between general plasticity and creep, if any, is thus marked by a thin line.

Defined as such, creep does offer a plausible explanation for the observed response. The exclusion of external factors suggests the explanation should be sought in the behaviour of the sand bed. The excellent reproducibility and consistent tendencies with varying density subscribe to this. Furthermore, Figure 8.37 suggests that instabilities at a smaller scale precede the triggering of liquefaction. These increase in size towards the moment of triggering, which suggests that instability of the soil skeleton yields the instant rise in excess pore pressure. The aged tests demonstrate the importance of time effects for the moment of triggering. Finally, the creep response is rate dependent. Yamamuro and Lade [7] demonstrate that instability increases with increasing strain rate, which is in line with the results of the tilting tests.

It is concluded that the triggering of liquefaction during the tilting tests in the liquefaction tank should be understood from the rate dependent plasticity of the soil at relatively low shear stresses. This is a feature that is, as yet, poorly understood. To the Author's knowledge, none of the existing constitutive models of sand can account for this. Further investigation on the scale of an element test or even the grain scale (by X-ray tomography or DEM) would be required to fully comprehend this mechanism. The numerical simulation of the overall response of the model slope may also be useful in elucidating the development of the observed instability.

8.4.3. Factors influencing the response

Section 8.3 gave an overview of factors that influence the response during the tilting tests, including density, ageing, rate of loading and direction of loading. In general, the derived tendencies correspond well with conceptions from element tests and case histories.

The density governs the observed response, the angle of triggering and the peak excess pore pressure. Liquefaction occurs at (average) porosities above $n^{av} = 0.469$, which corresponds with a relative density of $D_e = 34\%$. This is within the usual range of relative densities that are considered susceptible to flow liquefaction. However, as compared to field conditions the vertical effective stresses are significantly lower in the liquefaction tank. A lower, required relative density was anticipated beforehand, as the state parameter would be lower at the same density but lower effective stresses [8]. The relatively small stress effect may be explained by considering the critical state line at very low stresses. Been et al. [9] indicate that the critical state line tends to become flatter in plots of e-$\log p'$ at low stresses. This implies that the stress effect becomes less significant at low stresses. This should be verified by conducting element tests on the sand at the same, low effective stresses. Variability of the soil density had a limited effect on the results of the tilting tests. Even though liquefaction seems to be triggered in the loosest part, the overall response is represented best by the average porosity.

The increase of waiting time, *ageing*, increased the resistance against liquefaction in the tilting tests. This notion is consistent with case histories that report the liquefaction of relatively young deposits [10]. The tilting tests demonstrate that ageing already affects the response at a very early stage. The response after a few days waiting is substantially stronger than after tens of minutes. In addition, ageing overrules the tendency for an increasing triggering angle with increasing density. Provided that the ageing period was similar, the triggering angles for the aged test were practically constant, irrespective of the density. It is assumed that ageing created an additional bonding between the grains, for instance cementation at the contacts, which governed the first stage of loading. This additional bonding is presumably equal for tests with a similar waiting time. At the moment this strength is overcome, the soil skeleton will respond as if there was no ageing effect and the response is observed that could be anticipated based on the initial porosity. This conclusion corresponds with the findings of Cuccovillo and Coop [11]. Drained triaxial tests on a natural, cemented sand yielded a largely cohesive response. It was however anticipated that frictional behaviour would have been observed if the bonding could have been disrupted before failure.

The rate of loading had the anticipated effect, with liquefaction only occurring at the higher rate. However, the underlying mechanism does not meet the expectations. While the rate of loading is conventionally related to the rate of generation of excess pore pressures, the pre-triggering excess pore pressures during the tests that liquefied remain very small. The rate of loading mainly affects the (in)stability of the soil skeleton. The importance of the structure of the soil skeleton is further subscribed by the response during the reverse tilting of the denser sand. In spite of the densification during tilting, reverse tilting yields a larger rate of excess pore pressure increase. Furthermore, the excess pore pressures increase with decreasing tilting angle and, for some cases, the peak excess pore pressure are higher for reverse tilting as compared to tilting. Stress-induced anisotropy governs the generation of excess pore pressures. This conclusion is consistent with the results from element tests (see 2.3.2). It also emphasises the importance of the loading direction of triggers relative to the stress-induced anisotropy of the soil skeleton.

8.4.4. Implications for the assessment of flow liquefaction

The liquefaction tank eventually aims at improving the basis for the assessment of liquefaction flow slides. Chapter 2 raised questions related to the assessment. The results of the tilting tests may already provide some answers, but the results of the triggering of actual slope failures will remain indispensable.

The tilting tests endorse the importance of liquefaction flow slides as a failure mechanism of submerged, sandy slopes. Chapter 2 noted that the lack of knowledge of case histories, the similarities with the post-failure morphology after unstable breaching and the difficulties encountered to reproduce flow liquefaction in triaxial tests for undisturbed or water-pluviated samples may be reasons to inflict doubts on its importance. The tilting tests demonstrate that flow liquefaction can be reproduced in a fairly simple way, that is, using a relatively simple geometry and load and without imposing undrained con-

ditions. The results confirm the general conception that liquefaction flow slides occur at relatively gentle slopes, somewhat unexpectedly after a minor trigger, propagate at a high rate and produce very gentle slopes after failure.

During the tilting tests, liquefaction flow failures occurred at slopes approximately ranging between 1v:8h and 1v:10h. In contrast to case histories and the mobilised strengths deduced from element tests, these slopes are gentle. The tilting tests demonstrate that these gentle slopes are related to the response of the bed itself and not to secondary effects such as void ratio redistribution [12]. Furthermore, these shallow slopes confirm the limitations of undrained triaxial tests, that is, fixed principal effective stress directions. The instability line that follows from undrained triaxial tests [13] suggests mobilised strengths well above the failed slopes.

The flow failures in the tilting tests were truly static. They appeared without a clear sign of instability or significant excess pore pressure build-up. These observations correspond with the presumed spontaneous nature of flow slides encountered in engineering practice, although the triggering slope angle is demonstrated to be the actual cause. The results endorse the importance of the density for the response of the sand bed. In addition, ageing plays an important role, even for the very young deposits that were created in the tank. The results suggest that ageing creates a threshold strength, which should be overcome to trigger liquefaction. For strongly aged deposits it is anticipated that this threshold may be sufficiently large to prevent the triggering of flow liquefaction or delay it until the occurrence of a much more severe mobilised friction. This conclusion is in line with the notion that case histories only included young deposits [10]. The observed effect of stress-induced anisotropy stresses the importance of triggers that vary in direction, such as earthquakes.

The measured limited-liquefaction behaviour may offer an explanation for the relatively small differences between the peak excess pore pressures as measured for loose and dense packings. It also suggests the relative unimportance of the value of the peak excess pore pressure for the response. Since these excess pore pressures suddenly and instantly increase without a warning, the relevance of monitoring of excess pore pressures for liquefaction flow slides in engineering practice is questioned. Based on similar grounds, Jefferies and Been (p.29, [14]) consider the observational method as being unsuitable for flow liquefaction. The measurement of excess pore pressures implies instant failure of the slope and leaves no time to take measures.

The post-peak excess pore pressure response is governed by the reduction in excess pore pressure during limited liquefaction and consolidation. Even though none of the tests exhibited full (100%) liquefaction at the peak excess pore pressure, the bed was horizontal after failure. The Author believes that the horizontal surface is the result of the upward pore water flow during dissipation. In that case, the final geometry, i.e. the horizontal surface, is the result of secondary effects rather than the liquefied strength of the soil. This suggestion has far-reaching consequences, as many assessment methods are based on the liquefied strengths that have been derived from the post-failure geometries

of case histories (see Figure 2.31). Based on the test results, it is concluded that these liquefied strength values will underestimate the 'true' strength of the bed.

The waves that were induced by failure in the tank support the general belief that large, submerged slope failures may induce tsunamis. The results of the liquefaction tank tests can be used to improve the insight into the relation between submarine landslides and tsunamis. This research may contribute to filling one of the main gaps in the current knowledge: the effect of the rheology of submarine landslides on the properties of the generated tsunamis [15]. It is believed that the complex assessment of landslide-generated waves requires a numerical modelling approach. The liquefaction tank may provide additional experimental data for model benchmarking. It should be noted that the numerical modelling of landslide-generated tsunamis introduces additional complexities with respect to the modelling of the free water above the slope. Hence, the model discussed in Chapter 5 should be extended with a formulation for the free water, for instance using the Navier-Stokes equations, to describe the interaction between the liquefaction flow slide and the free water with some accuracy.

The generation of tsunamis by liquefaction flow slides can be used when assessing geohazards, but can also be used to detect submerged slope failures. As liquefaction flow failures often remain unnoticed until the mechanism appears above the phreatic surface, the monitoring of water waves can be used to detect the failure at an early stage. Moreover, the height of the wave can be used to distinguish between liquefaction flow failure and unstable breaching, which will yield far smaller waves.

References

[1] G. Castro, *Liquefaction of sands*, Ph.D. thesis, Harvard University, Cambridge, Massachutes (1969).

[2] H. Zhang and V. Garga, *Quasi-steady state: a real behaviour?* Canadian Geotechnical Journal **34**, 749–761 (1997).

[3] H. Zhang, V. Garga, Y. Vaid, A. Eliadorani, S. Sivathayalan, M. Uthayakumar, M. Yoshimine, and J. Chu, *Quasi-steady state: a real behaviour?: Discussion,* Canadian Geotechnical Journal **36**, 182–193 (1999).

[4] A. Andresen and L. Bjerrum, *Slides in subaqueous slopes in loose sand and silt,* Norwegian Geotechnical Institute Publication **081**, 1–9 (1968).

[5] P. Lade, *Static instability and liquefaction of loose fine sandy slopes,* Journal of Geotechnical Engineering **118**, 51–71 (1992).

[6] P. Lade and C.-T. Liu, *Experimental study of drained creep behavior of sand,* Journal of Engineering Mechanics **124**, 912–920 (1998).

[7] J. Yamamuro and P. Lade, *Effects of strain rate on instability of granular soils,* Geotechnical testing journal **16**, 304–313 (1993).

[8] K. Been and M. Jefferies, *A state parameter for sands,* Géotechnique **35**, 99–112 (1985).

[9] K. Been, M. Jefferies, and J. Hachey, *The critical state of sands,* Géotechnique **41**, 365–381 (1991).

[10] P. Robertson, *Evaluation of flow liquefaction and liquefied strength using the cone penetration test,* Journal of Geotechnical and Geoenvironmental Engineering **136**, 842–853 (2009).

[11] T. Cuccovillo and M. Coop, *On the mechanics of structured sands,* Géotechnique **49**, 741–760 (1999).

[12] H. B. Seed, *Design problems in soil liquefaction,* Journal of Geotechnical Engineering **113**, 827–845 (1987).

[13] J. Chu, S. Leroueil, and W. Leong, *Unstable behaviour of sand and its implication for slope instability,* Canadian Geotechnical Journal **40**, 873–885 (2003).

[14] M. Jefferies and K. Been, *Soil liquefaction: a critical state approach* (Taylor & Francis, 2006).

[15] S. Yavari-Ramshe and B. Ataie-Ashtiani, *Numerical modeling of subaerial and submarine landslide-generated tsunami waves—recent advances and future challenges,* Landslides **13**, 1325–1368 (2016).

9

Conclusions

Improving the assessment of liquefaction flow slides requires the consideration of different aspects. To this end, the thesis has treated liquefaction flow slides from different viewpoints. The previous chapters presented an extensive literature study, the framework of the governing equations, the numerical implementation and the experimental results with the liquefaction tank. The findings are numerous, novel and, in some cases, surprising. It is believed that these results can be used to improve the assessment of liquefaction flow slides. This chapter summarises the main findings and conclusions from the thesis, recognises the implications and presents the recommendations.

The introduction from Chapter 1 will be recalled. Using the key questions that were listed in Section 1.3, the Author first provides an overview of the main findings. Next, the main research question is separately addressed. The subsequent section discusses which implications can be expected for engineering practice. Finally, some recommendations are given with respect to future research and the assessment of liquefaction flow slides.

9.1. Overview of findings

The conclusions of this thesis are drawn in an overview of the main findings. The findings are presented in a number of subjects, which follow the structure of the thesis. Note that the key questions can be recognised among these subjects.

Underlying mechanisms of liquefaction flow slides

Chapter 2 considered the characteristics of liquefaction flow slides on the basis of literature about case histories, scale model testing and element testing. Even though liquefaction flow slides are considered a major hazard in engineering practice, it was concluded that case histories provide little detailed information. The main uncertainties include the soil conditions and the actual role of the trigger. Scale model tests enable a more detailed consideration of liquefaction flow slides, but generally suffer from a lack of reproducibility. The trigger is enforced but not well-controlled, whilst the soil conditions are

uncertain. The results of element tests do provide detailed information about the underlying mechanisms of liquefaction flow slides. The undrained instability corresponding with the generation of excess pore water pressures initiates flow liquefaction, which is followed by a diffusive mechanism through the slope. Engineering practice relies mostly on undrained triaxial tests conducted on loose reconstituted samples. This approach leaves many essential aspects under-exposed, such as the stress path, strain path, the fabric of the soil and void ratio redistribution. Ignoring these aspects yields an oversimplified, and sometimes even incorrect, assessment of liquefaction flow slides. It is thus concluded that there is a large gap between the detailed and essential information that is provided by element tests, and the response that is encountered during field events.

Coupled equations for saturated soils

The underlying mechanisms of liquefaction flow slides require a coupled analysis, including the conservation of mass and momentum of the saturated soil. Chapter 3 elaborated these governing equations using mixture theory. The most striking result is the heterogeneous interaction term that is required for the correct description of the hydrostatic paradox. This term is self-equilibrating; it is by definition eliminated from the momentum equations of the pore fluid and soil skeleton. This thesis also presented an alternative novel derivation of the momentum equations, using hydrostatics as the starting points. It was shown that a different, but essentially equivalent set of equations can be derived in this way. This set is a convenient alternative for the conventional set that is derived from mixture theory, as it allows for a direct expression of the effective stress. The resulting sets of equations were employed to describe the phenomena that appear during the different stages of liquefaction flow slides.

Heterogeneous interaction term in thermodynamics

In order to demonstrate that the derived framework is consistent, the role of the heterogeneous interaction term was considered for thermodynamics. The elimination of the heterogeneous interaction term in the momentum equations does not necessarily mean that the term does not play a role in thermodynamics. Chapter 4 considered the conservation of energy and the requirement of non-negative entropy production for the pore fluid and soil skeleton. The heterogeneous interaction term produces work and thus leads to an additional term in the energy conservation equations. The elaboration of the requirement of non-negative entropy production shows that the largest part of this work is exchanged and accounted for by the mechanical part of the energy interaction term. Hence, this term is also self-equilibrating. The complementary part of the work produced by the heterogeneous interaction term results in work exerted by the pore fluid stress on the compressing particles. This term will be part of the rate of internal strain energy of the soil skeleton. It is concluded that including the heterogeneous interaction term in the momentum equations leads to a consistent framework.

Validity of stress measures for soils

This thesis considered the limitations of the stress measures of saturated and unsaturated soils. First, it was demonstrated how the saturated stress measures can be extended to keep the unsaturated stress measures physically justified. As a result, the amendments to constitutive relations are minimal or none, which allows one to take advantage of the

vast experience and data that were obtained for the saturated case. Furthermore, the effect of fabric anisotropy was introduced for the stress measures. It is anticipated that the additional parameters in the stress measures for unsaturated soil can be determined using inverse modelling of experimental data. Second, the effect of interparticle sliding and particle rolling on the stress measures was investigated. Particle rolling is an important mode during the post-liquefaction phase. Using upscaling from the particle scale, it was demonstrated that the interparticle stress tensor is symmetric, even when accounting for particle rotations. However, this common, translational intergranular stress is not sufficient to describe the stresses in an assembly of particles that include both interparticle sliding and particle rotations. In this case the non-symmetric, total intergranular stress tensor should be used, which is composed of the symmetric translational and non-symmetric rotational part of the intergranular stress. The non-symmetry of the total intergranular stress tensor implies that the conservation of angular momentum should be taken into account as a field equation for particle rotations.

Implementation into the Finite Element Method
Chapter 5 discussed the implementation of the governing equations into a finite element code. Its performance was verified for the quasi-static one-dimensional consolidation problem. The code reproduced the analytical solution quite well for a mesh subdivided into two or more elements, and different types of elements. When it comes to abrupt changes in the loading conditions, three-node triangular elements performed better than four-node and eight-node quadrilateral elements for this problem. The modelling of dynamics requires the consideration of additional accuracy and stability conditions. The simultaneous satisfaction of the conditions that are set for statics and dynamics leads to unrealistically small values of the time step and element size. Hence, an adaptive strategy is recommended when the subsequent stages of liquefaction flow slides are modelled. The final section of Chapter 5 elaborated on the extension of the MONOT-model with a critical state-formulation. The incorporation of the critical state allows for the modelling of large deformations. The resulting formulation is compatible with the state parameter concept, while still taking advantage of the firm theoretical basis provided by the MONOT-model.

Design of the liquefaction tank
The main result of this research project is the development of a novel experimental facility: the liquefaction tank. Intended to bridge the gap between element tests and field events, the liquefaction tank has dimensions that are compatible with the stress levels that can be established in element tests. The liquefaction tank should produce liquefaction flow slides that are reproducible in terms of the monitored pore pressures and the failure mode. To this end, special attention was given to the triggering of liquefaction flow slides and the preparation of the sand bed.

The tank was designed to enable different triggering mechanisms. The tests described in this thesis were conducted using the tilting of the liquefaction tank as the trigger. The Author considers tilting the purest and simplest possible trigger. The load is applied uniformly over the sand bed, while the initiation of liquefaction flow slides can be identified accurately. Furthermore, the tilting can be reproduced easily in a finite element model,

by rotation of the gravity vector.

A fluidisation system was designed to establish a loose and uniform sand bed. It has been assumed that a uniform stress distribution along the fluidisation system will yield a uniform sand bed. Subsection 6.2.3 described the design of the fluidisation system, which was based on a finite element analysis of the pressure distribution. The results demonstrated that the pressure drop along the fluidisation system is expected to be sufficiently small for the considered range of design parameters. It was recognised that energy losses due to turbulence were not accounted for in the finite element analysis. To minimise this effect, a relatively large diameter of the tubes was selected, and the holes were drilled at a relatively large, mutual distance.

Novel preparation procedure for triaxial test
Subsection 6.3 discussed the development of a novel preparation procedure for triaxial tests, which is compatible with the procedure used in the liquefaction tank. The challenge is to mimic the low density, low mean effective stress and novel preparation procedure by fluidisation in the triaxial test. Two possible procedures were considered, using either a high column and sand suction or one-dimensional compression to mimic the stress history in the liquefaction tank. Based on the expected disturbance, it is concluded that the second procedure, using one-dimensional compression, is expected to yield the better performance. Both the established density and imposed stresses are expected to be rather uniform over the height of the sample. It is concluded that reasonably accurate liquefaction-related mechanical characteristics can be measured for the sand in the liquefaction tank, by means of triaxial tests.

Performance of fluidisation system
Chapter 7 discussed the performance of the fluidisation system. The measured pressure gradient along the fluidisation system was larger than anticipated, which is presumably caused by energy losses due to turbulence. Nonetheless, the anticipated effect on the density distribution along the sand bed was shown to be negligible. It is thus concluded that the fluidisation system performs well. The fluidisation tests also allowed the Author to define the optimum range of the fluidisation flow rate, which was defined between $6\,\mathrm{l\,s^{-1}}$ and $12\,\mathrm{l\,s^{-1}}$. A novel elaboration of Kynch's graphical theory of sedimentation demonstrated that the grain size distribution governs the response of the sand bed during fluidisation. Even for the uniform sand that was used in this research project, the final stage of fluidisation is clearly governed by the finer fraction of the soil. One may use the results of the fluidisation tests to control the initial density after sedimentation in the liquefaction tank.

Production of liquefaction flow slides in the liquefaction tank
The liquefaction tank produced several liquefaction flow slides for a bed with an initial thickness of approximately 0.5 m. The results confirmed the main characteristics of liquefaction flow slides that were described in Chapter 2. Liquefaction flow slides appeared suddenly, at relatively gentle slopes, developed at a high rate and left a horizontal bed after failure. Furthermore, the initiation of the liquefaction flow failures involved the generation of excess pore water pressures. A surprising conclusion is that the liquefaction

flow slides were triggered at relatively gentle slopes, ranging between 1v:8h and 1v:10h. In addition, it is noted that the measured excess pore water pressures stayed well below the values that correspond with full liquefaction (and zero effective stress), in spite of the failure yielding a horizontal sand bed.

Minor role of the trigger
The conditions for the triggering of liquefaction flow slides in the liquefaction tank were surprising. It was anticipated that the initiation of a liquefaction flow slide required a dredged slope of approximately 1.5 m height before tilting, and a clear trigger, for instance by suddenly halting the tilting, to initiate liquefaction. Chapter 8 demonstrated that liquefaction flow slides were produced by the uniform tilting of a horizontal sand bed. An instant and sudden increase in the excess pore fluid stresses preceded liquefaction failure at a particular inclination of the liquefaction tank. There was no clear triggering agent, which implies that the soil was in a metastable state and that any small perturbation, e.g. creep of the soil, initiated liquefaction. The consistency and reproducibility of the results, as well as additional measurements with accelerometers, rule out the possibility of an artificial or coincidental trigger. To the Author's knowledge, this is the first time that truly static liquefaction flow slides are observed at this scale.

Effect of density in tilting tests
There was a clear relation between the possible failure mode and the average density in the liquefaction tank for the tested range of porosities ($0.443 > n^{av} > 0.482$). Below a particular average porosity ($n^{av} < 0.463$), the slope did not fail, whereas for $n^{av} > 0.468$ it did fail. In between, partial failure of the slope was observed. This sharp distinction between bed responses was not reflected by the measured pore pressures. Irrespective of the initial average porosity, all tests exhibit an instant rise in the excess pore water pressures. There was a consistent and smooth trend of decreasing triggering angle and increasing peak excess pore pressure with increasing porosity, but the differences in pore pressure response were relatively small.

It is concluded that the results are reproducible. Two sets of tests that were conducted at the same average porosity yielded approximately (in one case exactly) the same values of the triggering angle and peak excess pore pressure. The excellent reproducibility of the results affirms that the average porosity is an appropriate measure for the susceptibility to flow liquefaction. Furthermore, it is noted that liquefaction failure was observed for very low initial vertical effective stresses of below 5 kPa, at relative densities D_e ranging between 19% and 34% ($0.468 > n^{av} > 0.482$). The results suggest that the looser part of the sand bed controls the global response.

Pronounced role of ageing
The 'standard' tests were conducted after a resting time in the order of tens of minutes. In addition, a number of tests were conducted after a resting time in the order of days. It is concluded that ageing has a pronounced effect on the response of the sand bed during tilting. The triggering angle increases with increasing resting time, even for the relatively small time scale of resting times that has been considered in this thesis. Furthermore, the effect of the density on the triggering diminished for the tests that were

conducted after an increased resting time. The excess pore pressures were triggered at approximately the same inclination of the tank, irrespective of the initial average porosity ($0.449 > n^{av} > 0.479$).

It should be noted that the relation between the failure mode and the average density seemed to be unaffected by ageing. The same threshold values applied for a liquefaction or stable response. Furthermore, the measured peak excess pore pressures did fit the relationship with the average porosity that was derived for the 'standard' tests.

Tilting rate governs the occurrence of failure
Two tests were conducted at a high average porosity and a tilting rate that was ten times slower than the other tests. These tests did not show any sign of failure or generation of excess pore pressure. Therefore, it is concluded that, in addition to the density, the tilting rate governed the occurrence of failure in the liquefaction tank. The effect of an external artificial agent on the triggering of liquefaction flow slides in the liquefaction tank was ruled out. It also seems unlikely that the generation of excess pore pressures before the triggering and a possible groundwater flow had a critical effect on the initiation of the sudden rise in excess pore water pressures. Therefore, it is hypothesised that rate dependent plasticity in the low shear regime explains the effect of the tilting rate.

Direction of loading with respect to loading history
The effect of pre-loading was a stabilising factor during the tilting tests, provided that the direction of re-loading was the same. The tests that were conducted at a lower tilting rate hardly disturbed the sand bed. After reverse tilting of the tank in its horizontal position, tilting of the tank at the normal, high tilting rate did not result in any generation of pore pressures.

The opposite conclusion is drawn for the direction of re-loading opposite to the direction of pre-loading. Reverse tilting of the 'dilative' tests yielded a weaker response, in spite of the densification of the sand bed during tilting. Contrary to tilting, reverse tilting resulted in a gradual increase of the excess pore pressures from the moment reverse tilting started. Furthermore, the peak excess pore pressure was often larger than during tilting. The peak occurred when the tank was almost back in its horizontal position, and sometimes even a few seconds later.

Liquefaction-generated water waves
Liquefaction failure in the liquefaction tank involved the generation of a water wave. Surprisingly, the 'dilative' tests also resulted in a water wave, albeit with a significantly smaller amplitude. In addition to the density, the triggering angle also affected the amplitude of the generated water wave. The 'aged' tests failed at a higher triggering angle, which also led to a larger amplitude of the generated wave.

9.2. Improving the assessment of liquefaction flow slides

Section 1.3 defined the following research question for this thesis: "How can assessments of liquefaction flow slides be improved?". There is a large gap between the fundamental

knowledge about flow liquefaction from element tests and the practical approaches that are often used in engineering practice. These practical approaches complement the soil investigations, which often include cone or standard penetration tests and undrained triaxial tests. A number of essential features of soil behaviour that are believed to be essential for the assessment of liquefaction flow slides, are not accounted for. On the other hand, it is yet unclear how important these advanced features are and for which conditions. Furthermore, there are no practical methods that can account for them.

The Author believes that it is not feasible to conduct an advanced soil investigation and complex finite element analyses for each project in practice. At this moment, both can only be carried out by a selected group of highly specialised people, using equipment and models that most engineers are unfamiliar with. With increasing complexity, and number of input and output variables, the reproducibility of analyses may become an issue. The size of project sites and the variability of the subsoil may require a vast amount of tests and analyses.

The development of the liquefaction tank has provided a test environment to study the response of a sand bed during a liquefaction flow slide in detail. One can study the effect of the properties of the sand, such as the consolidation coefficient, on the initiation of a flow slide. By testing different triggers, the importance of stress paths can be investigated. The liquefaction tank also allows the testing of mitigating measures, and related mechanisms such as liquefaction during the saturation of unsaturated soils. Element tests should be performed, using the same preparation method, density and effective stresses as in the tank, to understand the underlying soil behaviour. Then, the level of quality of finite element models can be evaluated using the results of the liquefaction tank tests. Hence, finite element analyses relate the results of element tests to the outcome of the liquefaction tank tests. Subsequently, the Finite Element Method and the results of element tests at larger stresses can be employed to extrapolate the results to the larger slopes that are engineered in practice.

It is anticipated that the liquefaction tank will produce a vast amount of data on liquefaction flow slides. The Author believes that this database will be the basis for an improved understanding of liquefaction flow slides. This thesis lays the foundation for future projects with the liquefaction tank and a finite element formulation with a firm, theoretical basis. The main conclusion is that the liquefaction tank can produce liquefaction flow slides, and that the reproducibility of the results is excellent.

9.3. Further implications for engineering practice

The first test series with the liquefaction tank have demonstrated its capabilities in terms of obtaining reproducible measurements of liquefaction flow slides. In addition, these preliminary results already provide useful information that can change our view on how to treat liquefaction flow slides. There are a number of implications that are of importance for engineering practice.

The transition between a dilative and liquefaction response in the liquefaction tank, de-

fined by the difference in the observed bed response in this thesis, was associated with a relatively small difference in the average porosity of 0.005. The sharp transition confirms the importance of density for the susceptibility to liquefaction. Furthermore, it highlights the necessity to determine the in-situ density accurately. The Author recognises the challenge that lies ahead with respect to the determination of the in-situ density. At this moment, the conventional testing methods that are used to determine the in-situ density are far from accurate.

The rise in excess pore water pressure was instant and sudden in the liquefaction tank tests, and occurred for the full range of densities that was tested. There was no indication beforehand that announced the pore pressure increase. This implies that the observational method is not appropriate for the control of liquefaction flow slides in engineering practice. Furthermore, a pore pressure rise is not necessarily an indicator for a liquefaction flow slide, as it also can be followed by a dilative response.

The effect of the resting time ('ageing') on the triggering has implications for relatively young deposits, such as hydraulic fills. Even a resting time of a few days creates resistance against liquefaction. It is known that hydraulic fills gain strength during the days just after construction. The liquefaction tank tests demonstrate that the susceptibility to liquefaction is particularly high in the first few days after construction. The Author acknowledges that ageing is indeed considered to be of importance in engineering practice, but hardly ever explicitly accounted for. This may be attributed to the disturbance during the sampling of sands, and, as a consequence, the reconstitution of samples in element tests.

The slopes at which liquefaction was triggered in the liquefaction tank are more gentle than anticipated based on case histories and element tests. The rare case histories that do involve such gentle slopes are often explained by secondary effects, such as void ratio redistribution. The liquefaction tank tests show that this is not necessarily the case, and that an explanation should be sought in the soil behaviour. Many assessment methods rely on the instability line concept and undrained triaxial tests to predict the triggering of flow liquefaction. These methods will overestimate the triggering strength that was found in the liquefaction tank tests. The Author believes that more advanced features of soil behaviour, such as principal stress rotation, should be accounted for in the assessment of liquefaction flow slides.

The slope of the sand bed that is found after liquefaction failure is not an appropriate measure for the residual or liquefied strength of the soil. The failures in the liquefaction tank resulted in a horizontal sand bed, in spite of excess pore water pressures that stayed below 70% of the value corresponding to 'full liquefaction'. It is anticipated that the upward water flow following the triggering governs the post-liquefaction slope. Hence, values of the liquefied strength that are derived from case histories, and used in assessments, should be applied with great caution.

9.4. Recommendations

9.4.1. Research

It is recommended to follow an integral approach during further research in which the finite element model and the liquefaction tank are simultaneously developed. The evaluation of the model requires experimental input, whereas the interpretation of the liquefaction tank tests asks for numerical simulations. There are a number of specific recommendations, which apply for the development of the experimental research and the finite element model.

Pore pressures and accelerations in the sand bed

The first test series that is described in this thesis may serve as a starting point for future research. There are a number of options to gain further insight into the development of liquefaction flow slides. The number of sensors can be extended by placing accelerometers and pore pressures sensors in the sand bed. These will provide information about the location of initiation and the subsequent development of liquefaction flow slides.One question is whether pore pressures trigger deformations or the other way around. Besides, it is of interest to see how pore pressures migrate through the soil body and if void ratio redistribution plays a role during the development of liquefaction flow slides. The Author postulates that the upward flow following the triggering of excess pore water pressures plays an important role during the development of liquefaction flow slides. If this is indeed the case, one can specify the effect of mitigating measures, such as the application of a permeable surcharge layer of scour protection. Sensors that are placed in the sand bed are also of importance to understand why liquefaction flow slides do not occur. The Author hypothesised that the stable response that was observed for the dilative tests during the first test series may be attributed to the decrease of excess pore pressures during limit liquefaction behaviour. Additional tests with sensors installed in the sand bed may be used to test this hypothesis.

Deformations at the surface

For a detailed evaluation of the finite element model, it is recommended to measure the deformations in the sand bed in more detail. The accelerometers in the sand bed will give an impression of the deformations, but the amount of sensors will be limited due to the disturbance of the sand bed. One may measure the deformations of the sand bed at the surface, for instance by using high-speed cameras. Earlier attempts by the Author to apply cameras encountered problems with the resolution of the images. As a result of the low contrast in the fine sand, only a small part of the slope surface can be filmed with sufficient resolution, even for the large amount of pixels that cameras have these days. Hence, one should increase the contrast at the surface to enable high-speed camera measurements.

Increasing thickness of the sand bed

The thickness of the sand bed can be increased to study the influence of the effective stresses on the response. To this end, first the performance of the fluidisation system should be considered for a larger amount of sand. The Author expects that the amount of sand will have a small effect on the pressure drop along the fluidisation system, but this

should be verified. The thickness of the sand bed may affect the fluidisation response of the sand bed and, therefore, the density that is reached after sedimentation. A larger thickness of the sand bed will make it easier to flush out finer particles, as the distance to the overflow is decreased. The advantage is that the water on top of the sand bed can be cleared more easily. On the other hand, the segregation of particle sizes may have a stronger effect on the response during tilting. A thicker sand bed also allows measurements of the horizontal stress to be made. The development of the horizontal stress can be measured during fluidisation, sedimentation and the resting period ('ageing'). The K^0-measurements before tilting define the initial stresses of the test.

Density and variability

The results of the first test series suggest that the average porosity is an appropriate measure to predict the response during tilting. However, a more detailed investigation of the initiation and development of liquefaction flow slides in the liquefaction tank also requires more detailed information about the density of the sand bed. To this end, it is recommended to apply the same principle as the siphon tools that were developed for the permeameter (7.2.4) and triaxial cell (6.3). The size of the tank complicates the delicate and time-consuming layer-by-layer suction of sand. It is recommended to follow a step-by-step approach. First, one may use the dredging device (6.2.6) and the measurement tapes to remove a particular volume of sand. Then, the mass of the sand could be stored in a big-bag and measured using the same procedure as described in Section 7.3. The volume of removed sand will be relatively large. The result is a first indication of the variation of the density with depth. The advantage of removing a relatively large volume of sand is that the measurement error is expected to be small. Subsequently, one may consider following the same procedure after partitioning the sand bed, e.g. by placing vertical panels during fluidisation. The variation of the density along the bed can thus also be determined. For a more detailed determination of the in-situ density, a box with an open bottom and top can be hung into the tank during fluidisation. Provided that the box is sufficiently large, one of the suction heads of the dredging device can be used to remove the sand. It will be more complicated to remove a horizontal layer accurately, which should become apparent in the measurement error.

Mechanical characterisation of the sand

Triaxial tests using the novel preparation procedure (Section 6.3) may characterise the mechanical behaviour of the sand in the liquefaction tank. The Author acknowledges that the minimisation of the disturbance of the sample and the uniform application of the stresses will be a challenge. It is thus recommended to investigate these aspects first experimentally, before conducting a test series at the same range of stresses and densities that are encountered in the liquefaction tank. The results will provide a unique insight into the effect of fluidisation as a preparation method, and the mechanical response of sands at extremely low effective stresses. It is recommended to vary the stress path by conducting both triaxial compression and extension tests. The finite element model should be employed to transform the mechanical characterisation of the sand into a post-diction of the liquefaction tank tests. The results can be used as a starting point for the development of the material model. It is anticipated that more experimen-

tal research is required to account for the rate-dependence of the material response and the effect of principal stress rotation.

Dredging and triggering
The dredging of a slope will allow one to vary the stress path and triggering. The dredging device was designed to dredge a natural slope. The minimisation (and determination) of the disturbance of the sand bed during dredging will pose a major challenge. The natural slope is much steeper than the slopes that failed during the first test series. It is recommended to apply a very low rate of dredging to avoid any premature failures. Recall that the loading rate was a governing factor during the first test series. The dredging of the slope involves a different effective stress path than tilting with a stronger effect of the rotation of the principal stresses. The triggering of liquefaction can be established by either tilting (at different rates and profiles), applying a shock load at the crest, or by dredging at the toe. Each imposes a different stress path and is therefore expected to have a different effect.

Composing the database
The long-term objective is to compose a database with the measurements of liquefaction tank and corresponding element tests. To this end, different types of sands should be tested. The results will provide a basis for the evaluation of models. Furthermore, insight will be gained into the effect of soil properties, such as the grain size and shape, on the susceptibility to liquefaction. The intrinsic susceptibility of soils to flow liquefaction can thus be investigated. The database should contain the results of the liquefaction tank tests and the corresponding element tests. In the future, it is possible to use the liquefaction tank for research on different phenomena. Examples are the collapse behaviour and liquefaction during the saturation of unsaturated soils, unstable breaching and the generation of waves by slope failures.

Finite element formulation
It is recommended to concentrate the development of the finite element model on the first stages of liquefaction flow failures, i.e. starting from the initial hydrostatic stage, followed by a sudden accelerating deformation after triggering and large deformations of the soil body. The starting point is the formulation that was developed in Chapter 5. It is recommended to first test the performance of the model for dynamics. To this end, the performance of the model should be benchmarked with an initial-boundary value problem with an analytical solution. Subsequently, the numerical stability and accuracy during the transition from statics to dynamics should be tackled. It is anticipated that an adaptive mesh and time-step strategy has to be adopted. A formulation for large(r) deformations can be established by updating the volumes and surfaces of the elements (updated-Lagrange), while correcting the effective stresses for the rotations.

Extending the material model
The current material models are not able to reproduce the rate-dependent response of the first test series in the liquefaction tank. It is recommended to use the firm, theoretical basis of the MONOT-model and to extend the model with a rate-dependent formulation. The Author acknowledges that this requires the input from element tests. In addition,

the critical state formulation that was discussed in Section 5.5 should be implemented and tested in the MONOT-model, which allows the application of the model for large deformations. The third extension that should be implemented to fully comprehend the response during the tilting tests is a formulation for the principal stress rotation. Again, it is acknowledged that the performance of this formulation relies on the results of element tests, such as hollow cylinder torsional-shear tests.

9.4.2. Engineering practice

The success of the research with the liquefaction tank relies on the implementation of the results in engineering practice. The research should respond to the needs in engineering practice. This may be established by deriving simplified design rules from the liquefaction tank tests and element tests. In addition, the results of the research may be used to establish dredging and construction strategies. On the other hand, engineering practice should also contribute to the research by providing input from field experience.

The experiences that are gained in projects are indispensable to bridge the gap between engineering practice and research. There should be interaction between the field observations in practice and the research conducted in the liquefaction tank. At this moment, field observations contain too many uncertainties, which gives rise to more questions rather than providing answers. The Author believes that field tests give the opportunity to control the conditions of field events, at least to some extent. It is recommended to introduce a field test at the start of high-end projects that involve susceptible soils. The field test gives the contractor the opportunity to assess the site-specific susceptibility to liquefaction flow slides, and to verify the working method. The experience that is gained from these field tests enhances the empirical basis of liquefaction flow slides. It provides a reference for the upscaling of the results of the liquefaction tank and element tests. Hence, field tests would bring engineering practice and research with the liquefaction tank closer together.

Summary

The liquefaction flow slide is the main geohazard for subaqueous slopes composed of sand. Liquefaction flow slides occur unexpectedly, develop rapidly, and involve the displacement of large volumes of soils over large distances. Some of the most destructive failures in the history of geomechanics were liquefaction flow slides, causing considerable financial damage and numerous casualties. Liquefaction flow slides are in essence complex, fully coupled mechanisms. However, the available methods in engineering practice tend to uncouple and simplify the assessment. The lack of advanced models should mainly be attributed to the rather narrow empirical basis. The case histories lack the detailed information required to verify and validate advanced models. Element tests do provide detailed information on the soil response during flow liquefaction, but the relevance of specific stress and/or strain paths for the boundary value problem of slope stability is unclear. Hence, there is a knowledge gap between the elementary soil behaviour from element tests and the response during field events.

This thesis is aimed at improving the assessment of liquefaction flow slides. It treats a number of subjects related to the assessment of liquefaction flow slides. An extensive literature review of the liquefaction response during field events, scale model tests, and element tests lays the basis for the two subsequent parts of the thesis. These include a theoretical and experimental treatment of the subject. The theoretical part expresses the underlying physics in terms of the governing equations of heterogeneous, saturated, porous media. These involve the conservation of mass and momentum equations of the pore fluid, soil skeleton and bulk material, while specifying the respective stresses and interaction terms. The further examination of the conservation of energy, non-negative entropy production, and the stress measures elucidates the consistency and limitations of the framework. The Finite Element Method has been selected for the implementation of the governing equations. It suits the modelling of initial-boundary value problems that involve the history-dependent response of soils. The performance of the initial implementation has been evaluated for statics, while extensions of dynamics and large deformations have been suggested.

The experimental part of the thesis includes the development of a novel, experimental facility: the liquefaction tank. It has been developed to produce high quality data of liquefaction flow slides for the evaluation of numerical models. This thesis addresses the performance of the liquefaction tank in terms of a consistent and reproducible replication of liquefaction flow slides. To this end, the preparation of the sand bed by means of fluidisation is elaborately discussed. Fluidisation tests have been conducted to control the density and uniformity of the sand bed. Liquefaction flow slides have been produced by conducting tilting tests of the level sand bed. The results allow the evaluation of the performance of the liquefaction tank, as well as the factors that influence the response

of the sand bed.

Case histories of liquefaction flow slides provide little detailed information about the soil conditions and the actual role of the trigger. These can be controlled in scale model tests, but the results in literature show a lack of reproducibility for the tests that have been conducted so far. Our basis for understanding liquefaction flow slides is provided by element tests. These suggest that undrained instability corresponding with the generation of excess pore water pressure initiates flow liquefaction, which is followed by a diffusive mechanism through the soil body. Element tests also demonstrate the complex interdependence of liquefaction flow slides and the stress and strain path, the fabric of the soil and void ratio redistribution. Incorporating these aspects in the assessment of liquefaction flow slides requires a coupled analysis.

The coupled set of mass and momentum equations has been derived using mixture theory. The most striking result is the heterogeneous interaction term that is required for the correct description of the hydrostatic paradox. This term is self-equilibrating: it is by definition eliminated from the momentum equations of the pore fluid and soil skeleton. It has been demonstrated that an alternative derivation starting from hydrostatic does not require the incorporation of the heterogeneous interaction terms. The resulting, alternative set of equations is equivalent to the set derived from mixture theory, but it also allows for a direct expression of the effective stresses. The role of the heterogeneous interaction term has been further investigated by elaboration of the conservation and entropy production equations. The elaboration of the requirement of non-negative entropy production shows that the largest part of the work produced by the heterogeneous interaction term is exchanged and accounted for by the mechanical part of the energy interaction term. Hence, this term is also self-equilibrating. The complementary part of the work results in work exerted by the pore fluid stress on the compressing particles. This term will be part of the rate of internal strain energy of the soil skeleton.

The validity of the stress measures has been examined for saturated and unsaturated soils. First, it was demonstrated how the saturated stress measures can be extended to keep the unsaturated stress measures physically justified. As a result, the amendments to constitutive relations are minimal or none, which allows one to take advantage of the vast experience and data that were obtained for the saturated case. Second, the effect of interparticle sliding and particle rolling on the stress measures was investigated. Using upscaling from the particle scale, it was demonstrated that the interparticle stress tensor is symmetric, even when accounting for particle rotations. However, this common, translational intergranular stress tensor is not sufficient to describe the stresses in an assembly of particles that include both interparticle sliding and particle rotations. In this case the non-symmetric, total intergranular stress tensor should be used, which is composed of the symmetric translational and non-symmetric rotational part of the intergranular stress tensor. The non-symmetry of the total intergranular stress tensor implies that the conservation of angular momentum should be taken into account as a field equation for particle rotations.

The set of governing equations has been implemented into a finite element code. The verification of the one-dimensional consolidation problem demonstrates that the code performs well for static problems. The modelling of dynamics requires the consideration of additional accuracy and stability conditions. The simultaneous satisfaction of the conditions that are set for statics and dynamics leads to unrealistically small values of the time step and element size. Hence, an adaptive strategy is recommended when the subsequent stages of liquefaction flow slides are modelled. The modelling of large deformations also requires the incorporation of the critical state in the material model. An extension of the MONOT-model with a critical state formulation has been suggested, which is compatible with the state parameter concept.

The main result of this research project is the development of a novel experimental facility: the liquefaction tank. Intended to bridge the gap between element tests and field events, the liquefaction tank has dimensions that are compatible with the stress levels that can be established in element tests. The liquefaction tank should produce liquefaction flow slides that are reproducible in terms of the monitored pore pressures and the failure mode. To this end, special attention has been given to the triggering of liquefaction flow slides and the preparation of the sand bed. The triggering mechanism that has been considered in this thesis involves the uniform tilting of the sand bed. The load is applied uniformly over the sand bed, while the initiation of liquefaction flow slides can be identified accurately. A fluidisation system has been designed to establish a loose and uniform sand bed. It has been assumed that a uniform stress distribution along the fluidisation system will yield a uniform sand bed. In addition, the development of a novel preparation procedure for triaxial tests has been presented, which is compatible with the procedure used in the liquefaction tank. The procedure is expected to mimic the low density and mean effective stress in the liquefaction tank, which are furthermore expected to be rather uniform over the height of the sample.

The results of the fluidisation tests in the liquefaction tank show that the measured pressure gradient along the fluidisation system was larger than anticipated, which is presumably caused by energy losses due to turbulence. Nonetheless, the anticipated effect on the density distribution along the sand bed was shown to be negligible. The fluidisation tests also allowed the Author to define the optimum range of the fluidisation flow rate, which was defined between $6\,\mathrm{l\,s^{-1}}$ and $12\,\mathrm{l\,s^{-1}}$. A novel elaboration of Kynch's graphical method of sedimentation demonstrated that the grain size distribution governs the response of the sand bed during fluidisation. Even for the uniform sand that was used in this research project, the final stage of fluidisation is clearly governed by the finer fraction of the soil. One may use the results of the fluidisation tests to control the initial density after sedimentation in the liquefaction tank.

The liquefaction tank produced several liquefaction flow slides by tilting a bed with an initial thickness of approximately 0.5 m. The results confirm the main characteristics of liquefaction flow slides, i.e. they appeared suddenly, at relatively gentle slopes, developed at a high rate and left a horizontal bed after failure. Liquefaction was spontaneously initiated during uniform tilting. To the Author's knowledge, this is the first time

that truly static liquefaction flow slides have been observed at this scale. The initiation of the liquefaction flow failures involved the generation of excess pore water pressures. A surprising result is that the liquefaction flow slides were triggered at relatively gentle slopes, ranging between 1v:8h and 1v:10h. In addition, it is noted that the measured excess pore water pressures stayed well below the values that correspond with full liquefaction (and zero effective stress), in spite of the failure yielding a horizontal sand bed.

There was a clear relation between the possible failure mode and the average density in the liquefaction tank for the tested range of porosities. The sharp distinction between bed responses was not reflected by the measured pore pressures. Irrespective of the initial average porosity, all tests exhibited an instant rise in the excess pore water pressures. There was a consistent and smooth trend of decreasing triggering angle and increasing peak excess pore pressure with increasing porosity, but the differences in pore pressure response were relatively small. It is concluded that the results are reproducible. Two sets of tests that were conducted at the same average porosity yielded approximately (in one case exactly) the same values of the triggering angle and peak excess pore pressure. The excellent reproducibility of the results affirms that the average porosity is an appropriate measure for the susceptibility to flow liquefaction, even though the results do suggest that the looser part of the sand bed controls the global response.

The resting time between the sedimentation after fluidisation and the start of tilting ('ageing') had a pronounced effect on the results. The triggering angle increased with increasing resting time, even for the relatively small time scale of resting times that has been considered in this thesis. Furthermore, the effect of the density on the triggering diminished for the tests that were conducted after an increased resting time. It should be noted that the relation between the failure mode and the average density seemed to be unaffected by ageing; the same threshold values applied for a liquefaction or stable response. In addition to the density and resting time, the tilting rate governed the occurrence of failure of the sand bed in the liquefaction tank. Tests conducted at a tilting rate of ten times slower than the standard tests did not show any sign of neither failure nor excess pore pressures. The effect of an external artificial agent on the triggering of liquefaction flow slides in the liquefaction tank was ruled out. It is hypothesised that rate dependent plasticity in the low shear regime explains the effect of the tilting rate.

The effect of pre-loading was a stabilising factor during the tilting tests, provided that the direction of re-loading was the same. The tests that were conducted at a lower tilting rate hardly disturbed the sand bed. After reverse tilting of the tank in its horizontal position, tilting of the tank at the normal, high tilting rate did not result in any generation of pore pressures. The opposite conclusion is drawn for the direction of re-loading opposite to the direction of pre-loading. Reverse tilting of the 'dilative' tests yielded a weaker response, in spite of the densification of the sand bed during tilting. Liquefaction failure in the liquefaction tank involved the generation of a water wave. In addition to the density, the triggering angle also affected the amplitude of the generated water waves. The 'aged' tests failed at a higher triggering angle, which also led to a larger amplitude of the generated waves.

The development of the liquefaction tank has provided a test environment to study the response of a sand bed during a liquefaction flow slide in detail. One can study the effect of the properties of the sand, such as the consolidation coefficient, on the initiation of a flow slide. By testing different triggers, the importance of stress paths can be investigated. The liquefaction tank also allows the testing of mitigating measures, and related mechanisms such as liquefaction during the saturation of unsaturated soils. Element tests should be performed, using the same preparation method, density and effective stresses as in the tank, to understand the underlying soil behaviour. Then, the level of quality of finite element models can be evaluated using the results of the liquefaction tank tests. Hence, finite element analyses relate the results of element tests to the outcome of the liquefaction tank tests. Subsequently, the Finite Element Method and the results of element tests at larger stresses can be employed to extrapolate the results to the larger slopes that are engineered in practice.

It is anticipated that the liquefaction tank will produce a vast amount of data on liquefaction flow slides. The Author believes that this database will be the basis for an improved understanding of liquefaction flow slides. This thesis lays the foundation for future projects with the liquefaction tank and a finite element formulation with a firm, theoretical basis. The main conclusion is that the liquefaction tank can produce liquefaction flow slides, and that the reproducibility of the results is excellent.

Samenvatting

De zettingsvloeiing is het belangrijkste faalmechanisme voor onder water hellingen van zand. Zettingsvloeiingen treden onverwachts op, ontwikkelen zich zeer snel en verplaatsen grote hoeveelheden zand over grote afstanden. Enkele van de meest verwoestende bezwijkgevallen in de geschiedenis van de geotechniek waren zettingsvloeiingen, met significante financiele schade en vele slachtoffers tot gevolg. Zettingsvloeiingen zijn in beginsel complexe, volledig gekoppelde mechanismen. Echter, de beschikbare methoden in de ingenieurspraktijk hebben de neiging om de beoordeling van zettingsvloeiingen te ontkoppelen en te versimpelen. Het gebrek aan geavanceerde methoden moet vooral toegeschreven worden aan de smalle, empirische basis. Bij de bekende bezwijkgevallen ontbreekt het aan de gedetailleerde informatie die noodzakelijk is voor de verificatie en validatie van geavanceerde modellen. Elementtests leveren deze gedetailleerde informatie over de respons van de grond gedurende verweking wel, maar de relevantie van specifieke spannings- en/of rekpaden voor het randvoorwaardeprobleem van macrostabiliteit van taluds is niet duidelijk. Kortom, er is een kennisleemte tussen het elementaire grondgedrag uit elementtests en de response in het veld.

Dit proefschrift richt zich op het verbeteren van de beoordeling van zettingsvloeiingen. Het behandelt een aantal onderwerpen die gerelateerd zijn aan de beoordeling van zettingsvloeiingen. Een uitgebreide literatuurstudie naar bekende bezwijkgevallen, schaalproeven en elementtests legt de basis voor de twee volgende delen van het proefschrift. Deze omvatten een theoretische en experimentele beschouwing van de kwestie. Het theoretische deel drukt de onderliggende fysica uit in de basisvergelijkingen van heterogene, verzadigde poreuze media. Deze bestaan uit de behoudsvergelijkingen van de massa en het momentum voor de poriënvloeistof, het korrelskelet en het bulkmateriaal, waarbij de betreffende spanningen en interactietermen zijn gespecificeerd. De verdere beschouwing van de behoudsvergelijking van energie, de vereiste niet-negatieve entropie produktie en de spanningsmaten geeft opheldering over de consistentie en de grenzen van het raamwerk. De Eindige Elementen Methode is gekozen voor de implementatie van de basisvergelijkingen. De methode is geschikt voor het modelleren van randvoorwaardeproblemen, waarbij de afhankelijkheid van de belastingsgeschiedenis van grond een rol speelt. De doelmatigheid van het model is geëvalueerd voor statica, waarbij suggesties zijn gedaan voor de uitbreiding naar dynamica en grote vervormingen.

Het experimentele deel van het proefschrift omvat de ontwikkeling van een nieuwe, experimentele opstelling: de liquefactiontank. Deze is ontwikkeld voor het verkrijgen van kwaliteitsmetingen van zettingsvloeiingen voor het evalueren van numerieke modellen. Dit proefschrift addresseert de werking van de liquefactiontank met betrekking tot de consistente en reproduceerbare replicatie van zettingsvloeiingen. Hiertoe wordt de pre-

paratie van het zandbed door fluidisatie uitgebreid besproken. Fluidisatietests zijn uitgevoerd om de dichtheid en uniformiteit van het zandbed te beheersen. Zettingsvloeiingen zijn geproduceerd door het vlakke zandbed te kantelen. De resultaten maken het mogelijk om de werking van de liquefactiontank en de invloedsfactoren van de gemeten respons te beoordelen.

De bekende praktijkgevallen van zettingsvloeiingen verschaffen weinig gedetailleerde informatie over de grondcondities en de rol van de trigger. Deze kunnen worden opgelegd in schaalproeven, maar de beschikbare resultaten in de literatuur laten zien dat de tests die tot dusver zijn uitgevoerd niet reproduceerbaar zijn. Elementtests hebben de basis gelegd voor ons begrip van zettingsvloeiingen. De tests impliceren dat verweking wordt geïnitieerd door ongedraineerde instabiliteit tijdens de generatie van wateroverspanningen, die vervolgens leidt tot een diffuus mechanisme door het grondlichaam. Elementtests laten ook de complexe onderlinge afhankelijkheid zien tussen zettingsvloeiingen en het spannings- en rekpad, de structuur van het korrelskelet en de herverdeling van dichtheid. Het meenemen van deze aspecten in de beoordeling van zettingsvloeiingen vereist een gekoppelde analyse.

De gekoppelde set van behoudsvergelijkingen voor de massa en het momentum is afgeleid door gebruik te maken van de mengseltheorie. Het meest opvallende resultaat is de heterogene interactieterm die ingevoegd moet worden voor de juiste beschrijving van de hydrostatische paradox. Deze term is *self-equilibrating*: hij wordt per definitie geëlimineerd uit de momentum vergelijkingen van het korrelskelet en de poriënvloeistof. Er is aangetoond dat bij een alternatieve afleiding die uitgaat van hydrostatica, de heterogene interactieterm niet nodig is. De resulterende set van vergelijkingen is equivalent aan de set die op basis van de mengseltheorie is afgeleid, maar resulteert bovendien in een directe uitdrukking van de effectieve spanningen. De rol van de heterogene interactieterm is verder onderzocht door de vergelijkingen voor het behoud van energie en niet-negatieve entropieproduktie uit te werken. Het uitwerken van de vereiste niet-negatieve entropieproduktie laat zien dat het grootste deel van de arbeid die wordt geproduceerd door de heterogene interactieterm wordt meegenomen door het mechanische deel van de energetische interactieterm. Deze term is dus ook *self-equilibrating*. Het complementaire deel van de arbeid resulteert in arbeid die wordt geleverd door de spanning van de poriënvloeistof aan de samengedrukte korrels. Deze term zal onderdeel zijn van de toename van de interne rekenergie van het korrelskelet.

De geldigheid van de spanningsmaten is onderzocht voor verzadigde en onverzadigde grond. Eerst is aangetoond hoe de spanningsmaten voor verzadigde grond kunnen worden uitgebreid om de spanningsmaten voor onverzadigde grond fysisch te rechtvaardigen. Daardoor hoeven er minimale of geen aanpassingen te worden gedaan aan constitutieve relaties, wat het mogelijk maakt om voordeel te halen uit de ervaringen en data die zijn verkregen voor verzadigde grond. Vervolgens is de invloed van het schuiven en roteren van korrels op de spanningsmaten onderzocht. Door gebruik te maken van het opschalen vanaf de korrelschaal is aangetoond dat de intergranulaire spanningstensor symmetrisch is, zelfs als rotaties van korrels worden meegenomen. Echter, deze gebrui-

kelijke, translerende intergranulaire spanningstensor voldoet niet voor de beschrijving van een verzameling korrels waarin zowel verschuivingen als rotaties voorkomen. In dit geval moet de niet-symmetrische, totale intergranulaire spanningstensor worden gebruikt, die bestaat uit het symmetrische, translerende en het niet-symmetrische, roterende deel van de intergranulaire spanningstensor. Het niet-symmetrische deel van de totale intergranulaire spanningstensor impliceert dat het behoud van moment van momentum moet worden meegenomen als een veldvergelijking voor de rotatie van de korrels.

De set van basisvergelijkingen is geïmplementeerd in een eindige elementencode. De verificatie van het eendimensionale consolidatieprobleem laat zien dat de code goed werkt voor statische problemen. Het modelleren van dynamica vereist een nadere beschouwing van de aanvullende nauwkeurigheids- en stabiliteitsvoorwaarden. Het voldoen aan zowel de eisen die gesteld zijn aan statica als dynamica leidt tot een onrealistisch kleine waarde van de tijdstap en de afmeting van het element. Er wordt dus aangeraden om een adaptieve strategie te volgen tijdens het modelleren van de opvolgende fasen van zettingsvloeiingen. Het modelleren van grote vervormingen vereist dat ook de critical state meegenomen wordt in het materiaalmodel. Er is een suggestie gedaan voor een uitbreiding van het MONOT-model met een critical state-formulering, die aansluit op het *state parameter* concept.

Het belangrijkste resultaat van het onderzoeksproject is de ontwikkeling van een nieuwe experimentele opstelling: de liquefactiontank. Het doel is het dichten van het gat dat bestaat tussen elementtests en de respons in het veld. De afmetingen van de liquefactiontank sluiten dus aan op de spanningsniveaus die gehaald kunnen worden in elementtests. De liquefactiontank moet zettingsvloeiingen repliceren die reproduceerbaar zijn wat betreft de gemeten waterdrukken en het bezwijkmechanisme. Daarom is extra aandacht besteed aan het triggeren van zettingsvloeiingen en de preparatie van het zandbed. De trigger die in dit proefschrift beschouwd is, betreft het uniforme kantelen van het zandbed. De belasting wordt uniform toegepast op het zandbed, waarbij de initiatie van zettingsvloeiingen nauwkeurig vastgelegd kan worden. Een fluidisatiesysteem is ontworpen om een los en uniform zandbed te verkrijgen. Er is aangenomen dat een uniforme drukverdeling in het fluidisatiesysteem tot een uniform zandbed leidt. Aanvullend is een nieuwe preparatieprocedure voor triaxiaaltests gepresenteerd, die aansluit op de procedure die gebruikt wordt in de liquefactiontank. Er wordt verwacht dat de procedure de lage dichtheid en gemiddelde effectieve spanning in de liquefactiontank nabootst en dat deze uniform opgelegd zullen worden over de hoogte van het monster.

De resultaten van de fluidisatietests in de liquefactiontank laten zien dat de drukgradiënt in het fluidisatiesysteem hoger is dan verwacht, wat wordt toegeschreven aan energieverliezen door turbulentie. Desalniettemin is aangetoond dat de verwachte invloed op de dichtheidsverdeling over het zandbed verwaarsloosbaar klein is. De fluidisatietests maakten het ook mogelijk om het optimale bereik van het fluidisatiedebiet vast te stellen, dat ligt tussen $6\,\mathrm{l s^{-1}}$ en $12\,\mathrm{l s^{-1}}$. Een originele bewerking van Kynch's grafische methode voor sedimentatie heeft laten zien dat de korrelverdeling bepalend is voor de

respons van het zand tijdens fluidisatie. Zelfs voor het uniforme zand dat gebruikt is in dit onderzoeksproject, wordt de laatste fase van fluidisatie duidelijk bepaald door de fijnste fractie van het zand. Men kan de resultaten van de fluidisatietests gebruiken om de initiële dichtheid na sedimentatie in de liquefactiontank te beheersen.

De liquefactiontank heeft verscheidene zettingsvloeiingen geproduceerd door het kantelen van het zandbed met een initiële dikte van 0.5 m. De resultaten onderschrijven de belangrijkste eigenschappen van zettingsvloeiingen. Ze traden plotseling op bij relatief vlakke hellingen, ontwikkelden zich met grote snelheid en lieten een horizontaal zandbed achter na bezwijken. Verweking werd spontaan geïnitieerd tijdens het uniforme kantelen. Naar de Auteurs beste weten is dit de eerste keer dat daadwerkelijk statisch geïnitieerde zettingsvloeiingen op deze schaal geobserveerd zijn. De initiate van zettingsvloeiingen ging gepaard met de generatie van wateroverspanningen. Een verrassend resultaat is dat de zettingsvloeiingen getriggered zijn bij relatief vlakke hellingen variërend tussen 1v:8h en 1v:10h. Daarnaast wordt opgemerkt dat de gemeten wateroverspanningen ruim onder de waarden bleven die corresponderen met volledige verweking (en effectieve spanningen gelijk aan nul), ondanks het feit dat bezwijken leidde tot een horizontaal zandbed.

Er was een duidelijke relatie tussen het eventuele bezwijkmechanisme en de gemiddelde dichtheid in de liquefactiontank voor het beproefde bereik van porositeiten. Het scherpe onderscheid tussen responsen van het zandbed kon niet worden teruggezien in de gemeten waterspanningen. Onafhankelijk van de initiële, gemiddelde porositeit, lieten alle tests een plotselinge toename van de wateroverspanningen zien. Er was een consistente en geleidelijke trend van een afnemende hoek van triggeren en toenemende piek van de wateroverspanningen bij een toename van de porositeit, maar de verschillen in de respons waren relatief klein. Er wordt geconcludeerd dat de resultaten reproduceerbaar zijn. Twee keer zijn tests bij dezelfde gemiddelde porositeit uitgevoerd, wat resulteerde in dezelfde waarden (eenmaal bij benadering, eenmaal exact) van de hoek van triggeren en de piek van de wateroverspanningen. De uitstekende reproduceerbaarheid van de resultaten bekrachtigt dat de gemiddelde porositeit een geschikte maat is voor de gevoeligheid voor verweking, hoewel de resultaten ook suggereren dat het meest losse deel van het zandbed bepalend is voor de respons van het geheel.

De rusttijd tussen de sedimentatie na fluidisatie en het begin van kantelen (’*ageing*’) had een duidelijke invloed op de resultaten. De hoek van triggeren nam toe met een toename van de rusttijd, zelfs voor de relatief korte tijdsschaal van russtijden die beschouwd zijn in dit proefschrift. Bovendien verdwijnt de invloed van de dichtheid op het triggeren voor tests die uitgevoerd zijn na een langere rusttijd. Er dient opgemerkt te worden dat de relatie tussen het bezwijkmechanisme en de gemiddelde dichtheid niet beïnvloed leek te worden door de rusttijd. Dezelfde drempelwaarde markeerde de overgang tussen verweking en een stabiele respons. Naast de dichtheid en de rusttijd, was de kantelsnelheid een bepalende factor voor het bezwijken van het zandbed in de liquefactiontank. Tests die uitgevoerd zijn bij een kantelsnelheid die tien keer lager was dan tijdens de andere tests lieten geen enkel teken van bezwijken of wateroverspanning zien.

De mogelijkheid van een externe verstoring op het triggeren van zettingsvloeiingen in de liquefactiontank kon worden uitgesloten. Er wordt verondersteld dat de invloed van de kantelsnelheid kan worden verklaard door de afhankelijkheid van plasticiteit bij lage schuifspanningen van de belastingsnelheid.

De invloed van voorbelasten was een stabiliserende factor tijdens de kanteltests, mits de richting van voorbelasten en kantelen hetzelfde was. De tests die uitgevoerd werden bij een lagere kantelsnelheid verstoorden het zandbed nauwelijks. Na het terugkantelen van de tank in de oorspronkelijke, horizontal positie, leidde het kantelen van de tank met de normale, hoge kantelsnelheid niet tot wateroverspanningen. De tegengestelde conclusie wordt getrokken voor de richting van kantelen die tegengesteld is aan de richting van voorbelasten. Het terugkantelen van de 'dilatante' proeven resulteerde in een zwakkere response, ondanks het feit dat het zandbed verdicht was tijdens het kantelen. Verweking in de liquefactiontank ging gepaard met de generatie van golven in het water. Naast de dichtheid had ook de hoek van triggeren invloed op de amplitude van de veroorzaakte golven. De proeven die uitgevoerd zijn na een langere rusttijd bezweken bij een steilere hoek, wat ook leidde tot een grotere amplitude van de opgewekte golven.

De ontwikkeling van de liquefactiontank heeft een testomgeving gecreëerd, waarin de respons van een zandbed tijdens zettingsvloeiingen in detail bestudeerd kan worden. Men kan de invloed van de eigenschappen van het zand, zoals bijvoorbeeld de consolidatiecoëfficient, op de initiatie van een zettingsvloeiingen onderzoeken. Door verschillende triggers uit te proberen kan het belang van spanningspaden bekeken worden. De liquefactiontank maakt het ook mogelijk om mitigerende maatregelen te onderzoeken, of gerelateerde mechanismen zoals verweking tijdens het verzadigen van onverzadigde grond. Elementtests zouden moeten worden uitgevoerd, gebruikmakend van dezelfde preparatie methode en met dezelfde dichtheid en effectieve spanningen als in de tank, om het onderliggende grondgedrag te begrijpen. Dan kan het kwaliteitsniveau van eindige elementenmodellen geëvalueerd worden door de resultaten van de tests met de liquefactiontank te gebruiken. De eindige elementenanalyses relateren de resultaten van elementtests dus aan de uitkomsten van de tests met de liquefactiontank. Vervolgens kunnen de Eindige Elementen Methode en de resultaten van de elementtests aangewend worden om de resultaten te extrapoleren naar de schaal van de taluds die in de praktijk ontworpen moeten worden.

Het is de verwachting dat de liquefactiontank een grote hoeveelheid data van zettingsvloeiingen zal opleveren. De Auteur gelooft dat deze database het uitgangspunt zal zijn voor een beter begrip van zettingsvloeiingen. Dit proefschrift legt de basis voor toekomstige projecten met de liquefactiontank en een eindige elementen formulering met een stevige, theoretische basis. De belangrijkste conclusie is dat de liquefactiontank in staat is om zettingsvloeiingen te produceren en dat de reproduceerbaarheid hiervan uitstekend is.

Dankwoord

Liquefaction (verweking) is een van de meest fascinerende onderwerpen in de grondmechanica. Het blijft intrigeren hoe zand 'zomaar' instabiel kan worden, om zich vervolgens als een vloeistof te gaan gedragen. Voor de praktijk is dit een ongrijpbaar proces, dat steeds belangrijker wordt voor het ontwerp van zandlichamen. Kortom, een onderwerp waar nog het nodige aan te ontdekken en te verbeteren valt. Toen ik in 2008 de mogelijkheid kreeg om mijn afstudeeronderzoek over zettingsvloeiingen uit 2006 een vervolg te geven in een promotieonderzoek, heb ik dus niet lang hoeven nadenken. Ik had bovendien het geluk om als laatste promovendus te starten bij Professor Molenkamp, die voor mij als leermeester in de grondmechanica erg belangrijk is geweest. Daarnaast mocht ik het onderzoek in deeltijd uitvoeren, zodat ik me kon blijven ontwikkelen als ingenieur bij Boskalis. Ik ben de TU Delft en Boskalis dankbaar voor deze kans.

Allereerst wil ik mijn dankwoord richten aan mijn begeleider, professor Molenkamp. Ik heb ontzettend veel opgestoken van de vele gesprekken die we gevoerd hebben tijdens het onderzoek; gesprekken waarin u met potloodpen (waarvan het puntje steeds afbrak) en gummetje ('stuffi') al schetsend uw ideeën toelichtte. U had als projectleider van het onderzoeksproject de ondankbare taak om 'randzaken' af te handelen. Zonder uw tomeloze inzet en vasthoudendheid was de Liquefaction Tank er nooit gekomen. Dank voor uw nooit aflatende steun en intensieve begeleiding door de jaren heen. Helaas kon u de laatste jaren niet meer als officiële promotor optreden. Luckily, Professor Hicks was willing to become my promotor. Thank you for your support during the last stage of my PhD research.

Tijdens het ontwerp van de Liquefaction Tank heb ik veel steun gekregen van Arjan Tanis en Ed van Ginneken van Boskalis. Jullie technische kennis en input is van onschatbare waarde geweest. De technici op de TU (Han de Visser, Kees van Beek, Rein van den Oever en Jan Graafland) hebben mij geholpen bij de opbouw van de Liquefaction Tank en het uitvoeren van de experimenten. Ik wil in het bijzonder Han bedanken die altijd voor me klaarstond. Ik denk dat de TU jouw kennis en ervaring nog gaat missen als je komend jaar met pensioen gaat.

Ik wil STW en Boskalis bedanken voor de financiële steun en het vertrouwen tijdens het promotietraject. Corine Meuleman en Ruben Sharpe van STW hebben het project door dik en dun gesteund en hebben altijd meegedacht als het niet volgens planning verliep. Dankzij het management van Hydronamic (Arjan, Bart) heb ik mijn werkzaamheden bij Boskalis met mijn promotieonderzoek kunnen combineren. Mijn collega's bij Boskalis hebben altijd begrip getoond als ik mijn promotieonderzoek voorrang moest geven. Het zegt voor mij veel over het bedrijf Boskalis dat zij mij deze kans gegund hebben. Verder wil ik de leden van de gebruikerscommissie van STW bedanken voor hun input tijdens

de periodieke vergaderingen.

Tijdens mijn promotieonderzoek heb ik samengewerkt met een aantal afstudeerders. Anteneh, Louisa en Pascale hebben een bijdrage geleverd aan dit onderzoek. Dankzij mijn kamergenoten en collega's van de sectie Geotechnology heb ik een mooie tijd op de TU gehad. Er zijn vele vriendschappen ontstaan die mij veel waard zijn. Ik heb sinds mijn derde studiejaar, toen ik begon als studentassistent Grondmechanica, rondgelopen op de sectie en het is nog altijd een vertrouwde omgeving waar ik graag kom. Buiten de sectie kon ik altijd terecht voor een bak koffie bij Martin. Het was fijn om iemand te hebben die in dezelfde fase van zijn deeltijdonderzoek zat. Mooi dat we nu (bijna) tegelijk over de streep zijn gekomen. Mijn goede vrienden Timo en Alex zullen als paranimfen aan mijn zijde staan tijdens de verdediging, zoals ik dat tijdens hun verdediging gedaan heb. Bedankt voor de vele jaren van vriendschap. Tot slot, wil ik mijn waardering uitspreken voor mijn familie en, in het bijzonder, Wendy. Het betekent veel voor me dat jullie altijd met begrip en geduld mij de ruimte hebben gegeven om dit onderzoek uit te voeren.

Curriculum Vitæ

Richard Ruben DE JAGER

19-10-1981	Born in Sassenheim, the Netherlands.

Education

1994–2000	Gymnasium, Fioretti College Lisse
2000–2004	BSc. Civil Engineering Delft University of Technology
2004–2006	MSc. Civil Engineering (cum laude) Delft University of Technology *Thesis:* The behaviour of soils during static liquefaction (grade: $10^{-}/10$) *Supervisor:* Prof. dr. ir. F. Molenkamp

Professional experience

since 2007	Discipline Engineer (geotechnical engineering) Royal Boskalis Westminster

Awards

2007	Best Graduate 2006-2007 Civil Engineering and Geosciences
2007	The Netherlands Student Award for Engineering Geology 2006-2007

List of Publications

The following publications are related to this thesis:

8. **R.R. de Jager**, A. Maghsoudloo, A. Askarinejad, F. Molenkamp, *Preliminary results of instrumented laboratory flow slides*, MPM 2017, Proceedings of the 1st Material Point Method for "Modelling Large Deformation and Soil–Water–Structure Interaction", Procedia Engineering **175**, 212-219, Delft, the Netherlands, January 2017.

7. **R.R. de Jager**, F. Molenkamp, *Stress measures for interparticle sliding and particle rolling*, NUMGE 2014, Proceedings of the 8th European Conference on Numerical Methods in Geotechnical Engineering, 61-66, Delft, the Netherlands, June 2014.

6. F. Molenkamp, **R.R. de Jager**, F.A.J.M. Mathijssen, *Stress measures affecting deformation of granular materials*, Vadose Zone Journal **13**(5),2014.

5. **R.R. de Jager**, F.A.J.M. Mathijssen, F. Molenkamp, *Hydrostatics and relative motion of pore fluids*, COMGEO III, 359-370, International Symposium on Geomechanics, Krakow, Poland, August 2013.

4. **R.R. de Jager**, F. Molenkamp, *Fluidization system for liquefaction tank*, Eurofuge 2012, Proceedings of European Conference on Physical Modelling in Geotechnics 2012, Delft, the Netherlands, April 2012.

3. **R.R. de Jager**, L.C.H. Braakenburg, M.A. Hicks, F. Molenkamp, *Static liquefaction of saturated loose sand*, COMGEO II, 1-13, International Symposium on Geomechanics, Dubrovnik, Croatia, April 2011.

2. A.B. Tesegaye, V. Galavi, R.B.J. Brinkgreve, **R.R. de Jager**, F. Molenkamp, P.G. Bonnier, *Modelling liquefaction behaviour of sands by means of hypoplastic model*, NUMGE 2010, Proceedings of the 7th European Conference on Numerical Methods in Geotechnical Engineering, 95-100, Numerical Methods in Geotechnical Engineering, Trondheim, Norway, June 2010.

1. A.B. Tesegaye, F. Molenkamp, R.B.J. Brinkgreve, P.G. Bonnier, **R.R. de Jager**, V. Galavi, *Modelling liquefaction behaviour of sands by means of hypoplastic model*,NUMGE 2010, Proceedings of the 7th European Conference on Numerical Methods in Geotechnical Engineering, 81-88, Numerical Methods in Geotechnical Engineering, Trondheim, Norway, June 2010.